GEOCHEMICAL TRACERS OF PROCESSES AFFECTING THE FORMATION OF SEAFLOOR HYDROTHERMAL FLUIDS AND DEPOSITS IN THE MANUS BACK–ARC BASIN

By
Paul R. Craddock

Submitted to the MIT/WHOI Joint Program in Oceanography and Applied Ocean Science and Engineering in partial fulfillment of the requirements for the degree of Doctor of Philosophy

at the

MASSACHUSETTS INSTITUTE OF TECHNOLOGY

and the

WOODS HOLE OCEANOGRAPHIC INSTITUTION

February 2009

Signature of Author

.....

Paul R. Craddock
Joint Program in Chemical Oceanography
Massachusetts Institute of Technology and Woods Hole Oceanographic Institution
October 3, 2008

Certified by

.....

Margaret K. Tivey
Thesis Co-advisor

Wolfgang Bach
Thesis Co-advisor

Accepted by

.....

Mark D. Kurz
Chair, Joint Committee in Chemical Oceanography
Dept. Marine Chemistry and Geochemistry, Woods Hole Oceanographic Institution

GEOCHEMICAL TRACERS OF PROCESSES AFFECTING THE FORMATION OF SEAFLOOR HYDROTHERMAL FLUIDS AND DEPOSITS IN THE MANUS BACK–ARC BASIN

By

Paul R. Craddock

Submitted to the MIT/WHOI Joint Program in Oceanography and Applied Ocean Science and Engineering on October 3, 2008, in partial fulfillment of the requirements for the degree of Doctor of Philosophy in the field of Chemical Oceanography

THESIS ABSTRACT

Systematic differences in trace element compositions (rare earth element (REE), heavy metal, metalloid concentrations) of seafloor vent fluids and related deposits from hydrothermal systems in the Manus back–arc basin (Eastern Manus Basin, EMB and Manus Spreading Center, MSC) are used to investigate processes that affect their formation. Processes responsible for observed differences in fluids and deposits from distinct geologic settings include (a) fluid–rock interaction (with temperature, pressure and crustal composition as variables), (b) magmatic acid volatile input and, (c) local seawater entrainment and mixing with hydrothermal fluids, coupled with sulfide precipitation and metal remobilization. REE distributions in vent fluids in the Manus Basin exhibit a wide range of chondrite-normalized patterns that contrast with the relatively uniform distributions observed in mid-ocean ridge vent fluids. This heterogeneity is attributed to marked differences in fluid pH and fluoride and sulfate concentrations that significantly affect REE solubility. The data indicate that REEs can be used as indicators of the styles of magmatic acid volatile input in back-arc hydrothermal systems. Anhydrite in deposits record the same range of REE patterns, suggesting that REE distributions preserved in anhydrite can be used as indicators of past magmatic acid volatile input. Vent fluid heavy metal and metalloid concentrations also exhibit considerable differences. High metal concentrations in EMB versus MSC vent fluids reflect low pH, largely from input of magmatic acid volatiles (indicated by fluoride concentrations greater than seawater). In EMB, metal concentrations are locally affected by dissolution of previously deposited sulfide owing to low pH conditions affected by magmatic acid volatile input or seawater entrainment and mixing with hydrothermal fluid that leads to sulfide precipitation and secondary acidity generation. Massive sulfide deposits in the Manus Basin exhibit a wide range of mineral compositions and heavy metal enrichments. The formation of Zn-rich (sphalerite/wurtzite) deposits in the MSC and of Cu-Fe and Cu-As-rich (chalcopyrite, tennantite) deposits in the EMB reflects differences in the conditions of sulfide precipitation (temperature, pH) and in metal concentrations. The data suggest that heavy metal and metalloid distributions in massive sulfide deposits can be used as indicators of the conditions of vent deposit formation.

Thesis Co–Supervisor: Dr. Margaret K. Tivey
Title: Senior Scientist, Woods Hole Oceanographic Institution
Thesis Co–Supervisor: Prof. Wolfgang Bach
Title: Professor of Geochemistry, University of Bremen

ACKNOWLEDGEMENTS

Suddenly, I think it easier to discuss and distill five-plus of graduate education and research in a thesis dissertation than it is to appropriately pay homage to all those that made this academic journey possible in the first place. My advisors, Meg Tivey and Wolfgang Bach, were a solid foundation of scientific insight, discussion and advice, of much needed support, and of interminable patience. I think it necessary to acknowledge that I am, more likely than not, a wily sort of character who requires a delicate balance between academic freedom and restraint. Meg and Wolfgang provided just enough of each, culminating in the successful completion of this thesis; a work that I hope they are as rewarded by as I am. I cannot express my appreciation for them enough. My thesis committee members Jeff Seewald, Olivier Rouxel and Ed Boyle were an unlimited source of information related to both academia and the trials and tribulations of life itself. Their generosity of precious time allocated in pursuit of my successful navigation through graduate school is fondly remembered – as is Jeff's chuckle and grin that provided much welcome relief when times were not at all easy.

There are countless persons at WHOI and MIT who facilitated my research on a day-to-day basis. Margaret Sulanowska and Brian Schroeder in the McLean Laboratory were more help that I could ever as asked for. Their contributions to this thesis, from a technical standpoint, were as important as my advisor's. Lary Ball, Dave Schneider, Scot Birdwhistell and Jurey Blusztajn (WHOI Plasma Facility) supplied all the technical know-how that enabled the successful collection of much of the data used in this thesis. As did Neel Chatterjee (MIT Electron Microprobe Facility), who provided much help with the analysis of sulfide deposit samples at short notice late on in the thesis. The MIT and WHOI Academic Programs offices – Marsha Gomes, Julia Westwater, Jim Yoder, John Farrington, Jim Price, Judy McDowell, Christine Charette, Ronni Schwartz – are unbounding in their support of all students in the Program. Their general help in every aspect of graduate education makes the Joint Program all the more enjoyable and successful. Sheila Clifford, Donna Mortimer and everyone on the MC&G administrative staff are warmly acknowledged for saving me from certain failure when printing services, projectors, all manner of stationary and, most importantly, coffee were needed immediately (Sheila – thank you for printing all 400 pages of this tome).

All that said, graduate education does require time outside of the laboratory (no matter how much I like being there at 3.00 am at the weekend), and I've been accompanied by many excellent friends at those times. My boys in Woods Hole – Eric Montie, Rick Rupan, Scott Garvin and Nicholas Drenzek – were, and still are, my life line to academic sanity. They are my confidantes and true, trusted friends. The baseball games, rounds of billiards, surf, wine tasting, and everything else I have failed to mention made my experience in MA one to remember. Cheers. It's been a blast.

To everyone in the Joint Program past and present – Christian Miller, Desirée Plata, Dreux Chappell, Peter Canovas, Caleb Mills, Colleen Petrik, Cara and Jeff

Standish, Matt and Anna Jackson, Jessica Warren and Carlos Moffat, Linda Kalnejais, Margaret Boettcher, Eoghan Reeves, Erin Banning, Ari Shapiro, Annette Hynes and Kate Buckman, in particular – Woods Hole would be oh-so the worse without you. Your friendship is most humbly appreciated.

And then there are those who knew me before I even started graduate school. Ben Murphy, Jon Downes and Simon Granger, who had to endure living with me through undergraduate, are three of my most wonderful and long-time friends. Wherever I spend my life you are most welcome to come and visit anytime.

To my family – my mum Linda, dad Chris and sister Natalie – this thesis represents the best of everything you taught me growing up: Pursue your goals with vigor and never give up on them, take responsibility, work hard with pride (I could go on forever). I love you all dearly and always. None of this could possibly have happened without your love and support.

And to Michelle – I am sorry you have endured all the pains and frustrations that I have felt during the latter few years of this thesis. But, to have you by my side through it made this journey a pleasure. That we made it through this together and had such a great time throughout, is surely the perfect start for our future. I cannot look forward enough to spending my life and all life's journeys with you. I love you eternally.

The thesis research presented herein was funded by the National Science Foundation through grants OCE-0327448 (to W. Bach and M.K. Tivey) and OCE-0441796 (to M.K. Tivey) and by support to P.R. Craddock from the MIT Presidential Fellowship and Ocean Drilling Program Schlanger Fellowship, as well by WHOI Academic Programs Office.

TABLE OF CONTENTS

LIST OF FIGURES

LIST OF TABLES

CHAPTER 1

Introduction

Submarine hydrothermal circulation involves the convection of seawater through fractured crust at oceanic spreading centers that is driven largely by the availability of a heat source (e.g., magma intrusion or newly solidified crust) and a permeable medium (e.g., faulted ocean crust). This process transfers significant heat and mass between the oceanic lithosphere and the overlying seawater. In the presence of a heat source, seawater is conductively heated and undergoes chemical interactions with surrounding oceanic crustal rocks (Alt, 1995). These interactions modify the composition of seawater, forming high–temperature hydrothermal fluids. At elevated temperatures (in excess of 400 °C) and pressures (> 200 – 400 bars), these fluids are buoyant and rise rapidly back to the seafloor where they can exit as high–temperature, focused 'black–smoker' vent fluids (up to ~ 400 °C), lower–temperature focused 'white smoker' fluids (~ 250 – 280 °C) and still lower temperature, less focused and diffuse fluids (< 100 °C) that have cooled conductively or mixed with cold seawater prior to venting (Corliss et al., 1979; Edmond et al., 1979a; Spiess et al., 1980). These fluids exit the seafloor from a range of hydrothermal deposit structures, including metal–rich sulfide chimneys and metalliferous and oxide sediments (Haymon and Kastner, 1981; Goldfarb et al., 1983).

Hydrothermal processes are of importance to global geochemical cycles because

they affect the chemical composition of ocean crust (Humphris and Thompson, 1978b; Alt, 1995) and regulate the flux of many aqueous species to and from seawater (Edmond et al., 1979b; Palmer and Edmond, 1989; Mottl and Wheat, 1994; Elderfield and Schultz, 1996). The precipitation of precious and heavy metals from evolved hydrothermal fluids results in the formation of metalliferous sediments and metal–rich sulfide deposits on the seafloor. These sulfide deposits are likely modern analogs to many economically–important volcanogenic–hosted massive sulfide deposits (VHMS) exposed on land, and hence provide key information about the conditions (e.g., temperature, pH, fluid composition) and processes responsible for the formation of metal–rich deposits in the geologic past (Franklin et al., 1981; Sawkins, 1990; Hannington et al., 2005). In addition, dissolved components in hydrothermal fluids provide chemical energy that is exploited by communities of chemosynthetic microbes that, in turn, provide the basis for diverse macro–faunal populations (Jannasch, 1983; Grassle, 1986; Tunnicliffe, 1991).

1. SUB–SEAFLOOR HYDROTHERMAL PROCESSES AT OCEANIC SPREADING CENTERS

1.1. Formation of seafloor hydrothermal fluids

The formation and compositions of seafloor hydrothermal fluids are affected by a range of geochemical processes occurring in the ocean crust that, in turn, are controlled by several physical parameters. The structure of the ocean crust and the depth and size of the underlying heat source determines the depth and scale of fluid circulation in the crust and the temperatures and pressures at which fluid–rock interactions can occur. The compositions of hot fluids that exit the seafloor, reflecting primarily the integrated of

effects fluid–rock interactions, are influenced by the temperatures and pressures of fluid–rock interaction and by the composition of the ocean crust that reacts with circulating fluids (see review by Alt, 1995). Most mid–ocean ridge vent fields are hosted within basalt. Our understanding of fluid–rock interactions occurring sub–seafloor is based largely on observations of alteration mineral assemblages obtained from drill cores of the crust or from ophiolites representing sections of ocean crust now exposed on land (Alt et al., 1986; Gillis and Robinson, 1990; Alt, 1995) and from experimental studies that consider the reactions between seawater and basalt at elevated temperatures and pressures (Bischoff and Dickson, 1975; Humphris and Thompson, 1978a; Seyfried and Bischoff, 1979; Seyfried and Bischoff, 1981; Seyfried, 1987; Berndt et al., 1989; Seewald and Seyfried, 1990).

As seawater penetrates into ocean crust in the downwelling limb ("recharge zone") and is heated to temperatures ~ 50 to 60 °C, reactions of seawater with basalt result in alteration of olivine, plagioclase and matrix glass by low temperature oxidation to Mg– and Fe–bearing micas and clays (e.g., smectite) (Seyfried and Bischoff, 1979; Alt, 1995). At higher temperatures (above ~ 150 °C), precipitation of anhydrite ($CaSO_4$) (a mineral that exhibits retrograde solubility) removes all Ca and approximately one–third sulfate from seawater (Bischoff and Seyfried, 1978). Mg is removed from seawater during the formation of Mg–rich smectite and chlorite at temperatures less than and greater than ~ 200 °C, respectively (Alt, 1995). These reactions are important because they generate significant acidity that is used in later silicate hydrolysis.

At high temperatures (~ 400 °C or greater) and low pH (less than ~ 4 to 5) in the

hydrothermal "root zone" at depth, these hydrolysis reactions release large amounts of alkalis (K, Li, Rb, Cs), alkaline earth metals (Ca, Ba, but not Mg), base metals (e.g., Mn, Fe, Cu, Zn), aqueous SiO_2 and sulfur from crustal rocks into hydrothermal fluids. Removal of Ca from crustal rocks can result in precipitation of additional quantities of anhydrite, further depleting seawater of its initial sulfate. Other reactions that affect fluid compositions include the generation of H_2 as a result of reaction between water and ferrous (Fe(II)–bearing) minerals in crustal rocks and the reduction of remaining seawater sulfate to H_2S. The integrative result of fluid–rock interactions in the ocean crust is the removal of Mg, sulfate and alkalinity from seawater and the generation of a high–temperature acidic, reducing and metal–rich hydrothermal fluid (Von Damm, 1990, 1995).

When buoyant, high–temperature hydrothermal fluids rise toward the seafloor, they may pass through the boiling curve for seawater (e.g., as a result of reduction in pressure) and phase separate into a lower salinity fluid and a higher salinity brine (Bischoff and Rosenbauer, 1984). Evidence for phase separation in many submarine hydrothermal systems is obtained from chloride concentrations of seafloor vent fluids significantly less than or greater than that of initial seawater (~ 546 mmol/kg) from which hydrothermal fluids evolved (e.g., Von Damm, 1995). The formation of lower– and higher–salinity fluid affects the compositions of hydrothermal fluids because more volatile species (e.g., H_2, H_2S, CO_2) are partitioned preferentially into the lower salinity phase while metals are carried in solution as chloride complexes and partitioned into the higher salinity brine.

Other processes that may affect the formation and composition of seafloor hydrothermal fluids include addition of volatiles degassed from underlying magmas as evidenced from elevated concentrations of ^3He and CO_2 in hydrothermal fluids relative to seawater (e.g., Lupton and Craig, 1981; Welhan and Craig, 1983) and mixing of rising high–temperature hydrothermal fluids with locally entrained seawater prior to venting at the seafloor (Edmond et al., 1995). The extent and overall significance of these processes for submarine hydrothermal systems along mid-ocean ridge spreading centers is not fully constrained, but appears to be of lesser importance relative to fluid–rock interaction.

1.2. Formation of seafloor mineral deposits

There are several major factors controlling the formation and composition of mineral deposits related to submarine hydrothermal activity at and beneath the seafloor, including the temperature and chemical composition of hydrothermal fluids from which these deposits precipitate, and the physical structure of upper (approximately 100 – 400 m) oceanic crust (and existing mineral deposits) that determines the pathways of fluid flow near the seafloor (e.g., Tivey, 2007). The latter affects the styles of interaction and mixing among rising high–temperature hydrothermal fluids and locally entrained seawater in proximity to the seafloor. Differences in temperature, fluid composition (e.g., pH, metal and H_2S concentrations) and style of fluid flow significantly affect the morphology and composition of metal–sulfide vent deposits at the seafloor (Koski et al., 1985; Fouquet et al., 1993b; Koski et al., 1994; Tivey et al., 1995; Tivey et al., 1999; Kristall et al., 2006). Overall, metal–sulfide deposits forming at mid-ocean ridge spreading centers tend to be dominated by Fe–sulfides (pyrite, pyrrhotite), Cu–Fe–

sulfides (chalcopyrite) and Zn–sulfides (sphalerite, wurtzite).

In general, chalcopyrite ($CuFeS_2$) is present in the highest modal abundance in open conduit type chimneys precipitating from the highest temperature (> 300 – 350 °C) "black smoker" fluids. An accepted model for their formation has been proposed by Haymon and Kastner (1981) and Goldfarb et al. (1983). During initial chimney growth, moderately acidic, reducing, metal– and Ca–rich hydrothermal fluids exit the seafloor at velocities of meters–per–second and mix with cold, alkaline and oxic, sulfate– and Ca–rich and metal–poor seawater, resulting in the precipitation of anhydrite and trace amounts of sulfide. Growth rates during this stage are up to 30 cm/day (Goldfarb et al., 1983). The initial framework (wall) of anhydrite is highly permeable, but provides a substrate onto which minerals can precipitate. Continued mixing between hydrothermal fluid and seawater and precipitation of sulfate and sulfide reduces permeability across the chimney wall, isolating high–temperature fluids inside the chimney from seawater exterior to the chimney wall. As mixing is inhibited and temperatures inside the chimney increase to that of the hydrothermal fluid, an inner monomineralic layer of chalcopyrite is precipitated against the inner side of the open pipe–like conduit. Advection and/or diffusion of hydrothermal fluid and seawater across the chimney wall result in precipitation of a range of (lower–temperature) sulfide and sulfate minerals within pore spaces of the wall (Tivey and McDuff, 1990; Tivey, 1995). However, while the conduit remains open to fluid flow, the fraction of fluid mass migrating across the chimney walls is minor relative to the fraction of fluid flowing up and out of the central conduit.

Chimneys precipitating from lower–temperature (< 270 – 300 °C) "white smoker"

and clear fluids often exhibit very different morphologies and compositions relative to their highest temperature counterparts (Haymon and Kastner, 1981; Koski et al., 1994). These differences can be related to the different styles of fluid flow and mixing, and to different conditions of mineral precipitation within lower temperature diffuser–type chimneys. Fluids with temperatures of ~ 270 – 280 °C may have cooled conductively or mixed with cold seawater prior to venting. Consequently, they have lower buoyancies and slower fluid flow rates relative to higher temperature fluids. These slower fluid rates correlate with the formation of more porous, bulbous chimneys, rather than cylindrical or pipe–like chimneys (Koski et al., 1994). Mineral textures indicate that fluid flows through multiple, tortuous micro–channels instead of through a single central open conduit. Many of these diffuser–type chimneys contain significantly lesser amounts of anhydrite (or lack anhydrite entirely) relative to open conduit–type chimneys, suggesting lesser entrainment of seawater and consistent with a greater fraction of fluid flow outward through permeable chimney walls. Differences in styles of fluid flow lead to different environments of sulfide mineral precipitation and different mineral compositions in diffuser–type chimneys. In general, these chimneys contain high modal abundances of Zn–sulfide and lesser amounts of Cu–Fe–sulfides (Haymon and Kastner, 1981; Koski et al., 1994; Tivey et al., 1995). Petrographic studies suggest that dendritic sphalerite is precipitated early in chimney genesis, followed by replacement and overgrowth by colloform sphalerite in exterior portions and subhedral to euhedral sphalerite and wurtzite in interior portions of chimney walls, and then by chalcopyrite lining narrow micro–channels (Koski et al., 1994). This sequence is consistent with a

range of lower, but typically increasing, hydrothermal fluid temperatures during mineral precipitation. The presence of pyrrhotite ($Fe_{1-x}S$) and isocubanite ($CuFe_2S_3$) in some diffuser–type chimneys (Haymon and Kastner, 1981; Goldfarb et al., 1983; Koski et al., 1994) suggest lower oxidation and sulfidation states in these chimneys relative to open conduit chimneys.

In addition to differences in fluid composition and styles of fluid flow on the scales of centimeters to meters in chimney deposits, differences in styles of fluid flow and mixing on the scale of entire deposits (> 100 m) can significantly affect their evolution. For example, at the TAG active mound at 26 °N along the Mid–Atlantic Ridge, large scale entrainment of seawater and mixing with hydrothermal fluid beneath the mound (to depths of ~ 200 meters below seafloor) results in subsurface precipitation of large quantities of anhydrite, chalcopyrite and pyrite and the dissolution of other minerals, in particular of Zn–sulfide (Edmond et al., 1995; Tivey et al., 1995). Remobilized Zn is then re–deposited at the seafloor in a process of on–going zone–refinement (Tivey et al., 1995). Coupled mineralogical and geochemical studies of both seafloor vent fluids and related vent deposits at oceanic spreading centers have proved instructive for better understanding the origins of ancient massive sulfide ore deposits preserved in the geologic record. For example, the morphology, composition and mineral zonation of the TAG active mound hydrothermal deposit are similar to that observed in Cyprus–type ore bodies (Constantinou and Govett, 1973; Humphris et al., 1995; Tivey et al., 1995). The processes responsible for the formation of the TAG active mound, including seawater entrainment, fluid mixing, mineral precipitation and remobilization

and consequent modification of hydrothermal fluid compositions, may be similar to those associated with the formation of Cyprus–type massive sulfide deposits (Constantinou and Govett, 1973; Humphris et al., 1995; Tivey et al., 1995).

2. SUB–SEAFLOOR HYDROTHERMAL PROCESSES IN CONVERGENT PLATE MARGINS

Many detailed field and experimental studies have investigated geochemical processes associated with the formation of seafloor hydrothermal fluids and related mineral deposits in basalt–hosted systems at mid-ocean ridge (MOR) spreading centers. In contrast, relatively few studies have examined geochemical processes associated with hydrothermal activity occurring associated with convergent plate margin settings, including within back–arc basins and at submarine arc volcanoes. Such studies are essential for our understanding of global submarine hydrothermal activity because the hydrothermal processes occurring at convergent plate margin settings may differ significantly from those at MORs and may therefore result in a range of different fluid and vent deposit compositions. For example, convergent plate margin settings are characterized by diverse crustal compositions, magma types (ranging from mafic (basalt) to felsic (andesite, dacite and rhyolite)) and crustal thicknesses, variable styles of seafloor tectonism, and a wide range depths of the seafloor (less than 1000 m to greater than 2500 m below sea level) (e.g., Martinez and Taylor, 2003; Martinez et al., 2006). Accordingly, the compositions of crustal rocks with which circulating fluids interact, and the temperatures and pressures at which these interactions occur, can differ significantly from

those at MORs.

In addition, there is evidence to support that the styles of magmatic volatile degassing and the compositions of exsolved magmatic volatiles can differ markedly from that occurring at MORs. Felsic arc magmas in convergent plate margins are likely the products of partial melting caused by the addition of H_2O to the arc mantle from dehydration of subducting sediments and altered oceanic crust (e.g., Schmidt and Poli, 1998). Fluids released into the mantle result in oxidation of arc magmas and act as agents for the removal of water soluble species from the subducting plate and the arc mantle, including volatile species such as HCl, HF and SO_2 (Burnham, 1979). Degassing of reactive magmatic acid volatile phases (e.g., H_2O–CO_2–HCl–HF–SO_2) can contribute significant acidity to seafloor hydrothermal fluids in convergent plate margins, as evidenced by the very low pH of high–temperature hydrothermal fluids (pH (25 °C) ~ 1 – 3) sampled from some back–arc basin vent fluids relative to those sampled at MORs (pH (25 °C) ~ 4) (Fouquet et al., 1993a; Gamo et al., 1997; Douville et al., 1999).

Studies of hydrothermal fluid and mineral deposit compositions associated with convergent plate margin settings have highlighted both similarities and differences relative to those at mid–ocean ridges. Where data are available, endmember hydrothermal fluids sampled from back–arc basin hydrothermal systems exhibit a higher oxygen– and sulfur–fugacity (e.g., lower H_2) and are enriched in alkali and alkaline earth metals (e.g., K, Rb, Ba) and in many base metals and metalloids (e.g., Zn, Pb, Cd, As, Sb) relative to those from MORs (Fouquet et al., 1993a; Ishibashi and Urabe, 1995; Douville, 1999). The observed metal enrichments in back–arc hydrothermal fluids have been attributed to

interaction of seawater with felsic rocks (e.g., Fouquet et al., 1993a) that contain higher concentrations of these elements (e.g., Pb, Ba, As, Sb) (Stanton, 1994). However, these interpretations are complicated by the fact that the pH of these back–arc vent fluids is lower than that of most MOR vent fluids, likely resulting from the input of reactive magmatic acid volatiles (i.e., H_2O–HCl–HF–SO_2) in back–arc basins (e.g., Gamo et al., 1997). Thus, elevated metal concentrations in back–arc hydrothermal fluids relative to those from MORs may reflect higher aqueous metal solubilities as a result of more acid pH. Further, it has been speculated that magmatic acid volatiles degassed from felsic magmas may directly contribute base and precious metals (e.g., Cu, As, Au) to back–arc hydrothermal systems independent of fluid–water interaction (Ishibashi and Urabe, 1995; Yang and Scott, 1996, 2002).

Although differences in back-arc basin vent fluids relative to MOR vent fluids are recognized, it is difficult to determine which factors affect most their formation and composition. This is because the possible key factors, (e.g., different crustal rock composition, lower pH from addition of magmatic acid volatiles, possible addition of metals with magmatic volatiles) do not occur exclusive of one another. Further examination of vent fluid compositions in convergent plate margins is critical to resolve the influence that different geochemical processes, such as fluid–rock interaction with ocean crust with a range of composition and magmatic acid volatile input, exert in controlling observed fluid compositions.

Vent deposits found in convergent plate margin settings also exhibit both similarities and differences relative to those found along MORs. Massive sulfide deposits

located in back–arc basins display a wide range of mineral compositions and precious metal concentrations and, in general, have high concentrations of Zn, Pb, As, Sb, Ag and Ba relative to mid–ocean ridge vent deposits (Halbach et al., 1989; Binns and Scott, 1993; Fouquet et al., 1993a; Ishibashi and Urabe, 1995; Hannington et al., 2005). Massive sulfide deposits in convergent plate margins, such as those found in the Okinawa trough (e.g., JADE hydrothermal field), in the Lau Basin along the Valu Fa Ridge (e.g., Vai Lili hydrothermal field) and in the Manus Basin (e.g., PACMANUS hydrothermal system), are enriched in tennantite ($Cu_{12}As_4S_{13}$), galena (PbS) and barite ($BaSO_4$) and show a wide range of sphalerite/wurtzite modal abundance relative to mid–ocean ridge deposits (Halbach et al., 1989; Binns and Scott, 1993; Fouquet et al., 1993a). At the DESMOS caldera (Manus back–arc basin) and Brothers volcano (Kermadec island–arc), alteration assemblages are markedly different than those associated with most seafloor hydrothermal activity and are characterized by advanced argillic alteration (alunite–illite–pyrophyllite–quartz) and the presence of large quantities of native sulfur and lesser pyrite (Gamo et al., 1997; de Ronde et al., 2005). These sulfur–rich assemblages appear to reflect low pH conditions (< 2) likely related to extensive degassing and input of highly–acidic magmatic volatiles to these vent systems (e.g., Gamo et al., 1997; Seewald et al., 2006).

As with vent fluids, it is difficult to determine which processes and factors affect most observed metal enrichment and sulfide mineral compositions of back-arc vent deposits. Unraveling this is difficult in part because of a paucity of back-arc massive sulfide deposit composition data that can be directly related to parent hydrothermal fluid

compositions. It is uncertain, for example, whether elevated enrichments of Pb, As, Sb, Au and Ba in back–arc vent deposits correlate best with higher metal concentrations in vent fluids, differences in oxygen– and sulfur–fugacity, styles of fluid flow and the conditions (e.g., temperature and pH) of sulfide mineral precipitation, or some combination of these parameters. Further detailed studies of paired vent fluids and deposits are absolutely necessary to establish the influence that differences in crustal rock composition, crustal architecture, and input of magmatic acid volatile input exert on the formation and composition of back-arc massive sulfide deposits.

Finally, such studies will also lead to a better understanding of the evolution and formation of economically valuable ore deposit preserved in the rock record (e.g., the Kuroko ore deposits). Kuroko-type ore deposits are associated with felsic rocks and exhibit compositional similarities to modern submarine back–arc vent deposits, suggesting that they were formed in convergent plate margin settings (Franklin et al., 1981; Ohmoto and Skinner, 1983; Halbach et al., 1989; Sawkins, 1990).

3. THESIS DISSERTATION RESEARCH: THE MANUS BACK–ARC BASIN EXAMPLE

3.1. Objectives and rationale

This research examines and characterizes in detail the compositions of a wide range of seafloor vent fluids and related mineral deposits sampled from hydrothermal systems in the Manus back–arc basin, Papua New Guinea. These data are used to constrain the sub–seafloor processes controlling the evolution of both hydrothermal fluids and metal–rich vent deposits in convergent plate margin settings, to examine directly the

relationships between vent fluid and vent deposit formation, and to compare these processes to those occurring at hydrothermal systems along mid-ocean ridge spreading centers. My dissertation focuses on the rare earth elements (REEs) and base metals and metalloids (e.g., Fe, Zn, Cu, Pb, Cd, Ag, Au, As, Sb) because these elements are present in seafloor hydrothermal fluids *and* in a range of sulfate and sulfide minerals in related vent deposits. These elements exhibit a wide range of chemical behaviors and previous studies have demonstrated that these elements can provide important constraints on sub–seafloor hydrothermal processes. The over–arching objectives of this research are:

(1) to determine how and to what extent fluid interaction with crustal rocks with a range of chemical composition affects the chemical evolution of seafloor hydrothermal fluids;

(2) to assess the role that varying amounts of magmatic acid volatile input plays in determining vent fluid composition and whether magmatic acid volatiles contribute a significant source of base and precious metals;

(3) to examine the extent of local seawater entrainment in these back-arc basin hydrothermal systems and identify whether such seawater entrainment affects the compositions of seafloor vent fluids and deposits;

(4) to examine the geochemical relationships among vent fluids and associated mineral deposits and assess the processes affecting massive sulfide deposit formation in these back–arc basin hydrothermal systems

(5) to identify geochemical tracers of vent fluid compositions that are preserved in the deposits and that can be used as indicators of past conditions of hydrothermal activity.

The Manus back–arc basin in the Bismarck Sea is an excellent geological environment in which to examine the key factors that affect submarine hydrothermal activity in convergent plate margin settings. Present–day tectonic activity involves subduction of the Solomon Microplate beneath the New Britain volcanic arc and rapid (~ 100 mm/yr) opening of the back–arc behind New Britain (Taylor, 1979; Martinez and Taylor, 1996). A complex history of plate deformation and rotation has resulted in a range of crustal spreading, including eruption of new mafic–dominated crust along the Manus Spreading Center and extension and rifting of existing felsic–dominated crust in the Eastern Manus Basin (Martinez and Taylor, 1996). Prior to 2006, field studies in the Manus Basin had identified the presence of at least four major active hydrothermal systems that occur in a range of tectonic settings at different distances to the active volcanic arc and that are hosted on crustal rocks of different composition.

Vienna Woods is a basalt–hosted hydrothermal system occurring at a depth of ~ 2500 meters along the Manus Spreading Center (axial rift valley) distal to the active volcanic arc (Both et al., 1986; Tufar, 1990). Prior to 2006, existing data for hydrothermal fluid compositions indicated broad similarities to that of mid–ocean ridge vent fluids, suggesting that geochemical processes occurring at Vienna Woods may be comparable to those occurring at mid-ocean ridge spreading centers (Douville, 1999; Douville et al., 1999). Hydrothermal systems in the Eastern Manus Basin occur in geologic settings distinct to the Manus Spreading Center. A well-defined spreading axis is lacking in the Eastern Manus Basin. The PACMANUS, DESMOS and SuSu Knolls hydrothermal systems in the Eastern Manus Basin are hosted by felsic crustal rocks and

are located on neo-volcanic ridges and discrete volcanic domes in proximity to the active volcanic arc (Binns and Scott, 1993; Scott and Binns, 1995; Binns et al., 1997; Gamo et al., 1997; Parr and Binns, 1997; Yeats et al., 2000). Fluid data collected prior to 2006 showed marked differences relative to those from the Manus Spreading Center and from mid-ocean ridge spreading centers, including the prevalence of very acidic fluids (pH (25 °C) ~ 2 – 3) and evidence for the addition of magmatic acid volatiles HF and SO_2 (Gamo et al., 1997; Douville, 1999). Geologic sampling of hydrothermal mineral deposits and metalliferous sediment by dredge haul at these vent fields prior to 2006 suggested the presence of hydrothermal sulfide deposits with compositions different to those at mid-ocean ridge spreading centers, including abundant Cu–Fe–sulfides (chalcopyrite, bornite, fukuchilite), Cu–As–sulfosalts (enargite, tennantite), galena, barite (e.g., Binns and Scott, 1993; Scott and Binns, 1995; Moss et al., 2001; Hrischeva et al., 2007) and, at DESMOS, native sulfur (e.g., Gamo et al., 1997). These data strongly suggested that the key processes affecting vent fluid and vent deposit formation in the Eastern Manus Basin differed markedly from those occurring along the Manus Spreading Center and mid–ocean ridges. However, a detailed understanding of the specific processes affecting vent fluid formation in back–arc basins (e.g., fluid–rock interaction with crustal rocks of different composition, input of magmatic acid volatiles, different styles of fluid flow owing to different crustal architecture), including their relative influence and the extent to which these processes likely vary, was lacking. Similarly, our understanding of specific factors affecting the size, structure and composition of mineral deposits in back–arc basins (e.g., vent fluid composition, styles of sub–seafloor fluid flow and mixing) was

also incomplete.

In 2006, a suite of vent fluid and deposit samples, including 22 paired fluids and solids, were sampled from the Vienna Woods, PACMANUS, DESMOS and SuSu Knolls hydrothermal systems during cruise MGLN06MV (Tivey et al., 2007). In this thesis, by comparing in detail the hydrothermal fluids and related mineral deposits formed at at these vent systems in a range of distinct geologic environments within the Manus Basin, it is possible to better constrain the specific factors and processes that control their evolution and composition. The research presented in this dissertation represents an attempt to advance our understanding of geochemical process associated with submarine hydrothermal activity in convergent plate margins, and is valuable for the study of other hydrothermal systems both active and relict.

3.2. Outline of dissertation research

In Chapter 2, of this thesis the concentrations and relative distributions of rare earth elements (REEs) in seafloor vent fluids sampled from the Vienna Woods (Manus Spreading Center) and the PACMANUS, DESMOS and SuSu Knolls (Eastern Manus Basin) hydrothermal systems are examined. It constrains the extent to which REEs are affected by, and can be used as indicators of, (a) the conditions of fluid–rock interaction and, (b) the styles and extent of magmatic acid volatile degassing.

In Chapter 3, REE concentrations, and Sr and S isotope ratios recorded within the mineral anhydrite ($CaSO_4$) recovered from the PACMANUS and SuSu Knolls hydrothermal systems are characterized. Anhydrite has been recovered at and/or beneath the seafloor via submersible operations or deep drilling into the upper oceanic crust. Data

are used to (1) assess the extent to which REE distributions preserved in anhydrite reflect that of the source hydrothermal fluid from which anhydrite precipitated, and (2) determine whether these distributions can be used to constrain changes in the conditions of fluid–rock interaction and styles of magmatic acid volatile degassing that affect the formation of back–arc mineral deposits. The data are complemented by coupled Sr and S isotope data that provide insights into near–seafloor processes, including local entrainment of seawater and mixing with hydrothermal fluids, which may overprint signatures of geochemical processes occurring at depth. This study provides valuable information about the temporal evolution of seafloor hydrothermal systems that it may not be possible to obtain by the study of seafloor hydrothermal fluids alone.

In Chapter 4, the concentrations of heavy and precious (ore–forming) metals and metalloids (e.g., Fe, Zn, Cu, Pb, Ag, As, Sb) in Manus Basin seafloor vent fluids are characterized. It discusses the extent to which these elements are controlled by, and can be used as indicators of, the conditions of deep–seated fluid–rock interaction. The data are also used to (1) examine how differences in the compositions of magmatic acid volatiles degassed from underlying felsic magmas can affect the behavior and aqueous mobility of these elements and, (2) assess whether magmatic acid volatiles may be a significant and direct source for valuable metals. Data are also used to examine the extent to which transport of heavy metals and metalloids in Manus Basin seafloor vent fluids are affected by local seawater entrainment and mixing with rising high–temperature fluids, and subsequent mineral precipitation, secondary acidity formation and subsequent metal remobilization. This zone refinement process has been shown previously to affect the

cycling of metals in some mid-ocean ridge hydrothermal systems (e.g., Edmond et al., 1995; Tivey et al., 1995).

In Chapter 5, the mineralogy and precious metal geochemistry of seafloor massive sulfide deposits in the Manus Basin are described and compared to those of mineral deposits found at mid–ocean ridges. In addition, vent deposit compositions are compared directly to compositions of the vent fluids from which these vent deposits formed. This enables evaluation of the roles that vent fluid composition (e.g., temperature, pH, [metals], [H_2S]) and styles of fluid flow and mixing (and resulting conditions of mineral precipitation) play in affecting the composition of seafloor hydrothermal deposits. The data provide new insights into the processes and conditions that favor the formation of precious metal–enriched seafloor massive sulfide deposits. The data also demonstrate the potential for trace elements found in seafloor vent deposits to identify past conditions of seafloor hydrothermal activity (e.g., temperatures and pH of mineral deposition) in both active and relict hydrothermal systems. Chapter 6 is a summary of the major conclusions drawn from this thesis research and identifies areas of priority for future studies that will provide complementary data to further constrain and better understand geochemical processes associated with submarine hydrothermal activity in convergent plate margin settings.

REFERENCES

Alt J. C. (1995) Subseafloor processes in mid-ocean ridge hydrothermal systems. In

Seafloor Hydrothermal Systems: Physical, Chemical, Biological and Geological Interactions. Geophysical Monograph., Vol. 91 (ed. S. E. Humphris, R. A. Zierenberg, L. S. Mullineaux, and R. E. Thomson), pp. 85-114. American Geophysical Union.

Alt J. C., Honnorez J., Laverne C., and Emmermann R. (1986) Hydrothermal alteration of a 1 km section through the upper oceanic crust. DSDP Hole 504B: Mineralogy, chemistry and evolution of seawater-basalt interactions. *Journal of Geophysical Research* **91**, 309-335.

Berndt M. E., Seyfried W. E., Jr., and Janecky D. R. (1989) Plagioclase and epidote buffering of cation ratios in mid-ocean ridge hydrothermal fluids: Experimental results in and near the supercritical region. *Geochimica et Cosmochimica Acta* **53**(9), 2283-2300.

Binns R. A. and Scott S. D. (1993) Actively forming polymetallic sulfide deposits associated with felsic volcanic rocks in the eastern Manus back-arc basin, Papua New Guinea. *Economic Geology* **88**, 2226-2236.

Binns R. A., Scott S. D., Gemmell J. B., Crook K. A. W., and Shipboard Scientific Party. (1997) The SuSu Knolls hydrothermal field, eastern Manus Basin, Papua New Guinea. *EOS Trans. AGU. Fall Meet. Suppl.*, **78**(52), Abstract #V22E-02.

Bischoff J. L. and Dickson F. W. (1975) Seawater-basalt interaction at 200 °C and 500 bars: Implications for origin of seafloor heavy-metal deposits and regulations of seawater chemistry. *Earth and Planetary Science Letters* **25**, 385-397.

Bischoff J. L. and Rosenbauer R. J. (1984) The critical point and two-phase boundary of seawater, 200-500 C. *Earth and Planetary Science Letters* **68**(1), 172-180.

Bischoff J. L. and Seyfried W. E., Jr. (1978) Hydrothermal chemistry of seawater from 25° to 350°C. *American Journal of Science* **278**, 838-860.

Both R., Crook K., Taylor B., Brogan S., Chappell B., Frankel E., Liu L., Sinton J., and Tiffin D. (1986) Hydrothermal chimneys and associated fauna in the Manus back-arc basin, Papua New Guinea. *EOS Transactions, American Geophysical Union* **67**, 489.

Burnham C. W. (1979) Magmas and hydrothermal fluids. In *Geochemistry of Hydrothermal Ore Deposits, 2nd Edition* (ed. H. L. Barnes), pp. 71-136. Wiley-Interscience.

Constantinou G. and Govett G. J. S. (1973) Geology, geochemistry and genesis of Cyprus sulfide deposits. *Economic Geology* **68**, 843-858.

Corliss J. B., Dymond J., Gordon L. I., Edmond J. M., von Herzen R. P., Ballard R. D., Green K., Williams D., Bainbridge A., Crane K., and van Andel T. H. (1979) Submarine thermal springs on the Galapagos Rift. *Science* **203**, 1073-1083.

de Ronde C. E. J., Hannington M. D., Stoffers P., Wright I. C., Ditchburn R. G., Reyes A. G., Baker E. T., Massoth G. J., Lupton J. E., Walker S. L., Greene R. R., Soong C. W. R., Ishibashi J., Lebon G. T., Bray C. J., and Resing J. A. (2005) Evolution of a submarine magmatic-hydrothermal system: Brothers volcano, Southern Kermadec Arc, New Zealand. *Economic Geology* **100**, 1097-1133.

Douville E. (1999) Les fluides hydrothermaux oceaniques comportement géochimique des éléments traces et des terres rares. Processus associés et modélisation thermodynamique. Ph.D. Thesis, University of Brest.

Douville E., Bienvenu P., Charlou J. L., Donval J. P., Fouquet Y., Appriou P., and Gamo T. (1999) Yttrium and rare earth elements in fluids from various deep-sea hydrothermal systems. *Geochimica et Cosmochimica Acta* **63**(5), 627-643.

Edmond J. M., Campbell A. C., Palmer M. R., German C. R., Klinkhammer G. P., Edmonds H. N., Elderfield H., Thompson G., and Rona P. (1995) Time series studies of vent fluids from the TAG and MARK sites (1986, 1990) Mid-Atlantic Ridge and a mechanism for Cu/Zn zonation in massive sulphide orebodies. In *Hydrothermal Vents and Processes*, Vol. 87 (ed. L. M. Parson, C. L. Walker, and D. R. Dixon), pp. 77-86. Geological Society Special Publication.

Edmond J. M., Measures C., Mangum B., Grant B., Sclater F. R., Collier R., Hudson A., Gordon L. I., and Corliss J. B. (1979a) On the formation of metal-rich deposits at ridge crests. *Earth and Planetary Science Letters* **46**(1), 19-30.

Edmond J. M., Measures C., McDuff R. E., Chan L. H., Collier R., Grant B., Gordon L.

I., and Corliss J. B. (1979b) Ridge crest hydrothermal activity and the balances of the major and minor elements in the ocean: The Galapagos data. *Earth and Planetary Science Letters* **46**(1), 1-18.

Elderfield H. and Schultz A. (1996) Mid-ocean ridge hydrothermal fluxes and the chemical composition of the ocean. *Annual Review of Earth and Planetary Sciences* **24**(1), 191-224.

Fouquet Y., von Stackelberg U., Charlou J. L., Erzinger J., Herzig P. M., Muehe R., and Wiedicke M. (1993a) Metallogenesis in back-arc environments; The Lau Basin example. *Economic Geology* **88**(8), 2150.

Fouquet Y., Wafik A., Cambon P., Mevel C., Meyer G., and Gente P. (1993b) Tectonic setting and mineralogical and geochemical zonation in the Snake Pit sulfide deposit (Mid-Atlantic Ridge, at 23 °N). *Economic Geology* **88**, 2018-2036.

Franklin J. M., Lydon J. W., and Sangster D. F. (1981) Volcanic-associated massive sulfide deposits. *Economic Geology* **75**, 485–627.

Gamo T., Okamura K., Charlou J. L., Urabe T., Auzende J. M., Ishibashi J.-I., Shitashima K., Chiba H., Binns R. A., and Gena K. (1997) Acidic and sulfate-rich hydrothermal fluids from the Manus back-arc basin, Papua New Guinea. *Geology* **25**(2), 139-142.

Gillis K. M. and Robinson P. T. (1990) Patterns and processes of alteration in the lavas and dykes of the Troodos Ophiolite, Cyprus. *Journal of Geophysical Research* **95**(B13), 21523-21548.

Goldfarb M. S., Converse D. R., Holland H. D., and Edmond J. M. (1983) The genesis of hot spring deposits on the East Pacific Rise, 21 °N. In *The Kuroko and Related Volcanogenic Massive Sulfide Deposits. Economic Geology Monograph*, Vol. 5 (ed. H. Ohmoto and B. J. Skinner), pp. 184-197.

Grassle J. F. (1986) The ecology of deep-sea hydrothermal vent communities. *Advances in Marine Biology* **23**, 301-362.

Halbach P., Nakamura K., Wahsner M., Lange J., Sakai H., Kaeselitz L., Hansen R. D., Yamano M., Post J., and Prause B. (1989) Probable modern analogue of Kuroko-

type massive sulphide deposits in the Okinawa Trough back-arc basin. *Nature* **338**, 496-499.

Hannington M. D., De Ronde C. E. J., and Petersen S. (2005) Sea-floor tectonics and submarine hydrothermal systems. *Economic Geology* **100**, 111-141.

Haymon R. M. and Kastner M. (1981) Hot spring deposits on the East Pacific Rise at 21 °N: Preliminary description of mineralogy and genesis. *Earth and Planetary Science Letters* **53**, 363-381.

Hrischeva E., Scott S. D., and Weston R. (2007) Metalliferous sediments associated with presently forming volcanogenic massive sulfides: The SuSu Knolls hydrothermal field, Eastern Manus Basin, Papua New Guinea. *Economic Geology* **102**, 55-74.

Humphris S. E., Herzig P. M., Miller D. J., Alt J. C., Becker K., Brown D., Brügmann G., Chiba H., Fouquet Y., and Gemmell J. B. (1995) The internal structure of an active sea-floor massive sulphide deposit. *Nature* **377**(6551), 713-716.

Humphris S. E. and Thompson G. (1978a) Hydrothermal alteration of oceanic basalts by seawater. *Geochimica et Cosmochimica Acta* **42**(1), 107-125.

Humphris S. E. and Thompson G. (1978b) Trace element mobility during hydrothermal alteration of oceanic basalts. *Geochimica et Cosmochimica Acta* **42**(1), 127-136.

Ishibashi J.-I. and Urabe T. (1995) Hydrothermal activity related to arc-backarc magmatism in the Western Pacific. In *Backarc Basins: Tectonics and Magmatism* (ed. B. Taylor), pp. 451–495. Plenum Press, New York.

Jannasch H. W. (1983) Microbes in the oceanic environment. In *Hydrothermal Processes at Seafloor Spreading Centers* (ed. P. A. Rona, K. Boström, L. Laubier, and K. L. Smith), pp. 677-709. Plenum Press, New York.

Koski R. A., Jonasson I. R., Kadko D. C., Smith V. K., and Wong F. L. (1994) Compositions, growth mechanisms, and temporal relations of hydrothermal sulfide-sulfate-silica chimneys at the northern Cleft segment, Juan de Fuca Ridge. *Journal of Geophysical Research* **99**(B3), 4813-4832.

Koski R. A., Lonsdale P. F., Shanks W. C., Berndt M. E., and Howe S. S. (1985) Mineralogy and Geochemistry of a sediment-hosted hydrothermal sulfide deposit

from the Southern Trough of Guaymas Basin, Gulf of California. *Journal of Geophysical Research* **90**(B8), 6695-6708.

Kristall B., Kelley D. S., Hannington M. D., and Delaney J. R. (2006) Growth history of a diffusely venting sulfide structure from the Juan de Fuca Ridge: A petrological and geochemical study. *Geochemistry Geophysics Geosystems* **7**, Q07001, doi:10.1029/2005GC001166.

Lupton J. E. and Craig H. (1981) A major helium-3 source at 15 °S on the East Pacific Rise. *Science* **214**, 13-18.

Martinez F. and Taylor B. (1996) Backarc spreading, rifting, and microplate rotation, between transform faults in the Manus Basin. *Marine Geophysical Researches* **18**, 203-224.

Martinez F. and Taylor B. (2003) Controls on back-arc crustal accretion: insights from the Lau, Manus and Mariana basins. *Geological Society London Special Publications* **219**, 19-54.

Martinez F., Taylor B., Baker E. T., Resing J. A., and Walker S. L. (2006) Opposing trends in crustal thickness and spreading rate along the back-arc Eastern Lau Spreading Center: Implications for controls on ridge morphology, faulting, and hydrothermal activity. *Earth and Planetary Science Letters* **245**, 655-672.

Moss R., Scott S. D., and Binns R. A. (2001) Gold Content of Eastern Manus Basin Volcanic Rocks: Implications for Enrichment in Associated Hydrothermal Precipitates. *Economic Geology* **96**(1), 91-107.

Mottl M. J. and Wheat C. G. (1994) Hydrothermal circulation through mid-ocean ridge flanks: Fluxes of heat and magnesium. *Geochimica et Cosmochimica Acta* **58**(10), 2225-2237.

Ohmoto H. and Skinner B. J. (1983) The Kuroko and Related Volcanogenic Massive Sulfide Deposits. In *Economic Geology Monograph*, Vol. 5, pp. 604.

Palmer M. R. and Edmond J. M. (1989) The strontium isotope budget of the modern ocean. *Earth and Planetary Science Letters* **92**(1), 11-26.

Parr J. M. and Binns R. A. (1997) Report on the PACMANUS-III Cruise, RV "Franklin,"

eastern Manus basin, Papua New Guinea. CSIRO Division of Exploration and Mining, Exploration and Mining Report 345R, pp. 179.

Sawkins F. J. (1990) *Metal Deposits in Relation to Plate Tectonics*. Springer-Verlag.

Schmidt M. W. and Poli S. (1998) Experimentally based water budgets for dehydrating slabs and consequences for arc magma generation. *Earth and Planetary Science Letters* **163**(1-4), 361-379.

Scott S. D. and Binns R. A. (1995) Hydrothermal processes and contrasting styles of mineralization in the western Woodlark and eastern Manus basins of the western Pacific. In *Hydrothermal Vent and Processes, Geological Society of London Special Publication*, Vol. 87 (ed. L. M. Parson, C. L. Walker, and D. R. Dixon), pp. 191-205.

Seewald J. S., Reeves E., Saccocia P., Rouxel O. J., Walsh E., Price R. E., Tivey M., Bach W., and Tivey M. (2006) Water-rock reaction, substrate composition, magmatic degassing, and mixing as major factors controlling vent fluid compositions in Manus Basin hydrothermal systems. *EOS Trans. AGU. Fall Meet. Suppl.*, **87**(52), Abstract # B34A-02.

Seewald J. S. and Seyfried W. E., Jr. (1990) The effect of temperature on metal mobility in subseafloor hydrothermal systems: Constraints from basalt alteration experiments. *Earth and Planetary Science Letters* **101**, 388-403.

Seyfried W. E., Jr. (1987) Experimental and theoretical constraints on hydrothermal alteration processes at mid-ocean ridges. *Annual Review of Earth and Planetary Sciences* **15**, 317-335.

Seyfried W. E., Jr. and Bischoff J. L. (1979) Low temperature basalt alteration by seawater: an experimental study at 70 °C and 150 °C. *Geochimica et Cosmochimica Acta* **43**(12), 1937-1947.

Seyfried W. E., Jr. and Bischoff J. L. (1981) Experimental seawater-basalt interaction at 300°C, 500 bars, chemical exchange, secondary mineral formation and implications for the transport of heavy metals. *Geochimica et Cosmochimica Acta* **45**(2), 135-147.

Spiess F. N., Macdonald K. C., Atwater T., Ballard R., Carranza A., Cordoba D., Cox C., Garcia V. M. D., Francheteau J., Guerrero J., Hawkins J., Haymon R., Hessler R., Juteau T., Kastner M., Larson R., Luyendyk B., Macdougall J. D., Miller S., Normark W., Orcutt J., and Rangin C. (1980) East Pacific Rise: Hot springs and geophysical experiments. *Science* **207**, 1421-1433.

Stanton R. L. (1994) Ore elements in arc lavas. In *Oxford Monographs on Geology and Geophysics*, Vol. 29, pp. 391.

Taylor B. (1979) Bismarck Sea; Evolution of a back-arc basin. *Geology* **7**, 171-174.

Tivey M. A., Bach W., Seewald J. S., Tivey M. K., Vanko D. A., and Shipboard Science and Technical Teams. (2007) Cruise Report R/V Melville, MAGELLAN-06. Hydrothermal systems in the Eastern Manus Basin: Fluid chemistry and magnetic structures as guides to subseafloor processes, pp. 67. Woods Hole Oceanographic Institution.

Tivey M. K. (1995) The influence of hydrothermal fluid composition and advection rates on black smoker chimney mineralogy: Insights from modeling transport and reaction. *Geochimica et Cosmochimica Acta* **59**, 1933-1949.

Tivey M. K. (2007) Generation of seafloor hydrothermal vent fluids and associated mineral deposits. *Oceanography* **20**, 50-65.

Tivey M. K., Humphris S. E., Thompson G., Hannington M. D., and Rona P. A. (1995) Deducing patterns of fluid flow and mixing within the TAG active hydrothermal mound using mineralogical and geochemical data. *Journal of Geophysical Research* **100**(B7), 12527-12555.

Tivey M. K. and McDuff R. E. (1990) Mineral precipitation in the walls of black smoker chimneys: A quantitative model of transport and chemical reaction. *Journal of Geophysical Research* **95**(B8), 12617-12637.

Tivey M. K., Stakes D. S., Cook T. L., Hannington M. D., and Petersen S. (1999) A model for the growth of steep-sided vent structures on the Endeavour Segment of the Juan de Fuca Ridge: Results of a petrologic and geochemical study. *Journal of Geophysical Research* **104**(B10), 22,859.

Tufar W. (1990) Modern hydrothermal activity, formation of complex massive sulfide deposits and associated vent communities in the Manus back-arc basin (Bismarck Sea, Papua New Guinea). *Mitteilungen der Osterreichischen Geologischen Gesellschaft* **82**, 183-210.

Tunnicliffe V. (1991) The biology of hydrothermal vents: Ecology and evolution. *Oceanography and Marine Biology Annual Reviews* **29**, 319-407.

Von Damm K. L. (1990) Seafloor hydrothermal activity: Black smoker chemistry and chimneys. *Annual Review of Earth and Planetary Sciences* **18**(1), 173-204.

Von Damm K. L. (1995) Controls on the chemistry and temporal variability of seafloor hydrothermal fluids. In *Seafloor Hydrothermal Systems: Physical, Chemical, Biological and Geological Interactions. Geophysical Monograph.*, Vol. 91 (ed. S. E. Humphris, R. A. Zierenberg, L. S. Mullineaux, and R. E. Thomson), pp. 222-247. American Geophysical Union.

Welhan J. A. and Craig H. (1983) Methane, hydrogen and helium in hydrothermal fluids at 21°N East Pacific Rise. In *Hydrothermal Processes at Seafloor Spreading Centers* (ed. P. Rona, K. Boström, L. Laubier, and K. L. Smith), pp. 391-409. Plenum Press.

Yang K. and Scott S. D. (1996) Possible contribution of a metal-rich magmatic fluid to a sea-floor hydrothermal system. *Nature* **383**, 420-423.

Yang K. and Scott S. D. (2002) Magmatic Degassing of volatiles and ore metals into a hydrothermal system on the modern seafloor of the Eastern Manus Back-Arc Basin, Western Pacific. *Economic Geology* **97**(5), 1079-1100.

Yeats C. J., Binns R. A., and Parr J. M. (2000) Advanced argillic alteration associated with actively forming submarine polymetallic sulfide mineralization in the eastern Manus Basin, Papua New Guinea. *Geological Society of Australia Abstracts* **59**, 555.

CHAPTER 2

Sub–seafloor Processes Controlling Rare Earth Element Compositions of Vent Fluids in Hydrothermal Systems from the Manus Back–Arc Basin, Papua New Guinea

1. INTRODUCTION

The distribution and behavior of the rare earth elements (REEs) have been used extensively as a tracer of sub–seafloor processes associated with hydrothermal activity. The REEs are of interest because they provide information about a wide range of geochemical processes including fluid–rock interaction and conditions of mineral precipitation and/or remobilization in hydrothermal environments. Studies have examined the distributions of REEs in hydrothermal fluids (Michard et al., 1983; Michard and Albarede, 1986; Michard, 1989; Klinkhammer et al., 1994; Mitra et al., 1994; Bau and Dulski, 1999; Douville et al., 1999), in associated mineral deposits (Graf, 1977; Bau and Dulski, 1995; Mills and Elderfield, 1995; Smith et al., 2000; Bach et al., 2003; Humphris and Bach, 2005) and in hydrothermally–altered volcanic rocks (Alderton et al., 1980; Humphris, 1984; Lottermoser, 1990; Fulignati et al., 1999).

Studies of REEs in seafloor vent fluids have focused mostly on basalt–hosted hydrothermal systems along mid–ocean ridges (MORs). MOR hydrothermal fluids have remarkably uniform chondrite–normalized REE distributions (REE_N pattern shape) characterized by a light REE enrichment and large, positive Eu anomaly (Michard et al., 1983; Michard and Albarede, 1986; Klinkhammer et al., 1994; Mitra et al., 1994; Douville et al., 1999). Although REEs in hydrothermal fluids are derived primarily from the crust, sub–seafloor processes that regulate their composition in vent fluids are not well–constrained. It has been hypothesized that dissolution of REEs from plagioclase controls the pattern shape of these elements in seafloor hydrothermal fluids because the chondrite–normalized REE compositions of MOR hydrothermal fluids and of plagioclase in basalt are similar (Campbell et al., 1988; Klinkhammer et al., 1994). In contrast, results of experimental studies suggest that REE compositions of seafloor vent fluids are unrelated to primary rock composition (e.g., plagioclase alteration) because REE_N pattern shapes of experimental hydrothermal solutions are different from primary REE compositions of the volcanic rock or individual minerals with which these fluids have reacted (Bach and Irber, 1998; Möller, 2002; Allen and Seyfried, 2005). Rather, experimental studies suggest that seafloor vent fluid REE compositions reflect solubility controls influenced by aqueous REE speciation/complexation (c.f. Bau, 1991). Accordingly, REE compositions of hydrothermal fluids may be primarily controlled by aspects of fluid chemistry (e.g., temperature, pH, ligand concentrations) that can affect the mobility of REEs and potentially fractionate the REEs during sub–seafloor hydrothermal processes (e.g., fluid–rock interaction).

This study reports REE data for a large number of seafloor vent fluids from four active hydrothermal systems in the Manus back–arc basin, Papua New Guinea. Among these vent fields, the composition of underlying crustal host rocks differs significantly, ranging from basalt to rhyolite (Sinton et al., 2003; Bach et al., 2007). In addition, the compositions of vent fluids (e.g., temperature, pH, salinity, concentrations of complexing ligands) differ substantially (Seewald et al., 2006). This study examines the relationship between measured aqueous REE compositions and fluid and host rock compositions to identify whether aqueous REE distributions are controlled primarily by the REE composition of the host rock or by aspects of fluid chemistry that affect REE solubility and mobility during sub–seafloor fluid–rock interactions.

Limited data exists for REE compositions of vent fluids and deposits (anhydrite) recovered from the Manus Basin (Douville et al., 1999; Bach et al., 2003). Bach et al (2003) have proposed that heterogeneous chondrite–normalized REE pattern shapes recorded by anhydrite reflect changes in fluid composition (changes in Cl^-, F^- and SO_4^{2-} ligand concentrations) and differences in aqueous REE mobility resulting from varying inputs of magmatic volatiles (H_2O–CO_2–HCl–HF–SO_2) in the Manus Basin. Using new fluid data for the REEs, it is possible to test this hypothesis and therefore to better understand the potential for the REEs in seafloor hydrothermal fluids to constrain a wide range of sub–seafloor geochemical processes that affect the evolution of vent fluids in submarine hydrothermal systems.

2. GEOLOGIC SETTING

The Manus Basin in the Bismarck Sea, Papua New Guinea (Figure 2.1) is a rapidly–opening (~ 100 mm/yr) back–arc basin associated with subduction of the Solomon Microplate beneath the New Britain arc (Taylor, 1979; Davies et al., 1987; Martinez and Taylor, 1996). Crustal extension and spreading are complex and variable and occur along several distinct lineations.

Toward the west is the Manus Spreading Center (MSC) bounded between the Willaumez and Djaul transform faults (Martinez and Taylor, 1996). Lavas erupted at the MSC are dominantly basaltic in composition (Both et al., 1986; Sinton et al., 2003). Several areas of hydrothermal activity have been identified in the MSC (Figure 2.1a); Vienna Woods is the largest and most active of the known fields (Tufar, 1990). It is located slightly south of the major spreading center within an axial rift valley at a water depth of ~ 2500 m.

To the east, the Eastern Manus Basin (EMB) is bounded by the Djaul and Weitin transform faults where rapid spreading is accommodated primarily by rifting and extension of existing crust (Martinez and Taylor, 1996). Lavas are erupted as a series of discrete *en echelon* neovolcanic ridges and volcanic domes of felsic (andesite–to–rhyolite) composition (Sinton et al., 2003). The arc–affinity of volcanic lavas (Sinton et al., 2003) is consistent with the proximal location (< 200 km) of the EMB to the actively subducting margin. The EMB hosts several known active hydrothermal systems (Figure 2.1b). The Papua New Guinea–Australia–Canada–Manus

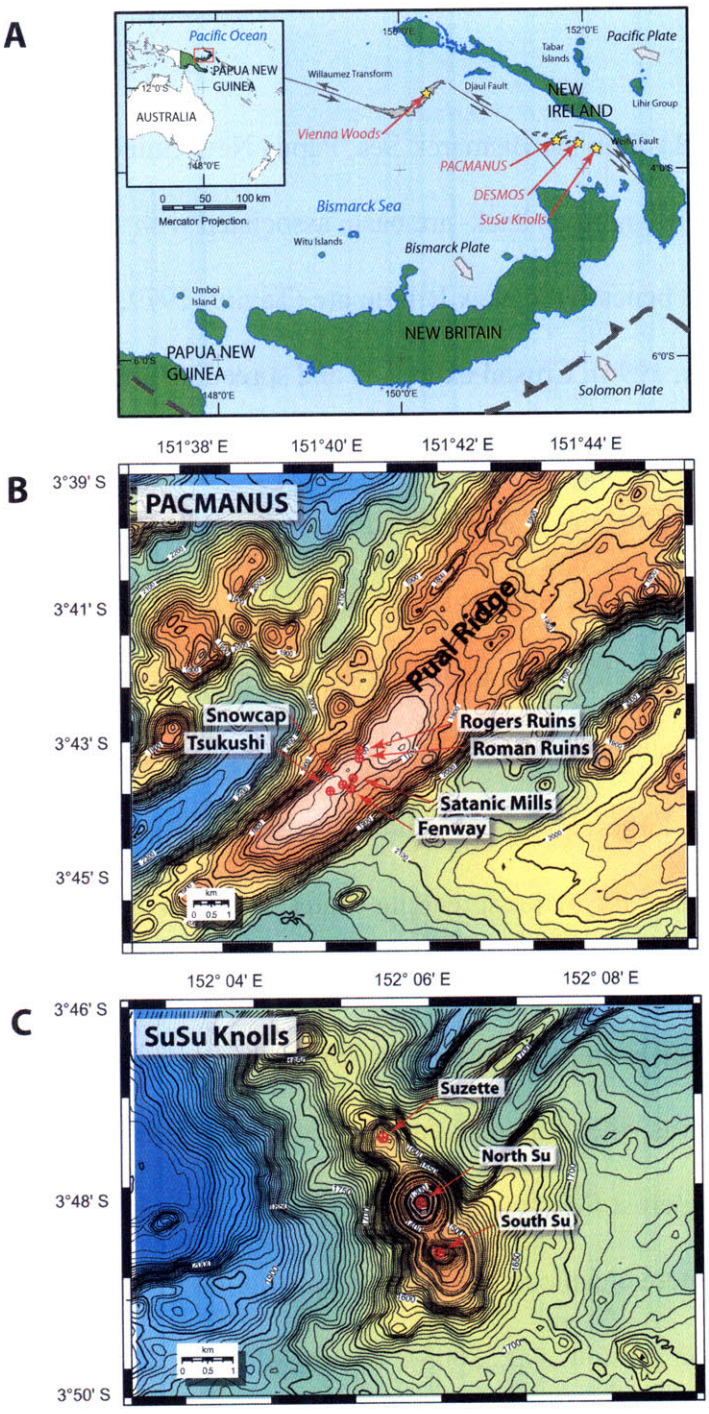

Figure 2.1. A) Regional tectonic setting of the Manus Basin, Papua New Guinea, indicating active plate motion and areas of known hydrothermal activity. Gray arrows indicate directions of plate motion. **B**) Distribution of hydrothermal deposits at PACMANUS. **C**) Distribution of hydrothermal deposits at SuSu Knolls. Bathymetry based on EM300 SeaBeam sonar (modified from Tivey et al., 2007).

(PACMANUS) hydrothermal system is located on the crest of the 35 km long, 500 m high Pual Ridge, between water depths of 1650 and 1740 m (Binns and Scott, 1993). The ridge is constructed of several sub–horizontal lava flows with compositions between andesite and dacite (Binns and Scott, 1993; Sinton et al., 2003). There are several discrete vent fields within the PACMANUS system (Figure 2.1b) that exhibit varying styles of hydrothermal activity from high–temperature (> 300 °C) black smoker fluid venting from sulfide–rich chimneys to low–temperature diffuse flows through cracks in lavas and sedimentary material. Further to the east, the DESMOS and SuSu Knolls hydrothermal systems are located on individual volcanic domes in environments markedly different from ridge–hosted hydrothermal fields. DESMOS (Onsen field, water depth of 1900 – 2000 m) is a collapse caldera that features a roughly crescent–shaped morphology with felsic pillow flows and hyaloclastite deposits arranged across several terraces forming the slopes of the caldera (Sakai et al., 1991; Gamo et al., 1997). Sedimentation and alteration of primary lavas is common and includes Fe–oxide staining, pervasive bleaching (acid–sulfate alteration), locally abundant native sulfur flows and extensive microbial mats (Sakai et al., 1991; Gamo et al., 1997). Further east, SuSu Knolls consists of three discrete volcanic cones (Suzette, North Su and South Su; Figure 2.1c) at water depths between ~ 1140 and 1510 m (Binns et al., 1997; Tivey et al., 2007). The North Su and South Su domes are composed of abundant porphyritic dacite flows showing variable acid–sulfate–type alteration (i.e., alunite, native sulfur) and sedimentation by mixed volcaniclastic and hydrothermal material (Binns et al., 1997; Yeats et al., 2000; Hrischeva et al., 2007; Tivey et al., 2007). The dome at Suzette

is extensively coated in metalliferous sediment and relic sulfide talus that overlies primary volcanic features (Hrischeva et al., 2007; Tivey et al., 2007) suggesting that hydrothermal activity has been long–lived.

2.1. Hydrothermal activity

2.1.1. Vienna Woods

Current hydrothermal activity is manifest as both focused and diffuse fluid venting within an area of ~ 150 m by 100 m (Tufar, 1990; Tivey et al., 2007). Inactive sulfide chimneys extend across a total area ~ 300 m by 100 m. The vent fluids sampled are black–gray smoker fluids that have temperatures between 273 and 283 °C and are mildly acidic (pH (25 °C) ~ 4.2 – 4.7) and that exit from the tops of large sulfide–rich chimneys up to 7 m in height (Seewald et al., 2006).

2.1.2. PACMANUS

Current hydrothermal activity occurs at several discrete vent fields (Roman Ruins, Roger's Ruins, Satanic Mills, Snowcap, Tsukushi and Fenway) that are between 50 and 200 m in diameter (Binns et al., 2007; Tivey et al., 2007). Vent fluids with a range of temperature and composition were sampled from these fields, including high temperature fluids (~ 300 – 358 °C) with focused discharges from black smoker chimneys, lower temperature white/gray smoker fluids (150 – 290 °C) discharging from "diffuser" chimneys, and low temperature diffuse fluids (< 100 °C) exiting through cracks in the volcanic basement or metalliferous deposits and sediments. The measured pH (25 °C) of all vent fluids with temperatures above 240 °C are low and between 2.3 and 2.8 (Seewald et al., 2006).

2.1.3. DESMOS

Hydrothermal activity occurs at the Onsen field (Gamo et al., 1997), which is a small (~ 30 m diameter) area of low–temperature fluid discharge located along the northern interior slope of the DESMOS caldera. Fluid venting is manifest as thick, milky–white smoke discharging directly through extensively altered volcanic breccia and hydrothermal sediments composed of abundant native sulfur and anhydrite (Gamo et al., 1997; Seewald et al., 2006; Bach et al., 2007). Despite the low temperature of sampled fluids (≤ 120 °C), the measured pH (25 °C) are very acidic < 1.5 (Seewald et al., 2006). Hydrothermal activity is markedly different from high–temperature black smoker fluids. On the basis of aqueous compositions, these fluids have been informally termed 'acid–sulfate' fluids (Gamo et al., 1997).

2.1.4. SuSu Knolls

At SuSu Knolls, hydrothermal activity and vent fluid compositions are remarkably diverse (Seewald et al., 2006). At North Su, the summit of the dome is dominated by a large sulfide–rich black smoker complex up to 11 m in height. Vent fluids sampled from this complex are similar to high–temperature black smoker fluids sampled from PACMANUS, with temperatures between 300 and 325 °C and moderately low pH (25 °C) between 2.8 and 3.2 (Seewald et al., 2006). In contrast, the flanks of the dome are dominated by extensive fluid discharge similar to that of acid–sulfate fluids sampled from DESMOS. Acid–sulfate fluids from North Su have a milky–white color, low temperatures (48 – 241 °C) and are very acidic (pH (25 °C) ≤ 1.8) (Seewald et al., 2006) and exit through cracks in hyaloclastite flows, extensively

altered volcanic breccia and hydrothermal sediments composed of native sulfur and anhydrite (Yeats et al., 2000; Bach et al., 2007; Tivey et al., 2007).

There is currently limited hydrothermal activity at South Su. This vent field is characterized by outcrops of both fresh and variably altered volcanics overlain by mostly inactive sulfide chimneys and scattered oxide–stained hydrothermal sediments (Yeats et al., 2000; Hrischeva et al., 2007; Tivey et al., 2007). In an area of diffuse venting toward the NW, extensively altered and bleached volcanic rocks were observed (Tivey et al., 2007). High–temperature fluid venting from scattered "beehive"–type chimneys was observed and sampled in two areas toward the S and SE. The temperatures of these fluids were up to 290 °C. The pH (25 °C) of these fluids is low ~ 2.6 – 2.7 (Seewald et al., 2006).

The smaller dome of Suzette, located NW of North Su and South Su, is extensively covered by volcanic breccia, hydrothermal sediment, mass–wasted sulfide talus, Fe–oxide crusts and limited exposures of possible hydrothermal stockwork (Hrischeva et al., 2007; Tivey et al., 2007). The summit is characterized by large expanses of both relic and scattered, active sulfide chimneys often buried within thick sediment. Hydrothermal activity is intermittent over broad sections of the Suzette mound. Five high–temperature fluids venting from sulfide–rich chimney edifices were sampled. The temperatures range from 226 – 303 °C and measured pH (25 °C) from 3.5 to 3.8 (Seewald et al., 2006). A sixth fluid was sampled from a cracked pavement structure; this fluid had a temperature of ~ 249 °C and a considerably more acidic pH (25 °C) of ~ 2.3 (Seewald et al., 2006).

3. METHODS

3.1. Sample collection and processing

Hydrothermal fluid samples were collected during *R/V Melville* cruise MGLN06MV (July – September, 2006) using discrete samplers mounted on and actuated by ROV *Jason II*. Samples were collected in 755 ml Ti–syringes ("major" samplers (Von Damm et al., 1985)) and 160 ml isobaric gas–tight samplers ("IGT" samplers (Seewald et al., 2002)) and were selected to represent the range of venting styles identified. In all cases, fluids were sampled in triplicate allowing an assessment of uncertainties and calculation of end–member fluid compositions (i.e., extrapolated to zero Mg (Von Damm et al., 1985)). Temperatures were measured with either the ROV temperature probe or with a thermocouple mounted directly on the IGT samplers.

Sample aliquots for chemical analysis were extracted immediately after recovery of samplers at the end of each dive operation. Fluid samples were drawn into clean polyethylene bottles. Aliquots of fluid drawn for REE and other trace element analysis were immediately acidified to pH < 2 by addition of Fisher Optima™ grade HCl to prevent precipitation of metal sulfides and sulfates from solution during storage prior to on–shore analysis. For Ti–syringe samples, this required addition of ~ 1 ml HCl to a volume of ~ 500 ml vent fluid and for gas–tight samples ~ 100 µl HCl to a volume of 25 ml vent fluid. These aliquots ("dissolved" fraction) were stored in acid cleaned, high–density polyethylene (HDPE) Nalgene™ bottles. In nearly all major and gas–tight samplers, a precipitate ("dregs" fraction) formed on the interior walls of the sampler as

the hydrothermal fluid cooled. The dregs were collected on a 0.22 μm pore–size, 45 mm diameter Nylon filter by rinsing with high–purity acetone and Milli–Q water. The Nylon filters were dried and stored in glass vials for on–shore processing. In addition, minor precipitates formed within several acidified aliquots during storage (referred to here as "bottle–filter" fraction). These precipitates were separated from the fluid by filtering through 0.22 μm pore–size, Nuclepore® filters as part of shore–based sample processing. The relative proportions of dregs and bottle–filter fractions formed was non–systematic among samples and was likely related to the variable time delay between sample collection and shipboard processing.

In order to obtain accurate data for concentrations of many trace elements in hydrothermal fluids (e.g., Fe, Cu, Zn, Pb, REE, etc.) it is essential to reconstitute the original sample by analyzing all dissolved, dregs and bottle–filter fractions (Trefry et al., 1994). This is best achieved by separate determination of element concentrations in each fraction followed by mathematical reconstitution of the fluid. A mass balance for REEs indicates that for fluids analyzed in this study, approximately 90 % of REEs remained in the dissolved phase.

Dissolved fractions were prepared for analysis by gravimetric dilution of a ~ 0.20 g split of each solution using ultra–pure 5% HNO_3 (Fisher Optima^{TM} grade nitric acid). Sample dilutions were normalized to a 6 mM Cl concentration. This equated to between 80 and 110 times dilution of the original sample and varied as a function of the chlorinity of the fluid. Normalization to uniform Cl content removed the effect of variable matrix (e.g., Na^+) on analyte behavior within the plasma interface of the ICP.

Dregs and bottle–filter fractions were treated separately. Particles were removed from filters into 30 ml Savillex™ vials by rinsing with 5 ml concentrated Fisher Optima™ HNO_3. The vials were sealed and placed on a hot–plate overnight (~ 70 °C) to digest particles. The resulting solutions were then taken to dryness. The acid digestion/evaporation step was repeated a further two times to achieve complete dissolution of the sulfide–sulfate mix. The digested particles were taken up in and quantitatively diluted in 5% HNO_3 acid for analysis.

3.2. Analytical

3.2.1. Determination of REE

Analyses of REEs were performed on a ThermoElectron *Element2* inductively coupled plasma–mass spectrometer (ICP–MS) at the Woods Hole Oceanographic Institution. Solutions were injected into the plasma using a Cetac Aridus® desolvating nebulizer to reduce isobaric interferences (e.g., $^{135}Ba^{16}O^{+}$ on $^{151}Eu^{+}$). Ba and REE oxide formation were monitored throughout the analytical session by periodic aspiration of Ba and Ce spikes. Ba–oxide formation was significantly less than 1 %. Any isobaric interference of BaO^{+} on Eu^{+} would bias (decrease) the naturally occurring $^{151}Eu/^{153}Eu$ ratio (~ 0.89) measured. In almost all samples no bias was observed and no correction for BaO interference was required. REE–oxide formation was typically less than ~ 4 %. Samples were spiked with 1 ppb ^{45}Sc and ^{115}In internal standards to correct for fluctuations of the plasma during the analytical session. Unknown sample concentrations were calibrated against matrix–matched, multi–REE–Y standards prepared from Specpure plasma solution standards. Background intensities were

measured periodically by aspirating ultra–pure 5% HNO_3 blanks. External precision, determined by triplicate analysis of randomly selected samples across multiple analytical sessions, was ~ 10 %.

3.2.2 Calculation of endmember fluid compositions

Artifacts from sampling of vent fluids can include entrainment of ambient seawater, entrainment of chimney and other particles, and precipitation of secondary minerals during cooling and storage of fluids. These artifacts may compromise sample quality and affect measured REE compositions. Typically, seafloor vent fluid compositions are calculated assuming that the hydrothermal fluid contains no Mg (Von Damm, 1983; Von Damm et al., 1985). Calculation of endmember concentrations allows direct comparison of REE compositions among different vent fluids. Endmember compositions were calculated by extrapolation of replicate vent fluid compositions to zero Mg using least–squares linear regression forced to pass through the composition of ambient seawater (Von Damm, 1983).

Acid–sulfate fluids sampled from DESMOS and SuSu Knolls (North Su) were excluded from this mathematical treatment. Measured Mg concentrations of all acid–sulfate fluids venting at the seafloor were consistently high ($\geq$ 39 mmol/kg). It is unlikely that high concentrations of Mg reflect dilution of hydrothermal fluid by seawater during sampling because the pH (25 °C) of all acid–sulfate fluids is extremely low ($\leq$ 1.8). Instead, acid–sulfate fluids venting at the seafloor contain significant amounts of Mg. Accordingly, REE concentrations of acid–sulfate are reported at the lowest measured Mg concentration of replicate fluid samples.

3.3. Thermodynamic species distribution calculations

Thermodynamic aqueous species distribution calculations were carried out for all hydrothermal fluids analyzed in this study to examine the factors that regulate the aqueous mobility of REEs. The calculations were carried out using the program SpecE8 (Geochemist's Workbench®, version 6.0 (Bethke, 1996)) incorporating a thermodynamic database for aqueous species calculated using SUPCRT92 (Johnson et al., 1992) at 50 MPa and 0 to 400°C. We used a SUPCRT92 database that has all updates for inorganic aqueous species up to November 2007 (see OBIGT database for detailed documentation: http://affinity.berkeley.edu/predcent/download/obigt). The extended Debye–Hückel equation was used to calculate activity coefficients with B–dot extended parameters and hard core diameters for each species from Wolery (2003). Dissolved neutral species were assigned an activity coefficient of one, except non–polar species for which CO_2 activity coefficients were used (Drummond, 1981). All aqueous REE species for which thermodynamic properties are known have been considered (Haas et al., 1995). Inclusion of thermodynamic data for Al–fluoride complexes (Tagirov and Schott, 2001) enabled us to examine competition between Al^{3+} and REE^{3+} to form complexes with fluoride (Gimeno Serrano et al., 2000). Reaction path models based on the REACT software package (Geochemist's Workbench®, version 6.0) and the thermodynamic database described above were used to assess changes in fluid composition and REE species distribution due to the titration of HF and SO_2 gas into hydrothermal fluids. In all calculations, mineral precipitation and redox reactions (except H^+/H_2, Fe^{3+}/Fe^{2+}, Mn^{3+}/Mn^{2+}, Cu^{2+}/Cu^+, and Eu^{3+}/Eu^{2+}) were suppressed. This

constraint reflects that calculations are used to predict species distributions prior to mineral precipitation knowing that these reactions can significantly affect fluid pH, redox and aqueous species concentrations.

4. Analytical Results

Calculated concentrations of REEs in hydrothermal fluids recovered from 36 vents (101 total fluid samples) in the Manus basin are reported in Tables 2.1 and 2.2. Concentrations of REEs in seawater and in mid–ocean ridge hydrothermal fluids (21 °N East Pacific Rise) are taken from Mitra et al (1994) and Klinkhammer et al. (1994). The chemical composition (temperature, pH, Na, Mg, Ca, Cl, Al, F, SO_4, CO_2, H_2, H_2S) of a subset of representative seafloor vent fluids used in thermodynamic calculations are reported in Table 2.3 (E. Reeves and J. Seewald, *unpubl. data*). Normalization of REE concentrations to chondrite values (Anders and Grevesse, 1989) is used to compare REE_N pattern shapes and to identify fractionation of REEs among different vent fluids.

4.1. Manus Spreading Center (Vienna Woods)

At Vienna Woods, total REE concentrations are low in all sampled vent fluids (ΣREE ~ 2.6 – 5.8 nmol/kg). Chondrite–normalized REE_N pattern shapes are near parallel, with uniform light–REE (La–Nd) enrichment and a large positive Eu–anomaly (Figure 2.2b). The data are consistent with REE compositions in Vienna Woods hydrothermal fluids determined by previous studies (Douville et al., 1999). The range of concentrations and pattern shapes are similar to abundances of REEs measured in high–

Table 2.1. Rare earth element concentrations (pmol/kg) in smoker vent fluids. Data are extrapolated to zero Mg.

Sample	Vent Site	Mg (mmol/kg)	La	Ce	Pr	Nd	Sm	Eu	Gd	Tb	Dy	Ho	Er	Yb	La_N/Yb_N	La_N/Sm_N	Sm_N/Yb_N	Eu_N/Eu^*_N
VW1	Vienna Woods	0.0	1700	1750	180	532	88	738	81	14	43	14	30	21	43.9	11.2	3.9	26.1
VW2	Vienna Woods	0.0	1021	1244	157	467	81	629	61	10	33	14	25	19	29.1	7.3	4.0	26.2
VW3	Vienna Woods	0.0	740	958	110	291	45	390	32	7	20	19	19	11	36.6	9.6	3.8	29.8
RMR1	Roman Ruins	8.0	9918	12164	977	2599	607	7996	219	31	154	24	67	76	70.8	9.5	7.5	55.0
RMR2	Roman Ruins	16.5	1392	3140	402	1612	395	4072	268	39	294	32	83	84	8.9	2.0	4.4	36.1
RMR3	Roman Ruins	6.4	10829	17413	2186	8326	1772	18162	1267	151	708	98	249	192	30.5	3.6	8.6	35.2
RMR4	Roman Ruins	3.2	13262	23871	3002	10835	2201	11863	1405	164	727	103	242	202	35.6	3.5	10.1	19.2
RGR1	Roger's Ruins	4.5	7071	12328	1540	6447	1511	8374	1044	111	476	60	147	92	41.5	2.7	15.2	19.3
RGR2	Roger's Ruins	9.0	1390	2653	274	1035	299	2042	277	34	161	21	51	53	14.2	2.7	5.2	21.2
SM1	Satanic Mills	8.8	1617	3950	570	2588	813	4058	647	87	424	69	170	143	6.1	1.2	5.3	16.5
SM2	Satanic Mills	17.4	480	1163	182	1009	566	984	2303	575	4039	697	1901	1404	0.2	0.5	0.4	2.2
SM3	Satanic Mills	10.1	1317	3031	501	2612	1283	3027	2084	315	1664	270	725	541	1.3	0.6	2.2	5.6
SC1	Snowcap	31.0	499	928	103	396	186	237	130	35	251	58	188	158	1.7	1.6	1.1	4.4
SC2	Snowcap	24.0	619	1454	123	500	99	246	88	21	123	28	70	70	4.8	3.7	1.3	7.9
TK1	Tsukushi	44.0	1470	3148	349	1397	379	881	335	81	452	135	357	262	3.0	2.3	1.3	7.3
F1	Fenway	5.8	959	2200	259	1397	2085	8217	2313	315	1493	226	592	448	1.2	0.3	4.3	11.3
F2	Fenway	4.7	21528	37103	4348	15794	3113	9296	2161	273	1321	180	442	343	34.0	4.0	8.4	10.4
F3	Fenway	4.5	16318	29560	3699	15230	3699	8431	2992	348	1632	223	511	315	28.0	2.6	10.9	7.5
F4	Fenway	9.4	3609	10984	1444	6328	1937	6087	2370	517	3729	463	1383	1083	1.8	1.1	1.7	8.6
F5	Fenway	44.7	9925	23799	2836	10482	2633	5443	3317	557	3848	N.D.	1063	506	10.6	2.2	4.8	5.6
SZ1	Suzette	4.4	3777	6228	788	2831	482	2976	316	35	177	27	70	67	30.7	4.6	6.7	21.8
SZ2	Suzette	8.6	3660	6209	738	2897	646	3194	441	48	227	32	90	78	25.3	3.3	7.7	17.3
SZ3	Suzette	5.5	3368	6921	1054	5162	1442	5324	933	97	386	55	122	92	19.8	1.4	14.5	13.1
SZ4	Suzette	8.3	1020	2077	301	1352	327	1888	251	36	147	50	63	48	11.6	1.8	6.4	19.3
SZ5	Suzette	6.4	2711	4625	755	4495	2893	1473	4525	834	5239	976	2808	2345	0.6	0.5	1.1	1.2
SZ6	Suzette	8.0	2711	4811	693	2976	708	5866	536	52	225	30	70	63	23.3	2.2	10.5	27.8
NS3	North Su	0.0	10689	18408	2075	6913	840	3089	424	41	179	29	66	60	96.5	7.4	13.0	14.1
NS5	North Su	7.4	964	1960	380	2342	867	2700	306	23	104	18	43	58	9.0	0.6	13.9	13.1
NS6	North Su	0.0	590	690	99	470	282	1502	399	59	318	54	142	147	2.2	1.2	1.8	13.5
SS1	South Su	5.3	592	1381	139	499	222	201	234	63	576	101	260	181	1.8	1.6	1.1	2.6
SS2	South Su	6.8	547	775	80	236	69	708	58	15	71	18	53	66	4.5	4.6	1.0	33.0
HG81[a]	21 °N EPR	0.0	2100	3980	510	1980	450	1980	440	56	310	49	108	67	17.0	2.7	6.3	13.3
Seawater[b]		52.7	29.0	5.5	4.4	21.4	4.1	1.1	6.3	0.9	6.4	1.7	5.5	5.4				

[a] HG81 is a vent fluid sampled from Hanging Garden, 21 °N East Pacific Rise in 1981. Data reported by Klinkhammer et al., (1994).

[b] Seawater data from Mitra et al., (1994).

N.D. = no data available.

Table 2.2. Rare earth element concentrations (pmol/kg) in acid-sulfate fluids. Data are reported at the lowest measured Mg.

Sample	Vent Site	Mg (mmol/kg)	La	Ce	Pr	Nd	Sm	Eu	Gd	Tb	Dy	Ho	Er	Yb	La_N/Yb_N	La_N/Sm_N	Sm_N/Yb_N	Eu_N/Eu^*_N
D1	DESMOS	46.0	17862	54166	7331	31845	7830	2948	7283	1160	6980	1330	4044	3826	2.5	1.3	1.9	1.2
D2	DESMOS	50.4	20805	71826	11431	55550	15736	6526	14321	2267	13865	2595	7773	7336	1.5	0.8	2.0	1.3
NS1	North Su	49.0	10923	35507	4755	19616	4699	1782	4452	718	4452	876	2793	2846	2.1	1.4	1.5	1.2
NS2	North Su	38.8	25597	98058	16244	83537	25511	8865	26764	4323	26644	5155	15724	15225	0.9	0.6	1.6	1.0
NS4	North Su	23.5	12657	47812	6540	29310	9834	3549	13534	2355	15301	3064	9287	8503	0.8	0.7	1.1	0.9

Table 2.3. Chemical compositions of vent fluids used for REE species distribution calculations

Sample [‡]	Vent Site	Temp (°C)	pH (25 °C)	Mg (mmol/kg)	Cl (mmol/kg)	Na (mmol/kg)	Ca (mmol/kg)	K (mmol/kg)	SiO_2 (mmol/kg)	Al (µmol/kg)	SO_4 (mmol/kg)	H_2S (mmol/kg)	H_2 (µmol/kg)	CO_2 (mmol/kg)	F (µmol/kg)
VW1	Vienna Woods	282	4.4	0.0	663	512	80.0	21.2	15.3	7.4	0.6	2.0	42	4.4	21
RMR2	Roman Ruins	272	2.3	16.5	529	435	10.5	50.5	13.5	5.6	3.0	2.9	29	18.8	92
RMR4	Roman Ruins	341	2.6	3.2	625	495	22.3	77.2	17.8	6.0	1.1	6.3	53	9.5	125
SM1	Satanic Mills	295	2.6	8.8	499	407	12.5	60.5	12.2	7.0	2.1	8.0	25	181.2	167
SM2	Satanic Mills	241	2.4	17.4	437	374	5.9	38.6	12.8	4.5	7.1	4.5	4	112.0	287
D1	DESMOS	117	1.0	46.0	475	391	9.4	8.3	8.1	480	147	0	4	26.7	137
NS2	North Su	215	0.9	38.8	425	340	8.9	7.8	10.0	1075	149	0	20	93.3	103
SZ5	Suzette	249	2.3	6.4	586	493	24.2	44.3	14.1	16.4	4.1	4.8	7	15.8	480
HG81	21 °N EPR	350	3.3	0.0	496	443	11.7	23.9	15.6	4.5	0.5	8.4	10	6.0	5

[‡] Fluid data provided by J. Seewald and E. Reeves (*unpublished data*) and P. Craddock (*unpublished data*), except for fluid sample HG81 (Hanging Gardens, 21 °N East Pacific Rise) taken from Welhan and Craig (1983) and Von Damm et al. (1985).

temperature (≥ 280 °C) vent fluids from basalt–hosted, mid–ocean ridge hydrothermal sites (Figure 2.2a) (Michard et al., 1983; Michard, 1989; Klinkhammer et al., 1994; Mitra et al., 1994; Douville et al., 1999).

4.2. Eastern Manus Basin (PACMANUS, DESMOS and SuSu Knolls)

Many hydrothermal fluids sampled from the Eastern Manus Basin have high REE concentrations, enriched by up to two orders of magnitude relative to fluids from Vienna Woods, and have different REE_N pattern shapes. At PACMANUS, total concentrations of REEs range from ~ 1.5 – 88 nmol/kg. The REE_N pattern shapes of most sampled fluids are variably light–REE enriched with a positive Eu–anomaly (Figure 2.3). Two vent fluids – Satanic Mills (sample "SM2") and Fenway (sample "F1") – have REE_N pattern shapes that show heavy–REE (Dy–Yb) enrichments and a range of positive Eu–anomalies (Figure 2.3).

At DESMOS, REE concentrations in acid–sulfate fluids (ΣREE ~ 147 – 236 nmol/kg) are significantly greater than those of sampled high–temperature black smoker fluids (see also Douville et al., 1999), but are similar to those measured in low pH acid–sulfate fluids from geothermal environments (e.g., Valles Caldera, N.M. (Michard, 1989); Rotokawa and Waiotapu, NZ (Wood, 2001)). Chondrite–normalized REE_N pattern shapes are broadly flat with a slight convex–upward curvature and no clear positive or negative Eu–anomaly (Figure 2.4a), and are clearly different than REE_N pattern shapes of seafloor smoker–type fluids sampled from the Manus Basin and mid–ocean ridges.

Rare earth element concentrations and chondrite–normalized REE_N pattern

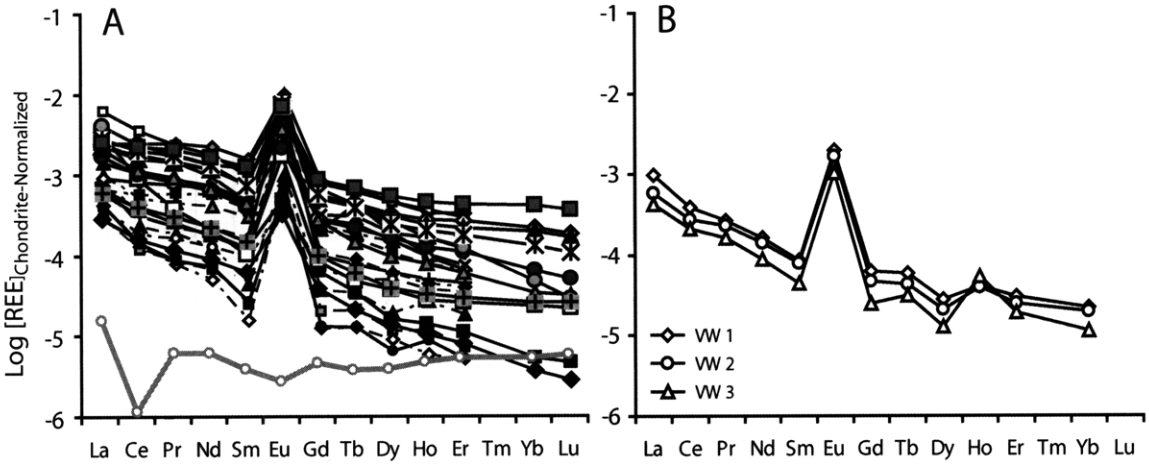

Figure 2.2. Chondrite-normalized REE patterns of **A**) modern seawater (—○—) and vent fluids from basalt-hosted, mid-ocean ridge hydrothermal sites, including samples from Escanaba Trough, Guaymas Basin, 21 °N EPR, 13 °N EPR, 17 °S EPR, Menez Gwen, TAG Active Mound, Lucky Strike and Snakepit. Data from Mitra et al., (1994); Klinkhammer et al., (1994) and Douville et al., (1999). **B**) vent fluids sampled from Vienna Woods, Manus Spreading Center (this study).

shapes differ significantly among hydrothermal fluids sampled from vent fields at SuSu Knolls (Figure 2.4b–d). Total concentrations of REEs in black/gray smoker fluids from North Su, South Su and Suzette range from ~ 6.5 to 43 nmol/kg. The REE_N pattern shapes of most black/gray smoker fluids are light–REE enriched with pronounced positive Eu–anomalies (Figure 2.4b, d). Some smoker fluids sampled from Suzette (sample "SZ5") and South Su (sample "SS1") have REE_N pattern shapes that exhibit greater enrichment of heavy REEs and smaller Eu–anomalies relative to other smoker fluids sampled from the same vent field (Figure 2.4b, d). Total concentrations of REEs in acid–sulfate fluids sampled from North Su range from ~ 93 to 350 nmol/kg. These fluids exhibit REE_N pattern shapes that are broadly flat with no clear Eu–anomaly (Figure 2.4c) and are similar to REE_N pattern shapes of acid–sulfate fluids sampled from DESMOS.

5. DISCUSSION

5.1. Controls on aqueous REE compositions of seafloor hydrothermal fluids

Rare earth elements (REE) in hydrothermal fluids are derived principally from the oceanic crust during high–temperature fluid–rock interaction. The primary factors that control the observed chondrite–normalized REE_N distribution of seafloor vent fluids, however, are unclear. It has been hypothesized that REE_N pattern shape of vent fluids directly reflects the REE composition of the crustal host rock (or minerals within the host–rock, such as plagioclase) subject to alteration and leaching (Campbell et al.,

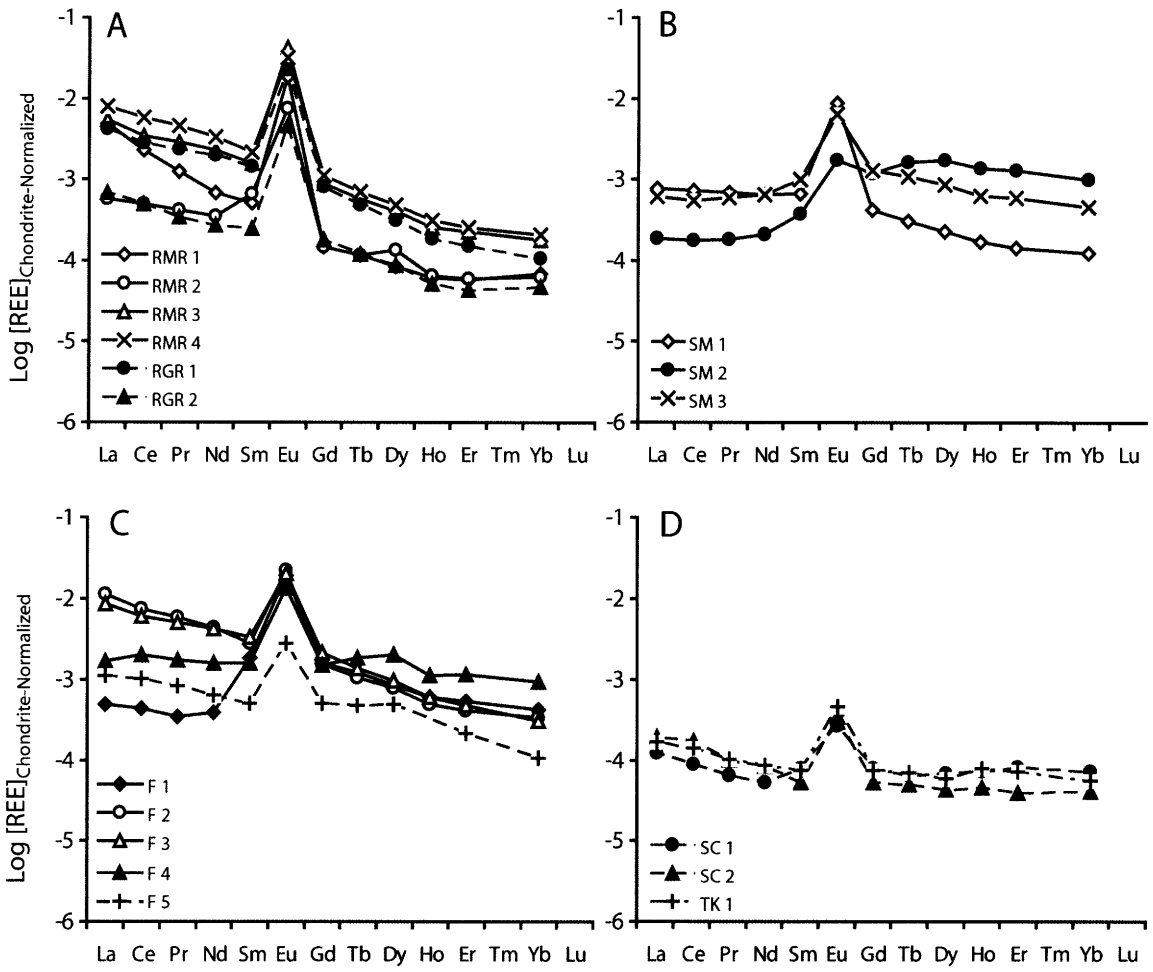

Figure 2.3. Chondrite-normalized REE patterns for high- and low-temperature smoker vent fluids sampled from the PACMANUS hydrothermal area, Eastern Manus Basin: **A**) Roman Ruins-Roger's Ruins, **B**) Satanic Mills, **C**) Fenway and, **D**) Snowcap and Tsukushi.

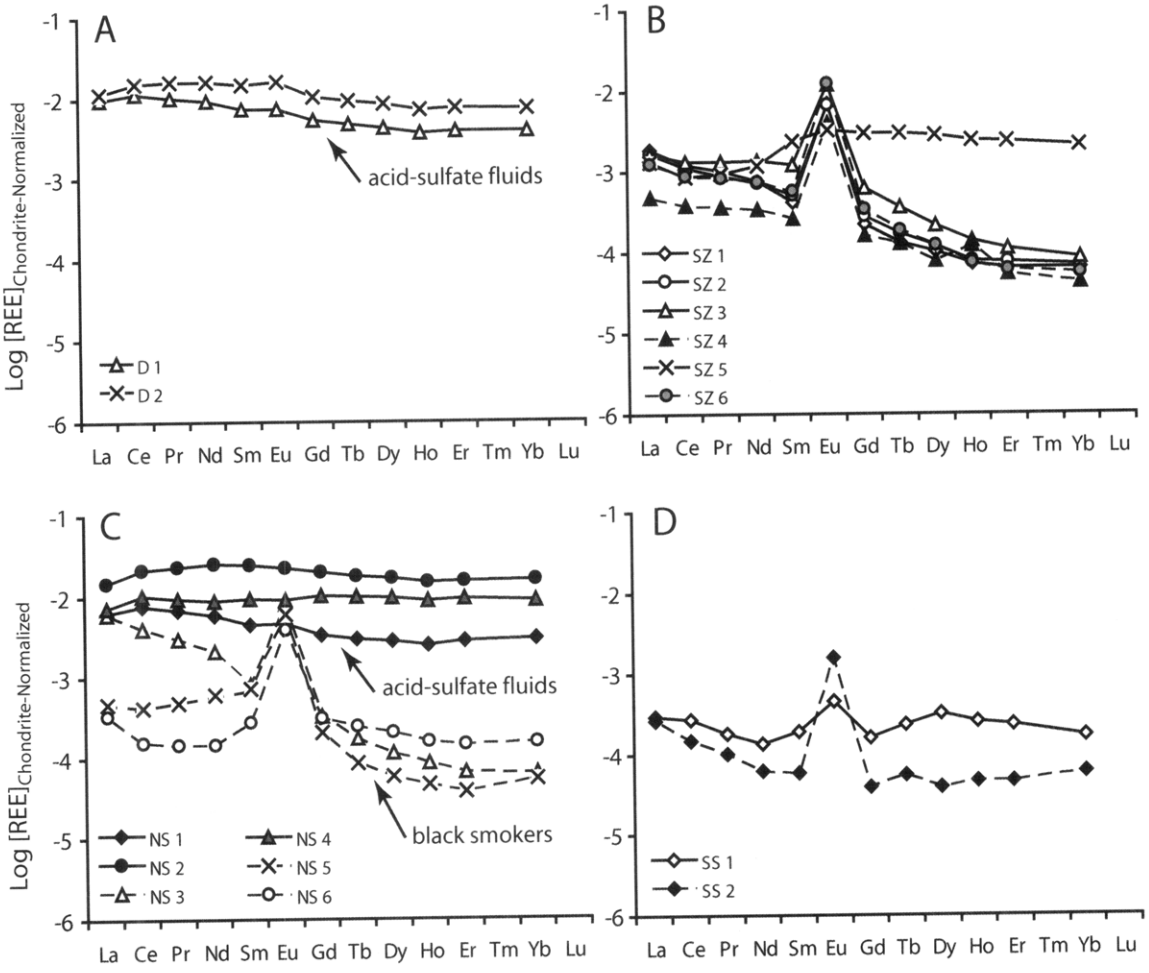

Figure 2.4. Chondrite-normalized REE patterns of fluids sampled from DESMOS and SuSu Knolls hydrothermal areas in the Eastern Manus Basin: **A**) acid-sulfate fluids from DESMOS, **B**) smoker fluids from Suzette, **C**) acid-sulfate (filled symbols) and smoker fluids (open symbols) from North Su, and **D**) smoker fluids from South Su.

1988; Klinkhammer et al., 1994). Alternatively, it has been proposed that REE_N pattern shapes of vent fluids are controlled primarily by fluid chemistry (e.g., pH, redox, ligand concentrations), temperature and alteration mineralogy that control the solubility and fractionation of REEs during fluid–rock interaction (Bau, 1991; Bach and Irber, 1998; Allen and Seyfried, 2005).

A plot of total REE concentration in Manus Basin vent fluids versus pH suggests that, overall, REE solubility in hydrothermal fluids increases with fluid acidity (Figure 2.5) although some differences between high– and low–temperature fluids are also apparent. REE concentrations in acid–sulfate fluids from DESMOS and SuSu Knolls are higher relative to black and gray smoker fluids sampled from all vent fields. Similarly, REE concentrations are higher in low pH smoker fluids from PACMANUS and SuSu Knolls relative to high pH smoker fluids sampled from Vienna Woods. Similar correlations in hydrothermal fluids sampled from a range of geologic environments, including basalt–hosted mid–ocean ridge (Michard and Albarede, 1986; Michard, 1989; Douville et al., 1999) and continental geothermal systems (Michard, 1989; Lewis et al., 1997; Wood, 2001) support this relationship. Departures from this pH relationship occur in several lower–temperature (~ 62 – 288 °C) vent fluids (Figure 2.5). Processes that may affect differences between high and low temperature fluids including phase separation and mineral precipitation/dissolution resulting from mixing between hydrothermal fluids and seawater and are discussed in Section 5.3. These trends support that changes in fluid acidity and temperature affect considerably mobilization of the REEs (and other elements) during sub–seafloor fluid–rock

interaction and may affect observed concentrations of REE in seafloor vent fluids.

Chondrite–normalized REE_N pattern shapes of vent fluids also correlate with differences in fluid composition, particularly differences in pH and ligand concentrations (e.g., chloride, fluoride and sulfate). For a given fluid pH, La_N/Yb_N and Eu_N/Eu^*_N ratios of high–temperature smoker fluids co–vary with $\Sigma Cl/\Sigma F$ (Figure 2.6). Increasing concentrations of fluoride (relative to chloride) correlate with greater enrichments of heavy–REEs relative to light–REEs, and lesser enrichments of Eu relative to neighboring REEs (Sm and Gd). For a given fluid pH, vent fluids exhibiting light–REE enriched pattern shapes and large positive Eu–anomalies have fluid compositions characterized by the lowest measured fluoride concentrations and highest $\Sigma Cl/\Sigma F$ ratios. Conversely, vent fluids with seafloor hydrothermal fluids vent fluids that have heavy–REE enriched chondrite–normalized pattern shapes (e.g., samples SM2 (Satanic Mills), F1 (Fenway), SZ5 (Suzette) and SS1 (South Su); Figures 2.3 and 2.4) are consistently correlated with remarkably high fluoride concentrations (> 300 – 500 μmol/kg; E. Reeves and J. Seewald, *unpubl. data*). These data suggest that the presence of high concentrations of fluoride in several vent fluids sampled from the Eastern Manus Basin preferentially enhances the aqueous solubility of the heavy–REEs (in particular relative to vent fluids sampled from Vienna Woods and from mid–ocean ridge hydrothermal systems).

Acid–sulfate fluids sampled from DESMOS (samples D1 and D2) and SuSu Knolls (samples NS1, NS2 and NS4) have flat REE_N pattern shapes (Figure 2.4), which are similar to that of acid–sulfate fluids sampled previously from DESMOS (e.g.,

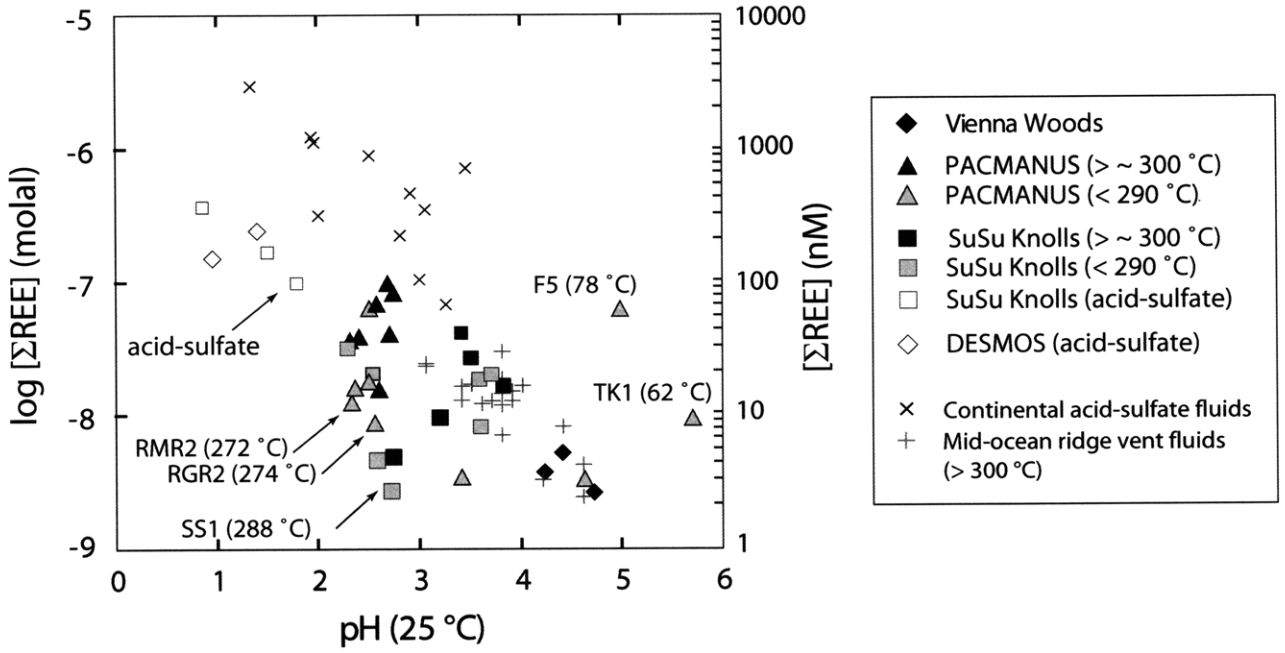

Figure 2.5. Total concentration of REEs vs. pH for hydrothermal vent fluids from the Manus Basin. The Highest temperature "smoker" fluids from each vent field are shown by black colored symbols and lower-temperature "smoker" fluids (< 62 - 288 ºC) are shown by gray colored symbols. Acid-sulfate fluids from DESMOS and SuSu Knoll are shown by white colored symbols. Also shown for comparison are data for high-temperature, endmember fluids from unsedimented, mid-ocean ridge hydrothermal systems (Klinkhammer et al., 1994; Douville et al., 1999) and for acid-sulfate fluids sampled from continental hydrothermal systems (Michard, 1989; Lewis et al., 1997). High-temperature black smoker fluids (~ 300 ºC) at all vent fields show a relatively good correlation between pH and REE concentration. Lower-temperature (<< 300 ºC) vent fluids show some significant departures. See text for discussion.

Douville et al., 1999). La_N/Yb_N and Eu_N/Eu^*_N ratios of acid–sulfate fluids are near unity for a wide range of chloride–to–fluoride ratios and varying fluoride concentrations do not obviously affect aqueous REE_N pattern shapes (Figure 2.6). In contrast, the unusual flat REE_N pattern shapes of acid–sulfate fluids are consistently correlated with very low pH (25 °C) of less than 1 – 1.8 and remarkably high sulfate concentrations (28 – 149 mmol/kg; E. Reeves and J. Seewald, *unpubl. data*). These data suggest that flat REE_N pattern shapes (and high REE abundances) of acid–sulfate fluids are influenced significantly by the extremely acidic pH, which likely leads to significantly solubility of all REEs.

The observed trends are consistent with experimental and thermodynamic studies that consider the aqueous speciation of the REEs (i.e., ligand complexation with chloride, fluoride, sulfate and hydroxide) in hydrothermal fluids with a range of chemical composition (e.g., Wood, 1990a; Wood, 1990b; Haas et al., 1995). These studies suggest that, for the compositions of most seafloor hydrothermal fluids (i.e., high chloride, low fluoride and low sulfate concentrations), REE–chloride complexes dominate. That REE–chloride complexes are stronger for the light–REEs and for divalent Eu relative to the mid– and heavy–REEs (Wood, 1990b; Haas et al., 1995) may enhance the aqueous stability of light–REEs and divalent Eu leading to their preferential enrichment in hydrothermal fluids during fluid–rock interaction. For several vent fluids sampled in the Manus Basin with high fluoride concentrations, REE–fluoride complexes are likely important aqueous species. The available thermodynamic data suggest that REE–fluoride complexes are stronger for the mid– and, in particular,

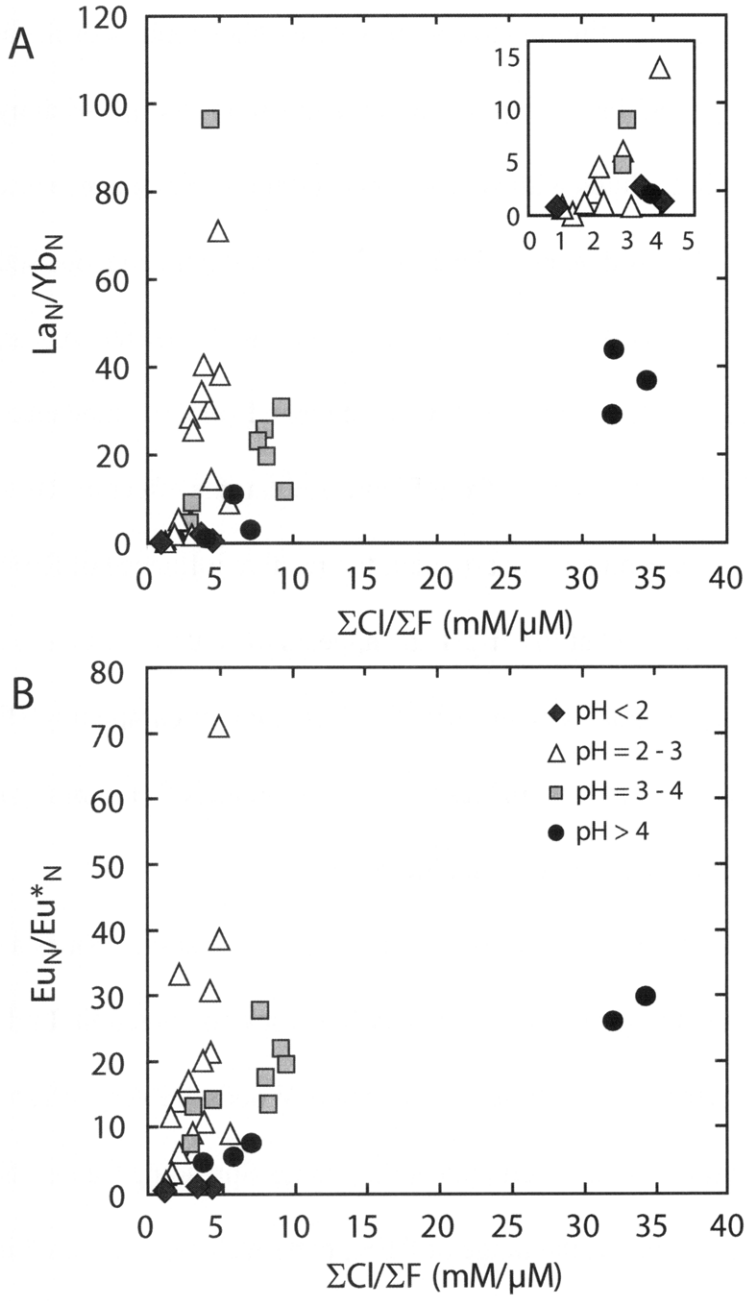

Figure 2.6. Trends between **A**) chondrite-normalized La/Yb ratios vs. ΣCl/ΣF ratios, and **B**) chondrite-normalized Eu-anomaly (Eu/Eu*) vs. ΣCl/ΣF ratios for all vent fluids sampled from the Manus Basin (Vienna Woods, PACMANUS, DESMOS and SuSu Knolls). Note the apparent influence of pH on the observed geochemical trends. See text for discussion.

heavy–REEs relative to the light–REEs (Wood, 1990b; Haas et al., 1995). Accordingly, the presence of significant fluoride to complex REEs likely enhances the aqueous stability of the heavy–REEs leading to their enrichment in fluoride–rich hydrothermal fluids. For acid–sulfate fluids with very low pH and high sulfate concentrations, free ions (REE^{3+}) and REE–sulfate complexes are likely important aqueous species (Wood, 1990b; Haas et al., 1995). The aqueous stability of all REEs as free ions and REE–sulfate complexes is similar, consistent with a high and similar abundance of all REEs in acid–sulfate fluids. It is apparent from Figure 2.6 that the effect of REE–ligand complexation is pH dependent. In particular, the relative influence of REE–fluoride complexation is diminished at lower pH and appears to be unimportant in acid–sulfate fluids. This is likely explained by the effective formation of competing HF^{o} (and other fluoride–complexes) at very low pH less than approximately 2, inhibiting the formation of REE–fluoride complexes in acid–sulfate fluids.

On the other hand, differences in vent fluid REE_N pattern shapes are not obviously correlated to differences in primary host rock composition. Light–REE enriched pattern shapes of vent fluids from Vienna Woods are very different to whole rock REE distributions of basalt erupted at the Manus Spreading Center (Sinton et al., 2003; Figure 2.7). Similarly, the range of REE_N pattern shapes measured in vent fluids from PACMANUS, DESMOS and SuSu Knolls is different relative to the uniform whole rock REE distributions of dacite and rhyolite erupted in the Eastern Manus Basin (Sinton et al., 2003; Figure 2.7). In addition, the range of REE_N pattern shapes measured in vent fluids in the Manus Basin are unlike the REE distributions in any specific

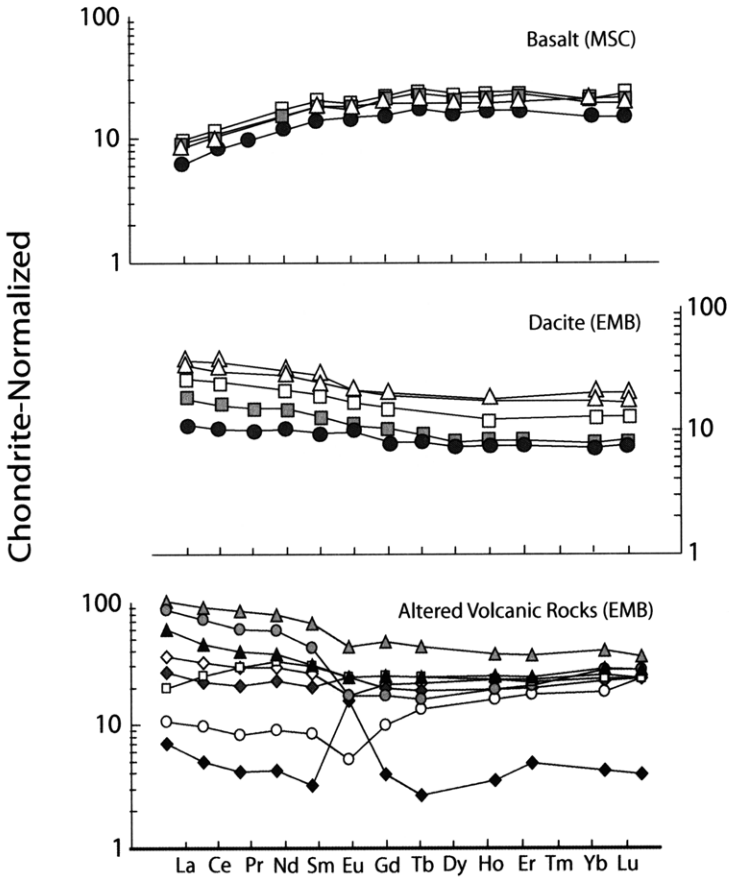

Figure 2.7. Chondrite-normalized REE pattern shapes of unaltered glass erupted at the Manus Spreading Center (basalt) and in the Eastern Manus Basin (dacite-rhyolite) compared to those of altered volcanic rocks in the Eastern Manus Basin. Data for fresh volcanic glasses are from Sinton et al. (2003) and for altered volcanic rocks from Beaudoin et al. (2007).

primary igneous mineral or in the range of alteration phases observed (e.g., Beaudoin et al., 2007). Significantly, REE concentrations and REE_N pattern shapes of Manus Basin hydrothermal fluids are markedly different within individual vent fields on spatial scales (< 100 – 500 m) over which the primary REE composition of volcanic rocks are uniform (e.g., Sinton et al., 2003).

Taken together, the data suggest that although the REEs are derived from volcanic rocks during fluid–rock interaction, the REE distribution of the volcanic rocks is a secondary control on the REE_N pattern shape of seafloor hydrothermal fluids. Instead, REE_N pattern shapes of vent fluids appear to be controlled primarily by different composition (i.e., pH and ligand concentrations) and temperature of circulating hydrothermal fluids, which influences the relative aqueous solubility and selective removal of REEs from the rock during fluid–rock interaction (e.g., Bau, 1991; Bach and Irber, 1998; Bach et al., 2003; Allen and Seyfried, 2005). These data suggest that the REE_N pattern shapes of seafloor vent fluids can be used as indicators of sub–seafloor geochemical processes associated with hydrothermal activity. Of particular significance, the apparent sensitivity of REEs to differences of fluid pH and elevated fluoride and sulfate concentrations suggests that REEs can be used as indicators for extensive inputs of exsolved magmatic acid volatiles (H_2O–CO_2–HCl–HF–SO_2) in submarine hydrothermal systems. This supports the original hypothesis put forward by Bach et al. (2003) that heterogeneous REE_N pattern shapes recorded by mineral deposit samples in the Manus Basin are related to varying inputs of magmatic acid volatile species.

5.2. Thermodynamic constraints

Given a lack of thermodynamic data for the behavior and partitioning of REEs alteration minerals at temperature and pressure conditions relevant to hydrothermal systems, it is not possible to model specific fluid–rock interactions to evaluate REE solubilities in different hydrothermal fluids sampled in the Manus Basin. However, it is possible using thermodynamic calculations to examine the aqueous species distributions of the REEs for the range of fluid temperature, pH and ligand concentrations measured for these hydrothermal fluids. Previous calculations suggest that changes of hydrothermal fluid pH, [ΣCl], [ΣF] and [ΣSO_4] significantly affect predicted aqueous REE species distributions (e.g., Douville et al., 1999; Bach et al., 2003). Differences in the stability of aqueous REE complexes (Wood, 1990a; Wood, 1990b; Bau, 1991; Haas et al., 1995) likely influence the solubilities of individual REEs to differing extents, thereby affecting their relative abundances. Results of representative thermodynamic species distribution calculations carried out for all Manus Basin hydrothermal fluids are presented in Figures 2.8 and 2.9. The results of species distribution calculations for mid–ocean ridge vent fluids from Hanging Garden, 21 °N East Pacific Rise (Von Damm et al., 1985; Klinkhammer et al., 1994) are provided for comparison.

5.2.1. REE species distributions in seafloor hydrothermal fluids

REEs in all high–temperature vent fluids with mildly–to–moderately acidic pH, low ΣF (< 20 – 200 μmol/kg) and low ΣSO_4 (< 1 – 10 mmol/kg) are present in solution predominantly as (trivalent) REE–chloride and REE–oxyhydroxide complexes (Figure 2.8). REE–fluoride complexes are present in varying and lesser amounts, and REE–sulfate complexes are present at relatively low abundances. REE–chloride complexes

are more abundant for the light–REEs relative to the heavy–REEs. The opposite is true of REE–fluoride complexes. Europium is predicted to be present as a divalent chloride complex, reflecting the stability of Eu^{2+} relative to Eu^{3+} at elevated temperatures above ~ 250 °C (Sverjensky, 1984). Small differences in the relative abundance of REE–chloride, REE–hydroxide and REE–fluoride complexes are due primarily to differences in aqueous pH; the relative abundances of REE–chloride complexes increase at lower pH. It has been suggested that theoretically–determined constants (Haas et al., 1995) over–predict the stability of REE–hydroxide complexes at elevated temperature and pressure (Gammons et al., 1996; Wood et al., 2002). If correct, predicted REE species distributions would be influenced even more by REE–chloride complexes. The predicted REE species distribution for moderately low pH, low ΣF and low ΣSO_4 hydrothermal fluids is similar across a range of geologic environments and host rock composition (i.e., hydrothermal systems in back–arc basins (Vienna Woods, PACMANUS and SuSu Knolls) and mid–ocean ridges (21 °N East Pacific Rise); see also Douville et al., 1999 and Bach et al., 2003). It is inferred from these data that the predominance of REE–chloride complexes in these fluids primarily controls the aqueous solubility of REEs (in particular the light–REEs and divalent Eu) and accounts for the REE_N pattern shapes (light–REE enrichment, large positive Eu–anomaly) in these fluids.

REEs in high–temperature vent fluids with moderately low pH, high ΣF (> 300 μmol/kg) and low ΣSO_4 (< 1 – 10 mmol/kg) have predicted REE species distributions that differ significantly to fluids with low fluoride (Figure 2.9a, b). In general, fluoride

complexes of all REEs are present in considerably higher abundances relative to low fluoride and low sulfate fluids. Light–REEs are present predominantly as REE–chloride complexes; light–REE–fluoride complexes are about a factor of five lower. In contrast, heavy–REEs are present predominantly as REE–fluoride complexes with lower abundances of REE–chloride complexes. In these fluids, Eu is again predicted to occur as a divalent chloride complex. REE–hydroxide and REE–sulfate complexes are present only at low abundances. It is inferred that the formation of stable REE–fluoride complexes, in particular of the heavy–REEs in moderately low pH fluoride–rich hydrothermal fluids, controls the heavy–REE enriched pattern shapes of these vent fluids.

Lower temperatures, extremely acidic pH, and high sulfate concentrations of acid–sulfate fluids result in predicted REE species distributions that differ even more relative to high–temperature smoker fluids from both mid–ocean ridges and back–arc basins (Figure 2.9c, d). Calculations indicate that in acid–sulfate fluids REEs are present dominantly as free REE^{3+}, REE–sulfate complexes and REE–chloride complexes (see also Douville et al., 1999 and Bach et al., 2003). REE–chloride complexes become more abundant at higher temperatures. Europium is predicted to exist predominantly as trivalent Eu^{3+} in most acid–sulfate fluids, primarily reflecting the lower temperature, and to a lesser extent more oxidizing composition, of these fluids (e.g., Sverjensky, 1984). Accordingly, the species distribution of Eu is similar to neighboring trivalent REEs (Figure 2.9c, d). REE–fluoride and REE–hydroxide complexes are insignificant. The low abundance of REE–fluoride complexes persists

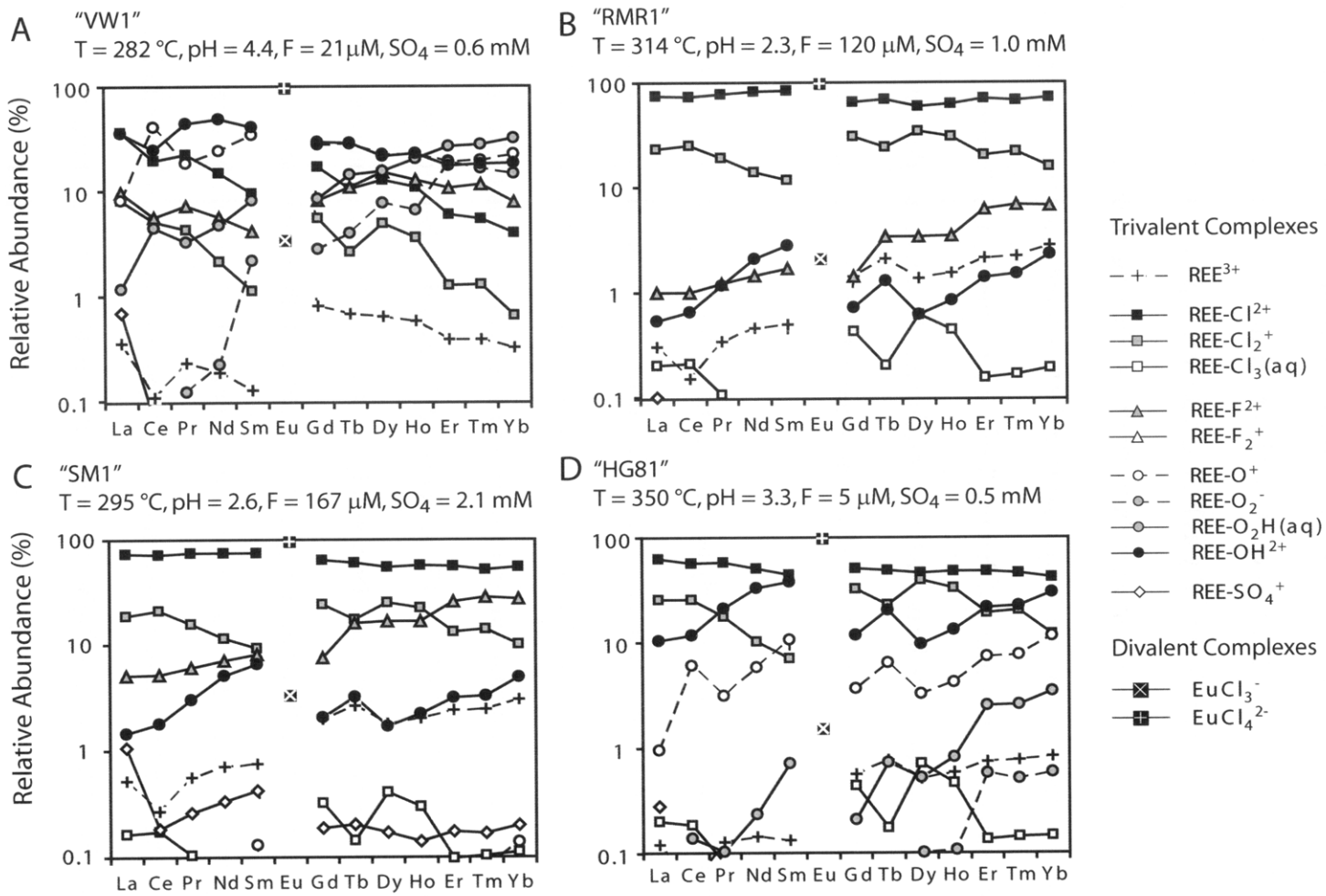

Figure 2.8. Results of thermodynamic species distribution calculations showing predicted REE complexation for vent fluids from **A**) Vienna Woods "VW2", Manus Spreading Center, **B-C**) PACMANUS "RMR1" and "SM1", Eastern Manus Basin and **D**) Hanging Garden, 21 °N EPR. Full fluid compositions used in calculation listed in Tables 2.1 through 2.3.

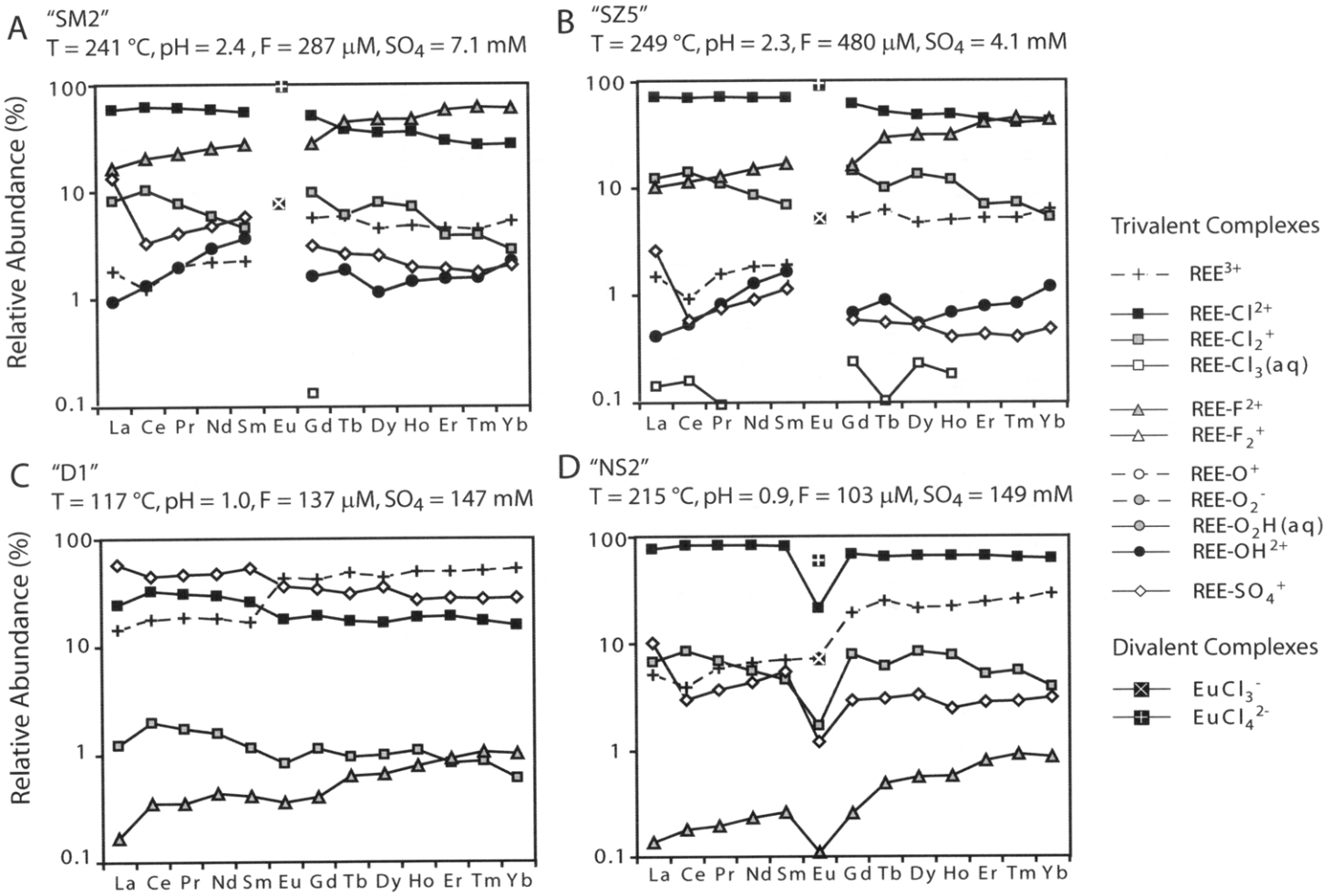

Figure 2.9. Results of thermodynamic species distribution calculations showing predicted REE complexation for vent fluids from **A**) PACMANUS "SM2", **B**) SuSu Knolls "SZ5", **C**) DESMOS acid-sulfate "D1", and **D**) SuSu Knolls acid-sulfate "NS2". Full fluid compositions used in calculation listed in Tables 2.1 through 2.3.

despite remarkably high ΣF in some of these fluids. This prediction supports the lack of sensitivity of REE_N pattern shapes to changes of $\Sigma Cl/\Sigma F$ and $\Sigma SO_4/\Sigma F$ ratios in acid–sulfate fluids (e.g., La_N/Yb_N; Figure 2.6). It has been suggested that the absence of REE–fluoride complexes is related to the competitive formation of Al–fluoride complexes in acid–sulfate fluids (Gimeno Serrano et al., 2000). Acid–sulfate fluids sampled from the Manus Basin have very high concentrations of dissolved Al (~ 150 – 1640 μmol/kg; see Chapter 4). Species distribution calculations indicate that abundances of Al–fluoride complexes can be important. However, the extent to which Al complexes with fluoride is dependent on pH and $\Sigma Al/\Sigma F$. In all acid–sulfate fluids the most common fluoride species is neutral HF^o and the formation of Al–fluoride complexes occurs at the expense of HF, not REE–fluoride complexes. The presence or absence of Al–fluoride complexes in extremely low pH acid–sulfate fluids does not affect the predicted absence of REE–fluoride complexes. pH is the most important control on the availability of free fluoride to complex with REEs (Figure 2.10). High REE concentrations and flat REE_N pattern shapes of acid–sulfate fluids appear to be influenced predominantly by the extremely acidic pH of these fluids, which likely results in substantial solubility and mobility of all REEs.

5.3. Other processes influencing REE compositions of seafloor hydrothermal fluids

5.3.1 Seawater entrainment, fluid mixing and mineral deposition and remobilization

Studies at mid–ocean ridges have demonstrated that local entrainment of seawater and sub–seafloor mixing with rising high–temperature hydrothermal fluids affects considerably seafloor vent fluid compositions via mineral deposition and/or

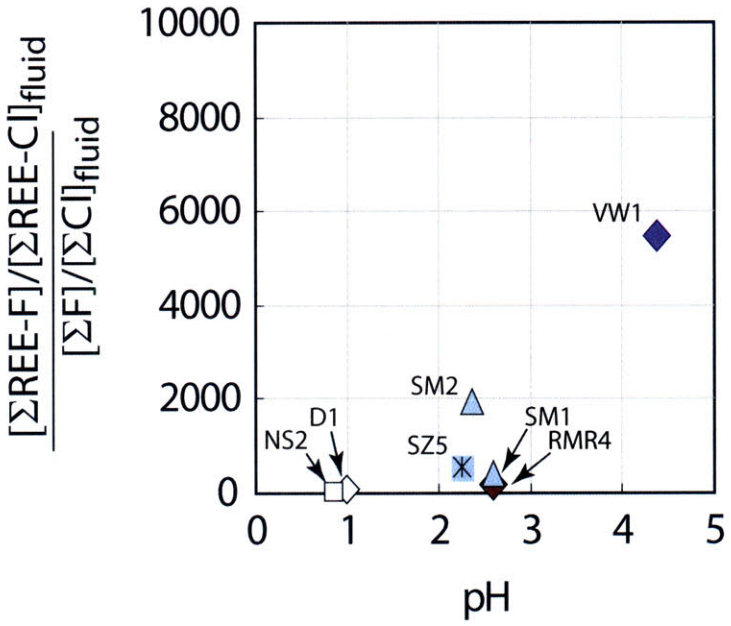

Figure 2.10. Comparison among measured pH (25 °C) and aqueous species distribution of REEs with fluoride and chloride predicted by thermodynamic calculations for selected Manu Basin hydrothermal fluids. Data shown as the ratio of total REE-fluoride and REE-chloride complex as a function of total fluoride and chloride concentration. As pH decreases, the fraction of REE complexed with fluoride decreases, likely resulting from increased association of HF and lower relative availability of fluoride to complex with REE at low pH. For low pH acid-sulfate fluids, there is essentially no REE-fluoride complex formation despite a range of fuoride concentations in these fluids. In contrast, the fraction of REE-fluoride complex formation increases with pH as HF is increasingly dissociated and free fluoride is present.

dissolution (Edmond et al., 1995). Deposition of anhydrite is a common product of this sub–seafloor mixing (Tivey et al., 1995; Mills et al., 1998; Tivey et al., 1998; Mills and Tivey, 1999; Humphris and Bach, 2005). Studies have shown that hydrothermal anhydrites typically contain significant amounts of REEs and may be the major sink of REEs from solution (Mills and Elderfield, 1995; Humphris, 1998).

Geological sampling has recovered substantial anhydrite in several vent deposits from the PACMANUS (Binns et al., 2007; Tivey et al., 2007) suggesting that near–seafloor mixing between locally entrained seawater and rising high–temperature hydrothermal fluid has impacted significantly the evolution of seafloor hydrothermal fluids in this system. At Roman Ruins, Satanic Mills and Snowcap, on–going anhydrite deposition is suggested by Ca and SO_4 concentrations in low–temperature (152 – 278 °C) mixed vent fluids (Mg > 16 mmol/kg) that are significantly less than that predicted by conservative mixing between endmember high–temperature hydrothermal fluid and seawater (Figure 2.11; E. Reeves and J. Seewald, *unpubl. data*). At these vent fields, concentrations of REEs are significantly lower in low–temperature fluids relative to that predicted by conservative mixing of seawater and endmember hydrothermal fluid, consistent with the removal of REEs by anhydrite (Figure 2.11). Sub–surface deposition of anhydrite at Fenway, either occurring at present or in the recent past, is indicated by the presence of massive anhydrite exposed at the seafloor of the Fenway mound. Dissolution of previously deposited anhydrite is suggested by relative enrichment of Ca and SO_4 in low–temperature fluids (sample F5; T ~ 78 °C) relative to high–temperature endmember hydrothermal fluids (Figure 2.11). At Fenway, the low–temperature fluid

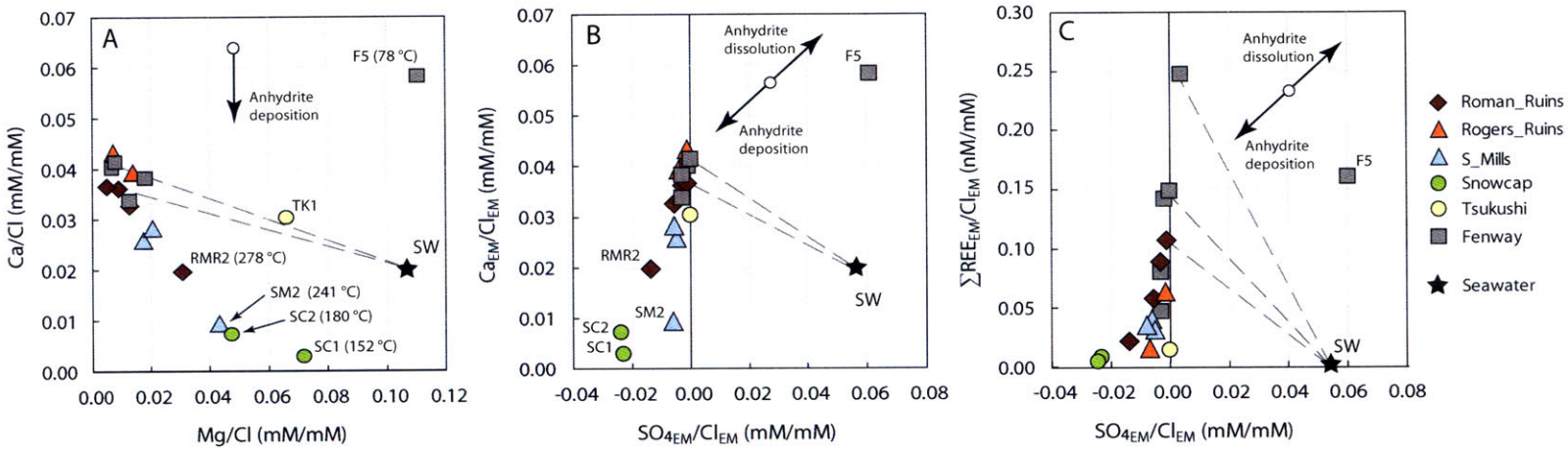

Figure 2.11. Geochemical variability and trends for vent fluids sampled from PACMANUS, resulting from local seawater entrainment and mixing between seawater (black star) and end-member hydrothermal fluid (Mg/Cl = 0; SO_4/Cl = 0). Data are normalized to chlorinity. Gray dashed lines show limits for conservative mixing for smoker fluids from PACMANUS. **A**) Ca vs. Mg. **B**) Ca vs. SO_4. C) REE vs. SO_4. The data suggest extensive depletion of calcium and sulfate during mixing (e.g., at Roman Ruins, Satanic Mills and Snowcap) likely resulting from anhydrite deposition, and in one vent field (Fenway) addition of calcium and sulfate resulting from anhydrite dissolution into low-temperature (< 100 ºC) fluids. REEs show similar behavior suggesting that anhydrite deposition and/or dissolution can influence the cycling of REEs in seafloor hydrothermal systems. Data for Mg, Ca and SO_4 from E. Reeves and J. Seewald (*unpubl. data*).

(sample F5) contains significantly higher REE concentrations than predicted by conservative mixing. The dissolution of REE–bearing anhydrite as predicted by excess Ca and SO_4 can explain relatively high concentrations of REEs in this extensively mixed, low–temperature hydrothermal fluid (Figures 2.6 and 2.11). Although precipitation and/or dissolution of anhydrite can affect the absolute concentrations of REEs in hydrothermal fluids, it does not appear that the precipitation of anhydrite also affects the relative REE_N pattern shape of the fluid. For example, at Roman Ruins there are no obvious differences among REE_N pattern shapes of endmember high–temperature fluids (samples RMR1, RMR4) and mixed lower–temperature fluids (sample RMR2; Figure 2.3) to suggest that the precipitation of anhydrite fractionates significantly the REEs from solution.

5.3.2. Phase separation and segregation of low– and high–salinity hydrothermal fluids

Phase separation of hydrothermal fluids in the oceanic crust is recognized as a fundamental process controlling the composition of many seafloor vent fluids (Von Damm, 1990; Von Damm, 1995). Phase separation and vapor–brine segregation is suggested by large ranges in chlorinity of seafloor vent fluids. Recent experiments have indicated that the REEs are not fractionated uniformly between vapor and brine (Shmulovich et al., 2002). Light–REEs and heavy–REEs are preferentially enriched in the brine and vapor phase, respectively.

Variable chlorinities of vent fluids sampled from the Manus Basin indicate on–going phase separation at most vent fields (E. Reeves and J. Seewald, *pers. commun.* 2008). To a minor extent, fluid phase separation may influence REE compositions

(REE_N pattern shapes) of seafloor hydrothermal fluids. Co–existing and phase separated low salinity and high salinity fluids were sampled from Fenway field at PACMANUS (Table 2). At Fenway, higher chlorinity fluids (samples F2, F3) have higher concentrations of light–REEs relative to lower chlorinity fluids (samples F1, F4; Figure 2.3) consistent with experimental predictions for REE fractionation during fluid phase separation (Shmulovich et al., 2002). Changes in $\Sigma Cl/\Sigma F$ ratios are limited among these fluids and so the effect of varying magmatic volatile degassing is likely not important for these pairs of fluids. However, phase separation as a process to affect the relative REE_N pattern shapes of seafloor vent fluids appears to be significantly less important than that of changes in hydrothermal fluid composition resulting from input of exsolved magmatic acid volatiles (H_2O–CO_2–HCl–HF–SO_2). Taken together, chondrite–normalized REE distributions of seafloor hydrothermal fluids appear to be a sensitive indicator used to track sub–seafloor inputs of magmatic acid volatiles.

6. Summary and Conclusions

Rare earth element data are reported for a wide range of seafloor vent fluids sampled from hydrothermal systems in the Manus back–arc basin. Chondrite–normalized REE_N pattern shapes show a range of variable distributions that is significantly greater than the relative uniform REE_N pattern shapes of mid–ocean ridge hydrothermal fluids. This variability is well correlated to differences in fluid composition, in particular pH and chloride, fluoride and sulfate concentrations.

Different vent fluid REE_N pattern shapes are not obviously correlated to differences in host rock REE compositions. The data suggest that aqueous REE compositions of hydrothermal fluids are affected primarily by the conditions of fluid–rock interaction, in particular pH, temperature and the availability of complexing ligands, as suggested by experimental studies (Bach and Irber, 1998; Allen and Seyfried, 2005).

The implications of these results are that if low pH and high fluoride and/or sulfate concentrations of seafloor hydrothermal fluids in the Manus Basin reflect inputs of magmatic volatiles HF and SO_2 (e.g., Gamo et al., 1997; Seewald et al., 2006), then REEs are sensitive to, and therefore can be used as indicators of, extensive magmatic degassing. This supports the study of Bach et al. (2003), which suggested that heterogeneous REE_N pattern shapes recorded in anhydrite from the Manus Basin reflected waxing and waning inputs of magmatic volatiles. It has been hypothesized that REE_N pattern shapes of mid–ocean ridge (MOR) hydrothermal fluids reflect exchange of REE from plagioclase in basalt and that MOR vent fluid REE compositions are uniform because crustal host rock composition is similar (Klinkhammer et al., 1994). Alternatively, the results of this study suggest that REE_N pattern shapes of MOR vent fluids may reflect a fluid composition that is similar at MOR hydrothermal systems, that is moderately acidic, chloride–rich, and fluoride– and sulfate–poor. Local processes, including sub–surface fluid mixing and mineral deposition and remobilization, may affect REE concentrations of seafloor hydrothermal fluids. However, these processes do not affect the relative REE distributions (REE_N pattern shape) of seafloor vent fluids to the same extent that changes in fluid composition resulting from inputs of exsolved

magmatic acid volatiles appear to.

This detailed study of REE compositions of seafloor vent fluids indicates that REEs can provide critical information about fundamental sub–seafloor geochemical processes associated with hydrothermal activity, in particular the influence of magmatic volatile input on fluid–rock interaction and REE mobility. A better understanding of aqueous REE behavior offers important constraints for interpreting REE signatures recorded in mineral deposits. Future studies of REE–bearing mineral deposits can be used to gain insight about geochemical processes pertaining to hydrothermal vent deposit formation and are essential for relict systems where access to hydrothermal fluids is precluded.

ACKNOWLEDGEMENTS

Wolfgang Bach (at University of Bremen), Jeffrey Seewald and Olivier Rouxel (both at Woods Hole Oceanographic Institution) are co-investigators in this study. Margaret K. Tivey, Susan Humphris and Edward Boyle provided stimulating discussions that benefited the outcome of this study. Dave Schneider and Scot Birdwhistell (at Woods Hole Oceanographic Institution) are acknowledged for assistance during rare earth element analysis on the ICP-MS. This study received financial support from NSF grant OCE-0327448 (to W. Bach, M. A. Tivey, M. K. Tivey and J. Seewald).

REFERENCES

Alderton D. H. M., Pearce J. A., and Potts P. J. (1980) Rare earth element mobility during granite alteration: Evidence from southwest England. *Earth and Planetary Science Letters* **49**(1), 149-165.

Allen D. E. and Seyfried W. E., Jr. (2005) REE controls in ultramafic hosted MOR hydrothermal systems: An experimental study at elevated temperature and pressure. *Geochimica et Cosmochimica Acta* **69**(3), 675-683.

Anders E. and Grevesse N. (1989) Abundances of the elements: Meteoritic and solar. *Geochimica et Cosmochimica Acta* **53**, 197-214.

Bach W. and Irber W. (1998) Rare earth element mobility in the oceanic lower sheeted dyke complex: evidence from geochemical data and leaching experiments. *Chemical Geology* **151**(1), 309-326.

Bach W., Roberts S., Vanko D. A., Binns R. A., Yeats C. J., Craddock P. R., and Humphris S. E. (2003) Controls of fluid chemistry and complexation on rare-earth element contents of anhydrite from the Pacmanus subseafloor hydrothermal system, Manus Basin, Papua New Guinea. *Mineralium Deposita* **38**(8), 916-935.

Bach W., Tivey M. A., Seewald J. S., Tivey M. K., Craddock P. R., Niedermeier D., and Yoerger D. (2007) Variable basement compostion and magma degassing affecting hydrothermal systems in the Eastern Manus Basin. *EOS Trans. AGU. Fall Meet. Suppl.,* **88**(52), Abstract #V21D-0749.

Bau M. (1991) Rare-earth element mobility during hydrothermal and metamorphic fluid-rock interaction and the significance of the oxidation state of europium. *Chemical Geology* **93**(3-4), 219-230.

Bau M. and Dulski P. (1995) Comparative study of yttrium and rare-earth element behaviours in fluorine-rich hydrothermal fluids. *Contributions to Mineralogy and Petrology* **119**(2), 213-223.

Bau M. and Dulski P. (1999) Comparing yttrium and rare earths in hydrothermal fluids from the Mid-Atlantic Ridge: implications for Y and REE behaviour during

near-vent mixing and for the Y/Ho ratio of Proterozoic seawater. *Chemical Geology* **155**(1), 77-90.

Beaudoin Y., Scott S. D., Gorton M. P., Zajacz Z., and Halter W. (2007) Effects of hydrothermal alteration on Pb in the active PACMANUS hydrothermal field, ODP Leg 193, Manus Basin, Papua New Guinea: A LA-ICP-MS study. *Geochimica et Cosmochimica Acta* **71**(17), 4256-4278.

Bethke C. M. (1996) *Geochemical Reaction Modeling*. Oxford University Press.

Binns R. A., Barriga F. J. A. S., and Miller D. J. (2007) Leg 193 synthesis: Anatomy of an active felsic-hosted hydrothermal system, eastern Manus Basin, Papua New Guinea. In *Proceedings of the Ocean Drilling Program, Scientific Results*, Vol. 193 (ed. F. J. A. S. Barriga, R. A. Binns, D. J. Miller, and P. M. Herzig), pp. 1-71. doi:10.2973/odp.proc.sr.193.201.2007. Ocean Drilling Program.

Binns R. A. and Scott S. D. (1993) Actively forming polymetallic sulfide deposits associated with felsic volcanic rocks in the eastern Manus back-arc basin, Papua New Guinea. *Economic Geology* **88**, 2226-2236.

Binns R. A., Scott S. D., Gemmell J. B., Crook K. A. W., and Shipboard Scientific Party. (1997) The SuSu Knolls hydrothermal field, eastern Manus Basin, Papua New Guinea. *EOS Trans. AGU. Fall Meet. Suppl.,* **78**(52), Abstract #V22E-02.

Both R., Crook K., Taylor B., Brogan S., Chappell B., Frankel E., Liu L., Sinton J., and Tiffin D. (1986) Hydrothermal chimneys and associated fauna in the Manus back-arc basin, Papua New Guinea. *EOS Transactions, American Geophysical Union* **67**, 489.

Campbell A. C., Palmer M. R., Klinkhammer G. P., Bowers T. S., Edmond J. M., Lawrence J. R., Casey J. F., Thompson G., Humphris S. E., and Rona P. (1988) Chemistry of hot springs on the Mid-Atlantic Ridge. *Nature* **335**(6190), 514-519.

Davies H. L., Honza E., Tiffin D. L., Lock J., Okuda Y., Keene J. B., Murakami F., and Kisimoto K. (1987) Regional setting and structure of the western Solomon Sea. *Geo-Marine Letters* **7**, 153-160.

Douville E., Bienvenu P., Charlou J. L., Donval J. P., Fouquet Y., Appriou P., and Gamo T. (1999) Yttrium and rare earth elements in fluids from various deep-sea hydrothermal systems. *Geochimica et Cosmochimica Acta* **63**(5), 627-643.

Drummond S. E., Jr. (1981) Boiling and Mixing of Hydrothermal Fluids: Chemical Effects on Mineral Precipitation, The Pennsylvania State University.

Edmond J. M., Campbell A. C., Palmer M. R., German C. R., Klinkhammer G. P., Edmonds H. N., Elderfield H., Thompson G., and Rona P. (1995) Time series studies of vent fluids from the TAG and MARK sites (1986, 1990) Mid-Atlantic Ridge and a mechanism for Cu/Zn zonation in massive sulphide orebodies. In *Hydrothermal Vents and Processes*, Vol. 87 (ed. L. M. Parson, C. L. Walker, and D. R. Dixon), pp. 77-86. Geological Society Special Publication.

Fulignati P., Gioncada A., and Sbrana A. (1999) Rare-earth element (REE) behaviour in the alteration facies of the active magmatic-hydrothermal system of Vulcano (Aeolian Islands, Italy). *Journal of Volcanology and Geothermal Research* **88**(4), 325-342.

Gammons C. H., Wood S. A., and Williams-Jones A. E. (1996) The aqueous geochemistry of the rare-earth elements and yttrium: VI. Stability of neodymium chloride complexes from 25 to 300 °C. *Geochimica et Cosmochimica Acta* **60**(23), 4615.

Gamo T., Okamura K., Charlou J. L., Urabe T., Auzende J. M., Ishibashi J., Shitashima K., Chiba H., Binns R. A., and Gena K. (1997) Acidic and sulfate-rich hydrothermal fluids from the Manus back-arc basin, Papua New Guinea. *Geology* **25**(2), 139-142.

Gimeno Serrano M. J., Auque Sanz L. F., and Nordstrom D. K. (2000) REE speciation in low-temperature acidic waters and the competitive effects of aluminum. *Chemical Geology* **165**(3-4), 167-180.

Graf J. L., Jr. (1977) Rare earth elements as hydrothermal tracers during the formation of massive sulfide deposits in volcanic rocks. *Economic Geology* **72**(4), 527-548.

Haas J. R., Shock E. L., and Sassani D. C. (1995) Rare earth elements in hydrothermal systems: Estimates of standard partial molal thermodynamic properties of aqueous complexes of the rare earth elements at high pressures and temperatures. *Geochimica et Cosmochimica Acta* **59**(21), 4329-4350.

Hrischeva E., Scott S. D., and Weston R. (2007) Metalliferous Sediments Associated with Presently Forming Volcanogenic Massive Sulfides: The SuSu Knolls Hydrothermal Field, Eastern Manus Basin, Papua New Guinea. *Economic Geology* **102**(1), 55-74.

Humphris S. E. (1984) The mobility of the rare earth elements in the crust. In *Rare Earth Element Geochemistry (Developments in Geochemistry)*, Vol. 2 (ed. P. Henderson), pp. 317-342. Elsevier.

Humphris S. E. (1998) Rare earth element composition of anhydrite: Implications for deposition and mobility within the TAG hydrothermal mound. In *Proceedings of the Ocean Drilling Program, Scientific Results*, Vol. 158 (ed. P. M. Herzig, S. E. Humphris, D. J. Miller, and R. A. Zierenberg), pp. 143-159. Ocean Drilling Program.

Humphris S. E. and Bach W. (2005) On the Sr isotope and REE compositions of anhydrites from the TAG seafloor hydrothermal system. *Geochimica et Cosmochimica Acta* **69**, 1511-1525.

Johnson J. W., Oelkers E. H., and Helgeson H. C. (1992) SUPCRT92: a software package for calculating the standard molal thermodynamic properties of minerals, gases, aqueous species and reactions from 1 to 5000 bar, and 0 to 1000 °C. *Computers and Geosciences* **18**(7), 899-947.

Klinkhammer G. P., Elderfield H., Edmond J. M., and Mitra A. (1994) Geochemical implications of rare earth element patterns in hydrothermal fluids from mid-ocean ridges. *Geochimica et Cosmochimica Acta* **58**(23), 5105-5113.

Lewis A. J., Palmer M. R., Sturchio N. C., and Kemp A. J. (1997) The rare earth element geochemistry of acid-sulphate and acid-sulphate-chloride geothermal systems from Yellowstone National Park, Wyoming, USA. *Geochimica et*

Cosmochimica Acta **61**(4), 695-706.

Lottermoser B. G. (1990) Rare-earth element and heavy-metal behaviour associated with epithermal gold deposits on Lihir Island, Papua New Guinea. *Journal of Volcanology and Geothermal Research* **40**, 269-289.

Martinez F. and Taylor B. (1996) Backarc spreading, rifting, and microplate rotation, between transform faults in the Manus Basin. *Marine Geophysical Researches* **18**, 203-224.

Michard A. (1989) Rare earth element systematics in hydrothermal fluids. *Geochimica et Cosmochimica Acta* **53**, 745-750.

Michard A. and Albarede F. (1986) The REE content of some hydrothermal fluids. *Chemical Geology* **55**(1-2), 51-60.

Michard A., Albarède F., Michard G., Minster J. F., and Charlou J. L. (1983) Rare-earth elements and uranium in high-temperature solutions from East Pacific Rise hydrothermal vent field (13 °N). *Nature* **303**(795-797).

Mills R. A. and Elderfield H. (1995) Rare earth element geochemistry of hydrothermal deposits from the active TAG Mound, 26 °N Mid-Atlantic Ridge. *Geochimica et Cosmochimica Acta* **59**, 3511-3524.

Mills R. A., Teagle D. A. H., and Tivey M. K. (1998) Fluid mixing and anhydrite precipitation within the TAG mound. In *Proceedings of the Ocean Drilling Program, Scientific Results*, Vol. 158 (ed. P. M. Herzig, S. E. Humphris, D. J. Miller, and R. A. Zierenberg), pp. 119-127. Ocean Drilling Program.

Mills R. A. and Tivey M. K. (1999) Sea water entrainment and fluid evolution within the TAG hydrothermal mound: Evidence from analyses of anhydrite. In *Mid-Ocean Ridges: Dynamics of Processes Associated with Creation of New Ocean Crust* (ed. J. R. Cann, H. Elderfield, and A. Laughton), pp. 225-248. Cambridge University Press.

Mitra A., Elderfield H., and Greaves M. J. (1994) Rare earth elements in submarine hydrothermal fluids and plumes from the Mid-Atlantic Ridge. *Marine Chemistry* **46**(3), 217-235.

Möller P. (2002) The distribution of rare earth elements and ytttrium in water-rock interactions: Field obsevations and experiments. In *Water-Rock Interaction* (ed. I. Stober and K. Bucher), pp. 97-123. Kluwer Academic Publishers.

Sakai H., Gamo T., and Scientific Crew of Cruise KH-90-3. (1991) Hydrothermal activity in the eastern Manus Basin, Bismarck Sea: A brief report of the Hakuho-Maru Cruise KH-90-3. *Ridge Events* **2**, 39,51.

Seewald J. S., Doherty K. W., Hammar T. R., and Liberatore S. P. (2002) A new gas-tight isobaric sampler for hydrothermal fluids. *Deep Sea Research Part I: Oceanographic Research Papers* **49**(1), 189-196.

Seewald J. S., Reeves E., Saccocia P., Rouxel O. J., Walsh E., Price R. E., Tivey M., Bach W., and Tivey M. (2006) Water-rock reaction, substrate composition, magmatic degassing, and mixing as major factors controlling vent fluid compositions in Manus Basin hydrothermal systems. *EOS Trans. AGU. Fall Meet. Suppl.,* **87**(52), Abstract # B34A-02.

Shmulovich K., Heinrich W., Möller P., and Dulski P. (2002) Experimental determination of REE fractionation between liquid and vapour in the systems NaCl-H_2O and $CaCl_2$-H_2O up to 450 °C. *Contributions to Mineralogy and Petrology* **144**(3), 257-273.

Sinton J. M., Ford L. L., Chappell B., and McCulloch M. T. (2003) Magma genesis and mantle heterogeneity in the Manus Back-Arc Basin, Papua New Guinea. *Journal of Petrology* **44**, 159-195.

Smith M. P., Henderson P., and Campbell L. S. (2000) Fractionation of the REE during hydrothermal processes: constraints from the Bayan Obo Fe-REE-Nb deposit, Inner Mongolia, China. *Geochimica et Cosmochimica Acta* **64**(18), 3141-3160.

Sverjensky D. A. (1984) Europium redox equilibria in aqueous solution. *Earth and Planetary Science Letters* **67**, 70-78.

Tagirov B. and Schott J. (2001) Aluminum speciation in crustal fluids revisited. *Geochimica et Cosmochimica Acta* **65**(21), 3965-3992.

Taylor B. (1979) Bismarck Sea; Evolution of a back-arc basin. *Geology* **7**, 171-174.

Tivey M. A., Bach W., Seewald J. S., Tivey M. K., Vanko D. A., and Shipboard Science and Technical Teams. (2007) Cruise Report R/V Melville, MAGELLAN-06. Hydrothermal systems in the Eastern Manus Basin: Fluid chemistry and magnetic structures as guides to subseafloor processes, pp. 67. Woods Hole Oceanographic Institution.

Tivey M. K., Humphris S. E., Thompson G., Hannington M. D., and Rona P. A. (1995) Deducing patterns of fluid flow and mixing within the TAG active hydrothermal mound using mineralogical and geochemical data. *Journal of Geophysical Research* **100**(B7), 12527-12555.

Tivey M. K., Mills R. A., and Teagle D. A. H. (1998) Temperature and salinity of fluid inclusions in anhydrite as indicators of seawater entrainment and heating within the TAG active mound. In *Proceedings of the Ocean Drilling Program, Scientific Results*, Vol. 158 (ed. P. M. Herzig, S. E. Humphris, D. J. Miller, and R. A. Zierenberg), pp. 179-190. Ocean Drilling Program.

Trefry J. H., Butterfield D. A., Metz S., Massoth G. J., Trocine R. P., and Feely R. A. (1994) Trace metals in hydrothermal solutions from Cleft segment on the southern Juan de Fuca Ridge. *Journal of Geophysical Research* **99**, 4925-4935.

Tufar W. (1990) Modern hydrothermal activity, formation of complex massive sulfide deposits and associated vent communities in the Manus back-arc basin (Bismarck Sea, Papua New Guinea). *Mitteilungen der Osterreichischen Geologischen Gesellschaft* **82**, 183-210.

Von Damm K. L. (1983) Chemistry of submarine hydrothermal solutions at 21° North, East Pacific Rise and Guaymas Basin, Gulf of California. Ph. D. Thesis, Massachusetts Institute of Technology-Woods Hole Oceanographic Institution.

Von Damm K. L. (1990) Seafloor hydrothermal activity: Black smoker chemistry and chimneys. *Annual Review of Earth and Planetary Sciences* **18**(1), 173-204.

Von Damm K. L. (1995) Controls on the chemistry and temporal variability of seafloor hydrothermal fluids. In *Seafloor Hydrothermal Systems: Physical, Chemical, Biological and Geological Interactions. Geophysical Monograph.*, Vol. 91 (ed.

S. E. Humphris, R. A. Zierenberg, L. S. Mullineaux, and R. E. Thomson), pp. 222-247. American Geophysical Union.

Von Damm K. L., Edmond J. M., Grant B., Measures C. I., Walden B., and Weiss R. F. (1985) Chemistry of submarine hydrothermal solutions at 21 °N, East Pacific Rise. *Geochimica et Cosmochimica Acta* **49**(11), 2197-2220.

Wolery T. J. and Jarek R. L. (2003) *Software User's Manual EQ3/6, Version 8.0.* Sandia National Laboratories - U.S. Department of Energy Report, Albuquerque, NM.

Wood S. A. (1990a) The aqueous geochemistry of the rare-earth elements and yttrium: 1. Review of available low-temperature data for inorganic complexes and the inorganic REE speciation of natural waters. *Chemical Geology* **82**, 159-186.

Wood S. A. (1990b) The aqueous geochemistry of the rare-earth elements and yttrium: 2. Theoretical predictions of speciation in hydrothermal solutions to 350 °C at saturation water vapor pressure. *Chemical Geology* **88**(1-2), 99-125.

Wood S. A. (2001) Behavior of rare earth elements in geothermal systems: A new exploration/exploitation tool? - U.S. Department of Energy Report, pp. 35. University of Idaho, Moscow, ID.

Wood S. A., Palmer D. A., Wesolowski D. J., and Bénézeth P. (2002) The aqueous geochemistry of the rare earth elements and yttrium: Part XI. The solubility of $Nd(OH)_3$ and hydrolysis of Nd^{3+} from 30 to 290 °C at saturated water vapor pressure with in-situ pH_m measurement. In *Water-Rock Interaction, Ore Deposits and Environmental Geochemistry: A Tribute to David A. Crerar. The Geochemical Society Special Publication*, Vol. 7 (ed. R. Hellmann and S. A. Wood), pp. 229-256.

Yeats C. J., Binns R. A., and Parr J. M. (2000) Advanced argillic alteration associated with actively forming submarine polymetallic sulfide mineralization in the eastern Manus Basin, Papua New Guinea. *Geological Society of Australia Abstracts* **59**, 555.

CHAPTER 3

Anhydrite as a Tracer of Magmatic–Hydrothermal Processes at the PACMANUS and SuSu Knolls Vent Fields, Manus Back–Arc Basin, Papua New Guinea

1. INTRODUCTION

The geochemical compositions of seafloor high–temperature vent fluids and related mineral deposits are affected by myriad sub–seafloor processes associated with submarine hydrothermal activity at mid–ocean ridge spreading centers. The fundamental processes controlling the formation and composition of seafloor hydrothermal fluids include fluid–rock interaction (Humphris and Thompson, 1978a; 1978b; Seyfried, 1987; Alt, 1995) and fluid phase separation (boiling) (Von Damm, 1995). Entrainment of seawater at the seafloor and sub–seafloor mixing with rising high–temperature hydrothermal fluids is known to significantly affect vent fluid compositions and the formation of associated mineral deposits on local spatial scales at some hydrothermal systems (Edmond et al., 1995; Tivey et al., 1995). At convergent plate margins, magmatic acid volatile phases (H_2O–CO_2–HCl–HF–SO_2) can be exsolved from oxidizing magmas and intersect

circulating hydrothermal fluids in subduction–related back–arc basins (Gamo et al., 1997; Seewald et al., 2006). The addition of acid volatile species in back–arc basins can lead to fundamental changes in fluid chemical characteristics, in particular the formation of hydrothermal fluids with very low pH relative to mid–ocean ridge hosted hydrothermal systems (Fouquet et al., 1993; Gamo et al., 1997; Douville et al., 1999; Seewald et al., 2006). Determining the extent and interplay among these processes is integral to our understanding of the evolution of hydrothermal systems in a range of geologic environments and the potential geochemical variability that can be expected in seafloor vent fluids and mineral deposits.

In the absence of direct and complete access to the sub–seafloor environment, it is necessary to use geochemical and isotopic information contained in vent fluids and/or related mineral deposits at the seafloor to infer environmental conditions and hydrothermal processes occurring at depth. Anhydrite ($CaSO_4$) is recognized is an important constituent of seafloor hydrothermal deposits, occurring within individual vent chimneys (Goldfarb, 1982; Haymon, 1983) and as veins and massive concretions (Humphris et al., 1995; Tivey et al., 1995). Anhydrite exhibits retrograde solubility and precipitates from seawater at temperatures above ~ 150 °C (at seafloor pressures), either from conductive heating of seawater, or by mixing between seawater and high–temperature hydrothermal fluids (Bischoff and Seyfried, 1978). Abundant massive anhydrite was first observed and sampled at the Trans–Atlantic Geotraverse (TAG) active hydrothermal mound at 26 °N, Mid–Atlantic Ridge (Thompson et al., 1988). Petrographic and geochemical studies of seafloor vent deposit and vent fluid chemistry suggest that local entrainment of seawater

and sub–seafloor mixing with rising hydrothermal fluid is occurring within the TAG mound, and predict the occurrence of significant anhydrite (Edmond et al., 1995; Tivey et al., 1995). Drilling of the mound (ODP Leg 158) recovered abundant anhydrite from multiple depths within the TAG mound (Humphris et al., 1995). Trace element (e.g., rare earth element, REE), isotope (e.g., strontium, $^{87}Sr/^{86}Sr$; sulfur, $\delta^{34}S$) and fluid inclusion data of sampled anhydrite (Chiba et al., 1998; Humphris, 1998; Mills et al., 1998; Teagle et al., 1998; Tivey et al., 1998; Humphris and Bach, 2005) are consistent with local seawater entrainment, mixing with high–temperature hydrothermal fluid and conductive heating of these fluid mixtures within the TAG mound. At TAG, sub–seafloor mixing between locally entrained seawater and rising hot hydrothermal fluids has resulted in precipitation of high–temperature sulfides (e.g., chalcopyrite, pyrite), generation of secondary acidity and dissolution of previously deposited sphalerite in a process of zone refinement (Tivey et al., 1995).

More recently, abundant anhydrite has been recovered from the active Papua New Guinea–Australia–Canada–Manus (PACMANUS) hydrothermal system, Manus back–arc basin (Binns et al., 2007). At PACMANUS, samples of anhydrite were recovered sub–seafloor to depths ~ 300 meters via drilling (ODP Leg 193) and include anhydrite as matrix within hydrothermal breccia, as well–developed veins often greater than 10 mm thickness, and as more massive anhydrite in brecciated pore space (Binns et al., 2007). Trace element (REE) and isotopic (Sr, S) studies of mineral separates from these anhydrite samples have enables the sub–seafloor processes associated with formation and evolution of hydrothermal fluids and mineral deposits at back–arc basins and mid–ocean ridges to be

compared and contrasted (Bach et al., 2003; Roberts et al., 2003; Bach et al., 2005). The PACMANUS data record significant geochemical and isotopic variability and indicate heterogeneous fluid mixing regimes during vent deposit formation (Bach et al., 2003; Roberts et al., 2003). Of particular significance, remarkable differences in REE contents (Bach et al., 2003) and S isotope compositions (Roberts et al., 2003) recorded in anhydrite have been interpreted to reflect variable degassing of magmatic acid volatiles at depth within back–arc basins. Exsolution of magmatic acid volatile phases (H_2O–CO_2–HCl–HF–SO_2) and resulting changes in fluid chemistry can impact substantially the processes associated with metal–rich sulfide deposit formation in back–arc hydrothermal environments (Sillitoe et al., 1996; Hannington et al., 2005).

Studies of anhydrite have the potential to identify sub–seafloor processes associated with high–temperature hydrothermal fluid activity and mineral deposition. However, conclusions drawn from previous studies have relied on data obtained via analysis of bulk homogenized materials (mineral separates). This technique is disadvantageous for two reasons: (1) data obtained from analysis of mineral separates for more than one geochemical tracer are typically obtained from multiple grains that may not have the same history of formation and are chemically unrelated, and (2) sample homogenization destroys chemical heterogeneity and thereby erases information recorded by the mineral. This study examines the geochemical signatures of anhydrite recovered from vent fields in the Manus back–arc basin (PACMANUS and SuSu Knolls) using fully coupled *in situ* analytical measurements of REEs and Sr and S isotopes. The results provide new constraints on sub–seafloor fluid evolution and mineral deposition processes

in hydrothermal systems in back–arc basins, including deep–seated seawater–rock interaction, inputs of magmatic volatiles and sub–seafloor fluid mixing. Extensive geochemical data available for seafloor hydrothermal fluids sampled from the same vent fields where anhydrite is deposited (see Chapter 2) are used to ground–truth mineral chemical signatures. The ability to use anhydrite as a recorder of sub–seafloor hydrothermal processes has particular importance for studies of relict systems where fluids are no longer present and information pertaining to the evolution of the deposit is preserved only in minerals.

2. GEOLOGIC SETTING

2.1. Regional setting

The Manus Basin in the Bismarck Sea, Papua New Guinea (Figure 3.1) is a rapidly–opening (~ 100 mm/yr) back–arc basin associated with subduction of the Solomon Microplate beneath the New Britain arc (Taylor, 1979; Davies et al., 1987; Martinez and Taylor, 1996). Crustal rifting and spreading occurs along several distinct lineations, including the Extensional Transform Zone, Manus Spreading Center and the Eastern Manus Basin (Martinez and Taylor, 1996; Sinton et al., 2003). The Eastern Manus Basin (EMB) is bounded by the Djaul and Weitin Transforms. Rapid spreading in the EMB is accommodated primarily by rifting and extension of existing crust. Lavas are erupted as a series of discrete *en echelon* neovolcanic ridges and volcanic cones of felsic composition (andesite–to–rhyolite) exhibiting distinct arc–affinity (Sinton et al., 2003). The EMB hosts

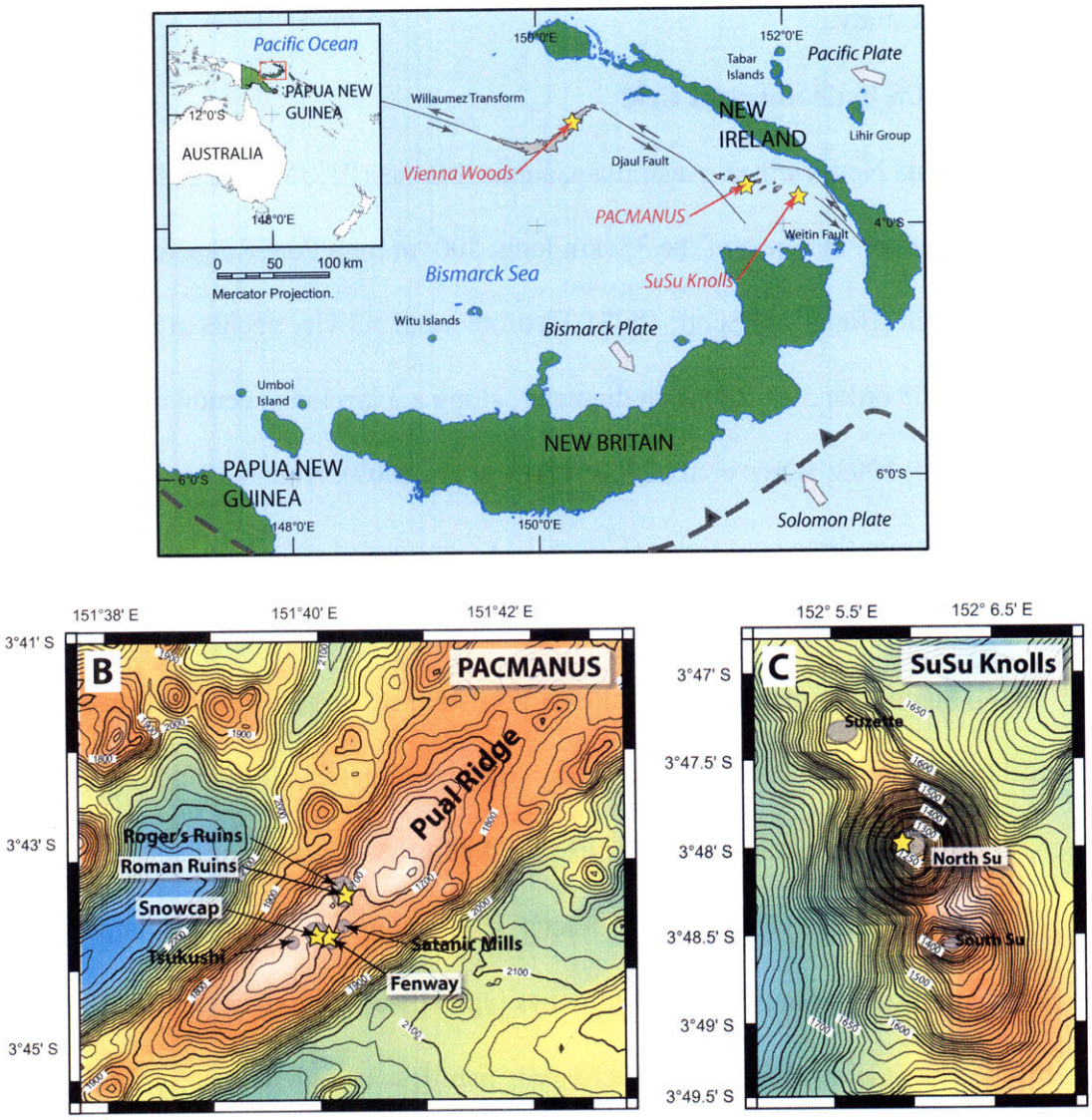

Figure 3.1. A) Regional tectonic setting of the Manus Basin indicating active plate motions and rifting, and areas of known hydrothermal activity in the Manus Basin. **B**) Distribution of known hydrothermal vent fields at PACMANUS. **C**) Known hydrothermal vent fields SuSu Knolls. Yellow stars indicate the locations where anhydrite was recovered (Roman Ruins, Snowcap and Fenway and North Su). Bathymetry based on EM300 SeaBeam sonar (modified from Tivey et al., 2007).

several active hydrothermal systems, including the PACMANUS (Binns and Scott, 1993; Scott and Binns, 1995)and SuSu Knolls (Binns et al., 1997), the deposits of which are examined in this study.

2.2. PACMANUS hydrothermal field

The Papua New Guinea–Australia–Canada–Manus (PACMANUS) hydrothermal systems is located on the crest of the 35–km long, 500–m high Pual Ridge at water depths of 1650 – 1740 m (Binns and Scott, 1993). Hydrothermal activity occurs at several discrete fields, each of the order 50 – 200 m in diameter, along a 3 km long section of Pual Ridge (Binns and Scott, 1993; Binns et al., 2007; Tivey et al., 2007). Abundant anhydrite has been recovered from three vent fields (Figure 3.1). Samples of anhydrite were recovered sub–seafloor by ocean drilling at Snowcap and Roman Ruins during ODP Leg 193 (Binns et al., 2007). Samples of massive anhydrite currently exposed at the seafloor were recovered by surface grab sampling at Fenway, which is a mound exhibiting high–temperature activity discovered during cruise MGLN06MV (Tivey et al., 2007).

The Roman Ruins vent field is characterized by numerous discrete columnar chimneys and clusters of multi–spired chimneys typically 5 – 7 m in height, overlying mostly fresh volcanic outcrop. Current activity is manifest as high temperature focused discharge (up to 341 °C) from black and gray smoker chimneys (Seewald et al., 2006; Tivey et al., 2007). More diffuse fluid, with temperatures ranging from 54 to 106 °C, discharges from fissures within the volcanic basement and through chimney and volcanic talus in areas surrounding sulfide deposits. Drilling of the Roman Ruins deposit and underlying basement (Holes 1189A and 1189B) recovered volcanic rocks and

hydrothermal material to depths of ~ 200 meters below seafloor (mbsf) (Binns et al., 2007). Except for relatively fresh lava flows recovered near the seafloor (< 30 mbsf), most volcanic rocks display moderate–to–extensive alteration, which continues without interruption to the base of the drill core. Alteration is primarily argillaceous (smectite–chlorite±illite±quartz) (Yeats et al., 2001; Lackschewitz et al., 2004). Hydrothermal stockwork is present to depths ~ 120 mbsf and is dominated by disseminated and locally massive veined pyrite (Binns et al., 2007). Anhydrite is a minor mineral interspersed throughout the drill core, occurring mostly as fine–grained disseminated matrix and locally as more massive anhydrite veins in both hydrothermal stockwork and alteration assemblages (Figure 3.2). The total abundance of anhydrite typically decreases with depth, although anhydrite is present to depths of at least 200 mbsf.

At the Snowcap vent field, hydrothermal activity is currently dominated by low temperature fluid discharge (< 180 °C) through bulbous sulfide chimneys across heavily–sedimented and altered terrain (Tivey et al., 2007). Surface outcrops of fresh massive lava flows are rare. Instead, hyaloclastite flows, volcaniclastic sediments, native sulfur, bleached alteration products and microbial mats are common (Yeats et al., 2000; Tivey et al., 2007). Drilling recovered core from two holes (Holes 1188A and 1188F) down to depths of 210 and 390 mbsf, respectively. Petrographic analyses indicate extensive and multi–stage alteration, including alternating argillaceous (smectite–chlorite) and advanced argillic (alunite–illite–pyrophyllite–quartz) assemblages and, with increasing depth, extensive silicification (Yeats et al., 2001; Lackschewitz et al., 2004). The occurrence of advanced argillic alteration and native sulfur is consistent with rock alteration by low pH

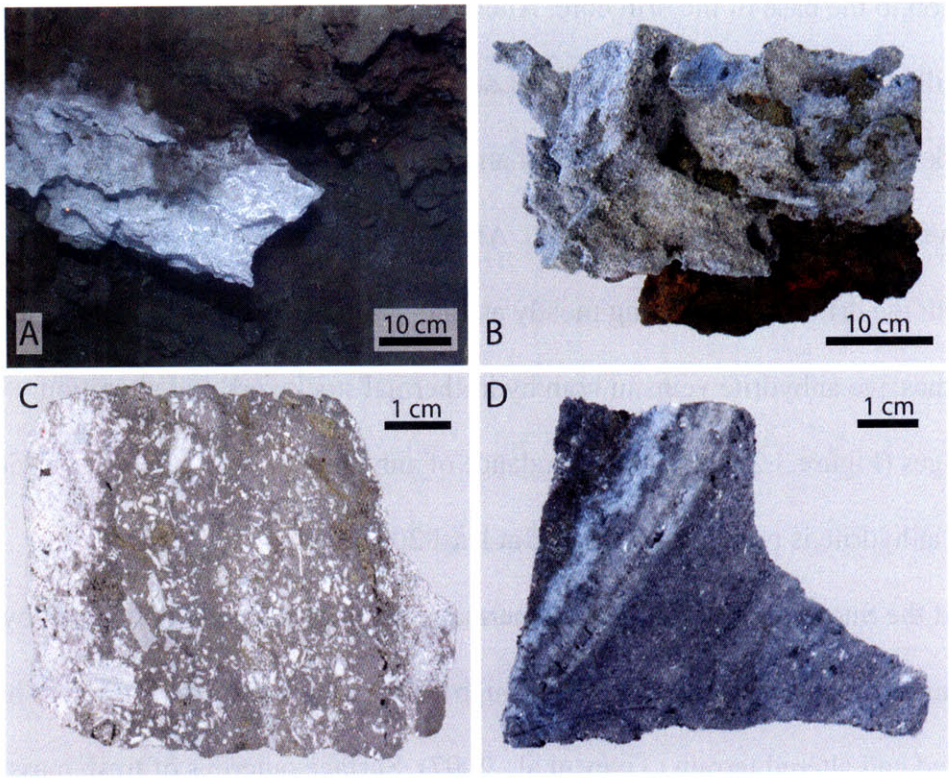

Figure 3.2. Photographs of **A**) massive anhydrite exposed at the seafloor (Fenway mound, PACMANUS). **B**) massive anhydrite (sample J2_212_7_R1 from Fenway). **C**) semi-massive sulfide (chalcopyrite+pyrite) within a matrix of anhydrite+silica (ODP drill core sample 193_1189A_12R_1, 120-128 cm, 105 mbsf, from Roman Ruins, PACMANUS). Photograph modified after Binns et al. (2007). **D**) cross-section through composite vein of massive anhydrite with frequent fine-to-medium grained chalcopyrite-rich sulfide dissemination (samples sample J2_227_7_R2 from North Su, SuSu Knolls).

(less than 3) fluids likely resulting from exsolution of a magmatic acid volatile phase beneath areas of the PACMANUS hydrothermal system. Anhydrite occurs throughout drill core to depths of at least 350 mbsf and does not appear associated within any single alteration stage. Anhydrite occurs commonly as composite veins and as matrix within brecciated and hydrothermally altered minerals.

At the Fenway vent field, the seafloor is dominated by a central, two–tiered mound approximately 40 m in diameter and 18 m in relief. The summit of the mound is composed of an extensive black smoker complex with fluids venting vigorously at temperatures up to 358 °C (Seewald et al., 2006; Tivey et al., 2007). Lower temperature focused fluid venting from chimneys and diffuse fluid venting from fissures and brecciated sediment are common from lower tiers and slopes of the mound. The entire mound is covered by extensive sulfide chimney debris and talus, outcrops of massive anhydrite, and brecciated sands. Several samples of massive anhydrite have been recovered from the seafloor (Tivey et al., 2007). Samples from Fenway are large (~ 5–10 kg) and coarse–grained with no obvious crystallographic zoning (Figure 3.2). Based on textural similarities with massive anhydrite recovered from the TAG active mound, Mid–Atlantic Ridge (Tivey et al., 1995), the massive anhydrite at Fenway was also likely precipitated within a porous sulfide–rich surface dome as a result of either conductive heating of seawater or mixing between entrained seawater and high–temperature hydrothermal fluids, and exposed following collapse of the dome. No anhydrite has been sampled from beneath the seafloor at this vent field.

2.3. SuSu Knolls (North Su) hydrothermal system

The SuSu Knolls hydrothermal area is located ~ 45 km east of PACMANUS and consists of three primary areas of activity (North Su, South Su and Suzette) located on individual volcanic domes at water depths between ~ 1140 and 1510 m (Binns et al., 1997). At North Su, hydrothermal activity on flanks of the dome is dominated by vigorous discharge of thick, yellowish–white fluids and liquid native sulfur through volcanic clasts and hydrothermal sediments. These fluids are hot (T = 48 – 241 °C) and extremely acidic (pH = 0.9 – 1.8, at 25 °C (Seewald et al., 2006)). This activity contrasts strongly with fluid discharge at the summit of the North Su mound, which is dominated by venting of high–temperature black smoker fluids (T = 296 – 325 °C; pH = 2.8 – 3.4, at 25 °C) from multi–spired sulfide chimney complexes up to 11 m tall (Seewald et al., 2006; Tivey et al., 2007). Seafloor rocks are composed of vesicular dacite flows and hyaloclastite flows, overlain by hydrothermal talus and sediments, abundant native sulfur flows and locally extensive sulfide deposits (Binns et al., 1997; Tivey et al., 2007). Exposed massive anhydrite was sampled near the base of the black smoker summit complex within sulfide–sulfate talus. This sample exhibits complex textures, including crustiform layering of anhydrite veins (Figure 3.2).

3. METHODS

3.1. Sample collection and preparation

Anhydrite analyzed during this study was recovered either from beneath the seafloor at the Roman Ruins and Snowcap vent fields during Ocean Drilling Program Leg

193 (Binns et al., 2007) or at the seafloor from the Fenway and North Su vent fields during *R/V Melville* cruise MGLN06MV (Tivey et al., 2007). A total of 12 drill core samples were selected from Roman Ruins and Snowcap and provide a representative down core profile of anhydrite from different lithologic units and textural settings, including a variety of veins, composite and cross–cutting growth bands and more massive anhydrite filling vugs and pore spaces. A total of seven massive anhydrite samples were recovered at the seafloor from the Fenway mound and a single massive anhydrite sample was recovered from the base of the black smoker complex at North Su.

Samples were prepared for analysis by one of two methods. Massive anhydrite samples recovered by ROV were initially sub–sampled using a tile saw and/or a Buehler Micromet saw. Working sections were impregnated with epoxy resin and cut into thin (~ 2 mm) wafers. These wafers were polished on both sides and mounted onto standard 45 x 25 mm petrographic slides for analysis. Six anhydrite samples from ODP drill core were provided by D. Vanko at the University of Towson, Maryland prepared using a similar method (Vanko et al., 2004). Six additional anhydrite samples recovered from ODP Leg 193 drill core were mounted with epoxy in 25 mm aluminum rings, cut to obtain a flat surface and polished on one side for analysis.

3.2 Analytical methods

3.2.1 Cathodoluminescence imaging

Cathodoluminescence (CL) reconnaissance imaging was performed to obtain semi–quantitative trace element distributions within each sample. In particular, CL imaging was used to differentiate chemical heterogeneities (crystal zoning) occurring within and

between individual anhydrite crystals, which would be a focus for subsequent *in situ*, quantitative geochemical analyses. Under excitation by a cathode beam, trivalent REEs (Sm^{3+} and Dy^{3+}) fluoresce and emit intense spectra within visible wavelengths with varying shades of tan (Marshall, 1988). CL was mapped using a Nuclide Corporation ELM–2B cold cathode generator, operated at ~ 10 keV and 0.8 mA and with a vacuum of 70 – 85 μtorr. Each sample was photographed using a Nikon D1x digital camera, mounted to a Nuclide Corporation ELM–2E microscope with 10x – 40x magnification. Photographs were captured using white balance set to fluorescent light and exposure times of 30 seconds. Photomosaics were generated using digital imaging software (Abode Photoshop CS2) without further manipulation.

3.2.2. Laser–ablation ICP–MS element analyses

Geochemical analyses were coordinated so that elemental and isotopic data were collected from adjacent locations within the same heterogeneous domains as identified by CL. Elemental and isotopic data are directly related spatially and texturally, and the full chemical heterogeneity as identified by CL imaging is faithfully captured.

In situ trace elemental (REE, Sr, Ba, Pb and Mg) analyses were performed using laser ablation–inductively coupled plasma–mass spectrometry (LA–ICP–MS) at the Woods Hole Oceanographic Institution (WHOI) and the University of Bremen. Anhydrite samples were loaded into a NewWave UP213 laser microprobe sample chamber coupled to a ThermoElectron *Element2* high resolution ICP–MS (Balaram, 1996). Operating parameters for the ICP–MS were configured for each session to obtain optimal signal response and stability. Laser ablation settings were identical for all elemental analyses. The

laser was operated in apertured mode, with a spot size of 60 μm diameter and a firing repetition rate of 10 Hz with a laser intensity of 65 %. Line scan ('raster') mode was used in preference to single spot mode, taking advantage of the movable stage beneath the laser. A line spacing of 15 μm and scan speed of 5 μm/s were used across a total raster area of 80 x 180 μm (total 13 lines). Total analysis time for a single measurement, including wash–out time, was of the order of 7 minutes. The certified reference material NIST SRM612 glass was used as the standard for trace element calibration (Pearce et al., 1997; Kent et al., 2004). Internal normalization of the data was achieved using CaO as the spike; concentrations in the standard and in anhydrite are 114000 and 411765 ppm, respectively. Blanks were monitored repeatedly during analytical sessions and used for data reduction. The formation of interfering oxides (e.g., $^{135}Ba^{16}O^{+}$ on $^{151}Eu^{+}$; $^{143}Nd^{16}O^{+}$ on $^{159}Tb^{+}$) can greatly degrade the accurate measurement of REEs. Contributions from BaO^{+} were assessed by monitoring simultaneously isotopes ^{151}Eu and ^{153}Eu. No significant bias of the naturally occurring $^{151}Eu/^{153}Eu$ ratio (~ 0.89) was observed, indicating no significant formation of oxide interferences during typical analysis. Chondritic values used for external normalization of REE (REE_N) data are taken from Anders and Grevesse (1989). Reproducibility for the method is typically within 5 – 8 %.

3.2.3. Laser–ablation MC–ICP–MS isotopic analyses

In situ isotope analyses were performed at WHOI using a ThermoElectron NEPTUNE multi–collector ICP–MS coupled to a NewWave UP213 laser microprobe. Strontium isotope ratios ($^{87}Sr/^{86}Sr$) were measured following a revised procedure from Hart et al. (2005), with laser and mass spectrometer operating parameters optimized for the

analysis of sulfates. The reference material NIST SRM987 was used as the external Sr isotopic standard (consensus $^{87}Sr/^{86}Sr$ ratio = 0.710248). Instrumental mass bias was calculated from deviation of the measured $^{86}Sr/^{88}Sr$ ratio from the canonical isotopic ratio in the standard ($^{86}Sr/^{88}Sr$ = 0.119400) and a mass bias correction applied to measured $^{87}Sr/^{86}Sr$ ratios using the exponential mass law relationship (Albarède and Beard, 2004). The calculated mass bias correction was then applied to the unknown anhydrite sample assuming linear interpolation of mass bias between replicate standards. Long–term reproducibility of $^{87}Sr/^{86}Sr$ isotope ratios, as determined by repeat analysis of an aragonite coral ('in–house' standard) grown in contemporaneous seawater, was better than 20 ppm (Sclerosponge; $^{87}Sr/^{86}Sr_{certified}$ = 0.70918; $^{87}Sr/^{86}Sr_{meas}$ = 0.70919 ± 0.00002; n = 15, 2σ uncertainty).

Isotopes of sulfur were measured using the analytical procedure detailed by Craddock et al. (2008). Briefly, the standard–sample bracketing method (Belshaw et al., 1998) was employed to calibrate unknown samples against isotopically characterized sulfur standards. Instrumental mass bias was calculated for the S isotopic standard and a correction applied to the unknown sample using linear interpolation of calculated mass biases from bracketing standards. Isobaric interferences (dominantly from molecular O_2 species) were resolved by operating the instrument in high–resolution mode (Weyer and Schwieters, 2003). Blank contamination was measured using ultra–clean 2% nitric acid and corrected by on–peak baseline subtraction. External reproducibility of the data is within ± 0.45 ‰ for laser ablation analyses.

4. RESULTS

Trace element (REE, Sr, Ba, Mg and Pb) and isotope (Sr, S) data are reported for 12 drill core samples from PACMANUS (8 from Snowcap and 4 from Roman Ruins) and 7 samples from exposed seafloor massive anhydrite (6 from Fenway and 1 from North Su). In total, approximately 500 multi–element analyses and 300 isotope analyses were carried out. A complete data report is provided in Appendix C1.

4.1. Trace element concentrations of anhydrite

All anhydrite samples examined exhibit significant variability in concentrations of trace elements. Detailed high–resolution analyses demonstrate that this variability exists on several spatial scales, ranging from sub–millimeter differences within single samples to differences among vent fields. Total concentrations of REEs (ΣREE) range from ~ 2 to 550 ppm, although most measurements fall in the range 5 to 70 ppm. Similar ranges and variability of REE concentrations were demonstrated previously by whole–rock analysis of anhydrite from PACMANUS (Bach et al., 2003; Bach et al., 2005).These concentrations are high relative to REE concentrations in anhydrite recovered from the TAG active mound, 26 °N mid–Atlantic Ridge (ΣREE ~ 1 – 10 ppm) (Humphris, 1998).

Strontium is a minor element in anhydrite, with concentrations in Manus Basin samples ranging from ~ 1000 – 5000 ppm. Magnesium and Ba are present in all Manus anhydrite samples at concentrations between 1 – 80 ppm and 4 – 250 ppm, respectively. In addition, local enrichments up to 1000 ppm Mg and Ba occur in some anhydrite grain domains. Lead is present as a trace element at concentrations of 0.01 – 10 ppm in most

within single samples. There is no clear correlation between the geochemistry of anhydrite and the depth below seafloor from which it was recovered.

At North Su (SuSu Knolls), composite veins within a single sample of massive anhydrite also exhibit different REE_N pattern shapes, ranging from light–REE depleted to relatively flat with variable, positive Eu–anomalies (La_N/Yb_N = 0.1 – 1.8, Sm_N/Yb_N = 0.6 – 4.6, Eu_N/Eu^*_N = 1.4 – 8.0; Figure 3.6).

4.2. Sr isotope ratios in anhydrites

Overall, Sr isotope ratios ($^{87}Sr/^{86}Sr$) in anhydrite range from 0.70429 to 0.70881 (Figure 3.7). These data reflect precipitation of anhydrite from a wide range of mixing ratios between seawater (radiogenic $^{87}Sr/^{86}Sr$ = 0.70918) and end–member hydrothermal fluids ($^{87}Sr/^{86}Sr$ ~ 0.70427; M. Rosner and W. Bach, *unpubl. data*). The Sr isotope ratio of end–member black–smoker hydrothermal fluids ($^{87}Sr/^{86}Sr$ ~ 0.70427 – 0.70460) is similar to that of host volcanics in the eastern Manus Basin ($^{87}Sr/^{86}Sr$ ~ 0.7035; Sinton et al., 2003). Where data exist, new results are compared against Sr isotope ratios for the same anhydrite samples determined using whole–rock isotope analysis (Roberts et al., 2003). In general, the data show excellent agreement (Figure 3.7). However, in situ analyses highlight a range of isotope compositions within individual anhydrite crystals, not identified by whole–rock isotope analysis and extend the overall range of Sr isotope ratios measured. The relative proportions of hydrothermal fluid and seawater in the mixture that precipitated anhydrite can be calculated from measured Sr isotope ratios (Mills et al., 1998; Mills and Tivey, 1999):

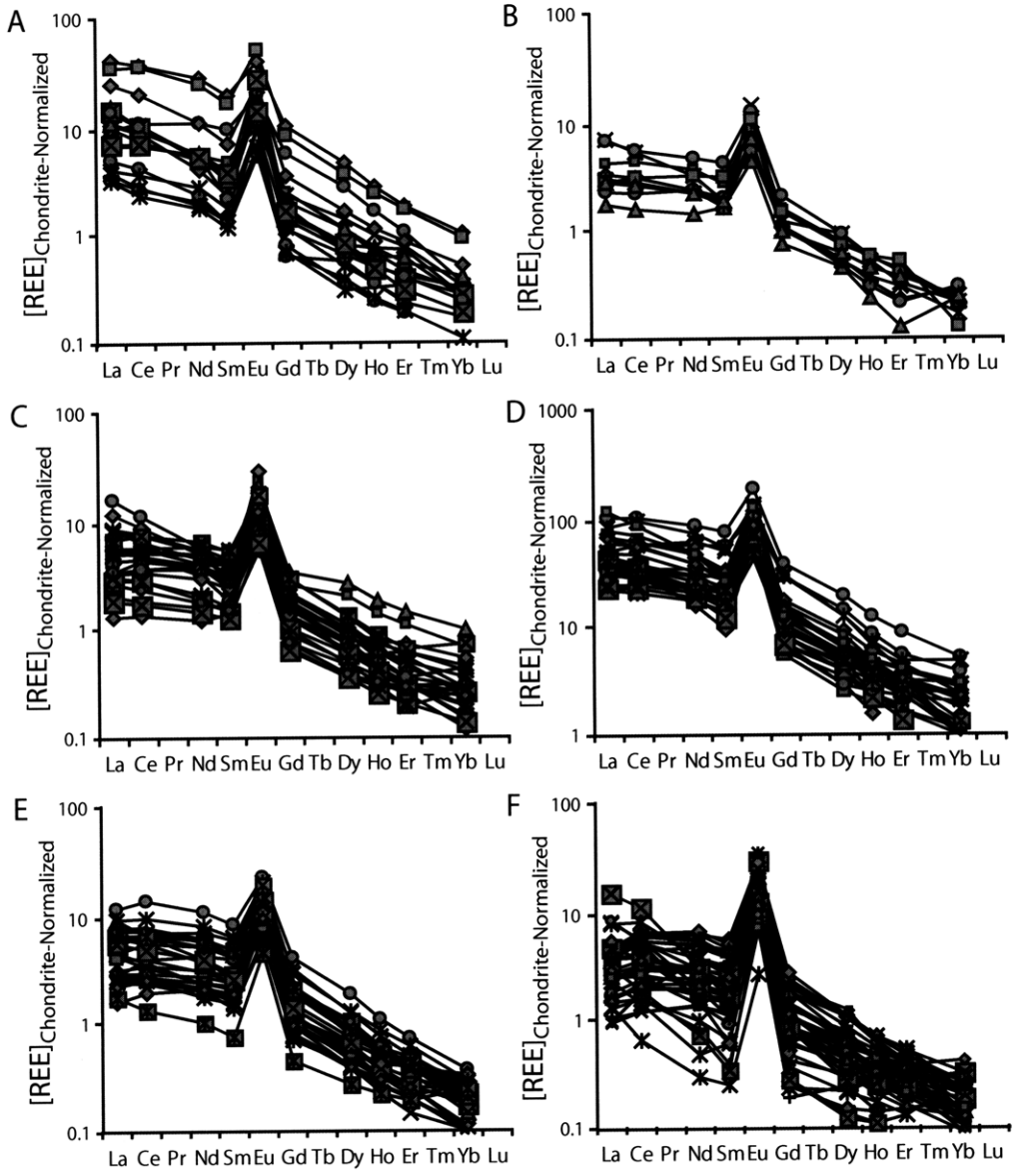

Figure 3.3. Condrite-normalized REE patterns for massive anhydrite recovered from the seafloor at Fenway, PACMANUS hydrothermal system. Individual patterns determined in situ by laser ablation ICP-MS. **A**) sample J2_210_8_R2, **B**) sample J2_212_7_R1, **C**) sample J2_216_1_R1, **D**) sample J2_216_5_R1, **E**) sample J2_216_12_R1, **F**) sample J2_216_14_R1. Chondritic values from Anders and Grevasse (1989).

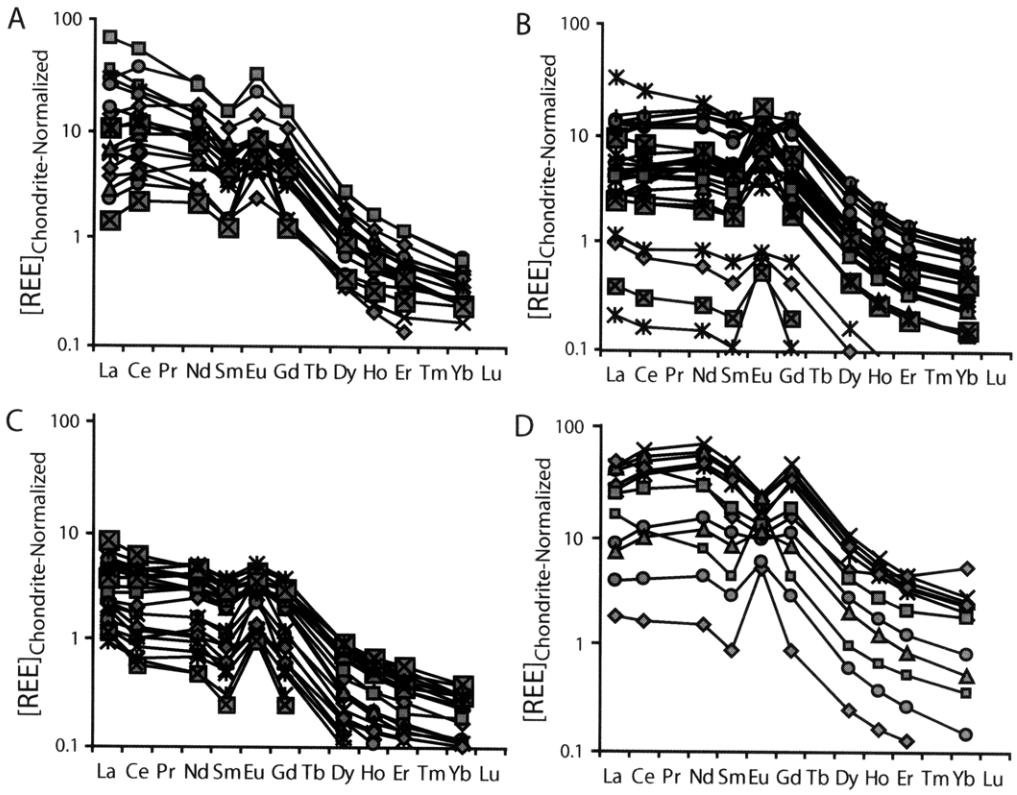

Figure 3.4. Condrite-normalized REE patterns for anhydrite recovered from site 1189 (Roman Ruins), PACMANUS hydrothermal system. Individual patterns determined in situ by laser ablation ICP-MS. **A**) sample 193_1189A_3R_1, 89-93cm, 20 mbsf, **B**) sample 193_1189A_7R_1, 19-23cm, 58 mbsf, **C**) sample 193_1189B_10R_1, 42-44cm, 118 mbsf, **D**) sample 193_1189B_14R_2, 0-3cm, 158 mbsf. Chondritic values from Anders and Grevasse (1989).

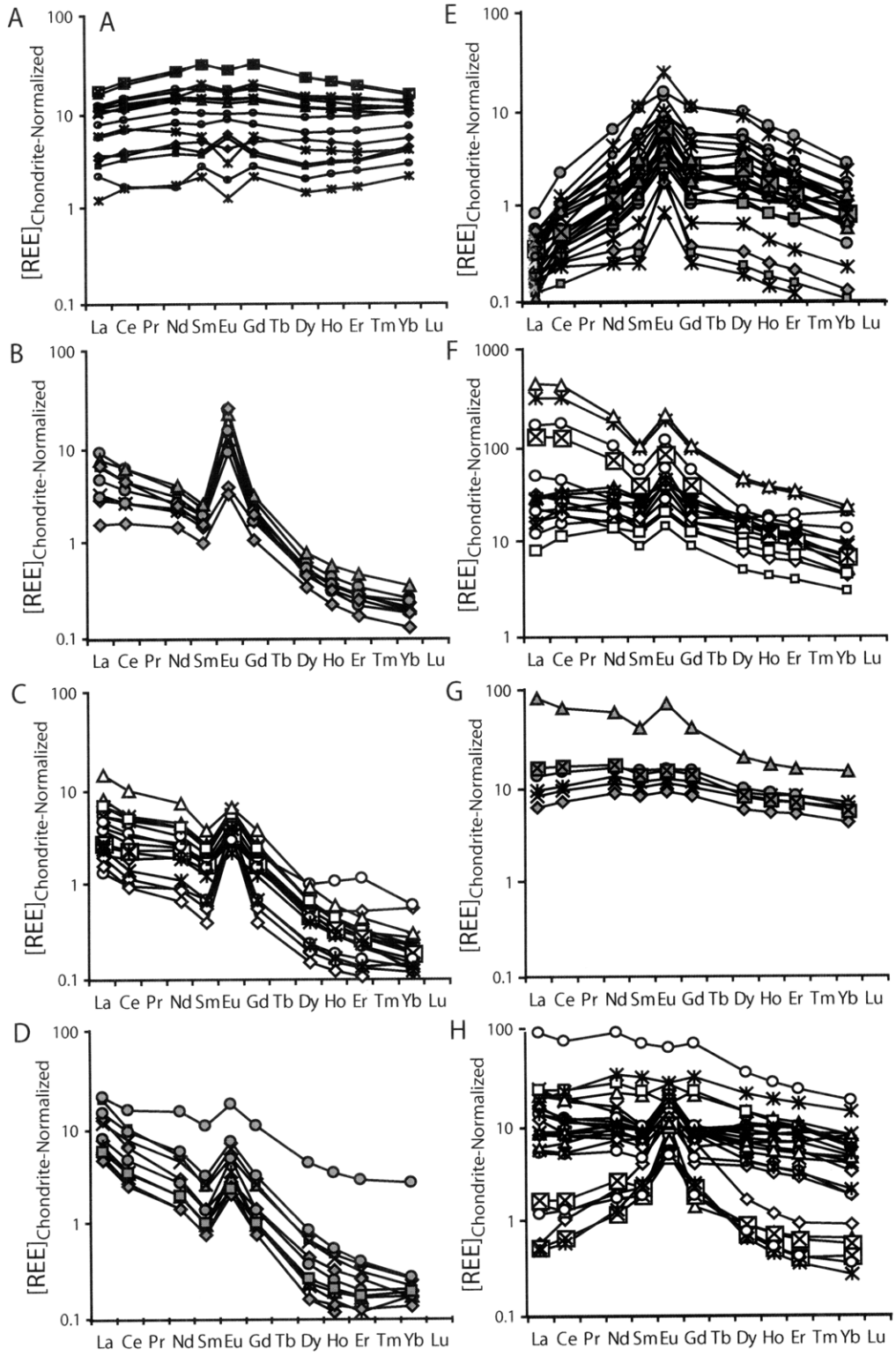

Figure 3.5. Condrite-normalized REE patterns for anhydrite from site 1188 (Snowcap), PAC-MANUS. **A**) 193_1188A_7R_1, 66-68cm, 50 mbsf, **B**) 193_1188A_15R_1, 14-20cm, 126 mbsf, **C**) 193_1188F_16R_2, 109-111cm, 137 mbsf, **D**) 193_1188A_17R_2, 6-9cm, 146 mbsf, **E**) 193_1188F_1Z_2, 32-34cm, 219 mbsf, **F**) 193_1188F_1Z_4, 100-104cm, 223 mbsf, **G**) 193_1188F_23Z_2, 22-26cm, 289 mbsf, **H**) 193_1188F_26Z_1, 62-69cm, 300 mbsf. Chondritic values from Anders and Grevasse (1989).

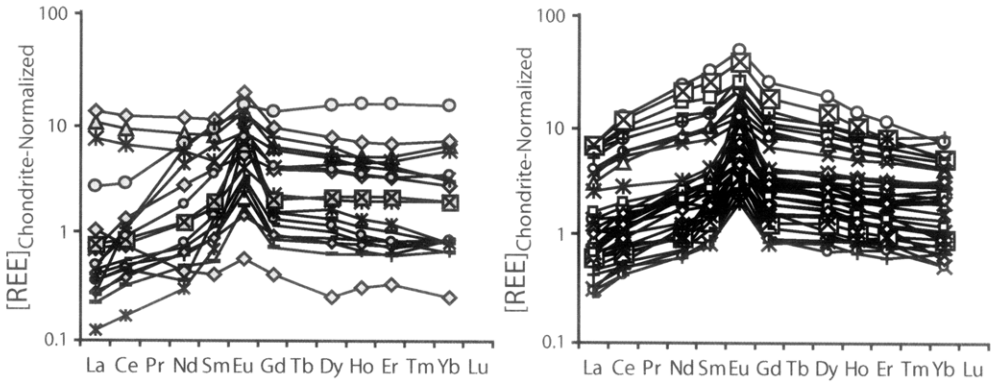

Figure 3.6. Condrite-normalized REE patterns for massive anhydrite recovered from the seafloor at North Su, SuSu Knolls hydrothermal system. Sample J2_227_7_R2. Chondritic values from Anders and Grevasse (1989).

% hydrothermal fluid =

$$\frac{\left[\left({}^{87}Sr/{}^{86}Sr_{SW} - {}^{87}Sr/{}^{86}Sr_{MIX}\right) \times [Sr]_{SW}\right]}{\left[{}^{87}Sr/{}^{86}Sr_{SW} \times [Sr]_{SW}\right] - \left[{}^{87}Sr/{}^{86}Sr_{HF} \times [Sr]_{HF}\right] + \left[{}^{87}Sr/{}^{86}Sr_{MIX} \times ([Sr]_{HF} - [Sr]_{SW})\right]}$$

where sub–scripts SW, HF and MIX are seawater, hydrothermal fluid and mixed component, respectively. This calculation assumes that the Sr concentration and isotope ratio in contemporary end–member hydrothermal fluids is representative of fluids from which anhydrite precipitated ($[Sr]_{HF,\ PACMANUS} \sim 120\ \mu M$, $[Sr]_{HF,\ SuSu\ Knolls} \sim 400\ \mu M$, $[Sr]_{seawater} \sim 90\ \mu M$; see Chapter 4).

At Snowcap (PACMANUS, Hole 1188A, F), in situ analyses demonstrate $^{87}Sr/^{86}Sr$ ratios of anhydrite cluster mostly in the range 0.7050 to 0.7075, corresponding to fluid mixes with between ~ 35 and 77 % hydrothermal fluid (Figure 3.7). This variability is observed on sub–centimeter spatial scales within most individual samples. There are no clear downhole trends for Sr isotope ratios recorded by anhydrite. A single anhydrite sample recovered at a depth ~ 50 mbsf has a uniform radiogenic $^{87}Sr/^{86}Sr$ ratio ~ 0.7087 and is calculated to have precipitated from a seawater dominated (> 90 – 95 %) fluid mix. Sr isotope ratios of anhydrite from Roman Ruins (PACMANUS, Hole 1189A, B) cluster mostly between 0.7055 and 0.7080 (Figure 3.7). Overall $^{87}Sr/^{86}Sr$ ratios span the range 0.7043 to 0.7082. Remarkable heterogeneity of Sr isotopes is apparent in all samples and occurs on spatial scales less than 1 mm. Mass balance calculations indicate anhydrite precipitated mostly from fluid mixes containing between ~ 32 – 83 % seawater (17 – 68 % hydrothermal fluid). However, the heterogeneity of Sr isotope ratios revealed by in situ

analyses indicates that the overall contribution of seawater was more variable and in some instances very low (1 – 5 %) in anhydrite recovered from depth (> 150 mbsf). Sr isotope ratios of seafloor massive anhydrite from Fenway (PACMANUS) vary between 0.7060 and 0.7082 (Figure 3.7). In most instances, the data indicate anhydrite precipitation from fluid mixes dominated by seawater (~ 55 to 84 %). Locally, greater contributions of hydrothermal fluid to the fluid mix precipitating anhydrite (up to 60 % hydrothermal fluid) are apparent in some samples.

At North Su (SuSu Knolls), Sr isotope ratios recorded in a single anhydrite sample are remarkably variable, ranging from 0.7046 to 0.7085 and indicating precipitation of anhydrite from a fluid mix with seawater containing 23 % to 96 % seawater.

4.3. S isotope ratios in anhydrite

At all vent fields, the S isotope compositions ($\delta^{34}S_{sulfate}$, hereafter referred to as $\delta^{34}S$) of anhydrite samples examined cluster mostly around that of contemporary seawater sulfate ($\delta^{34}S$ = +21.0 ‰ (Rees et al., 1978)). Seafloor massive anhydrite samples from Fenway have $\delta^{34}S$ compositions between +20.1 and +22.0 ‰. $\delta^{34}S$ compositions of anhydrite from Roman Ruins range from +19.6 and +23.1 ‰, with most $\delta^{34}S$ values equal to or slightly heavier than seawater sulfate (Figure 3.7). There is no clear downhole trend of S isotope compositions. Anhydrite samples from Snowcap display the greatest variation of S isotope compositions, ranging from $\delta^{34}S$ = +16.6 ‰ and +21.9 ‰. The $\delta^{34}S$ ratios of most anhydrite samples are lighter than seawater, in contrast to anhydrites examined at other vent fields. In general, $\delta^{34}S$ ratios trend toward lighter isotope composition with increasing depth beneath Snowcap. The data are largely in agreement with previous

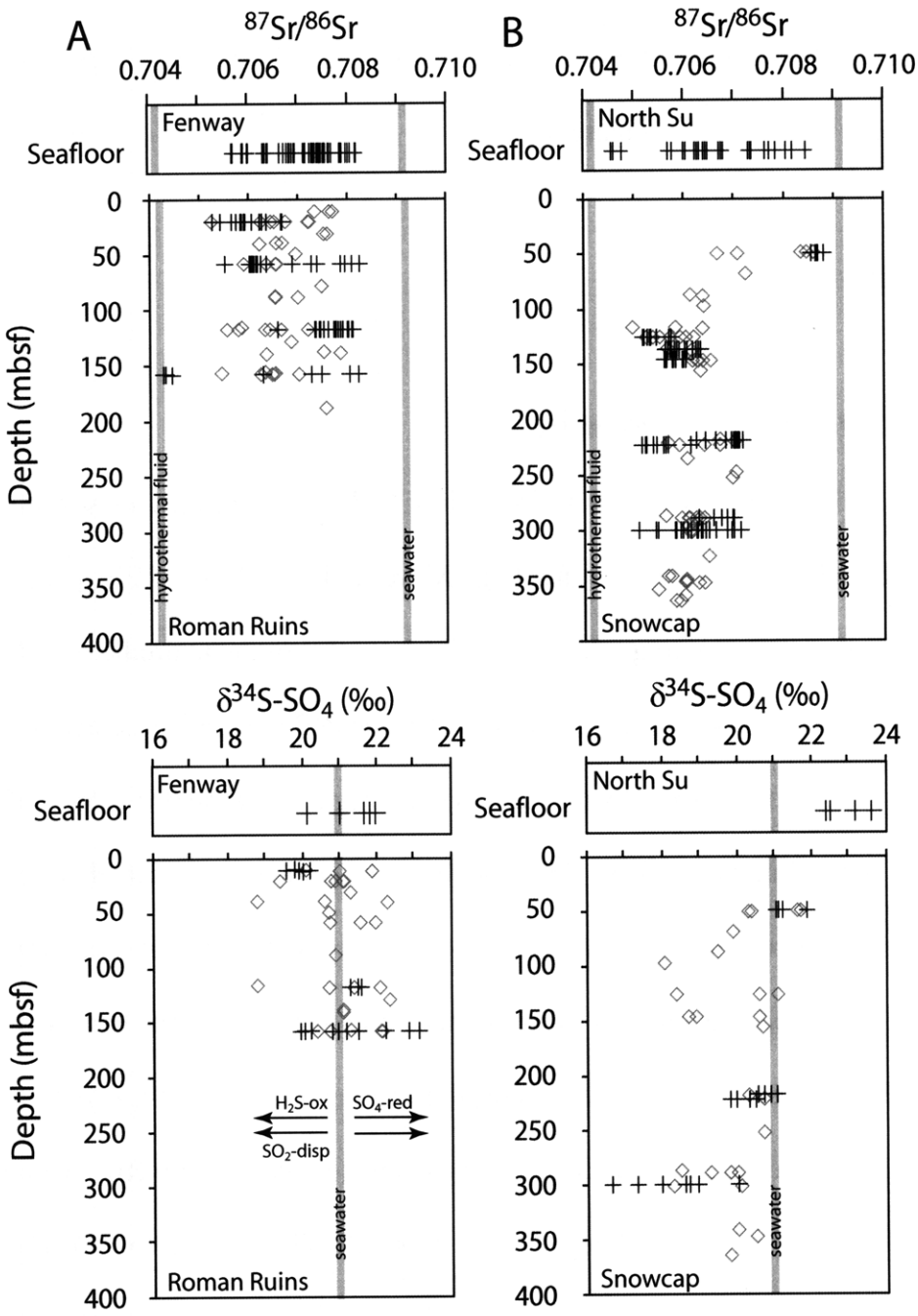

Figure 3.7. Sr isotope ($^{87}Sr/^{86}Sr$) and S isotope ($\delta^{34}S$) values determined by this study (black crosses) and compared with values determined by Roberts et al. (2003) and Bach et al. (2005) by whole rock analysis (gray diamonds). Concordance between the datasets is good, however the overall range of isotope values is greater for in situ analyses, reflecting the local ~ 1 mm heterogeneity recorded by in situ measurements. **A**) Fenway (seafloor) and Roman Ruins (drill core), **B**) Snowcap (drill core) and North Su (seafloor).

analyses of S isotope ratios of anhydrite within drill core from Roman Ruins and Snowcap (Roberts et al., 2003). At North Su, $\delta^{34}S$ compositions are all heavier than seawater sulfate, between +22.4 and +23.6 ‰ (Figure 3.7).

5. Discussion

5.1. Rare Earth Element geochemistry

Given that REE concentrations in seafloor hydrothermal fluids are several orders of magnitude enriched relative to seawater (e.g., Mitra et al., 1994), the REE_N pattern shape of a fluid resulting from mixing of the two will record that of the hydrothermal fluid. It has been shown in previous studies that, to first–order, the REEs (with the exception of Eu in some fluids) are incorporated into anhydrite without significant fractionation (Mills and Elderfield, 1995; Humphris, 1998). REE_N patterns preserved in anhydrite therefore record that of the source hydrothermal fluid. REE_N pattern shapes for anhydrites recovered from the PACMANUS and SuSu Knolls hydrothermal systems in the Manus Basin exhibit significant heterogeneity, with three patterns dominating: (1) light–REE enrichment, (2) light–REE depletion and heavy–REE enrichment, and (3) flat uniform REE enrichment, each with a range of positive and negative Eu–anomalies (Figures 3.3 to 3.6). These REE_N pattern shapes are similar to those identified by bulk analyses of the same samples (Bach et al., 2003). The heterogeneity of REE_N patterns recorded in anhydrite suggests that the mixed fluids (and therefore endmember hydrothermal fluids) from which anhydrite precipitated also exhibited a range of REE distributions.

Recent measurements of REE concentrations in seafloor vent fluids from hydrothermal systems in the Manus Basin have demonstrated a range of REE_N pattern shapes (see Chapter 2), which support the idea that differences in REE_N patterns recorded in anhydrite likely reflect differences in aqueous REE_N patterns. The range of measured aqueous REE distributions in Manus Basin vent fluids is consistently correlated with differences in pH and ligand concentrations (chloride, fluoride and sulfate) of the same fluids (see Chapter 2). These differences are best explained as a result of varying inputs of exsolved magmatic acid volatiles (H_2O–CO_2–HCl–HF–SO_2) into circulating hydrothermal fluids (e.g., Seewald et al., 2006), which affect significantly the pH, oxidation state and ligand concentrations (e.g., Cl^-, F^- and SO_4^{2-}), and the resulting aqueous REE species distribution and REE solubility in these fluids (Douville et al., 1999; Bach et al., 2003). The range of REE_N pattern shapes preserved in anhydrite analyzed during this study suggest that anhydrite also records episodes of extensive magmatic acid volatile input. This supports the original idea by Bach et al. (2003) that different REE_N patterns recorded in anhydrite samples recovered from PACMANUS result from varying contributions of exsolved magmatic acid volatile phases (H_2O–CO_2–HCl–HF–SO_2) in back–arc hydrothermal systems.

5.1.1. REE_N pattern shapes of seafloor massive anhydrite relative to hydrothermal fluid

At Fenway (PACMANUS), REE_N patterns in massive anhydrite are characterized by a light–REE enrichment and a positive Eu–anomaly and are similar to those of nearby high–temperature (> 300 °C) hydrothermal fluids (Figures 3.3 and 3.8). These fluids are acidic (pH (25 °C) between 2.4 and 2.7) and exhibit a range of elevated fluoride

concentrations ($\Sigma F \sim 160 - 285$ μmol/kg) relative to mid–ocean ridge hydrothermal fluids, suggesting some direct contribution from an exsolved magmatic acid volatile (H_2O–CO_2–HCl–HF–SO_2) phase (Seewald et al., 2006). The REE_N patterns preserved in anhydrite from Fenway are similar to those of neighboring hydrothermal fluids, suggesting that aqueous REE distributions of hydrothermal fluids in the past as recorded in anhydrite were similar to present. There are no significant differences in the REE_N patterns recorded in anhydrite to indicate that styles of magmatic acid volatile input or hydrothermal fluid circulation beneath Fenway were significantly different in the recent past.

At North Su (SuSu Knolls), REE_N pattern shapes of seafloor massive anhydrite exhibit a range of light–REE enrichments and depletions, and variable positive Eu–anomalies, which are different to those of anhydrite recovered from Fenway (Figure 3.6). Assuming that REEs are not fractionated during incorporation into anhydrite, it is likely that this heterogeneity records changes in REE composition and pattern of hydrothermal fluids from which anhydrite precipitated. REE_N pattern shapes measured in hydrothermal fluids from the North Su vent field show a similar range of REE_N patterns that support this hypothesis. REE_N pattern shapes range from light–REE enriched to light–REE depleted patterns with positive Eu–anomalies in high–temperature black smoker fluids, to flat REE patterns in milky–white "acid–sulfate" fluids (Figure 3.8). The geochemical and isotopic compositions of smoker fluids and acid–sulfate fluids suggest very different styles of fluid evolution. At North Su, the compositions of high–temperature smoker fluids (e.g., low pH, high F and high K, Li, Rb, Cs concentrations) are consistent with convective circulation of seawater–derived hydrothermal fluids that have mixed with varying amounts of magmatic

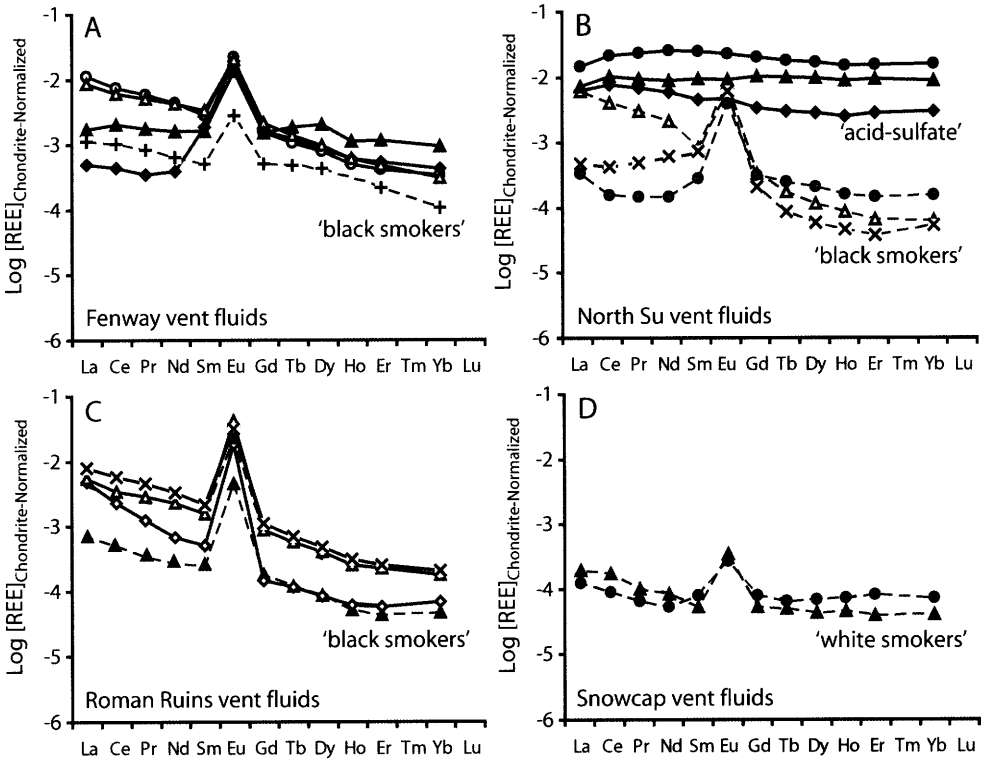

Figure 3.8. Condrite-normalized REE patterns for seafloor hydrothermal fluids sampled from the Manus Basin. **A**) black smoker fluids from Fenway, PACMANUS, **B**) black smoker fluids and acid-sulfate fluids from North Su, SuSu Knolls, **C**) black smoker fluids from Roman Ruins, PACMANUS, **D**) white/gray smoker fluids from Snowcap. (Data reported in Chapter 2.)

acid volatiles (H_2O–CO_2–HCl–HF–SO_2) and reacted extensively with crustal host rocks (see Chapters 2 and 4). In contrast, the compositions of acid–sulfate fluids (e.g., low pH, high SO_4, low K, Li, Rb, Cs concentrations) are more consistent with injection of a magmatic acid volatile phase into seawater in the absence of typical convecting high–temperature hydrothermal fluids and without significant interaction with fresh crustal host rocks (see Chapters 2 and 4). Correlated differences among fluid pH, fluoride and sulfate concentrations and REE_N pattern shapes suggest that aqueous REE distributions are sensitive to changes in fluid composition resulting from varying styles of magmatic acid volatile input and fluid evolution (Chapter 2). That REE_N pattern shapes preserved in anhydrite are similar to those of neighboring hydrothermal fluids suggests that anhydrite also records evidence for these processes at North Su.

5.1.2. REE_N pattern shapes of drill core anhydrite from PACMANUS

The geochemical compositions of anhydrite samples recovered in drill core can provide spatial constraints on the sub–seafloor evolution and chemical composition of circulating hydrothermal fluids. At Roman Ruins, REE_N patterns for anhydrite are light–REE enriched but with a range of positive and negative Eu–anomalies (Figure 3.4). In general, these REE distributions are similar to those of fluids sampled from this vent field, although negative Eu–anomalies are not observed (Figure 3.8). High–temperature hydrothermal fluids venting at Roman Ruins are characterized by low pH (2.3 – 2.6, at 25 °C) and low–to–moderate fluoride concentrations (92 – 155 μmol/kg; Seewald et al., 2006), suggesting some contribution from an exsolved magmatic acid volatile (H_2O–CO_2–HCl–HF–SO_2) phase. Similar patterns for anhydrites and vent fluids suggest that anhydrite

records sub–seafloor fluid compositions and chemical conditions in the recent geologic past that were similar to the present. It is unclear if pronounced negative Eu–anomalies recorded in sub–seafloor anhydrite are related to varying styles of magmatic acid volatile input or differences in fluid composition. The negative Eu–anomalies may reflect exclusion of Eu during incorporation of REEs into anhydrite. Changes in temperature and redox conditions can affect the valency of Eu (Sverjensky, 1984) and may fractionate divalent Eu from the remaining trivalent REE, but the effects of these redox changes on the partitioning of REEs between fluids and anhydrite are poorly understood. In general, REE_N patterns recorded in anhydrite from Roman Ruins are similar to Fenway, indicating similar histories of sub–seafloor fluid evolution. There are no REE_N patterns recorded in anhydrite samples from Roman Ruins that are similar to the flat REE_N pattern shapes recorded in anhydrite samples from North Su. Accordingly, there is no clear evidence to support the presence of acid–sulfate type fluids or to suggest that styles of fluid flow, compositions of exsolved magmatic acid volatiles or styles of fluid–rock interaction were also different in the geologic past at Roman Ruins.

Drill core anhydrite samples at Snowcap exhibit a large range of REE_N pattern shapes (Figure 3.5). The REE_N patterns in anhydrite from Snowcap are very different from those in anhydrite recovered from Roman Ruins and Fenway. Also, REE_N patterns in anhydrite are clearly different from those of hydrothermal fluids actively venting at Snowcap, which are characterized by light–REE enrichment and positive Eu–anomaly (Figure 3.8, see also Chapter 2). Present–day fluid activity at Snowcap is characterized by venting of lower temperature (< 180 °C) and moderately–acidic fluids with pH (25 °C) ≥

3.4 (Seewald et al., 2006). However, the range of REE_N patterns observed in anhydrite and differences to REE_N patterns in present–day fluids suggest that the provenance and chemical evolution of sub–seafloor hydrothermal fluids have changed significantly over time. Significantly, the range of REE_N patterns preserved in anhydrite at Snowcap is similar to that recorded in low pH fluids sampled from other vent fields in the Manus Basin. Heavy–REE enriched pattern shapes recorded in some Snowcap anhydrites (Figure 3.5e, h) are remarkably similar to REE_N patterns in low pH (~ 2.3, at 25 °C), fluoride–rich ($\Sigma F \sim 380 - 530$ μmol/kg; E. Reeves and J. Seewald, *unpubl. data*) seafloor hydrothermal fluids from the Satanic Mills (PACMANUS) and Suzette (SuSu Knolls) vent fields (Figure 3.9b). In addition, flat REE_N pattern shapes recorded in other Snowcap anhydrite samples (Figure 3.5a, g and h) closely resemble those of very acidic (pH (25 °C) ≤ 1.8), sulfate–rich ($\Sigma SO_4 \sim 28 - 150$ mmol/kg; E. Reeves and J. Seewald, *unpubl. data*) acid–sulfate fluids sampled from the DESMOS and North Su (SuSu Knolls) vent fields (Figure 3.9c; see also Chapter 2). The range of REE_N patterns preserved in Snowcap anhydrite, likely resulting from different REE_N patterns of source hydrothermal fluids from which anhydrite precipitated, appear to record changes in the compositions of magmatic acid volatiles injected into the Snowcap hydrothermal system. In particular, the range of REE_N pattern shapes recorded in anhydrite appears to document the past presence of acid–sulfate type fluids at Snowcap and thereby record fundamental changes in styles of fluid flow and fluid evolution at this vent field. The occurrence of acid–sulfate fluids in the recent past at Snowcap, which were likely similar to acid–sulfate fluids observed venting at the seafloor at DESMOS and North Su (SuSu Knolls), is supported by the presence of advanced argillic

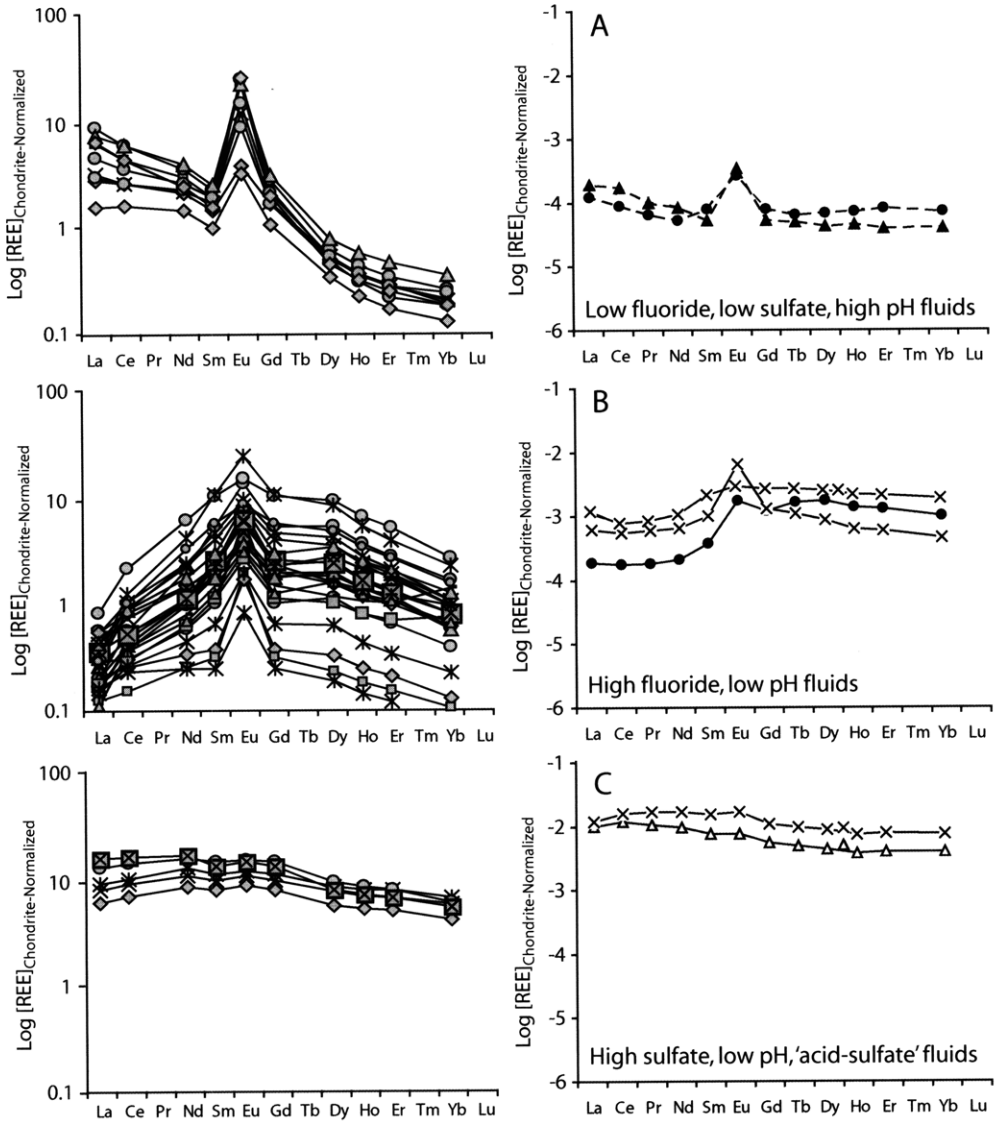

Figure 3.9. Summary of REE_N pattern shapes of Snowcap anhydrite samples (left) and comparison with REE_N pattern shapes of seafloor vent fluids from hydrothermal systems in the Manus Basin (right) that are variably affected by magmatic volatile degassing. The similarity between REE compositions of Snowcap anhydrites and of vent fluids is evidence for magmatic volatile degassing affecting the compositions of mineral deposits at Snowcap. **A**) Light-REE enriched patterns of low F and low SO4 fluids from Snowcap, **B**) Light-REE depleted, heavy-REE enriched patterns of high F, low pH fluids from Satanic Mills (PACMANUS) and Suzette (SuSu Knolls), **C**) Flat REE patterns with no Eu-anomaly of magmatic vapor-rich low pH acid-sulfate fluids from DESMOS.

(alunite–illite–pyrophyllite–quartz) alteration and native sulfur in proximity to anhydrite recovered from this vent field (Lackschewitz et al., 2004; Binns et al., 2007). Advanced argillic alteration is characteristic of extreme leaching and alteration of crustal host rocks under highly acidic conditions (pH < 2) resulting from the injection of reactive magmatic acid volatiles, in particular SO_2 and HCl (Meyer and Hemley, 1967; Brimhall and Ghiorso, 1983). This result is significant because it appears that REE signatures preserved in hydrothermal mineral deposits can provide information on the temporal chemical evolution of submarine hydrothermal systems, which is not necessarily obtainable from the study of actively circulating hydrothermal fluids.

5.1. Strontium and sulfur isotope geochemistry

Previous studies have demonstrated the use of $^{87}Sr/^{86}Sr$ and $\delta^{34}S$ isotope values of anhydrite to track the origin and sub–seafloor evolution of hydrothermal fluids (Chiba et al., 1998; Teagle et al., 1998; Roberts et al., 2003; Bach et al., 2005; Humphris and Bach, 2005). Differences of Sr and S isotope ratios of anhydrite sampled from PACMANUS (Snowcap, Fenway and Roman Ruins) and SuSu Knolls (North Su) indicate subtle distinctions in terms of fluid provenance and styles of fluid circulation and mixing at these vent fields.

The sulfur isotope ratios of most anhydrites from all vent fields cluster around that of contemporary seawater sulfate ($\delta^{34}S$–sulfate = + 21.0 ‰; Figure 3.7), although some anhydrite grains exhibit deviations from this isotopic ratio. These data indicate that sulfate required to precipitate anhydrite was supplied predominantly by SO_4–rich seawater, likely as a result of mixing between rising high–temperature hydrothermal fluid and locally

entrained seawater. This idea is supported by coupled $^{87}Sr/^{86}Sr$ ratios (of the same anhydrite grains) that cluster between that of contemporary seawater ($^{87}Sr/^{86}Sr \sim 0.70918$) and end–member hydrothermal fluids for each field ($^{87}Sr/^{86}Sr \sim 0.70427$; M. Rosner and W. Bach, *unpubl. data*), which suggest anhydrite precipitated from a mix of the two.

Sulfate–sulfur isotopic ratios of drill core anhydrites from Snowcap exhibit sulfate–sulfur isotope ratios significantly lighter than contemporary seawater in some grains ($\delta^{34}S$ = + 16.6 ‰ to + 21.9 ‰; Figure 3.7). In this study, the lightest S isotope ratios in anhydrite were measured in samples that were recovered from the greatest depths in Snowcap drill core (~ 300 mbsf; Figure 3.7) and that exhibited some of the lowest measured Sr isotope ratios ($^{87}Sr/^{86}Sr \sim 0.7050$; Figure 3.10). These data suggest that anhydrite carrying a light S isotope signature had precipitated from a fluid mixture containing a relatively small proportion of seawater. Potential sources of sulfate with S isotopic ratios less than seawater include the oxidation of aqueous H_2S in hydrothermal fluid (Shanks et al., 1995), equilibrium isotope exchange between aqueous sulfate and H_2S at high temperatures $\geq$ 360 – 380 °C (Ohmoto and Lasaga, 1982), and sulfate from the disproportionation of magmatic SO_2 (Drummond, 1981; Kusakabe et al., 2000). Oxidation of small amounts of H_2S in a fluid mixture containing little seawater–derived sulfate (as suggested by low Sr isotope ratios) could significantly perturb the S isotope ratio of sulfate. However, reaction path models that consider batch mixing of hydrothermal fluid and seawater do not predict significant increases in the oxidation state of the fluid mixture that would support significant oxidation of H_2S (e.g., Janecky and Seyfried, 1984). Indeed, assuming equilibrium between aqueous sulfate and sulfide, reaction path calculations tend to predict

reduction of seawater sulfate as a result of sulfide mineral deposition (Janecky and Seyfried, 1984), rather than oxidation of hydrothermal fluid H_2S. Temperatures of anhydrite formation at Snowcap as determined by fluid inclusion studies are mostly between 220 and 360 °C (Vanko et al., 2004). Accordingly, it is not clear that the temperatures of mixtures of hydrothermal fluid and seawater precipitating most anhydrite were sufficiently high (~ 380 °C) for equilibrium isotope fractionation between sulfate and H_2S to account for $\delta^{34}S$ isotopic ratios of sulfate significantly lighter than seawater. Alternatively, disproportionation of SO_2 ($\delta^{34}S \sim 0$ ‰), derived from degassing of shallow felsic magmas, according to a reaction similar to (Holland, 1965)

$$3SO_2 + 2H_2O \rightarrow S + 2H_2SO_4 (\rightarrow 2H^+ + 2HSO_4^-)$$

yields sulfate with an isotope composition ($\delta^{34}S$–sulfate ~ + 10 to + 15 ‰) significantly lighter than that of modern seawater (e.g., Kusakabe et al., 2000) and may account for the source of isotopically–light sulfate recorded in anhydrite from PACMANUS, as suggested previously by Roberts et al. (2003). These data are supported by the measurement of S isotope ratios in anhydrite grains sampled from sulfide chimney vent deposits, also from PACMANUS, that are lighter than seawater sulfate and that have been attributed to the input and disproportionation of magmatic SO_2 (Kim et al., 2004). The presence of significant amounts of sulfate of likely magmatic origin supports inferences from REE data recorded in the same anhydrites that low pH, acid–sulfate type fluids previously migrated through the Snowcap hydrothermal system. That the lightest $\delta^{34}S$ ratios are recorded in anhydrites sampled at depths several hundred meters beneath the seafloor in Snowcap drill core is consistent with a deep source for isotopically light sulfate from input of magmatic–

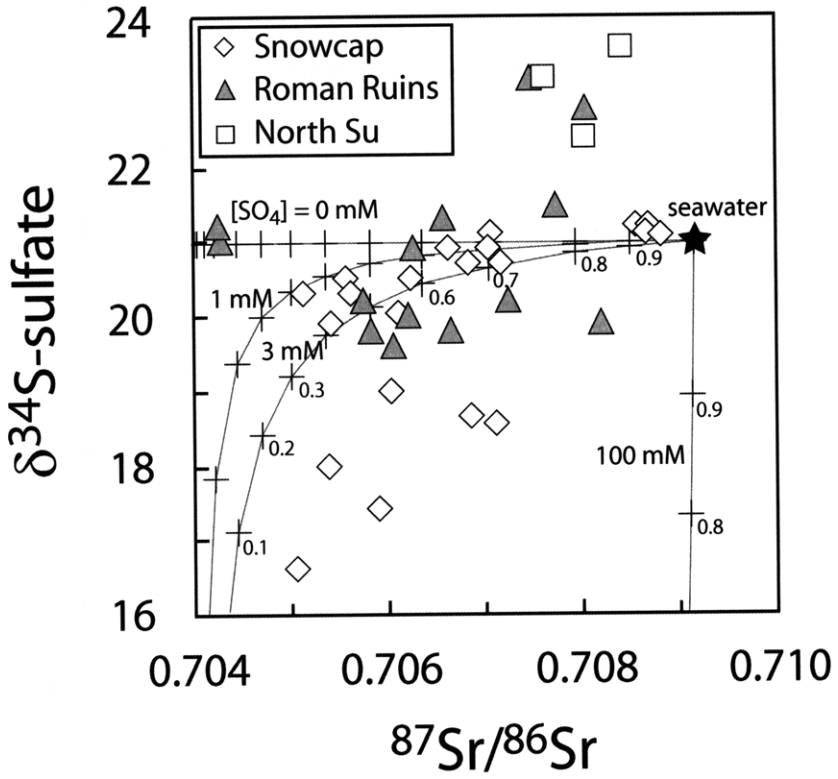

Figure 3.10. Sr isotopic ratios ($^{87}Sr/^{86}Sr$) versus S isotopic ratios ($\delta^{34}S$) for anhydrite samples from PACMANUS (Snowcap and Roman Ruins drill core samples) and SuSu Knolls (North Su massive anhydrite). Mixing lines show predicted isotopic evolution of hydrothermal fluids during mixing between seawater ([Sr] = 87 umol/kg, $^{87}Sr/^{86}Sr = 0.70918$, $[SO_4^{2-}] = 28$ mmol/kg, $\delta^{34}S = +21.0$ permil) and magmatic-hydrothermal fluid containing different concentrations of magmatic SO_2 (1, 3 and 100 mmol/kg sulfate). The isotopic composition of the magmatic-hydrothermal fluid is $^{87}Sr/^{86}Sr = 0.7043$ (the composition of endmember hydrothermal fluids in the Manus Basin; W. Bach, *unpubl. data*) and $\delta^{34}S = +10.0$ permil (the estimated composition of sulfate from disproportionation of magmatic SO_2 (Kusakabe et al., 2000). See also Roberts et al. (2003).

derived SO_2. The absence of anhydrite sulfate with light S isotope ratios (<< + 21 ‰) in drill core samples recovered at shallower depths (< 50 – 200 mbsf) does not necessarily indicate an absence of magmatic acid volatiles (i.e., an SO_2–bearing aqueous fluid) at the seafloor (Figure 3.7). Rather, greater extents of seawater entrainment in proximity to the seawater–crustal interface (as suggested by more seawater–like Sr isotopic ratios in anhydrites recovered from shallower depths; Figures 3.7) may contribute greater amounts of seawater–sulfate that overprints the isotopic signatures of magmatic sulfur species at the seafloor in most instances.

At other vent fields examined (Roman Ruins, Fenway and North Su), sulfur isotope ratios heavier than seawater are exhibited in some anhydrite grains (up to + 23.6 ‰; Figure 3.7). Similar S isotope ratios in the same anhydrite samples from Roman Ruins were measured by Roberts et al. (2003). At these vent fields, sulfate sulfur isotope ratios in anhydrite heavier than seawater likely reflect either partial reduction of seawater sulfate to sulfide (H_2S) by action of ferrous iron in hydrothermal fluid (Shanks et al., 1981; Janecky and Shanks, 1988) or equilibrium isotope exchange between aqueous sulfate and H_2S at temperatures less than ~ 350 °C (Ohmoto and Lasaga, 1982). The sluggish kinetics for equilibrium isotope exchange between sulfate and H_2S at relatively low temperature (Ohmoto and Lasaga, 1982) suggests that partial reduction of seawater sulfate is the more likely explanation (see also Roberts et al., 2003). However, there is no obvious relationship between the extent of mixing between hydrothermal fluid and seawater (as determined by Sr isotope ratios between hydrothermal fluid and seawater) and the extent of seawater sulfate reduction predicted at these vent fields to confirm this idea (Figure 3.10). The study

of multiple S isotopes (^{32}S, ^{33}S and ^{34}S; that is $\delta^{33}S$ and $\delta^{34}S$) show significant promise to better discriminate the geochemical processes affecting the cycling and isotope fractionation of sulfur among sulfate and sulfide in submarine hydrothermal systems (e.g., Ono et al., 2007). This is because sulfur isotope fractionation during equilibrium sulfur isotope exchange and sulfur oxidation–reduction, for example, follow measurably different $\delta^{33}S$ vs. $\delta^{34}S$ systematics that enable these processes to be distinguished.

There are no S isotope ratios recorded in anhydrite at Roman Ruins or Fenway from PACMANUS or at North Su from SuSu Knolls that are significantly lighter than seawater sulfate. Sulfur isotope ratios do not, therefore, provide evidence to support extensive inputs of magmatic acid volatiles (i.e., SO_2) that these vent fields. This is despite evidence to the contrary as inferred from heterogeneous REE_N patterns in the same anhydrite grains and from active venting of low pH and fluoride– and sulfate–rich hydrothermal fluids at these fields (Seewald et al., 2006). These data suggest that sulfate–sulfur isotopic ratios in anhydrite do not necessarily record signatures of inputs of magmatic acid volatiles (H_2O–CO_2–HCl–SO_2–HF). This likely reflects that most sulfate cycled through submarine hydrothermal systems, in particular close to the seawater–crustal interface, is derived from seawater, which overprints the weaker geochemical signatures contributed by magmatic acid volatiles. This is supported by the range of Sr isotopic ratios recorded in anhydrite, which demonstrate significant entrainment and mixing of seawater with hydrothermal (or hydrothermal–magmatic) fluids during the precipitation of anhydrite at all vent fields in the Manus Basin (Figure 3.10).

6. CONCLUSIONS

Coupled elemental (rare earth element) and isotopic (Sr, S) data for anhydrite are used to constrain the evolution and present and past sub–seafloor interactions of exsolved reactive magmatic acid volatiles (H_2O–CO_2–HCl–HF–SO_2), circulating hydrothermal fluid and locally entrained seawater within the active PACMANUS and SuSu Knolls hydrothermal systems in the Manus back–arc basin. Distributions of REEs (REE_N pattern shapes) in anhydrite samples from PACMANUS (Roman Ruins, Snowcap and Fenway) and SuSu Knolls (North Su) show remarkable heterogeneity and are very different to relatively uniform REE_N patterns in anhydrites from mid–ocean ridge deposits (e.g., Barrett et al., 1990; Mills and Elderfield, 1995; Humphris, 1998). To first–order, REE_N pattern shapes of anhydrite can be related to different REE compositions of the hydrothermal source fluids, as shown by similar ranges of REE_N pattern shapes measured in seafloor vent fluids from the same hydrothermal systems (see Chapter 2). The detailed measurements described here are supported by studies of REE in seafloor hydrothermal fluids, which have suggested that aqueous REE species distributions and REE solubility are affected by changes in pH and fluoride and sulfate ligand concentrations contributed by degassing of acid volatiles from felsic magmas (Bach et al., 2003; see also Chapter 2).

At SuSu Knolls (North Su), input of magmatic acid volatiles inferred from a range of REE_N pattern shapes in anhydrite are directly supported by the presence of low pH and fluoride– and sulfate–rich hydrothermal fluids (Seewald et al., 2006) that have similar REE distributions. The range of REE_N patterns in anhydrite sampled from PACMANUS

(Roman Ruins,. Snowcap and Fenway) suggest a history of hydrothermal activity characterized by differences in the styles of magmatic volatile degassing and in the compositions exsolved magmatic acid volatiles. In particular, flat enriched REE_N pattern shapes recorded in anhydrites from Snowcap are similar to REE_N patterns in low pH, acid–sulfate type fluids from DESMOS and SuSu Knolls and suggest that acid–sulfate fluids previously migrated through the Snowcap vent field. This is supported by the occurrence of advanced argillic (alunite–illite–pyrophyllite–quartz) alteration at Snowcap (Lackschewitz et al., 2004; Binns et al., 2007) characteristic of acid leaching of crustal host rocks under highly acidic aqueous conditions (Meyer and Hemley, 1967). The compositions of hydrothermal fluids exiting the seafloor presently at Snowcap, including moderately acid pH and low fluorine and/or sulfate concentrations relative to other vent fluids in the Manus Basin (Seewald et al., 2006), indicate different styles of, and less extensive, magmatic acid volatile degassing. Significantly, the REE_N patterns recorded in anhydrite can be used to infer past processes associated with hydrothermal activity that cannot be obtained from the study of present–day fluids alone. The REE_N patterns recorded in anhydrite also demonstrate the spatial heterogeneity in styles of magmatic acid volatile degassing beneath seafloor hydrothermal systems because there is no evidence to support similar occurrence of acid–sulfate type fluids at Roman Ruins or Fenway located only several hundreds of meters away from the Snowcap vent field.

Elemental data are complemented by those of S and Sr isotopes. The $^{87}Sr/^{86}Sr$ ratios of all anhydrite grains are between that of contemporary seawater and end–member hydrothermal (or magmatic–hydrothermal) fluids indicating that anhydrite was deposited

upon mixing of the two. Most $\delta^{34}S$ values of anhydrite from PACMANUS and SuSu Knolls cluster around that of contemporary seawater, suggesting that sulfate precipitating anhydrite was sourced from locally entrained seawater that mixed with rising hydrothermal fluids. Sulfate–sulfur isotope ratios in anhydrite lighter than that of modern seawater do support a magmatic component to some circulating hydrothermal fluids, specifically at Snowcap (c.f. Roberts et al., 2003). Light S isotope values of anhydrite recovered within drill core from Snowcap are consistent with disproportionation of SO_2 that was degassed from underlying felsic magmas. Similar S isotope ratios are not recorded in anhydrite from Roman Ruins or Fenway, despite that low pH, fluoride–rich hydrothermal fluids exit the seafloor (Seewald et al., 2006) indicating current degassing of magmatic acid volatiles at these vent fluids. The same true of S isotopes in anhydrite recovered from the seafloor at North Su, SuSu Knolls. Local entrainment of seawater and mixing (dilution) with rising magmatic–hydrothermal fluids likely overprints the weaker geochemical signatures of deep–seated magmatic acid volatile input at these, and potentially other, hydrothermal systems. However, the data indicate that REE distributions preserved in anhydrite are a sensitive indicator of these processes, likely reflecting that REE concentrations in evolved hydrothermal fluids are significantly higher that of seawater and are not therefore by dilution with seawater to a similar extent.

Sub–seafloor processes, including high–temperature hydrothermal fluid circulation, different styles and compositions of reactive magmatic acid volatile (H_2O–CO_2–HCl–HF–SO_2) degassing, seawater entrainment and fluid mixing have affected fluid evolution and mineral deposition at the PACMANUS and SuSu Knolls hydrothermal fields. Coupled

elemental and isotopic studies of mineral deposits, in this instance anhydrite, can identify interactions among these processes. In addition, elemental and isotopic signatures preserved in anhydrite can provide information about the temporal history of seafloor hydrothermal systems that are clearly variable over time and cannot be inferred from the study of seafloor vent fluids alone.

REFERENCES

Albarède F. and Beard B. (2004) Analytical Methods for Non–Traditional Isotopes. *Reviews in Mineralogy and Geochemistry* **55**, 113–152.

Alt J. C. (1995) Subseafloor processes in mid–ocean ridge hydrothermal systems. In *Seafloor Hydrothermal Systems: Physical, Chemical, Biological and Geological Interactions. Geophysical Monograph.*, Vol. 91 (ed. S. E. Humphris, R. A. Zierenberg, L. S. Mullineaux, and R. E. Thomson), pp. 85–114. American Geophysical Union.

Anders E. and Grevesse N. (1989) Abundances of the elements: Meteoritic and solar. *Geochimica et Cosmochimica Acta* **53**, 197–214.

Bach W., Roberts S., and Binns R. A. (2005) Data Report: Chemical and isotopic (S, Sr) composition of anhydrite from ODP Leg 193, PACMANUS hydrothermal system, Manus Basin, Papua New Guinea. In *Proceedings of the Ocean Drilling Program, Scientific Results*, Vol. 193 (ed. F. J. A. S. Barriga, R. A. Binns, D. J. Miller, and P. M. Herzig), pp. 1–23. doi:10.2973/odp.proc.sr.193.214.2005. Ocean Drilling Program.

Bach W., Roberts S., Vanko D. A., Binns R. A., Yeats C. J., Craddock P. R., and Humphris S. E. (2003) Controls of fluid chemistry and complexation on rare–earth element contents of anhydrite from the Pacmanus subseafloor hydrothermal system, Manus Basin, Papua New Guinea. *Mineralium Deposita* **38**(8), 916–935.

Balaram V. (1996) Recent trends in the instrumental analysis of rare earth elements in geological and industrial materials. *Trends in Analytical Chemistry* **15**(9), 475–486.

Barrett T. J., Jarvis I., and Jarvis K. E. (1990) Rare earth element geochemistry of massive sulfides–sulfates and gossans on the Southern Explorer Ridge. *Geology* **18**(7), 583–586.

Belshaw N. S., Freedman P. A., O'Nions R. K., Frank M., and Guo Y. (1998) A new variable dispersion double–focusing plasma mass spectrometer with performance illustrated for Pb isotopes. *International Journal of Mass Spectrometry* **181**, 51–58.

Binns R. A., Barriga F. J. A. S., and Miller D. J. (2007) Leg 193 synthesis: Anatomy of an active felsic–hosted hydrothermal system, eastern Manus Basin, Papua New Guinea. In *Proceedings of the Ocean Drilling Program, Scientific Results*, Vol. 193 (ed. F. J. A. S. Barriga, R. A. Binns, D. J. Miller, and P. M. Herzig), pp. 1–71. doi:10.2973/odp.proc.sr.193.201.2007. Ocean Drilling Program.

Binns R. A. and Scott S. D. (1993) Actively forming polymetallic sulfide deposits associated with felsic volcanic rocks in the eastern Manus back–arc basin, Papua New Guinea. *Economic Geology* **88**, 2226–2236.

Binns R. A., Scott S. D., Gemmell J. B., Crook K. A. W., and Shipboard Scientific Party. (1997) The SuSu Knolls hydrothermal field, eastern Manus Basin, Papua New Guinea. *EOS Trans. AGU. Fall Meet. Suppl.*, **78**(52), Abstract #V22E–02.

Bischoff J. L. and Seyfried W. E., Jr. (1978) Hydrothermal chemistry of seawater from 25° to 350°C. *American Journal of Science* **278**, 838–860.

Brimhall G. H., Jr. and Ghiorso M. S. (1983) Origin and ore–forming consequences of the advanced argillic alteration process in hypogene environments by magmatic gas contamination of meteoric fluids. *Economic Geology* **78**, 73–90.

Chiba H., Uchiyama N., and Teagle D. A. H. (1998) Stable isotope study of anhydrite and sulfide minerals at the TAG hydrothermal mound, Mid–Atlantic Ridge, 26 °N. In *Proceedings of the Ocean Drilling Program, Scientific Results*, Vol. 158 (ed. P. M. Herzig, S. E. Humphris, D. J. Miller, and R. A. Zierenberg), pp. 85–90. Ocean Drilling Program.

Craddock P. R., Rouxel O. J., Ball L. A., and Bach W. (2008) Sulfur isotope measurement of sulfate and sulfide by high–resolution MC–ICP–MS. *Chemical Geology* **253**, 102–113.

Davies H. L., Honza E., Tiffin D. L., Lock J., Okuda Y., Keene J. B., Murakami F., and Kisimoto K. (1987) Regional setting and structure of the western Solomon Sea. *Geo–Marine Letters* **7**, 153–160.

Douville E., Bienvenu P., Charlou J. L., Donval J. P., Fouquet Y., Appriou P., and Gamo T. (1999) Yttrium and rare earth elements in fluids from various deep–sea hydrothermal systems. *Geochimica et Cosmochimica Acta* **63**(5), 627–643.

Drummond S. E., Jr. (1981) Boiling and Mixing of Hydrothermal Fluids: Chemical Effects on Mineral Precipitation, The Pennsylvania State University.

Edmond J. M., Campbell A. C., Palmer M. R., German C. R., Klinkhammer G. P., Edmonds H. N., Elderfield H., Thompson G., and Rona P. (1995) Time series studies of vent fluids from the TAG and MARK sites (1986, 1990) Mid–Atlantic Ridge and a mechanism for Cu/Zn zonation in massive sulphide orebodies. In *Hydrothermal Vents and Processes*, Vol. 87 (ed. L. M. Parson, C. L. Walker, and D. R. Dixon), pp. 77–86. Geological Society Special Publication.

Fouquet Y., von Stackelberg U., Charlou J. L., Erzinger J., Herzig P. M., Muehe R., and Wiedicke M. (1993) Metallogenesis in back–arc environments; The Lau Basin example. *Economic Geology* **88**(8), 2150.

Gamo T., Okamura K., Charlou J. L., Urabe T., Auzende J. M., Ishibashi J., Shitashima K., Chiba H., Binns R. A., and Gena K. (1997) Acidic and sulfate–rich hydrothermal fluids from the Manus back–arc basin, Papua New Guinea. *Geology* **25**(2), 139–142.

Goldfarb M. S. (1982) Submarine Sulfide Deposits on the East Pacific Rise, 21 °N. Ph. D. Thesis, Massachusetts Institute of Technology.

Hannington M. D., De Ronde C. E. J., and Petersen S. (2005) Sea–floor tectonics and submarine hydrothermal systems. *Economic Geology* **100**, 111–141.

Hart S. R., Ball L., and Jackson M. J. (2005) Sr isotope by laser ablation PIMMS: Application to Cpx from Samoan peridotite xenoliths. WHOI Plasma Facility Open

File Technical Report 11, pp. 15. Woods Hole Oceanographic Institution, Woods Hole, MA.

Haymon R. M. (1983) Growth history of hydrothermal black smoker chimneys. *Nature* **301**(5902), 695–698.

Holland H. D. (1965) Some applications of thermochemical data to problems of ore deposits; [Part] 2, Mineral assemblages and the composition of ore forming fluids. *Economic Geology* **60**(6), 1101–1166.

Humphris S. E. (1998) Rare earth element composition of anhydrite: Implications for deposition and mobility within the TAG hydrothermal mound. In *Proceedings of the Ocean Drilling Program, Scientific Results*, Vol. 158 (ed. P. M. Herzig, S. E. Humphris, D. J. Miller, and R. A. Zierenberg), pp. 143–159. Ocean Drilling Program.

Humphris S. E. and Bach W. (2005) On the Sr isotope and REE compositions of anhydrites from the TAG seafloor hydrothermal system. *Geochimica et Cosmochimica Acta* **69**, 1511–1525.

Humphris S. E., Herzig P. M., Miller D. J., Alt J. C., Becker K., Brown D., Brügmann G., Chiba H., Fouquet Y., and Gemmell J. B. (1995) The internal structure of an active sea–floor massive sulphide deposit. *Nature* **377**(6551), 713–716.

Humphris S. E. and Thompson G. (1978a) Hydrothermal alteration of oceanic basalts by seawater. *Geochimica et Cosmochimica Acta* **42**(1), 107–125.

Humphris S. E. and Thompson G. (1978b) Trace element mobility during hydrothermal alteration of oceanic basalts. *Geochimica et Cosmochimica Acta* **42**(1), 127–136.

Janecky D. R. and Seyfried W. E., Jr. (1984) Formation of massive sulfide deposits on oceanic ridge crests: Incremental reaction models for mixing between hydrothermal solutions and seawater. *Geochimica et Cosmochimica Acta* **48**(12), 2723–2738.

Janecky D. R. and Shanks W. C., III. (1988) Computational modeling of chemical and sulfur isotopic reaction processes in seafloor hydrothermal systems: chimneys, massive sulfides, and subjacent alteration zones. *Canadian Mineralogist* **26**, 805–825.

Kent A. J. R., Jacobsen B., Peate D. W., Waight T. E., and Baker J. A. (2004) Isotope dilution MC–ICP–MS rare earth element analysis of geochemical reference materials NIST SRM 610, NIST SRM 612, NIST SRM 614, BHVO–2G, BHVO–2, BCR–2G, JB–2, WS–E, W–2, AGV–1 and AGV–2. *Geostandards and Geoanalytical Research* **28**(3), 417–429.

Kim J., Lee I., and Lee K.–Y. (2004) S, Sr, and Pb isotopic systematics of hydrothermal chimney precipitates from the Eastern Manus Basin, western Pacific: Evaluation of magmatic contribution to hydrothermal system. *Journal of Geophysical Research* **109**, B12210, doi:10.1029/2003JB002912.

Kusakabe M., Komoda Y., Takano B., and Abiko T. (2000) Sulfur isotopic effects in the disproportionation reaction of sulfur dioxide in hydrothermal fluids: Implications for the $\delta^{34}S$ variations of dissolved bisulfate and elemental sulfur from active crater lakes. *Journal of Volcanology and Geothermal Research* **97**(1–4), 287.

Lackschewitz K. S., Devey C. W., Stoffers P., Botz R., Eisenhauer A., Kummetz M., Schmidt M., and Singer A. (2004) Mineralogical, geochemical and isotopic characteristics of hydrothermal alteration processes in the active, submarine, felsic–hosted PACMANUS field, Manus Basin, Papua New Guinea. *Geochimica et Cosmochimica Acta* **68**(21), 4405–4427.

Marshall D. J. (1988) *Cathodoluminescence of Geological Materials*. Unwin Hyman Ltd.

Martinez F. and Taylor B. (1996) Backarc spreading, rifting, and microplate rotation, between transform faults in the Manus Basin. *Marine Geophysical Researches* **18**, 203–224.

Meyer C. A. and Hemley J. J. (1967) Wall–rock alteration. In *Geochemistry of Hydrothermal Ore Deposits, 1st Edition* (ed. H. L. Barnes), pp. 166–235. Holt, Rinehart and Winston.

Mills R. A. and Elderfield H. (1995) Rare earth element geochemistry of hydrothermal deposits from the active TAG Mound, 26 °N Mid–Atlantic Ridge. *Geochimica et Cosmochimica Acta* **59**, 3511–3524.

Mills R. A., Teagle D. A. H., and Tivey M. K. (1998) Fluid mixing and anhydrite precipitation within the TAG mound. In *Proceedings of the Ocean Drilling*

Program, Scientific Results, Vol. 158 (ed. P. M. Herzig, S. E. Humphris, D. J. Miller, and R. A. Zierenberg), pp. 119–127. Ocean Drilling Program.

Mills R. A. and Tivey M. K. (1999) Sea water entrainment and fluid evolution within the TAG hydrothermal mound: Evidence from analyses of anhydrite. In *Mid–Ocean Ridges: Dynamics of Processes Associated with Creation of New Ocean Crust* (ed. J. R. Cann, H. Elderfield, and A. Laughton), pp. 225–248. Cambridge University Press.

Mitra A., Elderfield H., and Greaves M. J. (1994) Rare earth elements in submarine hydrothermal fluids and plumes from the Mid–Atlantic Ridge. *Marine Chemistry* **46**(3), 217–235.

Ohmoto H. and Lasaga A. C. (1982) Kinetics of reactions between aqueous sulfates and sulfides in hydrothermal systems. *Geochimica et Cosmochimica Acta* **46**(10), 1727–1745.

Ono S., Shanks W. C., III, Rouxel O. J., and Rumble D. (2007) S–33 constraints on the seawater sulfate contribution in modern seafloor hydrothermal vent sulfides. *Geochimica et Cosmochimica Acta* **71**(5), 1170–1182.

Pearce N. J. G., Perkins W. T., Westgate J. A., Gorton M. P., Jackson S. E., Neal C. R., and Chenery S. P. (1997) A compilation of new and published major and trace element data for NIST SRM 610 and NIST SRM 612 glass reference materials. *Geostandards Newsletter* **21**(1), 115–144.

Rees C. E., Jenkins W. J., and Monster J. (1978) The sulphur isotopic composition of ocean water sulphate. *Geochimica et Cosmochimica Acta* **42**(4), 377–381.

Roberts S., Bach W., Binns R. A., Vanko D. A., Yeats C. J., Teagle D. A. H., Blacklock K., Blusztajn J. S., Boyce A. J., and Cooper M. J. (2003) Contrasting evolution of hydrothermal fluids in the PACMANUS system, Manus Basin: The Sr and S isotope evidence. *Geology* **31**(9), 805–808.

Scott S. D. and Binns R. A. (1995) Hydrothermal processes and contrasting styles of mineralization in the western Woodlark and eastern Manus basins of the western Pacific. In *Hydrothermal Vent and Processes, Geological Society of London*

Special Publication, Vol. 87 (ed. L. M. Parson, C. L. Walker, and D. R. Dixon), pp. 191–205.

Seewald J. S., Reeves E., Saccocia P., Rouxel O. J., Walsh E., Price R. E., Tivey M., Bach W., and Tivey M. (2006) Water–rock reaction, substrate composition, magmatic degassing, and mixing as major factors controlling vent fluid compositions in Manus Basin hydrothermal systems. *EOS Trans. AGU. Fall Meet. Suppl.*, **87**(52), Abstract # B34A–02.

Seyfried W. E., Jr. (1987) Experimental and theoretical constraints on hydrothermal alteration processes at mid–ocean ridges. *Annual Review of Earth and Planetary Sciences* **15**, 317–335.

Shanks W. C., III, Bischoff J. L., and Rosenbauer R. J. (1981) Seawater sulfate reduction and sulfur isotope fractionation in basaltic systems: Interaction of seawater with fayalite and magnetite at 200–350 °C. *Geochimica et Cosmochimica Acta* **45**, 1977–1995.

Shanks W. C., III, Bohlke J. K., and Seal R. R. (1995) Stable isotopes in mid–ocean ridge hydrothermal systems: Interaction between fluids, minerals and organisms. In *Seafloor Hydrothermal Systems: Physical, Chemical, Biological and Geological Interactions. Geophysical Monograph.*, Vol. 91 (ed. S. E. Humphris, R. A. Zierenberg, L. S. Mullineaux, and R. E. Thomson), pp. 194–221. American Geophysical Union.

Sillitoe R. H., Hannington M. D., and Thompson J. F. H. (1996) High sulfidation deposits in the volcanogenic massive sulfide environment. *Economic Geology* **91**(1), 204–212.

Sinton J. M., Ford L. L., Chappell B., and McCulloch M. T. (2003) Magma genesis and mantle heterogeneity in the Manus Back–Arc Basin, Papua New Guinea. *Journal of Petrology* **44**, 159–195.

Sverjensky D. A. (1984) Europium redox equilibria in aqueous solution. *Earth and Planetary Science Letters* **67**, 70–78.

Taylor B. (1979) Bismarck Sea; Evolution of a back–arc basin. *Geology* **7**, 171–174.

Teagle D. A. H., Alt J. C., Chiba H., and Halliday A. N. (1998) Dissecting an active hydrothermal deposit: The strontium and oxygen isotopic anatomy of the TAG hydrothermal mound – Anhydrite. In *Proceedings of the Ocean Drilling Program, Scientific Results*, Vol. 158 (ed. P. M. Herzig, S. E. Humphris, D. J. Miller, and R. A. Zierenberg), pp. 129–141. Ocean Drilling Program.

Thompson G., Humphris S. E., Schroeder B., Sulanowska M., and Rona P. A. (1988) Active vents and massive sulfides at 26 °N (TAG) and 23 °N (Snakepit) on the mid–Atlantic Ridge. *Canadian Mineralogist* **26**, 697–711.

Tivey M. A., Bach W., Seewald J. S., Tivey M. K., Vanko D. A., and Shipboard Science and Technical Teams. (2007) Cruise Report R/V Melville, MAGELLAN–06. Hydrothermal systems in the Eastern Manus Basin: Fluid chemistry and magnetic structures as guides to subseafloor processes, pp. 67. Woods Hole Oceanographic Institution.

Tivey M. K., Humphris S. E., Thompson G., Hannington M. D., and Rona P. A. (1995) Deducing patterns of fluid flow and mixing within the TAG active hydrothermal mound using mineralogical and geochemical data. *Journal of Geophysical Research* **100**(B7), 12527–12555.

Tivey M. K., Mills R. A., and Teagle D. A. H. (1998) Temperature and salinity of fluid inclusions in anhydrite as indicators of seawater entrainment and heating within the TAG active mound. In *Proceedings of the Ocean Drilling Program, Scientific Results*, Vol. 158 (ed. P. M. Herzig, S. E. Humphris, D. J. Miller, and R. A. Zierenberg), pp. 179–190. Ocean Drilling Program.

Vanko D. A., Bach W., Roberts S., Yeats C. J., and Scott S. D. (2004) Fluid inclusion evidence for subsurface phase separation and variable fluid mixing regimes beneath the deep–sea PACMANUS hydrothermal field, Manus Basin back arc rift, Papua New Guinea. *Journal of Geophysical Research* **109**, B03201, doi:10.1029/2003JB002579.

Von Damm K. L. (1995) Controls on the chemistry and temporal variability of seafloor hydrothermal fluids. In *Seafloor Hydrothermal Systems: Physical, Chemical, Biological and Geological Interactions. Geophysical Monograph.*, Vol. 91 (ed. S.

E. Humphris, R. A. Zierenberg, L. S. Mullineaux, and R. E. Thomson), pp. 222–247. American Geophysical Union.

Weyer S. and Schwieters J. B. (2003) High precision Fe isotope measurements with high mass resolution MC–ICPMS. *International Journal of Mass Spectrometry* **226**(3), 355–368.

Yeats C. J., Bach W., Vanko D. A., Roberts S., Lackschewitz K. S., and Paulick H. (2001) Fluid–dacite interaction in the PACMANUS subseafloor hydrothermal system – preliminary results from secondary mineral chemistry and geochemical modeling. *EOS Trans. AGU. Fall Meet. Suppl.,* **82**(47), Abstract # OS11A–0346.

Yeats C. J., Binns R. A., and Parr J. M. (2000) Advanced argillic alteration associated with actively forming submarine polymetallic sulfide mineralization in the eastern Manus Basin, Papua New Guinea. *Geological Society of Australia Abstracts* **59**, 555.

samples, with local enrichments of up to 20 – 400 ppm Pb. Concentrations of Sr, Mg, Ba and Pb show no obvious systematic differences among samples either within or between PACMANUS and SuSu Knolls vent fields. In drill core samples from Snowcap and Roman Ruins (PACMANUS), there are no obvious downhole trends or correlation of alteration lithology with concentrations of Sr, Mg, Ba and Pb. Neither are there obvious correlations among Sr, Mg, Ba and Pb concentrations and Sr and S isotope ratios related to different mixtures of hydrothermal fluid and seawater. Accordingly, the distributions of these elements in anhydrite are not discussed further.

Chondrite–normalized REE (REE_N) pattern shapes for anhydrite sampled from the Manus Basin exhibit remarkable heterogeneity. These data are supported by previous results of bulk REE analysis of the same anhydrite samples (Bach et al., 2003). REE_N patterns for seafloor massive anhydrite samples from Fenway show the most homogeneity with uniform light–REE enrichment and positive Eu–anomaly (La_N/Yb_N = 3.2 – 76, Sm_N/Yb_N = 3.0 – 32, Eu_N/Eu^*_N = 2.6 – 23; Figure 3.3). At Roman Ruins, measured REE_N pattern shapes for drill core anhydrite grains show a range of light–REE enrichment. Most grains have a positive Eu–anomaly, but some REE–rich domains show a pronounced negative Eu–anomaly (La_N/Yb_N = 7.8 – 108, Sm_N/Yb_N = 2.8 – 23, Eu_N/Eu^*_N = 0.4 – 6.5; Figure 3.4). Measured REE_N patterns for Snowcap anhydrite samples exhibit a range of shapes including light–REE enrichments, light–REE depletions and flat REE pattern shapes with both positive and negative Eu–anomalies (La_N/Yb_N = 0.3 – 74, Sm_N/Yb_N = 0.9 – 12.5, Eu_N/Eu^*_N = 0.5 – 14.3; Figure 3.5). Multiple REE_N pattern shapes can be observed

CHAPTER 4

Controls on the Concentrations of Trace Metals in Manus Back–Arc Basin Hydrothermal Fluids

1. INTRODUCTION

Combined results of field studies, laboratory experiments and theoretical calculations demonstrate that aqueous trace metal concentrations in hydrothermal fluids are affected by temperature, pH, redox and the availability of aqueous ligands such as chloride and sulfide. These factors are intimately related to high–temperature interaction between seawater and crustal host rock, and fluid phase separation and segregation (Bischoff and Dickson, 1975; Seyfried and Bischoff, 1981; Rosenbauer and Bischoff, 1983; Bischoff and Rosenbauer, 1987; Seyfried, 1987; Bowers et al., 1988; Seewald and Seyfried, 1990; Von Damm, 1990; Butterfield and Massoth, 1994; Butterfield et al., 1994; Metz and Trefry, 2000; Von Damm, 2000; Von Damm et al., 2003). It has been demonstrated at some vent fields that sub–seafloor mixing between locally entrained seawater and rising hot hydrothermal fluids can modify the concentrations of trace metals in solution through sulfide mineral precipitation and/or

dissolution reactions (Trefry et al., 1994; Edmond et al., 1995; Tivey et al., 1995). To date, these studies have largely focused on the effects of geochemical processes occurring at hydrothermal systems located along basalt–dominated mid–ocean ridge spreading centers.

In convergent plate margins (e.g., back–arc basins and island–arcs), a range of different geochemical processes associated with hydrothermal activity that can affect vent fluid compositions. For example, circulating seawater can interact with crustal rocks with different compositions ranging from basalt to rhyolite. Felsic crustal rocks are enriched in some trace elements (e.g., Pb, Ba, Sb) and depleted in others (e.g., Co, Ni) relative to basalt erupted along the mid–ocean ridges (e.g., Stanton, 1994; Sinton et al., 2003), and studies of back–arc basins vent fluids have shown that aqueous metal enrichments may directly reflect these differences (e.g., Fouquet et al., 1993a). Also, field studies have reported low pH and high CO_2, fluoride and sulfate (proxies for HF and SO_2) concentrations in many back–arc basin vent fluids, which have been attributed to input of magmatic acid volatile phases (i.e., H_2O–CO_2–HCl–HF–SO_2) degassed from felsic magmas (Sakai et al., 1990; Gamo et al., 1997; Douville et al., 1999; Seewald et al., 2006). Significant differences in the mode and composition of magmatic acid volatile input in convergent plate margins relative to that at mid–ocean ridges may significantly affect aqueous metal solubility during fluid–rock interaction as a result of the more acid pH. Further, it has been proposed that water and other magmatic volatiles degassed from felsic magmas can act as agents for the transport of heavy and precious metals (e.g., Cu) directly from the magma and may contribute significant quantities of

metals to seafloor metal–rich sulfide deposits (Yang and Scott, 1996; Kamenetsky et al., 2001). There is general acceptance that massive sulfide deposits found in felsic–dominated convergent plate margins may represent a modern submarine analog for volcanogenic hosted massive sulfide deposits preserved in the geologic record (e.g., the Kuroko formations (Halbach et al., 1989; Ohmoto, 1996; Iizasa et al., 1999)) and for epithermal–style Cu–Au mineralization in volcanic arcs (e.g., Tabar–Feni–Lihir ore deposits, Papua New Guinea (Petersen et al., 2002; Gemmell et al., 2004)). However, few studies have examined in detail the metal compositions of seafloor vent fluids from which these deposits may have formed (e.g., Fouquet et al., 1993a), and the specific factors affecting the evolution and composition of seafloor hydrothermal fluids and related deposits in convergent plate margins are not fully constrained.

Concentrations of trace metals and metalloids (Fe, Zn, Cu, Pb, Cd, As, Sb, Co, Ag and Au) in a comprehensive suite of seafloor hydrothermal fluids sampled from the Manus back–arc basin, Papua New Guinea, are presented in this study. The data are used to assess the roles that different sub–seafloor processes (e.g., interaction between seawater and crustal rocks with a range of compositions, differing extents and styles of magmatic acid volatile degassing, and local seawater entrainment and sub–seafloor mixing with high–temperature hydrothermal fluid) play in controlling the formation and composition of seafloor vent fluids in a back–arc basin. The results have particular relevance for understanding the processes responsible for the formation of many volcanogenic hosted massive sulfide deposits, which have been interpreted as forming within convergent margin settings.

2. Geologic Setting and Description of Vent Fields in the Manus Basin

The Manus Basin in the Bismarck Sea, Papua New Guinea (Figure 4.1) is a rapidly–opening (~ 100 mm/yr) back–arc basin associated with subduction of the Solomon Microplate beneath the New Britain arc (Taylor, 1979; Martinez and Taylor, 1996). Crustal extension is complex, involving spreading and generation of new oceanic crust extension toward the west and rifting of existing crust in the east. Toward the west is the Manus Spreading Center (MSC) bounded between the Willaumez and Djaul Transforms (Martinez and Taylor, 1996). Lavas erupted along the MSC are dominantly basalt and have mid–ocean ridge–like chemical affinity (Both et al., 1986; Sinton et al., 2003). Several areas of hydrothermal activity have been identified in the MSC. Vienna Woods is the largest and most active of the known fields (Figure 4.1) (Tufar, 1990). It is located slightly south of the major spreading center within an axial rift valley at a water depth of ~ 2500 m.

To the east, the Eastern Manus Basin (EMB) is bounded by the Djaul and Weitin Transforms where rapid spreading is accommodated primarily by rifting and extension of existing crust (Martinez and Taylor, 1996). Lavas are erupted as a series of discrete *en echelon* neovolcanic ridges and volcanic domes of felsic (andesite–to–rhyolite) composition (Sinton et al., 2003). The arc–like affinity of ocean crust (Sinton et al., 2003) is consistent with the proximal location (< 200 km) of the EMB to the actively subducting margin. The EMB hosts several known active hydrothermal systems (Figure 4.1). The Papua New Guinea–Australia–Canada–Manus

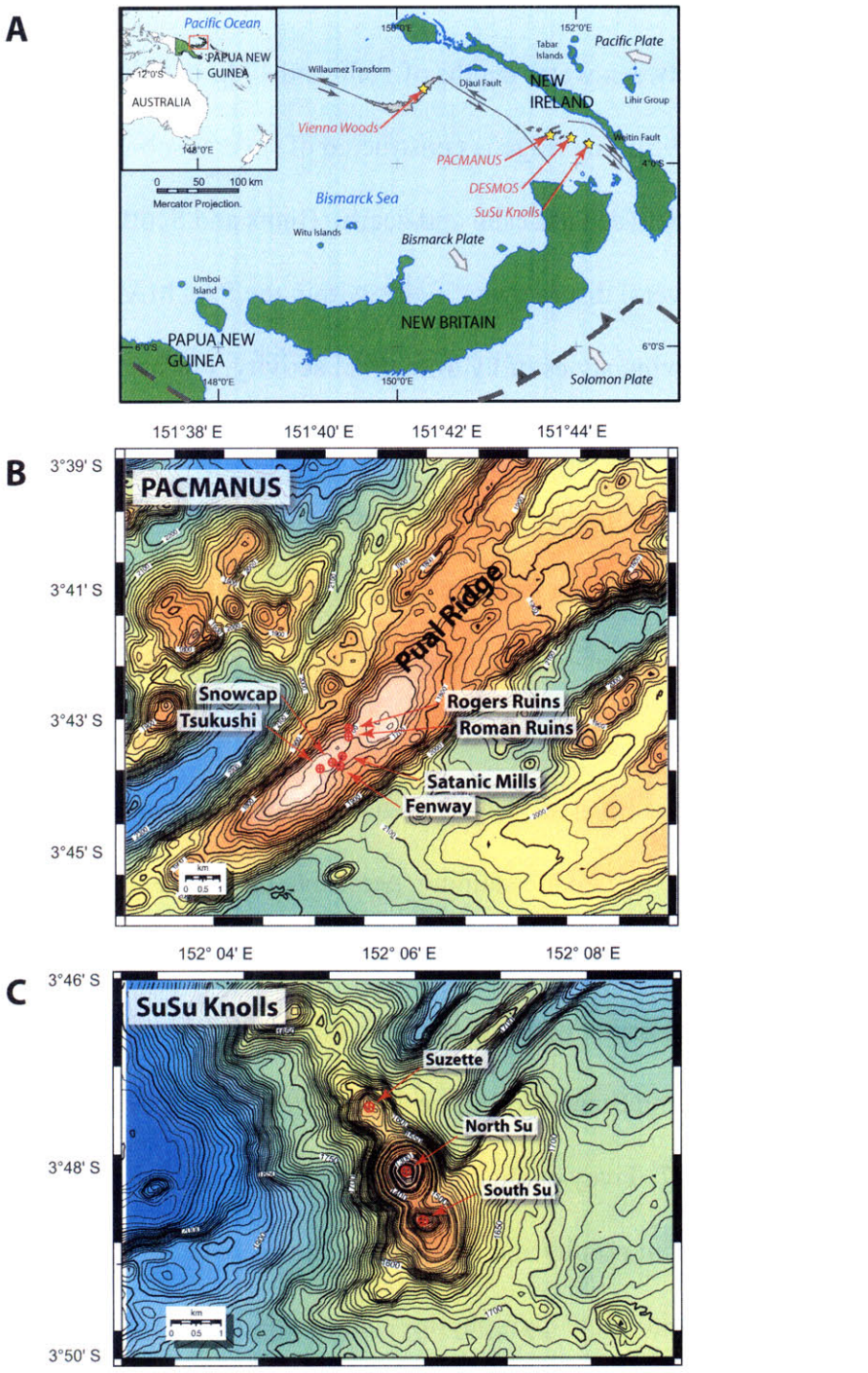

Figure 4.1. A) Regional tectonic setting of the Manus Basin, Papua New Guinea, indicating active plate motion and areas of known hydrothermal activity. Gray arrows indicate directions of plate motion. **B**) Distribution of hydrothermal deposits at PACMANUS. **C**) Distribution of hydrothermal deposits at SuSu Knolls. Bathymetry based on EM300 SeaBeam sonar (modified from Tivey et al., 2007).

(PACMANUS) hydrothermal system is located on the crest of the 35 km long, 500 m high Pual Ridge, between water depths of 1650 and 1740 m (Binns and Scott, 1993; Scott and Binns, 1995). The ridge is constructed of several sub–horizontal lava flows with compositions between andesite and dacite (Binns and Scott, 1993; Sinton et al., 2003). There are several discrete vent fields within the PACMANUS system (Figure 4.1) that exhibit varying styles of hydrothermal activity. Further to the east, the DESMOS and SuSu Knolls hydrothermal systems are located on individual volcanic domes in environments markedly different from ridge–hosted hydrothermal fields. DESMOS (Onsen field, water depth of 1900 to 2000 m) is a collapse caldera that features a roughly crescent–shaped morphology with felsic pillow flows and hyaloclastite deposits arranged across several terraces forming the slopes of the caldera (Sakai et al., 1991; Gamo et al., 1997). Sedimentation and alteration of primary lavas is common and includes Fe–oxide staining, pervasive bleaching (acid–sulfate alteration), locally abundant native sulfur flows and extensive microbial mats (Sakai et al., 1991; Gamo et al., 1997). Further east, SuSu Knolls consists of three discrete volcanic cones (Suzette, North Su and South Su; Figure 4.1) at water depths between ~ 1140 and 1510 m (Binns et al., 1997; Tivey et al., 2007). The North Su and South Su domes are composed of abundant porphyritic dacite flows showing variable advanced argillic alteration (e.g., alunite–illite–pyrophyllite–quartz and native sulfur) and sedimentation by mixed volcaniclastic and hydrothermal material (Binns et al., 1997; Auzende et al., 2000; Yeats et al., 2000; Hrischeva et al., 2007). The dome at Suzette is extensively coated in metalliferous sediment and relict sulfide talus (Binns et al., 1997; Hrischeva et

al., 2007) that mask primary volcanic features.

2.1. Hydrothermal activity

2.1.1. Vienna Woods

Current hydrothermal activity is manifest as both focused and diffuse fluid venting within an area ~ 150 m by 100 m (Tufar, 1990; Tivey et al., 2007). Inactive sulfide chimneys extend across a total area of ~ 300 m by 100 m. Black–gray smoker fluids were sampled exiting from the tops of large sulfide–rich chimneys up to 7 m in height; they have temperatures between 273 and 283 °C and are mildly acidic, with measured pH (25°C) between 4.2 and 4.7 (Douville et al., 1999; Seewald et al., 2006).

2.1.2. PACMANUS

Current hydrothermal activity occurs at several discrete vent fields (Roman Ruins, Roger's Ruins, Satanic Mills, Snowcap, Tsukushi and Fenway) that are between 50 and 200 m in diameter (Binns and Scott, 1993; Auzende et al., 1996; Binns et al., 2007; Tivey et al., 2007). Focused high temperature fluids (~ 300 – 358 °C) exiting black smoker chimneys, focused lower temperature white smoker fluids (150 – 290 °C) discharging from diffuser–type chimneys, and low temperature diffuse fluids (< 100 °C) exiting through cracks in the crust or metalliferous deposits and sediments were sampled from these vent fields. The measured pH (25 °C) of high–temperature vent fluids (≥ 250 °C) exiting sulfide chimney edifices ranges from 2.3 to 2.8 (Douville et al., 1999; Seewald et al., 2006).

2.1.3. DESMOS

Hydrothermal activity occurs at the Onsen field (Gamo et al., 1997), which is a

small (~ 30 m diameter) area of low–temperature fluid discharge located along the northern interior slope of the DESMOS caldera (Sakai et al., 1991; Auzende et al., 1996). Fluid venting is manifest as thick, milky–white smoke discharging directly through extensively altered volcanic breccia and hydrothermal sediments composed of abundant native sulfur and anhydrite (Gamo et al., 1997; Bach et al., 2007). Despite the low temperatures (≤ 120 °C) and high Mg concentrations (~ 40 – 50 mmol/kg) of sampled fluids, the measured pH (25 °C) are very acidic (< 1.5 to 2) (Gamo et al., 1997; Seewald et al., 2006). The compositions of these fluids are markedly different to those of high–temperature black smoker fluids. On the basis of aqueous composition, these fluids have been informally termed 'acid–sulfate' fluids (Gamo et al., 1997).

2.1.4. SuSu Knolls

On–going hydrothermal activity at SuSu Knolls is remarkably diverse, exhibiting a range of crustal rock alteration, mineral deposit composition and vent fluid compositions (Binns et al., 1997; Yeats et al., 2000; Seewald et al., 2006; Bach et al., 2007). The summit of the volcanic domes at North Su and South Su is characterized by high–temperature black and gray smoker fluids venting from scattered sulfide chimney edifices (Binns et al., 1997; Tivey et al., 2007). Black smoker fluids at North Su have temperatures between 300 and 325 °C and are relatively acidic with pH (25 °C) ranging from 2.8 to 3.2 (Seewald et al., 2006). High–temperature smoker fluids were sampled in two areas south and south–east of the South Su summit. Vent fluid temperatures were up to 290 °C. The measured pH (25 °C) of these fluids is low, approximately 2.6 to 2.7 (Seewald et al., 2006). The flanks of the North Su and South Su domes are

characterized by outcrops of volcanic rocks and breccia, some of which have been subject to extensive alteration and bleaching (Binns et al., 1997). Milky–white fluids exit through cracks in these brecciated volcanic flows and extensively altered material at North Su. These fluids exhibit a range of lower temperatures (48 – 241 °C), but are very acidic with measured pH (25 °C) of ≤ 1.8 (Seewald et al., 2006). These fluids show considerable similarity to acid–sulfate fluids sampled at DESMOS (e.g., Gamo et al., 1997).

The smaller dome of Suzette, located NW of North Su and South Su, is extensively covered by thick metalliferous sediment, mass–wasted sulfide talus, Fe–oxide crusts and limited exposures of possible hydrothermal stockwork (Binns et al., 1997; Moss and Scott, 2001; Hrischeva et al., 2007; Tivey et al., 2007). The summit is characterized by large expanses of relict and scattered active sulfide chimneys that are typically buried within sulfide–rich metalliferous sediment (Binns et al., 1997; Tivey et al., 2007). Five high–temperature fluids venting from sulfide–rich chimney edifices were sampled. Measured temperatures range from 226 – 303 °C and pH (25 °C) varies between 3.5 and 3.8 (Seewald et al., 2006). A sixth fluid was sampled from a cracked pavement structure. This fluid had a temperature of ~ 249 °C and was much more acidic with measured pH (25 °C) of 2.3 (Seewald et al., 2006).

3. METHODS

3.1. Sample collection

Hydrothermal fluid samples were collected in August and September 2006 during *R/V Melville* cruise MGLN06MV (Tivey et al., 2007) using discrete samplers actuated by ROV *Jason II*. Samples were collected in 755 ml Ti–syringes ("major" samplers (Von Damm et al., 1985)) and 160 ml isobaric gas–tight samplers ("IGT" samplers (Seewald et al., 2002)). Fluid sampling was coordinated to represent the range of fluid types identified at each vent field. In all cases, sampling of fluids in triplicate was attempted to obtain replicate analyses for quality assurance and to enable calculation of "endmember" fluid compositions. Temperatures were measured with either the ROV temperature probe or with a thermocouple mounted directly onto IGT fluid samplers. Because samples were taken during ROV dives, the location of fluid samples and their relations to geologic samples are known accurately. In total, 101 fluid samples were collected from 36 discrete vents.

Sample aliquots for chemical analysis were extracted immediately after recovery of samplers following the end of dive operations. Splits of each fluid sample were extracted for analysis of pH, gaseous species (e.g., H_2S, H_2, CO_2, F) and major aqueous species (e.g., Cl, Mg, Na, Ca, SO_4, SiO_2). Details of the chemical analysis for these species are provided in a separate study (E. Reeves and J. Seewald, *in prep*). Aliquots for metal analysis were also drawn from the samplers. These were collected in acid–washed, high–density polyethylene (HDPE) Nalgene^{TM} bottles and immediately acidified to pH < 2 by addition of Fisher Optima^{TM} grade HCl.

3.2. Sample processing

Dissolved fractions were prepared for analysis by gravimetric dilution of a ~

0.20 g split of each solution with Fisher Optima^{TM} grade 5 % HNO_3. For analysis of alkali metals (Li, K, Rb, Cs), alkaline earth metals (Sr, Ba), Fe and Mn fluid aliquots were diluted 5000 times. For analysis of trace elements (Al, Cu, Zn, Pb, Sb, Cd, Co, Ag and Au), fluid aliquots were diluted, normalizing to a chloride concentration of 6 mmol/kg. This equated to between 80 and 110 times dilution of the original sample and varied as a function of the chlorinity of the fluid. Normalization to uniform Cl concentrations minimized the effect that variable analyte matrix (predominantly from changes in Na^+ concentration in the fluid) exerted on the ionization and transmission of ions within the instrument. This enabled determination of trace elements without the need for extensive chemical purification to remove the complex analyte matrix. Differences in matrix composition resulting from other elements (e.g., different concentrations of Ca^{2+} and Mg^{2+} among hydrothermal fluid samples) are significantly less than differences in chlorinity (Na^+ and Cl^-) and are assumed not to impact analyte behavior in the instrument.

In nearly all fluid samples, a precipitate ("dregs" fraction) formed as the hydrothermal fluid cooled prior to extraction. The dregs were collected on a 0.22 μm pore–size, 45 mm diameter Nylon filter by rinsing with Milli–Q water and high–purity acetone. The Nylon filters were dried and stored in glass vials for on–shore processing. In addition, minor precipitates formed within several acidified aliquots during storage ("bottle–filter" fraction). These bottle–filter fractions were separated from aqueous samples by filtering through 0.22 μm pore–size, Nuclepore® filters as part of shore–based sample processing. The relative proportions of dregs and bottle–filter fractions

formed was variable among samples, likely related to the differences in time between sample collection and shipboard extraction. In order to obtain accurate data for trace metal concentrations (e.g., Fe, Cu, Zn, Pb) it is essential to reconstitute the original sample by analyzing all dissolved, dregs and bottle–filter fractions (Trefry et al., 1994). This is best achieved by separate determination of element concentrations in each fraction followed by mathematical reconstitution of the fluid.

Particle fractions were removed from filters into acid–washed 30 ml Savillex^{TM} vials by rinsing with 5 ml concentrated Fisher Optima^{TM} grade HNO_3. The vials were sealed and heated overnight on a hot–plate (~ 70 °C) to digest particulates. The resulting solutions were then evaporated to dryness. The acid digestion + evaporation step was repeated a further two times to achieve complete dissolution of the precipitates. The digested particles (dregs and bottle–filter fractions) were quantitatively diluted (100 times) in 5% HNO_3 acid ready for analysis.

3.3. Analytical

3.3.1. Inductively couple plasma–mass spectrometry

Metal concentrations were determined by inductively coupled plasma–mass spectrometry (ICP–MS) using a ThermoElectron *Element2* instrument at Woods Hole Oceanographic Institution. Metals were analyzed separately in the dissolved, dregs and bottle–filter fractions. The mass scan setup for determination of major and minor cations (5000 times diluted aliquots) was ^{7}Li, ^{25}Mg, ^{85}Rb, ^{88}Sr, ^{133}Cs, ^{137}Ba, ^{138}Ba (low resolution) and ^{27}Al, ^{55}Mn, ^{56}Fe, ^{66}Zn, ^{68}Zn, ^{63}Cu, ^{65}Cu (medium resolution) and ^{39}K (high resolution). The mass scan setup for determination of base metals and metlloids (~

100 fold diluted aliquots) was ^{7}Li, ^{59}Co, ^{111}Cd, ^{114}Cd, ^{133}Cs, ^{137}Ba, ^{197}Au, ^{208}Pb (low resolution) and ^{27}Al, ^{55}Mn, ^{56}Fe, ^{59}Co, ^{63}Cu, ^{65}Cu, ^{66}Zn, ^{68}Zn, ^{107}Ag, ^{109}Ag, ^{121}Sb, ^{123}Sb, ^{197}Au (medium resolution). All samples were spiked with 1 ppb ^{45}Sc and ^{115}In internal standards to correct for plasma fluctuations during analysis. Sample concentrations were determined against a six–point linear calibration. The external multi–element standard used for calibration was prepared from Specpure® plasma solutions. The chlorinity (NaCl content) of the standard was the same as for unknown samples (i.e., Cl = 6 mmol/kg) and concentrations of other elements in the standard (containing K, Li, Rb, Cs, Mg, Ca, Sr, Ba, Al, Mn, Fe, Cu, Zn, Pb, Cd, Co, Ni, Mo, Sb, Ag, Au) reflected the approximate distributions of these elements measured in seafloor hydrothermal fluids. Accordingly, the difference in matrix composition between fluid samples and standards was minimized as much as possible (see section 3.2). Bottom seawater sampled several kilometers away from known areas of hydrothermal activity was analyzed as an unknown sample. Baseline intensities were measured by aspirating a 5% HNO_3 acid blank and used for off–line data reduction. External precision of the analytical method determined by triplicate analysis of randomly selected fluids across multiple analytical sessions was approximately 10 %.

3.3.2. Hydride generation–atomic fluorescence spectrometry

Total arsenic concentrations in vent fluids were determined using hydride generation–atomic fluorescence spectrometry by Roy Price and Thomas Pichler (University of South Florida Center for Water and Environmental Analysis). Complete details on sample processing and analytical measurements are provided by Price and

Pichler (2005). Briefly, undiluted aliquots of dissolved and particle fractions were volumetrically mixed with solutions of concentrated HCl and saturated potassium iodide (KI) to obtain final fluid samples containing 30 % HCl and 2 % KI. The additions of HCl and KI were to quantitatively reduce As(V) to As(III) prior to analysis on a PSAnalytical 10.055 Milliennium Excalibur AFS system.

3.4 Calculation of vent fluid compositions

Vent fluid compositions were determined by addition of the concentrations determined in separate dissolved and particle fractions (Trefry et al., 1994). The fraction of trace elements contributed by residual particles varied considerably, from less than 1 % to greater than 95 %, similar to that shown in previous studies (Trefry et al., 1994; Metz and Trefry, 2000). Experimental studies have demonstrated quantitative removal of seawater Mg during high–temperature interaction with basalt (Seyfried and Mottl, 1982; Seyfried, 1987) and the highest temperature (> 300 – 350 °C) black–smoker hydrothermal fluids sampled from mid–ocean ridges typically contain close to zero Mg (Edmond et al., 1982; Von Damm et al., 1985; Campbell et al., 1988; Butterfield et al., 1994). When measured Mg concentrations are not zero, it reflects either the true Mg concentration in vent fluid at the seafloor (e.g., resulting from sub–seafloor mixing between zero–Mg hydrothermal fluid and seawater), or artifacts during sampling owing to entrainment of seawater into hydrothermal fluid at the sampler snorkel. When replicate vent fluid samples yield identical Mg concentrations, it can be assumed that the quality of samples is good and that measured Mg concentrations reflect those of the fluid exiting the vent orifice (at the seafloor).

In this study, Mg concentrations are reported at the lowest measured values of replicate fluids sampled from each vent orifice. Most sampled fluids exiting the seafloor in the Manus Basin contain measurable Mg. The concentrations of other elements in seafloor vent fluids are calculated by extrapolation of measured element concentrations in replicate samples to the lowest measured Mg concentration, using least–squares linear regression forced to pass through the composition of ambient seawater (Figure 4.2) (Von Damm, 1983). Vent fluid replicates characterized by anomalously low concentrations were assumed not to have fully recovered residual precipitates. Fluid samples with anomalously high trace metal concentrations were assumed to contain entrained chimney particles. These data were not used for regressions.

Metal concentrations of "smoker fluids" (sampled from Vienna Woods, PACMANUS and SuSu Knolls) are also reported by extrapolating data using least–squares linear regression to zero Mg to obtain "endmember" fluid compositions (Von Damm, 1983). The concept of a zero Mg, endmember hydrothermal fluid composition is useful for understanding the processes occurring in the sub-seafloor (i.e., high-temperature fluid-rock interaction) affecting the formation of high-temperature smoker fluids, prior to mixing between hydrothermal fluid and seawater (at or close to the seafloor). Reporting of endmember fluid compositions also allows for direct composition of fluids sampled from different vent orifices.

In contrast, metal concentrations of "acid–sulfate" fluids (sampled from DESMOS and SuSu Knolls) are not extrapolated to zero Mg. Acid–sulfate fluids sampled in triplicate contain similar and consistently high Mg concentrations ($\geq$ 24

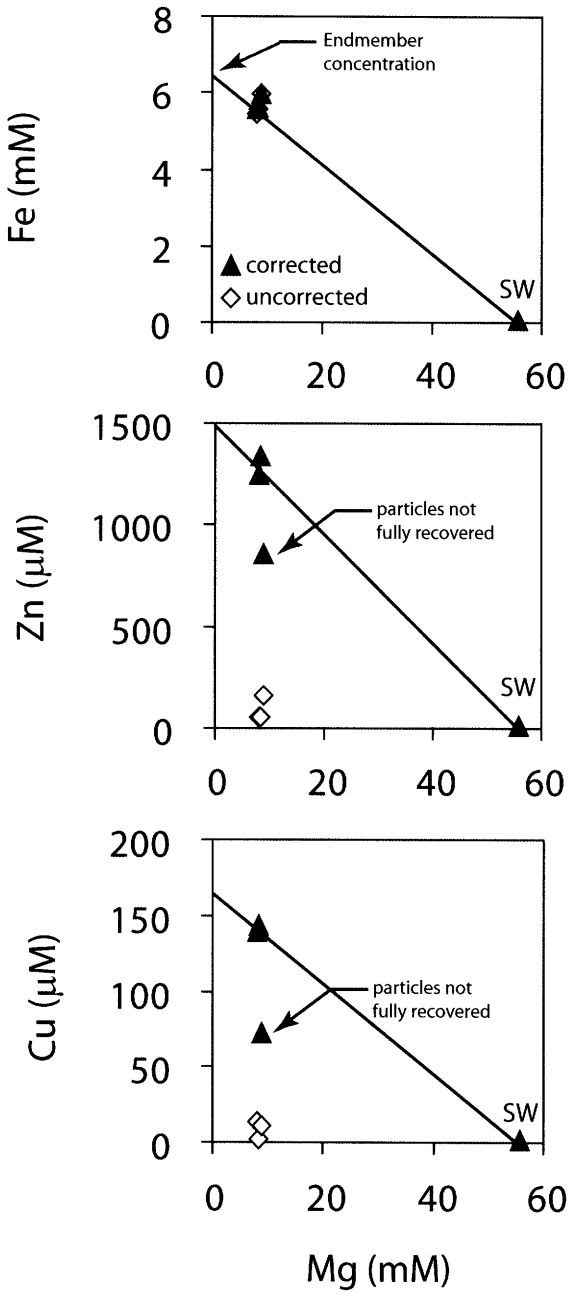

Figure 4.2. Concentrations of trace metals Fe, Zn and Cu in replicate fluids samples from vent "RMR1" (Roman Ruins, PACMANUS hydrothermal system) plotted versus Mg. Open and closed symbols denote fluid concentrations before and after correction for residual precipitates, respectively. For some samples complete recovery of metals from precipitates is not achieved and are excluded from regressions (solid black line) used to determine 'endmember' (zero Mg) concentrations.

mmol/kg), in contrast to high–temperature black smoker fluids that typically contain little or no Mg (see also Gamo et al., 1997). It is unlikely that high Mg concentrations are an artifact of seawater entrainment during vent fluid sampling because of the similar Mg concentrations and extremely low pH of these fluids. The data suggest that acid–sulfate fluids exiting the seafloor contain elevated Mg concentrations. Importantly, the concept of an endmember acid-sulfate hydrothermal fluid does not necessarily apply. There is no evidence to suggest that a zero Mg acid-sulfate fluid existed beneath the seafloor because acid-sulfate fluids do not appear to have formed during reaction of fresh crustal rocks with convecting seawater-derived hydrothermal fluids. Instead acid-sulfate fluids (the implication are discussed in Section 5).

4. RESULTS

4.1. Trace metals and metalloids

4.1.1. Manganese, Iron, Zinc and Copper

4.1.1.1. Vienna Woods

Endmember Mn (< 370 μmol/kg), Fe (< 170 μmol/kg), Zn (< 35 μmol/kg) and Cu (< 10 μmol/kg) concentrations of Vienna Woods vent fluids are low (Table 4.1a, b) but within the range measured in vent fluids with similar temperature (273 – 285 °C) and slightly acidic pH (4.2 – 4.7, at 25 °C) sampled from basalt–hosted mid–ocean ridge vent fields (Von Damm et al., 1985; Butterfield and Massoth, 1994; Trefry et al., 1994; Seyfried et al., 2003). Mn, Fe, Zn and Cu concentrations are low relative to those

from other vent fields in the Manus Basin.

4.2.1.2. PACMANUS

Substantially higher endmember concentrations of Mn (1813 – 4600 μmol/kg), Fe (70 – 14,400 μmol/kg), Zn (25 – 2970 μmol/kg) and Cu (6 – 800 μmol/kg) are observed in vent fluids at PACMANUS relative to Vienna Woods (Table 4.1a, b; Figure 4.3). In general, endmember concentrations of Mn, Fe and Cu are highest in high temperature black smoker fluids (295 – 358 °C) relative to lower–temperature fluids. The exceptions are fluid samples SM2 (Satanic Mills) and RGR2 (Roger's Ruins), which have high concentrations of Cu (475 – 800 μmol/kg) despite their relatively low temperatures (241 °C and 274 °C, respectively). Endmember concentrations of Zn are relatively uniform (~ 400 – 450 μmol/kg) in high temperature black smoker fluids sampled at all vent fields. Considerably higher Zn concentrations are measured in lower temperature fluids (~ 270 – 280 °C) at Roman Ruins (RMR2, RMR3; up to 2970 μmol/kg) and Roger's Ruins (RGR2; up to 566 μmol/kg). On a chloride–normalized basis, endmember Mn concentrations show little scatter among sampled vent fluids. In contrast, significant differences are still clear for Fe, Zn and Cu among sampled vent fluids, both within and between different vent fields.

4.2.1.3. DESMOS and SuSu Knolls

Concentrations of Mn, Fe, Zn and Cu in high–temperature smoker fluids sampled at SuSu Knolls vent fields are characterized by a high degree of variability (Table 4.2a, b). The concentration of Mn, Fe, Zn and Cu in acid-sulfate fluids are considerably different (Table 4.3). Endmember concentrations of Mn in smoker fluids

Table 4.1a. Measured compositions of seafloor hydrothermal (smoker-type) fluids collected from Vienna Woods and PACMANUS, Manus Basin.

Sample	Temp	pH	Mg[a]	Cl[b]	K	Li	Rb	Cs	Al	Mn	Fe	Zn	Cu	Co	As	Sb	Pb	Cd	Ag	Au
	(°C)	(25 °C)	mM	mM	mM	µM	µM	nM	µM	µM	µM	µM	µM	nM	µM	nM	µM	nM	nM	nM
Vienna Woods																				
VW1	282	4.4	0.0	663	21.2	1076	18	290	< 10	349	159	33	4	45	0.9	< 30	0.35	50	38	< 0.1
VW2	273	4.2	0.0	663	21.2	1157	18	286	< 10	365	165	30	(—)	30	0.4	< 30	0.30	57	28	< 0.1
VW3	285	4.7	0.0	641	20.1	1062	17	259	< 10	209	130	23	5	20	0.6	< 30	0.25	36	9	< 0.1
Roman Ruins-Rogers Ruins																				
RMR1	314	2.3	8.0	595	72.0	986	64	2233	< 10	3400	5619	1300	141	200	26.0	570	22.0	2450	690	1.7
RMR2	272	2.3	16.5	529	50.5	639	42	1575	< 10	2271	990	2200	44	50	33.6	3800	80.0	3200	1700	1.7
RMR3	278	2.5	6.4	680	86.4	1157	82	2852	< 10	4742	7385	927	38	59	30.0	690	25.0	1370	298	1.5
RMR4	341	2.6	3.2	625	77.2	1000	72	2250	< 10	2830	6468	440	190	256	18.0	250	8.0	590	190	1.6
RGR1	320	2.7	4.5	616	75.6	800	70	2030	< 10	2450	4150	460	195	27	15.7	300	3.4	667	212	1.8
RGR2	274	2.6	9.0	602	68.8	775	70	1714	< 10	2148	3173	474	400	34	15.9	1040	2.9	640	488	9.1
Satanic Mills																				
SM1	295	2.6	8.8	499	60.5	646	60	1800	< 10	2145	2790	300	120	76	16.6	350	5.8	365	103	2.0
SM2	241	2.4	17.4	437	38.6	441	37	1231	< 10	1853	1045	223	580	25	75.6	(1950)	5.0	155	91	12.4
SM3	288	2.5	10.1	490	57.0	600	56	1722	< 10	1821	960	135	115	9	13.2	225	4.0	134	67	2.0
Snowcap																				
SC1	152	4.6	31.0	480	25.0	300	20	654	< 10	993	32	80	15	30	4.4	(75)	20.0	42	65	7.5
SC2	180	3.4	24.0	510	34.4	499	27	1103	< 10	1625	135	15	4	35	6.6	60	0.5	10	17	0.4
Tsukushi																				
TK1	62	5.7	44.0	550	20.7	219	12	422	< 10	570	124	10	6	(—)	2.8	35	0.3	10	44	< 0.1
Fenway																				
F1	329	2.5	5.8	447	53.8	650	53	1847	< 10	2308	7373	304	263	35	17.7	320	5.8	367	186	1.8
F2	343	2.7	4.7	659	86.8	1067	87	2930	< 10	4218	13263	368	220	465	15.6	165	4.8	400	129	2.3
F3	358	2.7	4.5	562	73.9	900	74	2490	< 10	3800	11500	360	123	475	14.5	(350)	17.0	365	(265)	1.5
F4	284	2.4	9.4	507	61.0	700	57	2082	< 10	2950	6850	320	(260)	37	13.8	233	2.3	295	137	6.0
F5	78	5.0	44.7	497	15.0	110	9	230	< 10	368	600	(50)	9	26	(—)	99	(—)	39	25	< 0.1
Seawater[c]																				
Standard	2	7.8	52.7	546	10.2	27.4	1.4	2.2	0.04	0.005	0.001	0.003	0.01	0.3	0.027	1.2	0.001	0.8	0.035	0.001
Manus			55.7	522	9.8	28.0	1.4	2.1	0.08	(—)	(—)	0.5	0.09	(—)	0.030	1.1	0.002	0.9	0.8	(—)

[a] Mg are the minimum measured concentrations of replicate fluids sampled from each orifice. All data reported to lowest measured Mg.

[b] Cl concentrations provided by E. Reeves and J. Seewald (*unpubl. data*)

[c] Concentrations in "Standard" seawater are averages provided in the review by Bruland and Lohan (2003), except As from Price and Pichler (2005). Concentrations in "Manus" seawater are those determined in bottom seawater sampled from the Manus Basin for comparison (this study).

Values in parantheses denote data for which analyses of replicate fluid samples are reproducible to only 20 - 25 %; (—) indicates no data

A complete analytical dataset of measurements in separate dissolved and particle fractions is provided for reference in Appendix D1.

Table 4.1b. End-member compositions of seafloor hydrothermal (smoker-type) fluids collected from Vienna Woods and PACMANUS, Manus Basin. Data extrapolated to zero Mg.

Sample	Temp (°C)	pH (25 °C)	Mg[a] mM	Cl mM	K mM	Li µM	Rb µM	Cs nM	Al µM	Mn µM	Fe µM	Zn µM	Cu µM	Co nM	As µM	Sb nM	Pb µM	Cd nM	Ag nM	Au nM
Vienna Woods																				
VW1	282	4.4	0.0	663	21.2	1076	18	290	< 10	349	159	33	4	45	0.9	< 30	0.35	50	38	< 0.1
VW2	273	4.2	0.0	663	21.2	1157	18	286	< 10	365	165	30	(—)	30	0.4	< 30	0.30	57	28	< 0.1
VW3	285	4.7	0.0	641	20.1	1062	17	259	< 10	209	130	23	5	20	0.6	< 30	0.25	36	9	< 0.1
Roman Ruins-Rogers Ruins																				
RMR1	314	2.3	0.0	608	82.0	1137	76	2706	< 10	4155	6731	1499	165	234	30.4	678	22.0	2600	720	2.0
RMR2	272	2.3	0.0	532	67.5	880	60	2208	< 10	3345	1509	2970	62	71	47.7	5717	137.0	4000	3233	2.4
RMR3	278	2.5	0.0	700	95.7	1308	90	3131	< 10	5089	8079	1095	40	67	33.9	734	24.0	1620	328	1.6
RMR4	341	2.6	0.0	631	82.0	1083	76	2429	< 10	3005	6829	453	188	272	19.1	250	8.6	634	185	1.7
RGR1	320	2.7	0.0	625	81.3	890	79	2156	< 10	2906	4610	490	213	29	17.1	316	4.0	720	223	2.0
RGR2	274	2.6	0.0	624	79.8	893	79	2126	< 10	2822	3740	566	475	41	19.0	1106	2.9	770	580	10.8
Satanic Mills																				
SM1	295	2.6	0.0	497	69.7	771	71	2216	< 10	2745	3370	350	141	(90)	19.7	413	7.0	440	124	2.4
SM2	241	2.4	0.0	400	51.6	614	52	1747	< 10	2520	1475	265	800	(35)	109.9	(2800)	4.0	220	125	18.0
SM3	288	2.5	0.0	484	67.7	723	70	2140	< 10	2394	1298	175	140	10	16.1	281	5.0	155	75	2.4
Snowcap																				
SC1	152	4.6	0.0	430	43.7	663	42	1528	< 10	2240	70	179	34	(58)	9.9	(190)	31.0	100	155	17.0
SC2	180	3.4	0.0	505	53.9	857	50	2013	< 10	2880	241	25	6	(50)	11.6	98	2.0	23	32	0.7
Tsukushi																				
TK1	62	5.7	0.0	661	61.2	962	56	2063	< 10	3000	589	39	26	(—)	13.3	191	1.0	80	220	< 0.1
Fenway																				
F1	329	2.5	0.0	438	58.6	715	62	2144	< 10	2570	8500	330	291	39	19.8	353	6.0	410	210	2.0
F2	343	2.7	0.0	671	93.8	1142	96	3306	< 10	4600	14400	410	235	508	17.0	176	5.2	430	150	2.5
F3	358	2.7	0.0	562	79.5	960	77	2750	< 10	3962	12950	390	138	517	15.8	(420)	18.0	480	290	1.6
F4	284	2.4	0.0	502	70.7	842	65	2523	< 10	3599	8549	367	305	45	16.6	230	2.6	353	165	7.2
F5	78	5.0	0.0	402	34.7	472	43	1229	< 10	1813	3600	(320)	53	132	(—)	514	(—)	195	130	< 0.1

[a] Mg extrapolated to zero. All other data also extrapolated to zero Mg concentration.

Values in parantheses denote data for which analyses of replicate fluid samples are reproducible to only 20 - 25 %; (—) indicates no data

A complete analytical dataset of measurements in separate dissolved and particle fractions is provided for reference in Appendix D1.

Table 4.2a. Measured compositions of seafloor hydrothermal (smoker-type) fluids collected from SuSu Knolls, Manus Basin.

Sample	Temp	pH	Mg[a]	Cl[b]	K	Li	Rb	Cs	Al	Mn	Fe	Zn	Cu	Co	As	Sb	Pb	Cd	Ag	Au
	(°C)	(25 °C)	mM	mM	mM	μM	μM	nM	μM	μM	μM	μM	μM	nM	μM	nM	μM	nM	nM	nM
Suzette																				
SZ1	303	3.8	4.4	595	44.7	670	46	1988	< 10	246	682	20	49	212	14.0	172	1.6	76	35	(0.8)
SZ2	274	3.6	8.6	635	43.0	680	41	2023	< 10	309	702	25	22	85	12.0	166	2.9	81	50	(0.7)
SZ3	290	3.5	5.5	649	45.1	710	41	2250	< 10	294	783	30	38	80	13.0	160	2.1	113	53	(1.6)
SZ4	229	3.6	8.3	630	49.0	662	47	2147	< 10	279	430	26	11	104	24.0	224	2.3	79	28	(2.0)
SZ5	249	2.3	6.4	586	44.3	650	43	1877	< 10	243	3961	305	1030	70	103.0	590	14.7	860	1350	(2.5)
SZ6	226	3.7	8.0	662	45.5	694	44	2192	< 10	326	326	32	8	90	10.0	(200)	1.7	100	(25)	(0.5)
North Su																				
NS3	300	3.4	0.0	646	64.5	850	65	2836	< 10	421	2390	38	98	1003	18.7	214	1.4	99	52	1.8
NS5	299	3.2	7.4	527	43.7	562	45	1959	< 10	298	3463	13	425	150	15.8	92	1.6	71	50	1.9
NS6	325	2.8	0.0	710	63.4	900	65	2969	< 10	479	5858	17	99	2570	22.8	214	2.9	79	69	0.7
South Su																				
SS1	271	2.6	5.3	587	44.5	565	44	2074	< 10	500	1950	33	350	25	94.8	11850	1.1	(150)	250	15.0
SS2	288	2.7	6.8	579	43.7	552	45	1748	< 10	425	2230	25	115	37	15.9	234	2.1	99	50	3.6

[a] Mg are the minimum measured concentrations of replicate fluids sampled from each orifice. All data reported to lowest measured Mg.

[b] Cl concentrations provided by E. Reeves and J. Seewald (*unpubl. data*)

Values in parantheses denote data for which analyses of replicate fluid samples are reproducible to only 20 - 25 %; (—) indicates no data

A complete analytical dataset of measurements in separate dissolved and particle fractions is provided for reference in Appendix D1.

Table 4.2b. End-member compositions of seafloor hydrothermal (smoker-type) fluids collected from SuSu Knolls, Manus Basin. Data extrapolated to zero Mg.

Sample	Temp	pH	Mg[a]	Cl	K	Li	Rb	Cs	Al	Mn	Fe	Zn	Cu	Co	As	Sb	Pb	Cd	Ag	Au
	(°C)	(25 °C)	mM	mM	mM	µM	µM	nM	µM	µM	µM	µM	µM	nM	µM	nM	µM	nM	nM	nM
Suzette																				
SZ1	303	3.8	0.0	602	47.8	723	51	2162	< 10	265	720	22	53	230	14.5	188	1.7	85	35	(0.8)
SZ2	274	3.6	0.0	655	48.7	789	49	2443	< 10	360	880	29	27	101	14.6	195	3.4	96	60	(0.7)
SZ3	290	3.5	0.0	661	48.9	807	45	2495	< 10	329	916	32	44	89	15.2	178	2.4	125	58	(1.6)
SZ4	229	3.6	0.0	650	54.8	770	55	2558	< 10	324	495	31	13	122	28.2	265	2.7	93	34	(2.0)
SZ5	249	2.3	0.0	594	48.1	712	50	2125	18.1	271	4571	340	1170	79	116.4	750	15.5	800	1400	(3.0)
SZ6	226	3.7	0.0	685	51.5	812	53	2615	< 10	382	405	(35)	10	105	11.7	(225)	2.0	124	(25)	(0.5)
North Su																				
NS3	300	3.4	0.0	646	64.5	850	65	2836	< 10	421	2390	38	108	1003	15.0	214	1.4	99	52	1.8
NS5	299	3.2	0.0	528	48.7	662	51	2277	< 10	349	4021	15	480	173	18.2	105	1.8	82	52	2.2
NS6	325	2.8	0.0	710	63.4	900	65	2969	< 10	479	5858	17	99	2570	25.0	214	2.9	79	70	0.7
South Su																				
SS1	271	2.6	0.0	594	48.0	622	48	2266	< 10	550	2194	34	390	28	104.8	13000	1.2	(160)	270	16.6
SS2	288	2.7	0.0	585	48.1	627	49	2025	< 10	485	2562	23	136	42	18.1	275	2.4	110	60	4.1

[a] Mg extrapolated to zero. All other data also extrapolated to zero Mg concentration.

Values in parantheses denote data for which analyses of replicate fluid samples are reproducible to only 20 - 25 %; (—) indicates no data

A complete analytical dataset of measurements in separate dissolved and particle fractions is provided for reference in Appendix D1.

Table 4.3. Compositions of acid-sulfate fluids collected from DESMOS and SuSu Knolls (North Su), Manus Basin.

Sample	Temp	pH	Mg[a]	Cl[b]	K	Li	Rb	Cs	Al	Mn	Fe	Zn	Cu	Co	As	Sb	Pb	Cd	Ag	Au
	(°C)	(25 °C)	mM	mM	mM	µM	µM	nM	µM	µM	µM	µM	µM	nM	µM	nM	µM	nM	nM	nM
DESMOS																				
D1	117	1.0	46.0	475	8.3	24	3	11	480	40	12400	230	4	9630	11.7	15	6.5	140	(26)	1.4
D2	70	1.4	50.4	482	8.8	25	< 2	8	1640	43	5530	65	3	700	5.5	(—)	1.3	21	15	< 0.1
North Su																				
NS1	48	1.8	49.0	500	9.8	34	< 2	40	210	26	1627	80	6	96	3.2	163	0.7	13	20	< 0.1
NS2	215	0.9	38.8	425	7.8	37	< 2	64	1075	81	3103	63	6	813	18.4	(—)	1.6	80	7	0.2
NS4	241	1.5	23.5	540	31.3	399	31	1374	150	201	3199	55	14	50	9.2	(—)	(1.5)	74	14	< 0.1

[a] Mg are the minimum measured concentrations of replicate fluids sampled from each orifice. All data reported to lowest measured Mg.

[b] Cl concentrations provided by E. Reeves and J. Seewald (*unpubl. data*)

Values in parantheses denote data for which analyses of replicate fluid samples are reproducible to only 20 - 25 %; (—) indicates no data

A complete analytical dataset of measurements in separate dissolved and particle fractions is provided for reference in Appendix D1.

from SuSu Knolls range from 265 – 550 μmol/kg (Table 4.2b), but on a chloride–normalized basis are similar. Concentrations of Mn in acid–sulfate fluids from SuSu Knolls and DESMOS (~ 26 – 201 μmol/kg; Table 4.3) are lower than in smoker fluids. The abundance of Mn in vent fluids at DESMOS and SuSu Knolls are significantly lower than vent fluids at PACMANUS (Figure 4.3).

Endmember concentrations of Fe, Zn and Cu are low in most sampled Suzette vent fluids (Fe = 405 – 916 μmol/kg, Zn = 22 – 35 μmol/kg, Cu = 10 – 53 μmol/kg). The exception is the low pH fluid sample SZ5, which has order of magnitude higher Fe (4571 μmol/kg), Zn (340 μmol/kg) and Cu (1170 μmol/kg) concentrations. In general endmember Fe and Cu concentrations are higher in smoker fluids at North Su and South Su relative to those from Suzette (up to 5858 μmol/kg and 480 μmol/kg, respectively). At South Su, fluid sample SS1 has a higher endmember concentration of Cu (~ 390 μmol/kg) relative to other black smoker fluids, despite the lower temperature (271 °C) of this fluid. Endmember Zn concentrations of high–temperature smoker fluids at North Su and South Su (15 – 38 μmol/kg) are low and similar to vent fluids from Suzette. Acid–sulfate fluids sampled from North Su and DESMOS have uniformly low concentrations of Cu (4 – 14 μmol/kg). In contrast, and despite high Mg concentrations, acid–sulfate fluids have high Zn (55 – 230 μmol/kg) and Fe (1627 – 12,400 μmol/kg) concentrations relative to smoker fluids from SuSu Knolls (Table 4.3; Figure 4.3).

4.1.2. Lead, Cadmium, Cobalt, Silver and Gold

4.1.2.1. Vienna Woods

Endmember Pb (0.25 – 0.35 μmol/kg), Cd (< 60 nmol/kg), Co (≤ 45 nmol/kg)

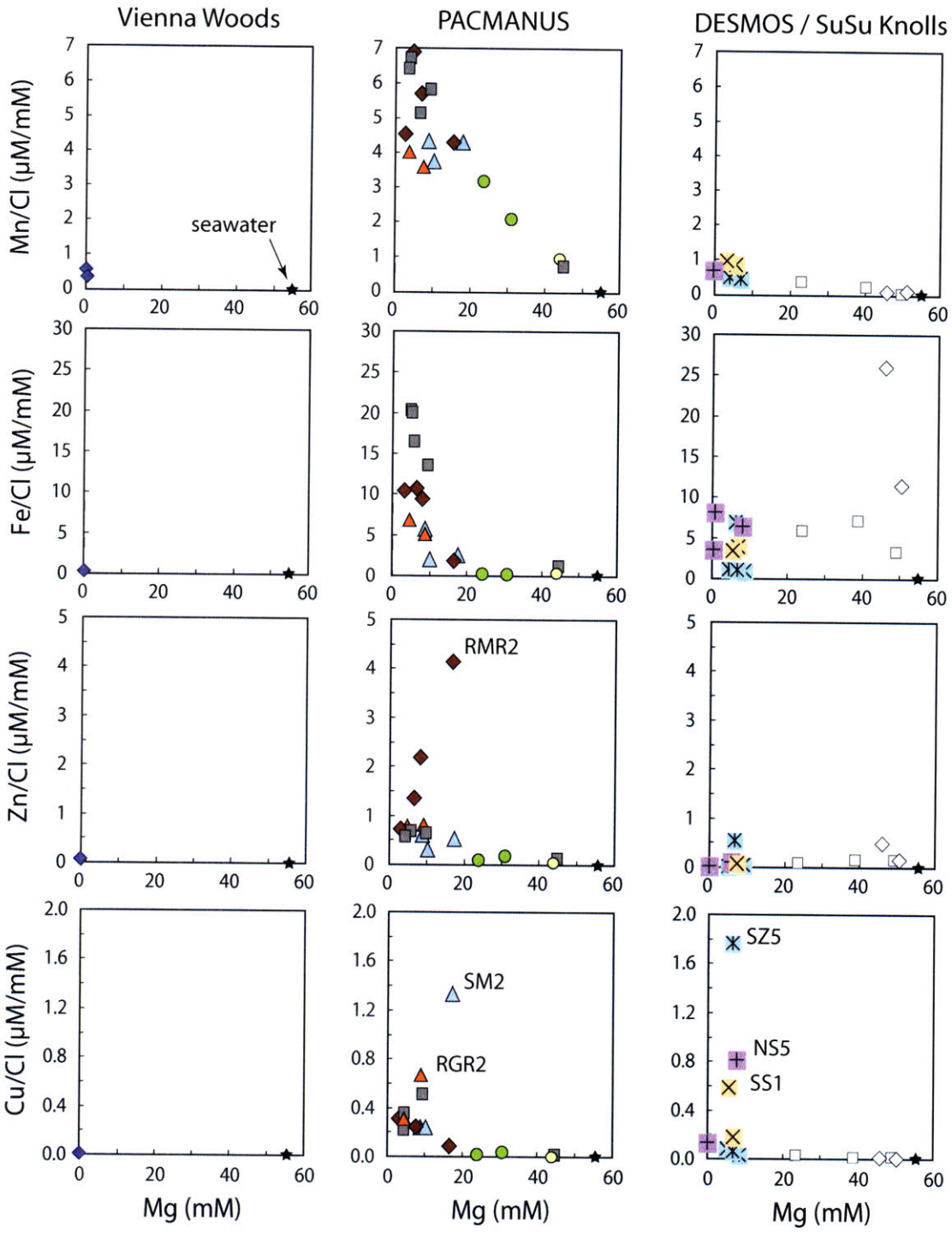

Figure 4.3. Chloride-normalized concentrations of Mn, Fe, Zn and Cu versus Mg in seafloor hydrothermal fluids from Vienna Woods (◆), PACMANUS (Roman Ruins ◆, Roger's Ruins ▲ Satanic Mills △, Snowcap ●, Tsukushi ○, Fenway ■), DESMOS (◇) and SuSu Knolls (Suzette ✳, North Su smoker fluids ⧾, North Su acid-sulfate fluids □, South Su ⧓).

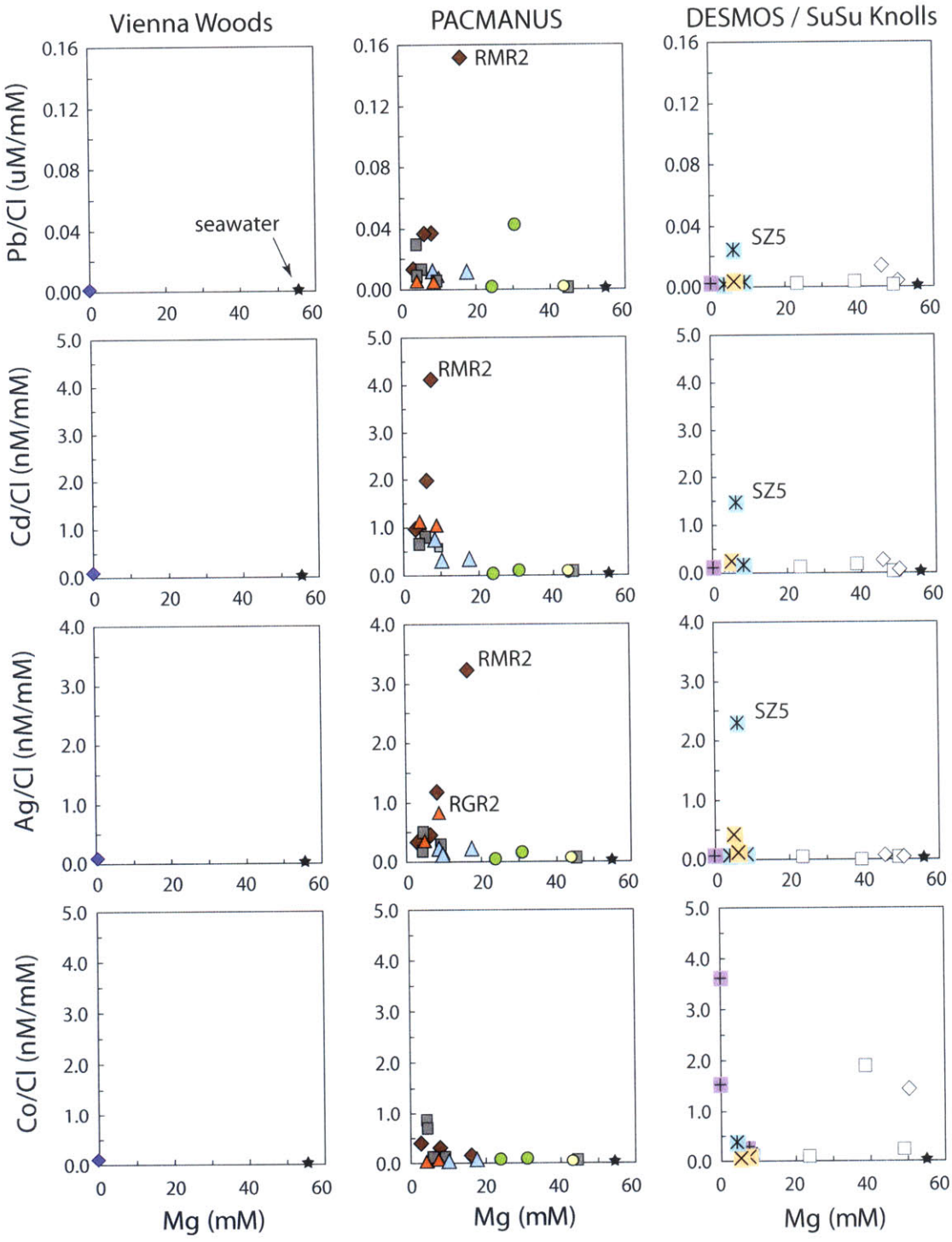

Figure 4.4. Chloride-normalized concentrations of Pb, Cd, Ag and Co versus Mg for seafloor hydrothermal fluids from Vienna Woods, PACMANUS, DESMOS and SuSu Knolls. Symbols as for Figure 4.3.

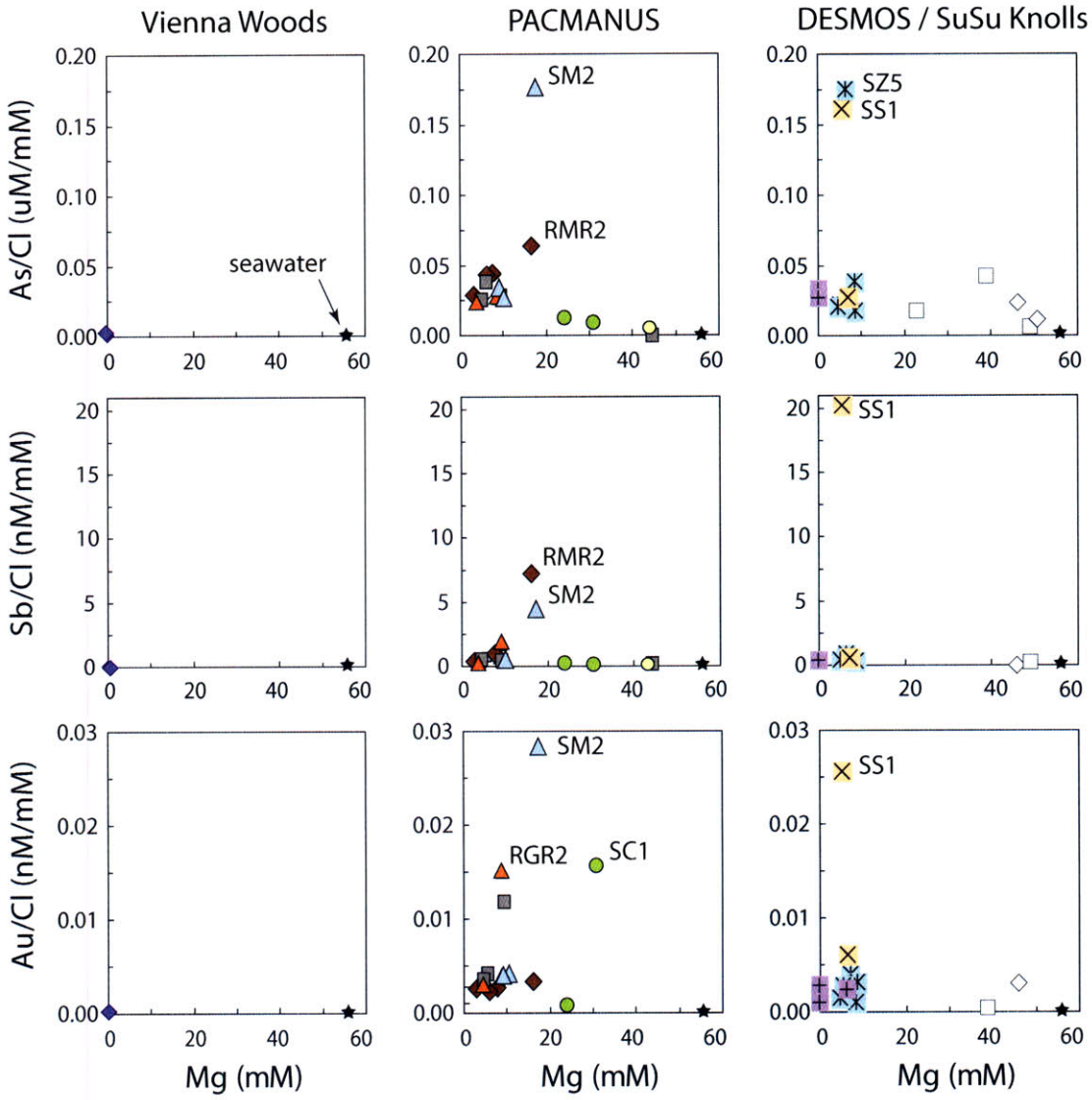

Figure 4.4. (contd) Chloride-normalized concentrations of As, Sb and Au versus Mg for seafloor hydrothermal fluids from Vienna Woods, PACMANUS, DESMOS and SuSu Knolls. Symbols as for Figure 4.3.

and Ag (< 40 nmol/kg) concentrations in Vienna Woods vent fluids are enriched relative to seawater but are low relative to hydrothermal fluids sampled from other vent fields in the Manus Basin (Table 4.1b; Figure 4.4). Concentrations of Au were below the detection limit (~ 0.2 nmol/kg) of the analytical method.

4.1.2.2. PACMANUS

Concentrations of Co, Pb, Cd, Ag and Au are high in most PACMANUS vent fluids relative to those of vent fluids from Vienna Woods and mid–ocean ridge hydrothermal systems (Table 4.1a, b; Figure 4.4). Endmember Co concentrations are highest (234 – 517 nmol/kg) in high temperature fluids (> 300 – 358 °C), and significantly less (29 – 132 nmol/kg) in lower temperature fluids. The aqueous distribution of Co is similar to Cu. Endmember Pb, Cd and Ag concentrations show a narrow range of relatively high concentrations in the highest temperature fluids sampled from PACMANUS vent fields (Pb = 4 – 18 μmol/kg, Cd = 440 – 720 nmol/kg, Ag = 124 – 290 nmol/kg). Significant enrichments of Pb (up to 137 μmol/kg), Cd (up to 4000 nmol/kg) and Ag (up to 3233 nmol/kg) are observed in lower temperature fluids from Roman Ruins (RMR2 and RMR3) and Roger's Ruins (RGR2; Table 4.1b), relative to higher temperature fluids. The distributions of Pb, Cd and Ag are generally similar to that of Zn. Endmember concentrations of Au are generally in the range 1 – 3 nmol/kg in all PACMANUS vent fluids, although significantly higher concentrations of Au are observed in low temperature fluids from Roger's Ruins (RGR2; T = 274 °C, Au = 10.8 nmol/kg), Satanic Mills (SM2; T = 241 °C, Au = 18 nmol/kg) and Snowcap (SC1; T = 152 °C, Au = 17 nmol/kg). Au enrichment of fluids from Roger's Ruins and Snowcap

are correlated with relative enrichments of Zn, Pb, Cd and Ag. High Au concentrations in Satanic Mills vent fluids are not correlated with high concentrations of Zn, Pb, Cd and Ag, but are correlated with high concentrations of As and Sb and fluoride (see below).

4.1.3.2. DESMOS and SuSu Knolls

In sampled black/gray smoker fluids, endmember concentrations of Co range from 28 – 173 nmol/kg in samples with temperatures below 300 °C, and from 230 – 2570 nmol/kg in samples with temperature above 300 °C (Table 4.2b). Endmember Co concentrations are generally higher in SuSu Knolls vent fluids relative to those from PACMANUS (Figure 4.4). In contrast, endmember concentrations of Pb (1.2 – 3.4 nmol/kg), Cd (80 – 125 nmol/kg), Ag (25 – 70 nmol/kg) and Au (1 – 4 nmol/kg) are generally lower in SuSu Knolls vent fluids compared to those from PACMANUS. Fluid sample SZ5 is different and has significantly higher endmember concentrations of Pb (15.5 μmol/kg) , Cd (800 nmol/kg) and Ag (1400 nmol/kg; Table 4.2). Fluid sample SS1 is also different, having somewhat elevated Ag (270 nmol/kg) and much higher Au (17 nmol/kg) than other smoker fluids from SuSu Knolls.

Acid–sulfate fluids from DESMOS and North Su exhibit concentrations of Pb, Cd, Ag and Au that are low relative to most black/gray smoker fluids from SuSu Knolls and PACMANUS (Table 4.3). In contrast, Co concentrations are variable but remarkably high (50 – 9630 nmol/kg) relative to most smoker fluids from all vent fields.

4.1.3. Arsenic and Antimony

4.1.3.1. Vienna Woods

Endmember As concentrations (0.4 – 0.9 μmol/kg) in fluids from Vienna Woods are the lowest of all sampled fluids in the Manus Basin (Figure 4.4). Concentrations of Sb exhibited significant scatter among replicate samples and the reproducibility of data obtained was not better than 25 %; however, calculated endmember concentrations in all Vienna Woods fluids are less than 30 nmol/kg.

4.1.3.2. PACMANUS

Endmember concentrations of As and Sb are high in vent fluids from PACMANUS relative to fluids from Vienna Woods and to mid–ocean ridge hydrothermal fluids (Von Damm et al., 1985; Trefry et al., 1994; Metz and Trefry, 2000). Endmember As and Sb concentrations of most high–temperature black/gray smoker fluids sampled from PACMANUS are in the range ~ 10 to 20 μmol/kg and 176 to 415 nmol/kg, respectively. High concentrations of As (up to 47.7 μmol/kg) and Sb (up to 5717 nmol/kg) are observed in lower temperature fluids from Roman Ruins and Roger's Ruins and are correlated with high concentrations of Zn. As is the case for Cu and Au, the Satanic Mills sample SM2 is an exception, having a very high concentration of both As (~ 110 μmol/kg) and Sb (2800 μmol/kg; Figure 4.4)

4.1.3.3. DESMOS and SuSu Knolls

In most black/gray smoker fluids sampled from SuSu Knolls, endmember As (12 – 28 μmol/kg) and Sb (105 – 265 nmol/kg) concentrations are similar to those of fluids from PACMANUS (Table 4.2b). Again, the exceptions are fluids SZ5 and SS1, which exhibit considerable enrichments of both elements (As = 105 – 116 μmol/kg; Sb

= 750 – 13,000 nmol/kg; Table 4.2b, Figure 4.4), relative to other vent fluids

Acid–sulfate fluids from North Su and DESMOS have variable concentrations of As (3.2 – 18.4 μmol/kg) and Sb (≤ 163 nmol/kg) and there is no evidence of systematically higher or lower concentrations of As or Sb in acid–sulfate fluids relative to smoker fluids (Table 4.3).

4.2. Alkali metals

Endmember concentrations of alkali metals (Li, K, Rb and Cs) in black/gray smoker fluids sampled at all vent fields in the Manus Basin are enriched by an order of magnitude relative to seawater (Tables 4.1b and 4.2b). At Vienna Woods, endmember concentrations of Li (1062 – 1157 μmol/kg), K (20.1 – 21.2 mmol/kg), Rb (17.0 – 18.4 μmol/kg) and Cs (259 – 290 nmol/kg) are relatively uniform and are comparable to those of high–temperature vent fluids from unsedimented mid–ocean ridge hydrothermal systems (Von Damm et al., 1985; Von Damm, 1990). The small amount of variability in the concentrations of these species (Figure 4.5) is reduced when the concentrations are normalized to chloride.

At PACMANUS, endmember Li (472 – 1308 μmol/kg), K (34.7 – 95.7 mmol/kg), Rb (42.3 – 95.7 μmol/kg) and Cs (1229 – 3306 nmol/kg) concentrations show more variability among sampled smoker fluids and are quite different to alkali concentrations of Vienna Woods fluids (Figure 4.5). This degree of variability is eliminated when the alkali concentrations are normalized to chloride.

Endmember Li (622 – 900 μmol/kg), K (48.0 – 64.5 mmol/kg), Rb, (48 – 65 μmol/kg) and Cs (2025 – 2969 nmol/kg) concentrations of sampled smoker fluids at

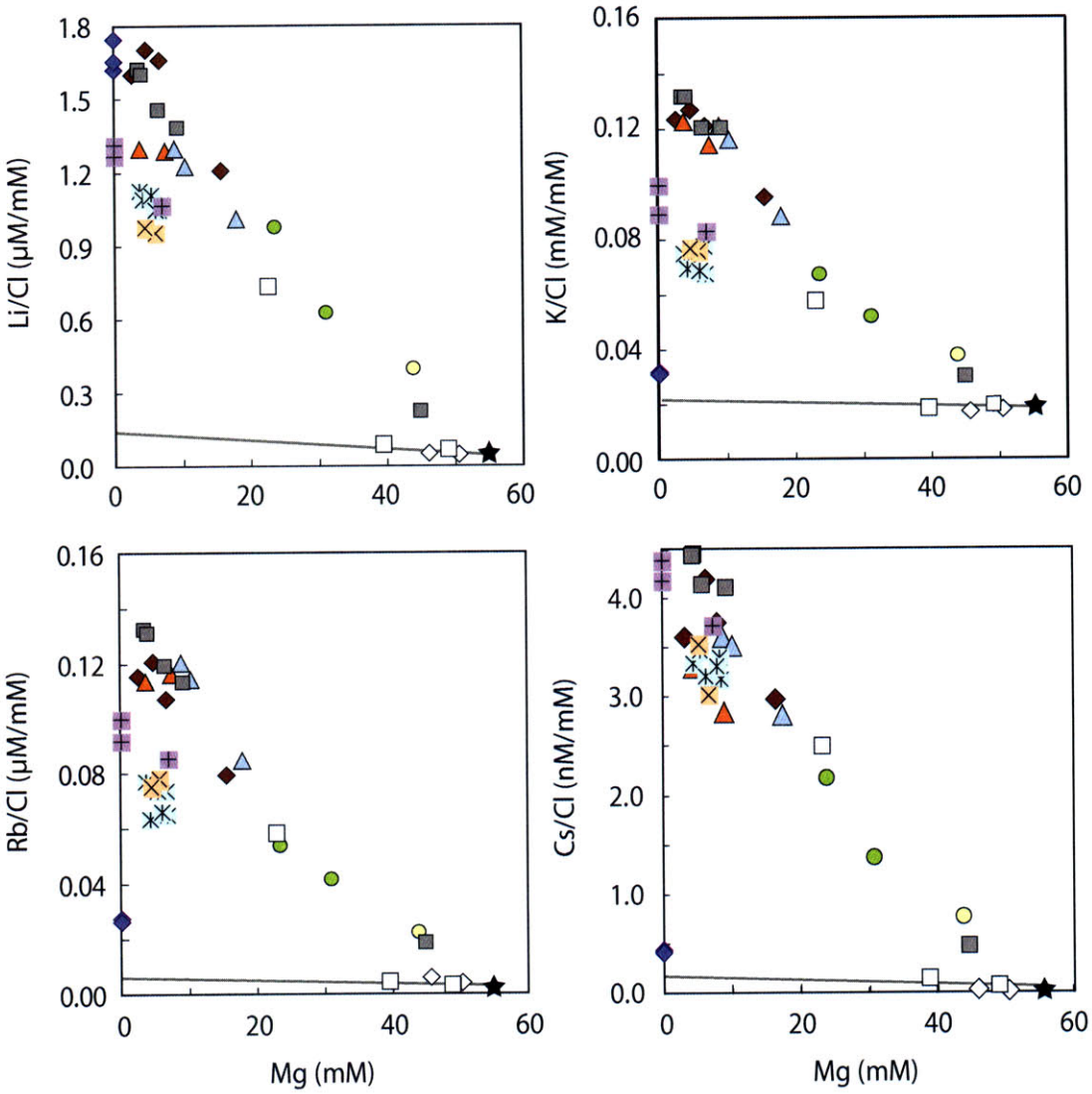

Figure 4.5. Chloride-normalized concentrations of alkali metals Li, K, Rb and Cs versus Mg in hydrothermal fluids from the Vienna Woods, PACMANUS, DESMOS and SuSu Knolls vent fields in the Manus Basin. Symbols as given in Figure 4.3.

SuSu Knolls are slightly lower than at PACMANUS (Figure 4.5). After normalization to chloride, it is apparent that alkali metal concentrations at SuSu Knolls fall on a chemical trend that is distinct from PACMANUS. Alkali concentrations are low in acid–sulfate fluids from DESMOS and SuSu Knolls and clearly different than smoker fluids sampled from all vent fields in the Manus Basin (Figure 4.5). Except for fluid sample NS4 (North Su), Li, Rb and Cs concentrations are elevated only slightly relative to local seawater and K concentrations are lower than local seawater (Table 4.3; Figure 4.5). Fluid sample NS4 has a fluid composition that is intermediate between acid–sulfate fluids and typical black smoker fluids.

4.3. Aluminum

In smoker fluids from Vienna Woods, PACMANUS and SuSu Knolls, endmember Al concentrations are similar and with few exceptions are less than 10 μmol/kg (Tables 4.1 and 4.2). This range is comparable to concentrations of dissolved Al measured in high–temperature mid–ocean ridge fluids (Von Damm, 1983, 1990; Seyfried et al., 2003). In contrast, acid–sulfate fluids sampled from DESMOS and North Su have remarkably high concentrations of Al ranging from 150 to 1640 μmol/kg (Table 4.3).

5. DISCUSSION

5.1. Formation of seafloor hydrothermal fluids during fluid–rock interaction

Experimental studies have shown that metal enrichments in seafloor

hydrothermal fluids from mid–ocean ridge spreading centers relative to seawater reflect the removal of metals from crustal rocks during alteration of primary silicates at elevated temperature and pressure (Bischoff and Dickson, 1975; Seyfried and Bischoff, 1977; Mottl and Holland, 1978; Mottl et al., 1979; Seyfried and Bischoff, 1981; Seyfried and Janecky, 1985; Seewald and Seyfried, 1990). The concentrations of mobile elements (such as Li, Rb, and to a lesser extent K) in seafloor hydrothermal fluids are primarily controlled by their concentrations in unaltered crustal rocks, the extent of previous rock alteration and the effective fluid/rock mass ratio (Mottl and Holland, 1978; Seyfried and Mottl, 1982; Seyfried et al., 1984). In contrast, concentrations of base and precious ('heavy') metals (e.g., Mn, Fe, Zn, Cu) in seafloor hydrothermal fluids are controlled by the aqueous solubility of these elements during fluid–rock interaction and secondary mineral precipitation, and are affected by changes in temperature, pressure and fluid composition (e.g., pH) in addition to primary rock composition (Bischoff and Dickson, 1975; Mottl et al., 1979; Seyfried and Bischoff, 1981; Rosenbauer and Bischoff, 1983; Seyfried and Janecky, 1985; Seewald and Seyfried, 1990).

The concentrations of alkali metals, alkaline earth metals and heavy metals and metalloids in high–temperature smoker fluids and acid–sulfate fluids sampled from vent fields in the Manus back–arc basin exhibit considerable differences. These differences reflect, in part, the influence of changes in host–rock composition (ranging from mafic (mid–ocean ridge–like) in the Manus Spreading Center to felsic (arc–like) in the Eastern Manus Basin), differences in the extent of previous crustal rock alteration, and marked

differences in the conditions (e.g., temperature, pressure, pH) of on–going fluid–rock interactions.

5.1.1. Factors affecting the formation of high–temperature black/gray smoker fluids

Alkali concentrations in vent fluids from Vienna Woods are consistent with interaction of circulating seawater and basalt at elevated temperatures and pressures. Ratios of Rb/K, Cs/Rb and Rb/Li (Figure 4.6) are similar to average ratios of fresh basalts erupted in the MSC (Sinton et al., 2003). Alkali ratios in Vienna Woods fluids (Cs/Rb molar ratio ~ 15 x 10^{-3}) are also similar to those from unsedimented mid–ocean ridge hydrothermal systems (Cs/Rb molar ratio ~ 11 x 10^{-3}) where hydrothermal fluids have interacted with basalt at depth (e.g., 21 °N East Pacific Rise (Von Damm et al., 1985); 11 – 13 °N East Pacific Rise (Von Damm, 1990)). Based on the enrichments of alkali metals relative to seawater and knowing the concentrations of the alkalis in primary basalts ([Li] ~ 6 ppm, [Rb] ~ 2 ppm; Sinton et al. 2003), an effective water/rock ratio (Seyfried and Mottl, 1982) of between 1 and 1.7 is calculated, indicating rock–dominated conditions for the formation of Vienna Woods fluids. That the measured pH (25 °C) of Vienna Woods fluids is mildly acidic (~ 4.2 – 4.7) is consistent, in part, with equilibrium fluid–basalt interaction under rock–dominated conditions. At low water/rock ratios, the acidity generated during uptake of Mg into secondary alteration minerals (e.g., Mg–smectite and Mg–chlorite) is effectively titrated by exchange of H^+ with Ca, Na and other cations during primary silicate hydrolysis (Seyfried and Bischoff, 1977; Seyfried and Mottl, 1982), thereby maintaining a relatively high fluid pH. Experimental studies have also demonstrated that fluid pH is a sensitive function of the

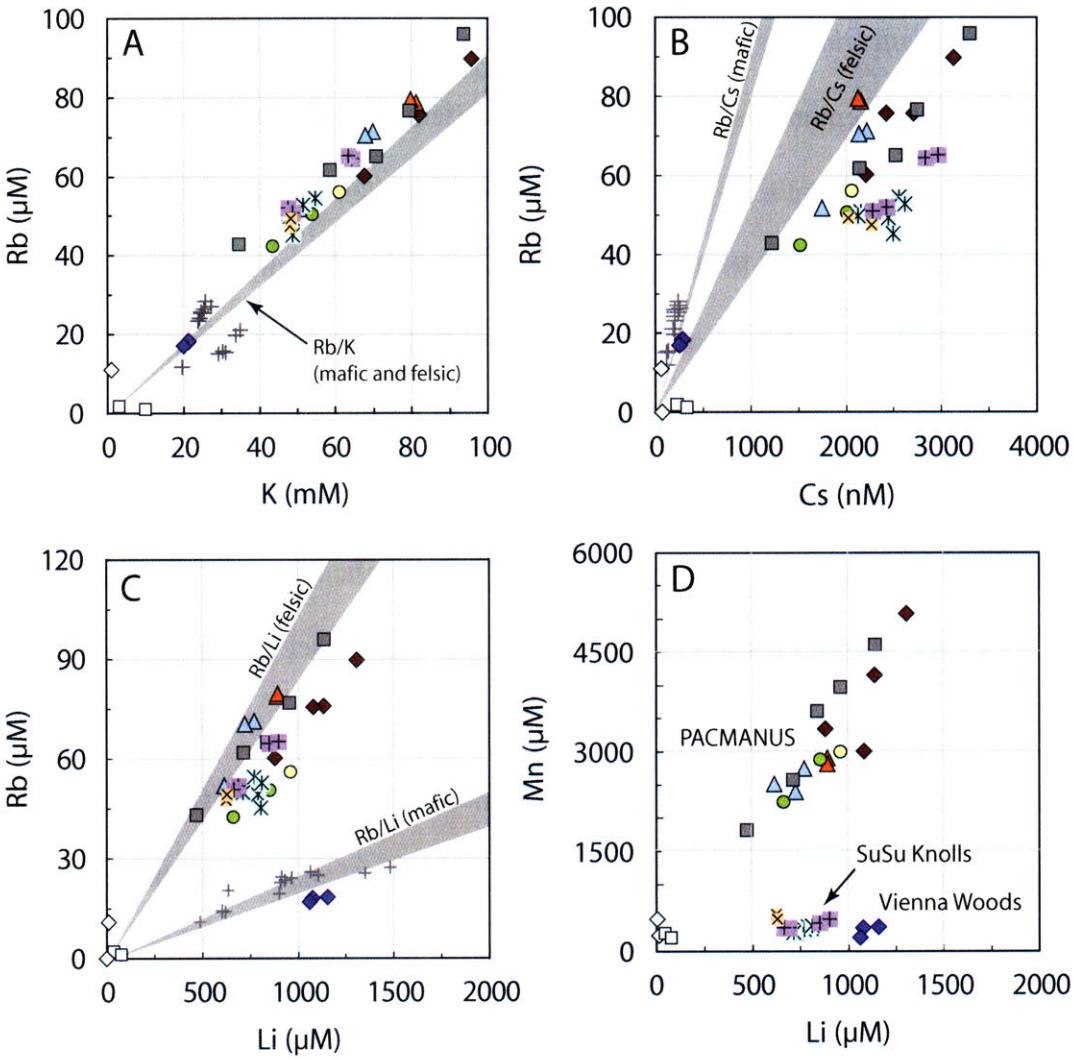

Figure 4.6. Concentrations of **A)** Rb versus K, **B)** Rb versus Cs, **C)** Rb versus Li and **D)** Mn versus Li in seafloor vent fluids from the Vienna Woods, PACMANUS, DESMOS and SuSu Knolls hydrothemal systems in the Manus Basin. Concentrations of alkali metals in mid-ocean ridge hydrothermal fluids are indicated by gray crosses; data from Palmer and Edmond (1989) and You et al. (1994). The shaded gray areas show the ratios of these elements in basalt erupted in the Manus Spreading Center ("mafic" line) and dacite/rhyolite erupted in the Eastern Manus Basin ("felsic" line); data from Sinton et al. (2003) and D. Niedermeier and W. Bach (*unpubl. data*) . Symbols as given in Figure 4.3.

temperature and pressure of fluid–rock interaction, with more acid fluids evolved at higher temperatures (Seyfried and Mottl, 1982; Seewald and Seyfried, 1990). The relatively high pH of Vienna Woods fluids relative to other hydrothermal fluids interacting with basalt along unsedimented mid–ocean ridge spreading centers (see Von Damm, 1990) likely reflects the combined effects of fluid–basalt interaction at lower temperatures (< 400 °C) and rock–dominated conditions. Concentrations of heavy metals (e.g., Mn, Fe, Cu, Zn, Pb) in Vienna Woods fluids are low relative to most high–temperature (~ 300 °C) mid–ocean ridge black smoker fluids, reflecting the low aqueous solubility of these metals as a result of moderate temperatures (~ 280 °C) and high pH (Mottl et al., 1979; Rosenbauer and Bischoff, 1983; Seyfried and Janecky, 1985).

Alkali concentrations in high–temperature smoker fluids from PACMANUS and SuSu Knolls in the Eastern Manus Basin are more consistent with fluid–rock interaction with felsic crustal rocks having arc–like chemical affinity. Higher concentrations of alkalis in PACMANUS and SuSu Knolls vent fluids relative to those from Vienna Woods likely reflect the higher concentrations of these elements in felsic crustal rocks erupted in the Eastern Manus Basin ([Li] ~ 10 ppm, [Rb] ~ 13 ppm; Sinton et al., 2003). Effective water/rock ratios calculated for high–temperature smoker fluids at PACMANUS and SuSu Knolls range from 1.5 to 2.5 and 2.2 to 3.5, respectively, indicating rock–dominated conditions at these hydrothermal systems. Similarly, elevated Cs/Rb and Rb/Li ratios in vent fluids from PACMANUS and SuSu Knolls relative to those from Vienna Woods (Figure 4.6) are likely related to higher primary

ratios in felsic crustal rocks (Sinton et al. 2003; D. Niedermeier and W. Bach, *unpubl. data*). However, it is apparent that Cs/Rb ratios in seafloor hydrothermal fluids (Cs/Rb molar ratio ~ 45 – 50 x 10^{-3}) at SuSu Knolls (and to a lesser extent at PACMANUS) are elevated relative to primary Cs/Rb ratios in fresh felsic crustal rocks (Cs/Rb molar ratio ~ 25 – 30 x 10^{-3}) sampled in the Eastern Manus Basin (D. Niedermeier and W. Bach, *unpubl. data*). The higher Cs/Rb ratios in sampled vent fluids may reflect the presence of a more enriched crustal source that is interacting with circulating fluids. Possibly, this may be weathered oceanic crust because low–temperature (~ 200 °C) fluid–rock interaction results in the formation of secondary minerals with Cs/Rb ratios higher than in primary igneous phases (e.g., Palmer and Edmond, 1989). Alternatively, fluids at SuSu Knolls may have reacted with terrigenous sediments resulting in elevated Cs/Rb ratios, similar to the high Cs/Rb ratios measured in seafloor vent fluids from sedimented hydrothermal systems such as Guaymas Basin (Cs/Rb molar ratio ~ 70 – 105 x 10^{-3}) (e.g., You et al., 1994). Elevated thermogenic methane concentrations in SuSu Knolls fluids support significant interaction with organic–bearing sediments that at this vent system (Seewald et al., 2006; E. Reeves and J. Seewald, *unpubl. data*).

Heavy metal and metalloid concentrations in high–temperature smoker fluids from PACMANUS are enriched by one to two orders of magnitude relative to those from Vienna Woods. Heavy metal concentrations in high–temperature smoker fluids from SuSu Knolls are similarly enriched, but to a lesser and more variable extent. Considering that alkali metal distributions in high–temperature smoker fluids are affected by interaction with crustal rocks of different composition, it is possible that

heavy metal concentrations also reflect the influence of source composition. Higher concentrations of some trace metals (e.g., Pb) and metalloids (e.g., As, Sb) in vent fluids from PACMANUS and SuSu Knolls (in the Eastern Manus Basin) can be correlated directly with considerable enrichments of these trace elements in differentiated felsic rocks relative to mafic rocks (Stanton, 1994; Sinton et al., 2003). Similar concentrations of Pb (up to 7 μmol/kg) and As (up to 11 μmol/kg) have been measured in high temperature, low pH seafloor vent fluids from the felsic–hosted Vai Lili hydrothermal system in the Lau back–arc basin (e.g., Fouquet et al., 1993a). The high concentrations of Pb and As are inferred to reflect directly the influence of fluid interaction with enriched felsic rocks (Fouquet et al., 1993a). However, higher concentrations of most heavy metals (including Mn, Fe, Cu and Zn) in PACMANUS and SuSu Knolls black fluids cannot be explained by higher contents of these elements in felsic rocks (dacite and rhyolite) erupted in the Eastern Manus Basin relative to basalt because their primary concentrations in basalt may exceed that of dacite and rhyolite (c.f. Sinton et al., 2003).

The concentrations of most heavy metals (e.g., Mn, Fe, Cu, Zn, Cd, Co, Ag, Au) appear to be solubility controlled and are therefore influenced by temperature, pressure and fluid composition (e.g., pH) during mineral alteration and precipitation. Endmember Mn concentrations in PACMANUS black smoker fluids up to 4 mmol/kg and in SuSu Knolls black smoker fluids up to 500 μmol/kg indicate temperatures of fluid–rock interaction of 450 – 500 °C and 400 – 450 °C, respectively, based on experimental results of basalt, dacite and rhyolite alteration at low water/rock ratios

(Mottl et al., 1979; Hajash and Chandler, 1981; Seewald and Seyfried, 1990). The low measured pH (25 °C) of high–temperature smoker fluids from PACMANUS (pH = 2.3 – 2.8) and SuSu Knolls (pH = 2.6 – 3.8) relative to vent fluids from Vienna Woods (Seewald et al., 2006) likely reflects, in part, the higher temperatures of fluid–rock interaction inferred at PACMANUS and SuSu Knolls relative to Vienna Woods. While higher temperatures during fluid-rock interaction result in higher aqueous metal concentrations owing to differences in resultant pH (Mottl et al., 1979; Seewald and Seyfried, 1990), the considerably lower fluid pH and higher metal concentrations in vent fluids from PACMANUS and (to a lesser extent) SuSu Knolls vent fluids relative to Vienna Woods do not appear to result only from difference in temperatures of crustal rock alteration.

The measured pH of vent fluids from PACMANUS and SuSu Knolls are significantly more acidic than the quench pH (25 °C) of hydrothermal fluids evolved during equilibrium reaction between seawater and dacite or rhyolite (pH ~ 3.5 – 4.5) at similar temperatures (400 – 500 °C) and water/rock ratios (w/r $\leq$ 5) (e.g., Hajash and Chandler, 1981). These data suggest that other factors must be affecting the pH of hydrothermal fluids in the Eastern Manus Basin. High–temperature smoker fluids sampled from PACMANUS and SuSu Knolls show a range of elevated CO_2 (up to ~ 300 mmol/kg) and fluoride concentrations (~ 65 – 527 μmol/kg; in excess of local seawater ~ 68 μmol/kg) relative to vent fluids from Vienna Woods (E. Reeves and J. Seewald, *unpubl. data*). Volatile enrichments of this magnitude are consistent with there being extensive degassing from underlying felsic magmas. Input of reactive magmatic

acid volatile phases (i.e., H_2O–HCl–CO_2–HF–SO_2) into hydrothermal systems in the Eastern Manus Basin (Douville, 1999; Seewald et al., 2006) is likely an important process affecting the acidity of seafloor vent fluids at PACMANUS and SuSu Knolls. The acidity contributed by the input of magmatic acid volatiles can significantly increase the solubility of heavy metals during fluid–rock interaction, thereby likely influencing the higher measured concentrations of these elements in seafloor hydrothermal fluids in the Eastern Manus Basin. If acidity generation owing to input of magmatic acid volatiles is important for the evolution of metal–rich hydrothermal fluids, this places valuable constraints on the geologic environments in which precious metal–rich mineral deposits can be expected to form. The occurrence of extensive magmatic acid volatile input may be one reason why many economically important, volcanogenic–hosted massive sulfide deposits preserved in the geologic record occur in tectonic settings similar to modern submarine island–arc and back–arc basins (Franklin et al., 1981; Sawkins, 1990; Hannington et al., 2005).

5.1.2. Evolution of low pH acid–sulfate fluids

Low concentrations of alkali metals in acid–sulfate fluids sampled at DESMOS and SuSu Knolls (North Su vent field) are a key difference relative to neighboring black smoker fluids from SuSu Knolls (Table 4.3; Figure 4.6). In contrast, acid–sulfate fluids have concentrations of Mg (~ 24 – 51 mmol/kg) significantly higher than in typical high–temperature smoker fluids. These fluids are characterized by a range of fluoride and extremely high sulfate (up to 150 mmol/kg) concentrations, and despite the high Mg concentration have a very low pH (25 °C) of less than 1.8 (E. Reeves and J.

Seewald, *unpubl. data*). That concentrations of alkalis (and other major metals Ca^{2+}, Sr^{2+}; E. Reeves and J. Seewalf, *unpubl. data*) are depleted in acid–sulfate fluids relative to ambient seawater suggests the absence of typical convective hydrothermal circulation and a lack of interaction between seawater–derived fluids and fresh crustal rocks at elevated temperatures and pressures. The compositions of acid–sulfate fluids are more consistent with mixing between exsolved magmatic fluids (H_2O–HCl–CO_2–HF–SO_2–bearing) and seawater. The exceptionally low pH and high sulfate concentrations of these fluids support the extensive input of magmatic SO_2 that disproportionates upon condensation with water (e.g., Holland, 1965);

$$4SO_2 + 4H_2O \rightarrow H_2S + 3HSO_4^- + 3H^+, \text{ or} \quad (4.1)$$

$$6SO_2 + 4H_2O \rightarrow 2S^\circ + 4HSO_4^- + 4H^+ \quad (4.2)$$

Aqueous sulfate in these fluids has an isotopic composition ($\delta^{34}S_{SO4} \sim +10$ to $+17$ ‰; W.C. Shanks III, *unpubl. data*) that is significantly lighter than seawater sulfate ($\sim +21$ ‰; Rees et al. (1978)), which is consistent with disproportionation of magmatically–derived SO_2 (e.g., Kusakabe et al., 2000).

The extremely low pH of acid–sulfate fluids indicates that there has not been significant titration of acidity owing to hydrothermal fluid–rock interaction with fresh crustal rocks. Low concentrations of fluid mobile elements, such as the alkalis, support this. Instead, very high concentrations of Fe and relatively immobile metals, including Al and the rare earth elements (see Chapter 2), suggest that very acid fluids containing residual magmatic volatiles migrate through and interact with previously altered and metal–depleted mineral assemblages. Measured Fe and Al concentrations are up to

12,400 μmol/kg and 1640 μmol/kg, respectively. If these concentrations are extrapolated to zero Mg, as is typically the case for high–temperature black smoker fluids, then Fe and Al concentrations would be even higher, up to ~ 70 mmol/kg and 17 mmol/kg, respectively. The occurrence of advanced argillic alteration (alunite–pyrophyllite–illite–quartz) and native sulfur in proximity to acid–sulfate discharges at the seafloor at both DESMOS and SuSu Knolls (Binns et al., 1997; Gamo et al., 1997; Auzende et al., 2000; Bach et al., 2007) is consistent is extreme metal leaching related to extensive crustal rock alteration at very low pH, much less than 2 to 3 (Hemley and Jones, 1964; Meyer and Hemley, 1967). In many respects, the chemical evolution of acid–sulfate fluids at DESMOS and North Su (SuSu Knolls) is similar to that described at continental epithermal hydrothermal systems where extensive acid alteration occurs owing to degassing of magmatic volatile (H_2O–HCl–CO_2–SO_2–bearing) fluids from felsic magmas (Heald et al., 1987; Stoffregen, 1987).

The concentrations of heavy metals and metalloids in acid–sulfate fluids are markedly different from high–temperature black/gray smoker fluids (Table 4.3). Relative to neighboring high–temperature smoker fluids, acid–sulfate fluids from both DESMOS and SuSu Knolls are significantly enriched in some metals (e.g., Fe, Co), but are depleted in others (e.g., Cu, Sb, Ag, Au). In part, different heavy metal concentrations in acid–sulfate fluids relative to smoker fluids reflect the very low pH and lower temperature of these fluids, and their influence on aqueous metal solubility. In addition, these differences must also affected by the markedly different compositions of crustal rocks with which acid–sulfate fluids interact. Low concentrations of some

heavy metals reflect that acid–sulfate fluids interact with previously altered crustal rocks that have likely been variably depleted of primary metal enrichments. There is an absence of typical high temperature and pressure interaction between convecting hydrothermal fluid and fresh crustal rocks. The lack of an available trace metal "reservoir" in extensively altered crustal rocks limits the potential for acid–sulfate fluids to gain significant heavy metal enrichment. The influence this exerts on the capacity of acid–sulfate fluids to form large metal–rich mineral deposits is not easy to assess.

5.2. Magmatic acid volatile degassing and metal input

The low pH and high concentrations of volatile species (e.g., CO_2, F) in seafloor vent fluids from PACMANUS, DESMOS and SuSu Knolls relative to those from Vienna Woods indicates that all vent fluids in the Eastern Manus Basin are affected by degassing of magmatic acid volatiles, although the styles and compositions of magmatic volatile input differ considerably (Gamo et al., 1997; Seewald et al., 2006). The evidence presented suggests that magmatic acid volatile input affects the styles and conditions of interaction between fluids and crustal rocks and the resulting solubility of heavy metals. Studies of co–existing brine and low salinity, vapor inclusions preserved in magmatic–hydrothermal Cu–Au–rich deposits have shown that more volatile elements (e.g., Cu, Cd, Se, As and Au) can be partitioned and concentrated in low–salinity fluids and segregated from refractory elements (e.g., Fe, Zn, Mn, Pb, Ag) that are preferentially retained within more saline fluids (e.g., Audétat et al., 1998; Heinrich et al., 1999; Ulrich et al., 1999; Baker et al., 2004). These observations are generally supported by experimental data that predict higher vapor partition coefficients for Cu,

As and Au relative to Fe, Zn, Ag and other refractory elements during separation of low salinity vapors and high salinity brines. There are two distinct mechanisms through which this fractionation can occur: (1) by exsolution of a low–salinity fluid phase (e.g., H_2O–CO_2–H_2S–SO_2) from a silicate melt–vapor–brine–sulfide assemblage (i.e., magmatic acid volatile degassing) at near magmatic temperatures and pressures (Simon et al., 2006, 2007) and, (2) by segregation of low– and high–salinity fluids during aqueous phase separation (i.e., boiling or condensation) of rising high–temperature hydrothermal fluids in the oceanic crust (Pokrovski et al., 2002; Pokrovski et al., 2008). It has been proposed that degassing magmatic acid volatiles (pathway #1) can act as agents for the direct transport of heavy metals from felsic magmas and may contribute a significant source of precious metals in both sub–aerial and submarine hydrothermal systems in convergent plate margins (e.g., Franklin et al., 1981; Hedenquist and Lowenstern, 1994).

If degassing of magmatic acid volatiles provides a direct and significant source of metals to seafloor hydrothermal systems, this should be most clearly expressed by the enrichment of "volatile" metals in acid–sulfate fluids at DESMOS and SuSu Knolls. Based on alkali metal data, these fluids appear not to have interacted with fresh crustal rocks, which are the primary source for metal enrichments in most seafloor hydrothermal fluids, but with extensively altered, metal–depleted mineral assemblages. Accordingly, acid–sulfate fluids are likely to carry a significantly lesser signature of heavy metal enrichment related to metal mobilization from crustal sources, which may overprint direct magmatic contributions. Heavy metals that are most enriched in acid–

sulfate fluids relative to high–temperature smoker fluids are Fe and Co, (and to a lesser extent Zn and Pb), which are elements considered more refractory and less likely to partition with an exsolved magmatic volatile fluid. In contrast, those elements considered more volatile and that are considered likely to partition with exsolved magmatic volatile fluids, including Cu, As, and Au, are generally depleted in acid–sulfate fluids relative to neighboring black smoker fluids (Table 4.3). At face value, the compositions of magmatic volatile–rich acid–sulfate fluids at DESMOS and SuSu Knolls do not support a significant and direct contribution of heavy metals within degassed magmatic acid volatile phases (c.f. Yang and Scott, 1996). Alternatively, it can be speculated that "volatile" heavy metals have been removed from acid–sulfate fluids resulting from temperature and pH controlled equilibrium sulfide precipitation reactions. Owing to the low temperatures of acid–sulfate fluids, Cu–bearing sulfides and sulfosalts are significantly less soluble (Crerar and Barnes, 1976; Barnes, 1979) and may have precipitated much of the aqueous Cu shallow within the crust prior to fluid discharge at the seafloor, thereby masking the fingerprints of a direct magmatic metal contribution.

Although acid–sulfate fluids evolve from mixing of magmatic acid volatiles and seawater, there are also smoker fluids that retain signatures of considerable magmatic acid volatile input. Vent fluids from Satanic Mills (SM2) at PACMANUS and from Suzette (SZ5) and South Su (SS1) at SuSu Knolls have low pH and the highest concentrations of fluoride ($\geq 380 - 527$ μmol/kg) relative to other smoker fluids sampled from the Eastern Manus Basin (Tables 4.1 and 4.2). These fluids show

consistent, and in some cases significant, enrichments of Cu, As, Sb and Au relative to neighboring smoker fluids with lower fluoride concentrations (Figure 4.7). High metal concentrations in fluoride–rich fluids may reflect vestiges of metals partitioned into degassed magmatic acid volatile (H_2O–HCl–CO_2–HF–SO_2–bearing) phases, which have subsequently intersected convecting high–temperature hydrothermal fluids. The factors that should enable the transport of metals to the seafloor within magmatic acid volatiles in fluoride–rich black smoker fluids, but apparently not in acid–sulfate fluids, are not clear. These may be related to differences in temperature and fluid composition (i.e., pH, availability of metal–complexing ligands) among these distinct fluid types owing to different chemical evolution in oceanic crust. Clearly, further study is required to assess the factors affecting both the compositions of magmatic acid volatiles during migration through oceanic crust (e.g., decoupling between HF and SO_2) and the resulting aqueous mobility of heavy metals in these fluids.

5.3. Remobilization of previously deposited metal sulfides

Experimental studies have demonstrated that Mn is a good indicator of the maximum temperatures of fluid–rock interaction in the reaction zone because of sluggish kinetics for Mn precipitation (Seewald and Seyfried, 1990). Endmember concentrations of Mn are similar among all high–temperature smoker fluids sampled *within* each hydrothermal system (Figure 4.3), suggesting that the reaction zone conditions influencing fluid–rock interaction at depth are similar, as also suggest by similar endmember alkali concentrations within each hydrothermal system. However, endmember concentrations of Fe, Cu, Zn and most other heavy metals and metalloids

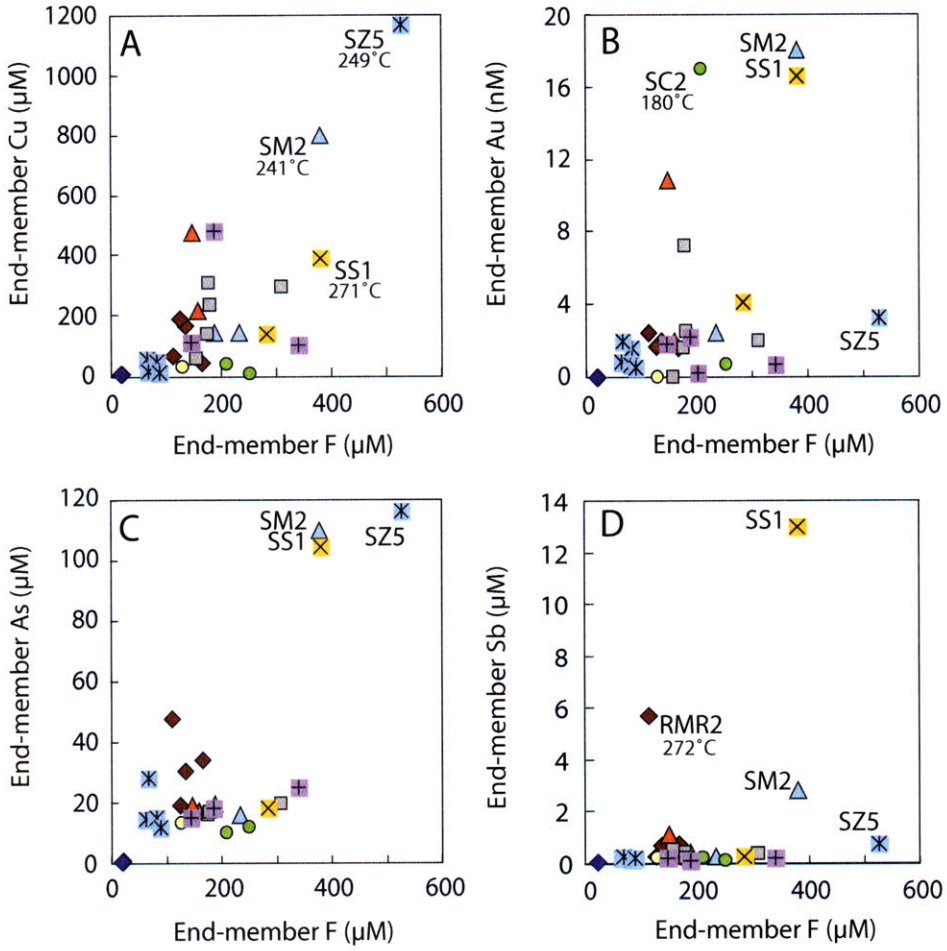

Figure 4.7. Concentrations of **A**) Cu versus F, **B**) Au versus F, **C**) As versus F, and **D**) Sb versus fluid in seafloor black/gray smoker fluids sampled from the Manus Basin. Measured temperatures of identified fluid samples are provided. Symbols as given in Figure 4.3.

show a considerable range of concentrations within the PACMANUS and SuSu Knolls hydrothermal systems (Figures 4.3 and 4.4). This variability can be related to processes other than interaction between circulating seawater and oceanic crust occurring on a local scale. Specifically, differences in heavy metal abundances appear to reflect localized sulfide mineralization and remobilization.

5.3.1. Magmatic volatile input, secondary acidity formation and metal remobilization

5.3.1.1. Acid–sulfate fluids

Pyrite is typically the most abundant sulfide associated with intermediate– and advanced–argillic alteration (illite–kaolinite and alunite–illite–pyrophyllite–silica), occurring predominantly as disseminated grains and veins within extensively altered host–rocks (Heald et al., 1987; Stoffregen, 1987). Pyrite precipitated within this environment is a product of reaction between H_2S derived from magmatic SO_2 disproportionation and Fe–bearing minerals within the host–rock. Although pyrite precipitation likely occurs at greater depths beneath the seafloor within more reducing fluids, disseminated and veined pyrite has been described in advanced–argillic alteration assemblages at seafloor at both DESMOS and SuSu Knolls (Binns et al., 1997; Gena et al., 2001; Bach et al., 2007).

While the considerable enrichment of Fe in acid–sulfate fluids can be largely attributed to extensive dissolution of Fe–bearing minerals from crustal rocks, it is possible that remobilization of pyrite may also contribute metals. Dissolution of pyrite may explain the considerable enrichment of Co (up to ~ 10 μmol/kg) in acid–sulfate fluids relative to black smoker fluids (Figure 4.4). Studies of seafloor massive sulfide

deposits have shown that Co is predominantly associated with Fe– and Cu–Fe–sulfides and occurs in pyrite at concentrations up to 0.5 wt % (Hannington et al., 1991; Tivey et al., 1995), although Co concentrations in wall–rock pyrite at DESMOS and SuSu Knolls are unknown. Minor enrichment of other metals (e.g., Zn, Pb) relative to high–temperature smoker fluids may also reflect pyrite re–working because analyses of pyrite grains have also demonstrated variable enrichment of Zn (< 0.07 – 0.93 wt%) and Pb (up to 1 – 4 wt%; see Chapter 5). The lack of H_2S, which should accompany pyrite dissolution, in acid–sulfate fluids is problematic, but may reflect oxidation of H_2S. A shift to more oxidizing conditions (i.e., SO_4–dominant) can result from continued degassing of SO_2 and alteration of crustal rocks that exhausts the capacity of the rock to buffer H_2S/SO_4^{2-}, similar to supergene alteration processes described for continental magmatic–hydrothermal processes (Giggenbach, 1997).

5.3.1.2. High–temperature smoker fluids

Variations in the concentrations of F and CO_2 in high–temperature smoker fluids from the Manus Basin (e.g., Douville et al., 1999; Seewald et al., 2006) indicate that magmatic acid volatile input does not affect equally the compositions of seafloor hydrothermal fluids. It has been hypothesized that heavy metal (Cu, As, Sb and Au) enrichments in low pH, fluoride–rich vent fluids (i.e., Suzette (SZ5), South Su (SS1) and Satanic Mills (SM2)) may reflect metals contributed by transport within degassing magmatic acid volatile phases (Section 5.2). Alternatively, varying enrichments of Cu, As, Sb and Au (and Fe, Zn, Pb, Cd) in these fluids may reflect local remobilization of previously deposited sulfide near the seafloor in response to the greater acidity that

results from a greater contribution of magmatic acid volatile input to these fluids, for example:

$$2H^+ + ZnS \rightarrow Zn^{2+} + H_2S \quad (4.3)$$

(sphalerite)

$$7.5H^+ + Cu_{12}As_4S_{13} + 17H_2O \rightarrow \quad (4.4)$$

(tennantite) $12Cu^+ + 4As(OH)_4^- + 12.75H_2S + 0.25SO_4^{2-}$

Seafloor drilling operations at the Suzette vent field (Nautilus Minerals Inc., Media Release 2007; http://www.nautilusminerals.com/i/pdf/2007–09–24_NR.pdf) indicates the presence of a large copper–rich (chalcopyrite + tennantite ± sphalerite) seafloor massive sulfide deposit that could support extensive metal remobilization and re–working.

5.3.2. Near–seafloor seawater entrainment, fluid mixing and metal sulfide re–working

At PACMANUS, the presence of abundant anhydrite at and beneath the seafloor (see Chapter 3, and references therein) and discharge of smoker fluids at the seafloor containing non–zero Mg and sulfate (E. Reeves and J. Seewald, *pers. commun.* 2007) provides evidence for widespread sub–seafloor entrainment of seawater by ascending hydrothermal fluids. Theoretical calculations that consider the effects of temperature and pH changes on the solubilities of various Fe–, Cu–Fe– and Zn–sulfide minerals demonstrate that sub–seafloor mixing between high–temperature hydrothermal fluids and seawater can result in deposition of high–temperature Cu–Fe–sulfide, generation of secondary acidity and the dissolution and re–working of previously deposited sulfide in a process of zone refinement (Tivey et al., 1995). This process was first described at the

TAG active mound, 26 °N Mid–Atlantic Ridge, and results in significant sub–seafloor deposition of chalcopyrite, pyrite and anhydrite and remobilization of previously deposited sphalerite (Edmond et al., 1995; Tivey et al., 1995). For example, deposition of chalcopyrite,

$$2Cu^{+} + 2Fe^{2+} + 3.75H_2S + 0.25SO_4^{2-} \rightarrow 2CuFeS_2 + 5.5H^{+} + H_2O \qquad (4.7)$$

results in acidity formation that can subsequently dissolve previously deposited sphalerite (and/or wurtzite; Eqn 5). According to this process, mixed vent fluids should exhibit lower concentrations of Cu, Fe and H_2S, lower pH and, depending on the extent of sphalerite or wurtzite remobilization, significant enrichment of Zn relative to endmember vent fluids.

Based on similar criteria, there is consistent evidence to support sub–seafloor fluid mixing and Fe– and Cu–Fe–sulfide precipitation accompanied by subsequent remobilization and re–working of previously deposited sulfide at the Roman Ruins and Roger's Ruins (PACMANUS) vent fields (Figure 4.8). At Roman Ruins, mixed hydrothermal fluids (RMR2; Table 4.2) contain significantly lesser Cu, Fe and H_2S but greater Zn relative to endmember black smoker fluids, consistent with the chalcopyrite deposition and sphalerite dissolution described (Figure 4.8). Mixed hydrothermal fluids contain significantly lesser Co relative to endmember black smoker fluids, likely reflecting incorporation of Co into high–temperature sulfides (Hannington et al., 1991; Tivey et al., 1995). In contrast, mixed fluids contain an order of magnitude higher Pb, Cd, Ag, As and Sb concentrations relative to endmember black smoker fluids, which can be explained by enrichment of these trace elements in sphalerite and other sulfides

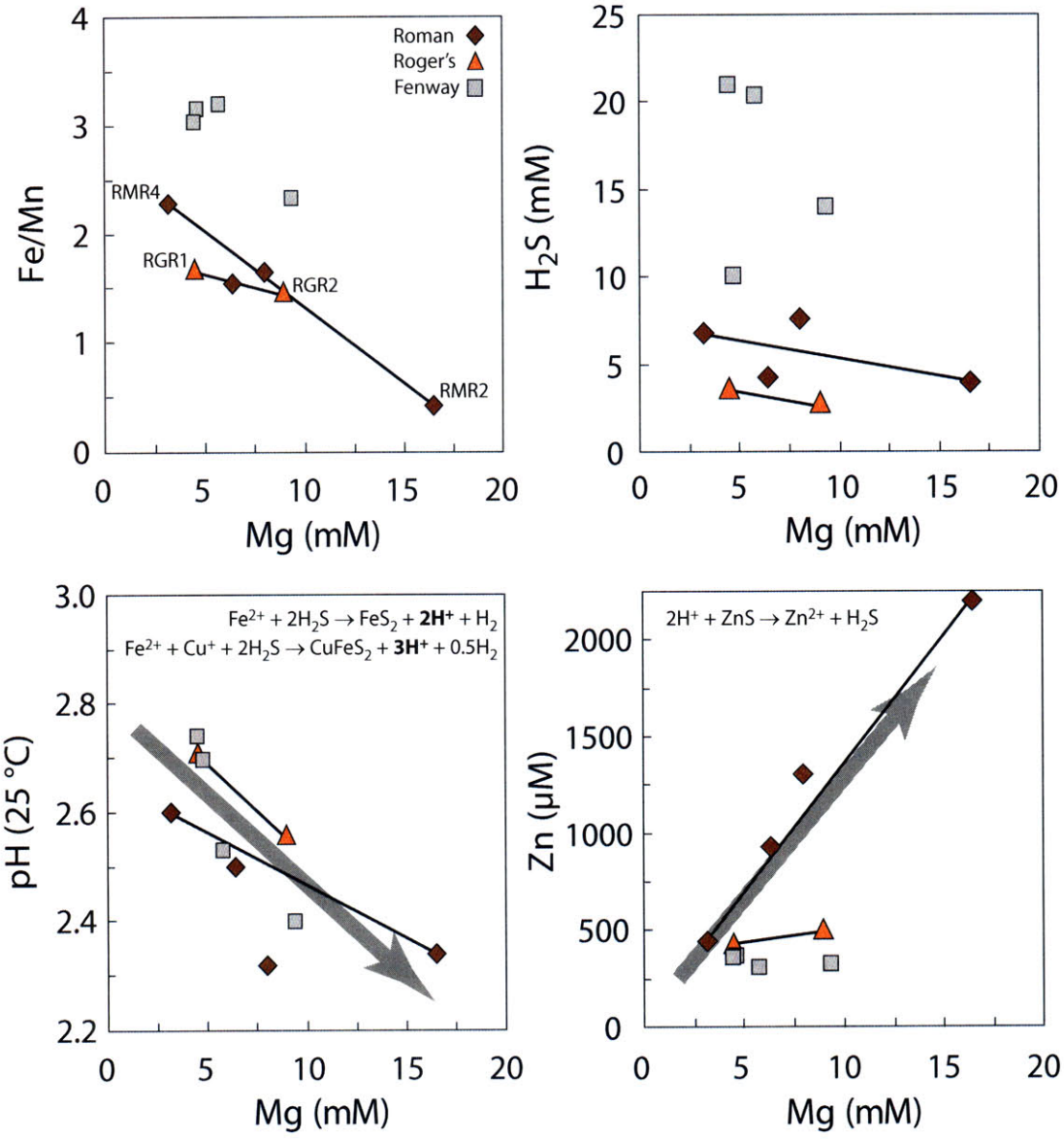

Figure 4.8. Correlation of **A**) Fe/Mn versus Mg, **D**) sulfide versus Mg, **A**) pH versus Mg, **A**) Zn versus Mg for seafloor hydrothermal fluids from PACMANUS (Roman Ruins, Roger's Ruins and Fenway vent fields). Sub-seafloor mixing between endmember (zero Mg) hydrothermal fluid and seawater can result in precipitation of Fe- and Cu-Fe-sulfides (e.g., pyrite, chalcopyrite) that lowers the Fe/Mn ratio, sulfide concentration and pH. The formation of secondary acidity can remobilize previously deposited sulfide (e.g., sphalerite/wurtzite) as shown by the increase in Zn concentration in mixed fluids with high Mg concentrations at Roman Ruins (RMR2) and Roger's Ruins (RGR2). On-going remobilization of previously deposited sulfide is not clear at other vent fields.

such as galena (PbS) (Hannington et al., 1991; Fouquet et al., 1993b; Koski et al., 1994; Tivey et al., 1995) and subsequent remobilization of these elements during ZnS (+ PbS) dissolution (Chapter 5).

At Roger's Ruins, mixed hydrothermal fluids (RGR2; Table 4.2) also contain lesser Fe and H_2S, and higher Zn, Sb, Ag and Au relative to highest–temperature endmember black smoker fluids from PACMANUS (e.g., RMR1, RGR2, F2, F3; Table 4.2). However, these fluids also contain high concentrations of Cu. Assuming removal of Fe and H_2S via deposition of pyrite (or chalcopyrite), requires remobilization of both Zn– and Cu–bearing sulfides to account for elevated Zn and Cu in mixed hydrothermal fluids. Enrichment of Zn in mixed hydrothermal fluid relative to endmember black smoker fluids can be explained by dissolution of sphalerite. Mineralogical and geochemical studies of seafloor vent deposits at PACMANUS and SuSu Knolls have shown the presence of abundant Cu–sulfosalts including tennantite, tetrahedrite and enargite (Binns and Scott, 1993; C. Yeats, *pers. commun.* 2007; see also Chapter 5). It is possible that Cu enrichments reflect the remobilization of one or more of these minerals. Remobilization of Cu–sulfosalts can also explain enrichment of Zn, Ag, As, Sb and Au in these fluids, because geochemical analyses of sulfosalts have shown significant enrichment of these elements in tennantite, tetrahedrite and enargite (C. Yeats, *pers. commun.* 2007; see Chapter 5).

6. Summary and Conclusions

Concentrations of heavy metals and metalloids (Fe, Mn, Zn, Cu, Cd, Pb, Co, Ag, Au, As and Sb) in seafloor vent fluids from the Manus back–arc basin are affected by deep–seated seawater–rock interaction, magmatic volatile input and near–seafloor sulfide deposition and re–working. Vent fluid metal concentrations show considerable differences among the different hydrothermal systems examined (Vienna Woods in the Manus Spreading Center and PACMANUS, DESMOS and SuSu Knolls in the Eastern Manus Basin), reflecting that these geochemical processes occur to differing extents at each vent field.

Alkali concentrations in seafloor vent fluids at Vienna Woods are consistent with fluid–rock interaction with fresh basalt. The pH (25 °C) of these vent fluids are high ($\geq$ 4.2) relative to most seafloor vent fluids suggesting seawater–rock interaction under rock–dominated conditions (low water/rock ratio) and low temperatures ($\leq$ 400 °C) (e.g., Seyfried and Bischoff, 1977; Hajash and Chandler, 1981; Seyfried and Mottl, 1982). Concentrations of heavy metals (e.g., Mn, Fe, Cu, Zn) are low in all Vienna Woods fluids, reflecting the moderate temperature and mildly acidic pH of these. In the Eastern Manus Basin, alkali and Mn concentrations in vent fluids from PACMANUS and SuSu Knolls are consistent with interaction between circulating seawater and felsic rocks with arc–like chemical affinities under rock dominated conditions and at high temperatures (> 400 – 500 °C). The measured pH of these vent fluids is considerably lower than that predicted by equilibrium reaction between seawater and dacite/rhyolite at these conditions, consistent with input of magmatic acid volatiles (H_2O–HCl–CO_2–HF–SO_2) in the Eastern Manus Basin. Degassing of magmatic acid volatiles is further

indicated by the high concentrations of fluoride and CO_2. In general, heavy metal concentrations are considerably higher in vent fluids from PACMANUS and SuSu Knolls relative to those at Vienna Woods and mid–ocean ridges, reflecting the low pH of these fluids and suggesting considerably greater metal solubility during seawater–rock interaction affected by magmatic volatile degassing.

Low concentrations of alkali metals in acid–sulfate fluids at DESMOS and SuSu Knolls are a key difference relative to high–temperature smoker fluids. The data do not support interaction between seawater–derived convecting hydrothermal fluids and fresh crustal rock. Acid–sulfate fluids appear to form from a magmatic vapor (i.e., H_2O–HCl–HF–SO_2–CO_2) that mixed with seawater, and is interacting with extensively altered and metal depleted rocks. This is consistent with the occurrence of advanced–argillic alteration at DESMOS and SuSu Knolls. The range of heavy metal concentrations (e.g., high Fe and Co, low Cu, As and Sb) appear to reflect the influence of interaction with extensively altered and trace metal depleted crustal rocks, but may also be related to dissolution of previously deposited sulfide. In particular high concentrations of Fe and Co may reflect dissolution of wall–rock pyrite that is commonly associated advanced–argillic alteration (Heald et al., 1987; Stoffregen, 1987).

Dissolution and remobilization of previously deposited sulfide variably impacts metal concentrations in smoker fluids sampled from PACMANUS and SuSu Knolls. Two mechanisms for local remobilization and re–working of an existing sulfide deposit are proposed. First, variable and locally greater contributions of magmatic acid volatiles in some vent fluids having low pH and high concentrations of magmatic gas species can

generate considerable fluid acidity. Local remobilization of previously deposited sulfide near the seafloor can occur in response to the greater acidity that results from a greater contribution of magmatic acid volatile input. Second, sub–seafloor mixing between locally entrained seawater and rising high–temperature hydrothermal fluid can result in a more acidic fluid, owing to the precipitation of high–temperature Cu–Fe– and Fe–sulfides (e.g., chalcopyrite) as fluid temperature decreases. The secondary acidity can then remobilize existing sulfides (in particular sphalerite and/or wurtzite), that are sensitive to changes in fluid pH. On–going modification of the Roman Ruins and Roger's Ruins vent deposits at PACMANUS are similar to the zone refinement process proposed for the TAG active mound, 26 °N Mid–Atlantic Ridge (Tivey et al., 1995).

From the data available, it does not appear that degassed magmatic acid volatiles contribute a direct and significant source of ore–forming metals to hydrothermal systems in the Eastern Manus Basin. Rather, magmatic acid volatile input primarily contributes acidity, which enhances significant metal solubility during alteration of crustal rocks (and possibly leaching of metal condensates trapped in vesicles (c.f. Yang and Scott, 1996)). A better understanding of the processes affecting metal cycling in seafloor hydrothermal systems in convergent plate margins is key to identifying the processes responsible for the formation of many economically–important volcanogenic massive sulfide deposits, because these deposits are thought to have been deposited within arc environments (Franklin et al., 1981; Sawkins, 1990).

REFERENCES

Audétat A., Günther D., and Heinrich C. A. (1998) Formation of a magmatic–hydrothermal ore deposit: Insights with LA–ICP–MS analysis of fluid inclusions. *Science* **279**, 2091–2094.

Auzende J. M., Ishibashi J., Beaudoin Y., Charlou J. L., Delteil J., Donval J. P., Fouquet Y., Gouillou J. P., Ildefonse B., and Kimura H. (2000) Rift Propagation and extensive off–axis volcanic and hydrothermal activity in the Manus Basin (Papua New Guinea): MANAUTE Cruise. *InterRidge News* **9**(2), 21–25.

Auzende J. M., Urabe T., Ruellan E., Charbroux D., Charlou J. L., Gena K., Gamo T., Henry K., Matsubayashi O., Matsumoto T., Naka J., Nagaya Y., and Okamura K. (1996) "Shinkai 6500" Dives in the Manus Basin: New STARMER Japanese–French Program. *JAMSTEC Journal of Deep Sea Research* **12**, 323–334.

Bach W., Tivey M. A., Seewald J. S., Tivey M. K., Craddock P. R., Niedermeier D., and Yoerger D. (2007) Variable basement compostion and magma degassing affecting hydrothermal systems in the Eastern Manus Basin. *EOS Trans. AGU. Fall Meet. Suppl.*, **88**(52), Abstract #V21D–0749.

Baker T., Van Achterberg E., Ryan C. G., and Lang J. R. (2004) Composition and evolution of ore fluids in a magmatic–hydrothermal skarn deposit. *Geology* **32**, 117–120.

Barnes H. L. (1979) Solubilities of ore minerals. In *Geochemistry of Hydrothermal Ore Deposits, 2nd Edition* (ed. H. L. Barnes), pp. 404–460. Wiley–Interscience.

Binns R. A., Barriga F. J. A. S., and Miller D. J. (2007) Leg 193 synthesis: Anatomy of an active felsic–hosted hydrothermal system, eastern Manus Basin, Papua New Guinea. In *Proceedings of the Ocean Drilling Program, Scientific Results*, Vol. 193 (ed. F. J. A. S. Barriga, R. A. Binns, D. J. Miller, and P. M. Herzig), pp. 1–71. doi:10.2973/odp.proc.sr.193.201.2007. Ocean Drilling Program.

Binns R. A. and Scott S. D. (1993) Actively forming polymetallic sulfide deposits associated with felsic volcanic rocks in the eastern Manus back–arc basin, Papua

New Guinea. *Economic Geology* **88**, 2226–2236.

Binns R. A., Scott S. D., Gemmell J. B., Crook K. A. W., and Shipboard Scientific Party. (1997) The SuSu Knolls hydrothermal field, eastern Manus Basin, Papua New Guinea. *EOS Trans. AGU. Fall Meet. Suppl.,* **78**(52), Abstract #V22E–02.

Bischoff J. L. and Dickson F. W. (1975) Seawater–basalt interaction at 200 °C and 500 bars: Implications for origin of seafloor heavy–metal deposits and regulations of seawater chemistry. *Earth and Planetary Science Letters* **25**, 385–397.

Bischoff J. L. and Rosenbauer R. J. (1987) Phase separation in seafloor geothermal systems; an experimental study of the effects on metal transport. *American Journal of Science* **287**(10), 953–978.

Both R., Crook K., Taylor B., Brogan S., Chappell B., Frankel E., Liu L., Sinton J., and Tiffin D. (1986) Hydrothermal chimneys and associated fauna in the Manus back–arc basin, Papua New Guinea. *EOS Transactions, American Geophysical Union* **67**, 489.

Bowers T. S., Campbell A. C., Measures C. I., Spivack A. J., Khadem M., and Edmond J. M. (1988) Chemical controls on the composition of vent fluids at 13–11 °N and 21 °N, East Pacific Rise. *Journal of Geophysical Research* **93**(B5), 4522–4536.

Butterfield D. A. and Massoth G. J. (1994) Geochemistry of north Cleft segment vent fluids: temporal changes in chlorinity and their possible relation to recent volcanism. *Journal of Geophysical Research* **99**(B3), 4951–4968.

Butterfield D. A., McDuff R. E., Mottl M. J., Lilley M. D., Lupton J. E., and Massoth G. J. (1994) Gradients in the composition of hydrothermal fluids from the Endeavour segment vent field: Phase separation and brine loss. *Journal of Geophysical Research* **99**, 9561–9583.

Campbell A. C., Palmer M. R., Klinkhammer G. P., Bowers T. S., Edmond J. M., Lawrence J. R., Casey J. F., Thompson G., Humphris S. E., and Rona P. (1988) Chemistry of hot springs on the Mid–Atlantic Ridge. *Nature* **335**(6190), 514–519.

Crerar D. A. and Barnes H. L. (1976) Ore solution chemistry. V. Solubilities of chalcopyrite and chalcocite assemblages in hydrothermal solution at 200 °C to 350 °C. *Economic Geology* **71**(772–794).

Douville E. (1999) Les fluides hydrothermaux oceaniques comportement géochimique des éléments traces et des terres rares. Processus associés et modélisation thermodynamique. Ph.D. Thesis, University of Brest.

Douville E., Bienvenu P., Charlou J. L., Donval J. P., Fouquet Y., Appriou P., and Gamo T. (1999) Yttrium and rare earth elements in fluids from various deep–sea hydrothermal systems. *Geochimica et Cosmochimica Acta* **63**(5), 627–643.

Edmond J. M., Campbell A. C., Palmer M. R., German C. R., Klinkhammer G. P., Edmonds H. N., Elderfield H., Thompson G., and Rona P. (1995) Time series studies of vent fluids from the TAG and MARK sites (1986, 1990) Mid–Atlantic Ridge and a mechanism for Cu/Zn zonation in massive sulphide orebodies. In *Hydrothermal Vents and Processes*, Vol. 87 (ed. L. M. Parson, C. L. Walker, and D. R. Dixon), pp. 77–86. Geological Society Special Publication.

Edmond J. M., von Damm K. L., McDuff R. E., and Measures C. I. (1982) Chemistry of Hot Springs on the East Pacific Rise and Their Effluent Dispersal. *Nature* **297**(5863), 187–191.

Fouquet Y., von Stackelberg U., Charlou J. L., Erzinger J., Herzig P. M., Muehe R., and Wiedicke M. (1993a) Metallogenesis in back–arc environments; The Lau Basin example. *Economic Geology* **88**(8), 2150.

Fouquet Y., Wafik A., Cambon P., Mevel C., Meyer G., and Gente P. (1993b) Tectonic setting and mineralogical and geochemical zonation in the Snake Pit sulfide deposit (Mid–Atlantic Ridge, at 23 °N). *Economic Geology* **88**, 2018–2036.

Franklin J. M., Lydon J. W., and Sangster D. F. (1981) Volcanic–associated massive sulfide deposits. *Economic Geology* **75**, 485–627.

Gamo T., Okamura K., Charlou J. L., Urabe T., Auzende J. M., Ishibashi J.–I., Shitashima K., Chiba H., Binns R. A., and Gena K. (1997) Acidic and sulfate–rich hydrothermal fluids from the Manus back–arc basin, Papua New Guinea.

Geology **25**(2), 139–142.

Gemmell J. B., Sharpe R., Jonasson I. R., and Herzig P. M. (2004) Sulfur Isotope Evidence for Magmatic Contributions to Submarine and Subaerial Gold Mineralization: Conical Seamount and the Ladolam Gold Deposit, Papua New Guinea. *Economic Geology* **99**(8), 1711–1725.

Gena K., Mizuta T., Ishiyama D., and Urabe T. (2001) Acid–sulphate type alteration and mineralization in the Desmos Caldera, Manus back–arc basin, Papua New Guinea. *Resource Geology* **51**(1), 31–44.

Giggenbach W. F. (1997) The origin and evolution of fluids in magmatic–hydrothermal systems. In *Geochemistry of Hydrothermal Ore Deposits, 3rd Edition* (ed. H. L. Barnes), pp. 737–796. Wiley–Interscience.

Hajash A. and Chandler G. W. (1981) An experimental investigation of high–temperature interactions between seawater and rhyolite, andesite, basalt and peridotite. *Contributions to Mineralogy and Petrology* **78**(3), 240–254.

Halbach P., Nakamura K., Wahsner M., Lange J., Sakai H., Kaeselitz L., Hansen R. D., Yamano M., Post J., and Prause B. (1989) Probable modern analogue of Kuroko–type massive sulphide deposits in the Okinawa Trough back–arc basin. *Nature* **338**, 496–499.

Hannington M., Herzig P., Scott S., Thompson G., and Rona P. (1991) Comparative mineralogy and geochemistry of gold–bearing sulfide deposits on the mid–ocean ridges. *Marine Geology* **101**, 217–248.

Hannington M. D., De Ronde C. E. J., and Petersen S. (2005) Sea–floor tectonics and submarine hydrothermal systems. *Economic Geology* **100**, 111–141.

Heald P., Foley N. K., and Hayba D. O. (1987) Comparative anatomy of volcanic–hosted epithermal deposits: Acid–sulfate and adularia–sericite types. *Economic Geology* **82**, 1–26.

Hedenquist J. W. and Lowenstern J. B. (1994) The role of magmas in the formation of hydrothermal ore deposits. *Nature* **370**, 519–527.

Heinrich C. A., Guenther D., Audetat A., Ulrich T., and Frischknecht R. (1999) Metal

fractionation between magmatic brine and vapor, determined by microanalysis of fluid inclusions. *Geology* **27**(8), 755–758.

Hemley J. J. and Jones W. R. (1964) Chemical aspects of hydrothermal alteration with emphasis on hydrogen metasomatism. *Economic Geology* **59**(538–569).

Holland H. D. (1965) Some applications of thermochemical data to problems of ore deposits; [Part] 2, Mineral assemblages and the composition of ore forming fluids. *Economic Geology* **60**(6), 1101–1166.

Hrischeva E., Scott S. D., and Weston R. (2007) Metalliferous sediments associated with presently forming volcanogenic massive sulfides: The SuSu Knolls hydrothermal field, Eastern Manus Basin, Papua New Guinea. *Economic Geology* **102**, 55–74.

Iizasa K., Fiske R. S., Ishizuka O., Yuasa M., Hashimoto J., Ishibashi J.–I., Naka J., Horii Y., Fujiwara Y., and Imai A. (1999) A Kuroko–Type Polymetallic Sulfide Deposit in a Submarine Silicic Caldera. *Science* **283**, 975–979.

Kamenetsky V. S., Binns R. A., Gemmell J. B., Crawford A. J., Mernagh T. P., Maas R., and Steele D. (2001) Parental basaltic melts and fluids in eastern Manus backarc Basin: implications for hydrothermal mineralisation. *Earth and Planetary Science Letters* **184**(3–4), 685–702.

Koski R. A., Jonasson I. R., Kadko D. C., Smith V. K., and Wong F. L. (1994) Compositions, growth mechanisms, and temporal relations of hydrothermal sulfide–sulfate–silica chimneys at the northern Cleft segment, Juan de Fuca Ridge. *Journal of Geophysical Research* **99**(B3), 4813–4832.

Kusakabe M., Komoda Y., Takano B., and Abiko T. (2000) Sulfur isotopic effects in the disproportionation reaction of sulfur dioxide in hydrothermal fluids: Implications for the $\delta^{34}S$ variations of dissolved bisulfate and elemental sulfur from active crater lakes. *Journal of Volcanology and Geothermal Research* **97**(1–4), 287.

Martinez F. and Taylor B. (1996) Backarc spreading, rifting, and microplate rotation, between transform faults in the Manus Basin. *Marine Geophysical Researches*

18, 203–224.

Metz S. and Trefry J. H. (2000) Chemical and mineralogical influences on concentrations of trace metals in hydrothermal fluids. *Geochimica et Cosmochimica Acta* **64**(13), 2267–2279.

Meyer C. A. and Hemley J. J. (1967) Wall–rock alteration. In *Geochemistry of Hydrothermal Ore Deposits, 1st Edition* (ed. H. L. Barnes), pp. 166–235. Holt, Rinehart and Winston.

Moss R. and Scott S. D. (2001) Geochemistry and mineralogy of gold–rich hydrothermal precipitates from the eastern Manus Basin, Papua New Guinea. *Canadian Mineralogist* **39**, 957–978.

Mottl M. J. and Holland H. D. (1978) Chemical exchange during hydrothermal alteration of basalt by seawater—I. Experimental results for major and minor components of seawater. *Geochimica et Cosmochimica Acta* **42**(8), 1103–1115.

Mottl M. J., Holland H. D., and Corr R. F. (1979) Chemical exchange during hydrothermal alteration of basalt by seawater—II. Experimental results for Fe, Mn, and sulfur species. *Geochimica et Cosmochimica Acta* **43**(6), 869–884.

Ohmoto H. (1996) Formation of volcanogenic massive sulfide deposits: The Kuroko perspective. *Ore Geology Reviews* **10**, 135–177.

Palmer M. R. and Edmond J. M. (1989) Cesium and rubidium in submarine hydrothermal fluids: Evidence for recycling of alkali elements. *Earth and Planetary Science Letters* **95**(1–2), 8–14.

Petersen S., Herzig P. M., Hannington M. D., Jonasson I. R., and Arribas A., Jr. (2002) Submarine gold mineralization near Lihir Island, New Ireland fore–arc, Papua New Guinea. *Economic Geology* **97**, 1795–1813.

Pokrovski G. S., Borisova A. Y., and Harrichoury J.–C. (2008) The effect of sulfur on vapor–liquid fractionation of metals in hydrothermal systems. *Earth and Planetary Science Letters* **266**(3–4), 345–362.

Pokrovski G. S., Zakirov I. V., Roux J., Testemale D., Hazemann J.–L., Bychkov A. Y., and Golikova G. V. (2002) Experimental study of arsenic speciation in vapor

phase to 500 °C: Implications for As transport and fractionation in low–density crustal fluids and volcanic gases. *Geochimica et Cosmochimica Acta* **66**(19), 3453–3480.

Price R. E. and Pichler T. (2005) Distribution, speciation and bioavailability of arsenic in a shallow–water submarine hydrothermal system, Tutum Bay, Ambitle Island, PNG. *Chemical Geology* **224**, 122–135.

Rees C. E., Jenkins W. J., and Monster J. (1978) The sulphur isotopic composition of ocean water sulphate. *Geochimica et Cosmochimica Acta* **42**(4), 377–381.

Rosenbauer R. J. and Bischoff J. L. (1983) Uptake and transport of heavy metals by heated seawater: A summary of the experimental results. In *Hydrothermal Processes at Seafloor Spreading Centers* (ed. P. A. Rona, K. Boström, L. Laubier, and K. L. Smith), pp. 177–197. Plenum Press.

Sakai H., Gamo T., Kim E. S., Tsutsumi M., Tanaka T., Ishibashi J., Wakita H., Yamano M., and Oomori T. (1990) Venting of carbon dioxide–rich fluid and hydrate formation in mid–Okinawa Trough backarc basin. *Science* **248**, 1093–1096.

Sakai H., Gamo T., and Scientific Crew of Cruise KH–90–3. (1991) Hydrothermal activity in the eastern Manus Basin, Bismarck Sea: A brief report of the Hakuho–Maru Cruise KH–90–3. *Ridge Events* **2**, 39,51.

Sawkins F. J. (1990) *Metal Deposits in Relation to Plate Tectonics*. Springer–Verlag.

Scott S. D. and Binns R. A. (1995) Hydrothermal processes and contrasting styles of mineralization in the western Woodlark and eastern Manus basins of the western Pacific. In *Hydrothermal Vent and Processes, Geological Society of London Special Publication*, Vol. 87 (ed. L. M. Parson, C. L. Walker, and D. R. Dixon), pp. 191–205.

Seewald J. S., Doherty K. W., Hammar T. R., and Liberatore S. P. (2002) A new gas–tight isobaric sampler for hydrothermal fluids. *Deep Sea Research Part I: Oceanographic Research Papers* **49**(1), 189–196.

Seewald J. S., Reeves E., Saccocia P., Rouxel O. J., Walsh E., Price R. E., Tivey M.,

Bach W., and Tivey M. (2006) Water–rock reaction, substrate composition, magmatic degassing, and mixing as major factors controlling vent fluid compositions in Manus Basin hydrothermal systems. *EOS Trans. AGU. Fall Meet. Suppl.,* **87**(52), Abstract # B34A–02.

Seewald J. S. and Seyfried W. E., Jr. (1990) The effect of temperature on metal mobility in subseafloor hydrothermal systems: Constraints from basalt alteration experiments. *Earth and Planetary Science Letters* **101**, 388–403.

Seyfried W. E., Jr. (1987) Experimental and theoretical constraints on hydrothermal alteration processes at mid–ocean ridges. *Annual Review of Earth and Planetary Sciences* **15**, 317–335.

Seyfried W. E., Jr. and Bischoff J. L. (1977) Hydrothermal transport of heavy metals by seawater: The role of seawater/basalt ratio. *Earth and Planetary Science Letters* **34**(1), 71–77.

Seyfried W. E., Jr. and Bischoff J. L. (1981) Experimental seawater–basalt interaction at 300°C, 500 bars, chemical exchange, secondary mineral formation and implications for the transport of heavy metals. *Geochimica et Cosmochimica Acta* **45**(2), 135–147.

Seyfried W. E., Jr. and Janecky D. R. (1985) Heavy metal and sulfur transport during subcritical and supercritical hydrothermal alteration of basalt: Influence of fluid pressure and basalt composition and crystallinity. *Geochimica et Cosmochimica Acta* **49**(12), 2545–2560.

Seyfried W. E., Jr., Janecky D. R., and Mottl M. J. (1984) Alteration of the oceanic crust: Implications for geochemical cycles of lithium and boron. *Geochimica et Cosmochimica Acta* **48**(3), 557–569.

Seyfried W. E., Jr. and Mottl M. J. (1982) Hydrothermal alteration of basalt by seawater under seawater–dominated conditions. *Geochimica et Cosmochimica Acta* **46**, 985–1002.

Seyfried W. E., Jr., Seewald J. S., Berndt M. E., Ding K., and Foustoukos D. I. (2003) Chemistry of hydrothermal vent fluids from the Main Endeavour Field, northern

Juan de Fuca Ridge: Geochemical controls in the aftermath of June 1999 seismic events. *Journal of Geophysical Research* **108**(B9), doi 10.1029/2002JB001957.

Simon A. C., Pettke T., Candela P. A., Piccoli P. M., and Heinrich C. A. (2006) Copper partitioning in a melt–vapor–brine–magnetite–pyrrhotite assemblage. *Geochimica et Cosmochimica Acta* **70**(22), 5583–5600.

Simon A. C., Pettke T., Candela P. A., Piccoli P. M., and Heinrich C. A. (2007) The partitioning behavior of As and Au in S–free and S–bearing magmatic assemblages. *Geochimica et Cosmochimica Acta* **71**(7), 1764–1782.

Sinton J. M., Ford L. L., Chappell B., and McCulloch M. T. (2003) Magma genesis and mantle heterogeneity in the Manus Back–Arc Basin, Papua New Guinea. *Journal of Petrology* **44**, 159–195.

Stanton R. L. (1994) Ore elements in arc lavas. In *Oxford Monographs on Geology and Geophysics*, Vol. 29, pp. 391.

Stoffregen R. E. (1987) Genesis of acid–sulfate alteration and Au–Cu–Ag mineralization at Summitville, Colorado. *Economic Geology* **82**, 1575–1591.

Taylor B. (1979) Bismarck Sea; Evolution of a back–arc basin. *Geology* **7**, 171–174.

Tivey M. A., Bach W., Seewald J. S., Tivey M. K., Vanko D. A., and Shipboard Science and Technical Teams. (2007) Cruise Report R/V Melville, MAGELLAN–06. Hydrothermal systems in the Eastern Manus Basin: Fluid chemistry and magnetic structures as guides to subseafloor processes, pp. 67. Woods Hole Oceanographic Institution.

Tivey M. K., Humphris S. E., Thompson G., Hannington M. D., and Rona P. A. (1995) Deducing patterns of fluid flow and mixing within the TAG active hydrothermal mound using mineralogical and geochemical data. *Journal of Geophysical Research* **100**(B7), 12527–12555.

Trefry J. H., Butterfield D. A., Metz S., Massoth G. J., Trocine R. P., and Feely R. A. (1994) Trace metals in hydrothermal solutions from Cleft segment on the southern Juan de Fuca Ridge. *Journal of Geophysical Research* **99**, 4925–4935.

Tufar W. (1990) Modern hydrothermal activity, formation of complex massive sulfide

deposits and associated vent communities in the Manus back–arc basin (Bismarck Sea, Papua New Guinea). *Mitteilungen der Osterreichischen Geologischen Gesellschaft* **82**, 183–210.

Ulrich T., Günther D., and Heinrich C. A. (1999) Gold concentrations of magmatic brines and the metal budget of porphyry copper deposits. *Science* **399**, 676–679.

Von Damm K. L. (1983) Chemistry of submarine hydrothermal solutions at 21° North, East Pacific Rise and Guaymas Basin, Gulf of California. Ph. D. Thesis, Massachusetts Institute of Technology–Woods Hole Oceanographic Institution.

Von Damm K. L. (1990) Seafloor hydrothermal activity: Black smoker chemistry and chimneys. *Annual Review of Earth and Planetary Sciences* **18**(1), 173–204.

Von Damm K. L. (2000) Chemistry of hydrothermal vent fluids from 9–10 °N, East Pacific Rise: "Time zero", the immediate posteruptive period. *Journal of Geophysical Research* **105**(B5), 11203–11222.

Von Damm K. L., Edmond J. M., Grant B., Measures C. I., Walden B., and Weiss R. F. (1985) Chemistry of submarine hydrothermal solutions at 21 °N, East Pacific Rise. *Geochimica et Cosmochimica Acta* **49**(11), 2197–2220.

Von Damm K. L., Lilley M. D., Shanks W. C., Brockington M., Bray A. M., O'Grady K. M., Olson E., Graham A., Proskurowski G., and SouEPR Scientific Party. (2003) Extraordinary phase separation and segregation in vent fluids from the southern East Pacific Rise. *Earth and Planetary Science Letters* **206**(3), 365–378.

Yang K. and Scott S. D. (1996) Possible contribution of a metal–rich magmatic fluid to a sea–floor hydrothermal system. *Nature* **383**, 420–423.

Yeats C. J., Binns R. A., and Parr J. M. (2000) Advanced argillic alteration associated with actively forming submarine polymetallic sulfide mineralization in the eastern Manus Basin, Papua New Guinea. *Geological Society of Australia Abstracts* **59**, 555.

You C.–F., Butterfield D. A., Spivack A. J., Gieskes J. M., Gamo T., and Campbell A. J. (1994) Boron and halide systematics in submarine hydrothermal systems:

Effects of phase separation and sedimentary contributions. *Earth and Planetary Science Letters* **123**, 227–238.

CHAPTER 5

Processes Affecting the Formation and Composition of Massive Sulfide Vent Deposits in the Manus Basin, Papua New Guinea

1. INTRODUCTION

Many economically important, volcanogenic–hosted massive sulfide (VHMS) deposits preserved in the geologic record are hosted by felsic rocks and occur in tectonic settings similar to modern submarine island–arc or back–arc marginal basins (Franklin et al., 1981; Ohmoto and Skinner, 1983; Sawkins, 1990; Hannington et al., 2005). It is the consensus that such deposits formed on the seafloor as a result of metal sulfide precipitation from high–temperature hydrothermal fluids, which gained at least some of their metal inventory during interaction with underlying crustal rocks (Franklin et al., 1981; Ohmoto and Skinner, 1983). Studies of actively–forming seafloor hydrothermal deposits in convergent plate margins are therefore integral to understanding the processes relevant to formation of these deposits. In particular, studies of active systems allow relations among source–rock lithology and composition, fluid source, fluid composition and vent deposit composition to be assessed, and the processes and conditions (e.g., temperature, pressure, pH, fO_2–fS_2) relevant to the formation of metal–rich sulfide deposits investigated.

This chapter discusses the processes controlling the chemical composition of actively–forming hydrothermal sulfide deposits in the Manus back–arc basin. Vent deposits in the Manus basin are ideal candidates for such a study because the seafloor hydrothermal fluids from which the deposits are forming have been studied in detail (see Chapter 4). The compositions of hydrothermal fluids (i.e., temperature, pH, [metals], [H_2S]) are known to vary significantly among the vent fields examined, reflecting different sub–seafloor processes of hydrothermal fluid formation and circulation (see Chapter 4). Accordingly, differences in vent deposit mineralogical and chemical composition and deposit morphology can be directly compared to differences in vent fluid composition and conditions of metal–sulfide deposition at these vent fields. This study provides further insight into the processes relevant to the formation of ancient volcanogenic massive sulfide deposits associated with hydrothermal activity in back–arc settings.

2. Geologic Setting Of The Manus Basin And Description Of Vent Deposits

The Manus Basin in the Bismarck Sea, Papua New Guinea (Figure 5.1) is a rapidly–opening (~ 100 mm/yr) back–arc basin associated with subduction of the Solomon Microplate beneath the New Britain arc (Taylor, 1979; Davies et al., 1987; Martinez and Taylor, 1996). A complex history of plate deformation and rotation has resulted in a range of crustal spreading, including eruption of new oceanic crust along the Manus Spreading Center (MSC) toward the west and rapid extension and rifting of existing crust in the Eastern Manus Basin toward the east. The MSC is bounded between the Willaumez and Djaul transform faults (Martinez and Taylor, 1996) where new lavas with basalt compositions are erupted along a well–defined

spreading axis (Both et al., 1986; Sinton et al., 2003). Several areas of hydrothermal activity have been identified in the MSC (Figure 5.1a). Vienna Woods is the largest and most active of the known fields and is located slightly south of the major spreading center within the axial rift valley at a water depth of ~ 2500 m (Tufar, 1990).

To the east, EMB is bounded by the Djaul and Weitin transform faults (Martinez and Taylor, 1996) where lavas are erupted as a series of *en echelon* neovolcanic ridges and volcanic domes with felsic (andesite to rhyolite) composition (Sinton et al., 2003). The arc–affinity of volcanic lavas (Sinton et al., 2003) is consistent with the proximal location (< 200 km) of the EMB to the actively subducting margin. The EMB hosts several known active hydrothermal systems (Figure 5.1). The Papua New Guinea–Australia–Canada–Manus (PACMANUS) hydrothermal complex is located on the crest of the 35 km long, 500 m high Pual Ridge, between water depths of 1650 and 1740 m (Binns and Scott, 1993). The ridge is constructed of several sub–horizontal lava flows with compositions ranging from andesite to dacite (Binns and Scott, 1993; Sinton et al., 2003). The PACMANUS system hosts several vent fields (Roman Ruins, Roger's Ruins, Satanic Mills, Fenway, Snowcap and Tsukushi) distributed over a 1 km long section of the Pual Ridge (Figure 5.1b) (Binns and Scott, 1993; Tivey et al., 2007). Further to the east, SuSu Knolls is a series of three northwest trending volcanic cones (Suzette, North Su and South Su; Figure 5.1c) at water depths between ~ 1140 and 1510 m (Binns et al., 1997; Auzende et al., 2000; Tivey et al., 2007). The North Su and South Su domes are composed of abundant pyroclastic dacite showing variable advanced–argillic alteration (alunite–illite–pyrophyllite–quartz and native sulfur) and sedimentation by mixed volcaniclastic and hydrothermal material (Binns et al., 1997; Tivey et al., 2007). The dome at Suzette is extensively coated in metalliferous sediment and massive sulfide talus that

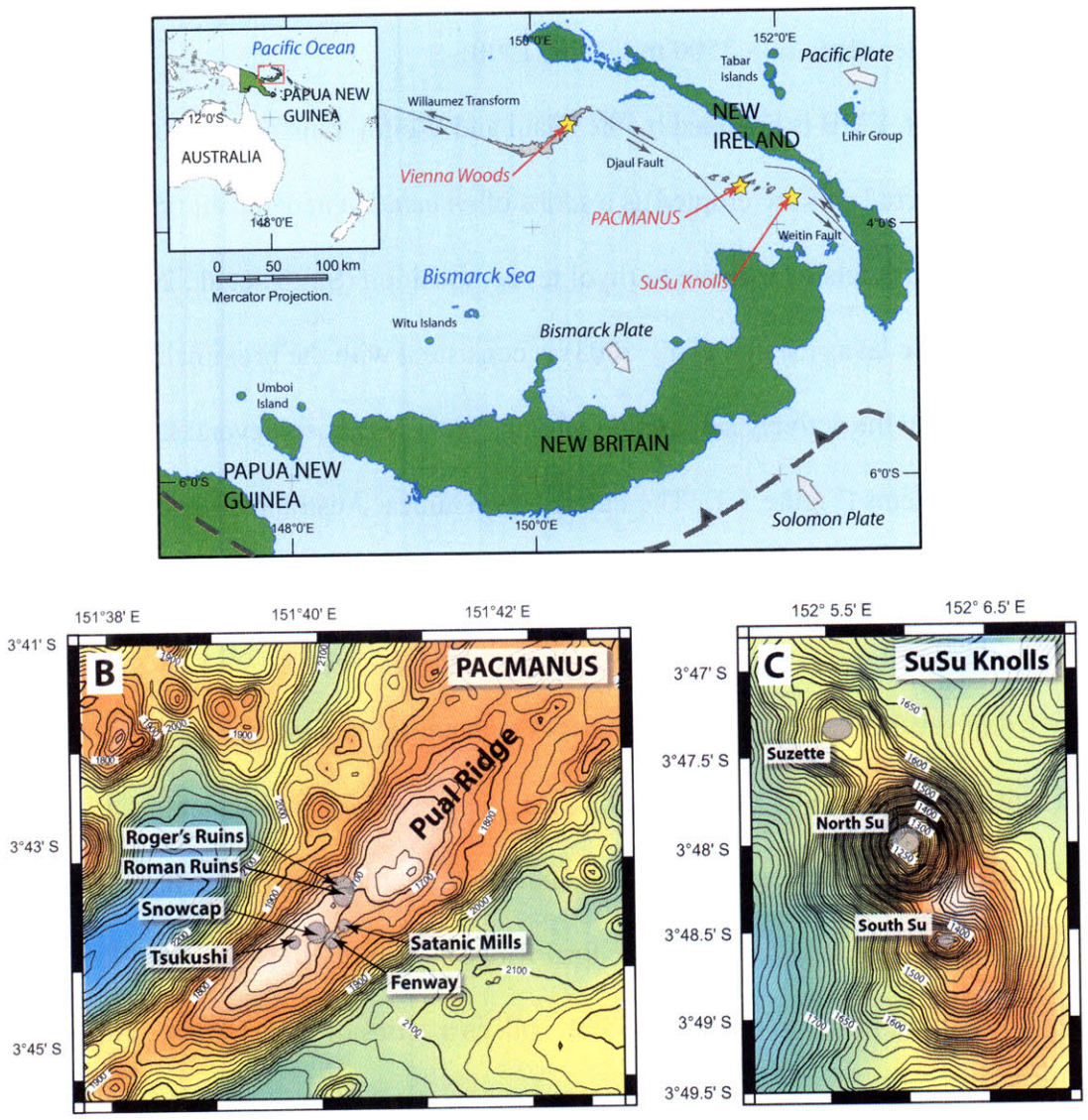

Figure 5.1. A) Regional tectonic setting of the Manus Basin indicating active plate motions and rifting, and areas of known hydrothermal activity in the Manus Basin. **B**) Distribution of known hydrothermal vent fields at PACMANUS. **C**) Known hydrothermal vent fields at SuSu Knolls. Bathymetry based on EM300 SeaBeam sonar (modified from Tivey et al., 2007).

mask primary volcanic features (Binns et al., 1997; Tivey et al., 2007).

2.1. Hydrothermal activity and vent deposit compositions

2.1.1. Vienna Woods

Hydrothermal activity at Vienna Woods is manifest as both focused and diffuse flows within an area of ~ 150 m by 100 m (Tufar, 1990; Tivey et al., 2007). The vent deposits at this field are characterized by numerous, mostly inactive, columnar sulfide spires up to 8 m tall that grow directly on the volcanic substrate (Figure 5.2a). The active sulfide chimneys recovered are cylindrical conduits for focused high temperature, mildly acidic fluid discharge (T up to 285 °C, pH (25 °C) ~ 4.2 – 4.7). The chimney deposits are notably zinc–rich but copper–poor, with an average of ~ 20 – 25 wt% in Zn and < 2 wt% in Cu reported (Tufar, 1990; Lisitsyn et al., 1993). Relict sulfide deposits have been observed and sampled at three other locations in the Manus Spreading Center, and have mineralogical compositions that are also Zn–rich (Tufar, 1990).

2.1.2. PACMANUS

Hydrothermal activity occurs at several discrete vent fields (Roman Ruins, Roger's Ruins, Satanic Mills, Snowcap, Tsukushi and Fenway; Figure 5.1), each between 50 and 200 m in diameter (Binns and Scott, 1993; Binns et al., 2007; Tivey et al., 2007). There are multiple styles of on–going seafloor vent fluid discharge. The Roman Ruins, Roger's Ruins and Satanic Mills vent fields consist of numerous large (up to 7 m tall) active and inactive sulfide chimneys. Many have complex morphologies, including peripheral spires growing around a central edifice. Several of these edifices form clusters of coalesced multi–spired chimneys (Moss and Scott, 2001; Tivey et al., 2007). Active chimneys discharge focused black–gray smoker fluids with a range of temperatures between 240 and 340 °C and low pH

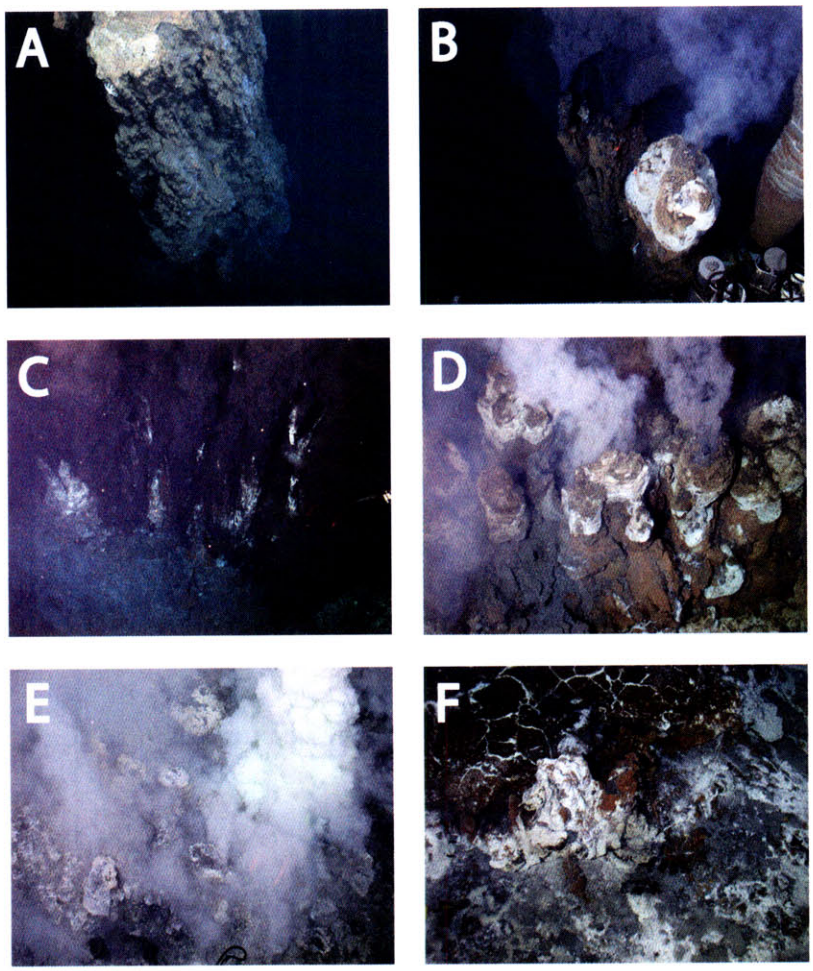

Figure 5.2. *Jason II* photographs of relict and active vent deposits at hydrothermal vent fields in the Manus Basin. (**A**) Approximately 5 m tall relict columnar chimney from the Vienna Woods vent field (top of chimney removed by prior sampling). (**B**) Contrasting venting characteristics of high-temperature black smoker fluids from open conduit chimneys (background) and lower-temperature gray smoker fluids from diffuser-type chimneys (foreground). From top of 3 m tall multi-spired, coalesced chimneys at the Roman Ruins vent field (PACMANUS). (**C**) Vigorous black smoker discharge from cracks and small open conduit orifices at the base of the black smoker complex at the Fenway vent field (PACMANUS). Field of view ~ 2 m. (**D**) Lower-temperature venting through multiple diffuser ("beehive") chimneys at Roman Ruins (PACMANUS). Field of view ~ 2 m. (**E**) Vigorous milky-white acid-sulfate fluid discharge (pH < 2, at 25 °C) from brecciated and altered rocks at the North Su vent field (SuSu Knolls). Field of view ~ 1.5 m. (**F**) Oxide-crusted sulfidic pavement (top of frame) on top of brecciated hydrothermal sulfidic sediment at the Suzette vent field (SuSu Knolls).

(25 °C) between 2.3 and 2.7 (Seewald et al., 2006). Seafloor hydrothermal activity at the Fenway mound consists of high–temperature (up to 358 °C) and acidic (pH (25 °C) ~ 2.3 – 2.8) black smoker discharge (Seewald et al., 2006) localized at a central ~ 10 m tall sulfide chimney complex (Figure 5.2c; Tivey et al., 2007). Substantial amounts of exposed massive anhydrite and massive sulfide talus were observed and recovered at the base and lower flanks of the black smoker complex (Tivey et al., 2007). The Snowcap vent field covers a volcanic knoll composed of dacite that has been variably altered and bleached (Binns et al., 2007; Tivey et al., 2007). Hydrothermal activity is limited to lower temperature fluid discharge (up to 180 °C) through diffuser–type chimneys located on the southern reaches of the knoll.

The sulfide chimney deposits from PACMANUS exhibit a wide range of mineralogical compositions, including a chalcopyrite + anhydrite (± bornite) assemblage in chimneys venting high–temperature (≥ 300 °C) black smoker fluids and a tennantite + bornite + sphalerite + barite (± galena) assemblage in diffuser chimneys venting lower temperature (~ 240 – 280 °C) gray smoker or clear fluids (Moss and Scott, 2001; Kim et al., 2004; Tivey et al., 2006; Craddock et al., 2007). Both active and relict chimney deposits at PACMANUS are enriched in Cu, Pb and Ba (average 8 wt% Cu, 1.5 wt% Pb, 7 wt% Ba and 22 wt% Zn (Moss and Scott, 2001)) relative to those from Vienna Woods. The mineralogical composition of chimney samples at PACMANUS is similar to that of massive sulfides recovered from felsic–hosted hydrothermal systems in the Lau back–arc basin (Fouquet et al., 1993a).

2.1.3. SuSu Knolls

On–going hydrothermal activity at SuSu Knolls is remarkably diverse, exhibiting a range of crustal rock alteration, mineral deposit composition and vent fluid compositions (Binns et al., 1997; Yeats et al., 2000; Seewald et al., 2006; Bach et al., 2007). The summit of

the North Su volcanic dome is characterized by high–temperature black and gray smoker fluids venting from scattered sulfide chimney edifices (Binns et al., 1997; Auzende et al., 2000; Tivey et al., 2007). Black smoker fluids at North Su, exiting primarily from multiple open conduit chimneys within a large ~ 11 m tall sulfide complex (Tivey et al., 2007), have temperatures between 300 and 325 °C and are relatively acidic with pH (25 °C) ranging from 2.8 to 3.2 (Seewald et al., 2006). Chimney deposits are located mostly on top of a convex shield of mixed sulfide–sulfate (chalcopyrite–pyrite–anhydrite) cemented material. Relict chimneys are observed in areas close to high–temperature black smoker fluid activity. The flanks of the North Su dome are characterized by extensive discharges of milky–white acid–sulfate fluids that have lower temperatures (48 – 241 °C) but very acidic pH (25°C) ≤ 1.8 (Seewald et al., 2006). These fluids exit through cracks in hyaloclastite and altered breccia (Figure 5.2e) (Bach et al., 2007; Tivey et al., 2007). Hydrothermal breccias are commonly bleached, do not retain primary volcanic textures and are mixed with broken anhydrite sediment, abundant native sulfur flows and contain interstitial veins of minor pyrite (Binns et al., 1997; Bach et al., 2007).

The South Su dome is a crescent–shaped volcanic feature characterized by outcrops of both fresh massive and variably altered volcanic (dacitic) rocks overlain by scattered, mostly inactive sulfide chimney deposits and oxide–stained hydrothermal sediments (Tivey et al., 2007). Altered material ranges from oxide–stained volcanic rock to more intensely bleached breccia, similar to that recovered from the flanks of North Su. Present–day hydrothermal activity occurs as black and gray smoker fluid discharge from scattered sulfide chimneys located along the summit ridge of the South Su dome (Tivey et al., 2007). Fluid temperatures are up to 290 °C and have moderately acidic pH (25 °C) approximately 2.6 (Seewald et al.,

2006).

The smaller Suzette dome, located NW of North Su and South Su, is extensively covered by thick metalliferous sediment, mass–wasted sulfide talus, Fe–oxide crusts and limited exposures of possible hydrothermal stockwork (Binns et al., 1997; Moss and Scott, 2001; Hrischeva et al., 2007; Tivey et al., 2007). The summit is characterized by large expanses of relict and scattered active sulfide chimneys that are typically buried within sulfide–rich metalliferous sediment (Binns et al., 1997; Tivey et al., 2007). The temperatures of hydrothermal fluids exiting from the tops of sulfide chimneys and from cracks in sulfide crusts (Figure 5.2f) range from 226 – 303 °C and have mildly–to–moderately acid pH (25 °C) between 2.3 and 3.8 (Seewald et al., 2006).

Sulfide mineralization at SuSu Knolls is generally Cu–rich and Zn–poor relative to other seafloor vent deposits from PACMANUS and, in particular, Vienna Woods (Binns et al., 1997; Kim et al., 2004; Craddock et al., 2007). Chimney deposits exhibit a range of mineralogical composition ranging from a high–temperature chalcopyrite + anhydrite assemblage (Figure 5.3c) to a lower temperature bornite + tennantite + barite (± sphalerite ± galena) assemblage (Tivey et al., 2006; Craddock et al., 2007).

3. METHODS

3.1. Sample processing and analysis

All vent deposit samples were recovered from the seafloor by Remotely Operated Vehicle (ROV *Jason II*) during cruise MGLN06MV (*R/V Meville*, July – September, 2006), allowing the relative locations of these samples at each vent field and relationship to present–

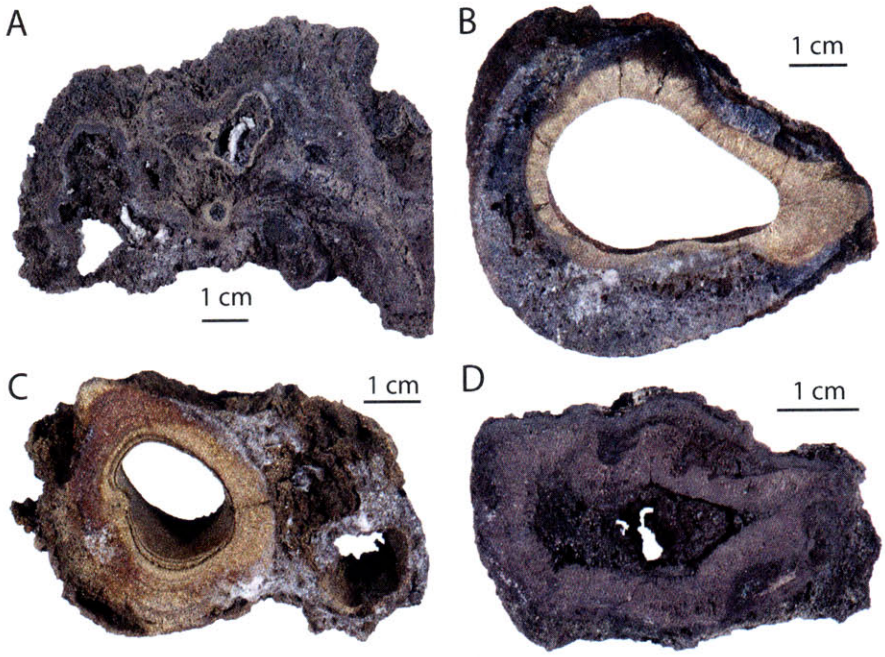

Figure 5.3. Cross sections of chimneys sampled from vent fields in the Manus Basin. **A)** Relict diffuser-type chimney from Vienna Woods, composed of a fine-grained Zn-sulfide matrix (gray) hosting minor amounts of pyrite and chalcopyrite (yellow) that are locally coarse-grained and form continuous rims around narrow channelways. Amorphous silica is present as a major (~ 25 wt% SiO_2), late mineral (sample J2_200_5_R1). **B)** Open conduit smoker from Roman Ruins (PACMANUS) with a central channel enclosed by an inner monomineralic chalcopyrite layer (yellow) and outer anhydrite-rich layer (light gray) and a thin exterior pyrite-marcasite and Fe-oxide rim (sample J2_213_2_R1). **C)** Open conduit smoker from North Su (SuSu Knolls) with two chalcopyrite-lined channelways coalesced by a fine-grained anhydrite-chalcoyprite matrix (sample J2_223_1_R1). **D)** Tennantite-lined (purple-gray) chimney from North Su (SuSu Knolls) with conduit infill of fine-grained tennantite and an outer layer of mixed barite and fine-grained tennantite and pyrite (dark gray) (sample J2_223_13_R1). Scale bar in figures is 1 cm.

day fluid activity to be determined. Sulfide–rich deposit samples were classified according to morphology, macroscopic texture and mineral composition. Samples of all types were cut and sub–sampled for petrographic, X–ray diffraction and geochemical studies. Mineral identifications were made using X–ray diffraction. Petrographic analyses, including mineral identification and textural interpretation, were made by examining singly–polished thin sections (30 μm or 40 μm) using reflected and transmitted light microscopy. Sphalerite and wurtzite were distinguished based on grain isotropy in transmitted light under crossed nicols and also by X–ray diffraction spectra.

Bulk geochemical analyses of all samples were performed by Activation Laboratories Ltd, Ontario (ActLabs) or ALS Laboratory Group, Brisbane (ALS Chemex). At ActLabs, concentrations of Cu, Pb, Mn, Cd, Ca, Sr and Ba were determined by inductively coupled plasma–emission spectroscopy (ICP–ES) following acid digestion and concentrations of Fe, Zn, Au, Ag, As, Sb, Co, Mo, Hg and Se were determined by instrumental neutron activation analysis (INAA). At ALS Chemex, concentrations of Au were determined by fire assay and atomic adsorption spectroscopy (AAS) and concentrations of Fe, Zn, Cu, Pb, Ag, As, Sb, Mn, Cd, Co, Mo, Hg, Se, Ca, Sr, Ba and SiO_2 were determined by ICP–ES following acid digestion. Quantitative analyses of trace elements in sulfide and sulfosalt grains (e.g., chalcopyrite, pyrite, sphalerite/wurtzite, tennantite) were carried out by electron probe micro–analysis using a JEOL 733 Superprobe equipped with Tracer Northern software at Massachusetts Institute of Technology (MIT). Natural and synthetic stoichiometric mineral standards were used for S, Fe, Cu, Zn, As, Sb, Pb, Cd, Ag, Se and Co. Analyses were made using an accelerating potential of 15 keV and a beam current of 10 nA. For analysis of Fe– and Cu–Fe–sulfides and sulfosalts, counting times were 20 s (S), 60 s (Fe, Zn, Cu and Cd),

120 s (Pb, As and Sb) and 180 s (Se, Co and Ag). For Zn– and Pb–sulfides, counting times were 20 s (S), 60 s (Fe, Cu, Zn and Pb), 120 s (Cd and Sb) and 180 s (As, Ag, Se and Co).

3.2. Thermodynamic Calculations

Thermodynamic calculations were performed for Manus Basin vent fluid compositions (see Chapter 4) to determine the equilibrium distribution of aqueous species and pH at in situ temperature and pressure, the saturation state (log Q/K) of sulfide minerals at in situ temperature and pressure, and the temperature at which various sulfides would be saturated (log $Q/K \geq 0$) if the fluid cooled via conduction. Mineral precipitation was suppressed during all calculations (see Tivey, 1995). Predicted mineral saturation states are compared to observed mineral assemblages in paired vent deposit samples.

Calculations were carried out using the computer program EQ3/6 (Wolery, 1992; Wolery and Daveler, 1992). The thermodynamic database used was generated by SUPCRT92 (Johnson et al., 1992), with thermodynamic properties of minerals, aqueous species and gases calculated at 250 bars and a temperature range of 25 to 350 °C. Modifications to the SUPCRT92 database included addition of aqueous species Na_2SO_4 and $MgSO_4$ (McCollom and Shock, 1997), $HCl_{(aq)}$ (Sverjensky et al., 1991), and $FeCl_{2(aq)}$ and $CuCl_{(aq)}$ at temperatures above 300 °C (Ding and Seyfried, 1992). Thermodynamic properties for the mineral tennantite taken from Knight (1977) were also added to the database. In the absence of thermodynamic properties of tennantite at in situ pressure (250 bars), vapor saturation data up to 350 °C were incorporated. The compositions of dissolved gases and major aqueous species used in thermodynamic calculations are from E. Reeves and J. Seewald (*unpubl. data*) and the compositions of dissolved trace metals are from Chapter 4. Activity diagrams to determine the stability relationships among sulfide minerals at various temperatures and fluid compositions

(e.g., aCu^{+}/aH^{+}, $aFe^{2+}/a^{2}H^{+}$, fO_2) were constructed using the thermodynamic data in SUPCRT92 and Knight (1977) (Appendix E1).

4. Mineralogy and Geochemistry of Sulfide Deposits in the Manus Basin

The morphology of the highest temperature open conduit, lower temperature diffuser and relict deposit samples are similar among all vent fields in the Manus Basin. However, the mineral contents and textures of open conduit, diffuser and relict samples differ. The mineral and chemical compositions of vent deposits in the Manus Basin exhibit some clear and considerable differences relative to seafloor deposits at mid-ocean ridge spreading centers

4.1. Open conduit chimneys

4.1.1. Vienna Woods

The few open conduit smokers sampled at Vienna Woods are composed of an interior lining of wurtzite with minor fine–grained chalcopyrite and trace pyrite, and an exterior layer of mixed wurtzite and anhydrite, with minor pyrite. Wurtzite in the interior layer forms coarse–grained (~ 1 mm) euhedral, hexagonal aggregates. Chalcopyrite occurs in minor amounts as fine–grained triangular inclusions (< 50 – 100 μm) along crystallographic boundaries in most wurtzite and in lesser amounts as subhedral grains (up to 250 μm) interstitial to wurtzite aggregates (Figure 5.4a). Euhedral chalcopyrite is present in one sample lining a ~ 1 cm^3 area of the interior conduit. Subhedral grains of chalcopyrite contain inclusions of fine–grained (most < 50 μm) euhedral pyrite. Wurtzite is honey–red in color when viewed in transmitted light (40 μm thick polished section; Figure 5.4b). The exterior layer is characterized by intergrowths of fine–grained wurtzite and tabular anhydrite (~100

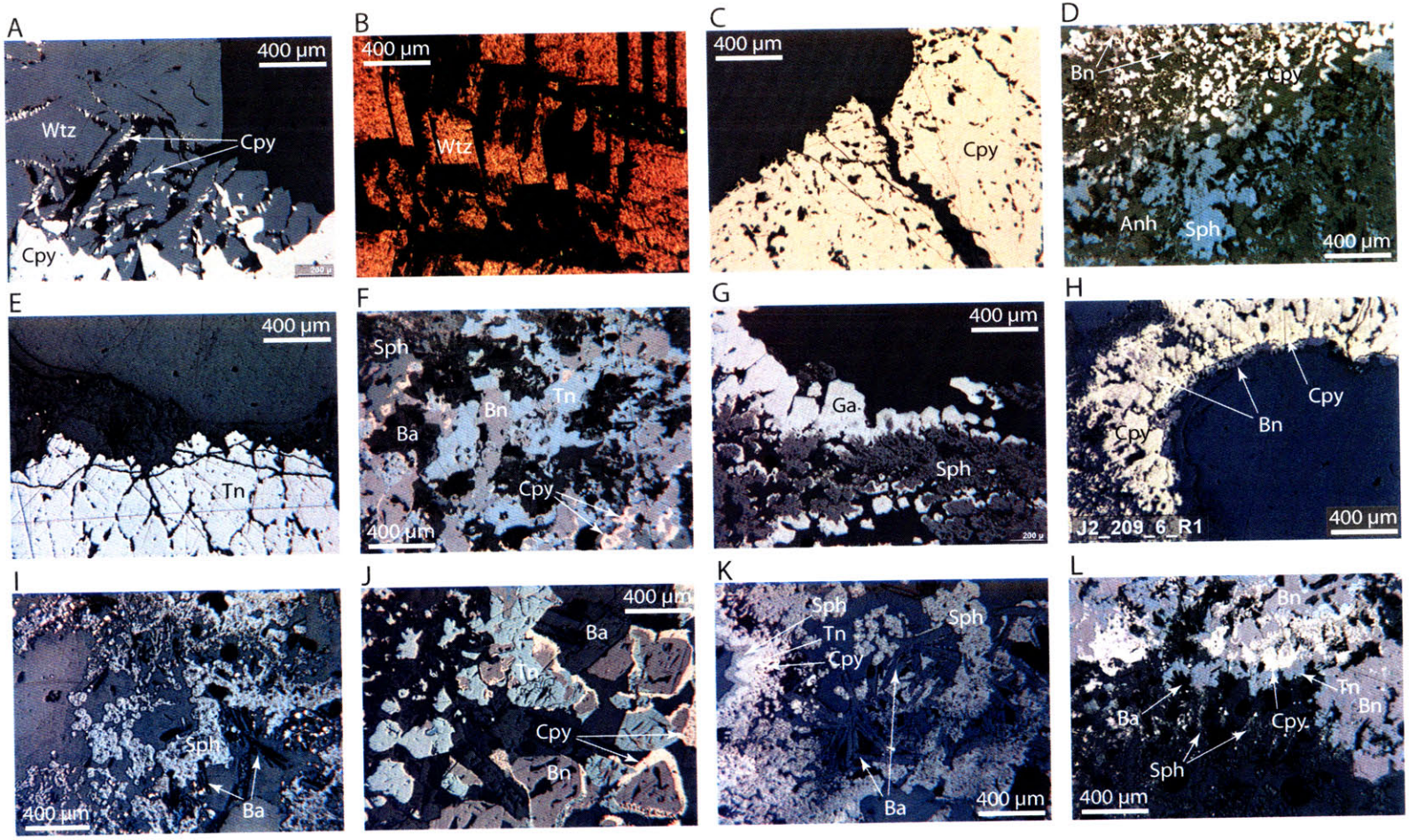
A
400 µm
Wtz
Cpy
Cpy
B
400 µm
Wtz
C
400 µm
Cpy
D
Bn
Cpy
Anh
Sph
400 µm
E
400 µm
Tn
F
Sph
Bn
Tn
Ba
Cpy
400 µm
G
400 µm
Ga
Sph
H
Cpy
Bn
Cpy
J2_209_6_R1
400 µm
I
Sph
Ba
400 µm
J
400 µm
Ba
Tn
Cpy
Bn
K
Sph
Tn
Cpy
Sph
Ba
400 µm
L
Bn
Tn
Bn
Ba
Cpy
Sph
400 µm

Figure 5.4. Photomicrographs of chimney samples from the Manus Basin. (**A**) Sample J2_207_1_R1 (Vienna Woods). Coarse-grained wurtzite (Wtz) and chalcopyrite (Cpy) lining high-temperature (285 °C) open conduit chimney typical of deposits at Vienna Woods. Common fine-grained inclusions of chalcopyrite are intergrown with or exsolved from wurtzite along crystallographic boundaries of wurtzite grains. (**B**) Sample J2_207_1_R1 (Vienna Woods). Cross-section through hexagonal platelets of wurtzite showing deep-red color, indicating elevated FeS content (6 – 7 mol% FeS) in ZnS. Transmitted light. (**C**) Sample J2_213_6_R1 (Roger's Ruins). Coarse-grained monomineralic chalcopyrite lining of high-temperature (320 °C) open conduit chimneys. (**D**) Sample J2_213_6_R1 (Roger's Ruins). Boundary between interior lining of monomineralic chalcopyrite and outer chimney wall layer of fine-grained tabular anhydrite (Anh) and anhedral and dendritic sphalerite (Sph). Trace amounts of bornite (Bn) are present at the outer edge of the chalcopyrite lining in some open conduit chimneys. (**E**) Sample J2_223_13_R1 (North Su). Interior monomineralic lining of coarse-grained tennantite (Tn) from low temperature (~ 212 °C) smoker. Trace amounts of acicular barite is plated on tennantite. (**F**) Sample J2_222_1_R1 (Roger's Ruins). Interior portion of active (274 °C) diffuser-type chimney. Anhedral sphalerite and tabular barite (Ba) present in exterior portions of diffuser chimneys at Roman Ruins and Roger's Ruins, succeeded toward interior portions of chimney walls by bornite (often rimmed by chalcopyrite) and tennantite. (**G**) Sample J2_208_2_R3 (Roman Ruins). Interior portion of active (272 °C) diffuser-type chimney. Dendritic low-Fe sphalerite forming a porous chimney framework that is plated by euhedral galena projecting into cavities and rimming micro-channels. (**H**) Sample J2_209_6_R1 (Satanic Mills). Cu-Fe-sulfide (chalcopyrite + bornite) rich lining around micro-channels from interior portions of diffuser type chimneys from the Satanic Mills vent field. (**I**) Sample J2_209_6_R1. Active 249 °C diffuser chimney. At Satanic Mills, Snowcap and Fenway vent fields, Zn-sulfide occurs only in trace-to-minor amounts in most sampled diffuser chimneys, as fine-grained dendrites of low-Fe sphalerite intergrown with fine-grained tabular barite in exterior portions of more massive diffuser chimney walls. (**J**) Sample J2_224_6_R1 (South Su). Cu-Fe-sulfide (bornite + chalcopyrite) and Cu-As-sulfosalt (tennantite) dominate the interior portions of most diffuser vent deposit samples recovered from SuSu Knolls vent fields. (**K**) Sample J2_226_2_R1 (Suzette) is different to most diffuser chimney samples from SuSu Knolls, being characterized by a high modal abundance of sphalerite, intergrown with tabular barite and plated by trace amounts of tennantite and rare fine-grained chalcopyrite around micro-channels through which fluid flow is likely focused. (**L**) Sample J2_210_1_R1 (Snowcap). Relic chimney exhibiting mineral textures and composition similar to active diffuser chimneys. Interior portions of relic chimneys at Satanic Mills, Snowcap and Fenway vent fields are mostly characterized by intergrown bornite, lesser chalcopyrite and tennantite, succeeded toward exterior chimney wall sections by fine-grained dendritic low-Fe sphalerite and minor amounts of fine-grained tabular barite.

μm). Minor amounts of subhedral fine–grained pyrite (< 40 μm) are disseminated within this layer, and in places colloform pyrite forms a discontinuous rim (< 200 μm thick) on the exterior of the chimney wall.

The mineralogy of Vienna Woods open conduit smokers is dominated by wurtzite, as reflected by modal mineral proportions calculated from bulk geochemical data (Table 5.1; Figure 5.5). Anhydrite is common, particularly in immature chimneys. Pyrite, chalcopyrite and barite are present only in trace–to–minor amounts. Galena is absent or present only in very trace amounts. Bulk chemical analyses of open conduit smokers show variable concentrations of Cd and low concentrations of Ag, Au, As, Sb, Mo, Co and Se (Figure 5.6). Electron microprobe analyses of active chimney samples document measurable Cd and Pb in wurtzite (Appendix E2). The Fe content of wurtzite in active samples is 3.2 to 4.2 wt % (6.1 – 7.3 mole % FeS). Chalcopyrite and pyrite grains in the same samples contain varying concentrations of Zn and Pb, while concentration of Ag, Sb, As, Se and Co are below detection in all grains analyzed (Figure 5.7; Appendix E2).

4.1.2. PACMANUS

The majority of open conduit chimneys at PACMANUS are lined with chalcopyrite and exhibit an exterior layer of anhydrite mixed with varying amounts of sulfides (Figure 5.3). Monomineralic chalcopyrite lining the open conduits is consolidated with grain size up to 1 mm (Figure 5.4c). Trace amounts of bornite are present in some samples rimming chalcopyrite at the boundary between the chalcopyrite lining and anhydrite–dominated layer (Figure 5.4d). The contact between the interior lining and exterior layer is sharp in most samples with only a thin (< 1 mm) mid–layer of mixed fine–grained chalcopyrite and anhydrite. Anhydrite in the outer layer is coarse–grained and tabular (> 500 μm, increasing

Table 5.1a. Chemical compositions of vent deposit samples from the Manus Spreading Center. Major elements

Sample	Location	Laboratory	Fe	Cu	Zn	Pb	As	S‡	Ca	Ba	SiO_2	Major	Minor	Trace
			Weight Percent (wt %)									X-ray Diffraction Mineral Identification§		
Open Conduit Chimneys														
J2-202-7-R1	V.W.	ALS Chemex	1.69	0.19	3.82	0.09	0.004	20.80	20.40	0.006	0.92	Anh	Sph	Cpy
J2-207-1-R1	V.W.	ActLabs	3.68	0.31	57.30	0.01	0.034	18.70	2.71	0.600	N.A.	Wtz	Anh	Cpy
J2-207-2-R1	V.W.	ActLabs	3.53	0.74	22.90	0.06	0.003	19.00	9.86	< 0.005	N.A.	Wtz, Anh		Cpy
Relic/Inactive Chimney														
J2-200-1-R1	V.W.	ALS Chemex	18.75	0.60	20.20	1.15	0.079	27.00	0.11	0.005	18.55	Sph	Py/Mc	Anh
J2-200-2-R1	V.W.	ALS Chemex	11.60	0.89	30.40	0.16	0.032	23.90	0.18	< 0.005	25.80	Sph	Py/Mc	Cpy, Anh
J2-200-3-R1	V.W.	ALS Chemex	17.20	0.62	28.10	0.25	0.034	29.60	0.08	< 0.005	20.80	Sph	Py/Mc	
J2-200-4-R1	V.W.	ALS Chemex	12.85	0.97	34.80	0.10	0.020	27.20	0.05	0.007	20.90	Sph	Py/Mc	Cpy, Wtz
J2-200-5-R1	V.W.	ALS Chemex	16.45	1.12	25.40	0.06	0.018	27.10	0.08	< 0.005	25.30	Sph	Py/Mc	Mc
J2-200-6-R1	V.W.	ALS Chemex	15.55	0.52	30.60	0.12	0.026	28.70	0.05	< 0.005	19.75	Sph		Py/Mc
J2-200-7-R1	V.W.	ALS Chemex	19.70	4.10	18.50	0.05	0.017	28.60	0.04	0.006	22.30	Sph	Cpy, Wtz	Py
J2-200-7-R2	V.W.	ALS Chemex	11.70	0.88	25.90	0.10	0.019	22.30	0.04	0.006	36.70	Sph		Cpy, Wtz, Py
J2-200-8-R1	V.W.	ALS Chemex	18.30	0.51	19.10	0.73	0.054	27.40	0.08	< 0.005	25.30	Sph	Py, Wtz	Cpy, Mc
J2-200-9-R1	V.W.	ALS Chemex	20.00	0.71	30.20	0.07	0.018	32.50	0.04	0.006	11.60	Sph	Py	Cpy
J2-200-10-R1	V.W.	ALS Chemex	12.95	4.28	31.70	0.05	0.012	25.40	0.06	0.006	18.70	Sph	Cpy, Wtz	Py
J2-200-12-R1	V.W.	ALS Chemex	10.40	0.82	28.10	0.08	0.022	19.30	0.04	0.007	23.70	Sph	Py	Mc
J2-200-13-R1	V.W.	ALS Chemex	8.32	1.15	42.30	0.17	0.015	22.30	0.09	0.006	16.20	Wtz, Sph		Py, Cpy
J2-200-14-R1	V.W.	ALS Chemex	22.60	0.39	16.65	0.25	0.033	27.80	0.12	0.025	17.65	Py, Wtz	Sph	Anh
J2-200-15-R1	V.W.	ALS Chemex	23.20	5.55	12.70	0.04	0.019	27.40	0.02	0.006	10.70	Py	Sph, Cpy	
J2-200-16-R1	V.W.	ALS Chemex	18.30	0.72	16.70	0.36	0.039	22.60	0.08	0.050	17.40	Sph	Py	Cpy, Ba
J2-200-17-R1	V.W.	ALS Chemex	15.70	1.02	34.50	0.12	0.022	25.90	0.05	0.006	10.15	Sph		Py, Cpy
J2-200-18-R1	V.W.	ALS Chemex	17.00	0.57	27.90	0.17	0.025	26.60	0.07	0.006	12.20	Sph	Py	Mc, (Ba?)
J2-200-19-R1	V.W.	ALS Chemex	20.80	0.40	22.50	0.30	0.028	27.90	0.11	0.010	17.60	Sph, Wtz	Py	Mc, (Ba?)
J2-200-20-R1	V.W.	ALS Chemex	20.10	0.27	17.55	0.36	0.023	26.50	0.08	0.010	25.10	Sph	Py	
J2-200-21-R1	V.W.	ALS Chemex	24.50	11.15	6.12	0.08	0.010	27.40	0.05	0.008	22.90	Cpy	Py, Sph	
J2-200-22-R1	V.W.	ALS Chemex	18.20	0.94	33.60	0.18	0.029	30.20	0.07	0.007	11.70	Sph	Py, Wtz	Mc
J2-202-3-R1	V.W.	ALS Chemex	15.15	0.69	22.00	0.26	0.042	25.50	0.05	0.014	27.90	Sph	Py	Mc, Cpy, (Ba?)
J2-202-4-R1	V.W.	ALS Chemex	9.96	1.06	23.40	0.37	0.030	20.70	0.43	0.017	33.40	Sph		Py, Anh, Cpy
J2-202-5-R1	V.W.	ALS Chemex	6.60	0.41	47.50	0.21	0.046	25.70	0.10	0.007	9.95		No powder	
J2-202-6-R1	V.W.	ALS Chemex	10.80	0.91	40.80	0.40	0.056	28.60	0.11	0.008	9.61		No powder	
J2-202-8-R1	V.W.	ALS Chemex	21.70	0.52	14.50	0.68	0.065	30.80	1.57	0.009	17.60		No powder	
J2-202-9-R1	V.W.	ALS Chemex	23.10	0.50	8.31	0.20	0.046	29.20	0.22	0.010	29.40	Py, Sph		Mc, Anh, (Ba?)
J2-202-11-R1	V.W.	ALS Chemex	35.90	0.05	0.67	0.31	0.075	37.10	0.13	0.010	7.08	Py, Mc		Sph
J2-202-15-R1	V.W.	ALS Chemex	9.87	1.05	27.40	0.30	0.021	22.40	0.05	0.009	33.60	Sph		Py, Cpy, Anh
J2-202-16-R1	V.W.	ALS Chemex	20.40	0.60	34.50	0.16	0.024	29.90	0.03	0.009	11.95	Sph		Cpy
J2-202-17-R1	V.W.	ALS Chemex	21.80	0.51	24.70	0.12	0.027	32.60	0.04	0.010	18.50	Sph	Py	Mc

‡ sulfur analysis is not quantitative owing to possible incomplete digestion of anhydrite and barite

§ X-ray diffraction carried out on splits of the same powders used for bulk geochemical analysis.

Locations: V.W. (Vienna Woods)

Table 5.1b. Chemical compositions of vent deposit samples from the Manus Spreading Center. Trace elements.

Sample	Location	Co	Se	Mo	Cd	Sb	Ag	Au	Mn	Sr
		Parts Per Million (ppm)								
				Open Conduit Chimneys						
J2-202-7-R1	V.W.	1	N.A.	12	137	3	32	0.8	238	1390
J2-207-1-R1	V.W.	4	< 1	15	6000	30	9	0.8	734	220
J2-207-2-R1	V.W.	< 1	13	48	1080	29	71	1.4	520	802
				Relic/Inactive Chimney						
J2-200-1-R1	V.W.	<1	N.A.	151	381	146	1040	22.7	1510	146
J2-200-2-R1	V.W.	<1	N.A.	190	808	70	352	6.7	1640	172
J2-200-3-R1	V.W.	<1	N.A.	120	587	66	341	9.4	1335	150
J2-200-4-R1	V.W.	<1	N.A.	157	1060	51	122	5.1	1205	138
J2-200-5-R1	V.W.	<1	N.A.	260	1150	37	77	2.7	884	115
J2-200-6-R1	V.W.	<1	N.A.	82	975	53	145	5.1	854	144
J2-200-7-R1	V.W.	<1	N.A.	151	1090	33	72	2.3	546	101
J2-200-7-R2	V.W.	<1	N.A.	119	933	45	103	3.4	655	98
J2-200-8-R1	V.W.	<1	N.A.	136	504	93	520	11.8	1760	186
J2-200-9-R1	V.W.	<1	N.A.	132	918	40	139	3.5	484	80
J2-200-10-R1	V.W.	5	N.A.	183	1795	39	66	2.4	705	109
J2-200-12-R1	V.W.	<1	N.A.	106	916	53	110	4.5	568	100
J2-200-13-R1	V.W.	<1	N.A.	86	1115	53	108	2.1	3420	280
J2-200-14-R1	V.W.	<1	N.A.	124	251	54	202	5.6	1355	215
J2-200-15-R1	V.W.	<1	N.A.	125	508	18	44	1.5	426	58
J2-200-16-R1	V.W.	<1	N.A.	90	321	60	255	8.5	965	190
J2-200-17-R1	V.W.	<1	N.A.	167	998	48	146	4.9	821	181
J2-200-18-R1	V.W.	<1	N.A.	59	1035	63	127	5.1	698	151
J2-200-19-R1	V.W.	<1	N.A.	93	341	74	415	9.6	730	168
J2-200-20-R1	V.W.	<1	N.A.	53	228	56	341	6.2	1550	184
J2-200-21-R1	V.W.	10	N.A.	80	198	26	93	1.8	484	112
J2-200-22-R1	V.W.	<1	N.A.	185	995	53	174	5.5	968	188
J2-202-3-R1	V.W.	<1	N.A.	157	674	71	310	6.6	1310	122
J2-202-4-R1	V.W.	<1	N.A.	120	720	71	259	8.5	1225	186
J2-202-5-R1	V.W.	<1	N.A.	35	1240	56	179	4.9	2870	224
J2-202-6-R1	V.W.	<1	N.A.	150	1350	95	407	11.4	1760	208
J2-202-8-R1	V.W.	<1	N.A.	184	228	135	560	11.7	1475	194
J2-202-9-R1	V.W.	<1	N.A.	165	102	82	336	7.5	2110	212
J2-202-11-R1	V.W.	<1	N.A.	66	9	100	227	9.2	4070	230
J2-202-15-R1	V.W.	<1	N.A.	45	755	98	274	8.3	974	102
J2-202-16-R1	V.W.	<1	N.A.	79	757	58	268	5.6	493	96
J2-202-17-R1	V.W.	<1	N.A.	87	616	56	198	6.3	821	109

N.A. indicates species not analyzed.

Locations: V W. (Vienna Woods)

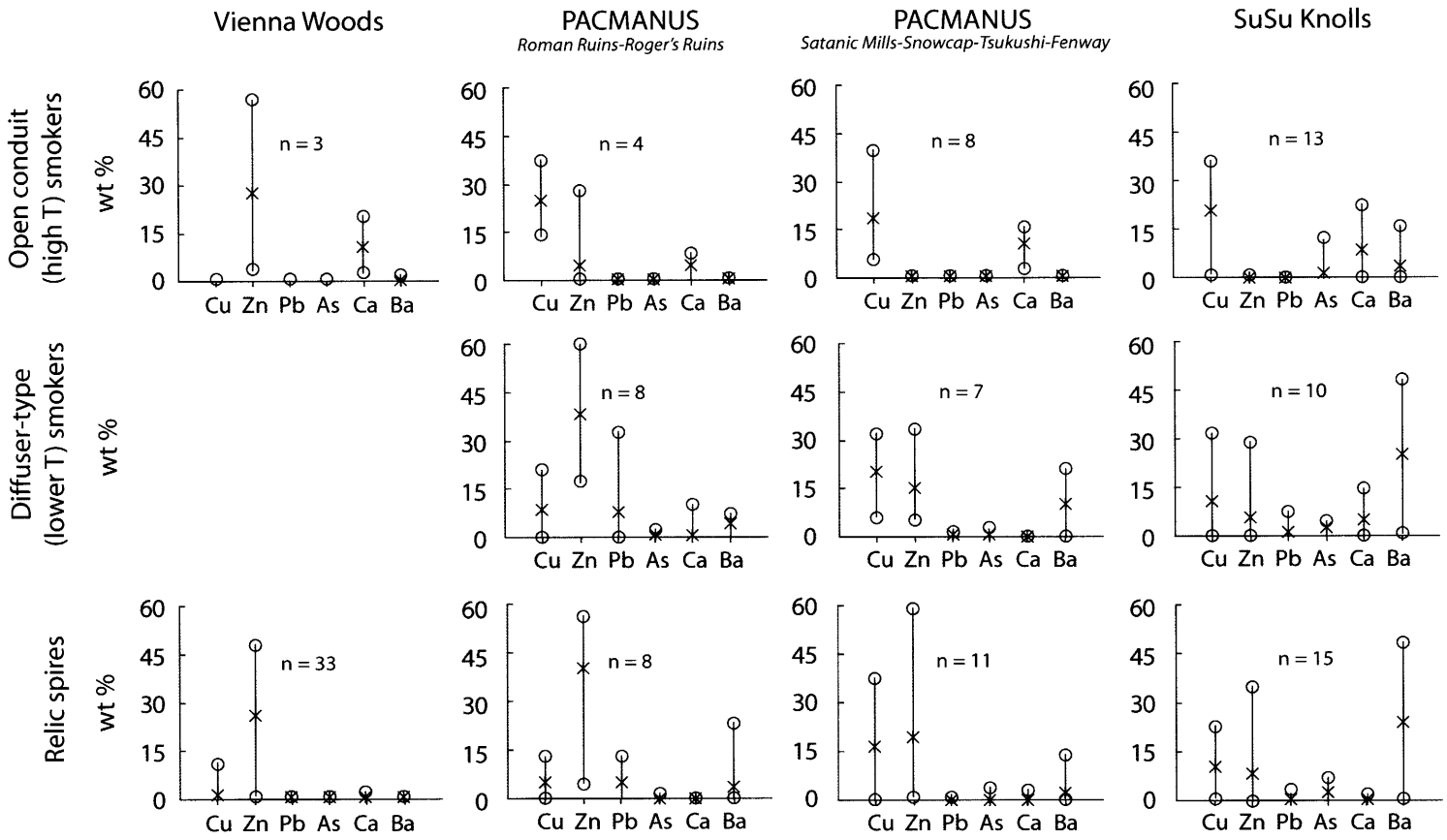

Figure 5.5. Summary of bulk geochemical analyses showing average (cross), maximum and minimum (circle) and range (line) of Cu, Zn, Pb, As, Ca and Ba concentrations in sulfide chimneys from the Manus Basin. Open conduit chimneys forming from high-temperature fluids, diffuser chimneys forming from lower temperature chimneys and relic chimneys shown. Samples from vent fields at PACMANUS are separated into those from Roman Ruins and Roger's Ruins and those from other vent fields (Satanic Mills, Snowcap, Fenway and one sample from Tsukushi).

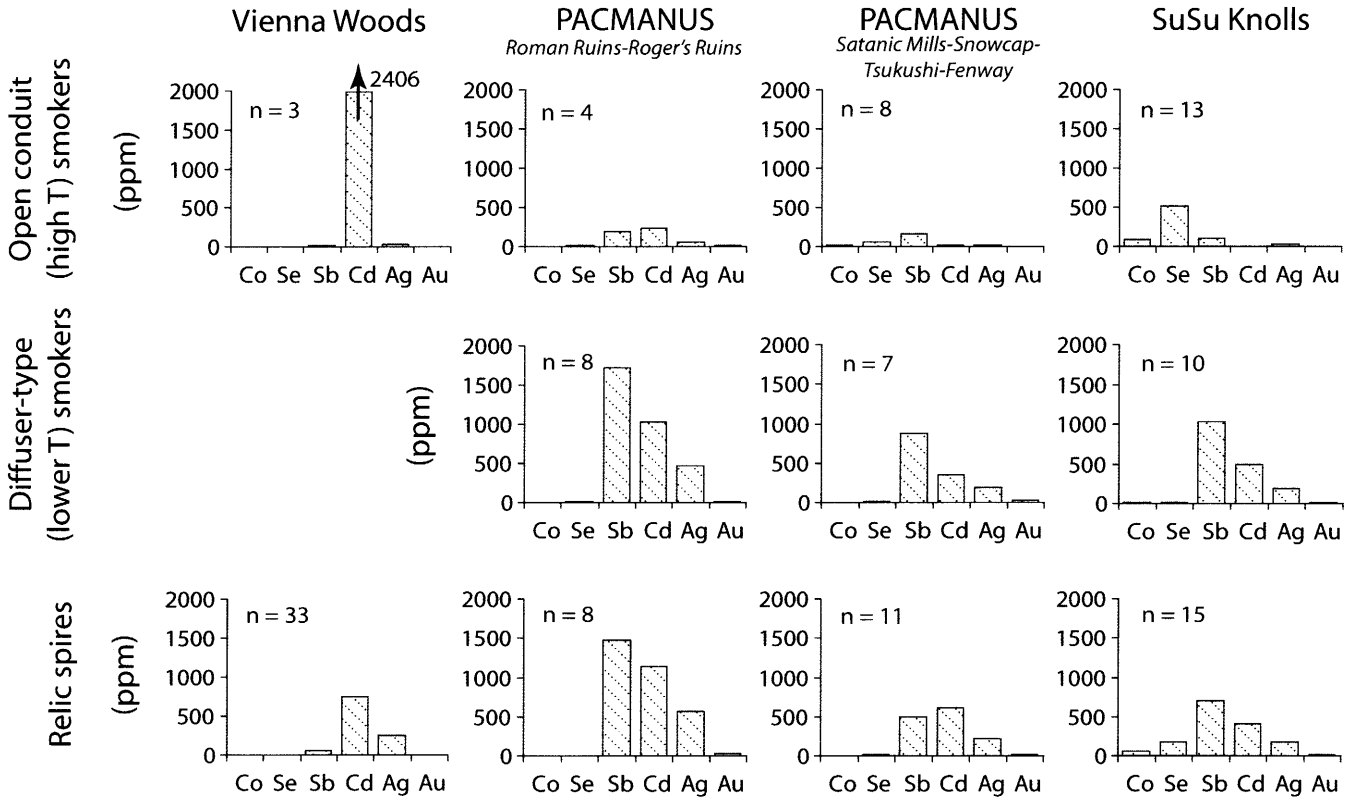

Figure 5.6. Average concentrations of trace elements (Co, Se, Sb, Cd, Ag and Au) in sample types from Vienna Woods, PACMANUS and SuSu Knolls. Number of samples (n) is given for each type.

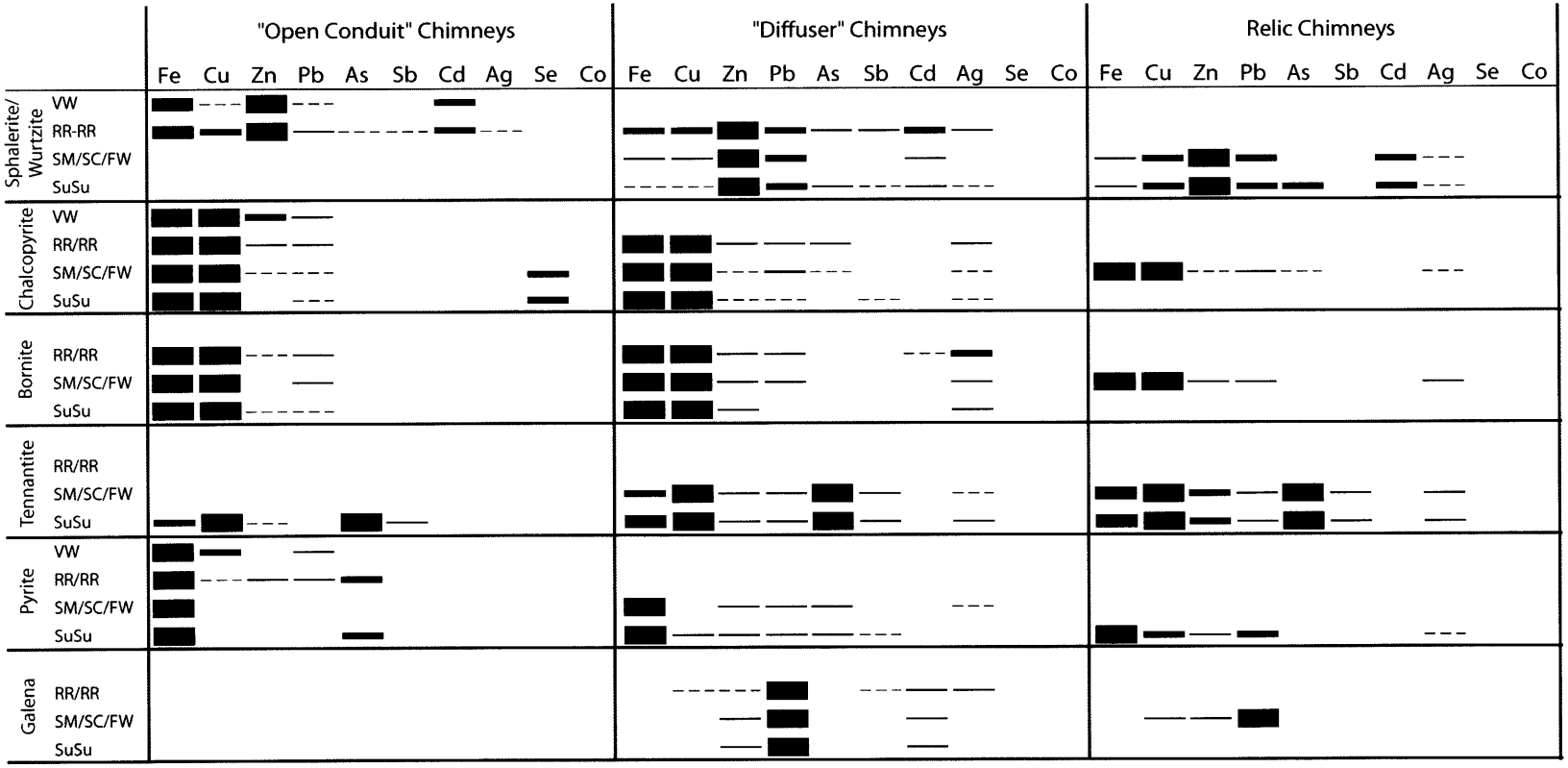

Figure 5.7. Summary of electron microprobe data showing major element composition of sulfide minerals (shown by thick black bar ▬) and distributions of trace elements in sulfides (▬ is common 5 - 11 wt%, ▬ is minor 1 - 5 wt%, —— is trace < 1 wt% and - - - is rare only in select grains << 1 wt%). Open conduit, diffuser and relic chimneys from each vent field shown separately. VW is Vienna Woods, RR/RR is Roman Ruins and Roger's Ruins (PACMANUS), SM/SC/FW is Satanic Mills, Snowcap and Fenway (PACMANUS) and SuSu is Suzette, North Su and South Su (SuSu Knolls). See appendix E2 for analytical data.

amounts of disseminated, fine–grained (< 50 – 100 μm) subhedral galena and pyrite.

Modal mineral abundances of diffuser chimneys as calculated from bulk geochemical analyses are consistent with polished section mineral identification. Diffuser chimneys recovered from PACMANUS have higher concentrations of Zn and Ba and lower concentrations of Cu relative to high–temperature open conduit chimneys (Figure 5.5). They also exhibit higher concentrations of Pb, Cd, As, Sb, Ag and Au and lower concentrations of Co, Se and Mo relative to open conduit chimneys (Table 5.2, Figure 5.6). Diffuser chimneys show higher concentrations of Zn, Pb, Cd, Sb and Ag in samples from Roman Ruins and Roger's Ruins relative to those from other PACMANUS (Satanic Mills, Fenway and Snowcap) vent fluids (Figures 5.5 and 5.6). Overall, diffuser chimneys from PACMANUS are enriched in Cu, As and Pb (occurring as bornite, tennantite and galena) relative to low–temperature chimney deposits from mid-ocean ridge spreading centers (see Hannington et al., 1991).

Electron microprobe analyses document measurable Cu, Pb and Cd in sphalerite in diffusers from all PACMANUS vent fields, and rarely of Ag, As and Sb in sphalerite from Roman Ruins and Roger's Ruins (Figure 5.7; Appendix E2). The Fe content of sphalerite is low (< 0.1 – 1.3 mol % FeS). At Roman Ruins and Roger's Ruins, electron microprobe analyses also document measurable concentrations of Zn, Pb, Ag and rarely of As in chalcopyrite, of Zn, Pb and Ag in bornite, and more variable concentrations of Zn, Cd, Ag, Sb and Cu in galena. At Satanic Mills, Snowcap and Fenway, electron microprobe analyses document the presence of Pb and rarely of Zn, As and Ag (in one or two grains) in chalcopyrite, of Zn, Pb and Ag in bornite, of Sb, Fe, Zn, Pb and Ag in tennantite, of Pb, Zn, As and rarely of Ag in pyrite, and of Zn and Cd in galena (Figure 5.7; Appendix E2).

with thickness of layer). At Roman Ruins and Roger's Ruins, colloform and dendritic sphalerite (up to 600 μm in length) and trace amounts of fine–grained pyrite (< 100 μm) are intergrown with anhydrite. At Satanic Mills and Fenway, subhedral bornite (± covellite) typically 200 – 300 μm in size are intergrown with anhydrite. Sphalerite is absent or present in only trace amounts in open conduit samples from Satanic Mills and Fenway. At all vent fields, a thin (~ 50 – 200 μm) discontinuous rim of colloform pyrite and/or marcasite and trace amounts of X–ray amorphous Fe–oxyhydroxide dendrites are present at the exterior of the chimney wall of some samples.

Bulk geochemical analyses of open conduit chimneys are consistent with observed mineral compositions (Table 5.1; Figure 5.5). Relative to open conduit samples from Vienna Woods, those from Roman Ruins and Rogers Ruins are enriched in Cu, Sb, Pb, Ag and Au but depleted in Zn and Cd, and those from Satanic Mills and Fenway are enriched in Cu, Co, Se, Sb and Au, but depleted in Zn, Cd and Ag. On average, Roman Ruins and Roger's Ruins samples are enriched in Zn, Pb, Cd, Ag and depleted in Co and Se relative to Satanic Mills and Fenway samples (Figure 5.6). Electron microprobe analyses show variable concentrations of Zn and Pb in chalcopyrite at Roman Ruins and Roger's Ruins and also of Se in chalcopyrite at Satanic Mills and Fenway. Within chalcopyrite, Se is present only in grains lining the highest–temperature conduits, whereas Zn and Pb are more abundant in grains toward the outer edge of the interior lining. Electron microprobe analyses also document measurable but variable concentrations of Pb, Cd, As, Sb and Ag in sphalerite, of Pb in bornite and of Zn, Pb and As in pyrite/marcasite in exterior sections (Figure 5.7; Appendix E2).

4.1.3. SuSu Knolls

Open conduit chimneys recovered from SuSu Knolls are similar to those from PACMANUS being composed of an interior lining of consolidated chalcopyrite and an exterior anhydrite–dominated layer (Figure 5.3). Rarely bornite and covellite are present rimming chalcopyrite at the boundary with the outer anhydrite–dominated layer. Anhydrite in the outer layer is intergrown with minor amounts of barite and sulfide minerals, predominantly fine–grained chalcopyrite and bornite and lesser pyrite. Sphalerite and galena are absent or present only in trace amounts. In some samples, trace–to–minor amounts of fine–grained tennantite (Cu–As–sulfosalt) are present in exterior sections of open conduit samples.

Bulk chemical analyses are consistent with modal mineral abundances dominated by chalcopyrite and anhydrite with lesser barite and trace tennantite (Table 5.2, Figure 5.5). They document enrichments of Mo, Co, Se and Sb relative to open conduit chimneys from other vent fields. Bulk concentrations of Zn, Pb, Cd and Ag are low relative to open conduit chimneys from PACMANUS, in particular Roman Ruins and Roger's Ruins (Table 5.2, Figure 5.6). Electron microprobe analyses document measurable Se in chalcopyrite, Zn and Pb in bornite and Fe, Zn and Sb in tennantite (Figure 5.7; Appendix E2).

4.2. Diffuser Smokers

4.2.1. Vienna Woods

Active diffuser smokers were not recovered from Vienna Woods. The morphology and composition of relict diffuser–type chimneys sampled from this vent field are discussed below (Section 4.3.1.)

4.2.2. PACMANUS

Examination of polished sections reveals that diffuser smokers at Roman Ruins and

Table 5.2a. Chemical compositions of vent deposit samples from the Eastern Manus Basin. Major elements

Sample	Location	Laboratory	Fe	Cu	Zn	Pb	As	S [‡]	Ca	Ba	SiO_2	Major	Minor	Trace
			Weight Percent (wt %)									X-ray Diffraction Mineral Identification [§]		
							Open Conduit Chimneys							
J2-213-2-R1	RMR.	ALS Chemex	21.20	29.40	4.14	0.24	0.05	20.50	4.20	0.52	N.A.		No powder	
J2-222-4-R1	RMR.	ActLabs	23.00	37.50	0.42	0.03	0.01	19.40	1.42	0.29	N.A.	Cpy	Anh	
J2-213-6-R1	RGR.	ActLabs	19.13	31.00	0.13	0.01	0.02	18.40	4.24	1.30	N.A.	Cpy	Anh	Sph/Wtz
J2-209-1-R1	S.M.	ActLabs	22.38	32.90	0.38	0.03	0.09	> 20.0	2.79	0.14	N.A.	Cpy	Anh	
J2-209-7-R1	S.M.	ActLabs	22.63	30.10	0.17	0.01	0.04	> 20.0	3.80	0.25	N.A.	Cpy	Anh	
J2-214-3-R1	S.M.	ALS Chemex	13.50	40.30	0.25	0.03	0.34	19.00	3.77	0.28	N.A.	Cpy	Bn	Anh
J2-212-1-R1	FW.	ALS Chemex	9.15	5.07	0.50	0.03	0.05	21.60	13.35	0.55	N.A.		No powder	
J2-212-2-R1	FW.	ActLabs	14.50	7.01	1.26	0.04	0.06	> 20.0	13.00	0.81	N.A.	Anh	Cpy	Py/Mc, Sph
J2-212-6-R1	FW.	ALS Chemex	9.28	5.96	0.41	0.02	0.04	23.10	16.00	0.49	N.A.		No powder	
J2-216-15-R1	FW.	ActLabs	7.29	5.67	0.86	0.03	0.03	17.30	15.40	0.29	N.A.	Anh	Cpy	
J2-216-16-R1	FW.	ALS Chemex	11.00	8.93	0.11	0.01	0.02	19.70	14.00	0.18	N.A.	Anh	Cpy	
J2-217-2-R1	SZ.	ActLabs	25.00	32.30	0.03	0.01	0.03	19.60	2.05	0.03	N.A.	Cpy		Anh
J2-217-2-R3	SZ.	ActLabs	28.00	33.80	0.03	0.02	0.02	> 20.0	0.20	0.16	N.A.	Cpy		Anh
J2-217-9-R1	SZ.	ActLabs	23.00	29.40	0.17	0.02	0.04	19.90	2.38	1.50	N.A.	Cpy	Anh	
J2-217-10-R1	SZ.	ActLabs	12.01	9.24	0.10	0.03	0.04	> 20.0	14.50	1.10	N.A.	Cpy, Anh		(Py/Mc?)
J2-219-3-R1	SZ.	ALS Chemex	24.30	25.80	0.11	0.03	0.07	22.40	4.46	1.81	N.A.		No powder	
J2-221-9-R2	N.Su	ALS Chemex	17.15	12.50	0.18	0.06	0.17	26.40	11.35	2.06	N.A.		No powder	
J2-223-1-R1	N.Su	ActLabs	25.50	36.00	0.13	0.03	0.10	> 20.0	0.13	0.61	N.A.	Cpy		Py, Anh
J2-223-13-R1	N.Su	ALS Chemex	2.20	31.60	0.05	0.01	11.95	21.00	0.19	19.95	N.A.	Tn		Py, Anh
J2-223-15-R1	N.Su	ALS Chemex	1.57	1.05	0.02	0.01	0.27	22.30	22.40	0.00	0.28	Anh		Cpy
J2-227-7-R1	N.Su	ActLabs	24.63	20.50	0.01	0.01	0.14	> 20.0	2.86	1.70	N.A.	Cpy, Anh		Ba
J2-227-10-R1	N.Su	ActLabs	12.11	8.53	0.32	0.02	0.13	15.40	5.79	16.00	N.A.	Cpy, Anh	Ba	Py
J2-224-8-R1	S.Su	ActLabs	13.88	13.70	0.03	0.01	0.19	18.30	9.98	5.40	N.A.	Anh, Cpy	Ba	
J2-224-12-R1	S.Su	ALS Chemex	6.25	24.10	1.87	0.29	0.12	21.30	17.35	1.66	N.A.		No powder	

[‡] sulfur analysis is not quantitative owing to possible incomplete digestion of anhydrite and barite

[§] X-ray diffraction carried out on splits of the same powders used for bulk geochemical analysis.

Locations: RMR (Roman Ruins), RGR (Roger's Ruins), S.M (Satanic Mills), SC (Snowcap), TSU (Tsukushi), FW (Fenway), SZ (Suzette), N.Su (North Su), S.Su (South Su).

Table 5.2a. (continued)

Sample	Location		Fe	Cu	Zn	Pb	As	S [‡]	Ca	Ba	SiO_2	Major	Minor	Trace
			Weight Percent (wt %)									X-ray Diffraction Mineral Identification[§]		
							Diffuser Chimneys							
J2-208-1-R3	RMR.	ALS Chemex	8.37	15.20	31.50	1.23	2.03	21.50	0.06	0.00	0.07	Sph	Tn, Cpy	Gal
J2-208-2-R3	RMR.	ALS Chemex	0.32	0.66	39.50	33.00	0.66	24.20	0.05	0.61	N.A.	Sph	Gal	Cpy
J2-208-9-R1	RMR.	ActLabs	0.43	0.13	53.20	2.11	0.53	17.80	0.06	5.00	N.A.	Sph	Ba	Gal
J2-208-10-R1	RMR.	ALS Chemex	19.90	3.61	21.40	6.39	0.52	30.40	0.03	7.38	N.A.		No powder	
J2-213-3-R1	RMR.	ActLabs	7.79	7.54	17.90	0.42	0.12	> 20.0	10.00	1.50	N.A.	Sph, Anh	Cpy	Gal
J2-222-7-R1	RMR.	ALS Chemex	0.70	0.73	59.80	3.50	0.60	28.70	0.05	6.07	N.A.		No powder	
J2-222-8-R2	RMR.	ALS Chemex	10.60	14.50	27.90	2.82	1.23	24.20	2.49	6.04	N.A.		No powder	
J2-222-1-R1	RGR.	ALS Chemex	3.84	21.10	21.10	0.51	1.77	16.90	0.04	0.00	0.26		No powder	
J2-209-5-R1	S.M.	ALS Chemex	3.52	14.10	29.00	1.61	1.69	20.30	0.03	21.40	N.A.		No powder	
J2-209-6-R1	S.M.	ALS Chemex	16.80	28.70	5.49	0.13	1.64	19.70	0.08	0.00	0.10	Cpy	Sph, Ba	
J2-211-4-R2	SC.	ALS Chemex	10.75	32.00	8.87	0.69	2.19	19.70	0.09	16.50	N.A.		No powder	
J2-212-3-R1	FW.	ALS Chemex	8.23	5.74	33.40	0.61	0.39	21.70	0.50	21.10	N.A.		No powder	
J2-212-9-R2	FW.	ALS Chemex	10.95	20.10	11.50	0.37	1.07	15.50	0.06	0.00	0.12	Cpy	Sph	Gal
J2-212-misc	FW.	ALS Chemex	14.20	10.40	14.05	0.40	0.26	19.50	0.57	0.00	0.22	Cpy	Sph	Ba
J2-216-2-R1	FW.	ActLabs	10.16	26.60	6.62	0.15	1.49	16.00	0.23	13.00	N.A.	Cpy	Tn, Ba, Sph	
J2-217-3-R1	SZ.	ALS Chemex	12.90	11.10	0.13	0.04	0.05	24.80	13.80	0.00	0.96	Cpy		Anh
J2-217-13-R1	SZ.	ActLabs	6.11	0.28	0.24	0.04	0.08	16.10	14.60	12.00	N.A.	Anh	Ba, Py	Cpy
J2-219-2-R2	SZ.	ALS Chemex	29.30	29.30	0.08	0.06	0.08	22.10	1.47	1.18	N.A.		No powder	
J2-219-10-R1	SZ.	ALS Chemex	6.03	0.60	4.65	0.65	0.24	10.30	1.04	46.40	N.A.		No powder	
J2-226-2-R1	SZ.	ActLabs	0.38	1.73	29.50	7.17	0.22	15.30	0.05	7.70	N.A.	Sph, Ba	Gal	Cpy
J2-226-4-R1	SZ.	ALS Chemex	9.79	0.74	4.95	0.58	0.43	13.70	0.14	46.50	N.A.		No powder	
J2-226-4-R4	SZ.	ALS Chemex	6.43	0.45	7.07	0.57	0.33	10.75	0.06	48.60	N.A.		No powder	
J2-224-6-R1	S.Su	ALS Chemex	4.11	22.30	2.54	0.03	3.40	12.70	0.56	17.00	N.A.	Tn	Ba, Sph	
J2-224-7-R1	S.Su	ALS Chemex	4.46	25.70	0.33	0.02	4.89	10.30	0.12	36.20	N.A.		No powder	
J2-224-7-R2	S.Su	ALS Chemex	7.56	6.05	0.03	0.01	4.29	11.95	0.06	38.50	N.A.	Tn	Ba	Cpy, Sph

[‡] sulfur analysis is not quantitative owing to possible incomplete digestion of anhydrite and barite

[§] X-ray diffraction carried out on splits of the same powders used for bulk geochemical analysis.

Locations: RMR (Roman Ruins), RGR (Roger's Ruins), S.M (Satanic Mills), SC (Snowcap), TSU (Tsukushi), FW (Fenway), SZ (Suzette), N.Su (North Su), S.Su (South Su).

Table 5.2a. (continued)

Sample	Location		Fe	Cu	Zn	Pb	As	S[‡]	Ca	Ba	SiO_2	Major	Minor	Trace
			Weight Percent (wt %)									X-ray Diffraction Mineral Identification[§]		
							Relic/Inactive Chimneys							
J2-208-1-R2	RMR.	ALS Chemex	1.44	0.72	53.10	2.02	0.82	24.70	0.04	0.00	0.31	Sph	Ba	
J2-208-1-R4	RMR.	ALS Chemex	4.61	1.66	4.45	0.25	0.12	4.66	0.90	0.01	55.20	Am.Si.	Sph	Cpy (Py?)
J2-208-2-R4	RMR.	ALS Chemex	1.30	2.14	56.10	1.34	0.24	26.30	0.06	7.46	N.A.		No powder	
J2-208-2-R4	RMR.	ALS Chemex	0.19	0.84	52.70	13.05	0.76	27.20	0.46	1.84	N.A.		No powder	
J2-208-4-R2	RMR.	ALS Chemex	0.47	0.37	45.80	8.97	1.07	21.70	0.04	0.00	1.79	Sph	Gal, Ba	
J2-222-4-R2	RMR.	ALS Chemex	13.35	13.30	26.20	1.08	0.62	24.10	0.08	0.00	1.81	Cpy, Sph		Ba
J2-222-8-R1	RMR.	ALS Chemex	2.48	5.53	52.20	5.84	1.40	26.20	0.04	5.18	N.A.		No powder	
J2-213-7-R1	RGR.	ALS Chemex	1.71	0.78	42.50	1.59	0.69	20.20	0.39	0.00	1.76	Sph	Cpy, Ba	
J2-222-1-R2	RGR.	ALS Chemex	2.38	11.65	33.50	1.48	1.93	19.85	0.04	22.90	N.A.		No powder	
J2-209-1-R2	S.M.	ALS Chemex	20.80	14.90	19.80	1.22	0.64	29.20	1.19	0.00	0.48		No powder	
J2-209-6-R2	S.M.	ALS Chemex	23.30	19.90	7.22	0.21	1.01	27.20	0.02	0.00	0.24	Cpy	Sph, Py	(Ba?)
J2-209-6-R3	S.M.	ALS Chemex	6.03	20.60	22.00	0.49	3.19	22.20	0.05	0.00	0.60	Sph	Cpy, Tn	(Ba?)
J2-209-7-R2	S.M.	ALS Chemex	27.10	26.90	3.85	0.29	0.32	22.10	0.36	2.74	N.A.		No powder	
J2-209-7-R5	S.M.	ALS Chemex	27.50	34.70	0.99	0.08	0.29	21.40	0.02	0.95	N.A.		No powder	
J2-210-1-R1	SC.	ALS Chemex	5.36	18.45	19.35	0.53	1.22	16.65	0.05	0.00	0.34	Sph	Cpy, Tn	(Ba?)
J2-211-7-R1	SC.	ALS Chemex	0.30	1.90	59.20	2.02	0.72	24.20	0.02	0.00	0.04	Sph	Ba	Tn
J2-214-15-R1	TSU.	ALS Chemex	3.29	0.83	62.20	0.19	0.14	28.10	0.36	0.00	0.54	Sph		
J2-210-4-R1	FW.	ALS Chemex	9.35	19.60	13.20	0.37	2.18	17.50	0.05	0.00	0.39	Tn	Sph, Cpy	Ba
J2-210-7-R1	FW.	ALS Chemex	18.25	38.20	5.35	0.21	0.81	> 20.0	0.14	2.00	N.A.	Cpy	Sph/Wtz	Ba, Tn
J2-210-7-R2	FW.	ALS Chemex	25.00	29.30	0.83	0.06	0.16	20.90	2.55	0.00	0.11	Cpy	Anh	Tn
J2-210-7-R3	FW.	ALS Chemex	10.49	22.50	1.45	0.01	0.65	13.40	0.07	14.00	N.A.	Cpy	Ba	Sph
J2-210-8-R3	FW.	ALS Chemex	4.74	0.64	57.80	0.48	0.24	26.90	0.03	0.00	0.01	Sph		
J2-212-9-R1	FW.	ALS Chemex	7.31	18.10	12.30	0.18	1.12	14.70	0.06	11.00	N.A.	Cpy, Ba		
J2-212-10-R1	FW.	ALS Chemex	1.65	0.51	55.90	0.75	0.57	25.50	0.03	0.00	0.03	Sph		Ba
J2-217-2-R2	SZ.	ALS Chemex	25.20	19.95	1.63	0.26	0.32	21.90	0.11	13.60	N.A.		No powder	
J2-219-1-R2	SZ.	ActLabs	2.56	0.16	11.00	3.12	0.24	8.34	0.05	24.00	N.A.	Ba	Sph	Pb
J2-219-2-R3	SZ.	ALS Chemex	19.30	14.50	8.54	1.15	0.77	23.30	0.07	0.00	4.27	Cpy	Sph	Ba
J2-219-12-R1	SZ.	ALS Chemex	6.83	22.70	2.73	0.26	7.36	15.00	0.04	29.40	N.A.		No powder	
J2-226-4-R3	SZ.	ALS Chemex	10.15	1.03	5.05	0.62	0.35	14.05	0.49	43.40	N.A.		No powder	
J2-226-5-R1	SZ.	ALS Chemex	0.65	0.08	10.85	2.85	0.67	6.99	0.07	50.10	N.A.		No powder	
J2-221-9-R1	N.Su	ALS Chemex	31.80	21.00	0.21	0.07	0.22	28.40	1.87	4.22	N.A.		No powder	
J2-227-9-R1	N.Su	ALS Chemex	15.45	0.07	5.91	0.88	0.71	15.35	0.06	0.00	20.50	Am.Si.	Py, Sph	(Ba?)
J2-227-10-R2	N.Su	ALS Chemex	21.10	17.80	0.41	0.12	0.36	19.05	0.06	25.90	N.A.		No powder	
J2-224-5-R1	S.Su	ALS Chemex	1.02	4.98	34.60	2.73	3.67	19.40	0.06	0.00	0.29	Tn, Sph	Gal, Ba	Cpy
J2-224-5-R2	S.Su	ActLabs	12.60	13.00	0.02	0.01	2.30	15.80	0.08	19.00	N.A.	Cpy, Ba	Tn	

[‡] sulfur analysis is not quantitative owing to possible incomplete digestion of anhydrite and barite

[§] X-ray diffraction carried out on splits of the same powders used for bulk geochemical analysis.

Locations: RMR (Roman Ruins), RGR (Roger's Ruins), S.M (Satanic Mills), SC (Snowcap), TSU (Tsukushi), FW (Fenway), SZ (Suzette), N.Su (North Su), S.Su (South Su).

Table 5.2a. (continued)

Sample	Location		Fe	Cu	Zn	Pb	As	S ‡	Ca	Ba	SiO_2	Major	Minor	Trace
			Weight Percent (wt %)									X-ray Diffraction Mineral Identification §		
							Fe-rich Massive Sulfide/Talus							
J2-212-4-R1	FW.	ALS Chemex	20.30	20.60	4.36	0.08	0.10	17.15	0.02	0.01	0.15	Cpy	Sph, Ba	
J2-212-5-R1	FW.	ALS Chemex	34.00	9.09	1.22	0.06	0.11	34.50	0.04	0.00	0.15	Py, Cpy		Ba
J2-212-7-R1	FW.	ALS Chemex	22.50	15.50	0.19	0.01	0.02	21.00	0.96	26.70	N.A.		No powder	
J2-216-7-R1	FW.	ALS Chemex	32.90	4.56	3.78	0.15	0.25	35.30	0.05	0.00	0.64	Py, Cpy	Cpy, Ba	Sph
J2-216-8-R1-GC	FW.	ALS Chemex	2.63	0.24	32.30	1.61	0.69	17.45	0.03	0.00	4.46	Sph	Ba	
J2-216-9-R1-GC	FW.	ALS Chemex	38.30	1.48	0.80	0.10	0.27	37.80	0.16	8.11	N.A.		No powder	
J2-217-12-R1	SZ.	ALS Chemex	35.40	18.50	0.05	0.07	0.46	33.50	0.03	0.72	N.A.		No powder	
J2-219-4-R1	SZ.	ALS Chemex	24.10	3.92	1.08	0.06	0.17	26.20	0.06	0.01	23.90	Py	Ba	
J2-219-5-R1	SZ.	ALS Chemex	29.10	27.90	0.02	0.03	0.11	22.80	0.02	0.00	0.88	Cpy	Py	
J2-219-5-R2	SZ.	ALS Chemex	30.00	29.10	0.14	0.02	0.11	22.70	0.02	0.00	1.69	Cpy	Py	
J2-226-1-R1	SZ.	ALS Chemex	27.13	29.40	0.08	0.04	0.10	21.60	0.82	0.12	N.A.	Cpy	Py	Ba, Anh
J2-226-1-R1	SZ.	ALS Chemex	25.30	22.10	1.04	0.20	0.19	23.30	0.04	0.01	9.03	Cpy	Py	Ba, Anh
J2-226-8-R1	SZ.	ALS Chemex	4.27	0.65	18.25	0.84	0.10	12.30	0.04	0.00	8.30	Sph	Ba	Cpy
J2-223-12-R2	N.Su	ALS Chemex	29.60	1.80	0.03	0.04	0.49	32.00	0.45	2.62	N.A.		No powder	

‡ sulfur analysis is not quantitative owing to possible incomplete digestion of anhydrite and barite

§ X-ray diffraction carried out on splits of the same powders used for bulk geochemical analysis.

Locations: RMR (Roman Ruins), RGR (Roger's Ruins), S.M (Satanic Mills), SC (Snowcap), TSU (Tsukushi), FW (Fenway), SZ (Suzette), N.Su (North Su), S.Su (South Su).

Table 5.2b. Chemical compositions of vent deposit samples from the Eastern Manus Basin. Trace elements.

Sample	Location	Co	Se	Mo	Cd	Sb	Ag	Au	Mn	Sr
		Parts Per Million (ppm)								
		Open Conduit Chimneys								
J2-213-2-R1	RMR.	<1	13	81	127	111	76	5.1	125	N.A.
J2-222-4-R1	RMR.	1	51	15	13	8	8	1.2	80	83
J2-213-6-R1	RGR.	1	< 1	15	4	43	22	11.2	210	184
J2-209-1-R1	S.M.	< 1	< 1	83	14	475	13	3.5	36	200
J2-209-7-R1	S.M.	< 1	44	76	6	133	8	3.0	14	296
J2-214-3-R1	S.M.	< 1	< 1	37	9	519	54	18.8	32	254
J2-212-1-R1	FW.	69	95	26	13	24	8	1.2	33	N.A.
J2-212-2-R1	FW.	22	58	55	26	31	16	1.7	33	790
J2-212-6-R1	FW.	50	107	38	11	24	8	1.2	21	N.A.
J2-216-15-R1	FW.	12	96	49	20	44	14	2.2	44	1310
J2-216-16-R1	FW.	4	108	31	3	14	10	1.1	130	1150
J2-217-2-R1	SZ.	39	1450	53	2	33	9	1.5	15	232
J2-217-2-R3	SZ.	56	878	59	3	21	22	1.6	17	47
J2-217-9-R1	SZ.	8	383	12	10	52	11	1.4	105	188
J2-217-10-R1	SZ.	21	111	26	8	93	23	3.9	80	1250
J2-219-3-R1	SZ.	9	264	31	9	94	15	2.8	33	N.A.
J2-221-9-R2	N.Su	260	378	574	9	67	23	7.8	10	N.A.
J2-223-1-R1	N.Su	125	1900	414	8	56	11	3.2	26	55
J2-223-13-R1	N.Su	3	48	18	2	4980	17	15.8	10	N.A.
J2-223-15-R1	N.Su	103	N.A.	13	1	105	1	0.8	8	3730
J2-227-7-R1	N.Su	472	593	652	1	280	17	9.2	8	303
J2-227-10-R1	N.Su	9	116	127	23	139	30	5.2	17	618
J2-224-8-R1	S.Su	3	< 1	22	1	229	3	7.8	6	865
J2-224-12-R1	S.Su	<1	3	39	2	96	140	3.2	3	N.A.

N.A. indicates species not analyzed.

Locations: RMR (Roman Ruins), RGR (Roger's Ruins), S.M (Satanic Mills), SC (Snowcap), TSU (Tsukushi), FW (Fenway), SZ (Suzette), N.Su (North Su), S.Su (South Su).

Table 5.2b. (continued)

Sample	Location	Co	Se	Mo	Cd	Sb	Ag	Au	Mn	Sr
		Parts Per Million (ppm)								
		Diffuser Chimneys								
J2-208-1-R3	RMR.	<1	N.A.	10	705	871	267	13.7	49	72
J2-208-2-R3	RMR.	<1	15	4	1125	5370	756	0.1	42	N.A.
J2-208-9-R1	RMR.	2	< 1	11	1560	209	111	0.0	36	17
J2-208-10-R1	RMR.	<1	18	90	307	779	278	5.0	466	N.A.
J2-213-3-R1	RMR.	< 1	< 1	9	791	597	143	67.9	107	571
J2-222-7-R1	RMR.	<1	23	6	1575	612	785	10.1	46	N.A.
J2-222-8-R2	RMR.	<1	11	99	831	2910	428	69.9	68	N.A.
J2-222-1-R1	RGR.	<1	N.A.	5	677	1520	566	2.1	22	114
J2-209-5-R1	S.M.	<1	12	42	803	35	333	17.2	26	N.A.
J2-209-6-R1	S.M.	<1	N.A.	52	122	919	87	26.9	31	104
J2-211-4-R2	SC.	<1	6	124	114	2610	234	97.8	215	N.A.
J2-212-3-R1	FW.	<1	17	22	802	869	363	41.1	53	N.A.
J2-212-9-R2	FW.	<1	N.A.	10	217	430	126	9.0	24	122
J2-212-misc	FW.	<1	N.A.	29	275	237	141	8.7	33	225
J2-216-2-R1	FW.	< 1	< 1	31	153	1050	98	50.4	17	45
J2-217-3-R1	SZ.	57	N.A.	64	7	66	14	2.6	53	1960
J2-217-13-R1	SZ.	19	< 1	7	18	73	24	4.3	124	1230
J2-219-2-R2	SZ.	29	146	58	5	152	19	4.3	57	N.A.
J2-219-10-R1	SZ.	14	13	27	299	834	60	5.9	119	N.A.
J2-226-2-R1	SZ.	< 1	< 1	31	3550	< 5	1030	0.4	9	87
J2-226-4-R1	SZ.	31	6	19	364	548	125	9.4	93	N.A.
J2-226-4-R4	SZ.	20	6	18	506	644	144	8.2	54	N.A.
J2-224-6-R1	S.Su	< 1	< 1	18	134	5280	367	17.5	7	347
J2-224-7-R1	S.Su	<1	2	13	20	1195	103	15.5	6	N.A.
J2-224-7-R2	S.Su	<1	3	16	72	1420	2	11.9	8	N.A.

N.A. indicates species not analyzed.

Locations: RMR (Roman Ruins), RGR (Roger's Ruins), S.M (Satanic Mills), SC (Snowcap), TSU (Tsukushi), FW (Fenway), SZ (Suzette), N.Su (North Su), S.Su (South Su).

Table 5.2b. (continued)

Sample	Location	Co	Se	Mo	Cd	Sb	Ag	Au	Mn	Sr
		Parts Per Million (ppm)								
		Relic/Inactive Chimneys								
J2-208-1-R2	RMR.	<1	N.A.	5	1640	1280	632	15.4	60	77
J2-208-1-R4	RMR.	10	N.A.	11	147	159	56	5.4	1100	242
J2-208-2-R4	RMR.	<1	20	13	1815	4100	910	118.0	61	N.A.
J2-208-2-R4	RMR.	<1	23	4	1550	2580	1005	2.1	26	N.A.
J2-208-4-R2	RMR.	<1	N.A.	6	755	1120	567	3.3	52	104
J2-222-4-R2	RMR.	<1	N.A.	127	738	731	340	50.9	46	92
J2-222-8-R1	RMR.	<1	22	5	1440	262	577	2.5	36	N.A.
J2-213-7-R1	RGR.	<1	N.A.	8	1415	1475	613	7.5	53	84
J2-222-1-R2	RGR.	<1	13	5	1035	1535	500	1.5	34	N.A.
J2-209-1-R2	S.M.	13	N.A.	74	354	541	154	13.8	2520	122
J2-209-6-R2	S.M.	<1	N.A.	20	153	688	79	8.7	991	38
J2-209-6-R3	S.M.	<1	N.A.	23	343	687	175	16.1	3230	62
J2-209-7-R2	S.M.	<1	10	97	88	453	67	10.2	196	N.A.
J2-209-7-R5	S.M.	<1	18	158	24	626	30	12.8	29	N.A.
J2-210-1-R1	SC.	<1	N.A.	12	499	38	310	3.9	929	176
J2-211-7-R1	SC.	<1	N.A.	4	1675	11	516	1.8	82	118
J2-214-15-R1	TSU.	<1	N.A.	40	2160	925	251	66.5	264	85
J2-210-4-R1	FW.	<1	N.A.	18	264	82	203	10.9	47	126
J2-210-7-R1	FW.	< 1	< 1	56	140	797	95	17.4	28	46
J2-210-7-R2	FW.	<1	N.A.	59	16	236	40	7.4	8	351
J2-210-7-R3	FW.	4	< 1	27	69	530	82	10.3	34	124
J2-210-8-R3	FW.	<1	N.A.	9	1430	924	534	10.5	72	96
J2-212-9-R1	FW.	< 1	< 1	15	308	499	127	13.0	22	33
J2-212-10-R1	FW.	<1	N.A.	6	1775	338	611	15.4	546	92
J2-217-2-R2	SZ.	106	320	148	97	225	59	4.6	38	N.A.
J2-219-1-R2	SZ.	< 1	< 1	9	718	1260	194	0.6	33	91
J2-219-2-R3	SZ.	60	N.A.	232	437	922	302	32.1	328	320
J2-219-12-R1	SZ.	<1	3	10	326	47	501	1.9	7	N.A.
J2-226-4-R3	SZ.	32	7	18	363	565	133	10.3	88	N.A.
J2-226-5-R1	SZ.	1	5	5	551	1430	113	1.6	489	N.A.
J2-221-9-R1	N.Su	413	1050	870	12	88	36	7.6	65	N.A.
J2-227-9-R1	N.Su	3	N.A.	21	252	481	79	7.5	76	514
J2-227-10-R2	N.Su	<1	60	1360	24	295	33	6.7	29	N.A.
J2-224-5-R1	S.Su	<1	N.A.	31	1690	968	419	3.6	22	172
J2-224-5-R2	S.Su	< 1	< 1	15	1	1440	38	6.2	1420	273

N.A. indicates species not analyzed.

Locations: RMR (Roman Ruins), RGR (Roger's Ruins), S.M (Satanic Mills), SC (Snowcap), TSU (Tsukushi), FW (Fenway), SZ (Suzette), N.Su (North Su), S.Su (South Su).

Table 5.2b. (continued)

Sample	Location	Co	Se	Mo	Cd	Sb	Ag	Au	Mn	Sr
		Parts Per Million (ppm)								
		Fe-rich Massive Sulfide/Talus								
J2-212-4-R1	FW.	<1	N.A.	24	92	90	58	3.7	27	46
J2-212-5-R1	FW.	<1	N.A.	35	26	57	31	5.4	37	70
J2-212-7-R1	FW.	2	12	34	6	25	7	3.4	12	N.A.
J2-216-7-R1	FW.	5	N.A.	83	62	75	57	3.5	287	115
J2-216-8-R1-GC	FW.	<1	N.A.	7	992	1065	297	7.7	135	120
J2-216-9-R1-GC	FW.	<1	2	47	15	21	15	4.2	358	N.A.
J2-217-12-R1	SZ.	430	202	149	3	111	33	10.4	32	N.A.
J2-219-4-R1	SZ.	6	N.A.	86	63	153	48	2.4	95	219
J2-219-5-R1	SZ.	133	N.A.	48	1	140	20	6.8	28	161
J2-219-5-R2	SZ.	84	N.A.	55	4	185	49	14.8	33	158
J2-226-1-R1	SZ.	233	811	419	6	36	11	4.3	35	87
J2-226-1-R1	SZ.	348	N.A.	554	52	130	71	6.6	56	254
J2-226-8-R1	SZ.	2	N.A.	24	1125	370	187	31.5	39	216
J2-223-12-R2	N.Su	5	74	5	2	81	32	2.2	166	N.A.

N.A. indicates species not analyzed.

Locations: RMR (Roman Ruins), RGR (Roger's Ruins), S.M (Satanic Mills), SC (Snowcap), TSU (Tsukushi), FW (Fenway), SZ (Suzette), N.Su (North Su), S.Su (South Su).

Roger's Ruins are composed of a porous exterior framework of dendritic and anhedral sphalerite, intergrown with minor amounts of barite. In most sections examined, anhydrite is absent or present only in trace amounts. Galena is a trace–to–minor constituent of these chimneys, occurring as fine–grained disseminated euhedral grains in outer portions of walls. Sphalerite is over–plated by sulfide minerals within interior portions of chimneys, predominantly by subhedral grains (~ 200 to 250 μm) of bornite, covellite and trace chalcopyrite that form rims around anastomosing micro–channels (Figure 5.4f). In one section (J2–208–2–R3, Roman Ruins), galena is abundant (~ 33 wt % Pb) and forms consolidated aggregates up to 400 – 500 μm around narrow micro–channels (Figure 5.4g).

Examination of polished sections of diffusers from Satanic Mills, Snowcap and Fenway reveals that they are characterized by thick chimney walls composed of a porous framework of fine–grained Cu–Fe–sulfide (bornite + chalcopyrite), with minor tennantite and sphalerite, intergrown with minor amounts of barite laths in exterior portions of chimneys walls. Cu–Fe–sulfides are most abundant in interior portions of chimneys, locally forming rims up to 200 to 250 μm thick around numerous tortuous micro–channels (Figure 5.4h). Bornite is rimmed by chalcopyrite, and in places exsolved with chalcopyrite. Bornite is also intergrown and rimmed with trace amounts of covellite, chalcocite and digenite in some samples, particularly at the exterior of Cu–Fe–sulfide dominated inner portions. Tennantite is present in minor amounts as fine–grained subhedral grains (< 20 – 140 μm) disseminated within subhedral bornite distal from fluid conduits. Sphalerite is limited to exterior layers of chimney walls where Cu–Fe–sulfides are absent or present only in trace amounts. Sphalerite forms small dendrites (< 100 μm to 300 μm in length) that are over–grown by later colloform Fe–poor sphalerite (Figure 5.4i). Interstices between sphalerite dendrites contain trace

4.2.3. SuSu Knolls

In general, diffuser smokers recovered from SuSu Knolls are composed of a thick outer chimney wall of fine–to–medium grained (~ 200 – 250 μm) subhedral Cu–Fe–sulfide (as bornite and lesser chalcopyrite) and minor Cu–As–sulfosalt (tennantite), intergrown with minor amounts of acicular barite laths (mostly < 300 μm in length; Figure 5.4j). Sphalerite is present only in minor amounts and galena present in only trace amounts in most diffuser samples. In some samples, sphalerite and galena are absent entirely. In larger samples, tennantite and, to a lesser extent, bornite form consolidated thin rims around anastomosing channelways in interior portions of diffusers. At SuSu Knolls, only one active lower–temperature (249 °C) sample (J2–226–2–R1, Suzette) forming at the cusp of a sulfide–rich crust or pavement contains significant sphalerite. The sample is composed predominantly of dendritic low–Fe sphalerite intergrown with minor acicular barite (Figure 5.4k). Sphalerite in interior portions of sample is over–plated by trace amounts of tennantite and sphalerite in outer portions contains disseminated fine–grained euhedral galena.

Bulk chemical analyses show that, on average, diffuser chimneys at SuSu Knolls are Cu– and Ba–rich and Zn– and Pb–poor relative to those from PACMANUS (Roman Ruins and Roger's Ruins) and contain variable As (Figure 5.5). Bulk chemical analyses show variable concentrations of Se, Co, Mo and Sb, but low concentrations of Cd, Ag and Au (Table 5.2; Figure 5.6). Sample J2–226–2–R1 exhibits high concentrations of Zn, Pb, Cd and Ag, and low concentrations of Cu, Co, Se, As and Sb relative to other SuSu Knolls diffuser samples. Electron microprobe analyses document measurable concentrations of Pb and rarely of Zn, As, Sb and Ag in chalcopyrite, of Zn and Ag in bornite and of Fe, Sb, Zn, Pb and Ag in tennantite. Electron microprobe analyses also document the presence of Pb, Cd and, in some

grains, of Cu, As, Sb and Ag in sphalerite, and variable concentrations of Zn and Cd in galena (Figure 5.7; Appendix E2).

4.3. Relict Chimneys

4.3.1. Vienna Woods

As presented in hand specimen, most relict chimney structures comprise a porous framework of Zn–sulfide (sphalerite and wurtzite) forming thick walls containing multiple tortuous micro–channels typically < 5 mm in diameter (Figure 5.3). These channelways are commonly lined by thin (mostly < 1 mm) layers of pyrite or chalcopyrite that, in turn, may also be enclosed in Zn–sulfide, the hexagonal crystal habit of which indicates likely wurtzite in some samples. Chalcopyrite and pyrite are present in lesser amounts in the Zn–sulfide matrix away from obvious channelways. Anhydrite and barite are absent in most relict chimneys, or occur in only trace amounts. X–ray amorphous silica is common. Polished sections are not available for relict chimneys sampled from Vienna Woods and so unambiguous identification of sulfide and other minerals, and of textural and paragenetic relationships among minerals, is precluded. These samples appear similar in morphology and mineralogy to Zn–rich chimneys forming from lower–temperature (< 280 °C) white smoker fluids sampled at the Cleft Segment, Juan de Fuca Ridge (Koski et al., 1984; Koski et al., 1994) and TAG active mound, 26 °N Mid–Atlantic Ridge (Tivey et al., 1995).

Bulk chemical and XRD analyses are consistent with mineralogical compositions dominated by sphalerite and/or wurtzite, lesser amounts of pyrite and/or marcasite and amorphous silica, and trace amounts of chalcopyrite, galena, anhydrite and barite (Table 5.1; Figure 5.5). Bulk geochemical analyses show lower concentrations of Pb, Co, Se, As, Sb and Au in relict chimneys from Vienna Woods relative to relict and diffuser chimney deposits

from PACMANUS and SuSu Knolls (Table 5.1, Figure 5.6). Relative to high–temperature open conduit chimneys recovered from Vienna Woods, concentrations of Pb, Ag, As, Sb and Au are higher and concentrations of Co and Se lower in relict deposits (Figure 5.5 and 5.6).

4.3.2. PACMANUS

In general, the morphology and composition of relict deposits at PACMANUS are similar to active diffuser smokers recovered from the same vent field (Section 4.2.2.). At Roman Ruins and Roger's Ruins, most relict chimneys are composed of an exterior wall of dendritic and colloform sphalerite intergrown with minor amounts of barite laths (200 – 400 μm in length) and containing trace amounts of disseminated fine–grained (< 100 μm) euhedral galena. Minor amounts of Cu–Fe–sulfides (bornite + chalcopyrite ± covellite ± chalcocite) are present in interior portions of relict chimneys, in places forming rims around former micro–channels for fluid flow. Bulk chemical analyses are consistent with modal mineral assemblages dominated by sphalerite and/or wurtzite, minor Cu–Fe–sulfides and barite, and trace galena (Table 5.2; Figure 5.5). Concentrations of As, Sb, Cd, Ag and Au are similar in relict samples relative to active diffuser samples, but high relative to active open conduit smokers (Figure 5.6). In contrast, concentrations of Co, Mo and Se are lower in relict deposits relative to active open conduit chimney samples (Table 5.2; Figure 5.6).

At Satanic Mills, Snowcap and Fenway, most relict chimneys comprise a porous exterior framework of mixed fine–grained anhedral bornite and tennantite intergrown with minor amounts of fine–grained acicular barite and very variable amounts of dendritic and colloform sphalerite (Figure 5.4l). Bulk chemical analyses show that relict deposits from Satanic Mills, Snowcap and Fenway have higher Cu and lower Zn and Pb relative to relict deposits from Roman Ruins and Roger's Ruins (Figure 5.5). Relict deposits exhibit lower

concentrations of Sb, Cd, Ag and Au relative to those from Roman Ruins and Roger's Ruins. Electron microprobe analyses document measurable concentrations of Pb, Zn and Ag in some chalcopyrite and bornite grains, Fe, Cu, Cd, Pb and variable Ag in sphalerite grains, Fe, Zn, Pb, Sb and Ag in tennantite grains, and Cu and Zn in galena (Figure 5.7; Appendix E2).

4.3.3. SuSu Knolls

Relict samples recovered from SuSu Knolls are similar in morphology and texture to active diffuser–type chimney samples from the same vent field. Relict chimneys are composed of a several cm thick exterior framework of variable amounts of fine–grained subhedral Cu–Fe–sulfide (bornite) and/or dendritic Zn–sulfide (sphalerite), intergrown with minor amounts of barite laths. In some inner portions of relict chimneys Cu–Fe–sulfides (bornite ± chalcopyrite) and Cu–sulfosalts (tennantite) plate the sulfide framework forming discontinuous rims around anastomosing micro–channels in the absence of a well–defined central open conduit (Figure 5.4). Bulk chemical analyses are consistent with modal mineral compositions dominated by Cu–Fe–sulfides (bornite, chalcopyrite) and barite, minor and variable sphalerite and tennantite, and trace pyrite and galena (Table 5.2). At SuSu Knolls, chemical compositions of relict samples are comparable to those of active diffuser samples (Figure 5.5). Bulk chemical analyses of relict samples document concentrations of Zn, Pb, As, Sb, Ag and Au similar to active diffuser smokers, but higher than open conduit smokers. In contrast, relict samples have lower concentrations of Cu, Co and Se relative to open conduit smokers (Table 5.2, Figure 5.6). Where electron microprobe analyses are available, the data document measurable concentrations of Cu, Pb, As, Cd and Ag in sphalerite grains, Fe, Zn, Sb, Pb and Ag in tennantite grains and Cu, Pb, Zn and rarely Ag in pyrite (Figure 5.7; Appendix E2).

5. DISCUSSION

5.1. Mineral chemistry of Manus Basin vent deposits: Influence of fluid composition and conditions of mineral precipitation

Open conduit chimneys recovered from all vent fields are cylindrical and composed of an inner sulfide lining and an outer more porous mixture of anhydrite and lesser finer–grained sulfide (e.g., Figure 5.3b, c). These chimneys are conduits for focused high–temperature seafloor fluid venting. The physical characteristics of the growth of these chimneys have been discussed in detail previously (Goldfarb et al., 1983; Haymon, 1983; Tivey and McDuff, 1990). In contrast, diffuser chimneys are typically composed of a porous framework of fine–grained sulfide and minor barite, with different sulfide minerals forming linings along networks of narrow anastomosing micro–channels (Figure 5.3a). The morphology of these chimneys is consistent with the formation of these chimneys from lower temperature, less focused fluids (e.g., Fouquet et al., 1993b; Koski et al., 1994) with styles fluid flow and conditions of sulfide precipitation very different to those for open conduit smokers. Relict chimneys have textures, morphologies and mineral compositions similar to diffuser chimneys, and the conditions of formation relevant to relict chimneys are inferred to be similar to active diffusers.

5.1.1. Vienna Woods Open Conduit and Diffuser–type chimneys

Active high–temperature open conduit chimneys from Vienna Woods are Zn–rich but Cu–poor relative to most high–temperature deposits from basalt–hosted mid–ocean ridge systems (Haymon and Kastner, 1981; Goldfarb et al., 1983; Fouquet et al., 1988; Fouquet et

al., 1993b; Tivey et al., 1995). The presence of wurtzite and trace amounts of co–precipitated chalcopyrite lining open conduit chimneys at Vienna Woods indicates saturation of Zn–sulfide at relatively high–temperatures, approximately that of hydrothermal fluids exiting from these chimneys (~ 270 – 280 °C). A temperature for wurtzite precipitation can be estimated from the FeS content in ZnS knowing the activity (or fugacity) of sulfur (fS_2) in the fluid (Scott, 1976, 1983). The sulfur fugacity can be calculated using thermodynamic calculations that predict aqueous species distributions at in situ temperatures and pressures. For Vienna Woods fluid compositions (sample VW1; Table 5.3), the calculated $\log fS_2$ is approximately – 10.7 to – 10.5. This sulfur fugacity occurs in the region of FeS activity buffered by chalcopyrite–pyrite stability (as opposed to pyrite–pyrrhotite, for example), as supported by the presence of minor chalcopyrite and trace pyrite in Vienna Woods open conduit chimneys. For a measured FeS content of ~ 6 – 7 mol% in wurtzite from Vienna Woods and sulfur fugacity of – 10.5, a temperature of between 275 and 285 °C for the precipitation of wurtzite is calculated (see Figure 1 of Scott, 1983). This is in the range of measured temperatures of hydrothermal fluids exiting from wurtzite–lined chimneys at Vienna Woods (~ 273 – 282 °C).

Geochemical calculations that consider the VW1 fluid composition (Table 5.3) also indicate fluid pH at in situ temperature (280 °C) and pressure (~ 250 bars) of ~ 5.1 (Figure 5.8a). (In situ pH was calculated by obtaining total proton concentration by distributing aqueous species at 25 °C using measured pH and then re–distributing aqueous species using the resulting proton–balanced composition at in situ temperature and pressure with mineral saturation suppressed; e.g., Tivey and McDuff (1990), Tivey(1995)). At this pH, sphalerite is calculated to be saturated at temperatures less than ~ 290 °C (Figure 5.8b), similar to

Table 5.3. Chemical compositions of vent fluids used for aqueous species distribution calculations

	V. Woods	PACMANUS				DESMOS	SuSu Knolls	
		Roman Ruins		Satanic Mills			North Su	Suzette
	VW1	RMR2	RMR4	SM1	SM2	D1	NS2	SZ5
Temperature (°C)	282	272	341	295	241	117	215	249
pH (25 °C)	4.4	2.3	2.6	2.6	2.4	1.0	0.9	2.3
Mg (mmol/kg)	0.0	16.5	3.2	8.8	17.4	46.0	38.8	6.4
Cl (mmol/kg) ‡	663	529	625	499	437	475	425	586
SO_4 (mmol/kg) ‡	0.6	3.0	1.1	2.1	7.1	147	149	4.1
Na (mmol/kg) ‡	512	435	495	407	374	391	340	493
K (mmol/kg)	21.2	50.5	77.2	60.5	38.6	8.3	7.8	44.3
Ca (mmol/kg) ‡	80.0	10.5	22.3	12.5	5.9	9.4	8.9	24.2
Ba (μmol/kg) ‡	55	18	92	20	16	1	N.D.	16
Mn (μmol/kg)	349	2271	2830	2145	1853	40	81	243
Fe (μmol/kg)	159	990	6468	2790	1045	12400	3103	3961
Zn (μmol/kg)	33	2200	440	300	223	230	63	305
Cu (μmol/kg)	4.0	44	190	120	580	4.1	5.6	1030
Pb (μmol/kg)	0.3	80.0	8.0	5.8	5.0	6.5	1.6	14.7
SiO_2 (mmol/kg) ‡	15.3	13.5	17.8	12.2	12.8	8.1	10.0	14.1
H_2S (mmol/kg) ‡	2.0	2.9	6.3	8.0	4.5	0.0	0.0	4.8
H_2 (μmol/kg) ‡	42.0	28.5	53.0	25.0	4.3	4.0	20.0	7.4
CO_2 (mmol/kg) ‡	4.4	18.8	9.5	181	112	26.7	93	15.8
F (μmol/kg) ‡	21	92	125	167	287	137	103	480

‡ Data for dissolved gases and major aqueous species provided by E. Reeves and J. Seewald (*unpublished data*). Metal data are taken from Chapter 4. N.D. denotes no data.

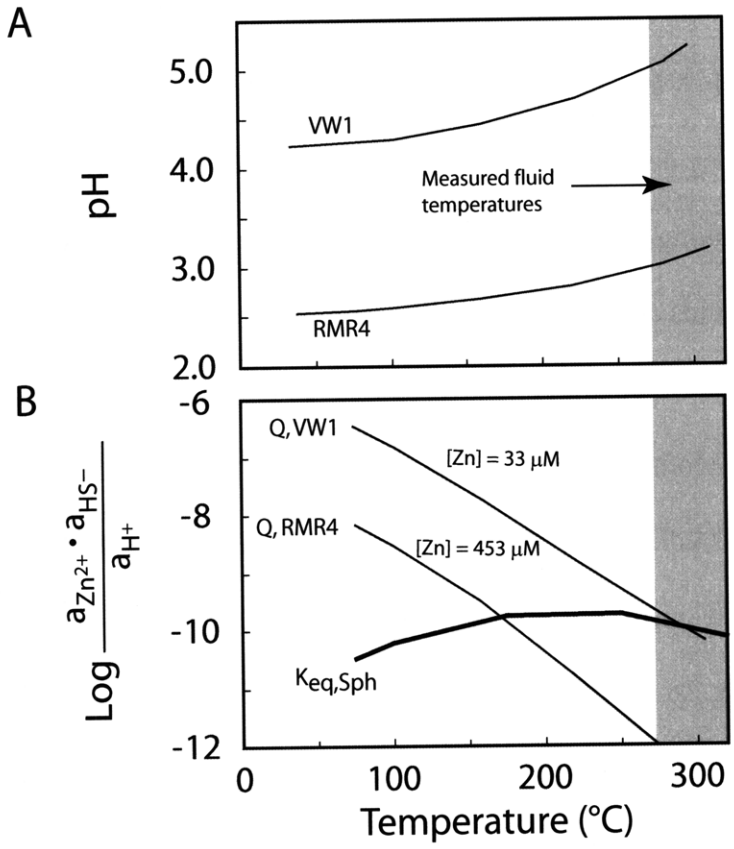

Figure 5.8. Results of species distribution calculations for high-temperature vent fluids exiting Open Conduit chimneys from from Vienna Woods (VW1) and PACMANUS (RMR4). (**A**) pH as a function of temperature. pH is calculated up to 350 °C by speciating the fluid composition at incremental temperatures with mineral precipitation suppressed. (**B**) Equilibrium constant (K) for sphalerite (thick black line) compared with the reaction quotient (Q) for each fluid for a range of temperature. The reaction quotient is calculated as the product of the Zn^{2+} and HS^- activity divided by the proton activity for each vent fluid. Sphalerite is predicted to be saturated at all temperatures where Q > K. Owing to the high pH of vent fluids from Vienna Woods, sphalerite is saturated at significantly higher temperature despite lower concentrations of Zn in these fluids relative to those from PACMANUS. Fluid compositions used in calculations are shown in table 5.3.

temperatures estimated using the ZnS geobarometer and similar to the temperatures of fluids exiting the seafloor at Vienna Woods. Chalcopyrite is calculated to be saturated at temperatures < 300 – 310 °C (i.e., saturated at temperature at which Vienna Woods fluids exit the seafloor). Saturation of sphalerite occurs at high temperatures despite the low concentrations of Zn in Vienna Woods vent fluids (< 33 μmol/kg; see Chapter 4). When Vienna Woods chimney deposit compositions are compared to those of the fluids from which chimneys are precipitating (Figure 5.9a), it is clear that Vienna Woods deposits are Zn–rich, but not because the fluids are also Zn–rich. The lack of correlation between Zn concentrations in vent deposits and Zn concentrations in vent fluids with high pH has been described for the Main Endeavour and Mothra vent fields (Tivey et al., 1999; Kristall et al., 2006).

Experimental studies (e.g., Ruaya and Seward, 1986; Barrett and Anderson, 1988) and theoretical calculations (e.g., Janecky and Shanks, 1988; Tivey and McDuff, 1990; Tivey, 1995) have shown that Zn–sulfides are under–saturated in most seafloor hydrothermal fluids to temperatures ~ 220 – 240 °C. Primarily, this reflects the influence of moderately acid pH (25 °C), between 3.5 and 4, of many seafloor vent fluids (Von Damm, 1990, 1995). In contrast, at Vienna Woods measured fluid pH (25 °C) is higher (≥ 4.2 – 4.7) and in situ pH is greater than 5. The prevalence of wurtzite in high–temperature vent deposits at Vienna Woods reflects higher pH, which results in saturation of Zn–sulfide (sphalerite and wurtzite) at significantly higher temperatures, as it does at the Main Endeavour and Mothra vent fields along the Endeavour Segment, Juan de Fuca Ridge (Tivey et al., 1999; Kristall et al., 2006). The high pH of the Vienna Woods vent fluids, relative to that of most mid–ocean ridge fluids, is likely related to fluid–rock interaction occurring at lower temperatures (< 400 °C) and rock–dominated conditions (low effective water/rock ratio; see chapter 4). The pH of evolved

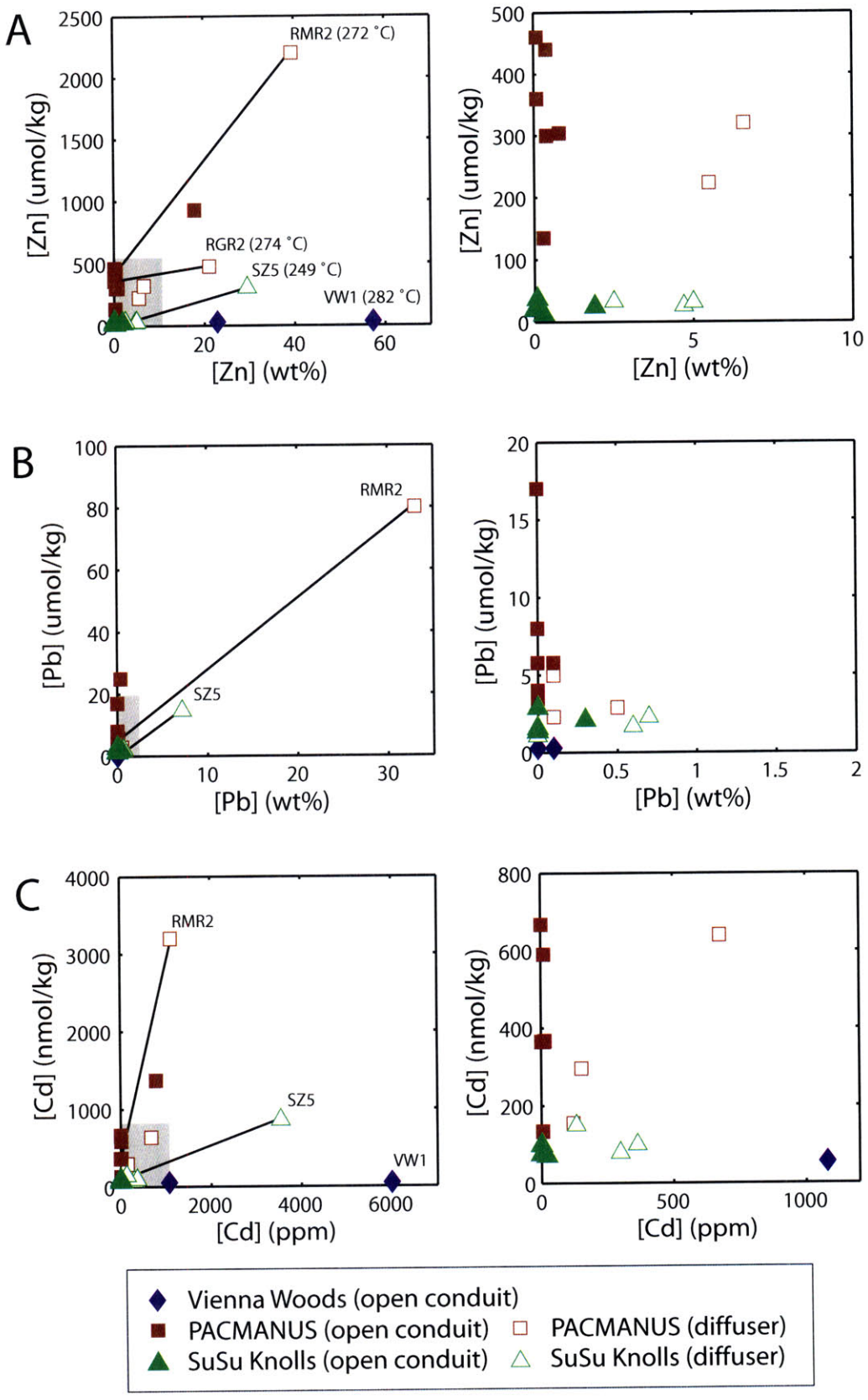
A
[Zn] (umol/kg)
[Zn] (wt%)
RMR2 (272 °C)
RGR2 (274 °C)
SZ5 (249 °C)
VW1 (282 °C)
B
[Pb] (umol/kg)
[Pb] (wt%)
RMR2
SZ5
C
[Cd] (nmol/kg)
[Cd] (ppm)
RMR2
SZ5
VW1
Vienna Woods (open conduit)
PACMANUS (open conduit)
SuSu Knolls (open conduit)
PACMANUS (diffuser)
SuSu Knolls (diffuser)

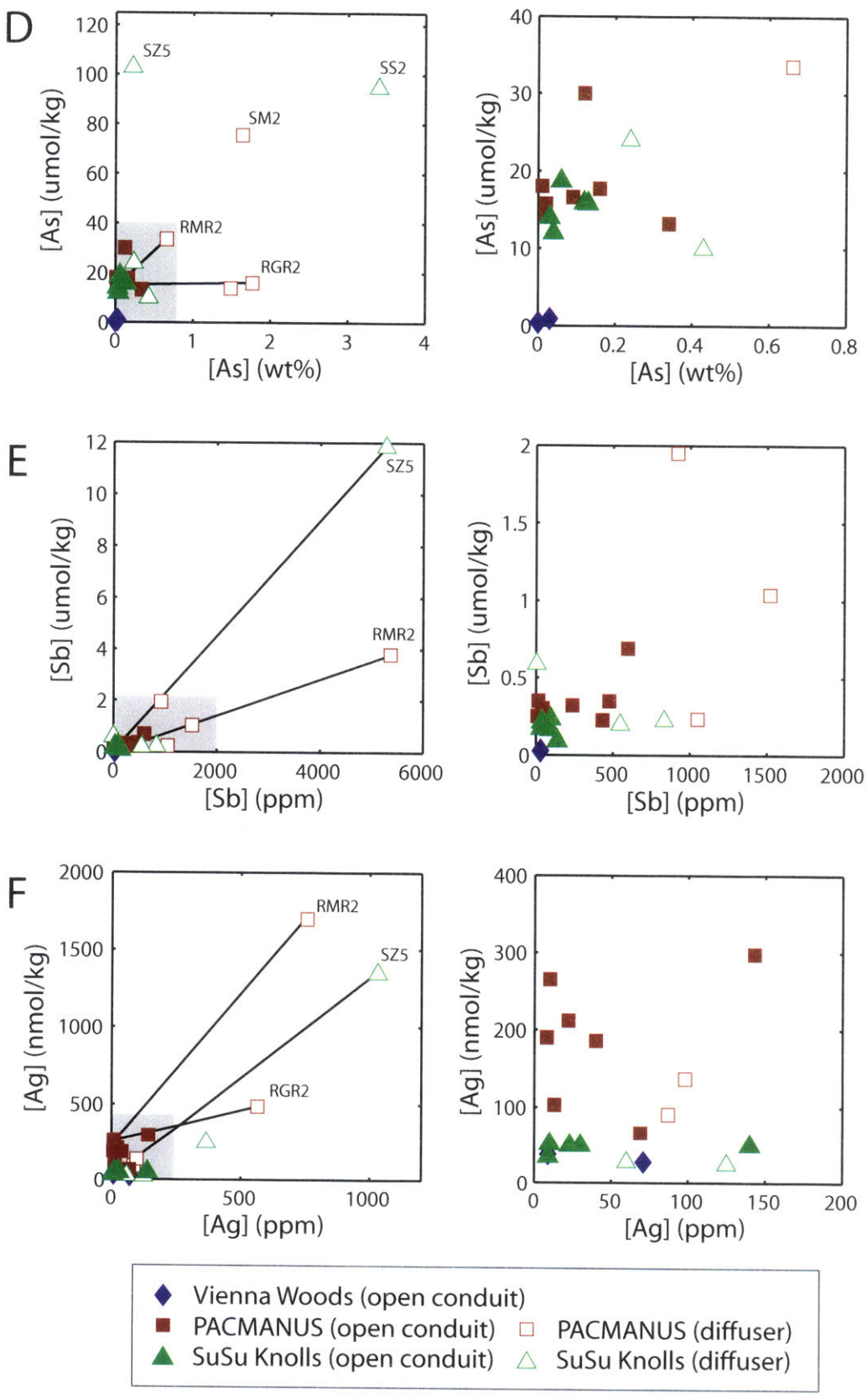
D
[As] (umol/kg)
[As] (wt%)
SZ5
SS2
SM2
RMR2
RGR2
E
[Sb] (umol/kg)
[Sb] (ppm)
SZ5
RMR2
F
[Ag] (nmol/kg)
[Ag] (ppm)
RMR2
SZ5
RGR2
Vienna Woods (open conduit)
PACMANUS (open conduit)
PACMANUS (diffuser)
SuSu Knolls (open conduit)
SuSu Knolls (diffuser)

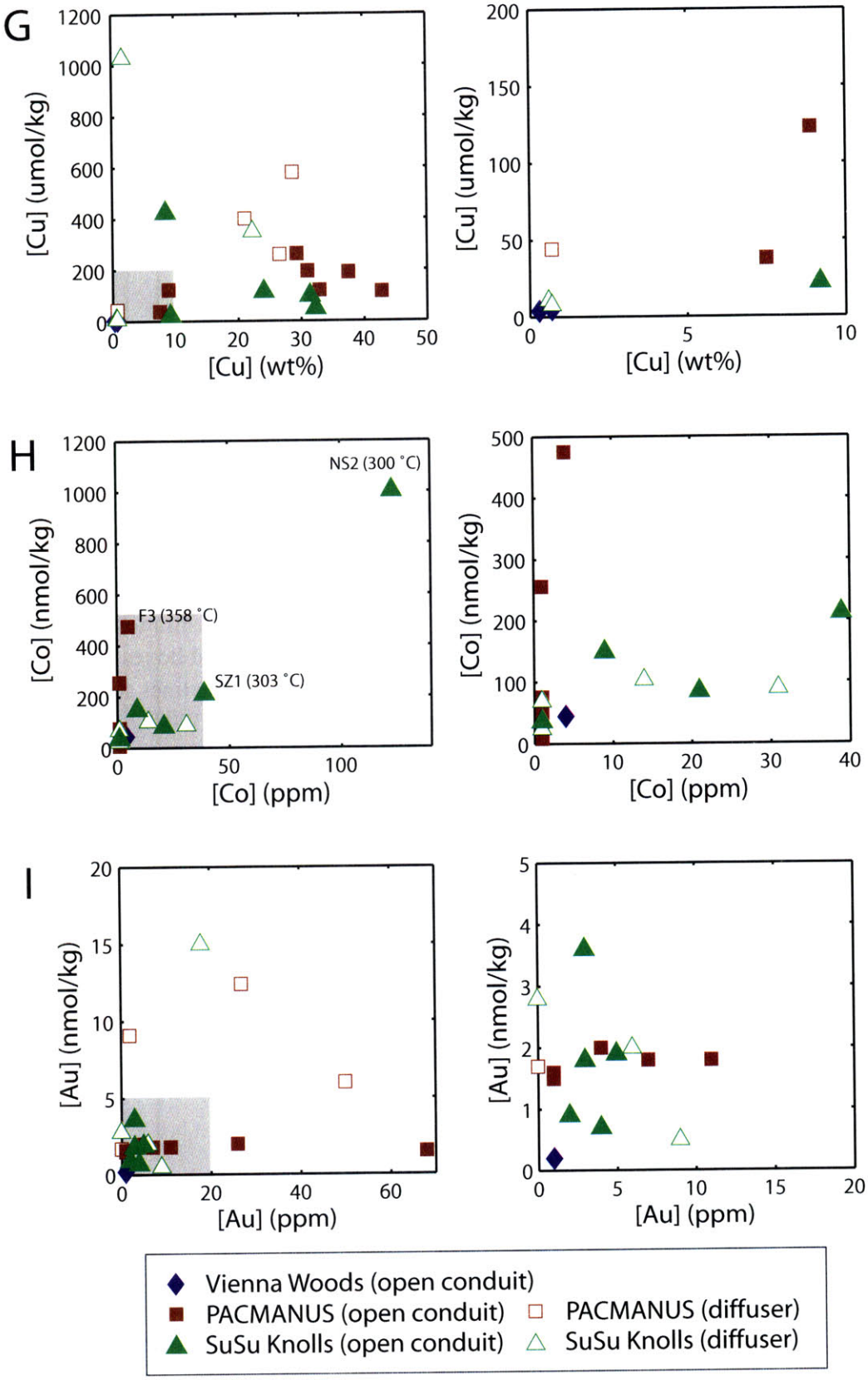
G
[Cu] (umol/kg)
[Cu] (wt%)
[Cu] (umol/kg)
[Cu] (wt%)
H
NS2 (300 °C)
F3 (358 °C)
SZ1 (303 °C)
[Co] (nmol/kg)
[Co] (ppm)
[Co] (nmol/kg)
[Co] (ppm)
I
[Au] (nmol/kg)
[Au] (ppm)
[Au] (nmol/kg)
[Au] (ppm)
Vienna Woods (open conduit)
PACMANUS (open conduit)
PACMANUS (diffuser)
SuSu Knolls (open conduit)
SuSu Knolls (diffuser)

Figure 5.9. Comparison of bulk metal compositions in seafloor chimney deposit samples from Vienna Woods (Manus Spreading Center) and PACMANUS and SuSu Knolls (Eastern Manus Basin) compared to metal concentrations in paired fluids from which chimney deposits precipitated. Gray shaded boxes (left panel) denote the area enlarged on the right panel of each figure. Tie lines relate low temperature (< 280 °C) mixed fluids to high-temperature (> 300 °C) endmember hydrothermal fluids at the same vent field. (A) Zn, (B) Pb, (C) Cd, (D) As, (E) Sb, (F) Ag, (G) Cu, (H) Co and (I) Au.

hydrothermal fluids has been shown experimentally to be a sensitive function of the maximum temperature and pressure conditions of fluid–rock interaction (Seyfried and Mottl, 1982; Seewald and Seyfried, 1990).

The formation of Zn–rich, Cu–poor vent deposits at Vienna Woods is significantly affected by pH, reflecting precipitation from metal–poor, high pH fluids. The absence of significant amounts of Cu–Fe–sulfide minerals reflects low Cu concentrations (< 5 μmol/kg) in Vienna Woods vent fluids. Low Cu concentrations are likely owing to the limited aqueous solubility of Cu in Vienna Woods fluids at temperatures below ~ 300 °C (e.g., Crerar and Barnes, 1976). That the mineral chemistry of relict (diffuser–type) deposits is similar to open conduit deposits and dominated by Zn–sulfide suggests that relict deposits may have formed from vent fluid with similar compositions.

5.1.2. PACMANUS and SuSu Knolls Open Conduit and Diffuser–type chimneys

Active open conduit chimneys from all PACMANUS and SuSu Knolls vent fields are characterized by linings of monomineralic chalcopyrite indicative of mineral precipitation at temperatures above 300 °C (Crerar and Barnes, 1976). In general, low–temperature mineral assemblages (e.g., low–Fe sphalerite, colloform pyrite and marcasite; Koski et al., 1994) are absent or present only in trace amounts at the exterior of these chimneys. The thick walls of diffuser and relict samples are characterized by a predominance of Cu–Fe–sulfides (bornite + chalcopyrite ± covellite) and lesser tennantite (Cu–As–sulfosalt) within interior portions, and minor tennantite with variable amounts of trace–to–minor sphalerite in exterior portions. The mineral compositions of diffuser and relict chimneys from PACMANUS and SuSu Knolls contrast markedly with that of low temperature vent deposits at most mid–ocean ridges, where compositions characterized by sphalerite (± wurtzite), pyrite, pyrrhotite and minor cubanite

dominate (e.g., Koski et al., 1984; Koski et al., 1994; Tivey et al., 1995).

Geochemical calculations were used to examine the significance of differences in observed mineral compositions of PACMANUS and SuSu Knolls vent deposits. The stability of Fe– and Cu–Fe–sulfides in representative fluid samples from each vent field (Table 5.3) is plotted in Figure 5.10 as a function of log $[a(Fe^{2+})/a(H^{+})^2]$ versus log $[a(Cu^{+})/a(H^{+})]$ for temperatures of 325, 275 and 250 °C. The compositions of the highest–temperature vent fluids (300 – 358 °C) exiting open conduit chimneys at PACMANUS and SuSu Knolls plot within the chalcopyrite field, consistent with chalcopyrite lining open conduits (e.g., samples RMR4 and SM1; Figure 5.10a). The highest temperature fluids do not plot in the stability fields of pyrite or lower temperature Cu–Fe–sulfides such as bornite. The compositions of Vienna Woods fluids also plot within the chalcopyrite stability field (e.g., sample VW1; Figure 5.10b), although the temperatures of fluids venting at this field are slightly lower (~ 280 °C). The general lack of low–temperature minerals in open conduit chimneys is a function of the composition of high–temperature fluids and the dynamics of fluid flow in open conduit chimney edifices (Tivey and McDuff, 1990; Tivey, 1995). Following early precipitation of quenched anhydrite and formation of a porous chimney framework during mixing of hydrothermal fluid and seawater, continued precipitation of anhydrite and minor sulfide in pore space reduces porosity and permeability across the chimney wall. Chalcopyrite precipitates along the interior of (and possibly replacing) the anhydrite framework and results in the development of a low permeability monomineralic chalcopyrite conduit lining (e.g., Goldfarb et al., 1983; Haymon, 1983). Hydrothermal fluid discharge is focused through the open conduit (flow rates approximately 1 – 2 m/s) and the flux of fluid across the chimney wall due to diffusion and/or advection (approximately 10^{-7} m/s) is low (Tivey, 1995). Low

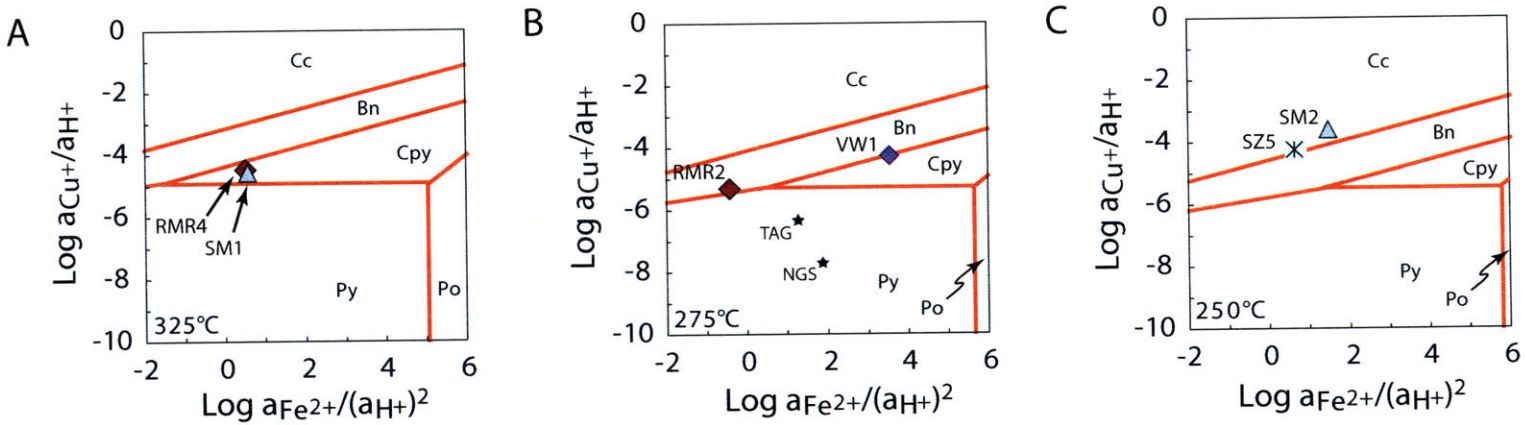

Figure 5.10. Log [$a(Fe^{2+})/a(H^{+})^2$] versus Log [$a(Cu^{+})/a(H^{+})$] diagrams for the system S-Cu-Fe constructed using data from the SUPCRT92 database (Johnson et al., 1992) at a pressure of 250 bars. Modifications to the database as detailed in text. Aqueous species distributions for Manus Basin vent fluids are calculated using the software package EQ3/6 (Wolery, 1992; Wolery and Daveler, 1992) and are super-imposed on diagrams at relevant temperatures to show predicted mineral assemblage in equilibrium with each fluid. (A) 325 °C, (B) 275 °C, (C) 250 °C. Fixed activity of Log $a(H_2)$ = - 5.0. Compositions of mid-ocean ridge vent fluids from Edmond et al. (1995) and Tivey et al. (1995) for TAG white smokers and Von Damm et al. (1985) for NGS, 21 °N East Pacific Rise are shown for comparison. (Py = pyrite, Po = pyrrhotite, Cpy = chalcopyrite, Bn = bornite, Cc = chalcocite). Fluid compositions used in calculations are shown in Table 5.3.

temperatures and low fluxes of metal–bearing fluid across exterior portions of open conduit chimney walls are unlikely to favor significant amounts of low–temperature sulfide precipitation. The low abundance of sulfide minerals precipitating at lower temperatures in these chimney walls relative to significantly greater amounts of sulfide mineral precipitating at high temperature along the conduit lining affects considerably the incorporation and enrichment of heavy and precious metals (e.g., Pb, Cd, Ag, Au) in these deposit types (discussed in Section 5.2).

The compositions of lower temperature fluids (~ 250 – 280 °C) exiting from the tops of diffuser type chimneys plot within the bornite and chalcocite stability fields (e.g., samples RMR2, SM2 and SZ5; Figure 5.10b). This contrasts markedly with mid–ocean ridge fluids of similar temperature (e.g., TAG white smoker (Edmond et al., 1995), 21°N East Pacific Rise (Von Damm et al., 1985) fluids), which plot within the pyrite stability field (Figure 5.10b). The predicted stability of bornite in most lower temperature vent fluids is consistent with the presence of abundant bornite in interior portions of diffuser chimneys from which these fluids exit, and reflects the high Cu^{+}/H^{+} activity and low $Fe^{2+}/(Cu^{+})^{2}$ activity (high Cu concentrations) and high fO_2 conditions (low H_2(aq) concentrations; E. Reeves and J. Seewald, *unpubl. data*) of low–temperature vent fluids from PACMANUS and SuSu Knolls relative to those of mid–ocean ridge vent fluids. The presence of minor chalcopyrite (with bornite) in many diffuser samples lining micro–channels within interior portions of the chimney wall suggests temperatures of precipitation in the interior of diffuser chimneys locally higher than that of measured temperatures of fluids exiting the tops of these chimneys (~ 280 °C). However, bulk compositions of diffuser samples are characterized by the predominance of lower–temperature mineral assemblages including bornite (± chalcocite),

tennantite (at Satanic Mills, Snowcap, Fenway and SuSu Knolls) and dendritic low–Fe sphalerite (at Roman Ruins and Roger's Ruins), occurring in a range of modal mineral abundance. This suggests that the bulk mass of sulfide is precipitated at a range of lower temperatures (~ 250 °C or below). The range of mineral textures and compositions can be related to different dynamics of fluid flow and conditions of mineral precipitation in diffuser chimney walls relative to open conduit chimneys (Fouquet et al., 1993b; Koski et al., 1994). Diffuser chimneys are characterized by sluggish vertical fluid flow rates relative to black smoker chimneys (referred to here as open conduit chimneys) and significant advective fluid flux across more permeable, fine–grained mineral frameworks. The high lateral permeability of diffuser chimneys relative to open conduit chimneys favors significant lateral (radial) fluid flow through chimney walls (Koski et al., 1994); ponding of hydrothermal fluid in interstices can result in conductive cooling of these fluids and the precipitation of a range of minerals at lower temperatures in exterior portions of chimney walls before fluids exit through the sides of these chimneys. This idea provides an explanation for the predominance of lower temperature minerals present in diffuser chimneys.

Geochemical calculations do not predict saturation of tennantite or sphalerite at in situ temperature and pressure for most fluids exiting tops of diffuser chimneys. The stability of tennantite relative to Fe– and Cu–Fe–sulfides is plotted in Figure 5.11 as a function of log $[a(Cu^{+})/a(H^{+})]$ and temperature. As indicated, most fluids exiting from the tops of diffuser chimneys are stable with respect to bornite, but are in equilibrium with tennantite if fluids are conductively cooled within the chimney edifice. The extent of cooling required is a function of the initial Cu, Fe and As activity (Figure 5.11). For compositions of most sampled vent fluids exiting diffuser chimneys at PACMANUS and SuSu Knolls (pH (25 °C) ~ 2.3 – 2.8,

[Cu] ~ 40 – 580 μmol/kg, [As] ~ 14 – 19 μmol/kg), geochemical calculations predict that conductively cooling vent fluids between 5 and 50 °C (to temperatures ~ 220 – 270 °C) is sufficient to saturate vent fluids with respect to tennantite (Figure 5.12a). Precipitation of bornite and tennantite owing to cooling of hydrothermal fluid likely explains the presence of bornite and tennantite in both active diffuser and relict chimney deposits from Satanic Mills, Snowcap, Fenway and SuSu Knolls. That tennantite is observed also in the very interior of some diffuser–type chimneys or in one sample from North Su (SuSu Knolls) lining an interior conduit (Figures 5.3 and 5.4) suggests that some chimneys are deposited at low temperatures (~ 220 °C) or, if deposited at higher temperatures, that concentrations of Cu and As in these vent fluids can be even higher than those measured (see Chapter 4). Sphalerite is absent from these diffuser chimneys, or is present only in trace amounts, despite concentrations of Zn up to an order of magnitude higher in Satanic Mills, Snowcap, Fenway and SuSu Knolls vent fluids relative to those from Vienna Woods (see Chapter 4). This is likely related to the effect of low pH of Eastern Manus Basin vent fluids on sphalerite saturation. Geochemical calculations predict that sphalerite is saturated in vent fluids at Satanic Mills, Snowcap, Fenway and SuSu Knolls only at temperatures below ~ 170 °C, and considerably less than the temperatures at which tennantite is predicted to be saturated in these fluids (Figure 5.12).

Diffuser (and relict) chimneys recovered from the Roman Ruins and Roger's Ruins vent fields are the most enriched in sphalerite (±galena). The likely explanation for the higher modal abundance of sphalerite and galena in these samples is that the vent fluids from which Roman Ruins and Roger's Ruins diffuser deposits are precipitating exhibit considerably higher concentrations of Zn and Pb relative to other PACMANUS vent fluids (Figure 5.9; see Chapter 4). The high concentrations of Zn in low temperature vent fluids from Roman Ruins

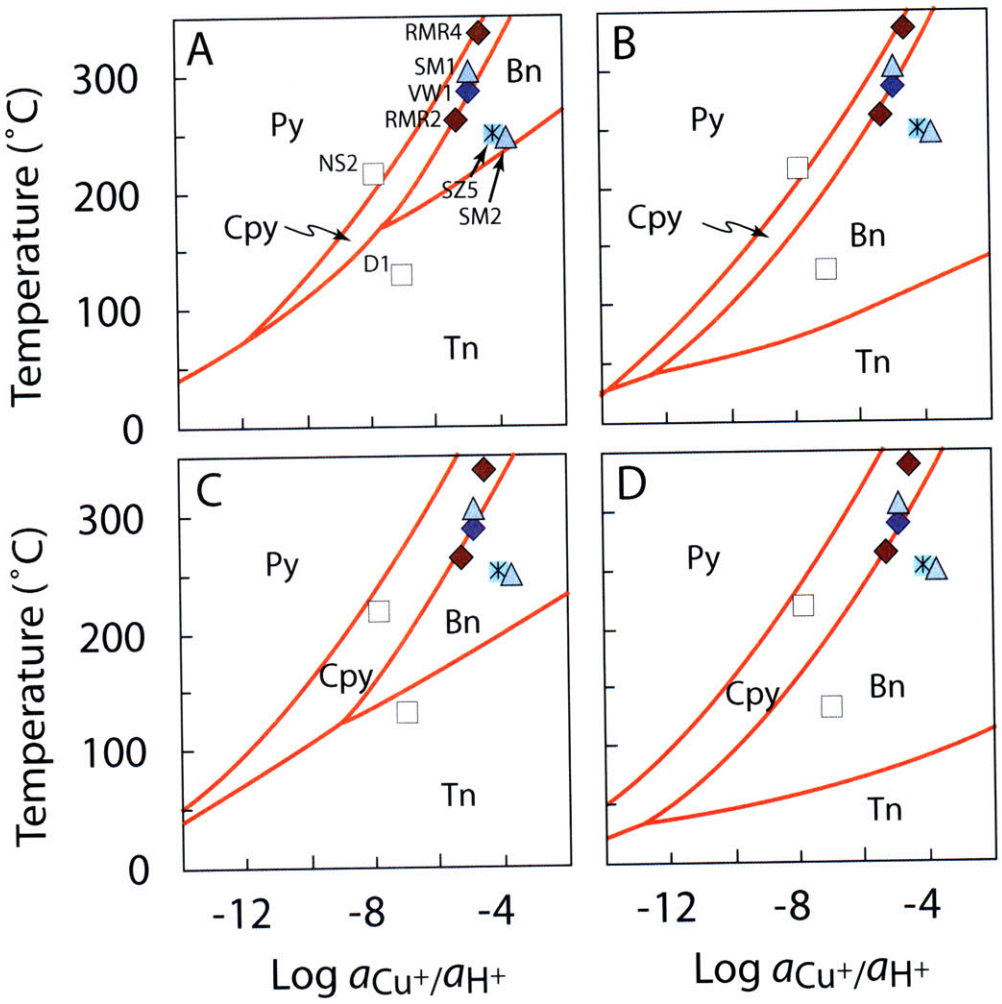

Figure 5.11. Temperature versus Log [$a(Cu^+)/a(H^+)$] diagrams for the system S-Cu-Fe-As. Aqueous species distributions of Manus Basin vent fluids super-imposed on diagrams. Fluid compositions relevant to most PACMANUS and SuSu Knolls high-temperature black and gray smoker vent fluids are for diagrams (**A**) and (**B**). Highest-temperature fluids exiting open conduit chimneys plot in the boundary of chalcopyrite stability. Lower-temperature fluids exiting diffuser chimneys plot within the bornite stability field and with conductive cooling pass to equilibrum with tennantite. (Py = pyrite, Cpy = chalcopyrite, Bn = bornite, Tn = tennantite).

Fixed activity ratios are:
(**A**) Log [$a(Fe^{2+})/a(H^+)^2$] = 2, Log [$a(As(OH)_4^-)\cdot a(H^+)$] = -12, Log $a(H_2S)$ = -2
(**B**) Log [$a(Fe^{2+})/a(H^+)^2$] = 2, Log [$a(As(OH)_4^-)\cdot a(H^+)$] = -16, Log $a(H_2S)$ = -2
(**C**) Log [$a(Fe^{2+})/a(H^+)^2$] = 4, Log [$a(As(OH)_4^-)\cdot a(H^+)$] = -12, Log $a(H_2S)$ = -2
(**D**) Log [$a(Fe^{2+})/a(H^+)^2$] = 4, Log [$a(As(OH)_4^-)\cdot a(H^+)$] = -16, Log $a(H_2S)$ = -2

and Roger's Ruins have been attributed to remobilization of previously deposited Zn–sulfide owing to a more acidic fluid pH resulting from sub–seafloor entrainment of seawater, mixing with high–temperature hydrothermal fluid and precipitation of high–temperature Cu–Fe–sulfides (see Chapter 4). The higher abundance of sphalerite is not related to a higher fluid pH (c.f., Vienna Woods) because the pH (25 °C) of all vent fluids exiting from diffuser chimneys at Roman Ruins and Roger's Ruins are low (~ 2.3 – 2.6) and similar to those at other PACMANUS vent fields. Geochemical calculations support that sphalerite is saturated at higher temperatures in vent fluids exiting diffuser chimneys at Roman Ruins and Roger's Ruins (~ 200 °C) relative to other PACMANUS and SuSu Knolls vent fluids (Figure 5.12) owing to the significantly higher dissolved Zn concentrations. Significantly, sphalerite is predicted to be saturated at temperatures similar to tennantite in the Roman Ruins and Roger's Ruins low temperature fluids (Figure 5.12). Tivey (1995) has suggested that the association constant for $ZnCl^+$ in the SUPCRT92 database is too large (compare with Bourcier and Barnes (Bouricer and Barnes, 1987)) and thus under–estimates the temperature of sphalerite and wurtzite precipitation. Accordingly, sphalerite may be saturated at temperatures higher than tennantite in Roman Ruins and Roger's Ruins fluids.

Similarly, a sulfide crust recovered from a large pavement–type edifice at Suzette (SuSu Knolls, sample J2–226–2–R1) exhibits significantly higher modal abundance of sphalerite relative to other SuSu Knolls vent deposit samples. The precipitation of abundant sphalerite in this sample also reflects the markedly higher concentrations of Zn in vent fluids exiting this edifice (sample SZ5; Table 5.3). The order of magnitude higher concentrations of Zn (and Cu and As) in vent fluids exiting through the crust are also attributed to remobilization of previously deposited sphalerite (and tennantite) owing to interaction with a

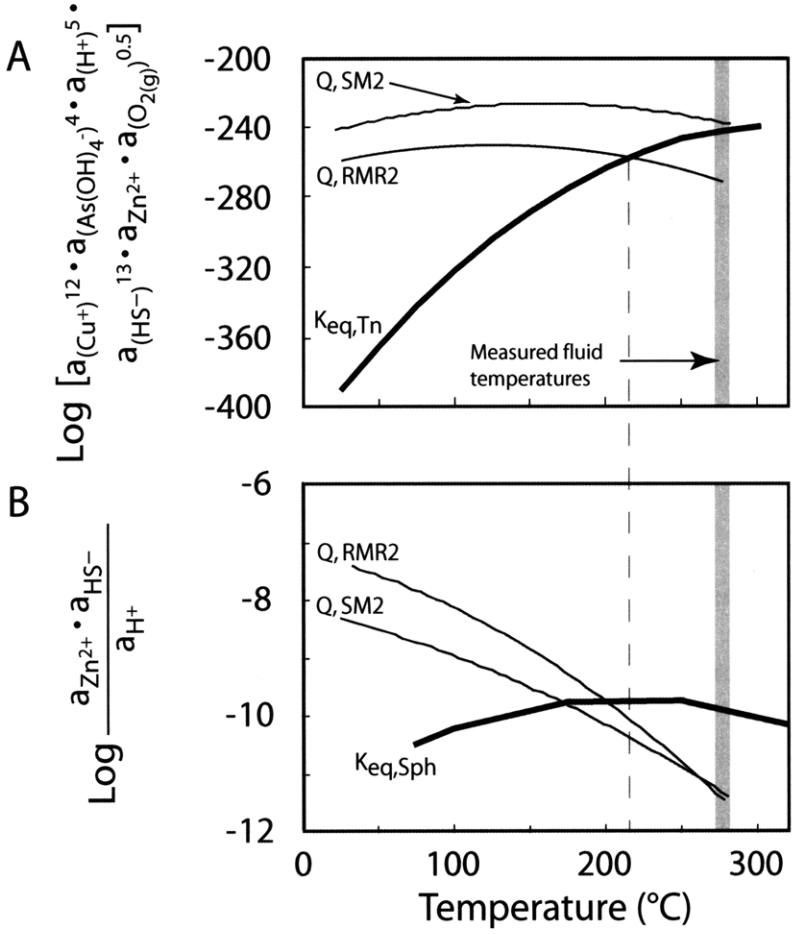

Figure 5.12. Calculated equilibrium species distribution and mineral saturation state (equilibrium constan K versus reaction quotient Q) for vent fluids exiting Diffuser chimneys from PACMANUS (Roman Ruins RMR2 and Satanic Mills SM2) and from SuSu Knolls (South Su SS1). (**A**) Tennantite and (**B**) Sphalerite. Fluid compositions used in calculations shown in Table 5.3. See text for description of calculations and discussion.

fluid with a lower pH than that at which the sulfides originally precipitated. In this case, the significantly lower measured pH (25 °C) of fluids venting through the sulfide crust (~ 2.3) relative to high–temperature fluids exiting sulfide chimneys (3.4 – 3.8) is hypothesized to have resulted from locally higher contributions of degassed magmatic acid volatiles (i.e., H_2O–HCl–CO_2–HF–SO_2) beneath some areas of the Suzette mound (see Chapter 4). The remobilization of sulfide minerals within these existing sulfide bodies suggests that on–going zone–refinement is a process that affects significantly the evolution and spatial distribution of metal sulfides in seafloor vent deposits in the Manus Basin, as has been described previously for vent deposits at the TAG active mound, 26 °N mid–Atlantic Ridge (e.g., Tivey et al., 1995).

5.2. Factors affecting precious metal enrichment in Manus Basin vent deposits: Effect of fluid composition and conditions of mineral precipitation

The different morphology and mineral composition of cylindrical, pipe–like open conduit chimneys versus more uniformly porous diffuser chimneys reflects differences in fluid composition and dynamics of fluid flow, both of which affect conditions (e.g., temperature, pH, fO_2–fS_2, metal concentrations) of mineral precipitation. These factors affect significantly the incorporation and enrichment of trace and precious metals (e.g., Ag, Au, Cd, Se) in sulfide minerals and leads to large differences in observed trace metal concentrations among the Manus Basin vent deposits.

5.2.1. Trace metal enrichment in Vienna Woods vent deposits

In general, concentrations of trace elements in both open conduit and relict (diffuser–type) chimneys are low in Vienna Woods vent deposit samples relative to those from PACMANUS and SuSu Knolls (e.g., Co, Se, Pb, Sb, Ag and Au; Figure 5.6). To first–order

the low concentrations of most trace and precious metals in vent deposit samples from Vienna Woods (excluding Cd, see below) can be directly correlated with low concentrations of these elements in Vienna Woods vent fluids (Figure 5.9). This correlation suggests that fluid composition is a key variable influencing precious metal enrichment in seafloor hydrothermal mineral deposits.

Within Vienna Woods chimney deposits, however, there are considerable differences in trace element concentrations among active open conduit and relict (diffuser–type) chimneys. Concentrations of Co are higher and concentrations of Pb, As, Sb, Ag and Au considerably lower in open conduit chimneys relative to relict chimney samples (Figures 5.5 and 5.6). In general, Co is positively correlated with Cu (Table 5.4), indicating that Co is likely distributed primarily with or in chalcopyrite, within higher–temperature sulfide mineral assemblages, although absolute concentrations are too low to be determined by electron microprobe data (< 350 ppm; Appendix E2). This correlation is similar to that observed and described in most mid–ocean ridge seafloor vent deposits (Hannington et al., 1991; Fouquet et al., 1993b; Koski et al., 1994; Tivey et al., 1995). In contrast, Cd is positively correlated with Zn (Table 5.4). Electron microprobe analyses have documented that Cd is precipitated predominantly in Zn–sulfide (up to 0.9 wt% Cd in wurtzite; Appendix E2). Owing to the fact that Cd behaves similar to Zn and partitions effectively into Zn–sulfide during mineral precipitation (Fleischer, 1955) results in significant Cd enrichment in the Zn–rich Vienna Woods vent deposits, even though Cd concentrations in Vienna Woods vent fluids from which the deposits form are low relative to other vent fluids in the Manus Basin.

The lack of correlation between Zn and Pb, As, Sb, Ag and Au in active or relict deposits from Vienna Woods (Table 5.4) contrasts with Zn–rich chimneys sampled from most

Table 5.4. Correlation Factors r for bulk chemical analyses of Vienna Woods vent deposits

	Cu	Zn	Pb	As	Cd	Sb	Ag	Au	Co	Mo	Ca	Ba	Sr	Mn
Fe	0.22	-0.56	0.22	0.40	-0.49	0.31	0.26	0.31	0.07	0.26	-0.49	-0.29	-0.48	0.22
Cu		-0.26	-0.25	-0.34	-0.07	-0.36	-0.27	-0.31	**0.81**	0.08	-0.12	-0.08	-0.19	-0.28
Zn			-0.21	-0.11	**0.72**	-0.10	-0.17	-0.17	-0.07	-0.04	-0.25	**0.45**	-0.25	0.01
Pb				**0.77**	-0.31	**0.85**	**0.94**	**0.93**	-0.21	0.14	-0.15	-0.16	-0.10	0.32
As					-0.12	**0.85**	**0.76**	**0.82**	-0.23	0.17	-0.32	0.04	-0.25	**0.60**
Cd						-0.27	-0.33	-0.33	0.23	-0.18	-0.01	**0.89**	-0.07	-0.15
Sb							**0.87**	**0.91**	-0.28	0.22	-0.37	-0.18	-0.31	**0.47**
Ag								**0.96**	-0.23	0.23	-0.22	-0.20	-0.18	0.27
Au									-0.27	0.22	-0.28	-0.20	-0.23	0.32
Co										-0.10	-0.04	0.26	-0.09	-0.20
Mo											-0.40	-0.32	-0.41	-0.03
Ca												0.07	**0.98**	-0.25
Ba													0.00	-0.10
Sr														-0.09

Correlations based on 35 samples. Correlation coefficients greater than 0.45 are statistically significant at the 95% confidence interval (highlighted in bold type)

mid–ocean ridge vent fields, where Zn, Cd, Pb, As, Sb, Ag and Au are generally positively correlated (Hannington et al., 1991; Fouquet et al., 1993b; Tivey et al., 1995). At most mid–ocean ridge vent fields, Pb, As, Sb, Ag and Au are precipitated predominantly in, or with, Zn–sulfide, during deposition of low–temperature Zn–rich mineral assemblages (< 200 – 250 °C). The distributions of Pb, Ag, As, Sb and Au at Vienna Woods are similar to those of Zn–rich vent deposits at the Endeavour Segment, Juan de Fuca Ridge (Tivey et al., 1999) (Kristall et al., 2006). At Endeavour, Zn–sulfide is precipitating at high temperatures (~ 280 °C) owing to the high measured pH (25 °C) of Endeavour fluids between 4.2 and 4.5 (Butterfield et al., 1994). The lack of a correlation between Zn and Pb, As, Sb, Ag and Au within Endeavour vent deposits has been attributed to exclusion of these trace elements during Zn–sulfide precipitation at high temperatures (Tivey et al., 1999). Similarly, the lack of correlation between Zn and Pb, As, Sb, Ag and Au at Vienna Woods likely reflects precipitation of Zn–sulfide at higher temperatures (~ 280 °C) also owing to high pH, as demonstrated by the thermodynamic calculations presented, and the resultant exclusion of these trace elements from Zn–sulfide. The good correlations among Pb, As, Sb, Ag and Au in Vienna Woods vent deposit samples (Table 5.4) suggest that these trace elements are likely incorporated together with or in sulfide minerals, other than wurtzite/sphalerite, that precipitated at a range of lower temperatures. The low concentrations of trace metals (Pb, As, Sb, Ag and Au) in Vienna Woods open conduit chimneys reflect the absence of significant amounts of sulfide minerals precipitating at low temperature. In contrast, the higher concentrations of trace metals in relict diffuser–type chimneys reflects the higher modal abundance of sulfide minerals (e.g., pyrite, marcasite) likely precipitated at lower–temperatures as a result of ponding and cooling of hydrothermal fluid within diffuser chimney edifices, explaining both their higher

concentrations in diffuser chimneys and lack of correlation with Zn.

5.2.2. Trace metal enrichment in PACMANUS and SuSu Knolls vent deposits

The different mineralogical compositions of vent deposits in the PACMANUS and SuSu Knolls (e.g., Cu– and As–rich) relative to Vienna Woods (e.g., Zn–rich, Cu– and As–poor) are explained by the markedly different compositions of vent fluids (i.e., pH, temperature, metal concentrations) sampled at these vent fields (see Chapter 4) and the resulting differences in conditions of sulfide mineral precipitation. The differences in fluid compositions and in the conditions of sulfide mineral precipitation also both affect the enrichment of base and precious metals in these sulfide deposits. In general, the concentrations of trace elements (e.g., Pb, Ag, As, Sb, Au and Co) are significantly higher in all types of sulfide chimneys sampled at PACMANUS and SuSu Knolls (i.e., open conduit, diffuser and relict chimneys) relative to sulfide chimneys sampled from Vienna Woods (Figure 5.9). This enrichment can be correlated directly with the higher concentrations of trace elements in seafloor vent fluids from the PACMANUS and SuSu Knolls relative to those in vent fluids from Vienna Woods (Figure 5.9). The higher concentrations of trace metals in hydrothermal fluids from PACMANUS and SuSu Knolls reflect the higher temperatures and considerably lower pH of vent fluids in the Eastern Manus Basin; the latter resulting, in large part, from input of magmatic acid volatiles exsolved from underlying felsic magmas in this area (see Chapter 4). To first–order, trace metal concentrations in seafloor hydrothermal fluids do control the resulting trace metal enrichment in related massive sulfide deposits.

The influence that fluid composition exerts is also apparent when the compositions of vent deposits within PACMANUS and SuSu Knolls are compared. Lower temperature Zn–

rich diffuser chimneys from Roman Ruins and Roger's Ruins (e.g., samples J2–208–2–R2 and J2–222–1–R1) are enriched in trace elements Pb, Cd, Ag, As and Sb relative to most diffuser chimneys from Satanic Mills, Fenway and Snowcap (the PACMANUS hydrothermal system). Likewise, the low temperature Zn–rich sulfide crust deposited at Suzette (J2–226–2–R1) is significantly enriched in Pb, Ag and Cd relative to all other lower temperature diffuser–type chimneys sampled within SuSu Knolls. In general, the enrichments of trace metals in these Zn–rich deposits can be directly correlated with high concentrations of Pb, Cd, Ag, As and Sb in seafloor hydrothermal fluids from which these deposits are forming (c.f., fluid samples RMR2 (Roman Ruins), RGR2 (Roger's Ruins) and SZ5 (Suzette) shown in Figure 5.9). As discussed earlier, the enrichment of Zn in these same fluids likely reflects remobilization of previously deposited Zn–sulfide beneath the seafloor at Roman Ruins and Roger's Ruins (PACMANUS) and Suzette (SuSu Knolls). Remobilization of Zn also appears to correlate with remobilization of Pb, Cd, Ag, As and Sb resulting in their higher concentrations in these fluids and is likely related to enrichment of these trace metals in Zn–sulfide. Positive correlations among Zn, Pb, Cd, Sb and Ag in Roman Ruins and Roger's Ruins vent deposit samples (Table 5.5) indicate that Pb, Cd, Sb and Ag are re–precipitated predominantly in sphalerite (as demonstrated by electron microprobe analyses; Figure 5.7), during zone–refinement of the Roman Ruins and Roger's Ruins sulfide deposits. High concentrations of Pb also reflect the presence of trace–to–minor galena occurring with sphalerite in low temperature diffuser chimneys at Roman Ruins and Roger's Ruins. The absence of significant amounts of sphalerite and galena in most chimney deposits recovered from other fields in the Eastern Manus Basin (i.e., at Satanic Mills, Fenway and Snowcap and at SuSu Knolls) reflects lower concentrations of Zn and Pb in the vent fluids from which these

Table 5.5. Correlation Factors r for bulk chemical analyses of Roman Ruins-Roger's Ruins (PACMANUS) vent deposits

	Cu	Zn	Pb	As	Cd	Sb	Ag	Au	Co	Mo	Ca	Ba	Sr	Mn
Fe	**0.79**	-0.80	-0.33	-0.40	-0.81	-0.43	-0.70	-0.01	-0.10	**0.59**	0.37	-0.15	0.09	0.18
Cu		-0.76	-0.38	-0.12	-0.71	-0.36	-0.58	-0.08	-0.19	0.25	0.33	-0.12	-0.04	-0.10
Zn			0.30	0.34	**0.95**	0.40	**0.79**	0.11	-0.30	-0.32	-0.50	0.21	-0.41	-0.46
Pb				0.05	0.23	**0.69**	**0.47**	-0.23	-0.13	-0.16	-0.24	-0.09	-0.23	-0.14
As					0.25	0.15	0.33	-0.19	-0.25	-0.15	-0.44	0.35	-0.40	-0.35
Cd						**0.45**	**0.78**	0.23	-0.28	-0.35	-0.36	0.23	-0.25	-0.47
Sb							**0.69**	0.37	-0.21	-0.08	-0.24	0.12	-0.19	-0.27
Ag								0.16	-0.32	-0.28	-0.47	0.17	-0.31	-0.41
Au									-0.12	0.29	0.31	0.08	**0.70**	-0.12
Co										-0.11	-0.04	-0.14	0.17	**0.91**
Mo											0.08	-0.02	-0.12	0.08
Ca												-0.16	**0.92**	0.04
Ba													0.00	-0.10
Sr														0.27

Correlations based on 20 samples (11 samples for Sr). Correlation coefficients greater than 0.45 are statistically significant at the 95% confidence interval (highlighted in bold type)

deposits are precipitating. There does not appear to be significant on–going zone refinement at these vent fields. Lower concentrations of trace and precious elements (e.g., Cd, Ag, Au and Sb) in chimney samples from these vent fields, relative to those at Roman Ruins and Roger's Ruins, likely reflect lower concentrations of these trace elements in vent fluids from which they are forming (owing to the absence of on–going zone refinement).

Concentrations of Co and Se are significantly higher in open conduit chimneys precipitating from the highest–temperature fluids, relative to diffuser chimneys forming at lower temperatures (Tables 5.2a, b). High concentrations of Co and Se in open conduit chimneys reflect both higher concentrations of Co and Se in high–temperature fluids, but also temperature effects because Co and Se are effectively incorporated into chalcopyrite that is precipitated as temperature decreases below ~ 300 °C owing to the markedly decreased solubility of Cu in lower temperature fluids (e.g., Crerar and Barnes, 1976). Bulk concentrations of Co and Se (up to 125 and 2000 ppm, respectively) in a few chimney sampled from Fenway (PACMANUS) and SuSu Knolls are considerably higher than those of most deposits in back–arc hydrothermal systems (c.f., Lau Basin; Fouquet, et al., 1993). The presence of high Co in the deposits is correlated with high concentrations vent fluids from which these deposits are forming. Possibly, high concentrations of Se in these deposits also reflect high concentrations of Se in parent hydrothermal fluids from which the deposits formed, however no fluid data for Se are available to confirm this.

In contrast, average concentrations of Pb, Cd, As, Sb, Ag and Au are higher in diffuser and relict chimney deposits relative to open conduit smokers at PACMANUS and SuSu Knolls (Figure 5.6). This is similar to the relative concentrations of Pb, As, Sb, Ag and Au in diffuser versus open conduit chimneys at Vienna Woods (section 5.2.1.). The higher

concentrations of Pb, As, Sb, Ag and Au in diffuser–type chimneys likely reflect the preferential incorporation of these trace elements in sulfide minerals precipitating at a range of lower temperatures (~ 200 – 250 °C), and their exclusion from sulfide minerals (e.g., chalcopyrite and wurtzite) precipitated at high temperatures (~ 280 °C). Likewise, higher concentrations of Pb, Cd, As, Sb, Ag and Au in diffuser chimneys relative to open conduit chimneys at PACMANUS and SuSu Knolls reflect their effective incorporation into sulfide minerals precipitated at a range of lower–temperatures. The differences in metal enrichment between open conduit and diffuser chimneys at each vent field does not appear to be obviously related to different metal enrichments in the fluids from which they precipitated (the trace metal rich low–temperature deposits from Roman Ruins and Roger's Ruins are excluded from the following discussion, these deposits having precipitated from remarkably Pb, Cd, Sb, As and Ag rich hydrothermal fluids). As shown in Figure 5.9 (enlarged panels on the right), bulk concentrations of Pb, Cd, Sb, As and Ag are higher in diffuser type chimneys relative to most open conduit chimneys from the same vent field, even though concentrations of these trace elements are similar in both low–temperature and high–temperature fluids from which the respective deposits are forming. Indeed, trace metal concentrations of lower–temperature fluids from which diffuser chimneys precipitate are mostly lower than in high–temperature vent fluids from the same vent field (Figure 5.9). These data strongly support that the conditions of sulfide mineral precipitation, affecting the mineralogical composition of the vent deposits (e.g., chalcopyrite versus sphalerite), also affect trace metal enrichment. The good correlations among Pb, Cd, Ag and Zn and between Sb and As in vent deposits at PACMANUS and SuSu Knolls (Tables 5.6 and 5.7) support that Pb, Cd and Ag are distributed within sphalerite and Sb within sphalerite and tennantite (as documented at

Table 5.6. Correlation Factors r for bulk chemical analyses of Satanic Mills-Snowcap-Fenway (PACMANUS) vent deposits

	Cu	Zn	Pb	As	Cd	Sb	Ag	Au	Co	Mo	Ca	Ba	Sr	Mn
Fe	**0.65**	-0.63	-0.41	-0.26	-0.62	0.05	-0.64	-0.17	-0.10	**0.68**	-0.05	-0.24	0.01	-0.02
Cu		-0.61	-0.32	0.25	-0.61	0.34	-0.49	0.15	-0.36	**0.55**	-0.34	0.05	-0.27	-0.04
Zn			**0.62**	0.08	**0.98**	0.09	**0.90**	0.23	-0.24	-0.42	-0.40	0.04	-0.35	0.15
Pb				0.31	**0.55**	-0.01	**0.70**	0.09	-0.21	-0.18	-0.38	0.26	-0.30	0.26
As					-0.02	0.39	0.22	0.37	-0.32	-0.11	-0.49	0.29	-0.46	0.47
Cd						0.05	**0.85**	0.24	-0.21	-0.39	-0.35	0.01	-0.31	0.05
Sb							0.14	**0.87**	-0.30	0.37	-0.43	0.40	-0.57	0.08
Ag								0.20	-0.31	-0.42	-0.47	0.19	-0.39	0.10
Au									-0.24	0.27	-0.35	0.50	-0.38	-0.01
Co										-0.06	0.72	-0.16	**0.57**	-0.06
Mo											-0.01	0.05	0.24	-0.06
Ca												-0.25	**0.97**	-0.19
Ba													-0.20	-0.19
Sr														-0.20

Correlations based on 30 samples (23 samples for Sr). Correlation coefficients greater than 0.45 are statistically significant at the 95% confidence interval (highlighted in bold type)

Table 5.7. Correlation Factors r for bulk chemical analyses of SuSu Knolls (Suzette-North Su-South Su) vent deposits

	Cu	Zn	Pb	As	Cd	Sb	Ag	Au	Co	Mo	Ca	Ba	Sr	Mn
Fc	**0.60**	-0.46	-0.43	-0.40	-0.42	-0.42	-0.43	-0.03	**0.49**	**0.48**	-0.15	-0.48	-0.35	-0.05
Cu		-0.43	-0.43	0.23	-0.38	0.09	-0.22	0.05	0.17	0.20	-0.15	-0.43	-0.40	-0.14
Zn			**0.86**	0.03	**0.90**	0.02	**0.77**	-0.09	-0.21	-0.18	-0.28	0.05	-0.29	-0.02
Pb				-0.08	**0.95**	-0.02	**0.81**	-0.19	-0.19	-0.16	-0.25	0.09	-0.28	0.01
As					-0.01	**0.67**	0.16	0.34	-0.22	-0.19	-0.28	0.24	-0.21	0.00
Cd						-0.04	**0.89**	-0.16	-0.18	-0.16	-0.25	0.04	-0.26	-0.05
Sb							0.10	**0.51**	-0.22	-0.18	-0.30	0.27	-0.19	0.11
Ag								0.01	-0.21	-0.17	-0.27	0.05	-0.30	-0.07
Au									0.06	0.10	-0.26	0.13	-0.16	0.07
Co										**0.58**	0.09	-0.30	0.04	-0.12
Mo											-0.09	-0.14	-0.22	-0.11
Ca												-0.41	**0.92**	-0.15
Ba													-0.22	0.15
Sr														-0.12

Correlations based on 34 samples (18 samples for Sr). Correlation coefficients greater than 0.45 are statistically significant at the 95% confidence interval (highlighted in bold type)

electron microprobe data; Figure 5.7). Geochemical calculations have indicated that the saturation and precipitation of sphalerite and tennantite occurs at a range of lower temperatures (< 200 – 260 °C) in diffuser–type deposits but not at high temperatures of ~ 300 °C (the conditions dominating precipitation in open conduit chimneys). The association of Pb, Cd and Ag (and to a lesser extent Sb) with sphalerite at PACMANUS and SuSu Knolls (but not at Vienna Woods, as discussed) reflects that sphalerite is precipitated at significantly lower temperatures at PACMANUS and SuSu Knolls (e.g., Figure 5.12) relative to sphalerite and wurtzite precipitated at Vienna Woods (e.g., Figure 5.8). This results from the affect of low pH on sphalerite saturation at PACMANUS and SuSu Knolls. The precipitation of large quantities of sulfide assemblages at low temperature in diffuser–type chimneys (e.g., sphalerite, tennantite, bornite) versus at high temperature sulfide assemblages in open conduit chimneys (e.g., chalcopyrite) significantly affects the bulk enrichment of trace metals (i.e., Pb, Cd, As, Sb, Ag versus Co, Se). This is despite that metal concentrations in lower temperature fluids are often lower than in higher temperature "endmember" hydrothermal fluids (see Chapter 4).

6. Summary and Conclusions

Mineralogical and chemical compositions of vent deposits show considerable differences among different vent fields in the Manus Basin and among different chimney deposit types. At Vienna Woods in the Manus Spreading Center, both active (high–temperature ~ 280 °C open conduit chimneys) and relict (diffuser–type) deposits are dominated by Zn–sulfide (wurtzite and sphalerite) and contain only trace–to–minor amounts

of Cu and Pb. In the Eastern Manus Basin, vent deposits at PACMANUS and SuSu Knolls contain significantly more Cu and less Zn relative to those from Vienna Woods. At all PACMANUS and SuSu Knolls vent fields, open conduit chimneys (precipitating from highest temperature > 300 °C focused fluids) are dominated by chalcopyrite and anhydrite and contain only trace–to–minor amounts of lower temperature sulfide assemblages. Diffuser–type chimneys from Roman Ruins and Roger's Ruins (PACMANUS) vent fields (precipitating from lower temperature ~ 240 – 280 °C less focused fluids) are dominated by Cu–Fe–sulfides (bornite and chalcopyrite), with minor sphalerite and trace galena. At Satanic Mills, Fenway and Snowcap (PACMANUS) and at SuSu Knolls, diffuser chimneys are dominated by Cu–Fe–sulfides (bornite and chalcopyrite), minor tennantite and, in general, significantly lesser sphalerite and galena.

Differences in chimney morphology and mineral composition can be explained by differences in fluid composition and styles of fluid flow and interaction with seawater within chimney edifices where sulfides are precipitated. Open conduit chimneys are characterized by the precipitation of an impermeable lining that focuses fluid flow vertically up through a central conduit and greatly reduces radial fluid flow through chimney walls (Goldfarb et al., 1983; Tivey and McDuff, 1990; Tivey, 1995). In contrast, diffuser chimneys are precipitated from fluids with lower vertical advection rates and higher lateral fluid flow through a porous and often thicker chimney wall without a well–defined central open conduit, which likely leads to some ponding and conductive cooling of hydrothermal fluid within chimney edifices (Fouquet et al., 1993b; Koski et al., 1994).

At Vienna Woods, predominance of Zn–sulfide in both active open conduit and relict deposits reflects mineral precipitation from high pH (> 4 – 5), metal–poor vent fluids. The

high pH of these fluids relative to those from the Eastern Manus Basin allows for precipitation of Zn–sulfide at high temperatures (~ 280 °C), despite low concentrations of Zn in Vienna Woods fluids. Similar conditions of mineral precipitation have been described to explain the precipitation of abundant Zn–sulfide in seafloor vent deposits at the Endeavour Segment, Juan de Fuca Ridge (Tivey et al., 1999; Kristall et al., 2006).

At PACMANUS and SuSu Knolls, high–temperature (> 300 °C) open conduit chimneys are rich in Cu–Fe–sulfides but lacking in sphalerite, even though concentrations of Zn in parent hydrothermal fluids are up to an order of magnitude enriched relative to those from Vienna Woods. This reflects the low pH (25 °C) of high–temperature black smoker fluids (~ 2.3 – 3.8) and the lack of saturation of sphalerite in these fluids. The predominance of bornite (± chalcopyrite) with minor tennantite and/or sphalerite in diffuser and relict chimneys at PACMANUS and SuSu Knolls reflects formation from lower–temperature fluids (< 280 °C) coupled with conductive cooling of hydrothermal fluid within more porous chimney walls. The higher modal abundance of sphalerite (± galena) in vent deposits from Roman Ruins and Roger's Ruins (PACMANUS) and one sample at Suzette (SuSu Knolls) relative to other PACMANUS and SuSu Knolls chimney deposits reflects the very high concentrations of Zn and Pb in vent fluids from which these deposits are precipitating. It has been proposed (see Chapter 4) that high Zn and Pb concentrations in low temperature vent fluids at Roman Ruins and Roger's Ruins and at one vent at Suzette reflect dissolution and remobilization of previously deposited sulfide beneath the seafloor. These data suggest that on–going zone–refinement is significantly affecting the composition and distribution of the seafloor massive sulfide deposits at Roman Ruins and Roger's Ruins and to a lesser extent at Suzette. The presence of minor tennantite in vent deposit samples from Satanic Mills,

Snowcap and Fenway (PACMANUS) and from North Su and South Su (SuSu Knolls) reflects that tennantite is saturated at temperatures significantly higher than sphalerite in vent fluids from which these deposits are precipitating. This can be related to the low vent fluid pH and lower Zn concentrations in the absence of significant on–going zone refinement at these vent fields.

Differences in fluid composition and style and condition of mineral precipitation significantly affect trace and precious metal enrichments. Vent deposits at PACMANUS and SuSu Knolls are enriched in trace elements (e.g., Co, Se, Sb, Ag, Au) relative to those at Vienna Woods. To first–order, these enrichments reflect higher concentrations of heavy and precious metals in seafloor vent fluids at PACMANUS and SuSu Knolls from which the vent deposits are forming. However, there are also considerable differences among open conduit and diffuser and relict chimneys at each vent field, with open conduit chimneys more enriched in Co and Se and less enriched in Pb, Sb, Ag and Au. Precipitation of wurtzite (at Vienna Woods) and chalcopyrite (at PACMANUS and SuSu Knolls) at high temperatures in open conduit chimneys does not favor the incorporation of most heavy and precious metals. In contrast, precipitation of a range of sulfide minerals at significantly lower temperatures in diffuser chimneys provides more suitable hosts for the enrichment of economically valuable ore metals. The trace metal compositions of diffuser–type chimney deposits are more representative of the compositions of vent fluids from which they precipitated. Consequently, trace metal distributions within diffuser–type chimneys may provide important information about the processes and conditions (e.g., temperature, pH) influencing the formation of seafloor massive sulfide deposits. Sulfide deposits forming at lower temperatures from low pH, metal–rich seafloor hydrothermal fluids, in particular those having experienced

significant zone–refinement of an existing sulfide deposit, are particular enriched in precious metals and may present the most attractive targets for the exploration of economically valuable massive sulfide deposits.

REFERENCES

Auzende J. M., Ishibashi J., Beaudoin Y., Charlou J. L., Delteil J., Donval J. P., Fouquet Y., Gouillou J. P., Ildefonse B., and Kimura H. (2000) Rift Propagation and extensive off–axis volcanic and hydrothermal activity in the Manus Basin (Papua New Guinea): MANAUTE Cruise. *InterRidge News* **9**(2), 21–25.

Bach W., Tivey M. A., Seewald J. S., Tivey M. K., Craddock P. R., Niedermeier D., and Yoerger D. (2007) Variable basement compostion and magma degassing affecting hydrothermal systems in the Eastern Manus Basin. *EOS Trans. AGU. Fall Meet. Suppl.,* **88**(52), Abstract #V21D–0749.

Barrett T. J. and Anderson G. M. (1988) The solubility of sphalerite and galena in 1–5 m NaCl solutions to 300 °C. *Geochimica et Cosmochimica Acta* **52**, 813–820.

Binns R. A., Barriga F. J. A. S., and Miller D. J. (2007) Leg 193 synthesis: Anatomy of an active felsic–hosted hydrothermal system, eastern Manus Basin, Papua New Guinea. In *Proceedings of the Ocean Drilling Program, Scientific Results*, Vol. 193 (ed. F. J. A. S. Barriga, R. A. Binns, D. J. Miller, and P. M. Herzig), pp. 1–71. doi:10.2973/odp.proc.sr.193.201.2007. Ocean Drilling Program.

Binns R. A. and Scott S. D. (1993) Actively forming polymetallic sulfide deposits associated with felsic volcanic rocks in the eastern Manus back–arc basin, Papua New Guinea. *Economic Geology* **88**, 2226–2236.

Binns R. A., Scott S. D., Gemmell J. B., Crook K. A. W., and Shipboard Scientific Party. (1997) The SuSu Knolls hydrothermal field, eastern Manus Basin, Papua New Guinea. *EOS Trans. AGU. Fall Meet. Suppl.,* **78**(52), Abstract #V22E–02.

Both R., Crook K., Taylor B., Brogan S., Chappell B., Frankel E., Liu L., Sinton J., and Tiffin D. (1986) Hydrothermal chimneys and associated fauna in the Manus back–arc basin,

Papua New Guinea. *EOS Transactions, American Geophysical Union* **67**, 489.

Bouricer W. L. and Barnes H. L. (1987) Ore solution chemistry: VI. Stabilities of chloride and bisulphide complexes of zinc to 350°C. *Economic Geology* **82**, 1839–1863.

Butterfield D. A., McDuff R. E., Mottl M. J., Lilley M. D., Lupton J. E., and Massoth G. J. (1994) Gradients in the composition of hydrothermal fluids from the Endeavour segment vent field: Phase separation and brine loss. *Journal of Geophysical Research* **99**, 9561–9583.

Craddock P. R., Tivey M. K., Seewald J. S., Rouxel O. J., and Bach W. (2007) The role of magmatic volatile input, near–surface seawater entrainment and sulfide deposition in regulating metal concentrations within Manus Basin hydrothermal systems. *EOS Trans. AGU. Fall Meet. Suppl.,* **88**(52), Abstract #V34B–05.

Crerar D. A. and Barnes H. L. (1976) Ore solution chemistry. V. Solubilities of chalcopyrite and chalcocite assemblages in hydrothermal solution at 200 °C to 350 °C. *Economic Geology* **71**(772–794).

Davies H. L., Honza E., Tiffin D. L., Lock J., Okuda Y., Keene J. B., Murakami F., and Kisimoto K. (1987) Regional setting and structure of the western Solomon Sea. *Geo–Marine Letters* **7**, 153–160.

Ding K. and Seyfried W. E., Jr. (1992) Determination of Fe–Cl complexing in the low pressure supercritical region (NaCl fluid): Iron solubility constraints on pH of subseafloor hydrothermal fluids. *Geochimica et Cosmochimica Acta* **56**(10), 3681–3692.

Edmond J. M., Campbell A. C., Palmer M. R., German C. R., Klinkhammer G. P., Edmonds H. N., Elderfield H., Thompson G., and Rona P. (1995) Time series studies of vent fluids from the TAG and MARK sites (1986, 1990) Mid–Atlantic Ridge and a mechanism for Cu/Zn zonation in massive sulphide orebodies. In *Hydrothermal Vents and Processes*, Vol. 87 (ed. L. M. Parson, C. L. Walker, and D. R. Dixon), pp. 77–86. Geological Society Special Publication.

Fleischer M. (1955) Minor elements in some sulfide minerals. *Economic Geology* **50**, 970–1024.

Fouquet Y., Auclair G., Cambon P., and Etoubleau J. (1988) Geological setting and mineralogical and geochemical investigations on sulfide deposits near 13 °N on the

East Pacific Rise. *Marine Geology* **84**(3–4), 145–178.

Fouquet Y., von Stackelberg U., Charlou J. L., Erzinger J., Herzig P. M., Muehe R., and Wiedicke M. (1993a) Metallogenesis in back–arc environments; The Lau Basin example. *Economic Geology* **88**(8), 2150.

Fouquet Y., Wafik A., Cambon P., Mevel C., Meyer G., and Gente P. (1993b) Tectonic setting and mineralogical and geochemical zonation in the Snake Pit sulfide deposit (Mid–Atlantic Ridge, at 23 °N). *Economic Geology* **88**, 2018–2036.

Franklin J. M., Lydon J. W., and Sangster D. F. (1981) Volcanic–associated massive sulfide deposits. *Economic Geology* **75**, 485–627.

Goldfarb M. S., Converse D. R., Holland H. D., and Edmond J. M. (1983) The genesis of hot spring deposits on the East Pacific Rise, 21 °N. In *The Kuroko and Related Volcanogenic Massive Sulfide Deposits. Economic Geology Monograph*, Vol. 5 (ed. H. Ohmoto and B. J. Skinner), pp. 184–197.

Hannington M., Herzig P., Scott S., Thompson G., and Rona P. (1991) Comparative mineralogy and geochemistry of gold–bearing sulfide deposits on the mid–ocean ridges. *Marine Geology* **101**, 217–248.

Hannington M. D., De Ronde C. E. J., and Petersen S. (2005) Sea–floor tectonics and submarine hydrothermal systems. *Economic Geology* **100**, 111–141.

Haymon R. M. (1983) Growth history of hydrothermal black smoker chimneys. *Nature* **301**(5902), 695–698.

Haymon R. M. and Kastner M. (1981) Hot spring deposits on the East Pacific Rise at 21 °N: Preliminary description of mineralogy and genesis. *Earth and Planetary Science Letters* **53**, 363–381.

Hrischeva E., Scott S. D., and Weston R. (2007) Metalliferous sediments associated with presently forming volcanogenic massive sulfides: The SuSu Knolls hydrothermal field, Eastern Manus Basin, Papua New Guinea. *Economic Geology* **102**, 55–74.

Janecky D. R. and Shanks W. C., III. (1988) Computational modeling of chemical and sulfur isotopic reaction processes in seafloor hydrothermal systems: chimneys, massive sulfides, and subjacent alteration zones. *Canadian Mineralogist* **26**, 805–825.

Johnson J. W., Oelkers E. H., and Helgeson H. C. (1992) SUPCRT92: a software package for calculating the standard molal thermodynamic properties of minerals, gases, aqueous

species and reactions from 1 to 5000 bar, and 0 to 1000 °C. *Computers and Geosciences* **18**(7), 899–947.

Kim J., Lee I., and Lee K.–Y. (2004) S, Sr, and Pb isotopic systematics of hydrothermal chimney precipitates from the Eastern Manus Basin, western Pacific: Evaluation of magmatic contribution to hydrothermal system. *Journal of Geophysical Research* **109**, B12210, doi:10.1029/2003JB002912.

Knight J. E. (1977) A thermochemical study of alunite, enargite, luzonite and tennantite deposits. *Economic Geology* **72**, 1321–1336.

Koski R. A., Clague D. A., and Oudin E. (1984) Mineralogy and chemistry of massive sulfide deposits from the Juan de Fuca Ridge. *Geological Society of America Bulletin* **95**(8), 930–945.

Koski R. A., Jonasson I. R., Kadko D. C., Smith V. K., and Wong F. L. (1994) Compositions, growth mechanisms, and temporal relations of hydrothermal sulfide–sulfate–silica chimneys at the northern Cleft segment, Juan de Fuca Ridge. *Journal of Geophysical Research* **99**(B3), 4813–4832.

Kristall B., Kelley D. S., Hannington M. D., and Delaney J. R. (2006) Growth history of a diffusely venting sulfide structure from the Juan de Fuca Ridge: A petrological and geochemical study. *Geochemistry Geophysics Geosystems* **7**, Q07001, doi:10.1029/2005GC001166.

Lisitsyn A. P., Crook K. A. W., Bogdanov Y. A., Zonenshayn L. P., Muravyev K. G., Tufar W., Gurvich Y. G., Gordeyev V. V., and Ivanov G. V. (1993) A hydrothermal field in the rift zone of the Manus Basin, Bismarck Sea. *International Geology Review* **35**, 105–126.

Martinez F. and Taylor B. (1996) Backarc spreading, rifting, and microplate rotation, between transform faults in the Manus Basin. *Marine Geophysical Researches* **18**, 203–224.

McCollom T. M. and Shock E. L. (1997) Geochemical constraints on chemolithoautotrophic metabolism by microorganisms in seafloor hydrothermal systems. *Geochimica et Cosmochimica Acta* **61**(4375–4391).

Moss R. and Scott S. D. (2001) Geochemistry and mineralogy of gold–rich hydrothermal precipitates from the eastern Manus Basin, Papua New Guinea. *Canadian Mineralogist* **39**, 957–978.

Ohmoto H. and Skinner B. J. (1983) The Kuroko and Related Volcanogenic Massive Sulfide Deposits. In *Economic Geology Monograph*, Vol. 5, pp. 604.

Ruaya J. R. and Seward T. M. (1986) The stability of chlorozinc (II) complexes in hydrothermal solutions up to 350 °C. *Geochimica et Cosmochimica Acta* **50**, 651–661.

Sawkins F. J. (1990) *Metal Deposits in Relation to Plate Tectonics*. Springer–Verlag.

Scott S. D. (1976) Application of the sphalerite geobarometer to regionally metamorphosed terrains. *American Mineralogist* **61**, 661–670.

Scott S. D. (1983) Chemical behaviour of sphalerite and arsenopyrite in hydrothermal and metamorphic environments. *Mineralogical Magazine* **47**, 427–435.

Seewald J. S., Reeves E., Saccocia P., Rouxel O. J., Walsh E., Price R. E., Tivey M., Bach W., and Tivey M. (2006) Water–rock reaction, substrate composition, magmatic degassing, and mixing as major factors controlling vent fluid compositions in Manus Basin hydrothermal systems. *EOS Trans. AGU. Fall Meet. Suppl.,* **87**(52), Abstract # B34A–02.

Seewald J. S. and Seyfried W. E., Jr. (1990) The effect of temperature on metal mobility in subseafloor hydrothermal systems: Constraints from basalt alteration experiments. *Earth and Planetary Science Letters* **101**, 388–403.

Seyfried W. E., Jr. and Mottl M. J. (1982) Hydrothermal alteration of basalt by seawater under seawater–dominated conditions. *Geochimica et Cosmochimica Acta* **46**, 985–1002.

Sinton J. M., Ford L. L., Chappell B., and McCulloch M. T. (2003) Magma genesis and mantle heterogeneity in the Manus Back–Arc Basin, Papua New Guinea. *Journal of Petrology* **44**, 159–195.

Sverjensky D. A., Hemley J. J., and D'Angelo W. M. (1991) Thermodynamic assessment of hydrothermal alkali feldspar–mica–aluminosilicate equilibria. *Geochimica et Cosmochimica Acta* **55**(4), 989–1004.

Taylor B. (1979) Bismarck Sea; Evolution of a back–arc basin. *Geology* **7**, 171–174.

Tivey M. A., Bach W., Seewald J. S., Tivey M. K., Vanko D. A., and Shipboard Science and Technical Teams. (2007) Cruise Report R/V Melville, MAGELLAN–06. Hydrothermal systems in the Eastern Manus Basin: Fluid chemistry and magnetic structures as guides to subseafloor processes, pp. 67. Woods Hole Oceanographic

Institution.

Tivey M. K. (1995) The influence of hydrothermal fluid composition and advection rates on black smoker chimney mineralogy: Insights from modeling transport and reaction. *Geochimica et Cosmochimica Acta* **59**, 1933–1949.

Tivey M. K., Bach W., Tivey M. A., Seewald J. S., Craddock P. R., Rouxel O. J., Yoerger D. R., Yeats C. J., McConachy T., Quigley M., Vanko D. A., and MGLN06MV Scientific Party. (2006) Investigating the influence of magmatic volatile input and seawater entrainment on vent deposit morphology and composition in Manus Basin (back–arc) hydrothermal systems. *EOS Trans. AGU. Fall Meet. Suppl.,* **87**(52), Abstract #B34A–01.

Tivey M. K., Humphris S. E., Thompson G., Hannington M. D., and Rona P. A. (1995) Deducing patterns of fluid flow and mixing within the TAG active hydrothermal mound using mineralogical and geochemical data. *Journal of Geophysical Research* **100**(B7), 12527–12555.

Tivey M. K. and McDuff R. E. (1990) Mineral precipitation in the walls of black smoker chimneys: A quantitative model of transport and chemical reaction. *Journal of Geophysical Research* **95**(B8), 12617–12637.

Tivey M. K., Stakes D. S., Cook T. L., Hannington M. D., and Petersen S. (1999) A model for the growth of steep–sided vent structures on the Endeavour Segment of the Juan de Fuca Ridge: Results of a petrologic and geochemical study. *Journal of Geophysical Research* **104**(B10), 22,859.

Tufar W. (1990) Modern hydrothermal activity, formation of complex massive sulfide deposits and associated vent communities in the Manus back–arc basin (Bismarck Sea, Papua New Guinea). *Mitteilungen der Osterreichischen Geologischen Gesellschaft* **82**, 183–210.

Von Damm K. L. (1990) Seafloor hydrothermal activity: Black smoker chemistry and chimneys. *Annual Review of Earth and Planetary Sciences* **18**(1), 173–204.

Von Damm K. L. (1995) Controls on the chemistry and temporal variability of seafloor hydrothermal fluids. In *Seafloor Hydrothermal Systems: Physical, Chemical, Biological and Geological Interactions. Geophysical Monograph.*, Vol. 91 (ed. S. E. Humphris, R. A. Zierenberg, L. S. Mullineaux, and R. E. Thomson), pp. 222–247.

American Geophysical Union.

Von Damm K. L., Edmond J. M., Grant B., Measures C. I., Walden B., and Weiss R. F. (1985) Chemistry of submarine hydrothermal solutions at 21 °N, East Pacific Rise. *Geochimica et Cosmochimica Acta* **49**(11), 2197–2220.

Wolery T. J. (1992) *EQ3NR, A Computer Program for Geochemical Aqueous Speciation–Solubility Calculations: Theoretical Manual, User's Guide and Related Documentation (Version 7.0).* Lawerence Livermore National Laboratory, Livermore, CA.

Wolery T. J. and Daveler S. A. (1992) *EQ6, A Computer Program for Reaction Path Modeling of Aqueous Geochemical Systems: Theoretical Manual, User's Guide and Related Documentation (Version 7.0).* Lawerence Livermore National Laboratory, Livermore, CA.

Yeats C. J., Binns R. A., and Parr J. M. (2000) Advanced argillic alteration associated with actively forming submarine polymetallic sulfide mineralization in the eastern Manus Basin, Papua New Guinea. *Geological Society of Australia Abstracts* **59**, 555.

CHAPTER 6

Summary and Concluding Remarks

This thesis examines in detail and characterizes the chemical compositions of a range of seafloor hydrothermal fluids and related vent mineral deposits recovered from hydrothermal systems in the Manus back–arc basin, Papua New Guinea, including from the Vienna Woods vent field (Manus Spreading Center, MSC) and the PACMANUS, DESMOS and SuSu Knolls vent fields (Eastern Manus Basin, EMB). The important processes affecting the formation and composition of seafloor vent fluids and related vent deposits in back–arc basin hydrothermal systems are (1) deep–seated fluid–rock interactions at a range of elevated temperature and pressure and rock composition, overprinted by (2) varying magmatic acid volatile (H_2O–CO_2–HCl–HF–SO_2) input beneath the seafloor and (3) local near–seafloor seawater entrainment and mixing with rising high–temperature hydrothermal (or magmatic–hydrothermal) fluids. Magmatic volatile inputs contribute significant acidity, thereby considerably increasing metal mobility during fluid–rock interaction. In addition, the acidity that accompanies magmatic volatile input may lead to remobilization of previously deposited metal sulfides. Local entrainment of seawater and mixing with hydrothermal fluids can result in sub–seafloor mineral deposition, formation of secondary acidity and subsequent sulfide remobilization.

In this thesis, concentrations and distributions of rare earth elements (REEs) and

heavy metals (Mn, Fe, Cu, Zn, Pb, Ag, Cd, Au, As, Sb, Co) in seafloor vent fluids and related vent deposits are used as indicators of these processes. Seafloor vent fluids from the MSC and EMB exhibit a range of chondrite–normalized REE_N pattern shapes distinct from the uniform pattern shape of mid–ocean ridge vent fluids (Michard and Albarede, 1986; Klinkhammer et al., 1994; Mitra et al., 1994). The REEs are solubility controlled and their concentrations are affected by the conditions (e.g., temperature, pressure and resulting pH) of fluid–rock interaction and by hydrothermal fluid composition. In particular, vent fluid REE concentrations and REE_N pattern shapes are affected by differences in fluid pH and ligand concentrations (e.g., Cl^-, F^-, SO_4^{2-}) related to different styles and compositions of magmatic acid volatile input (HF, SO_2) in back–arc hydrothermal systems (c.f., Douville et al., 1999; Bach et al., 2003). The REE_N pattern shapes of seafloor hydrothermal fluids are not sensitive indicators of the extent of sub–seafloor mixing between rising hydrothermal fluid and locally entrained seawater, because the concentrations of REEs in seafloor vent fluids are orders of magnitude more enriched relative to seawater.

To first–order, REE_N pattern shapes preserved in anhydrite vent deposit samples are the same as those of hydrothermal fluids from which anhydrite precipitated (see also Mills and Elderfield, 1995), suggesting that anhydrite is a faithful recorder of the REE composition of the hydrothermal fluid. Of significance, the range of REE_N pattern shapes preserved in anhydrite sampled from vent fields in the Eastern Manus Basin records a history of varying extent and composition of magmatic acid volatile input. REE compositions preserved in anhydrite are particularly useful for inferring the temporal evolution of seafloor hydrothermal systems, or the conditions of vent deposit formation

in relict systems where hydrothermal fluids from which the vent deposit formed no longer exist. Sulfur isotope ratios ($\delta^{34}S$–sulfate) of the same anhydrite samples are used to provide complementary evidence to support the input of magmatic volatiles (i.e., SO_2) (e.g., Roberts et al., 2003). However, isotopic signatures of magmatic sulfur input appear to be often overprinted by mixing of magmatic–hydrothermal fluids with sulfate–rich seawater sulfate at or close to the seafloor where seafloor hydrothermal fluids and related vent deposits are sampled. The available data suggest that sulfur isotopic compositions in anhydrite are less sensitive indicators of magmatic acid volatile input than are REE_N pattern shapes.

Concentrations of heavy metals and metalloids (e.g., Mn, Fe, Cu, Zn, Pb, Cd, As, Sb) in seafloor hydrothermal fluids are also solubility controlled and affected by conditions of fluid–rock interaction (e.g., temperature, pressure, and resultant pH). Similar to the REEs, higher concentrations of heavy metals in seafloor vent fluids from the EMB relative to those from the MSC reflect their higher solubility during fluid–rock interaction owing to a lower pH of fluid–rock interaction. In part, the lower pH can be related to higher temperatures of fluid–rock interaction; however, the input of magmatic acid volatiles significantly affects metal solubility during alteration of oceanic crust. Magmatic acid volatile input may also locally affect aqueous metal concentrations because the acidity that accompanies input of magmatic vapors can result in dissolution of previously deposited sulfide. From the data available, there is no clear evidence to support that the degassing of magmatic acid volatile fluids contributes a direct and significant source of metals to seafloor hydrothermal systems. In contrast to the REEs, concentrations and distributions of ore–forming metals are sensitive to local entrainment

of seawater and mixing with high–temperature hydrothermal fluids because mixing can result in substantial precipitation of high–temperature Cu–Fe–sulfides (e.g., chalcopyrite) and generation of secondary acidity, which leads to remobilization of previously deposited sulfide (e.g., sphalerite and/or wurtzite). This process of zone–refinement, as described at the TAG active mound, 26 °N Mid–Atlantic Ridge (Tivey et al., 1995), appears to be important for the chemical evolution of at least some seafloor hydrothermal fluids and massive sulfide deposits in the Manus Basin.

Related seafloor massive sulfide deposits in the Manus Basin exhibit a wide range of chimney morphologies and mineral compositions. On the Manus Spreading Center (Vienna Woods), both active open conduit and relic diffuser–type deposits are dominated by Zn–sulfide (as wurtzite and/or sphalerite). In the Eastern Manus Basin (PACMANUS and SuSu Knolls), active high–temperature open conduit chimneys are dominated by Cu–Fe–sulfides (as chalcopyrite), and lower–temperature diffuser chimneys are dominated by Cu–Fe–sulfides (as bornite ± chalcopyrite) with different amounts of lesser Cu–As–sulfosalts (as tennantite) and Zn–sulfide (as sphalerite). Comparison to paired hydrothermal fluids suggests that differences in chimney morphology and mineral composition are related to differences in styles of fluid flow and to differences in fluid composition. In particular, the high pH of vent fluids from Vienna Woods and low pH of vent fluids from PACMANUS and SuSu Knolls affects considerably the solubility of sulfide minerals (e.g., sphalerite) and their resulting chimney mineralogical compositions. Although high concentrations of heavy and precious metals (e.g., Ag, Pb, Co, Au) in seafloor vent deposit samples reflect high concentrations in parental hydrothermal fluids, enrichment of trace metals is affected significantly by the conditions of mineral sulfide

precipitation. In particular, precipitation of sulfides at low temperatures (< 200 – 220 °C) within diffuser–type chimneys appears to favor the enrichment of trace metals versus deposition at high–temperatures in open conduit chimneys, even though metal concentrations in high–temperature fluids exiting open conduit chimneys may be higher. The available data suggest that the distributions of trace metals in a range of sulfide minerals in high–and low–temperature mineral assemblages (e.g., open conduit versus diffuser–type chimneys) can be used to infer the temperature and pH conditions of massive sulfide deposit formation in this and other active and relict submarine hydrothermal systems.

6.1. Future research directions

There are several topics of scientific interest and debate that have not been fully addressed in this thesis research and that are recommended as a foci for future studies. The first concerns the use of stable isotopes as tracers of magmatic volatile input to seafloor hydrothermal systems. The isotopes of sulfur (sulfur being a primary constituent of seafloor hydrothermal vent (sulfide–sulfate) deposits) can provide considerable information about the sources of S in seafloor vent fluids and related mineral deposits, and about the geochemical processes affecting the cycling of S and, by association, of other elements (Shanks et al., 1995; Shanks, 2001). Experimental studies have shown that isotopes of S are affected significantly by input and disproportionation of SO_2 to H_2S (or S°) and H_2SO_4 (Kusakabe et al., 2000). Sulfate–sulfur and sulfide–sulfur of direct magmatic origin have isotope compositions distinct (isotopically lighter) than sulfur derived from sulfate–sulfur in seawater or reaction of sulfide–sulfur in volcanic rocks (Kusakabe et al., 2000). Although the data for sulfate–sulfur isotope ratios of anhydrite

(δ^{34}S–sulfate) recovered from vent fields in the Manus Basin (PACMANUS and SuSu Knolls) suggest that sulfate–sulfur isotopes can be used to track deep–seated magmatic volatile input (Chapter 2, see also Roberts et al., 2003), sulfate–sulfur isotope compositions in the near–seafloor hydrothermal environment can be significantly compromised by input by large volumes of seawater sulfate, which overprint the isotopic signatures of magmatic sulfate–sulfur contributions . In contrast, isotope ratios of sulfide–sulfur, as measured in seafloor hydrothermal fluids (as H_2S,aq) and in sulfide and sulfosalt minerals (e.g., chalcopyrite, pyrite, tennantite), should provide a better indication of magmatic acid volatile inputs into hydrothermal systems in convergent plate margins, because sulfide is absent from ambient seawater. Indeed, recent studies examining the sulfide–sulfur (δ^{34}S–sulfide) ratios of chimney sulfides recovered from vent fields in the Lau back–arc basin (e.g., Herzig et al., 1998) and the Manus back–arc basin (e.g., Kim et al., 2004) have identified isotopically light δ^{34}S–sulfide ratios (< 0 ‰). The data are consistent with direct and significant contributions of magmatic acid volatiles to these hydrothermal systems. However, other processes including equilibrium isotope exchange between seawater sulfate and sulfide at low temperatures (< 300 °C) (Ohmoto and Lasaga, 1982) and microbial sulfate reduction (Canfield, 2001) can result in isotopically light δ^{34}S–sulfide ratios that can resemble those of magmatically–derived sulfide–sulfur. Recent advances in analytical capabilities have now made it possible to determine precisely multiple sulfur isotope compositions (δ^{34}S, δ^{33}S and δ^{36}S) of seafloor vent fluid H_2S and of related sulfide minerals (e.g., Ono et al., 2007). Preliminary studies suggest that multiple sulfur isotope compositions reflecting different geochemical and biological processes in hydrothermal systems follow measurably different isotope

fractionation pathways (Ono et al., 2007). Future studies should focus on the multiple sulfur isotope ratios as a means to characterize the multiple sulfur isotope compositions of magmatic sulfur (both sulfate and sulfide) and to distinguish the sulfide–sulfur isotope compositions arising from chemical disproportionation of magmatic S versus other processes.

The second, and perhaps most controversial, unresolved issue concerns the possible sources of ore–forming metals to seafloor hydrothermal systems in back–arc basins. Evidence for the addition of metal–bearing (e.g., Cu, Zn) magmatic volatile fluids to submarine hydrothermal fluids in the Manus Basin is centered on the presence of metal–bearing precipitates within vesicles of erupted felsic volcanic rocks (Yang and Scott, 1996, 2002). Experiments have shown that volatile elements (such as Cu, Au, As) can be effectively partitioned into volatile–rich fluids exsolving from melts at magmatic conditions (Simon et al., 2006, 2007). Heavy metal concentrations in Manus Basin seafloor hydrothermal fluids examined as part of this thesis do not provide clear and definitive evidence to support a direct and significant input of metals carried within an exsolved magmatic volatile–rich fluids (Chapter 4). The available data suggest that enhanced removal of metals from crustal rocks (or metal condensates; c.f., Yang and Scott, 1996) or from previously deposited sulfide, owing to low pH conditions as a result of magmatic volatile input, is the predominant source for metals in these seafloor hydrothermal fluids.

Non–traditional stable metal isotope studies, in particular of Cu, may provide constraints on the sources of Cu and associated heavy metals in Manus Basin seafloor hydrothermal fluids that cannot be obtained from determinations of metal concentrations

alone. In particular, theoretical calculations (e.g., Seo et al., 2007) predict significant fractionation of Cu isotopes during exsolution and segregation of low salinity vapors and higher salinity liquids (between ~ 0.8 and 2.9 ‰, as a function of decreasing temperature from 500 to 150 °C). It is possible that if Cu is partitioned preferentially into a degassing magmatic acid volatile fluid from a melt, there may measurable isotopic fractionation of Cu associated with this process. Further, studies of Cu isotope ratios in Cu–Fe–sulfides from both ancient (e.g., Larson et al., 2003) and modern (e.g., Rouxel et al., 2004) hydrothermal systems have indicated Cu isotopes to be fractionated significantly during hydrothermal weathering and sulfide remobilization (resulting mineral deposits enriched in heavy Cu isotopes). Cu isotope studies of paired seafloor hydrothermal fluids and related vent sulfide deposits may provide valuable constraints on the extent to which these processes affect the sources and cycling of Cu in seafloor hydrothermal systems in back–arc basins. In particular, it should be a priority to determine the Cu isotope compositions of fluoride–rich (380 – 530 μmol/kg; E. Reeves and J. Seewald, *unpubl. data*), magmatically–influenced vent fluids and related vent deposits from the PACMANUS and SuSu Knolls hydrothermal systems (e.g., vent fluids from Satanic Mills, Suzette and South Su), because it is unclear if marked Cu–enrichments (up to 1100 μmol/kg; Chapter 4) in fluoride–rich seafloor vent fluids reflect remobilization of previously deposited Cu–bearing sulfides and/or sulfosalts as a result of low pH, or reflect a direct contribution of Cu (and Au, As and Sb) in exsolved magmatic vapors. In addition, it should be a priority to determine the Cu isotope ratios of high–temperature vent fluids exiting open conduit black smoker chimneys and apparently related low–temperature vent fluids exiting diffuser–type chimneys at the Roman Ruins and Roger's

Ruins vent fields (PACMANUS hydrothermal system) because seafloor vent fluids and related vent deposits at these vent fields appear to be impacted significantly by sub–seafloor mineral precipitation and sulfide remobilization (Chapters 4 and 5) and may carry with them Cu isotope compositions diagnostic of such sulfide re–working. Stable metal isotope studies can provide further insights and complementary information to support the ideas put forward in this thesis regarding the fundamental processes affecting the formation and composition of seafloor vent fluids and related mineral deposits.

REFERENCES

Bach W., Roberts S., Vanko D. A., Binns R. A., Yeats C. J., Craddock P. R., and Humphris S. E. (2003) Controls of fluid chemistry and complexation on rare–earth element contents of anhydrite from the Pacmanus subseafloor hydrothermal system, Manus Basin, Papua New Guinea. *Mineralium Deposita* **38**(8), 916–935.

Canfield D. E. (2001) Biogeochemistry of Sulfur Isotopes. *Reviews in Mineralogy and Geochemistry* **43**, 607–636.

Douville E., Bienvenu P., Charlou J. L., Donval J. P., Fouquet Y., Appriou P., and Gamo T. (1999) Yttrium and rare earth elements in fluids from various deep–sea hydrothermal systems. *Geochimica et Cosmochimica Acta* **63**(5), 627–643.

Herzig P. M., Hannington M. D., and Arribas A., Jr. (1998) Sulfur isotopic composition of hydrothermal precipitates from the Lau back–arc: Implications for magmatic contributions to seafloor hydrothermal systems. *Mineralium Deposita* **33**(3), 226–237.

Kim J., Lee I., and Lee K.–Y. (2004) S, Sr, and Pb isotopic systematics of hydrothermal chimney precipitates from the Eastern Manus Basin, western Pacific: Evaluation of magmatic contribution to hydrothermal system. *Journal of Geophysical Research* **109**, B12210, doi:10.1029/2003JB002912.

Klinkhammer G., German C. R., Elderfield H., Greaves M. J., and Mitra A. (1994) Rare

earth elements in hydrothermal fluids and plume particulates by inductively coupled plasma mass spectrometry. *Marine Chemistry* **45**(3), 179–186.

Kusakabe M., Komoda Y., Takano B., and Abiko T. (2000) Sulfur isotopic effects in the disproportionation reaction of sulfur dioxide in hydrothermal fluids: Implications for the $\delta^{34}S$ variations of dissolved bisulfate and elemental sulfur from active crater lakes. *Journal of Volcanology and Geothermal Research* **97**(1–4), 287.

Larson P. B., Maher K., Ramos F. C., Chang Z., Gaspar M., and Meinert L. D. (2003) Copper isotope ratios in magmatic and hydrothermal ore–forming environments. *Chemical Geology* **201**, 337–350.

Michard A. and Albarede F. (1986) The REE content of some hydrothermal fluids. *Chemical Geology* **55**(1–2), 51–60.

Mills R. A. and Elderfield H. (1995) Rare earth element geochemistry of hydrothermal deposits from the active TAG Mound, 26 °N Mid–Atlantic Ridge. *Geochimica et Cosmochimica Acta* **59**, 3511–3524.

Mitra A., Elderfield H., and Greaves M. J. (1994) Rare earth elements in submarine hydrothermal fluids and plumes from the Mid–Atlantic Ridge. *Marine Chemistry* **46**(3), 217–235.

Ohmoto H. and Lasaga A. C. (1982) Kinetics of reactions between aqueous sulfates and sulfides in hydrothermal systems. *Geochimica et Cosmochimica Acta* **46**(10), 1727–1745.

Ono S., Shanks W. C., III, Rouxel O. J., and Rumble D. (2007) S–33 constraints on the seawater sulfate contribution in modern seafloor hydrothermal vent sulfides. *Geochimica et Cosmochimica Acta* **71**(5), 1170–1182.

Roberts S., Bach W., Binns R. A., Vanko D. A., Yeats C. J., Teagle D. A. H., Blacklock K., Blusztajn J. S., Boyce A. J., and Cooper M. J. (2003) Contrasting evolution of hydrothermal fluids in the PACMANUS system, Manus Basin: The Sr and S isotope evidence. *Geology* **31**(9), 805–808.

Rouxel O. J., Fouquet Y., and Ludden J. N. (2004) Copper isotope systematics of the Lucky Strike, Rainbow, and Logatchev sea–floor hydrothermal fields on the Mid–Atlantic Ridge. *Economic Geology* **99**(3), 585.

Seo J. H., Lee S. K., and Lee I. (2007) Quantum chemical calculations of equilibrium

copper (I) isotope fractionations in ore–forming fluids. *Chemical Geology* **243**, 225–237.

Shanks W. C., III. (2001) Stable Isotopes in Seafloor Hydrothermal Systems: Vent fluids, hydrothermal deposits, hydrothermal alteration and microbial processs. *Reviews in Mineralogy and Geochemistry* **43**, 469–525.

Shanks W. C., III, Bohlke J. K., and Seal R. R. (1995) Stable isotopes in mid–ocean ridge hydrothermal systems: Interaction between fluids, minerals and organisms. In *Seafloor Hydrothermal Systems: Physical, Chemical, Biological and Geological Interactions. Geophysical Monograph.*, Vol. 91 (ed. S. E. Humphris, R. A. Zierenberg, L. S. Mullineaux, and R. E. Thomson), pp. 194–221. American Geophysical Union.

Simon A. C., Pettke T., Candela P. A., Piccoli P. M., and Heinrich C. A. (2006) Copper partitioning in a melt–vapor–brine–magnetite–pyrrhotite assemblage. *Geochimica et Cosmochimica Acta* **70**(22), 5583–5600.

Simon A. C., Pettke T., Candela P. A., Piccoli P. M., and Heinrich C. A. (2007) The partitioning behavior of As and Au in S–free and S–bearing magmatic assemblages. *Geochimica et Cosmochimica Acta* **71**(7), 1764–1782.

Tivey M. K., Humphris S. E., Thompson G., Hannington M. D., and Rona P. A. (1995) Deducing patterns of fluid flow and mixing within the TAG active hydrothermal mound using mineralogical and geochemical data. *Journal of Geophysical Research* **100**(B7), 12527–12555.

Yang K. and Scott S. D. (1996) Possible contribution of a metal–rich magmatic fluid to a sea–floor hydrothermal system. *Nature* **383**, 420–423.

Yang K. and Scott S. D. (2002) Magmatic Degassing of volatiles and ore metals into a hydrothermal system on the modern seafloor of the Eastern Manus Back–Arc Basin, Western Pacific. *Economic Geology* **97**(5), 1079–1100.

Appendix B-1.

Complete listing of analytical data for rare earth element concentrations measured in seafloor hydrothermal fluids sampled from the Manus Basin (Vienna Woods, PACMANUS, DESMOS and SuSu Knolls vent fields) during cruise MGLN06MV (Tivey et al., 2007). Analytical measurements were performed separately on dissolved and particle fractions ("bottle-filter" and "dregs") and mathematically re-constituted to obtain the precipitate- and contaminant-corrected fluid composition.

The following abbreviation(s) is used in the tables:

N/A = fraction not available for analysis.

Appendix B1. Measured Rare Earth Element concentrations (pmol/kg) in "dissolved" fractions of sampled vent fluids from Vienna Woods

Fluid Sampler ID	Vent Site	Vent Orifice	Mg (mmol/kg)	La	Ce	Pr	Nd	Sm	Eu	Gd	Tb	Dy	Ho	Er	Yb
J2-207-1-W1-IGT7	Vienna Woods	VW1	3.36	1459	1396	132	408	59	550	77	15	37	13	30	22
J2-207-1-W2-IGT3	Vienna Woods	VW1	1.55	1641	1727	171	520	78	722	68	10	38	14	23	18
J2-207-1-W3-M2	Vienna Woods	VW1	1.44	2077	1915	243	963	291	813	274	45	241	55	135	133
J2-207-2-W1-IGT4	Vienna Woods	VW2	1.02	948	886	105	299	38	522	32	7	19	12	17	16
J2-207-3-W1-IGT8	Vienna Woods	VW3	1.11	780	624	73	181	22	280	14	5	10	17	14	8
J2-207-3-W2-IGT6	Vienna Woods	VW3	14.90	399	429	41	112	7	103	6	4	5	15	8	4

Appendix B1. Measured Rare Earth Element concentrations (pmol/kg) in "dregs" fractions of sampled vent fluids from Vienna Woods

Fluid Sampler ID	Vent Site	Vent Orifice	Mg (mmol/kg)	La	Ce	Pr	Nd	Sm	Eu	Gd	Tb	Dy	Ho	Er	Yb
J2-207-1-W1-IGT7	Vienna Woods	VW1	3.36		191	21	87	32	28	11	1	8	1	6	1
J2-207-1-W2-IGT3	Vienna Woods	VW1	1.55												
J2-207-1-W3-M2	Vienna Woods	VW1	1.44		42	9	41	7	0	4	0	3	0	1	0
J2-207-2-W1-IGT4	Vienna Woods	VW2	1.02	54	335	48	160	42	96	29	3	13	2	8	3
J2-207-3-W1-IGT8	Vienna Woods	VW3	1.11	48	285	32	101	21	100	18	2	10	2	5	3
J2-207-3-W2-IGT6	Vienna Woods	VW3	14.90		302	16	47	28	100	13	1	10	1	4	4

Appendix B1. Measured Rare Earth Element concentrations (pmol/kg) in "dissolved" fractions of sampled vent fluids from PACMANUS

Fluid Sampler ID	Vent Site	Vent Orifice	Mg (mmol/kg)	La	Ce	Pr	Nd	Sm	Eu	Gd	Tb	Dy	Ho	Er	Yb
J2-208-1-W1-IGT8	Roman Ruins	RMR1	8.01	8307	10075	811	2133	282	6769	171	25	109	19	54	56
J2-208-1-W2-IGT5	Roman Ruins	RMR1	8.28	8635	11043	911	2293	75	6933	153	20	79	20	47	123
J2-208-1-W3-M4	Roman Ruins	RMR1	8.90	6510	8566	741	2049	278	6704	177	23	108	19	53	66
J2-208-2-W2-IGT2	Roman Ruins	RMR2	16.56	979	2158	276	1097	278	2833	187	27	132	22	58	58
J2-208-2-W1-IGT1	Roman Ruins	RMR2	16.55	726	4146	235	956	215	2728	160	25	114	19	48	50
J2-208-2-W3-M2	Roman Ruins	RMR2	27.50	343	1045	208	1077	390	2020	308	55	315	55	156	174
J2-213-3-W1-IGT7	Roman Ruins	RMR3	23.36	5505	9640	1244	4865	978	10371	839	105	533	87	246	221
J2-213-3-W3-M4	Roman Ruins	RMR3	6.39	9304	14964	1887	7210	1395	15879	1100	131	602	84	214	154
J2-222-4-W2-IGT1	Roman Ruins	RMR4	3.63	13638	23722	2798	10130	1928	11097	1314	153	674	96	225	184
J2-222-4-W3-M4	Roman Ruins	RMR4	4.71	10897	19320	2469	9421	1888	10622	1309	148	668	96	223	176
J2-213-6-W1-IGT3	Roger's Ruins	RGR1	5.63	6740	11371	1447	5870	1218	7662	926	96	406	51	127	91
J2-213-6-W2-IGT4	Roger's Ruins	RGR1	8.10	5081	8783	1173	4833	1059	6893	795	86	369	47	111	80
J2-213-6-W3-M2	Roger's Ruins	RGR1	4.68	6068	11059	1388	5824	1255	7671	945	100	426	54	131	82
J2-222-1-W1-IGT4	Roger's Ruins	RGR2	22.64	445	931	123	513	162	1001	159	24	75	16	29	32
J2-222-1-W2-IGT3	Roger's Ruins	RGR2	9.45	880	1747	201	796	233	1523	219	25	106	17	40	41
J2-222-1-W3-M2	Roger's Ruins	RGR2	9.03	815	1551	206	837	257	1695	208	25	115	16	35	42
J2-209-1-W1-IGT6	Satanic Mills	SM1	10.52	1198	2980	450	2103	608	3431	529	70	339	58	140	120
J2-209-1-W1-IGT7	Satanic Mills	SM1	9.63	1552	4027	626	2902	831	3676	701	98	474	72	184	162
J2-209-1-W3-M4	Satanic Mills	SM1	8.84	1042	2525	410	2013	613	3393	539	73	351	54	135	111
J2-209-6-W1-IGT4	Satanic Mills	SM2	27.50	404	1055	147	663	334	413	1053	266	1792	324	846	629
J2-209-6-W2-M2	Satanic Mills	SM2	17.37	110	356	86	586	493	431	1566	392	2675	476	1298	953
J2-214-3-W1-IGT8	Satanic Mills	SM3	10.29	1574	3371	430	2114	955	2331	1632	252	1335	215	564	442
J2-214-3-W2-IGT5	Satanic Mills	SM3	10.17	982	2249	391	2095	1006	2401	1697	257	1353	220	591	440
J2-214-3-W3-M4	Satanic Mills	SM3	10.07	494	1900	282	1721	953	2336	1676	260	1375	221	585	451

Appendix B1. Measured Rare Earth Element concentrations (pmol/kg) in "dregs" fractions of sampled vent fluids from PACMANUS

Fluid Sampler ID	Vent Site	Vent Orifice	Mg (mmol/kg)	La	Ce	Pr	Nd	Sm	Eu	Gd	Tb	Dy	Ho	Er	Yb
J2-208-1-W1-IGT8	Roman Ruins	RMR1	8.01	187	341	26	93	674	78	16	1	23	2	3	3
J2-208-1-W2-IGT5	Roman Ruins	RMR1	8.28	N/A	N/A	N/A	N/A	N/A	N/A	N/A	N/A	N/A	N/A	N/A	N/A
J2-208-1-W3-M4	Roman Ruins	RMR1	8.90	137	184	15	51	242	24	6	1	15	1	2	2
J2-208-2-W2-IGT2	Roman Ruins	RMR2	16.56		52	7	38		33	1	0	75	1	1	2
J2-208-2-W1-IGT1	Roman Ruins	RMR2	16.55	47	189	18	113		99	5	1	471	1	2	4
J2-208-2-W3-M2	Roman Ruins	RMR2	27.50	62	113	14	109	692	13	7	1	61	1	3	3
J2-213-3-W1-IGT7	Roman Ruins	RMR3	23.36	N/A	N/A	N/A	N/A	N/A	N/A	N/A	N/A	N/A	N/A	N/A	N/A
J2-213-3-W3-M4	Roman Ruins	RMR3	6.39	281	448	48	159	173	195	21	3	24	2	6	16
J2-222-4-W2-IGT1	Roman Ruins	RMR4	3.63	260	412	32	82	147	84	10	1	11	1	3	7
J2-222-4-W3-M4	Roman Ruins	RMR4	4.71	72	117	10	29	78	36	5	1	6	1	2	2
J2-213-6-W1-IGT3	Roger's Ruins	RGR1	5.63	448	690	59	219	117	86	21	2	17	2	7	9
J2-213-6-W2-IGT4	Roger's Ruins	RGR1	8.10	1195	1631	113	264	135	130	30	2	10	1	3	6
J2-213-6-W3-M2	Roger's Ruins	RGR1	4.68	135	274	28	102	134	27	15	2	12	1	4	3
J2-222-1-W1-IGT4	Roger's Ruins	RGR2	22.64	253	426	31	76	19	71	15	2	15	1	4	5
J2-222-1-W2-IGT3	Roger's Ruins	RGR2	9.45	286	478	29	65	17	56	13	3	24	1	3	3
J2-222-1-W3-M2	Roger's Ruins	RGR2	9.03	29	77	7	31	323	17	9	2	27	1	4	3
J2-209-1-W1-IGT6	Satanic Mills	SM1	10.52	163	346	30	76	69	114	9	1	9	1	3	6
J2-209-1-W1-IGT7	Satanic Mills	SM1	9.63	N/A	N/A	N/A	N/A	N/A	N/A	N/A	N/A	N/A	N/A	N/A	N/A
J2-209-1-W3-M4	Satanic Mills	SM1	8.84	92	175	16	55	72	24	5	0	6	0	1	1
J2-209-6-W1-IGT4	Satanic Mills	SM2	27.50	53	196	18	50	55	47	12	1	31	1	3	3
J2-209-6-W2-M2	Satanic Mills	SM2	17.37	220	223	33	108	61	246	18	3	102	3	9	12
J2-214-3-W1-IGT8	Satanic Mills	SM3	10.29	136	243	24	56	43	148	10	1	8	1	3	8
J2-214-3-W2-IGT5	Satanic Mills	SM3	10.17	96	232	19	43	45	76	8	1	9	0	2	3
J2-214-3-W3-M4	Satanic Mills	SM3	10.07	46	125	12	49	35	30	7	1	7	1	3	5

Appendix B1. Measured Rare Earth Element concentrations (pmol/kg) in "dissolved" fractions of sampled vent fluids from PACMANUS

Fluid Sampler ID	Vent Site	Vent Orifice	Mg (mmol/kg)	La	Ce	Pr	Nd	Sm	Eu	Gd	Tb	Dy	Ho	Er	Yb
J2-210-1-W1-IGT8	Snowcap	SC1	31.05	163	220	28	106	31	37	49	14	103	24	78	61
J2-210-1-W2-IGT5	Snowcap	SC1	48.96	108	153	17	60	9	10	1	3	21	8	20	13
J2-210-1-W3-M2	Snowcap	SC1	31.85	173	277	42	182	43	34	65	16	121	28	81	65
J2-211-9-W1-IGT4	Snowcap	SC2	24.55	248	601	54	197	29	48	16	6	39	11	24	30
J2-211-9-W2-IGT3	Snowcap	SC2	25.18	309	804	94	362	72	134	43	10	56	16	31	30
J2-211-9-W3-M4	Snowcap	SC2	24.52	201	343	55	229	53	36	38	10	63	13	37	40
J2-211-2-W1-IGT7	Tsukushi	TK1	43.96	284	469	55	249	46	107	65	12	82	27	67	53
J2-214-14-W1-IGT2	Tsukushi	TK1	44.94	53	238	58			205	38	25	105	249	88	54
J2-214-14-W2-M2	Tsukushi	TK1	44.62		38	11			172		15	82	189	77	50
J2-210-7-W1-IGT1	Fenway	F1	5.97	867	1854	223	1461	1827	7360	2033	263	1287	194	489	379
J2-210-7-W2-M4	Fenway	F1	5.84	226	507	125	1159	1816	7339	2055	279	1314	198	518	390
J2-214-4-W1-IGT1	Fenway	F1	39.99		349	38	209	235	1786	538	97	406	279	175	
J2-212-2-W1-IGT8	Fenway	F2	4.90	20011	34019	4001	14442	2801	8695	1960	250	1183	166	414	299
J2-212-2-W2-IGT5	Fenway	F2	5.26	18664	32508	3880	14173	2751	8451	1954	244	1179	163	397	309
J2-212-2-W3-M4	Fenway	F2	4.66	18013	32710	3939	14402	2800	8652	1985	257	1214	167	406	298
J2-212-6-W1-IGT2	Fenway	F3	4.52	13983	25214	3116	11661	2387	7657	1751	222	1039	145	356	258
J2-212-6-W2-IGT1	Fenway	F3	4.74	15746	32842	4613	19173	4364	7969	3324	413	1888	254	568	354
J2-212-6-W3-M2	Fenway	F3	9.70	7696	19994	3239	14705	3621	6843	2827	354	1634	221	497	305
J2-216-2-W1-IGT7	Fenway	F4	9.86	2311	7820	1078	6115	1497	4568	1938	337	2070	366	1074	904
J2-216-2-W2-IGT6	Fenway	F4	9.38	2178	7359	1076	4968	1498	4975	1933	345	2115	384	1099	897
J2-216-2-W3-M2	Fenway	F4	10.96	640	4357	764	3782	1353	4169	1837	341	2117	368	1080	895
J2-216-5-W1-IGT4	Fenway	F5	44.66	1439	3953	491	1840	425	970	610	103	430	404	182	90
J2-216-5-W2-IGT3	Fenway	F5	45.53	1449	3711	428	1510	345	919	596	101	440	492	204	95
J2-216-5-W3-M4	Fenway	F5	50.46	544	1586	195	330	30	351	181	48	195	550	102	31

Appendix B1. Measured Rare Earth Element concentrations (pmol/kg) in "dregs" fractions of sampled vent fluids from PACMANUS

Fluid Sampler ID	Vent Site	Vent Orifice	Mg (mmol/kg)	La	Ce	Pr	Nd	Sm	Eu	Gd	Tb	Dy	Ho	Er	Yb
J2-210-1-W1-IGT8	Snowcap	SC1	31.05	59	191	18	69	52	69	8	2	8	2	5	9
J2-210-1-W2-IGT5	Snowcap	SC1	48.96	243	489	71	304	259	107	80	22	158	36	125	137
J2-210-1-W3-M2	Snowcap	SC1	31.85	137	210	22	81	55	11	11	2	13	2	7	7
J2-211-9-W1-IGT4	Snowcap	SC2	24.55	104	226	23	71	23	92	9	2	11	2	5	9
J2-211-9-W2-IGT3	Snowcap	SC2	25.18	138	452	46	167	35	71	20	4	21	4	11	12
J2-211-9-W3-M4	Snowcap	SC2	24.52	30	51	7	55	3	6	3	1	4	1	2	2
J2-211-2-W1-IGT7	Tsukushi	TK1	43.96	25	193	18	44	33	72	5	1	8	1	5	8
J2-214-14-W1-IGT2	Tsukushi	TK1	44.94	N/A	N/A	N/A	N/A	N/A	N/A	N/A	N/A	N/A	N/A	N/A	N/A
J2-214-14-W2-M2	Tsukushi	TK1	44.62	17	89	10	38	27	20	6	2	10	2	6	7
J2-210-7-W1-IGT1	Fenway	F1	5.97		117	9	19	128	70	1	0	8	1	2	4
J2-210-7-W2-M4	Fenway	F1	5.84	57	186	22	93	52	23	18	4	24	4	12	11
J2-214-4-W1-IGT1	Fenway	F1	39.99	525	839	57	131	71	98	20	2	11	1	3	4
J2-212-2-W1-IGT8	Fenway	F2	4.90	600	935	76	215	107	76	34	6	32	6	18	16
J2-212-2-W2-IGT5	Fenway	F2	5.26	1052	1472	103	292	100	62	25	2	11	1	4	5
J2-212-2-W3-M4	Fenway	F2	4.66	328	476	45	135	62	155	14	2	10	1	3	7
J2-212-6-W1-IGT2	Fenway	F3	4.52	1371	1958	142	354	378	95	33	2	18	2	5	7
J2-212-6-W2-IGT1	Fenway	F3	4.74	4739	9263	941	3354	876	503	525	76	319	41	87	37
J2-212-6-W3-M2	Fenway	F3	9.70	1117	2278	213	717	147	87	100	14	59	8	18	8
J2-216-2-W1-IGT7	Fenway	F4	9.86	691	1312	122	340	116	127	53	4	15	2	7	5
J2-216-2-W2-IGT6	Fenway	F4	9.38	573	1090	111	293	77	88	38	2	9	1	3	2
J2-216-2-W3-M2	Fenway	F4	10.96	201	702	81	262	60	47	29	2	9	1	4	2
J2-216-5-W1-IGT4	Fenway	F5	44.66	524	748	70	228	95	105	46	5	25	4	10	9
J2-216-5-W2-IGT3	Fenway	F5	45.53	376	457	34	79	25	127	19	1	5	1	2	2
J2-216-5-W3-M4	Fenway	F5	50.46	181	302	18	48	4	11	12	0	2	0	1	1

Appendix B1. Measured Rare Earth Element concentrations (pmol/kg) in "dissolved" fractions of sampled vent fluids from DESMOS

Fluid Sampler ID	Vent Site	Vent Orifice	Mg (mmol/kg)	La	Ce	Pr	Nd	Sm	Eu	Gd	Tb	Dy	Ho	Er	Yb
J2-220-5-W1-IGT1	DESMOS	D1	45.97	17862	54166	7331	31845	7830	2948	7283	1160	6980	1330	4044	3826
J2-220-5-W2-IGT2	DESMOS	D1	46.20	18149	53073	7232	31638	7802	3099	7212	1147	6941	1324	4025	3790
J2-220-5-W3-M4	DESMOS	D1	51.04	7906	22210	3133	13911	3438	1456	3167	501	3024	580	1754	1638
J2-220-15-W1-IGT4	DESMOS	D2	50.50	20829	70503	11394	56330	15908	6138	14573	2300	13887	2613	7790	7380
J2-220-15-W2-IGT3	DESMOS	D2	50.43	20640	71571	11415	55512	15722	6472	14309	2266	13573	2538	7561	7158
J2-220-15-W3-M2	DESMOS	D2	50.62	20281	68927	11313	56043	15803	6001	14675	2302	13865	2595	7773	7336

Appendix B1. Measured Rare Earth Element concentrations (pmol/kg) in "dregs" fractions of sampled vent fluids from DESMOS

Fluid Sampler ID	Vent Site	Vent Orifice	Mg (mmol/kg)	La	Ce	Pr	Nd	Sm	Eu	Gd	Tb	Dy	Ho	Er	Yb
J2-220-5-W1-IGT1	DESMOS	D1	45.97	N/A	N/A	N/A	N/A	N/A	N/A	N/A	N/A	N/A	N/A	N/A	N/A
J2-220-5-W2-IGT2	DESMOS	D1	46.20	N/A	N/A	N/A	N/A	N/A	N/A	N/A	N/A	N/A	N/A	N/A	N/A
J2-220-5-W3-M4	DESMOS	D1	51.04	N/A	N/A	N/A	N/A	N/A	N/A	N/A	N/A	N/A	N/A	N/A	N/A
J2-220-15-W1-IGT4	DESMOS	D2	50.50	121	147	12	23	9	51	8	1	6	1	3	4
J2-220-15-W2-IGT3	DESMOS	D2	50.43	165	255	16	38	13	54	12	1	6	1	2	4
J2-220-15-W3-M2	DESMOS	D2	50.62	N/A	N/A	N/A	N/A	N/A	N/A	N/A	N/A	N/A	N/A	N/A	N/A

Appendix B1. Measured Rare Earth Element concentrations (pmol/kg) in "dissolved" fractions of sampled vent fluids from SuSu Knolls

Fluid Sampler ID	Vent Site	Vent Orifice	Mg (mmol/kg)	La	Ce	Pr	Nd	Sm	Eu	Gd	Tb	Dy	Ho	Er	Yb
221-3-W1-IGT8	North Su	NS1	49.84	8755	29170	3935	16175	3890	1351	3650	594	3720	739	2320	2383
221-3-W2-IGT7	North Su	NS1	49.01	10646	35127	4729	19568	4682	1637	4440	717	4448	875	2792	2842
221-3-W3-M4	North Su	NS1	49.36	10563	32762	4394	18109	4264	1497	4066	654	4071	802	2513	2610
221-5-W1-IGT6	North Su	NS2	38.82	25597	98058	16244	83537	25511	8865	26764	4323	26644	5155	15724	15225
221-5-W2-IGT5	North Su	NS2	40.95	21229	81099	13649	71219	21715	7493	22974	3698	22806	4400	13469	12959
221-5-W3-M2	North Su	NS2	40.89	24225	87213	14621	75390	22978	8021	24244	3913	24296	4677	14375	13885
J2-223-1-W1-IGT8	North Su	NS3	21.22	2630	4691	534	1914	247	1025	147	16	86	14	41	40
J2-223-1-W2-IGT7	North Su	NS3	3.42	9530	16763	1894	6326	751	2779	373	37	160	27	62	58
J2-223-1-W3-M2	North Su	NS3	1.62	10478	17782	2021	6759	820	3007	414	39	174	28	62	53
J2-223-11-W1-IGT5	North Su	NS4	23.89	12657	47812	6540	29310	9834	3549	13534	2355	15301	3064	9287	8503
J2-223-11-W2-IGT6	North Su	NS4	24.63	4957	33521	5715	28009	9868	3484	12854	2349	14936	3014	9134	8237
J2-227-10-W1-IGT2	North Su	NS5	7.42	253	900	116	650	209	1153	78	6	29	6	11	22
J2-227-10-W2-IGT1	North Su	NS5	7.51	393	1154	271	1830	664	1246	238	18	71	11	25	32
J2-227-10-W3-M2	North Su	NS5	27.43	227	734	176	1143	358	626	192	22	111	33	53	52
J2-227-8-W1-IGT4	North Su	NS6	2.03	362	493	76	362	209	1264	348	51	268	46	129	123
J2-227-8-W2-IGT3	North Su	NS6	1.57	461	668	101	434	245	1270	378	55	302	51	136	138
J2-227-8-W3-M4	North Su	NS6	5.09	223	424	72	370	245	1273	405	60	317	58	149	123
J2-223-15-W1-M4	North Su	NS6	3.37	536	536	90	470	328	1390	520	77	402	69	175	148
J2-224-6-W1-IGT4	South Su	SS1	5.30	473	920	115	428	112	112	205	56	433	90	233	162
J2-224-6-W2-IGT3	South Su	SS1	5.52	206	1305	54	226	71	98	177	51	409	86	222	155
J2-224-6-W3-M2	South Su	SS1	37.81	135	257	40	187	56	54	115	26	199	43	107	76
J2-224-12-W1-IGT1	South Su	SS2	6.77	427	681	63	207	32	327	51	9	57	13	39	53
J2-224-12-W2-IGT2	South Su	SS2	8.43	384	581	61	187	34	271	49	9	56	19	43	46
J2-224-12-W3-M4	South Su	SS2	9.23	N/A	N/A	N/A	N/A	N/A	N/A	N/A	N/A	N/A	N/A	N/A	N/A

Appendix B1. Measured Rare Earth Element concentrations (pmol/kg) in "dregs" fractions of sampled vent fluids from SuSu Knolls

Fluid Sampler ID	Vent Site	Vent Orifice	Mg (mmol/kg)	La	Ce	Pr	Nd	Sm	Eu	Gd	Tb	Dy	Ho	Er	Yb
221-3-W1-IGT8	North Su	NS1	49.84	248	267	20	39	11	167	10	1	6	1	2	5
221-3-W2-IGT7	North Su	NS1	49.01	277	380	26	47	18	145	12	1	4	1	1	4
221-3-W3-M4	North Su	NS1	49.36	N/A	N/A	N/A	N/A	N/A	N/A	N/A	N/A	N/A	N/A	N/A	N/A
221-5-W1-IGT6	North Su	NS2	38.82	N/A	N/A	N/A	N/A	N/A	N/A	N/A	N/A	N/A	N/A	N/A	N/A
221-5-W2-IGT5	North Su	NS2	40.95	N/A	N/A	N/A	N/A	N/A	N/A	N/A	N/A	N/A	N/A	N/A	N/A
221-5-W3-M2	North Su	NS2	40.89	N/A	N/A	N/A	N/A	N/A	N/A	N/A	N/A	N/A	N/A	N/A	N/A
J2-223-1-W1-IGT8	North Su	NS3	21.22	473	622	46	98	17	99	20	1	4	1	1	3
J2-223-1-W2-IGT7	North Su	NS3	3.42	305	433	31	60	19	86	16	1	3	0	0	2
J2-223-1-W3-M2	North Su	NS3	1.62	47	89	8	25	10	12	5	0	3	0	1	1
J2-223-11-W1-IGT5	North Su	NS4	23.89	N/A	N/A	N/A	N/A	N/A	N/A	N/A	N/A	N/A	N/A	N/A	N/A
J2-223-11-W2-IGT6	North Su	NS4	24.63	N/A	N/A	N/A	N/A	N/A	N/A	N/A	N/A	N/A	N/A	N/A	N/A
J2-227-10-W1-IGT2	North Su	NS5	7.42	439	693	88	334	83	309	82	12	62	11	30	29
J2-227-10-W2-IGT1	North Su	NS5	7.51	443	395	59	201	88	1095	27	2	8	1	3	17
J2-227-10-W3-M2	North Su	NS5	27.43	683	390	59	231	85	2638	21	3	13	2	10	33
J2-227-8-W1-IGT4	North Su	NS6	2.03	164	98	16	39	50	431	8	1	9	1	4	11
J2-227-8-W2-IGT3	North Su	NS6	1.57	96	116	10	24	34	140	7	1	6	1	3	6
J2-227-8-W3-M4	North Su	NS6	5.09	37	43	4	15	19	78	6	1	6	1	3	3
J2-223-15-W1-M4	North Su	NS6	3.37	22	38	4	16	11	27	12	2	11	2	5	3
J2-224-6-W1-IGT4	South Su	SS1	5.30	63	99	10	24	77	70	7	1	88	1	2	3
J2-224-6-W2-IGT3	South Su	SS1	5.52	102	127	10	22	51	120	6	1	78	1	2	3
J2-224-6-W3-M2	South Su	SS1	37.81	90	95	12	28	104	120	8	1	75	1	3	4
J2-224-12-W1-IGT1	South Su	SS2	6.77					32	294		5	5	1	8	6
J2-224-12-W2-IGT2	South Su	SS2	8.43	149	74	10	17	20	306	4	1	4	0	1	7
J2-224-12-W3-M4	South Su	SS2	9.23	N/A	N/A	N/A	N/A	N/A	N/A	N/A	N/A	N/A	N/A	N/A	N/A

Appendix B1. Measured Rare Earth Element concentrations (pmol/kg) in "dissolved" fractions of sampled vent fluids from SuSu Knolls

Fluid Sampler ID	Vent Site	Vent Orifice	Mg (mmol/kg)	La	Ce	Pr	Nd	Sm	Eu	Gd	Tb	Dy	Ho	Er	Yb
J2-217-2-W1-IGT8	Suzette	SZ1	4.40	3232	5547	703	2545	416	2234	281	31	157	24	62	53
J2-217-2-W2-IGT5	Suzette	SZ1	5.36	2888	5103	642	2385	412	2171	265	30	147	19	61	56
J2-217-2-W3-M2	Suzette	SZ1	5.47	2777	5253	685	2688	457	2238	308	33	173	24	65	58
J2-217-10-W1-IGT1	Suzette	SZ2	8.58	2659	4716	594	2383	513	2178	358	40	188	27	74	59
J2-217-10-W2-IGT2	Suzette	SZ2	8.56	2803	5255	698	2925	598	2259	445	51	259	43	122	101
J2-217-10-W3-M4	Suzette	SZ2	14.69	954	2971	374	1003	130	1620	200	24	127	15	40	15
J2-219-2-W1-IGT7	Suzette	SZ3	7.16	2448	5456	874	4326	1213	4267	799	85	334	49	98	63
J2-219-2-W2-IGT6	Suzette	SZ3	6.13	2619	5616	885	4330	1226	4410	832	87	341	49	95	74
J2-219-8-W3-M2	Suzette	SZ3	5.51	2848	5883	947	4736	1398	4705	919	96	384	60	104	70
J2-219-10-W1-IGT8	Suzette	SZ4	8.32	868	1767	256	1150	279	1607	214	31	125	42	53	41
J2-219-10-W1-IGT5	Suzette	SZ4	8.62	894	1783	243	1085	284	1542	190	26	119	36	48	38
J2-226-2-W1-IGT6	Suzette	SZ5	40.66	677	1834	257	1274	683	371	1090	200	1269	245	718	636
J2-226-2-W2-IGT5	Suzette	SZ5	6.31	1361	3635	633	3891	2542	1261	3983	736	4619	861	2477	2069
J2-226-2-W3-M2	Suzette	SZ5	20.75	179	702	188	1437	1101	640	1916	360	2342	451	1343	1205
J2-226-4-W1-IGT7	Suzette	SZ6	9.08	1875	3608	490	2190	556	4289	403	40	164	24	49	36
J2-226-4-W2-IGT8	Suzette	SZ6	8.02	2015	3801	540	2330	549	4431	419	39	165	19	45	39
J2-226-4-W3-M4	Suzette	SZ6	8.57	1806	3131	451	2195	582	4598	434	42	177	25	45	36

Appendix B1. Measured Rare Earth Element concentrations (pmol/kg) in "dregs" fractions of sampled vent fluids from SuSu Knolls

Fluid Sampler ID	Vent Site	Vent Orifice	Mg (mmol/kg)	La	Ce	Pr	Nd	Sm	Eu	Gd	Tb	Dy	Ho	Er	Yb
J2-217-2-W1-IGT8	Suzette	SZ1	4.40	246	189	23	62	28	507	10	1	6	1	3	9
J2-217-2-W2-IGT5	Suzette	SZ1	5.36	197	173	17	37	24	264	8	1	5	0	1	5
J2-217-2-W3-M2	Suzette	SZ1	5.47	31	61	7	25	17	9	5	1	4	0	2	1
J2-217-10-W1-IGT1	Suzette	SZ2	8.58	367	351	30	66	33	523	14	1	3	0	2	7
J2-217-10-W2-IGT2	Suzette	SZ2	8.56	341	324	36	110	42	646	21	2	13	2	8	14
J2-217-10-W3-M4	Suzette	SZ2	14.69	243	629	78	323	74	78	53	6	28	4	11	7
J2-219-2-W1-IGT7	Suzette	SZ3	7.16	233	211	25	74	54	427	13	1	8	1	4	10
J2-219-2-W2-IGT6	Suzette	SZ3	6.13	179	188	20	54	35	276	9	1	7	1	3	7
J2-219-8-W3-M2	Suzette	SZ3	5.51	187	355	60	254	66	93	49	7	35	6	17	14
J2-219-10-W1-IGT8	Suzette	SZ4	8.32	N/A	N/A	N/A	N/A	N/A	N/A	N/A	N/A	N/A	N/A	N/A	N/A
J2-219-10-W1-IGT5	Suzette	SZ4	8.62	N/A	N/A	N/A	N/A	N/A	N/A	N/A	N/A	N/A	N/A	N/A	N/A
J2-226-2-W1-IGT6	Suzette	SZ5	40.66	510	1006	122	464	134	393	125	22	137	22	71	66
J2-226-2-W2-IGT5	Suzette	SZ5	6.31	282	459	35	88	19	43	22	2	19	2	8	7
J2-226-2-W3-M2	Suzette	SZ5	20.75	1490	1507	213	757	455	4239	85	8	43	7	27	67
J2-226-4-W1-IGT7	Suzette	SZ6	9.08	251	166	20	42	32	431	8	1	5	1	5	12
J2-226-4-W2-IGT8	Suzette	SZ6	8.02	307	319	53	218	57	593	40	5	27	3	15	18
J2-226-4-W3-M4	Suzette	SZ6	8.57	35	64	8	29	11	40	9	1	8	1	4	4

Appendix C-1.

Complete listing of element concentrations (rare earth element, Mg, Sr, Ba and Pb) and isotope ($^{87}Sr/^{86}Sr$ and $\delta^{34}S$) ratios measured in anhydrite grains by in situ laser ablation ICP-MS. Samples recovered from subsurface via sub-seafloor drilling during ODP Leg 193 (Binns et al., 2007) or from seafloor by submersible operations during cruise MGLN06MV (Tivey et al., 2007).

The following abbreviation(s) is used in the tables:

N.D. = element and/or isotope analysis not performed on sample.

Appendix C1. Trace element (Sr, Mg, Ba, Pb, REE) and isotope (Sr, S) compositions of anhydrite determined by Laser Ablation ICP-MS and MC-ICP-MS.

(ppm)	Sr	Mg	Ba	Pb	La	Ce	Pr	Nd	Sm	Eu	Gd	Tb	Dy	Ho	Er	Yb	Lu	ΣREE	La_N/Yb_N	Sm_N/Yb_N	Eu_N/Eu^*_N	$^{87}Sr/^{86}Sr$	$\delta^{34}S$ (‰)
Snowcap, 193_1188A_7R_1, 66-68cm, 50mbsf																							
Spot #1	2664	3	18	0.54	0.77	2.41	N.D.	1.96	0.57	0.33	0.84	N.D.	0.68	0.16	0.50	0.68	N.D.	9.0	0.8	0.9	1.6	0.70865	21.9
Spot #2	2689	9	23	0.87	0.65	1.98	N.D.	1.68	0.52	0.30	0.76	N.D.	0.65	0.16	0.48	0.62	N.D.	7.9	0.7	0.9	1.5	0.70856	21.2
Spot #4	3913	10	64	0.91	1.29	3.91	N.D.	3.53	1.11	0.47	1.64	N.D.	1.49	0.34	1.00	1.13	N.D.	16.0	0.8	1.1	1.1	0.70869	21.2
Spot #5	4930	28	115	1.25	2.27	6.91	N.D.	6.53	2.06	0.74	3.01	N.D.	2.74	0.59	1.69	1.76	N.D.	28.4	0.9	1.3	0.9	0.70866	21.1
Spot #6	4731	28	111	1.02	2.78	8.67	N.D.	8.10	2.59	0.89	3.79	N.D.	3.40	0.73	2.11	2.07	N.D.	35.3	0.9	1.3	0.9	0.70881	21.1
Spot #7	4919	32	103	1.12	1.75	5.15	N.D.	4.63	1.44	0.54	2.25	N.D.	2.13	0.48	1.43	1.57	N.D.	21.4	0.8	1.0	1.0	0.70879	
Spot #8	5003	35	94	0.96	2.34	6.79	N.D.	6.16	1.93	0.68	2.91	N.D.	2.67	0.59	1.70	1.73	N.D.	27.6	0.9	1.2	0.9		
Spot #19	N.D.	N.D.	N.D.	N.D.	0.29	1.00	N.D.	0.80	0.31	0.07	0.46	N.D.	0.35	0.08	0.26	0.34	N.D.	4.0	0.6	1.0	0.6		
Spot #20	N.D.	N.D.	N.D.	N.D.	0.83	2.19	N.D.	2.15	0.73	0.23	1.08	N.D.	1.25	0.26	0.73	0.83	N.D.	10.3	0.7	0.9	0.8		
Spot #21	N.D.	N.D.	N.D.	N.D.	2.48	6.51	N.D.	6.06	2.08	0.77	3.06	N.D.	2.70	0.57	1.59	1.50	N.D.	27.3	1.1	1.5	1.0		
Spot #22	N.D.	N.D.	N.D.	N.D.	2.57	7.46	N.D.	6.54	2.62	0.97	3.86	N.D.	3.25	0.68	1.85	1.75	N.D.	31.5	1.0	1.6	1.0		
Spot #23	N.D.	N.D.	N.D.	N.D.	3.60	11.94	N.D.	11.83	4.85	1.51	7.14	N.D.	5.62	1.13	2.92	2.37	N.D.	52.9	1.0	2.2	0.8		
Spot #24	N.D.	N.D.	N.D.	N.D.	3.98	12.96	N.D.	12.39	4.76	1.57	7.01	N.D.	5.62	1.15	3.06	2.43	N.D.	54.9	1.1	2.1	0.9		
Spot #25	N.D.	N.D.	N.D.	N.D.	2.69	8.27	N.D.	7.51	2.93	0.92	4.32	N.D.	3.59	0.78	2.23	1.95	N.D.	35.2	0.9	1.6	0.8		
Spot #26	N.D.	N.D.	N.D.	N.D.	0.51	1.04	N.D.	0.75	0.40	0.11	0.59	N.D.	0.49	0.12	0.39	0.46	N.D.	4.9	0.8	0.9	0.7		
Spot #27	N.D.	N.D.	N.D.	N.D.	1.34	4.15	N.D.	2.86	0.84	0.16	1.23	N.D.	0.98	0.21	0.60	0.64	N.D.	13.0	1.4	1.4	0.5		

Appendix C1.Contd

(ppm)	Sr	Mg	Ba	Pb	La	Ce	Pr	Nd	Sm	Eu	Gd	Tb	Dy	Ho	Er	Yb	Lu	ΣREE	La_N/Yb_N	Sm_N/Yb_N	Eu_N/Eu^*_N	$^{87}Sr/^{86}Sr$	$\delta^{34}S$ (‰)
Snowcap, 193_1188A_15R_1, 14-20cm, 126mbsf																							
Spot #2	2891	4	6	0.04	0.68	1.67	N.D.	1.01	0.22	0.22	0.34	N.D.	0.13	0.02	0.05	0.03	N.D.	4.6	14.3	7.4	2.5	0.70570	
Spot #3	2601	14	186	0.12	1.51	2.81	N.D.	1.40	0.30	1.29	0.47	N.D.	0.13	0.02	0.05	0.03	N.D.	9.2	29.2	9.2	10.5	0.70532	
Spot #4	2525	12	1073	0.15	2.11	3.86	N.D.	1.71	0.35	1.43	0.57	N.D.	0.16	0.02	0.06	0.04	N.D.	11.5	33.3	8.7	9.8	0.70546	
Spot #5	2563	5	314	0.06	0.79	1.66	N.D.	1.06	0.26	0.68	0.35	N.D.	0.14	0.02	0.05	0.03	N.D.	5.6	15.6	8.3	6.8	0.70533	
Spot #15	2843	156	170	1.49	0.72	1.67	N.D.	1.10	0.26	0.50	0.34	N.D.	0.12	0.02	0.04	0.03	N.D.	5.3	16.0	9.2	5.1	0.70545	
Spot #16	1256	29	6	0.21	1.10	2.27	N.D.	1.22	0.29	0.85	0.43	N.D.	0.14	0.02	0.05	0.04	N.D.	7.3	18.2	7.7	7.3	0.70518	
Spot #17	1428	10	8	0.01	1.81	3.82	N.D.	1.85	0.39	1.27	0.63	N.D.	0.20	0.03	0.08	0.06	N.D.	11.4	20.7	7.1	7.7	0.70526	
Spot #18	3468	72	69	2.89	0.38	1.04	N.D.	0.68	0.15	0.19	0.22	N.D.	0.09	0.01	0.03	0.02	N.D.	3.0	11.9	7.6	3.1	0.70575	
Spot #19	3291	6	1288	0.16	1.58	2.76	N.D.	1.16	0.24	1.45	0.40	N.D.	0.11	0.02	0.04	0.03	N.D.	8.9	34.6	8.3	14.2	0.70520	

Appendix C1 Contd

(ppm)	Sr	Mg	Ba	Pb	La	Ce	Pr	Nd	Sm	Eu	Gd	Tb	Dy	Ho	Er	Yb	Lu	ΣREE	La_N/Yb_N	Sm_N/Yb_N	Eu_N/Eu^*_N	$^{87}Sr/^{86}Sr$	$\delta^{34}S$ (‰)
Snowcap, 193_1188A_17R_2, 6-9cm, 146mbsf																							
Spot #1	12013	5	57	7.24	2.93	3.93	N.D.	1.38	0.22	0.16	0.91	N.D.	0.11	0.02	0.04	0.03	N.D.	9.9	72.5	8.5	2.0	0.70599	
Spot #2	13380	5	105	6.59	4.65	6.16	N.D.	2.35	0.37	0.28	1.58	N.D.	0.17	0.03	0.06	0.04	N.D.	15.9	73.5	9.3	2.0	0.70604	
Spot #3	7415	7	223	3.35	3.40	5.75	N.D.	2.66	0.49	0.42	1.59	N.D.	0.22	0.03	0.07	0.04	N.D.	15.0	51.2	11.6	2.3	0.70578	
Spot #4	7537	7	180	3.04	2.68	4.63	N.D.	2.06	0.39	0.34	1.24	N.D.	0.16	0.02	0.05	0.04	N.D.	11.9	50.1	11.5	2.3	0.70577	
Spot #5	8966	5	196	3.18	1.86	2.86	N.D.	1.25	0.21	0.27	0.74	N.D.	0.09	0.01	0.03	0.03	N.D.	7.6	36.6	6.7	3.4	0.70583	
Spot #6	3555	1468	21	0.45	5.04	9.59	N.D.	6.93	1.60	0.99	3.61	N.D.	1.08	0.19	0.46	0.43	N.D.	30.7	7.9	4.0	1.6	0.70596	
Spot #9	5205	25	98	1.92	1.53	2.15	N.D.	0.92	0.15	0.17	0.46	N.D.	0.06	0.01	0.03	0.03	N.D.	5.7	35.9	5.6	3.1	0.70563	
Spot #10	5126	9	143	1.61	1.55	2.20	N.D.	0.90	0.15	0.20	0.49	N.D.	0.06	0.01	0.02	0.03	N.D.	5.8	36.7	5.6	3.6	0.70562	
Spot #11	4582	11	80	1.45	1.25	1.67	N.D.	0.67	0.12	0.14	0.30	N.D.	0.04	0.01	0.02	0.03	N.D.	4.4	29.2	4.4	3.1	0.70560	
Spot #12	3902	8	57	1.09	1.11	1.58	N.D.	0.68	0.12	0.12	0.32	N.D.	0.04	0.01	0.02	0.02	N.D.	4.1	33.5	5.7	2.6	0.70566	
Spot #13	3527	28	38	1.13	1.38	2.12	N.D.	0.92	0.15	0.13	0.43	N.D.	0.07	0.01	0.03	0.03	N.D.	5.4	29.1	5.1	2.3	0.70561	

Appendix C1.Contd

(ppm)	Sr	Mg	Ba	Pb	La	Ce	Pr	Nd	Sm	Eu	Gd	Tb	Dy	Ho	Er	Yb	Lu	ΣREE	La_N/Yb_N	Sm_N/Yb_N	Eu_N/Eu^*_N	$^{87}Sr/^{86}Sr$	$\delta^{34}S$ (‰)
Snowcap, 193_1188F_16R_2, 109-111cm, 137mbsf																							
Spot #1	4494	597	169	1.97	0.47	1.09	N.D.	0.85	0.20	0.23	0.58	N.D.	0.12	0.03	0.08	0.09	N.D.	4.0	3.7	2.5	3.0	0.70589	
Spot #2	4297	40	92	1.69	0.44	0.78	N.D.	0.49	0.15	0.21	0.55	N.D.	0.29	0.07	0.19	0.15	N.D.	3.5	1.9	1.0	3.8	0.70571	
Spot #3	5054	34	122	2.10	1.20	2.57	N.D.	1.44	0.30	0.30	0.89	N.D.	0.24	0.06	0.18	0.09	N.D.	7.6	8.8	3.5	2.6	0.70566	
Spot #4	3569	12	54	1.68	1.17	2.80	N.D.	1.74	0.37	0.28	0.88	N.D.	0.15	0.02	0.05	0.03	N.D.	7.8	23.4	11.7	2.0	0.70601	
Spot #5	5203	28	125	2.14	0.85	1.63	N.D.	1.08	0.26	0.25	0.63	N.D.	0.13	0.02	0.04	0.03	N.D.	5.2	18.7	9.1	2.5	0.70633	
Spot #6	5573	23	122	1.56	0.30	0.58	N.D.	0.40	0.10	0.16	0.29	N.D.	0.06	0.01	0.02	0.02	N.D.	2.1	10.2	5.2	4.3	0.70623	
Spot #7	5962	13	108	2.13	1.77	3.13	N.D.	1.92	0.37	0.29	0.96	N.D.	0.16	0.02	0.05	0.03	N.D.	9.0	34.5	11.6	2.0	0.70607	
Spot #8	6175	11	242	2.26	1.51	3.06	N.D.	1.75	0.35	0.33	0.83	N.D.	0.16	0.02	0.05	0.04	N.D.	8.5	24.5	9.0	2.5	0.70587	
Spot #9	6192	17	156	1.75	0.44	0.69	N.D.	0.38	0.08	0.16	0.26	N.D.	0.05	0.01	0.02	0.02	N.D.	2.3	16.2	4.7	5.2	0.70616	
Spot #10	7204	16	497	1.77	0.36	0.56	N.D.	0.29	0.06	0.17	0.21	N.D.	0.04	0.01	0.02	0.01	N.D.	2.0	19.3	4.8	8.1	0.70618	
Spot #11	5551	12	153	2.28	1.50	2.85	N.D.	1.76	0.34	0.29	0.84	N.D.	0.16	0.02	0.05	0.03	N.D.	8.2	33.9	12.2	2.2	0.70585	
Spot #12	7298	13	62	2.86	3.17	5.70	N.D.	3.11	0.54	0.34	1.46	N.D.	0.22	0.03	0.07	0.05	N.D.	15.0	46.6	12.5	1.7	0.70564	
Spot #13	2842	13	4	1.56	0.62	1.34	N.D.	1.00	0.23	0.17	0.50	N.D.	0.11	0.02	0.04	0.03	N.D.	4.2	14.6	8.7	2.0	0.70628	
Spot #14	6559	57	248	2.53	0.53	0.83	N.D.	0.49	0.10	0.20	0.26	N.D.	0.05	0.01	0.02	0.02	N.D.	2.8	16.2	4.7	5.6	0.70581	
Spot #15	5364	14	40	1.65	1.02	2.02	N.D.	1.13	0.22	0.16	0.56	N.D.	0.10	0.02	0.03	0.03	N.D.	5.5	27.6	9.4	1.9	0.70567	
Spot #16	3375	0	4	0.06	0.57	1.31	N.D.	0.81	0.18	0.12	0.45	N.D.	0.09	0.02	0.04	0.02	N.D.	3.7	20.4	9.9	1.8	0.70589	
Spot #17	5340	4	192	0.46	0.91	1.89	N.D.	1.18	0.24	0.21	0.62	N.D.	0.12	0.02	0.03	0.02	N.D.	5.5	27.3	11.2	2.3	0.70574	

Appendix C1 Contd

(ppm)	Sr	Mg	Ba	Pb	La	Ce	Pr	Nd	Sm	Eu	Gd	Tb	Dy	Ho	Er	Yb	Lu	ΣREE	La_N/Yb_N	Sm_N/Yb_N	Eu_N/Eu^*_N	$^{87}Sr/^{86}Sr$	$\delta^{34}S$ (‰)
Snowcap, 193_1188F_1Z_2, 32-34cm, 219mbsf																							
Spot #1	3133	20	103	1.10	0.05	0.17	N.D.	0.16	0.06	0.10	0.16	N.D.	0.08	0.01	0.03	0.02	N.D.	1.0	1.6	2.9	4.6	0.70718	20.7
Spot #2	3303	62	103	0.85	0.03	0.10	N.D.	0.13	0.05	0.11	0.10	N.D.	0.06	0.01	0.03	0.02	N.D.	0.8	1.2	2.9	6.1	0.70707	21.1
Spot #3	7267	21	453	10.24	0.07	0.20	N.D.	0.28	0.16	0.35	0.29	N.D.	0.29	0.05	0.11	0.07	N.D.	2.3	0.7	2.5	6.0	0.70663	20.9
Spot #4	3058	8	27	0.09	0.13	0.67	N.D.	1.13	0.63	0.48	0.95	N.D.	0.90	0.13	0.29	0.16	N.D.	5.8	0.6	4.3	2.0	0.70683	20.7
Spot #5	2329	16	25	0.91	0.05	0.37	N.D.	0.99	0.82	0.77	1.31	N.D.	1.34	0.20	0.46	0.28	N.D.	7.2	0.1	3.2	2.5	0.70625	20.5
Spot #6	2649	351	48	0.73	0.14	0.35	N.D.	0.47	0.29	0.22	0.43	N.D.	0.47	0.08	0.19	0.10	N.D.	2.9	1.0	3.1	2.0	0.70704	20.9
Spot #7	3128	92	82	1.83	0.05	0.27	N.D.	0.50	0.30	0.25	0.48	N.D.	0.50	0.08	0.18	0.09	N.D.	2.9	0.4	3.4	2.2	0.70700	
Spot #8	3795	38	20	0.22	0.11	0.58	N.D.	1.08	0.62	0.48	0.99	N.D.	0.90	0.14	0.32	0.18	N.D.	5.7	0.4	3.8	2.1		
Spot #9	4858	30	80	0.13	0.14	0.53	N.D.	0.71	0.31	0.23	0.46	N.D.	0.39	0.07	0.16	0.10	N.D.	3.3	0.9	3.3	2.0		
Spot #10	2696	118	27	1.00	0.04	0.27	N.D.	0.52	0.36	0.33	0.59	N.D.	0.64	0.10	0.22	0.13	N.D.	3.4	0.2	2.8	2.4		
Spot #11	3444	571	35	0.37	0.04	0.19	N.D.	0.30	0.18	0.15	0.24	N.D.	0.26	0.05	0.12	0.12	N.D.	1.8	0.2	1.5	2.3		
Spot #12	3473	13	43	0.20	0.07	0.30	N.D.	0.51	0.27	0.21	0.39	N.D.	0.50	0.08	0.18	0.10	N.D.	2.7	0.5	3.0	2.0		
Spot #13	4926	17	55	0.30	0.09	0.34	N.D.	0.54	0.39	0.35	0.64	N.D.	0.62	0.09	0.21	0.13	N.D.	3.7	0.5	3.2	2.4		
Spot #14	4424	209	43	0.38	0.04	0.15	N.D.	0.12	0.04	0.05	0.03	N.D.	0.05	0.01	0.02	0.01	N.D.	0.6	2.3	3.5	3.4	0.70643	
Spot #15	2903	20	68	2.43	0.20	1.41	N.D.	2.83	1.58	0.85	2.24	N.D.	2.32	0.37	0.86	0.45	N.D.	13.6	0.3	3.8	1.4	0.70662	
Spot #16	2459	44	50	0.49	0.07	0.56	N.D.	1.15	0.71	0.54	1.05	N.D.	1.04	0.16	0.35	0.18	N.D.	6.2	0.3	4.3	2.0	0.70710	
Spot #17	3000	784	86	1.16	0.04	0.25	N.D.	0.38	0.23	0.19	0.25	N.D.	0.30	0.06	0.17	0.23	N.D.	2.2	0.1	1.1	2.2	0.70703	
Spot #20	3659	314	57	0.30	0.04	0.17	N.D.	0.22	0.10	0.11	0.10	N.D.	0.16	0.02	0.06	0.04	N.D.	1.1	0.7	3.0	3.0	0.70694	
Spot #21	2744	6034	36	0.16	0.01	0.15	N.D.	0.20	0.11	0.11	0.10	N.D.	0.17	0.03	0.07	0.04	N.D.	1.1	0.1	3.2	2.6	0.70700	
Spot #22	3709	8	136	0.72	0.11	0.57	N.D.	0.83	0.46	0.48	0.75	N.D.	0.87	0.14	0.34	0.21	N.D.	5.2	0.3	2.4	2.8	0.70699	
Spot #23	2838	21	50	0.22	0.03	0.24	N.D.	0.33	0.19	0.18	0.24	N.D.	0.40	0.07	0.18	0.11	N.D.	2.1	0.2	1.9	2.5	0.70707	
Spot #24	4986	70	184	0.56	0.10	0.48	N.D.	0.68	0.34	0.34	0.55	N.D.	0.69	0.12	0.30	0.16	N.D.	4.0	0.5	2.4	2.6	0.70717	
Spot #25	2971	5	4	0.15	0.08	0.81	N.D.	2.00	1.60	1.37	2.25	N.D.	2.08	0.30	0.64	0.38	N.D.	12.6	0.1	4.5	2.3	0.70706	
Spot #26	2130	42	19	0.47	0.07	0.66	N.D.	1.57	0.87	0.50	1.10	N.D.	1.23	0.19	0.45	0.26	N.D.	7.2	0.2	3.6	1.5	0.70718	
Spot #27	3281	513	46	2.61	0.04	0.24	N.D.	0.46	0.36	0.42	0.31	N.D.	0.40	0.07	0.20	0.16	N.D.	3.1	0.2	2.5	3.1		
Spot #28	1916	807	31	4.04		0.11	N.D.	0.31	0.22	0.31	0.11	N.D.	0.17	0.03	0.09	0.09	N.D.	1.7		2.6	3.6		

Appendix C1.Contd

(ppm)	Sr	Mg	Ba	Pb	La	Ce	Pr	Nd	Sm	Eu	Gd	Tb	Dy	Ho	Er	Yb	Lu	ΣREE	La_N/Yb_N	Sm_N/Yb_N	Eu_N/Eu^*_N	$^{87}Sr/^{86}Sr$	$\delta^{34}S$ (‰)
Snowcap, 193_1188F_1Z_4, 100-104cm, 223mbsf																							
Spot #1	3635	26	77	2.74	7.36	16.29	N.D.	8.92	1.95	1.22	3.54	N.D.	1.89	0.36	0.96	0.70	N.D.	44.1	7.1	3.0	1.7	0.70525	
Spot #2	3816	42	64	4.26	5.19	11.73	N.D.	6.27	1.31	0.80	2.25	N.D.	1.20	0.23	0.64	0.47	N.D.	30.6	7.5	3.0	1.6	0.70567	
Spot #4	3557	3146	2655	5.31	11.40	26.87	N.D.	12.28	3.03	3.17	5.72	N.D.	4.28	0.99	2.96	3.17	N.D.	75.5	2.4	1.0	2.8	0.70538	
Spot #5	3127	563	482	3.92	6.60	18.74	N.D.	12.17	3.14	2.19	4.99	N.D.	3.67	0.71	1.91	1.50	N.D.	57.1	3.0	2.2	1.9	0.70521	
Spot #6	2465	726	705	3.55	2.84	9.46	N.D.	7.83	2.35	2.03	3.36	N.D.	3.15	0.60	1.61	1.09	N.D.	35.5	1.8	2.3	2.3		
Spot #7	2381	123	64	4.04	1.90	6.85	N.D.	6.26	1.83	1.10	2.55	N.D.	2.21	0.42	1.12	0.72	N.D.	25.6	1.8	2.7	1.6	0.70612	20.0
Spot #8	4699	30	13	0.27	102.73	264.36	N.D.	92.09	14.90	11.76	29.45	N.D.	10.92	2.03	5.33	3.65	N.D.	547.1	19.0	4.4	2.1		20.0
Spot #10	5126	17	66	0.57	29.88	75.01	N.D.	32.45	5.76	4.54	10.36	N.D.	3.67	0.64	1.59	1.08	N.D.	168.8	18.6	5.7	2.1	0.70559	20.5
Spot #11	4489	17	82	8.12	6.66	19.08	N.D.	15.21	4.08	2.46	5.72	N.D.	4.49	0.83	2.18	1.41	N.D.	63.6	3.2	3.1	1.6	0.70515	20.3
Spot #12	3637	14	60	0.26	38.52	103.90	N.D.	45.91	8.21	6.42	13.57	N.D.	5.06	0.92	2.40	2.09	N.D.	232.6	12.5	4.2	2.1	0.70545	19.9
Spot #14	2855	351	328	1.28	3.73	13.53	N.D.	11.76	3.72	2.43	5.14	N.D.	3.89	0.67	1.67	1.06	N.D.	49.3	2.4	3.8	1.7	0.70563	20.3
Spor #20	3261	50	67	3.52	4.95	13.66	N.D.	9.03	2.38	1.54	3.64	N.D.	2.79	0.53	1.40	0.96	N.D.	41.9	3.5	2.7	1.7		
Spor #21	2468	14	14	0.77	6.76	20.71	N.D.	16.91	4.18	2.23	5.86	N.D.	3.86	0.65	1.59	0.82	N.D.	65.1	5.6	5.5	1.4		
Spor #22	4476	19	5	0.09	74.87	191.54	N.D.	78.15	13.60	10.08	26.41	N.D.	10.51	1.92	5.02	3.28	N.D.	423.6	15.4	4.4	2.0		
Spor #23	4766	18	222	0.58	7.16	12.85	N.D.	5.36	0.86	1.73	1.64	N.D.	0.42	0.08	0.19	0.18	N.D.	32.0	27.5	5.2	5.3		
Spor #25	3624	809	755	5.04	3.85	11.43	N.D.	7.30	2.63	2.37	5.16	N.D.	4.32	0.71	1.71	1.05	N.D.	41.8	2.5	2.7	2.4		

Appendix C1 Contd

(ppm)	Sr	Mg	Ba	Pb	La	Ce	Pr	Nd	Sm	Eu	Gd	Tb	Dy	Ho	Er	Yb	Lu	ΣREE	La_N/Yb_N	Sm_N/Yb_N	Eu_N/Eu^*_N	$^{87}Sr/^{86}Sr$	$\delta^{34}S$ (‰)
Snowcap, 193_1188F_23Z_2, 22-26cm, 289mbsf																							
Spot #1	2989	33	103	1.96	1.49	4.43	N.D.	4.15	1.24	0.52	2.18	N.D.	1.48	0.31	0.87	0.69	N.D.	17.5	1.5	1.9	1.1	0.70698	
Spot #2	2443	17	33	0.92	2.29	6.42	N.D.	6.18	1.76	0.70	3.16	N.D.	2.18	0.46	1.32	1.11	N.D.	25.8	1.4	1.7	1.1	0.70697	
Spot #3	2761	42	64	1.29	3.16	9.12	N.D.	7.57	2.28	0.89	3.77	N.D.	2.46	0.48	1.32	1.03	N.D.	32.5	2.1	2.4	1.0	0.70659	
Spot #4	2688	121	140	0.96	1.98	5.80	N.D.	5.20	1.55	0.63	2.78	N.D.	1.98	0.40	1.12	0.99	N.D.	22.6	1.4	1.7	1.1	0.70673	
Spot #5	3347	275	185	1.62	3.94	10.50	N.D.	8.15	2.05	0.86	3.66	N.D.	2.04	0.41	1.15	0.93	N.D.	34.0	2.9	2.4	1.1	0.70686	
Spot #6	2494	9222	3340	1.58	20.34	42.30	N.D.	28.61	6.30	4.25	12.93	N.D.	5.06	0.97	2.59	2.34	N.D.	128.3	5.9	2.9	1.8	0.70630	

Appendix C1 Contd

(ppm)	Sr	Mg	Ba	Pb	La	Ce	Pr	Nd	Sm	Eu	Gd	Tb	Dy	Ho	Er	Yb	Lu	ΣREE	La_N/Yb_N	Sm_N/Yb_N	Eu_N/Eu^*_N	$^{87}Sr/^{86}Sr$	$\delta^{34}S$ (‰)
Snowcap, 193_1188F_26Z_1, 62-69cm, 300mbsf																							
Spot #1	2577	65	63	0.35	0.14	0.66	N.D.	1.05	0.64	0.91	0.72	N.D.	0.98	0.18	0.49	0.30	N.D.	6.8	0.3	2.2	3.8	0.70642	
Spot #2	2103	45	50	0.75	5.41	13.16	N.D.	6.70	1.49	1.13	4.00	N.D.	1.95	0.40	1.11	0.80	N.D.	36.9	4.5	2.0	2.0	0.70614	
Spot #3	2347	7	23	0.45	3.86	8.04	N.D.	5.28	1.49	1.28	3.47	N.D.	2.60	0.56	1.59	0.99	N.D.	29.9	2.6	1.6	2.3	0.70508	16.6
Spot #4	2209	194	134	0.55	6.18	12.00	N.D.	7.76	1.55	0.97	4.31	N.D.	2.09	0.48	1.43	1.38	N.D.	38.5	3.0	1.2	1.7	0.70546	
Spot #5	2832	99	89	0.37	3.36	7.78	N.D.	5.91	1.59	0.46	3.24	N.D.	1.58	0.32	0.89	0.70	N.D.	26.0	3.2	2.4	0.8	0.70694	
Spot #6	2821	185	155	0.59	1.33	3.26	N.D.	2.60	0.71	0.67	1.23	N.D.	1.08	0.21	0.56	0.31	N.D.	12.4	2.9	2.5	2.5	0.70635	
Spot #7	2566	1098	41	0.39	5.33	12.53	N.D.	11.05	3.38	1.63	6.06	N.D.	3.65	0.69	1.85	1.35	N.D.	48.4	2.7	2.7	1.3	0.70592	17.4
Spot #8	2991	29	41	1.06	1.41	3.44	N.D.	3.44	1.16	1.01	1.69	N.D.	1.12	0.21	0.54	0.35	N.D.	15.1	2.7	3.5	2.2	0.70596	
Spot #9	2103	19	53	0.46	3.02	5.52	N.D.	4.37	1.08	0.86	1.84	N.D.	0.42	0.07	0.16	0.15	N.D.	18.3	13.4	7.6	2.1	0.70583	
Spot #10	1393	20	12	0.33	2.04	5.11	N.D.	3.62	0.94	0.73	1.85	N.D.	1.72	0.34	0.93	0.56	N.D.	18.2	2.5	1.8	2.1	0.70623	
Spot #11	2468	20	73	310.43	6.15	15.75	N.D.	14.07	3.71	1.03	7.15	N.D.	3.63	0.64	1.62	1.13	N.D.	55.2	3.7	3.5	0.7	0.70626	
Spot #12	2442	356	205	27.53	0.37	0.82	N.D.	0.95	0.35	0.42	0.29	N.D.	0.23	0.04	0.11	0.11	N.D.	4.0	2.4	3.5	3.9	0.70712	18.6
Spot #13	3316	10	106	0.47	0.13	0.43	N.D.	0.56	0.28	0.60	0.15	N.D.	0.23	0.04	0.10	0.09	N.D.	3.2	0.9	3.2	5.7	0.70581	
Spot #14	2516	338	157	2.84	2.19	5.67	N.D.	4.97	1.40	1.20	2.25	N.D.	1.37	0.27	0.75	0.68	N.D.	21.6	2.2	2.2	2.3	0.70625	
Spot #15	1928	24	52	0.49	24.56	51.94	N.D.	46.97	11.86	3.92	22.93	N.D.	9.38	1.65	4.18	3.14	N.D.	182.9	5.3	4.0	0.9	0.70542	18.0
Spot #16	2304	25	64	0.88	4.85	15.05	N.D.	16.92	5.22	1.70	8.29	N.D.	5.65	1.10	2.97	2.39	N.D.	64.7	1.4	2.3	0.9	0.70606	19.0
Spot #17	2768	29	21	0.21	0.41	1.06	N.D.	1.30	0.35	0.29	0.40	N.D.	0.18	0.03	0.07	0.07	N.D.	4.4	4.0	5.5	2.2	0.70686	18.7
Spot #18	3380	11	46	0.25	0.12	0.38	N.D.	0.64	0.39	0.32	0.15	N.D.	0.17	0.03	0.06	0.04	N.D.	2.6	1.8	9.2	2.2	0.70699	
Spot #19	2080	39	115	0.39	4.07	7.65	N.D.	4.39	1.13	1.19	2.94	N.D.	2.62	0.55	1.58	1.02	N.D.	27.7	2.7	1.2	2.8	0.70542	
Spot #20	2561	193	126	0.27	2.08	5.58	N.D.	5.08	1.38	0.63	2.30	N.D.	1.54	0.31	0.87	0.76	N.D.	20.8	1.8	1.9	1.2	0.70663	
Spot #21	2060	14	23	0.53	1.48	4.39	N.D.	4.72	1.44	0.64	2.16	N.D.	1.75	0.38	1.11	1.35	N.D.	19.7	0.7	1.1	1.2	0.70648	
Spot #22	1691	9	18	0.35	2.06	5.21	N.D.	3.99	1.19	1.08	2.40	N.D.	2.79	0.59	1.67	1.02	N.D.	22.5	1.4	1.3	2.4	0.70635	
Spot #23	1789	224	142	0.58	3.41	7.17	N.D.	4.96	1.37	1.09	2.95	N.D.	2.32	0.47	1.33	0.84	N.D.	26.4	2.7	1.7	2.1	0.70633	
Spot #24	2547	59	42	0.27	0.29	0.85	N.D.	0.83	0.29	0.29	0.14	N.D.	0.19	0.03	0.07	0.06	N.D.	3.3	3.4	5.4	2.6	0.70613	

Appendix C1 Contd

(ppm)	Sr	Mg	Ba	Pb	La	Ce	Pr	Nd	Sm	Eu	Gd	Tb	Dy	Ho	Er	Yb	Lu	ΣREE	La_N/Yb_N	Sm_N/Yb_N	Eu_N/Eu^*_N	$^{87}Sr/^{86}Sr$	$\delta^{34}S$ (‰)
Roman Ruins, 193_1189A_3R_1, 89-93cm, 20mbsf																							
Spot #1	2989	4	197	1.49	3.27	9.93	N.D.	7.66	1.52	0.75	1.36	N.D.	0.48	0.07	0.14	0.08	N.D.	26.0	27.0	19.9	1.3	0.70576	20.2
Spot #2	4127	1	170	1.78	8.35	15.59	N.D.	6.19	1.00	0.48	1.25	N.D.	0.33	0.05	0.11	0.08	N.D.	33.9	74.2	14.0	1.3	0.70586	19.8
Spot #3	3391	1	108	1.96	3.74	7.78	N.D.	3.35	0.49	0.34	0.63	N.D.	0.17	0.03	0.07	0.04	N.D.	17.0	57.8	12.1	1.8	0.70623	20.0
Spot #4	3267	3	75	1.41	1.44	3.09	N.D.	1.39	0.23	0.23	0.26	N.D.	0.09	0.01	0.03	0.03	N.D.	7.0	35.6	9.0	2.7	0.70594	
Spot #5	1378	5	28	0.60	6.85	22.45	N.D.	12.42	2.18	1.24	2.24	N.D.	0.65	0.09	0.19	0.11	N.D.	49.5	41.9	21.2	1.5	0.70527	
Spot #6	1820	4	30	0.42	0.54	1.94	N.D.	1.27	0.22	0.51	0.24	N.D.	0.11	0.02	0.06	0.05	N.D.	5.5	7.8	5.1	6.1	0.70565	
Spot #7	1819	4	147	0.37	0.66	2.44	N.D.	2.26	0.51	0.47	0.46	N.D.	0.24	0.04	0.08	0.05	N.D.	7.7	8.3	10.2	2.4	0.70607	19.6
Spot #8	615	4	1	0.01	1.42	4.55	N.D.	2.57	0.47	0.24	0.48	N.D.	0.22	0.03	0.07	0.04	N.D.	10.3	23.4	12.2	1.3	0.70666	19.8
Spot #9	872	3	24	0.02	0.86	2.41	N.D.	1.24	0.23	0.13	0.23	N.D.	0.09	0.01	0.02	0.02	N.D.	5.4	38.8	16.2	1.5		19.8
Spot #10	807	1	4	0.01	1.05	3.84	N.D.	2.36	0.54	0.29	0.53	N.D.	0.24	0.03	0.06	0.04	N.D.	9.2	17.5	14.5	1.4		19.9
Spot #11	2077	14	37	0.36	16.17	33.10	N.D.	11.67	2.17	1.80	2.74	N.D.	0.67	0.09	0.19	0.10	N.D.	70.5	107.7	23.0	2.2	0.70628	
Spot #12	620	1	4	0.00	1.56	5.58	N.D.	4.06	1.11	0.37	1.06	N.D.	0.44	0.06	0.10	0.06	N.D.	14.7	19.1	21.6	0.9	0.70544	
Spot #13	908	2	8	0.06	2.48	6.90	N.D.	3.59	0.67	0.30	0.71	N.D.	0.23	0.03	0.07	0.04	N.D.	15.3	41.9	17.9	1.2	0.70583	
Spot #14	3335	5	56	0.12	6.87	13.54	N.D.	6.41	0.86	0.47	1.18	N.D.	0.31	0.05	0.10	0.07	N.D.	30.2	69.2	13.7	1.5	0.70667	
Spot #15	4124	1	282	2.06	5.88	12.52	N.D.	5.20	0.78	0.49	1.02	N.D.	0.30	0.05	0.11	0.07	N.D.	26.9	56.7	12.0	1.7	0.70591	
Spot #16	2046	1	40	0.52	2.34	7.36	N.D.	4.15	0.78	0.29	0.79	N.D.	0.32	0.04	0.09	0.06	N.D.	16.5	26.0	13.8	1.0	0.70637	
Spot #17	1579	1	26	0.22	0.34	1.34	N.D.	0.98	0.19	0.46	0.17	N.D.	0.11	0.02	0.04	0.04	N.D.	4.1	5.9	5.2	6.5	0.70565	

Appendix C1.Contd

(ppm)	Sr	Mg	Ba	Pb	La	Ce	Pr	Nd	Sm	Eu	Gd	Tb	Dy	Ho	Er	Yb	Lu	ΣREE	La_N/Yb_N	Sm_N/Yb_N	Eu_N/Eu^*_N	$^{87}Sr/^{86}Sr$	$\delta^{34}S$ (‰)
Roman Ruins, 193_1189A_7R_1, 19-23cm, 58mbsf																							
Spot #1	1629	11	124	0.80	0.93	2.55	N.D.	2.28	0.61	0.50	0.84	N.D.	0.30	0.05	0.10	0.08	N.D.	8.7	8.2	8.5	2.1	0.70610	
Spot #2	1477	3	137	0.39	1.03	2.94	N.D.	2.62	0.71	0.51	0.98	N.D.	0.35	0.05	0.11	0.08	N.D.	9.8	8.7	9.5	1.9	0.70612	
Spot #3	1582	3	151	0.36	1.03	3.04	N.D.	2.80	0.77	0.50	0.98	N.D.	0.36	0.05	0.11	0.08	N.D.	10.2	8.5	10.1	1.8	0.70604	
Spot #4	1613	4	147	0.38	0.61	2.14	N.D.	2.60	0.72	0.63	0.91	N.D.	0.37	0.05	0.12	0.09	N.D.	8.8	4.6	8.6	2.4	0.70604	
Spot #5	3203	2	211	0.84	1.21	3.13	N.D.	2.72	0.62	0.71	0.91	N.D.	0.30	0.05	0.11	0.08	N.D.	10.5	10.2	8.3	2.9	0.70611	
Spot #6	1855	2	48	0.61	2.78	6.89	N.D.	5.15	1.33	0.71	1.88	N.D.	0.62	0.09	0.18	0.13	N.D.	20.4	14.3	10.8	1.4	0.70611	
Spot #7	1026	2	11	0.21	0.65	1.87	N.D.	1.46	0.39	0.21	0.54	N.D.	0.19	0.03	0.06	0.04	N.D.	5.6	10.8	10.3	1.4	0.70617	
Spot #8	1300	1	70	0.37	0.88	2.51	N.D.	1.82	0.50	0.28	0.70	N.D.	0.23	0.03	0.07	0.05	N.D.	7.3	11.7	10.4	1.4	0.70626	
Spot #9	1269	1	30	0.28	0.96	2.78	N.D.	2.04	0.56	0.28	0.73	N.D.	0.25	0.03	0.07	0.05	N.D.	8.0	12.0	11.2	1.3	0.70611	
Spot #10	1356	2	51	0.39	1.08	2.90	N.D.	2.12	0.57	0.29	0.80	N.D.	0.24	0.03	0.07	0.05	N.D.	8.4	14.9	12.5	1.3	0.70606	
Spot #11	1515	3	199	1.06	0.95	2.44	N.D.	1.67	0.43	0.38	0.61	N.D.	0.19	0.03	0.06	0.04	N.D.	7.1	16.3	11.7	2.3	0.70608	
Spot #12	1751	4	264	1.38	0.58	1.39	N.D.	0.99	0.27	0.41	0.39	N.D.	0.12	0.02	0.04	0.02	N.D.	4.5	16.2	11.7	3.8	0.70617	
Spot #13	1879	3	233	1.52	0.58	1.41	N.D.	0.94	0.27	0.42	0.36	N.D.	0.11	0.02	0.03	0.03	N.D.	4.5	14.4	10.6	4.1		
Spot #14	1996	4	131	0.65	0.66	1.62	N.D.	1.08	0.27	0.24	0.39	N.D.	0.12	0.02	0.03	0.02	N.D.	4.6	18.4	11.9	2.3	0.70637	
Spot #15	2950	1	127	2.46	2.99	7.30	N.D.	5.43	1.20	0.78	1.97	N.D.	0.48	0.07	0.15	0.11	N.D.	21.1	17.7	11.3	1.5	0.70601	
Spot #16	2063	2	165	1.78	7.26	14.36	N.D.	8.41	1.96	0.83	3.56	N.D.	0.81	0.11	0.22	0.16	N.D.	38.3	30.4	13.0	1.1	0.70552	
Spot #17	4624	2	678	2.71	2.11	4.85	N.D.	3.12	0.65	0.98	1.26	N.D.	0.28	0.04	0.09	0.07	N.D.	14.2	20.3	9.8	3.3	0.70624	
Spot #18	1429	4	98	0.61	1.28	3.97	N.D.	3.19	0.77	0.49	1.25	N.D.	0.36	0.05	0.11	0.09	N.D.	12.0	10.1	9.8	1.5	0.70626	
Spot #19	3942	24	35	0.43	0.23	0.45	N.D.	0.28	0.07	0.04	0.14	N.D.	0.03	0.00	0.01	0.01	N.D.	1.3	20.6	9.2	1.8	0.70809	
Spot #20	2088	6	48	0.04	0.05	0.11	N.D.	0.07	0.02	0.04	0.03	N.D.	0.01	0.00	0.00	0.00	N.D.	0.4	11.4	6.0	6.0	0.70787	
Spot #21	2429	7	29	0.07	0.10	0.20	N.D.	0.13	0.03	0.03	0.05	N.D.	0.01	0.00	0.00	0.00	N.D.	0.6	34.6	18.4	2.6	0.70796	
Spot #22	2769	4	14	0.20	0.28	0.54	N.D.	0.39	0.10	0.05	0.17	N.D.	0.04	0.01	0.01	0.01	N.D.	1.6	25.6	14.7	1.2	0.70824	
Spot #23	2962	11	27	1.96	1.46	3.24	N.D.	2.36	0.62	0.18	0.91	N.D.	0.28	0.04	0.07	0.05	N.D.	9.4	21.4	14.4	0.8	0.70739	
Spot #24	1445	37	24	0.22	2.90	8.44	N.D.	7.11	2.04	0.57	2.93	N.D.	0.88	0.12	0.23	0.16	N.D.	25.9	12.3	13.8	0.7	0.70617	
Spot #25	1449	84	35	0.18	3.33	9.28	N.D.	7.44	1.94	0.57	3.06	N.D.	0.82	0.11	0.22	0.17	N.D.	27.4	13.1	12.2	0.8	0.70689	
Spot #26	1521	15	34	0.30	2.18	7.12	N.D.	6.36	1.81	0.51	2.60	N.D.	0.73	0.10	0.18	0.14	N.D.	22.1	10.4	13.8	0.7	0.70728	
Spot #27	1256	32	12	0.24	2.26	7.33	N.D.	6.47	1.69	0.53	2.69	N.D.	0.72	0.10	0.20	0.14	N.D.	22.6	10.5	12.6	0.8		

Appendix C1 Contd

(ppm)	Sr	Mg	Ba	Pb	La	Ce	Pr	Nd	Sm	Eu	Gd	Tb	Dy	Ho	Er	Yb	Lu	ΣREE	La_N/Yb_N	Sm_N/Yb_N	Eu_N/Eu^*_N	$^{87}Sr/^{86}Sr$	$\delta^{34}S$ (‰)
Roman Ruins, 193_1189B_10R_1, 42-44cm, 118mbsf																							
Spot #1	3063	46	144	0.24	0.99	2.27	N.D.	1.75	0.42	0.18	0.60	N.D.	0.17	0.03	0.06	0.04	N.D.	6.6	17.8	11.9	1.1	0.70786	
Spot #2	2810	30	126	0.32	0.69	1.76	N.D.	1.30	0.34	0.16	0.46	N.D.	0.16	0.02	0.06	0.04	N.D.	5.1	11.5	9.0	1.2	0.70781	
Spot #3	2884	27	145	0.30	0.50	1.02	N.D.	0.70	0.16	0.13	0.22	N.D.	0.07	0.01	0.03	0.02	N.D.	3.0	17.5	9.1	2.0	0.70778	
Spot #4	2439	34	54	0.58	0.28	0.52	N.D.	0.34	0.09	0.07	0.13	N.D.	0.04	0.01	0.02	0.01	N.D.	1.6	18.6	9.6	2.0	0.70786	
Spot #5	1996	12	125	0.29	0.34	0.72	N.D.	0.48	0.13	0.12	0.17	N.D.	0.04	0.01	0.01	0.01	N.D.	2.1	22.3	13.5	2.4	0.70762	
Spot #6	2493	7	184	0.71	1.12	2.01	N.D.	1.23	0.27	0.21	0.45	N.D.	0.08	0.01	0.02	0.02	N.D.	5.6	39.0	14.9	2.0	0.70736	
Spot #7	2955	12	160	0.68	1.19	2.23	N.D.	1.28	0.28	0.18	0.54	N.D.	0.08	0.01	0.03	0.02	N.D.	6.0	40.9	15.3	1.7	0.70744	
Spot #8	2781	34	203	0.42	0.47	1.01	N.D.	0.71	0.17	0.20	0.31	N.D.	0.06	0.01	0.02	0.02	N.D.	3.1	17.1	10.0	3.1	0.70791	
Spot #9	3170	24	185	0.17	0.52	1.20	N.D.	1.08	0.28	0.17	0.35	N.D.	0.11	0.02	0.04	0.03	N.D.	3.9	12.6	10.8	1.6		
Spot #10	2629	14	19	0.12	0.29	0.62	N.D.	0.55	0.12	0.06	0.21	N.D.	0.05	0.01	0.02	0.02	N.D.	2.0	11.4	7.7	1.2	0.70808	
Spot #11	2928	17	112	0.39	0.62	1.57	N.D.	1.30	0.32	0.16	0.49	N.D.	0.13	0.02	0.03	0.03	N.D.	4.8	13.8	11.4	1.3		
Spot #12	3122	26	181	8.47	1.11	2.56	N.D.	2.07	0.51	0.24	0.80	N.D.	0.23	0.03	0.08	0.06	N.D.	7.9	12.4	9.0	1.3	0.70773	
Spot #13	2898	17	174	0.23	0.83	2.13	N.D.	1.74	0.43	0.22	0.65	N.D.	0.18	0.03	0.06	0.05	N.D.	6.5	11.5	9.4	1.4	0.70774	
Spot #20	2411	24	8	2.83	1.23	2.62	N.D.	1.56	0.34	0.15	0.70	N.D.	0.20	0.03	0.07	0.04	N.D.	7.0	20.3	8.9	1.1	0.70734	
Spot #21	2206	52	10	2.49	1.23	2.66	N.D.	1.66	0.36	0.16	0.71	N.D.	0.19	0.03	0.07	0.05	N.D.	7.2	16.9	7.9	1.2	0.70742	
Spot #22	2381	14	7	2.74	1.42	3.07	N.D.	2.07	0.43	0.19	0.87	N.D.	0.23	0.04	0.09	0.05	N.D.	8.6	19.3	9.2	1.2	0.70742	
Spot #23	2940	46	14	4.21	1.82	3.49	N.D.	2.00	0.41	0.18	1.01	N.D.	0.23	0.04	0.09	0.06	N.D.	9.5	19.7	7.0	1.2	0.70752	
Spot #24	2635	11	69	0.05	0.27	0.38	N.D.	0.22	0.05	0.06	0.10	N.D.	0.02	0.00	0.01	0.01	N.D.	1.2	30.4	8.2	3.5	0.70800	
Spot #25	2746	19	62	0.05	0.48	0.77	N.D.	0.49	0.09	0.08	0.21	N.D.	0.03	0.00	0.01	0.01	N.D.	2.2	37.0	11.2	2.2		21.6
Spot #26	2984	36	59	0.09	0.44	0.64	N.D.	0.42	0.07	0.06	0.18	N.D.	0.03	0.00	0.01	0.01	N.D.	1.9	46.1	12.1	2.2	0.70811	
Spot #27	2999	29	58	0.05	0.27	0.35	N.D.	0.22	0.04	0.05	0.10	N.D.	0.01	0.00	0.00	0.00	N.D.	1.1	47.8	10.7	3.7	0.70802	
Spot #28	3285	38	202	22.93	1.00	2.54	N.D.	2.08	0.53	0.26	0.82	N.D.	0.22	0.03	0.07	0.05	N.D.	7.8	13.7	11.5	1.3	0.70774	21.5
Spot #29	3162	22	194	0.22	0.22	0.41	N.D.	0.31	0.08	0.14	0.13	N.D.	0.03	0.00	0.01	0.01	N.D.	1.4	12.8	7.2	4.9	0.70659	21.3

Appendix C1 Contd

(ppm)	Sr	Mg	Ba	Pb	La	Ce	Pr	Nd	Sm	Eu	Gd	Tb	Dy	Ho	Er	Yb	Lu	ΣREE	La_N/Yb_N	Sm_N/Yb_N	Eu_N/Eu^*_N	$^{87}Sr/^{86}Sr$	$\delta^{34}S$ (‰)
Roman Ruins, 193_1189B_14R_2, 0-3cm, 158mbsf																							
Spot #1	2856	10	187	1.37	0.44	1.03	N.D.	0.71	0.14	0.29	0.24	N.D.	0.06	0.01	0.02	0.01	N.D.	3.2	21.2	10.5	5.6	0.70628	20.9
Spot #2	2479	9	261	4.53	3.71	7.07	N.D.	3.57	0.65	1.06	1.33	N.D.	0.25	0.04	0.09	0.06	N.D.	18.7	41.2	11.5	4.3	0.70427	
Spot #3	785	3	26	0.31	9.56	30.63	N.D.	25.82	5.65	1.25	8.28	N.D.	2.03	0.28	0.56	0.38	N.D.	85.4	17.0	15.9	0.6	0.70432	21.0
Spot #5	447	4	1	0.13	10.39	37.67	N.D.	32.62	7.15	1.39	10.46	N.D.	2.63	0.36	0.71	0.46	N.D.	104.9	15.2	16.6	0.5	0.70727	20.2
Spot #6	2291	32	68	4.78	0.93	2.51	N.D.	1.97	0.44	0.33	0.66	N.D.	0.16	0.02	0.04	0.03	N.D.	7.4	24.8	18.7	2.0	0.70822	19.9
Spot #7	1445	6	43	0.42	2.06	7.44	N.D.	6.82	1.62	0.54	2.31	N.D.	0.68	0.10	0.21	0.14	N.D.	22.4	10.2	12.7	0.9	0.70429	21.2
Spot #9	686	1	15	0.42	10.11	33.58	N.D.	27.82	6.11	1.31	8.90	N.D.	2.31	0.32	0.63	0.42	N.D.	92.5	16.3	15.7	0.6	0.70804	22.8
Spot #10	443	1	1	0.02	6.38	23.15	N.D.	20.01	4.54	0.91	6.46	N.D.	1.75	0.25	0.51	0.33	N.D.	65.0	12.9	14.6	0.5	0.70748	23.2
Spot #11	545	10	8	0.05	7.00	24.63	N.D.	21.30	5.09	0.84	7.18	N.D.	2.05	0.28	0.57	0.38	N.D.	69.9	12.3	14.2	0.4		21.5
Spot #12	263	723	41	1.68	11.39	26.65	N.D.	13.87	2.26	0.59	4.73	N.D.	1.22	0.26	0.72	0.87	N.D.	62.9	8.9	2.8	0.7		21.4
Spot #13	1818	270	68	0.83	5.87	17.04	N.D.	13.52	2.75	0.72	4.08	N.D.	1.04	0.16	0.34	0.30	N.D.	46.4	13.2	9.8	0.7		22.1
Spot #14	1900	12	47	0.20	1.75	6.01	N.D.	5.31	1.22	0.63	1.68	N.D.	0.50	0.07	0.14	0.09	N.D.	18.0	13.7	15.2	1.4		21.2

Appendix C1 Contd

(ppm)	Sr	Mg	Ba	Pb	La	Ce	Pr	Nd	Sm	Eu	Gd	Tb	Dy	Ho	Er	Yb	Lu	ΣREE	La_N/Yb_N	Sm_N/Yb_N	Eu_N/Eu^*_N	$^{87}Sr/^{86}Sr$	$\delta^{34}S$ (‰)
Fenway, J2_210_8_R1																							
Spot #1	842	2	93	0.19	2.59	5.57	N.D.	1.93	0.35	1.37	0.23	N.D.	0.17	0.03	0.07	0.05	N.D.	13.7	33.2	7.2	13.9		
Spot #2	2258	5	33	0.65	1.61	4.31	N.D.	2.56	0.73	0.67	0.51	N.D.	0.29	0.04	0.08	0.05	N.D.	11.5	21.9	15.7	3.2		
Spot #3	1417	112	217	2.66	2.34	6.79	N.D.	5.18	1.43	1.11	1.17	N.D.	0.70	0.09	0.18	0.06	N.D.	20.1	27.1	26.4	2.5		
Spot #4	2762	39	161	1.16	2.35	4.72	N.D.	2.33	0.59	0.70	0.47	N.D.	0.35	0.06	0.13	0.05	N.D.	12.4	29.0	11.6	4.0		
Spot #5	2447	9	73	1.84	0.80	1.68	N.D.	0.98	0.21	0.33	0.17	N.D.	0.09	0.01	0.03	0.01	N.D.	4.6	36.5	15.5	5.1		
Spot #7	1911	10	118	1.95	1.19	2.64	N.D.	1.10	0.20	0.54	0.13	N.D.	0.15	0.02	0.04	0.03	N.D.	6.5	27.8	7.3	9.7		
Spot #8	1703	4	531	2.27	2.66	5.73	N.D.	2.67	0.61	0.65	0.41	N.D.	0.29	0.04	0.09	0.07	N.D.	13.8	26.5	9.6	3.8		
Spot #9	1372	12	455	0.94	3.20	6.59	N.D.	2.47	0.49	1.06	0.31	N.D.	0.20	0.04	0.12	0.04	N.D.	15.6	48.9	11.8	7.8		
Spot #10	1423	18	560	0.69	6.00	12.89	N.D.	5.15	1.08	1.43	0.70	N.D.	0.42	0.06	0.14	0.08	N.D.	29.3	48.3	13.9	4.7		
Spot #11	1216	43	396	0.32	10.08	23.91	N.D.	13.45	3.01	2.29	2.07	N.D.	1.15	0.16	0.31	0.17	N.D.	58.8	40.2	19.0	2.7		
Spot #12	1098	7	81	0.44	8.47	22.64	N.D.	11.47	2.50	2.89	1.68	N.D.	0.93	0.13	0.29	0.15	N.D.	54.0	37.1	17.4	4.1		
Spot #13	1831	81	514	3.00	3.74	6.51	N.D.	2.63	0.54	1.55	0.37	N.D.	0.18	0.04	0.10	0.04	N.D.	17.2	58.0	13.2	10.0		
Spot #14	1654	199	626	6.49	3.47	6.42	N.D.	2.42	0.52	1.59	0.30	N.D.	0.21	0.03	0.06	0.05	N.D.	16.5	50.6	12.0	11.3		
Spot #15	2829	7	102	3.80	0.92	1.79	N.D.	0.89	0.20	0.38	0.14	N.D.	0.08	0.01	0.06	0.01	N.D.	4.8	49.5	17.4	6.4		
Spot #16	2630	22	123	3.17	3.41	6.50	N.D.	2.48	0.33	0.87	0.29	N.D.	0.18	0.03	0.07	0.04	N.D.	15.0	57.4	8.8	8.5		
Spot #17	1509	42	28	1.36	0.97	2.33	N.D.	1.29	0.28	0.57	0.24	N.D.	0.13	0.10	0.04	0.01	N.D.	6.4	48.0	21.6	6.7		
Spot #18	1437	52	31	1.13	1.71	4.40	N.D.	2.54	0.58	0.81	0.34	N.D.	0.21	0.03	0.05	0.03	N.D.	11.4	36.5	19.6	5.2		
Spot #19	2867	91	59	1.95	0.76	1.49	N.D.	0.83	0.18	0.31	0.14	N.D.	0.10	0.01	0.03	0.02	N.D.	4.2	27.7	10.4	5.9		

Appendix C1 Contd

(ppm)	Sr	Mg	Ba	Pb	La	Ce	Pr	Nd	Sm	Eu	Gd	Tb	Dy	Ho	Er	Yb	Lu	ΣREE	La_N/Yb_N	Sm_N/Yb_N	Eu_N/Eu^*_N	$^{87}Sr/^{86}Sr$	$\delta^{34}S$ (‰)
Fenway, J2_210_8_R2																							
Spot #1	2449	8	45	0.91	0.66	1.81	N.D.	1.09	0.25	0.66	0.15	N.D.	0.10	0.02	0.04	0.03	N.D.	5.5	16.3	9.8	9.6	0.70694	21.0
Spot #2	2245	73	75	6.32	0.73	2.18	N.D.	1.26	0.33	0.59	0.19	N.D.	0.13	0.02	0.04	0.02	N.D.	6.1	29.6	21.0	6.7		
Spot #3	2517	89	88	17.32	0.92	2.08	N.D.	0.99	0.22	0.57	0.15	N.D.	0.09	0.01	0.03	0.02	N.D.	5.6	29.1	11.3	9.0	0.70757	
Spot #4	2819	66	73	2.42	1.47	3.22	N.D.	1.44	0.31	0.70	0.23	N.D.	0.15	0.02	0.05	0.04	N.D.	8.3	25.4	8.5	7.6	0.70768	
Spot #5	3669	14	67	1.60	0.44	1.05	N.D.	0.69	0.18	0.19	0.13	N.D.	0.08	0.01	0.04	0.02	N.D.	3.0	13.8	8.7	3.7		
Spot #6	2162	66	64	2.40	0.99	2.74	N.D.	1.53	0.35	0.70	0.23	N.D.	0.13	0.02	0.04	0.04	N.D.	7.4	18.8	10.5	7.2	0.70763	
Spot #7	1762	5	50	2.10	2.07	4.81	N.D.	2.26	0.48	0.65	0.31	N.D.	0.18	0.03	0.06	0.03	N.D.	11.6	40.7	15.0	4.8	0.70673	21.7
Spot #8	2178	6	212	1.88	1.27	3.04	N.D.	1.60	0.37	0.44	0.22	N.D.	0.13	0.02	0.04	0.02	N.D.	7.6	38.6	18.0	4.3		
Spot #9	2447	75	134	0.77	0.58	1.46	N.D.	0.84	0.21	0.26	0.17	N.D.	0.08	0.01	0.03	0.02	N.D.	3.9	25.9	15.1	4.1	0.70806	
Spot #10	3059	11	352	1.30	0.51	1.08	N.D.	0.56	0.13	0.22	0.09	N.D.	0.06	0.01	0.02	0.02	N.D.	2.9	19.1	7.4	6.1		
Spot #11	2420	11	83	0.58	0.26	0.59	N.D.	0.37	0.08	0.19	0.06	N.D.	0.04	0.01	0.02	0.02	N.D.	1.8	8.7	4.2	7.9	0.70803	
Spot #12	2403	7	37	0.37	0.87	2.47	N.D.	1.46	0.37	0.37	0.23	N.D.	0.15	0.02	0.04	0.02	N.D.	6.4	30.1	20.5	3.6	0.70790	
Spot #13	2379	7	119	0.74	0.47	0.98	N.D.	0.48	0.12	0.24	0.10	N.D.	0.06	0.01	0.02	0.02	N.D.	2.7	18.2	7.5	6.5		
Spot #14	2231	2	200	1.68	0.42	1.08	N.D.	0.53	0.15	0.31	0.09	N.D.	0.08	0.01	0.03	0.02	N.D.	3.0	13.8	7.6	7.7	0.70752	
Spot #15	2082	32	59	2.18	1.50	3.18	N.D.	1.54	0.34	0.90	0.24	N.D.	0.15	0.02	0.05	0.03	N.D.	8.8	37.4	13.5	9.2		
Spot #16	3047	139	159	3.44	1.39	2.85	N.D.	1.47	0.33	0.49	0.23	N.D.	0.15	0.02	0.04	0.03	N.D.	7.4	33.7	12.6	5.2		
Spot #17	2192	91	136	1.49	0.74	2.08	N.D.	1.44	0.42	0.41	0.33	N.D.	0.20	0.03	0.06	0.04	N.D.	6.1	11.4	10.1	3.3		
Spot #18	2617	44	82	0.51	0.47	1.18	N.D.	0.67	0.14	0.15	0.11	N.D.	0.06	0.01	0.03	0.01	N.D.	3.0	24.3	11.4	3.6		
Spot #19	2977	59	428	3.29	2.98	6.00	N.D.	3.12	0.74	0.80	0.54	N.D.	0.30	0.04	0.08	0.06	N.D.	15.4	31.9	12.5	3.7		
Spot #20	2591	37	122	126.61	0.42	1.21	N.D.	0.66	0.17	0.37	0.12	N.D.	0.08	0.01	0.02	0.01	N.D.	3.5	19.2	11.9	7.6		21.8

Appendix C1 Contd

(ppm)	Sr	Mg	Ba	Pb	La	Ce	Pr	Nd	Sm	Eu	Gd	Tb	Dy	Ho	Er	Yb	Lu	ΣREE	La_N/Yb_N	Sm_N/Yb_N	Eu_N/Eu^*_N	$^{87}Sr/^{86}Sr$	$\delta^{34}S$ (‰)
Fenway, J2_212_7_R1																							
Spot #1	3185	7	73	0.04	0.81	1.98	N.D.	1.12	0.24	0.33	0.22	N.D.	0.13	0.02	0.04	0.04	N.D.	5.2	12.2	5.9	4.4		
Spot #2	2900	30	44	0.39	1.03	2.72	N.D.	1.72	0.42	0.49	0.32	N.D.	0.19	0.03	0.07	0.04	N.D.	7.5	19.2	12.3	3.9		
Spot #3	2968	9	63	0.39	0.55	1.39	N.D.	1.11	0.30	0.31	0.22	N.D.	0.12	0.02	0.03	0.05	N.D.	4.4	7.5	6.6	3.5		
Spot #4	3174	191	147	2.49	1.70	3.39	N.D.	1.51	0.28	0.82	0.24	N.D.	0.23	0.03	0.05	0.03	N.D.	9.1	33.5	8.8	9.4		
Spot #5	3286	12	31	0.31	1.31	2.54	N.D.	1.08	0.19	0.94	0.15	N.D.	0.08	0.01	0.11	0.03	N.D.	7.3	28.4	6.6	16.4		
Spot #7	3096	29	76	0.99	1.61	3.52	N.D.	2.15	0.64	0.71	0.41	N.D.	0.23	0.03	0.07	0.03	N.D.	10.1	32.7	20.6	4.0	0.70762	
Spot #10	3359	34	68	0.39	0.41	0.98	N.D.	0.67	0.25	0.25	0.15	N.D.	0.11	0.01	0.02	0.04	N.D.	3.1	7.3	7.0	3.7	0.70789	
Spot #11	2524	475	30	2.16	0.71	1.79	N.D.	1.02	0.26	0.59	0.20	N.D.	0.13	0.02	0.05	0.03	N.D.	5.3	17.6	10.2	7.6	0.70785	
Spot #12	1904	128	26	5.71	0.36	1.03	N.D.	0.74	0.33	0.63	0.26	N.D	0.25	0.02	0.23	0.05	N.D.	4.5	5.0	7.2	6.4	0.70746	
Spot #16	2232	24	39	0.43	1.47	4.11	N.D.	3.13	0.92	0.85	0.58	N.D.	0.36	0.03	N.D.	0.12	N.D.	12.4	8.3	8.2	3.3	0.70697	
Spot #17	2893	85	37	0.79	0.67	1.97	N.D.	1.49	0.47	0.59	0.30	N.D.	0.18	0.03	0.08	0.02	N.D.	6.3	21.6	24.1	4.5		
Spot #18	3484	7	110	1.73	0.68	1.66	N.D.	1.04	0.28	0.40	0.20	N.D.	0.15	0.03	0.06	0.04	N.D.	4.9	11.8	7.8	4.9	0.70732	

Appendix C1 Contd

(ppm)	Sr	Mg	Ba	Pb	La	Ce	Pr	Nd	Sm	Eu	Gd	Tb	Dy	Ho	Er	Yb	Lu	ΣREE	La_N/Yb_N	Sm_N/Yb_N	Eu_N/Eu^*_N	$^{87}Sr/^{86}Sr$	$\delta^{34}S$ (‰)
Fenway, J2_216_1_R1																							
Spot #1	2181	4	30	0.44	0.31	0.84	N.D.	0.56	0.21	0.31	0.14	N.D.	0.09	0.02	0.04	0.04	N.D.	2.8	4.7	5.0	5.3	0.70788	
Spot #2	2499	2	26	3.40	1.37	3.53	N.D.	1.84	0.61	1.34	0.52	N.D.	0.50	0.08	0.18	0.11	N.D.	11.3	8.3	5.9	7.1		
Spot #3	3315	1	97	2.64	3.72	6.97	N.D.	2.64	0.68	0.96	0.36	N.D.	0.22	0.03	0.08	0.04	N.D.	16.4	64.2	18.6	5.4	0.70736	
Spot #4	3232	50	87	2.67	2.06	4.86	N.D.	2.55	0.59	0.96	0.40	N.D.	0.25	0.04	0.08	0.06	N.D.	12.7	24.0	10.9	5.8	0.70664	
Spot #5	2144	3	19	0.38	1.18	3.41	N.D.	2.32	0.65	0.66	0.43	N.D.	0.25	0.03	0.07	0.04	N.D.	9.7	18.2	16.1	3.6		
Spot #6	1995	5	13	0.42	1.20	3.13	N.D.	1.46	0.28	0.77	0.20	N.D.	0.12	0.02	0.05	0.05	N.D.	8.1	16.0	5.9	9.6	0.70689	
Spot #8	2503	57	24	2.78	0.82	2.65	N.D.	1.76	0.37	0.41	0.27	N.D.	0.16	0.02	0.05	0.02	N.D.	6.9	23.4	16.6	3.9		
Spot #9	2615	15	236	0.97	1.94	4.06	N.D.	2.06	0.50	0.45	0.31	N.D.	0.18	0.03	0.05	0.03	N.D.	10.0	51.4	20.8	3.3		
Spot #10	2420	6	32	0.16	0.78	2.11	N.D.	1.35	0.37	0.47	0.26	N.D.	0.15	0.02	0.05	0.03	N.D.	6.0	16.2	12.2	4.5		
Spot #11	2708	8	34	0.18	0.50	1.15	N.D.	0.75	0.26	0.39	0.15	N.D.	0.12	0.02	0.04	0.02	N.D.	3.7	17.0	14.1	5.5		
Spot #12	2640	2	55	19.52	1.03	2.83	N.D.	1.67	0.42	0.91	0.37	N.D.	0.14	0.03	0.10	0.07	N.D.	8.5	9.6	6.2	6.9		
Spot #13	2822	11	82	31.39	0.78	2.24	N.D.	1.78	0.63	1.21	0.67	N.D.	0.67	0.10	0.24	0.16	N.D.	9.6	3.2	4.1	5.7		
Spot #14	3351	7	45	2.10	0.70	1.81	N.D.	0.88	0.22	0.53	0.21	N.D.	0.15	0.02	0.05	0.04	N.D.	5.1	11.0	5.6	7.4		
Spot #15	2673	8	39	0.58	1.26	3.30	N.D.	2.20	0.56	0.56	0.37	N.D.	0.23	0.03	0.06	0.07	N.D.	9.2	11.9	8.4	3.6		
Spot #16	2669	5	76	0.56	0.82	2.29	N.D.	1.69	0.44	0.48	0.27	N.D.	0.18	0.03	0.06	0.05	N.D.	6.7	11.7	9.9	3.9		
Spot #17	2247	5	126	2.45	1.19	3.20	N.D.	2.27	0.66	0.60	0.43	N.D.	0.28	0.04	0.08	0.04	N.D.	9.3	19.7	17.2	3.3		
Spot #18	2715	18	51	1.09	0.45	1.08	N.D.	0.67	0.19	0.35	0.13	N.D.	0.09	0.01	0.03	0.02	N.D.	3.4	13.6	9.1	6.6		
Spot #19	2486	10	34	0.92	0.74	1.81	N.D.	0.99	0.24	0.50	0.18	N.D.	0.13	0.02	0.03	0.04	N.D.	5.1	11.3	5.9	7.0		
Spot #20	2224	6	5469	175.05	2.73	5.53	N.D.	2.29	0.43	1.67	0.33	N.D.	0.23	0.04	0.12	0.09	N.D.	15.0	21.0	5.3	13.0	0.70686	
Spot #21	1980	7	18	1.08	1.93	4.62	N.D.	2.45	0.58	1.03	0.33	N.D.	0.24	0.04	0.10	0.07	N.D.	12.4	19.3	9.2	6.6		
Spot #22	1755	5	42	1.85	1.62	4.59	N.D.	3.02	0.80	1.00	0.59	N.D.	0.34	0.05	0.11	0.12	N.D.	13.1	9.2	7.2	4.3	0.70740	
Spot #23	2367	5	86	1.95	1.16	3.58	N.D.	2.68	0.82	0.59	0.60	N.D.	0.33	0.05	0.09	0.05	N.D.	10.5	17.3	19.4	2.5	0.70766	
Spot #24	2929	43	2017	1.20	1.48	2.95	N.D.	1.84	0.46	0.61	0.32	N.D.	0.20	0.03	0.05	0.03	N.D.	8.6	31.8	15.8	4.6		
Spot #25	2760	51	165	2.52	0.63	1.48	N.D.	0.83	0.23	0.69	0.15	N.D.	0.10	0.02	0.05	0.04	N.D.	4.9	11.2	6.3	10.8	0.70602	

Appendix C1.Contd

(ppm)	Sr	Mg	Ba	Pb	La	Ce	Pr	Nd	Sm	Eu	Gd	Tb	Dy	Ho	Er	Yb	Lu	ΣREE	La_N/Yb_N	Sm_N/Yb_N	Eu_N/Eu^*_N	$^{87}Sr/^{86}Sr$	$\delta^{34}S$ (‰)
Fenway, J2_216_5_R1																							
Spot #1	2038	19	227	0.78	1.65	3.85	N.D.	2.17	0.50	0.50	0.35	N.D.	0.23	0.03	0.07	0.04	N.D.	9.9	29.4	14.1	3.5	0.70672	
Spot #2	2537	8	77	0.86	0.87	2.34	N.D.	1.41	0.34	0.40	0.28	N.D.	0.16	0.02	0.05	0.04	N.D.	6.2	14.9	9.2	4.0		
Spot #3	1922	7	49	0.32	1.19	3.59	N.D.	2.67	0.85	0.58	0.59	N.D.	0.36	0.05	0.09	0.06	N.D.	10.6	12.8	14.5	2.4		
Spot #4	2299	16	70	23.28	1.21	3.57	N.D.	2.84	0.75	0.77	0.60	N.D.	0.31	0.04	0.06	0.05	N.D.	10.9	17.2	17.0	3.4	0.70685	
Spot #6	1674	9	18	0.70	2.44	6.39	N.D.	3.99	1.12	1.08	0.77	N.D.	0.48	0.07	0.14	0.09	N.D.	17.6	19.3	14.1	3.4	0.70714	
Spot #7	1980	7	65	0.27	0.76	1.78	N.D.	1.03	0.31	0.30	0.21	N.D.	0.13	0.02	0.04	0.02	N.D.	4.9	25.0	16.3	3.4	0.70754	
Spot #8	2123	2	99	1.16	0.92	2.25	N.D.	1.35	0.28	0.41	0.23	N.D.	0.14	0.02	0.04	0.04	N.D.	6.1	15.5	7.6	4.7	0.70749	
Spot #9	2291	4	143	5.93	0.54	1.31	N.D.	0.81	0.21	0.37	0.12	N.D.	0.09	0.01	0.03	0.01	N.D.	3.8	25.7	15.9	6.6		
Spot #11	2657	4	148	7.44	1.00	2.03	N.D.	0.72	0.14	0.37	0.13	N.D.	0.07	0.01	0.01	0.01	N.D.	4.9	56.9	12.9	8.3		
Spot #13	3131	9	89	214.52	0.90	2.33	N.D.	1.36	0.46	0.60	0.20	N.D.	0.14	0.02	0.05	0.02	N.D.	6.7	35.3	28.6	5.2		
Spot #14	2581	21	125	4.48	0.79	1.84	N.D.	0.80	0.21	0.30	0.11	N.D.	0.06	0.01	0.03	0.02	N.D.	4.5	29.2	12.3	5.5		
Spot #15	2004	4	94	0.80	0.80	1.94	N.D.	1.03	0.25	0.32	0.17	N.D.	0.10	0.01	0.03	0.02	N.D.	5.0	34.2	17.1	4.6	0.70730	
Spot #16	2165	3	34	4.36	0.56	1.43	N.D.	0.86	0.18	0.31	0.14	N.D.	0.10	0.01	0.02	0.02	N.D.	3.9	24.1	12.5	5.8		
Spot #17	2128	6	38	0.49	0.81	2.01	N.D.	1.11	0.26	0.32	0.16	N.D.	0.12	0.02	0.05	0.02	N.D.	5.2	31.1	15.7	4.5	0.70742	
Spot #18	3015	7	60	2.55	1.02	2.20	N.D.	0.96	0.25	0.43	0.14	N.D.	0.07	0.01	0.04	0.03	N.D.	5.5	20.9	8.1	6.6		
Spot #19	2713	4	37	10.20	0.72	1.81	N.D.	1.06	0.32	0.50	0.20	N.D.	0.12	0.02	0.04	0.02	N.D.	5.3	27.7	19.5	5.6	0.70713	
Spot #20	2255	8	254	1.48	1.02	2.23	N.D.	1.07	0.26	0.41	0.14	N.D.	0.10	0.02	0.05	0.01	N.D.	5.7	46.3	19.0	5.9		
Spot #21	2017	11	150	1.07	1.41	3.63	N.D.	1.75	0.40	0.47	0.27	N.D.	0.16	0.02	0.05	0.03	N.D.	8.6	33.0	14.7	4.1		
Spot #22	2969	11	57	5.84	1.07	2.41	N.D.	1.37	0.35	0.34	0.18	N.D.	0.13	0.02	0.05	0.05	N.D.	6.3	14.6	7.6	3.7		
Spot #23	2310	3	31	0.85	1.98	5.94	N.D.	3.41	0.80	0.70	0.58	N.D.	0.31	0.04	0.08	0.08	N.D.	14.5	16.8	10.7	3.0	0.70725	
Spot #24	2146	4	55	1.23	0.81	2.26	N.D.	1.24	0.33	0.39	0.21	N.D.	0.12	0.02	0.05	0.02	N.D.	5.8	25.4	16.4	4.2		
Spot #25	2618	4	60	4.30	1.14	2.89	N.D.	1.51	0.40	0.42	0.30	N.D.	0.16	0.02	0.05	0.03	N.D.	7.3	22.9	12.9	3.5	0.70745	
Spot #26	2346	2	209	1.25	0.60	1.55	N.D.	0.96	0.34	0.27	0.18	N.D.	0.12	0.02	0.04	0.02	N.D.	4.4	25.7	22.8	3.0		
Spot #27	1983	5	59	9.68	0.66	2.15	N.D.	1.58	0.48	0.75	0.32	N.D.	0.21	0.03	0.05	0.03	N.D.	7.0	12.9	15.0	5.6	0.70802	
Spot #28	2156	5	35	1.19	0.86	2.12	N.D.	1.03	0.27	0.30	0.25	N.D.	0.13	0.02	0.04	0.02	N.D.	5.3	33.0	16.3	3.5		
Spot #29	2207	5	58	0.35	0.75	1.77	N.D.	0.94	0.23	0.24	0.17	N.D.	0.11	0.01	0.03	0.01	N.D.	4.5	35.0	16.8	3.7		
Spot #30	3194	7	56	1.40	1.89	4.45	N.D.	2.15	0.46	0.48	0.31	N.D.	0.16	0.03	0.06	0.04	N.D.	10.5	28.8	11.2	3.7		
Spot #31	2638	5	136	6.31	1.58	3.42	N.D.	1.78	0.42	0.50	0.28	N.D.	0.17	0.03	0.05	0.04	N.D.	8.7	28.8	12.2	4.1		
Spot #32	2919	3	91	4.00	2.83	5.46	N.D.	2.20	0.39	0.70	0.25	N.D.	0.18	0.03	0.07	0.05	N.D.	12.9	38.5	8.5	6.4		

Appendix C1.Contd

(ppm)	Sr	Mg	Ba	Pb	La	Ce	Pr	Nd	Sm	Eu	Gd	Tb	Dy	Ho	Er	Yb	Lu	ΣREE	La_N/Yb_N	Sm_N/Yb_N	Eu_N/Eu^*_N	$^{87}Sr/^{86}Sr$	$\delta^{34}S$ (‰)
Fenway, J2_216_14_R1																							
Spot #1	2065	55	379	317.4	0.37	1.38	N.D.	0.78	0.24	0.79	0.13	N.D.	0.09	0.02	0.05	0.02	N.D.	4.5	10.5	10.7	12.7		
Spot #2	1488	23	105	71.6	0.86	3.21	N.D.	1.66	0.41	1.51	0.28	N.D.	0.15	0.02	0.06	0.03	N.D.	9.6	21.8	16.7	12.9	0.70635	22.0
Spot #3	2305	81	192	32.6	0.56	1.79	N.D.	1.23	0.29	0.98	0.22	N.D.	0.13	0.02	0.05	0.05	N.D.	6.3	7.4	6.0	11.5		
Spot #4	2537	86	358	2734.5	0.64	1.98	N.D.	1.35	0.39	1.26	0.26	N.D.	0.16	0.02	0.05	0.04	N.D.	7.4	10.9	10.6	11.4	0.70592	
Spot #5	2971	336	113	4782.2	0.91	2.44	N.D.	1.29	0.28	0.67	0.22	N.D.	0.13	0.02	0.04	0.02	N.D.	6.6	26.4	12.8	8.0	0.70679	
Spot #6	2365	160	325	514.1	0.40	1.20	N.D.	0.88	0.20	0.73	0.17	N.D.	0.11	0.02	0.04	0.02	N.D.	4.4	17.7	14.2	11.8		
Spot #7	2401	239	171	185.2	0.60	1.80	N.D.	1.23	0.32	1.00	0.25	N.D.	0.19	0.02	0.04	0.12	N.D.	6.6	17.2	14.5	10.5	0.70600	
Spot #8	2693	5	234	10.6	1.12	3.65	N.D.	2.45	0.55	1.32	0.36	N.D.	0.26	0.04	0.09	0.04	N.D.	11.2	21.6	16.9	8.5		
Spot #9	2048	111	481	108.7	0.90	3.47	N.D.	2.80	0.81	1.57	0.47	N.D.	0.26	0.03	0.06	0.03	N.D.	11.9	19.3	27.6	7.2		
Spot #10	2068	7	242	116.0	0.93	3.85	N.D.	2.95	0.74	1.57	0.54	N.D.	0.27	0.04	0.08	0.05	N.D.	12.6	12.2	15.5	7.2		
Spot #11	1851	105	410	48.1	0.35	1.20	N.D.	0.75	0.21	0.75	0.11	N.D.	0.08	0.01	0.01	0.02	N.D.	4.2	11.9	11.3	13.7	0.70592	
Spot #12	2202	314	496	990.8	0.86	3.32	N.D.	2.25	0.66	1.16	0.36	N.D.	0.17	0.02	0.05	0.03	N.D.	10.2	20.2	24.6	6.7		
Spot #16	2398	3	110	4.1	1.09	2.31	N.D.	0.85	0.42	0.67	0.16	N.D.	0.08	0.01	0.04	0.05	N.D.	6.4	14.4	8.9	6.6	0.70642	
Spot #17	1624	7	44	4.3	0.53	0.90	N.D.	0.23	0.09	0.55	0.05	N.D.	0.05	0.02	0.05	0.03	N.D.	3.1	11.1	3.1	22.6		20.1
Spot #18	1352	28	72	3.0	0.59	1.57	N.D.	0.63	0.14	0.84	0.10	N.D.	0.07	0.01	0.03	0.02	N.D.	4.8	20.2	7.4	21.0		
Spot #20	3509	9	165	3.8	1.86	3.45	N.D.	0.89	0.16	0.56	0.12	N.D.	0.10	0.02	0.08	0.03	N.D.	7.8	39.2	5.3	12.0		
Spot #21	2157	115	73	10.5	3.43	6.64	N.D.	1.37	0.23	1.60	0.17	N.D.	0.07	0.01	0.04	0.03	N.D.	15.1	76.0	8.2	23.7	0.70641	
Spot #22	2315	2	31	2.6	0.31	0.97	N.D.	0.46	0.10	0.55	0.06	N.D.	0.03	0.01	0.02	0.01	N.D.	3.0	21.6	11.2	20.5		
Spot #23	2348	0	52	5.4	1.25	3.18	N.D.	0.68	0.09	1.58	0.05	N.D.	0.04	0.01	N.D.	0.03	N.D.	8.5	29.6	3.4	65.9	0.70571	
Spot #24	3546	2	181	5.8	0.32	0.41	N.D.	0.14	0.04	0.15	0.02	N.D.	0.01	0.00	0.00	0.01	N.D.	1.3	29.7	5.6	15.4	0.70589	
Spot #25	2343	0	68	5.9	0.74	1.16	N.D.	0.33	0.05	0.50	0.06	N.D.	0.03	0.01	0.02	0.02	N.D.	3.4	30.6	3.4	28.1		
Spot #26	1898	31	88	3.2	1.82	4.90	N.D.	1.69	0.38	1.08	0.22	N.D.	0.16	0.02	0.05	0.04	N.D.	11.3	31.9	10.6	10.4	0.70632	20.2
Spot #27	1263	54	126	3.7	0.86	2.35	N.D.	0.73	0.22	0.84	0.07	N.D.	0.05	0.01	0.02	0.05	N.D.	6.0	12.3	5.0	16.1		
Spot #28	2041	109	181	5.0	0.11	0.19	N.D.	0.09	0.19	0.25	0.02	N.D.	0.02	0.01	0.01	0.01	N.D.	1.2	5.1	13.8	6.6	0.70568	
Spot #29	1777	13	139	2.1	0.35	0.98	N.D.	0.39	0.06	0.37	0.04	N.D.	0.06	0.01	0.01	N.D.	N.D.	2.6	N.D.	N.D.	22.3		
Spot #30	4990	5	109	0.3	0.13	0.46	N.D.	0.38	0.12	0.13	0.13	N.D.	0.18	0.04	0.13	0.11	N.D.	1.9	0.8	1.2	3.0	0.70630	
Spot #31	2610	167	441	3178.3	1.10	4.09	N.D.	2.78	0.66	1.23	0.43	N.D.	0.27	0.04	0.07	0.04	N.D.	11.8	17.5	16.8	6.6		
Spot #32	2801	137	349	69.3	1.14	3.91	N.D.	2.52	0.59	1.09	0.40	N.D.	0.26	0.04	0.08	0.04	N.D.	11.2	18.4	15.0	6.5		
Spot #33	2624	216	522	926.0	0.58	1.93	N.D.	1.35	0.32	0.76	0.23	N.D.	0.14	0.02	0.06	0.07	N.D.	6.2	5.7	5.0	8.3		
Spot #34	2428	99	394	740.2	0.42	1.49	N.D.	1.12	0.32	0.74	0.21	N.D.	0.15	0.02	0.06	0.05	N.D.	5.2	6.3	7.5	8.3		
Spot #35	1849	94	198	10.1	0.38	1.22	N.D.	0.89	0.24	0.78	0.17	N.D.	0.14	0.02	0.04	0.04	N.D.	4.7	6.1	6.1	11.1		
Spot #36	2440	123	70	4.8	0.23	0.76	N.D.	0.63	0.16	0.55	0.08	N.D.	0.08	0.01	0.03	0.02	N.D.	3.1	9.1	10.3	12.9		
Spot #38	2115	29	117	16.4	0.23	1.11	N.D.	1.70	0.46	1.91	0.28	N.D.	0.17	0.03	0.06	0.04	N.D.	7.9	4.2	13.0	15.2	0.70639	
Spot #39	3395	24	93	4.3	1.94	3.27	N.D.	1.34	0.32	0.51	0.17	N.D.	0.12	0.02	0.04	0.02	N.D.	8.3	61.9	16.0	6.0	0.70686	
Spot #40	2154	4	82	153.0	1.01	3.31	N.D.	2.24	0.60	0.99	0.37	N.D.	0.22	0.03	0.06	0.02	N.D.	9.8	30.6	28.8	6.0		
Spot #41	2000	15	94	30.0	0.83	2.73	N.D.	2.17	0.54	1.05	0.39	N.D.	0.31	0.03	0.04	0.02	N.D.	9.2	31.3	32.6	6.7	0.70633	
Spot #42	2124	44	207	9.6	0.25	0.74	N.D.	0.62	0.17	0.63	0.17	N.D.	0.08	0.01	0.02	0.02	N.D.	3.3	8.0	8.9	11.2		
Spot #43	2159	70	102	21.3	0.70	2.22	N.D.	1.37	0.37	0.63	0.23	N.D.	0.11	0.02	0.03	0.02	N.D.	6.3	22.7	19.1	6.2	0.70733	
Spot #44	2015	13	78	5.8	0.58	1.60	N.D.	0.99	0.24	0.39	0.17	N.D.	0.09	0.01	0.03	0.02	N.D.	4.5	15.7	10.3	5.7		
Spot #45	2090	14	378	11.0	0.37	1.32	N.D.	0.98	0.26	0.66	0.16	N.D.	0.10	0.01	0.03	0.01	N.D.	4.5	16.9	18.8	9.3	0.70736	

Appendix C1.Contd

(ppm)	Sr	Mg	Ba	Pb	La	Ce	Pr	Nd	Sm	Eu	Gd	Tb	Dy	Ho	Er	Yb	Lu	ΣREE	La_N/Yb_N	Sm_N/Yb_N	Eu_N/Eu^*_N	$^{87}Sr/^{86}Sr$	$\delta^{34}S$ (‰)
North Su, J2_227_7_R2																							
Spot #1	5826	31	57	1.92	0.25	0.46	N.D.	0.20	0.02	0.03	0.08	N.D.	0.06	0.02	0.05	0.04	N.D.	1.2	4.2	0.6	2.0	0.70805	22.4
Spot #3	3626	111	107	0.06	N.D.	N.D.	N.D.	N.D.	N.D.	N.D.	N.D.	N.D.	N.D.	N.D	N.D.	N.D.	N.D.	N.D.	N.D.	N.D.	N.D	0.70845	23.6
Spot #4	3539	17	50	0.41	0.33	1.11	N.D.	0.89	0.27	0.16	0.31	N.D.	0.37	0.07	0.19	0.16	N.D.	3.9	1.4	1.8	1.6	0.70763	23.2
Spot #5	2342	9	13	2.53	0.07	0.34	N.D.	0.54	0.21	0.17	0.32	N.D.	0.26	0.05	0.14	0.08	N.D.	2.3	0.6	2.8	1.9		22.5
Spot #8	2799	3	39	1.80	1.58	7.43	N.D.	10.85	4.79	2.77	4.99	N.D.	4.65	0.74	1.75	1.12	N.D.	42.7	1.0	4.6	1.7		
Spot #9	2255	1	192	0.99	1.39	4.73	N.D.	5.01	1.90	1.20	1.98	N.D.	2.02	0.39	1.04	1.16	N.D	21.7	0.8	1.8	1.9		
Spot #10	3967	1	758	0.11	2.36	5.40	N.D.	3.61	1.15	0.72	1.22	N.D.	1.27	0.28	0.79	1.00	N.D.	18.2	1.6	1.2	1.8		
Spot #11	3009	5	583	0.08	1.68	3.85	N.D.	2.55	0.68	0.48	0.78	N.D.	1.04	0.24	0.72	0.90	N.D.	13.1	1.3	0.8	2.0		
Spot #12	3885	1	898	0.10	3.02	7.16	N.D.	5.08	1.59	1.09	1.81	N.D.	1.83	0.37	1.04	1.10	N.D.	24.8	1.8	1.5	2.0	0.70649	
Spot #13	3872	23	33	5.05	0.25	0.62	N.D.	0.58	0.21	0.25	0.31	N.D.	0.36	0.08	0.25	0.14	N.D.	3.2	1.2	1.6	3.0	0.70640	
Spot #14	3989	10	73	4.59	1.48	5.99	N.D.	7.46	2.67	1.40	2.74	N.D.	2.47	0.46	1.21	0.83	N.D.	27.6	1.2	3.4	1.6		
Spot #15	3621	20	90	3.05	0.70	2.86	N.D.	3.73	1.48	0.81	1.64	N.D.	1.67	0.32	0.84	0.64	N.D.	15.2	0.7	2.5	1.6	0.70675	
Spot #16	3543	14	81	1.93	1.56	7.07	N.D.	9.60	3.78	2.21	3.55	N.D.	3.30	0.54	1.27	0.80	N.D.	35.4	1.3	5.1	1.8		
Spot #17	3650	0	118	0.38	0.58	1.71	N.D.	1.45	0.61	0.64	0.79	N.D.	0.91	0.18	0.49	0.49	N.D.	8.3	0.8	1.3	2.8	0.70627	
Spot #18	2748	15	44	38.66	0.62	1.72	N.D.	2.98	1.31	0.83	2.55	N.D.	3.64	0.83	2.44	2.36	N.D.	19.3	0.2	0.6	1.4	0.70675	
Spot #19	3218	12	714	22.56	0.17	0.48	N.D.	0.56	0.25	0.22	0.44	N.D.	0.49	0.11	0.31	0.31	N.D.	3.4	0.4	0.9	2.0		
Spot #20	3092	14	505	8.96	0.15	0.41	N.D.	0.44	0.20	0.18	0.26	N.D.	0.32	0.06	0.16	0.14	N.D.	2.4	0.7	1.5	2.4	0.70578	
Spot #21	3226	9	102	1.11	0.15	0.46	N.D.	0.45	0.23	0.19	0.30	N.D.	0.36	0.07	0.20	0.17	N.D.	2.7	0.6	1.4	2.2	0.70600	
Spot #22	2963	2	95	0.25	0.17	0.82	N.D.	1.25	0.58	0.29	0.75	N.D.	0.91	0.18	0.51	0.44	N.D.	6.1	0.3	1.4	1.4		
Spot #23	3301	1	89	0.12	0.51	1.54	N.D.	1.09	0.29	0.22	0.37	N.D.	0.44	0.10	0.28	0.31	N.D.	5.3	1.1	1.0	2.1	0.70679	
Spot #24	3495	1	34	0.20	0.18	0.54	N.D.	0.58	0.29	0.37	0.40	N.D.	0.53	0.12	0.35	0.31	N.D.	3.9	0.4	1.0	3.3		
Spot #25	4166	0	69	0.81	0.32	0.91	N.D.	0.99	0.35	0.52	0.55	N.D.	0.75	0.16	0.45	0.45	N.D.	5.8	0.5	0.8	3.6	0.70624	
Spot #26	4632	2	111	0.24	0.16	0.50	N.D.	0.40	0.12	0.11	0.17	N.D.	0.21	0.05	0.15	0.12	N.D.	2.1	0.9	1.1	2.4		
Spot #27	4587	34	104	3.29	0.07	0.26	N.D.	0.29	0.12	0.23	0.18	N.D.	0.17	0.04	0.12	0.08	N.D.	1.7	0.6	1.5	4.7		
Spot #28	4371	29	159	3.09	0.10	0.31	N.D.	0.28	0.13	0.13	0.17	N.D.	0.20	0.04	0.10	0.11	N.D.	1.7	0.6	1.3	2.7		
Spot #29	3393	76	117	1.65	0.06	0.26	N.D.	0.29	0.13	0.16	0.18	N.D.	0.22	0.05	0.13	0.11	N.D.	1.7	0.4	1.3	3.2	0.70818	
Spot #30	3644	31	105	0.52	0.05	0.20	N.D.	0.22	0.08	0.10	0.14	N.D.	0.16	0.04	0.10	0.14	N.D.	1.3	0.3	0.6	2.7		

Appendix C1 Contd

(ppm)	Sr	Mg	Ba	Pb	La	Ce	Pr	Nd	Sm	Eu	Gd	Tb	Dy	Ho	Er	Yb	Lu	ΣREE	La_N/Yb_N	Sm_N/Yb_N	Eu_N/Eu^*_N	$^{87}Sr/^{86}Sr$	$\delta^{34}S$ (‰)
North Su, J2_227_7_R2 (contd)																							
Spot #31	3124	16	59	0.95	0.07	0.24	N.D.	0.30	0.13	0.08	0.19	N.D.	0.20	0.04	0.12	0.14	N.D.	1.6	0.3	1.0	1.5		
Spot #32	3425	8	74	3.45	0.18	0.81	N.D.	1.16	0.45	0.39	0.62	N.D.	0.69	0.14	0.39	0.35	N.D.	5.4	0.4	1.4	2.3	0.70736	
Spot #33	3533	4	40	2.75	0.22	1.01	N.D.	1.36	0.54	0.53	0.83	N.D.	0.84	0.18	0.53	0.46	N.D.	6.8	0.3	1.3	2.4		
Spot #34	4456	3	55	1.90	0.28	1.31	N.D.	1.93	0.69	0.44	0.79	N.D.	0.79	0.15	0.39	0.32	N.D.	7.4	0.6	2.3	1.8	0.70734	
Spot #35	3213	10	53	0.57	0.17	0.79	N.D.	1.08	0.44	0.35	0.51	N.D.	0.59	0.11	0.30	0.25	N.D.	4.8	0.4	1.8	2.3		
Spot #36	3153	38	77	0.22	0.09	0.29	N.D.	0.36	0.21	0.58	0.26	N.D.	0.29	0.05	0.14	0.14	N.D.	2.9	0.4	1.7	7.6		
Spot #37	2413	5	35	0.22	0.08	0.30	N.D.	0.32	0.22	0.76	0.38	N.D.	0.42	0.08	0.19	0.16	N.D.	3.6	0.3	1.5	8.0	0.70671	
Spot #38	2859	8	56	1.34	0.12	0.40	N.D.	0.46	0.32	1.17	0.56	N.D.	0.53	0.09	0.24	0.22	N.D.	5.2	0.4	1.6	8.4	0.70461	
Spot #39	2787	12	67	0.33	0.09	0.28	N.D.	0.17	0.20	0.59	0.31	N.D.	0.33	0.06	0.16	0.13	N.D.	2.9	0.4	1.7	7.2		
Spot #40	2140	1	55	0.12	0.26	0.97	N.D.	0.90	0.44	0.61	0.66	N.D.	0.73	0.16	0.46	0.51	N.D.	6.1	0.3	0.9	3.4	0.70729	
Spot #41	4316	38	217	2.82	0.38	1.23	N.D.	1.17	0.43	0.43	0.56	N.D.	0.59	0.12	0.33	0.37	N.D.	5.9	0.7	1.2	2.7		
Spot #42	3283	7	182	8.79	0.16	0.70	N.D.	1.04	0.46	0.26	0.51	N.D.	0.58	0.12	0.34	0.31	N.D.	4.6	0.3	1.6	1.6		
Spot #44	3632	11	94	0.24	0.87	3.27	N.D.	3.17	1.13	0.60	1.27	N.D.	1.33	0.27	0.76	0.64	N.D.	13.6	0.9	1.9	1.5		
Spot #45	3876	3	124	2.55	0.11	0.67	N.D.	1.94	0.95	0.47	1.12	N.D.	1.19	0.23	0.60	0.52	N.D.	8.1	0.1	2.0	1.4		
Spot #46	3586	22	80	0.77	0.94	3.60	N.D.	3.55	1.38	0.69	1.54	N.D.	1.72	0.33	0.89	0.75	N.D.	15.7	0.9	2.0	1.4		
Spot #47	4491	5	161	4.57	0.07	0.67	N.D.	2.69	1.44	0.69	1.49	N.D.	1.49	0.26	0.66	0.48	N.D.	10.4	0.1	3.2	1.4		
Spot #48	2833	76	233	14.12	0.11	0.34	N.D.	0.33	0.17	0.18	0.23	N.D.	0.25	0.05	0.12	0.13	N.D.	2.0	0.6	1.3	2.9	0.70649	
Spot #49	4583	10	190	44.64	0.17	0.67	N.D.	1.01	0.35	0.23	0.53	N.D.	0.70	0.14	0.37	0.42	N.D.	4.6	0.3	0.9	1.6	0.70643	
Spot #50	2895	3	132	0.28	0.14	0.56	N.D.	0.82	0.38	0.40	0.58	N.D.	0.68	0.12	0.31	0.34	N.D.	4.6	0.3	1.2	2.6		
Spot #51	3394	5	69	22.14	0.16	0.71	N.D.	0.96	0.39	0.26	0.44	N.D.	0.46	0.09	0.22	0.19	N.D.	4.0	0.6	2.2	1.9	0.70771	
Spot #52	1691	2	6	0.15	0.08	0.36	N.D.	0.49	0.24	0.69	0.52	N.D.	0.54	0.12	0.35	0.23	N.D.	4.2	0.2	1.1	5.9	0.70456	
Spot #53	1887	0	24	0.07	0.10	0.40	N.D.	0.56	0.44	1.40	0.71	N.D.	0.66	0.12	0.30	0.27	N.D.	6.3	0.3	1.8	7.6	0.70477	
Spot #54	1306	1	45	0.03	0.03	0.11	N.D.	0.14	0.11	0.39	0.30	N.D.	0.40	0.07	0.19	0.13	N.D.	2.2	0.2	0.9	6.2	0.70569	
Spot #55	1503	2	10	0.07	0.12	0.57	N.D.	0.84	0.51	0.41	0.81	N.D.	0.92	0.19	0.52	0.55	N.D.	5.7	0.1	1.0	2.0	0.70783	
Spot #56	3965	573	100	237.50	1.20	4.69	N.D.	5.02	1.95	1.63	2.43	N.D.	2.51	0.48	1.27	1.27	N.D.	23.5	0.6	1.6	2.3	0.70604	
Spot #57	3712	85	50	8.38	0.83	3.51	N.D.	3.86	1.37	1.03	1.78	N.D.	1.64	0.31	0.84	0.66	N.D.	16.5	0.8	2.2	2.0		
Spot #58	4807	11	59	0.85	1.45	5.27	N.D.	5.78	2.02	1.24	2.11	N.D.	2.21	0.40	1.04	0.80	N.D.	23.2	1.2	2.7	1.8	0.70631	
Spot #59	4097	15	27	1.66	0.24	0.77	N.D.	0.76	0.27	0.24	0.37	N.D.	0.41	0.07	0.19	0.09	N.D.	3.6	1.7	3.1	2.3		

Appendix D-1.

Complete listing of analytical data for trace metal concentrations measured in seafloor hydrothermal fluids sampled from the Manus Basin (Vienna Woods, PACMANUS, DESMOS and SuSu Knolls vent fields) during cruise MGLN06MV (Tivey et al., 2007). Analytical measurements were performed separately on dissolved and particle fractions ("bottle-filter" and "dregs") and mathematically re-constituted to obtain the precipitate- and contaminant-corrected fluid composition. Blank spaces for concentrations below element limit of detection for analytical method.

The following abbreviation(s) is used in the tables:

N/A = fraction not available for analysis.

Appendix D1. Measured metal concentrations in "dissolved" fractions of sampled vent fluids from Vienna Woods

Fluid Sampler ID	Vent Site	Vent Orifice	Mg (mmol/kg)	Li (µmol/kg)	Rb (µmol/kg)	Cs (nmol/kg)	Al (µmol/kg)	Mn (µmol/kg)	Fe (µmol/kg)	Zn (µmol/kg)	Cu (µmol/kg)	Pb (µmol/kg)	Co (nmol/kg)	Cd (nmol/kg)	Ag (nmol/kg)	Sb (nmol/kg)	Au (nmol/kg)
J2-207-1-W1-IGT7	Vienna Woods	VW1	3.36	1022	15.8	267	< 10	326	139	25.8	1.0	0.20	14.2	39.2	6.4	0.6	BDL
J2-207-1-W2-IGT3	Vienna Woods	VW1	1.55	1055	17.5	283	< 10	339	152	24.7	0.6	0.26	13.2	34.7	5.4	1.3	BDL
J2-207-1-W3-M2	Vienna Woods	VW1	1.44	1032	19.4	288	< 10	388	139	36.7	1.7	0.32	BDL	39.2	BDL	1.4	0.02
J2-207-2-W1-IGT4	Vienna Woods	VW2	1.02	1069	18.1	281	< 10	356	158	20.2	0.6	0.21	2.8	22.0	3.8	1.2	BDL
J2-207-3-W1-IGT8	Vienna Woods	VW3	1.11	1061	16.6	256	< 10	206	111	16.8	0.1	0.11	7.2	19.7	BDL	BDL	BDL
J2-207-3-W2-IGT6	Vienna Woods	VW3	14.90	759	13.0	188	< 10	148	81	10.9	1.3	0.14	3.3	16.9	5.7	BDL	BDL

-/- denotes elements for which no analytical measurement was carried out. BDL denotes elements for which aqueous fluid concentrations were below the analytical detection limit of the method or otherwise not obtainable.

Appendix D1. Measured metal concentrations in "bottle-filter" fractions of sampled vent fluids from Vienna Woods

Fluid Sampler ID	Vent Site	Vent Orifice	Mg (mmol/kg)	Li (µmol/kg)	Rb (µmol/kg)	Cs (nmol/kg)	Al (µmol/kg)	Mn (µmol/kg)	Fe (µmol/kg)	Zn (µmol/kg)	Cu (µmol/kg)	Pb (µmol/kg)	Co (nmol/kg)	Cd (nmol/kg)	Ag (nmol/kg)	Sb (nmol/kg)	Au (nmol/kg)
J2-207-1-W1-IGT7	Vienna Woods	VW1	3.36	-/-	-/-	-/-	-/-	1.1	1.7	0.3	1.1	0.04	BDL	3.4	4.9	BDL	BDL
J2-207-1-W2-IGT3	Vienna Woods	VW1	1.55	-/-	-/-	-/-	-/-	1.7	3.3	0.2	0.4	0.02	BDL	2.3	BDL	BDL	BDL
J2-207-1-W3-M2	Vienna Woods	VW1	1.44	-/-	-/-	-/-	-/-	0.3	0.1	0.1	BDL	0.02	BDL	BDL	1.3	BDL	BDL
J2-207-2-W1-IGT4	Vienna Woods	VW2	1.02	-/-	-/-	-/-	-/-	0.8	2.2	0.2	0.6	0.02	BDL	2.3	6.6	BDL	BDL
J2-207-3-W1-IGT8	Vienna Woods	VW3	1.11	-/-	-/-	-/-	-/-	0.6	0.8	0.9	0.8	0.09	BDL	9.5	6.7	BDL	BDL
J2-207-3-W2-IGT6	Vienna Woods	VW3	14.90	-/-	-/-	-/-	-/-	1.6	1.5	0.2	0.4	0.01	BDL	BDL	BDL	BDL	BDL

-/- denotes elements for which no analytical measurement was carried out. BDL denotes elements for which aqueous fluid concentrations were below the analytical detection limit of the method or otherwise not obtainable.

Appendix D1. Measured metal concentrations in "dregs" fractions of sampled vent fluids from Vienna Woods

Fluid Sampler ID	Vent Site	Vent Orifice	Mg (mmol/kg)	Li (µmol/kg)	Rb (µmol/kg)	Cs (nmol/kg)	Al (µmol/kg)	Mn (µmol/kg)	Fe (µmol/kg)	Zn (µmol/kg)	Cu (µmol/kg)	Pb (µmol/kg)	Co (nmol/kg)	Cd (nmol/kg)	Ag (nmol/kg)	Sb (nmol/kg)	Au (nmol/kg)
J2-207-1-W1-IGT7	Vienna Woods	VW1	3.36	-/-	-/-	-/-	-/-	0.7	6.7	5.6	1.8	0.05	31.1	9.9	26.8	21.0	0.12
J2-207-1-W2-IGT3	Vienna Woods	VW1	1.55	-/-	-/-	-/-	-/-	-/-	-/-	-/-	-/-	-/-	-/-	-/-	-/-	-/-	-/-
J2-207-1-W3-M2	Vienna Woods	VW1	1.44	-/-	-/-	-/-	-/-	0.1	1.2	0.8	0.1	0.00	5.6	2.1	BDL	35.3	0.01
J2-207-2-W1-IGT4	Vienna Woods	VW2	1.02	-/-	-/-	-/-	-/-	0.7	1.4	8.5	10.1	0.06	27.2	31.3	16.8	67.2	0.15
J2-207-3-W1-IGT8	Vienna Woods	VW3	1.11	-/-	-/-	-/-	-/-	0.1	15.4	4.7	4.1	0.04	12.4	5.8	1.9	0.0	0.01
J2-207-3-W2-IGT6	Vienna Woods	VW3	14.90	-/-	-/-	-/-	-/-	-/-	-/-	-/-	-/-	-/-	-/-	-/-	-/-	-/-	-/-

-/- denotes elements for which no analytical measurement was carried out. BDL denotes elements for which aqueous fluid concentrations were below the analytical detection limit of the method or otherwise not obtainable.

Appendix D1. Measured metal concentrations in "dissolved" fractions of sampled vent fluids from PACMANUS

Fluid Sampler ID	Vent Site	Vent Orifice	Mg (mmol/kg)	Li (µmol/kg)	Rb (µmol/kg)	Cs (nmol/kg)	Al (µmol/kg)	Mn (µmol/kg)	Fe (µmol/kg)	Zn (µmol/kg)	Cu (µmol/kg)	Pb (µmol/kg)	Co (nmol/kg)	Cd (nmol/kg)	Ag (nmol/kg)	Sb (nmol/kg)	Au (nmol/kg)
J2-208-1-W1-IGT8	Roman Ruins	RMR1	8.01	986	63.8	2233	< 10	3362	5471	50	13.7	0.28	10.0	20.0	3.6	6.0	BDL
J2-208-1-W2-IGT5	Roman Ruins	RMR1	8.28	957	62.6	2241	< 10	3268	5555	51	1.8	0.23	6.8	16.2	4.4	2.0	BDL
J2-208-1-W3-M4	Roman Ruins	RMR1	8.90	968	67.2	2423	< 10	3905	5950	164	12.6	2.02	1.4	229.0	65.0	93.1	0.05
J2-208-2-W2-IGT2	Roman Ruins	RMR2	16.56	620	42.3	1575	< 10	2241	958	88	BDL	3.96	15.2	17.0	BDL	BDL	BDL
J2-208-2-W1-IGT1	Roman Ruins	RMR2	16.55	639	41.2	1504	< 10	2252	946	213	0.1	3.29	8.6	85.0	3.3	10.8	BDL
J2-208-2-W3-M2	Roman Ruins	RMR2	27.50	453	33.9	1156	< 10	1946	726	482	2.5	36.93	BDL	230.7	100.1	7.4	BDL
J2-213-3-W1-IGT7	Roman Ruins	RMR3	23.36	778	48.8	1691	< 10	2537	4154	31	0.6	0.37	3.2	29.5	0.1	2.4	0.04
J2-213-3-W3-M4	Roman Ruins	RMR3	6.39	1200	80.9	2852	< 10	4732	7292	313	4.9	6.81	BDL	426.8	80.5	211.8	0.33
J2-222-4-W2-IGT1	Roman Ruins	RMR4	3.63	1059	74.5	2234	< 10	2820	6390	27	0.0	0.05	12.5	4.1	BDL	BDL	BDL
J2-222-4-W3-M4	Roman Ruins	RMR4	4.71	980	71.5	2261	< 10	2717	6069	121	47.7	2.52	BDL	169.1	48.1	50.9	BDL
J2-213-6-W1-IGT3	Roger's Ruins	RGR1	5.63	788	68.6	1928	< 10	2402	4046	42	18.3	0.72	BDL	55.0	10.3	15.6	0.09
J2-213-6-W2-IGT4	Roger's Ruins	RGR1	8.10	765	65.2	1786	< 10	2289	3830	26	12.1	0.44	7.7	31.5	7.4	8.3	0.06
J2-213-6-W3-M2	Roger's Ruins	RGR1	4.68	832	76.4	2036	< 10	3022	4823	314	126.2	5.50	2.9	423.2	136.2	146.4	BDL
J2-222-1-W1-IGT4	Roger's Ruins	RGR2	22.64	498	42.3	1194	< 10	1434	2012	20	13.1	0.18	3.8	17.2	11.5	4.9	BDL
J2-222-1-W2-IGT3	Roger's Ruins	RGR2	9.45	753	66.7	1714	< 10	2138	3083	43	14.8	0.24	6.3	27.1	11.6	7.0	BDL
J2-222-1-W3-M2	Roger's Ruins	RGR2	9.03	775	70.0	1878	< 10	2713	3624	215	28.9	1.76	BDL	162.2	56.3	69.9	0.08
J2-209-1-W1-IGT6	Satanic Mills	SM1	10.52	641	57.9	1766	< 10	2033	2637	16	3.3	0.12	13.3	5.9	0.3	1.1	0.02
J2-209-1-W1-IGT7	Satanic Mills	SM1	9.63	638	57.2	1800	< 10	2131	2770	15	3.8	0.12	4.8	6.1	BDL	2.2	0.00
J2-209-1-W3-M4	Satanic Mills	SM1	8.84	646	62.4	1927	< 10	2600	3162	161	60.5	3.56	BDL	188.1	50.5	163.6	0.02
J2-209-6-W1-IGT4	Satanic Mills	SM2	27.50	311	24.8	844	< 10	1104	383	39	2.1	0.17	4.4	11.9	BDL	0.7	BDL
J2-209-6-W2-M2	Satanic Mills	SM2	17.37	441	37.6	1231	< 10	1850	586	183	64.5	3.59	BDL	51.3	23.4	1.6	BDL
J2-214-3-W1-IGT8	Satanic Mills	SM3	10.29	601	56.0	1711	< 10	1810	941	22	12.5	0.31	4.7	15.2	1.6	8.1	0.05
J2-214-3-W2-IGT5	Satanic Mills	SM3	10.17	587	56.2	1722	< 10	1816	949	19	9.7	0.26	7.7	15.6	0.8	6.1	0.00
J2-214-3-W3-M4	Satanic Mills	SM3	10.07	600	61.1	1814	< 10	2225	1042	72	BDL	2.84	0.4	83.0	34.6	108.1	0.07

-/- denotes elements for which no analytical measurement was carried out. BDL denotes elements for which aqueous fluid concentrations were below the analytical detection limit of the method or otherwise not obtainable.

Appendix D1. Measured metal concentrations in "bottle-filter" fractions of sampled vent fluids from PACMANUS

Fluid Sampler ID	Vent Site	Vent Orifice	Mg (mmol/kg)	Li (µmol/kg)	Rb (µmol/kg)	Cs (nmol/kg)	Al (µmol/kg)	Mn (µmol/kg)	Fe (µmol/kg)	Zn (µmol/kg)	Cu (µmol/kg)	Pb (µmol/kg)	Co (nmol/kg)	Cd (nmol/kg)	Ag (nmol/kg)	Sb (nmol/kg)	Au (nmol/kg)
J2-208-1-W1-IGT8	Roman Ruins	RMR1	8.01	-/-	-/-	-/-	-/-	36.9	60.3	2.5	1.7	0.36	BDL	43.5	9.7	20.2	BDL
J2-208-1-W2-IGT5	Roman Ruins	RMR1	8.28	-/-	-/-	-/-	-/-	15.0	28.2	2.5	2.7	0.46	BDL	52.0	7.2	27.9	BDL
J2-208-1-W3-M4	Roman Ruins	RMR1	8.90	-/-	-/-	-/-	-/-	2.9	4.8	0.5	0.3	0.08	BDL	2.3	1.7	2.2	0.25
J2-208-2-W2-IGT2	Roman Ruins	RMR2	16.56	-/-	-/-	-/-	-/-	15.0	7.9	56.9	2.1	BDL	BDL	118.0	142.6	169.4	BDL
J2-208-2-W1-IGT1	Roman Ruins	RMR2	16.55	-/-	-/-	-/-	-/-	18.5	8.8	18.2	1.5	BDL	BDL	69.1	71.0	267.5	BDL
J2-208-2-W3-M2	Roman Ruins	RMR2	27.50	-/-	-/-	-/-	-/-	1.2	0.9	1.6	0.3	1.05	BDL	7.1	14.1	25.5	BDL
J2-213-3-W1-IGT7	Roman Ruins	RMR3	23.36	-/-	-/-	-/-	-/-	13.2	21.7	BDL	0.2	0.32	BDL	9.5	BDL	14.5	BDL
J2-213-3-W3-M4	Roman Ruins	RMR3	6.39	-/-	-/-	-/-	-/-	9.7	15.6	1.0	0.1	0.13	BDL	2.7	10.9	6.3	0.37
J2-222-4-W2-IGT1	Roman Ruins	RMR4	3.63	-/-	-/-	-/-	-/-	11.6	30.2	10.1	16.4	0.68	BDL	44.7	9.0	19.5	BDL
J2-222-4-W3-M4	Roman Ruins	RMR4	4.71	-/-	-/-	-/-	-/-	10.4	19.5	0.8	0.8	0.09	BDL	1.2	1.8	2.8	0.36
J2-213-6-W1-IGT3	Roger's Ruins	RGR1	5.63	-/-	-/-	-/-	-/-	12.4	21.0	0.2	0.5	0.07	BDL	1.3	BDL	BDL	0.42
J2-213-6-W2-IGT4	Roger's Ruins	RGR1	8.10	-/-	-/-	-/-	-/-	5.8	10.9	1.3	1.8	0.08	BDL	5.0	BDL	BDL	BDL
J2-213-6-W3-M2	Roger's Ruins	RGR1	4.68	-/-	-/-	-/-	-/-	8.2	15.4	4.0	3.5	0.18	BDL	9.5	7.3	3.7	1.46
J2-222-1-W1-IGT4	Roger's Ruins	RGR2	22.64	-/-	-/-	-/-	-/-	12.5	24.1	1.2	27.9	0.05	BDL	4.3	22.6	60.4	5.97
J2-222-1-W2-IGT3	Roger's Ruins	RGR2	9.45	-/-	-/-	-/-	-/-	9.0	16.5	1.6	16.4	0.20	BDL	17.4	13.3	65.5	1.27
J2-222-1-W3-M2	Roger's Ruins	RGR2	9.03	-/-	-/-	-/-	-/-	0.1	0.4	0.1	0.4	0.01	BDL	BDL	1.4	6.5	0.23
J2-209-1-W1-IGT6	Satanic Mills	SM1	10.52	-/-	-/-	-/-	-/-	15.8	21.2	1.1	4.5	0.25	BDL	11.5	BDL	14.2	BDL
J2-209-1-W1-IGT7	Satanic Mills	SM1	9.63	-/-	-/-	-/-	-/-	13.5	20.5	0.9	3.0	0.27	BDL	10.0	BDL	13.2	BDL
J2-209-1-W3-M4	Satanic Mills	SM1	8.84	-/-	-/-	-/-	-/-	2.5	3.6	2.1	2.0	0.20	BDL	5.4	4.8	8.3	0.42
J2-209-6-W1-IGT4	Satanic Mills	SM2	27.50	-/-	-/-	-/-	-/-	3.2	11.9	1.1	18.1	0.36	BDL	13.5	BDL	68.6	BDL
J2-209-6-W2-M2	Satanic Mills	SM2	17.37	-/-	-/-	-/-	-/-	2.1	16.7	0.4	28.4	0.16	BDL	BDL	8.2	353.8	0.57
J2-214-3-W1-IGT8	Satanic Mills	SM3	10.29	-/-	-/-	-/-	-/-	9.1	6.4	0.6	5.0	0.23	BDL	3.7	BDL	11.9	BDL
J2-214-3-W2-IGT5	Satanic Mills	SM3	10.17	-/-	-/-	-/-	-/-	5.0	9.1	0.4	6.0	0.24	0.6	2.6	BDL	BDL	BDL
J2-214-3-W3-M4	Satanic Mills	SM3	10.07	-/-	-/-	-/-	-/-	1.8	1.7	0.2	1.5	0.08	BDL	BDL	2.1	4.9	1.66

-/- denotes elements for which no analytical measurement was carried out. BDL denotes elements for which aqueous fluid concentrations were below the analytical detection limit of the method or otherwise not obtainable.

Appendix D1. Measured metal concentrations in "dregs" fractions of sampled vent fluids from PACMANUS

Fluid Sampler ID	Vent Site	Vent Orifice	Mg (mmol/kg)	Li (µmol/kg)	Rb (µmol/kg)	Cs (nmol/kg)	Al (µmol/kg)	Mn (µmol/kg)	Fe (µmol/kg)	Zn (µmol/kg)	Cu (µmol/kg)	Pb (µmol/kg)	Co (nmol/kg)	Cd (nmol/kg)	Ag (nmol/kg)	Sb (nmol/kg)	Au (nmol/kg)
J2-208-1-W1-IGT8	Roman Ruins	RMR1	8.01	-/-	-/-	-/-	-/-	1.2	25.9	1195	124.3	17.44	195	2251	596	552	0.13
J2-208-1-W2-IGT5	Roman Ruins	RMR1	8.28	-/-	-/-	-/-	-/-	1.6	35.6	1284	138.8	18.89	175	2453	727	532	2.17
J2-208-1-W3-M4	Roman Ruins	RMR1	8.90	-/-	-/-	-/-	-/-	0.4	25.6	694	59.0	2.87	24	1109	284	492	0.75
J2-208-2-W2-IGT2	Roman Ruins	RMR2	16.56	-/-	-/-	-/-	-/-	-/-	-/-	-/-	-/-	-/-	-/-	-/-	-/-	-/-	-/-
J2-208-2-W1-IGT1	Roman Ruins	RMR2	16.55	-/-	-/-	-/-	-/-	1.0	35.9	1977	41.4	106.14	24	3051	2504	3514	2.08
J2-208-2-W3-M2	Roman Ruins	RMR2	27.50	-/-	-/-	-/-	-/-	0.3	28.5	841	26.9	13.33	32	1326	1080	3190	0.73
J2-213-3-W1-IGT7	Roman Ruins	RMR3	23.36	-/-	-/-	-/-	-/-	29.6	146.9	671	14.2	12.02	27	1002	178	341	5.25
J2-213-3-W3-M4	Roman Ruins	RMR3	6.39	-/-	-/-	-/-	-/-	0.5	77.3	613	32.7	15.06	59	940	207	475	0.41
J2-222-4-W2-IGT1	Roman Ruins	RMR4	3.63	-/-	-/-	-/-	-/-	0.6	47.5	359	174.5	6.77	243	535	184	273	1.43
J2-222-4-W3-M4	Roman Ruins	RMR4	4.71	-/-	-/-	-/-	-/-	0.4	76.9	320	108.9	5.91	11	420	99	115	1.20
J2-213-6-W1-IGT3	Roger's Ruins	RGR1	5.63	-/-	-/-	-/-	-/-	0.7	20.3	247	113.3	2.62	27	403	121	269	0.26
J2-213-6-W2-IGT4	Roger's Ruins	RGR1	8.10	-/-	-/-	-/-	-/-	1.3	45.3	358	173.7	2.37	43	569	172	313	2.04
J2-213-6-W3-M2	Roger's Ruins	RGR1	4.68	-/-	-/-	-/-	-/-	0.4	36.5	158	65.3	2.59	17	234	68	90	0.26
J2-222-1-W1-IGT4	Roger's Ruins	RGR2	22.64	-/-	-/-	-/-	-/-	0.9	93.1	251	384.9	1.86	32	336	470	312	4.50
J2-222-1-W2-IGT3	Roger's Ruins	RGR2	9.45	-/-	-/-	-/-	-/-	1.3	73.7	376	375.7	1.67	27	596	384	901	7.89
J2-222-1-W3-M2	Roger's Ruins	RGR2	9.03	-/-	-/-	-/-	-/-	0.3	111.2	351	358.7	6.40	13	714	431	985	8.63
J2-209-1-W1-IGT6	Satanic Mills	SM1	10.52	-/-	-/-	-/-	-/-	1.1	84.3	240	102.2	4.43	63	300	84	270	2.95
J2-209-1-W1-IGT7	Satanic Mills	SM1	9.63	-/-	-/-	-/-	-/-	-/-	-/-	-/-	-/-	-/-	-/-	-/-	-/-	-/-	-/-
J2-209-1-W3-M4	Satanic Mills	SM1	8.84	-/-	-/-	-/-	-/-	0.4	47.4	154	60.7	2.72	26	215	64	223	0.65
J2-209-6-W1-IGT4	Satanic Mills	SM2	27.50	-/-	-/-	-/-	-/-	1.0	309.8	37	393.3	1.44	22	81	59	1334	9.70
J2-209-6-W2-M2	Satanic Mills	SM2	17.37	-/-	-/-	-/-	-/-	0.6	441.5	40	623.0	2.92	14	84	60	5277	11.41
J2-214-3-W1-IGT8	Satanic Mills	SM3	10.29	-/-	-/-	-/-	-/-	0.8	34.6	107	93.4	2.75	35	115	44	176	1.70
J2-214-3-W2-IGT5	Satanic Mills	SM3	10.17	-/-	-/-	-/-	-/-	0.8	BDL	135	BDL	2.70	21	168	53	BDL	3.40
J2-214-3-W3-M4	Satanic Mills	SM3	10.07	-/-	-/-	-/-	-/-	0.3	96.2	71	123.7	2.06	9	135	41	155	1.25

-/- denotes elements for which no analytical measurement was carried out. BDL denotes elements for which aqueous fluid concentrations were below the analytical detection limit of the method or otherwise not obtainable.

Appendix D1. Measured metal concentrations in "dissolved" fractions of sampled vent fluids from PACMANUS

Fluid Sampler ID	Vent Site	Vent Orifice	Mg (mmol/kg)	Li (µmol/kg)	Rb (µmol/kg)	Cs (nmol/kg)	Al (µmol/kg)	Mn (µmol/kg)	Fe (µmol/kg)	Zn (µmol/kg)	Cu (µmol/kg)	Pb (µmol/kg)	Co (nmol/kg)	Cd (nmol/kg)	Ag (nmol/kg)	Sb (nmol/kg)	Au (nmol/kg)
J2-210-1-W1-IGT8	Snowcap	SC1	31.05	298	18.2	654	< 10	988	10.9	0.4	BDL	0.13	2.2	BDL	BDL	BDL	BDL
J2-210-1-W2-IGT5	Snowcap	SC1	48.96	89	6.0	141	< 10	207	4.2	BDL	BDL	0.40	BDL	0.1	BDL	BDL	0.02
J2-210-1-W3-M2	Snowcap	SC1	31.85	313	20.2	683	< 10	1227	BDL	0.3	BDL	0.01	0.3	BDL	BDL	2.3	BDL
J2-211-9-W1-IGT4	Snowcap	SC2	24.55	486	27.4	1103	< 10	1611	127	4.5	0.1	0.02	BDL	BDL	BDL	BDL	0.08
J2-211-9-W2-IGT3	Snowcap	SC2	25.18	476	27.2	1093	< 10	1542	150	44.5	0.1	0.32	9.9	6.6	BDL	BDL	BDL
J2-211-9-W3-M4	Snowcap	SC2	24.52	503	31.1	1159	< 10	2031	126	12.9	0.7	0.78	BDL	BDL	BDL	1.2	BDL
J2-211-2-W1-IGT7	Tsukushi	TK1	43.96	219	12.2	422	< 10	565	119	5.7	0.1	0.01	0.8	BDL	BDL	0.0	BDL
J2-214-14-W1-IGT2	Tsukushi	TK1	44.94	209	11.3	401	< 10	556	68	10.1	0.1	0.27	2.7	0.9	12.2	6.4	BDL
J2-214-14-W2-M2	Tsukushi	TK1	44.62	219	13.4	422	< 10	648	114	1.4	0.3	0.01	BDL	BDL	BDL	3.4	BDL
J2-210-7-W1-IGT1	Fenway	F1	5.97	637	53.2	1847	< 10	2296	7233	21.3	2.4	0.79	7.6	16.6	0.9	3.8	BDL
J2-210-7-W2-M4	Fenway	F1	5.84	654	58.1	1963	< 10	2804	8266	220.2	176.2	4.28	BDL	253.4	92.4	173.6	0.07
J2-214-4-W1-IGT1	Fenway	F1	39.99	198	15.5	484	< 10	654	1883	6.5	0.0	0.03	9.1	2.8	BDL	BDL	BDL
J2-212-2-W1-IGT8	Fenway	F2	4.90	1033	87.2	2920	< 10	4188	13109	12.8	1.6	0.05	352.2	1.7	0.1	BDL	0.03
J2-212-2-W2-IGT5	Fenway	F2	5.26	1028	82.2	2932	< 10	4119	12870	20.3	3.5	0.13	358.6	5.9	1.6	BDL	0.06
J2-212-2-W3-M4	Fenway	F2	4.66	1067	92.6	3179	< 10	5253	15482	169.4	88.4	2.75	437.8	162.2	53.9	67.2	0.03
J2-212-6-W1-IGT2	Fenway	F3	4.52	904	73.5	2489	< 10	3584	11350	12.8	1.3	0.22	411.2	7.4	0.4	BDL	0.01
J2-212-6-W2-IGT1	Fenway	F3	4.74	748	60.0	2173	< 10	3065	9599	17.2	0.3	0.32	324.7	9.5	BDL	BDL	0.11
J2-212-6-W3-M2	Fenway	F3	9.70	793	71.5	2381	< 10	3907	11563	118.9	62.5	2.43	286.2	121.8	49.8	65.1	0.50
J2-216-2-W1-IGT7	Fenway	F4	9.86	713	57.5	2074	< 10	2940	6671	52.8	6.7	0.12	BDL	12.1	1.4	1.3	0.06
J2-216-2-W2-IGT6	Fenway	F4	9.38	685	57.3	2082	< 10	2923	6575	26.0	4.0	0.11	0.2	6.2	1.6	0.5	0.21
J2-216-2-W3-M2	Fenway	F4	10.96	688	59.8	2047	< 10	3492	7320	223.6	111.2	3.75	BDL	195.0	73.8	91.7	0.03
J2-216-5-W1-IGT4	Fenway	F5	44.66	109	9.3	218	< 10	322	393	30.7	0.0	0.60	BDL	5.1	BDL	BDL	BDL
J2-216-5-W2-IGT3	Fenway	F5	45.53	119	9.3	256	< 10	365	450	13.2	0.0	0.44	1.2	3.2	BDL	BDL	BDL
J2-216-5-W3-M4	Fenway	F5	50.46	65	4.6	108	< 10	176	197	1.0	0.7	0.08	BDL	0.2	BDL	BDL	BDL

-/- denotes elements for which no analytical measurement was carried out. BDL denotes elements for which aqueous fluid concentrations were below the analytical detection limit of the method or otherwise not obtainable.

Appendix D1. Measured metal concentrations in "bottle-filter" fractions of sampled vent fluids from PACMANUS

Fluid Sampler ID	Vent Site	Vent Orifice	Mg (mmol/kg)	Li (µmol/kg)	Rb (µmol/kg)	Cs (nmol/kg)	Al (µmol/kg)	Mn (µmol/kg)	Fe (µmol/kg)	Zn (µmol/kg)	Cu (µmol/kg)	Pb (µmol/kg)	Co (nmol/kg)	Cd (nmol/kg)	Ag (nmol/kg)	Sb (nmol/kg)	Au (nmol/kg)
J2-210-1-W1-IGT8	Snowcap	SC1	31.05	-/-	-/-	-/-	-/-	3.5	0.4	0.9	1.8	0.15	BDL	BDL	BDL	BDL	BDL
J2-210-1-W2-IGT5	Snowcap	SC1	48.96	-/-	-/-	-/-	-/-	2.2	0.5	1.0	0.2	0.10	BDL	1.4	BDL	BDL	BDL
J2-210-1-W3-M2	Snowcap	SC1	31.85	-/-	-/-	-/-	-/-	4.6	4.3	9.7	2.1	4.00	1.8	4.5	9.4	9.6	0.74
J2-211-9-W1-IGT4	Snowcap	SC2	24.55	-/-	-/-	-/-	-/-	13.1	1.8	0.0	0.3	0.21	BDL	BDL	BDL	BDL	BDL
J2-211-9-W2-IGT3	Snowcap	SC2	25.18	-/-	-/-	-/-	-/-	11.9	5.3	0.6	0.1	0.08	BDL	BDL	BDL	6.6	BDL
J2-211-9-W3-M4	Snowcap	SC2	24.52	-/-	-/-	-/-	-/-	1.8	1.8	0.7	2.3	0.11	BDL	BDL	BDL	8.6	BDL
J2-211-2-W1-IGT7	Tsukushi	TK1	43.96	-/-	-/-	-/-	-/-	2.8	1.3	BDL	0.1	BDL	BDL	BDL	BDL	BDL	BDL
J2-214-14-W1-IGT2	Tsukushi	TK1	44.94	-/-	-/-	-/-	-/-	2.0	2.5	BDL	0.1	BDL	BDL	BDL	BDL	BDL	BDL
J2-214-14-W2-M2	Tsukushi	TK1	44.62	-/-	-/-	-/-	-/-	0.6	0.1	BDL	BDL	BDL	BDL	BDL	BDL	BDL	BDL
J2-210-7-W1-IGT1	Fenway	F1	5.97	-/-	-/-	-/-	-/-	10.8	40.8	3.8	15.8	0.75	BDL	10.9	8.6	29.4	BDL
J2-210-7-W2-M4	Fenway	F1	5.84	-/-	-/-	-/-	-/-	3.1	15.5	2.8	5.8	0.26	BDL	6.6	4.2	13.6	0.83
J2-214-4-W1-IGT1	Fenway	F1	39.99	-/-	-/-	-/-	-/-	3.4	18.0	0.9	7.7	0.16	BDL	4.6	BDL	BDL	BDL
J2-212-2-W1-IGT8	Fenway	F2	4.90	-/-	-/-	-/-	-/-	28.9	92.6	2.7	7.5	0.23	6.7	10.9	BDL	BDL	BDL
J2-212-2-W2-IGT5	Fenway	F2	5.26	-/-	-/-	-/-	-/-	36.1	114.9	4.0	9.6	0.34	BDL	15.1	BDL	BDL	BDL
J2-212-2-W3-M4	Fenway	F2	4.66	-/-	-/-	-/-	-/-	5.0	12.4	10.1	8.8	0.21	3.0	13.8	6.5	6.2	0.32
J2-212-6-W1-IGT2	Fenway	F3	4.52	-/-	-/-	-/-	-/-	16.7	54.1	1.7	5.6	0.43	BDL	6.5	BDL	BDL	BDL
J2-212-6-W2-IGT1	Fenway	F3	4.74	-/-	-/-	-/-	-/-	21.8	72.7	2.1	8.6	0.61	BDL	9.7	BDL	13.9	BDL
J2-212-6-W3-M2	Fenway	F3	9.70	-/-	-/-	-/-	-/-	3.9	16.0	1.2	1.4	0.07	4.3	1.2	1.1	3.6	BDL
J2-216-2-W1-IGT7	Fenway	F4	9.86	-/-	-/-	-/-	-/-	9.6	23.3	1.4	8.3	0.32	BDL	11.5	BDL	10.6	BDL
J2-216-2-W2-IGT6	Fenway	F4	9.38	-/-	-/-	-/-	-/-	12.0	26.5	2.8	9.7	0.32	BDL	16.0	BDL	8.8	BDL
J2-216-2-W3-M2	Fenway	F4	10.96	-/-	-/-	-/-	-/-	2.9	5.9	1.9	4.7	0.16	BDL	2.9	5.1	4.6	0.52
J2-216-5-W1-IGT4	Fenway	F5	44.66	-/-	-/-	-/-	-/-	1.6	26.2	26.0	6.9	2.15	BDL	19.3	BDL	10.5	BDL
J2-216-5-W2-IGT3	Fenway	F5	45.53	-/-	-/-	-/-	-/-	2.3	11.6	4.3	3.0	0.52	BDL	4.9	BDL	BDL	BDL
J2-216-5-W3-M4	Fenway	F5	50.46	-/-	-/-	-/-	-/-	0.2	0.4	0.0	0.1	0.00	BDL	BDL	BDL	0.4	BDL

-/- denotes elements for which no analytical measurement was carried out. BDL denotes elements for which aqueous fluid concentrations were below the analytical detection limit of the method or otherwise not obtainable.

Appendix D1. Measured metal concentrations in "dregs" fractions of sampled vent fluids from PACMANUS

Fluid Sampler ID	Vent Site	Vent Orifice	Mg (mmol/kg)	Li (µmol/kg)	Rb (µmol/kg)	Cs (nmol/kg)	Al (µmol/kg)	Mn (µmol/kg)	Fe (µmol/kg)	Zn (µmol/kg)	Cu (µmol/kg)	Pb (µmol/kg)	Co (nmol/kg)	Cd (nmol/kg)	Ag (nmol/kg)	Sb (nmol/kg)	Au (nmol/kg)
J2-210-1-W1-IGT8	Snowcap	SC1	31.05	-/-	-/-	-/-	-/-	1.0	17.9	78.3	11.5	16.71	34.8	45.2	60.3	44.5	7.26
J2-210-1-W2-IGT5	Snowcap	SC1	48.96	-/-	-/-	-/-	-/-	2.4	167.5	452.1	34.8	34.81	37.5	361.8	283.2	173.5	2.19
J2-210-1-W3-M2	Snowcap	SC1	31.85	-/-	-/-	-/-	-/-	0.4	28.0	66.5	14.5	20.66	13.2	32.2	65.9	89.9	6.81
J2-211-9-W1-IGT4	Snowcap	SC2	24.55	-/-	-/-	-/-	-/-	0.8	11.8	9.0	13.0	0.18	23.4	7.9	15.3	126.3	0.27
J2-211-9-W2-IGT3	Snowcap	SC2	25.18	-/-	-/-	-/-	-/-	0.9	13.9	8.4	1.7	0.13	28.3	7.4	20.3	54.4	0.39
J2-211-9-W3-M4	Snowcap	SC2	24.52	-/-	-/-	-/-	-/-	0.2	1.4	0.9	1.2	0.08	7.1	0.9	BDL	33.4	0.11
J2-211-2-W1-IGT7	Tsukushi	TK1	43.96	-/-	-/-	-/-	-/-	1.9	4.0	6.6	5.6	0.30	22.9	13.1	38.7	16.6	0.14
J2-214-14-W1-IGT2	Tsukushi	TK1	44.94	-/-	-/-	-/-	-/-	157.1	217.0	19.4	4.5	3.59	28.4	27.5	36.9	25.2	0.25
J2-214-14-W2-M2	Tsukushi	TK1	44.62	-/-	-/-	-/-	-/-	0.8	3.6	1.7	2.7	0.04	5.8	2.9	0.8	36.4	0.09
J2-210-7-W1-IGT1	Fenway	F1	5.97	-/-	-/-	-/-	-/-	1.0	99.5	259.0	201.8	13.33	27.1	334.2	176.1	286.4	1.88
J2-210-7-W2-M4	Fenway	F1	5.84	-/-	-/-	-/-	-/-	0.3	58.2	81.3	80.8	1.25	9.0	106.9	46.3	111.8	0.13
J2-214-4-W1-IGT1	Fenway	F1	39.99	-/-	-/-	-/-	-/-	0.8	130.0	91.5	105.4	2.54	32.1	110.4	70.9	148.4	0.80
J2-212-2-W1-IGT8	Fenway	F2	4.90	-/-	-/-	-/-	-/-	1.4	61.6	307.5	187.9	4.56	99.4	340.6	112.3	75.2	0.17
J2-212-2-W2-IGT5	Fenway	F2	5.26	-/-	-/-	-/-	-/-	2.1	71.9	343.6	203.4	3.99	106.3	377.9	126.7	164.6	2.10
J2-212-2-W3-M4	Fenway	F2	4.66	-/-	-/-	-/-	-/-	1.4	105.5	214.4	130.6	3.58	74.2	219.9	68.7	168.4	2.72
J2-212-6-W1-IGT2	Fenway	F3	4.52	-/-	-/-	-/-	-/-	1.1	89.6	349.8	115.5	34.01	63.4	447.2	566.9	470.7	0.65
J2-212-6-W2-IGT1	Fenway	F3	4.74	-/-	-/-	-/-	-/-	0.9	155.1	307.2	140.4	15.76	215.3	347.2	264.0	335.7	1.30
J2-212-6-W3-M2	Fenway	F3	9.70	-/-	-/-	-/-	-/-	0.3	91.1	63.9	33.5	0.63	98.6	65.5	23.0	80.6	0.70
J2-216-2-W1-IGT7	Fenway	F4	9.86	-/-	-/-	-/-	-/-	1.2	156.8	255.0	236.4	1.41	51.5	271.6	135.6	221.4	60.24
J2-216-2-W2-IGT6	Fenway	F4	9.38	-/-	-/-	-/-	-/-	1.0	52.3	229.9	156.6	1.83	29.4	249.1	97.3	203.3	6.59
J2-216-2-W3-M2	Fenway	F4	10.96	-/-	-/-	-/-	-/-	0.3	204.3	110.3	222.1	0.20	10.6	103.9	49.2	154.9	4.71
J2-216-5-W1-IGT4	Fenway	F5	44.66	-/-	-/-	-/-	-/-	1.2	449.1	1195.1	78.5	52.67	41.4	494.3	112.2	221.8	2.78
J2-216-5-W2-IGT3	Fenway	F5	45.53	-/-	-/-	-/-	-/-	0.9	110.2	64.6	5.8	2.29	24.8	30.8	25.5	99.6	1.29
J2-216-5-W3-M4	Fenway	F5	50.46	-/-	-/-	-/-	-/-	0.1	28.0	16.5	6.1	0.54	7.9	10.6	3.3	34.7	0.10

-/- denotes elements for which no analytical measurement was carried out. BDL denotes elements for which aqueous fluid concentrations were below the analytical detection limit of the method or otherwise not obtainable.

Appendix D1. Measured metal concentrations in "dissolved" fractions of sampled vent fluids from DESMOS

Fluid Sampler ID	Vent Site	Vent Orifice	Mg (mmol/kg)	Li (μmol/kg)	Rb (μmol/kg)	Cs (nmol/kg)	Al (μmol/kg)	Mn (μmol/kg)	Fe (μmol/kg)	Zn (μmol/kg)	Cu (μmol/kg)	Pb (μmol/kg)	Co (nmol/kg)	Cd (nmol/kg)	Ag (nmol/kg)	Sb (nmol/kg)	Au (nmol/kg)
J2-220-5-W1-IGT1	DESMOS	D1	45.97	24	2.8	11	479.9	39	12383	231	4.1	6.51	9598	138	25.9	19.4	2.16
J2-220-5-W2-IGT2	DESMOS	D1	46.20	25	3.3	9	466.7	37	11746	129	1.3	4.84	9337	73	1.1	12.5	1.37
J2-220-5-W3-M4	DESMOS	D1	51.04	29	1.6	8	208.7	28	5618	402	3.5	2.93	3995	140	0.6	39.4	0.53
J2-220-15-W1-IGT4	DESMOS	D2	50.50	31	3.1	8	1620.1	45	5484	60	0.4	1.30	678	18	BDL	0.6	0.15
J2-220-15-W2-IGT3	DESMOS	D2	50.43	21	0.3	8	1637.9	45	5440	51	0.1	1.22	661	18	BDL	0.4	0.13
J2-220-15-W3-M2	DESMOS	D2	50.62	25	1.0	11	1579.6	43	5532	99	0.2	0.50	674	17	BDL	1.3	0.04

-/- denotes elements for which no analytical measurement was carried out. BDL denotes elements for which aqueous fluid concentrations were below the analytical detection limit of the method or otherwise not obtainable.

Appendix D1. Measured metal concentrations in "bottle-filter" fractions of sampled vent fluids from DESMOS

Fluid Sampler ID	Vent Site	Vent Orifice	Mg (mmol/kg)	Li (µmol/kg)	Rb (µmol/kg)	Cs (nmol/kg)	Al (µmol/kg)	Mn (µmol/kg)	Fe (µmol/kg)	Zn (µmol/kg)	Cu (µmol/kg)	Pb (µmol/kg)	Co (nmol/kg)	Cd (nmol/kg)	Ag (nmol/kg)	Sb (nmol/kg)	Au (nmol/kg)
J2-220-5-W1-IGT1	DESMOS	D1	45.97	-/-	-/-	-/-	-/-	0.1	44	0.6	0.0	0.02	33.3	BDL	BDL	BDL	BDL
J2-220-5-W2-IGT2	DESMOS	D1	46.20	-/-	-/-	-/-	-/-	0.4	121	1.0	0.1	0.05	93.3	BDL	BDL	BDL	BDL
J2-220-5-W3-M4	DESMOS	D1	51.04	-/-	-/-	-/-	-/-	BDL	6	0.4	0.2	0.01	4.6	BDL	BDL	BDL	BDL
J2-220-15-W1-IGT4	DESMOS	D2	50.50	-/-	-/-	-/-	-/-	0.5	59	0.4	0.8	0.03	7.6	BDL	BDL	BDL	BDL
J2-220-15-W2-IGT3	DESMOS	D2	50.43	-/-	-/-	-/-	-/-	0.1	11	0.0	0.3	0.02	BDL	BDL	5.6	7.9	BDL
J2-220-15-W3-M2	DESMOS	D2	50.62	-/-	-/-	-/-	-/-	BDL	2	0.1	BDL	BDL	BDL	BDL	6.2	BDL	BDL

-/- denotes elements for which no analytical measurement was carried out. BDL denotes elements for which aqueous fluid concentrations were below the analytical detection limit of the method or otherwise not obtainable.

Appendix D1. Measured metal concentrations in "dregs" fractions of sampled vent fluids from DESMOS

Fluid Sampler ID	Vent Site	Vent Orifice	Mg (mmol/kg)	Li (μmol/kg)	Rb (μmol/kg)	Cs (nmol/kg)	Al (μmol/kg)	Mn (μmol/kg)	Fe (μmol/kg)	Zn (μmol/kg)	Cu (μmol/kg)	Pb (μmol/kg)	Co (nmol/kg)	Cd (nmol/kg)	Ag (nmol/kg)	Sb (nmol/kg)	Au (nmol/kg)
J2-220-5-W1-IGT1	DESMOS	D1	45.97	-/-	-/-	-/-	-/-	-/-	-/-	-/-	-/-	-/-	-/-	-/-	-/-	-/-	-/-
J2-220-5-W2-IGT2	DESMOS	D1	46.20	-/-	-/-	-/-	-/-	-/-	-/-	-/-	-/-	-/-	-/-	-/-	-/-	-/-	-/-
J2-220-5-W3-M4	DESMOS	D1	51.04	-/-	-/-	-/-	-/-	-/-	-/-	-/-	-/-	-/-	-/-	-/-	-/-	-/-	-/-
J2-220-15-W1-IGT4	DESMOS	D2	50.50	-/-	-/-	-/-	-/-	0.7	14	8.2	3.1	0.29	36.2	4.9	6.7	36.5	0.07
J2-220-15-W2-IGT3	DESMOS	D2	50.43	-/-	-/-	-/-	-/-	0.7	6	1.0	2.2	0.07	27.5	3.5	13.4	50.3	0.07
J2-220-15-W3-M2	DESMOS	D2	50.62	-/-	-/-	-/-	-/-	-/-	-/-	-/-	-/-	-/-	-/-	-/-	-/-	-/-	-/-

-/- denotes elements for which no analytical measurement was carried out. BDL denotes elements for which aqueous fluid concentrations were below the analytical detection limit of the method or otherwise not obtainable.

Appendix D1. Measured metal concentrations in "dissolved" fractions of sampled vent fluids from SuSu Knolls

Fluid Sampler ID	Vent Site	Vent Orifice	Mg (mmol/kg)	Li (µmol/kg)	Rb (µmol/kg)	Cs (nmol/kg)	Al (µmol/kg)	Mn (µmol/kg)	Fe (µmol/kg)	Zn (µmol/kg)	Cu (µmol/kg)	Pb (µmol/kg)	Co (nmol/kg)	Cd (nmol/kg)	Ag (nmol/kg)	Sb (nmol/kg)	Au (nmol/kg)
221-3-W1-IGT8	North Su	NS1	49.84	30	0.7	33	180.2	21	1279	84.8	0.2	0.57	53	8.3	0.4	1.4	0.05
221-3-W2-IGT7	North Su	NS1	49.01	35	1.9	40	210.8	25	1615	72.6	0.2	0.57	66	6.1	0.3	BDL	0.04
221-3-W3-M4	North Su	NS1	49.36	34	1.2	38	210.7	22	1413	56.6	2.1	0.59	29	13.8	BDL	4.1	BDL
221-5-W1-IGT6	North Su	NS2	38.82	27	1.0	64	1075.6	80	3098	63.1	3.6	1.60	1444	38.3	6.1	9.8	0.17
221-5-W2-IGT5	North Su	NS2	40.95	34	2.7	56	928.0	67	2568	156.6	1.2	2.27	813	82.3	6.2	12.1	0.16
221-5-W3-M2	North Su	NS2	40.89	34	1.0	56	941.7	66	2466	53.4	5.5	0.88	591	73.1	BDL	24.7	0.37
J2-223-1-W1-IGT8	North Su	NS3	21.22	509	40.5	1643	< 10	247	1120	2.7	BDL	0.05	40	3.1	BDL	BDL	BDL
J2-223-1-W2-IGT7	North Su	NS3	3.42	806	60.6	2687	< 10	395	2079	4.6	0.2	0.03	693	0.1	BDL	BDL	0.02
J2-223-1-W3-M2	North Su	NS3	1.62	834	62.8	2799	< 10	412	2134	33.5	42.5	2.06	730	75.7	30.1	117.8	0.18
J2-223-11-W1-IGT5	North Su	NS4	23.89	419	31.4	1374	115.0	201	3187	55.4	BDL	0.15	33	52.1	BDL	BDL	0.03
J2-223-11-W2-IGT6	North Su	NS4	24.63	380	28.4	1362	152.9	189	1844	54.8	BDL	0.94	56	70.3	BDL	BDL	0.03
J2-227-10-W1-IGT2	North Su	NS5	7.42	562	42.6	1959	< 10	293	2755	4.1	BDL	0.01	16	3.4	BDL	BDL	0.02
J2-227-10-W2-IGT1	North Su	NS5	7.51	593	45.0	1980	< 10	297	2739	4.7	BDL	0.01	12	1.4	BDL	BDL	BDL
J2-227-10-W3-M2	North Su	NS5	27.43	348	28.2	1162	< 10	198	1788	9.9	22.9	0.81	10	34.1	20.4	46.8	BDL
J2-227-8-W1-IGT4	North Su	NS6	2.03	908	63.9	3005	< 10	468	5717	9.9	BDL	0.02	2550	5.9	0.2	BDL	0.07
J2-227-8-W2-IGT3	North Su	NS6	1.57	833	59.7	2915	< 10	434	5330	8.8	2.7	0.10	2718	6.5	0.3	1.3	0.05
J2-227-8-W3-M4	North Su	NS6	5.09	766	61.0	2597	< 10	475	5662	48.3	41.6	2.18	2150	67.8	45.6	102.2	BDL
J2-223-15-W1-M4	North Su	NS6	3.37	862	62.7	2707	< 10	435	5306	47.3	56.5	3.02	2470	61.7	44.7	125.7	BDL
J2-224-6-W1-IGT4	South Su	SS1	5.30	559	43.1	2074	< 10	496	1896	9.4	30.7	0.29	0.2	16.9	4.9	36.5	0.26
J2-224-6-W2-IGT3	South Su	SS1	5.52	571	43.5	2017	< 10	495	1869	13.4	0.3	0.04	0.9	1.6	BDL	BDL	0.17
J2-224-6-W3-M2	South Su	SS1	37.81	215	14.6	BDL	< 10	165	611	BDL	BDL	BDL	BDL	BDL	BDL	BDL	BDL
J2-224-12-W1-IGT1	South Su	SS2	6.77	552	44.6	1748	< 10	420	2185	5.2	1.1	0.01	10	4.7	BDL	BDL	0.29
J2-224-12-W2-IGT2	South Su	SS2	8.43	539	40.8	1751	< 10	411	2148	9.1	17.3	0.08	7	9.3	0.5	4.0	0.35
J2-224-12-W3-M4	South Su	SS2	9.23	-/-	-/-	-/-	-/-	-/-	-/-	-/-	-/-	-/-	-/-	-/-	-/-	-/-	-/-

-/- denotes elements for which no analytical measurement was carried out. BDL denotes elements for which aqueous fluid concentrations were below the analytical detection limit of the method or otherwise not obtainable.

Appendix D1. Measured metal concentrations in "bottle-filters" fractions of sampled vent fluids from SuSu Knolls

Fluid Sampler ID	Vent Site	Vent Orifice	Mg (mmol/kg)	Li (µmol/kg)	Rb (µmol/kg)	Cs (nmol/kg)	Al (µmol/kg)	Mn (µmol/kg)	Fe (µmol/kg)	Zn (µmol/kg)	Cu (µmol/kg)	Pb (µmol/kg)	Co (nmol/kg)	Cd (nmol/kg)	Ag (nmol/kg)	Sb (nmol/kg)	Au (nmol/kg)
221-3-W1-IGT8	North Su	NS1	49.84	-/-	-/-	-/-	-/-	0.1	8.2	0.2	1.0	0.02	BDL	BDL	7.3	BDL	BDL
221-3-W2-IGT7	North Su	NS1	49.01	-/-	-/-	-/-	-/-	0.1	6.8	2.4	3.2	0.02	BDL	BDL	4.8	49.4	BDL
221-3-W3-M4	North Su	NS1	49.36	-/-	-/-	-/-	-/-	0.0	1.6	0.1	0.1	0.01	BDL	BDL	4.8	1.6	BDL
221-5-W1-IGT6	North Su	NS2	38.82	-/-	-/-	-/-	-/-	0.1	5.2	BDL	BDL	0.01	BDL	BDL	BDL	BDL	BDL
221-5-W2-IGT5	North Su	NS2	40.95	-/-	-/-	-/-	-/-	0.1	4.3	BDL	BDL	BDL	BDL	BDL	BDL	BDL	BDL
221-5-W3-M2	North Su	NS2	40.89	-/-	-/-	-/-	-/-	1.6	7.1	0.2	0.1	0.02	1.2	BDL	1.3	1.6	BDL
J2-223-1-W1-IGT8	North Su	NS3	21.22	-/-	-/-	-/-	-/-	1.2	12.4	0.0	4.2	0.09	19.8	BDL	14.2	9.2	BDL
J2-223-1-W2-IGT7	North Su	NS3	3.42	-/-	-/-	-/-	-/-	3.6	23.3	9.5	8.9	0.42	18.7	15.3	4.5	26.2	BDL
J2-223-1-W3-M2	North Su	NS3	1.62	-/-	-/-	-/-	-/-	0.5	5.4	0.1	2.2	0.06	5.1	1.2	5.5	9.9	0.41
J2-223-11-W1-IGT5	North Su	NS4	23.89	-/-	-/-	-/-	-/-	0.7	11.4	BDL	13.7	0.73	BDL	BDL	8.4	9.8	BDL
J2-223-11-W2-IGT6	North Su	NS4	24.63	-/-	-/-	-/-	-/-	1.0	13.8	0.3	4.0	1.19	BDL	2.5	14.2	BDL	BDL
J2-227-10-W1-IGT2	North Su	NS5	7.42	-/-	-/-	-/-	-/-	1.3	57.1	1.7	43.8	0.84	6.5	26.6	9.6	77.3	0.91
J2-227-10-W2-IGT1	North Su	NS5	7.51	-/-	-/-	-/-	-/-	0.7	49.7	0.6	26.7	0.38	11.5	12.6	6.1	32.8	BDL
J2-227-10-W3-M2	North Su	NS5	27.43	-/-	-/-	-/-	-/-	0.1	11.2	0.1	3.3	0.11	7.8	0.5	2.6	2.5	0.44
J2-227-8-W1-IGT4	North Su	NS6	2.03	-/-	-/-	-/-	-/-	1.4	27.3	BDL	21.3	0.56	8.7	9.6	8.5	49.5	BDL
J2-227-8-W2-IGT3	North Su	NS6	1.57	-/-	-/-	-/-	-/-	0.9	16.9	BDL	15.8	0.47	5.8	7.4	5.7	30.9	BDL
J2-227-8-W3-M4	North Su	NS6	5.09	-/-	-/-	-/-	-/-	0.5	6.8	0.2	0.3	0.03	5.4	BDL	8.4	1.7	0.35
J2-223-15-W1-M4	North Su	NS6	3.37	-/-	-/-	-/-	-/-	0.5	9.1	0.1	3.8	0.09	8.5	1.7	8.0	11.2	0.35
J2-224-6-W1-IGT4	South Su	SS1	5.30	-/-	-/-	-/-	-/-	2.2	22.8	0.9	88.9	0.58	BDL	16.8	33.7	3319.9	5.25
J2-224-6-W2-IGT3	South Su	SS1	5.52	-/-	-/-	-/-	-/-	1.8	24.1	1.6	97.1	0.24	BDL	7.6	29.6	3048.1	2.43
J2-224-6-W3-M2	South Su	SS1	37.81	-/-	-/-	-/-	-/-	0.2	3.7	0.3	8.5	0.10	1.2	0.6	4.1	BDL	BDL
J2-224-12-W1-IGT1	South Su	SS2	6.77	-/-	-/-	-/-	-/-	4.5	30.2	1.4	39.9	0.79	BDL	26.9	16.5	51.1	0.77
J2-224-12-W2-IGT2	South Su	SS2	8.43	-/-	-/-	-/-	-/-	1.9	14.0	1.8	19.8	0.62	BDL	18.7	7.1	36.2	0.59
J2-224-12-W3-M4	South Su	SS2	9.23	-/-	-/-	-/-	-/-	-/-	-/-	-/-	-/-	-/-	-/-	-/-	-/-	-/-	-/-

-/- denotes elements for which no analytical measurement was carried out. BDL denotes elements for which aqueous fluid concentrations were below the analytical detection limit of the method or otherwise not obtainable.

Appendix D1. Measured metal concentrations in "dregs" fractions of sampled vent fluids from SuSu Knolls

Fluid Sampler ID	Vent Site	Vent Orifice	Mg (mmol/kg)	Li (µmol/kg)	Rb (µmol/kg)	Cs (nmol/kg)	Al (µmol/kg)	Mn (µmol/kg)	Fe (µmol/kg)	Zn (µmol/kg)	Cu (µmol/kg)	Pb (µmol/kg)	Co (nmol/kg)	Cd (nmol/kg)	Ag (nmol/kg)	Sb (nmol/kg)	Au (nmol/kg)
221-3-W1-IGT8	North Su	NS1	49.84	-/-	-/-	-/-	-/-	0.8	34	2.9	3.0	0.46	42.2	5.9	7.7	133.0	1.47
221-3-W2-IGT7	North Su	NS1	49.01	-/-	-/-	-/-	-/-	0.7	6	2.0	3.0	0.14	30.0	3.6	25.4	113.9	0.44
221-3-W3-M4	North Su	NS1	49.36	-/-	-/-	-/-	-/-	-/-	-/-	-/-	-/-	-/-	-/-	-/-	-/-	-/-	-/-
221-5-W1-IGT6	North Su	NS2	38.82	-/-	-/-	-/-	-/-	-/-	-/-	-/-	-/-	-/-	-/-	-/-	-/-	-/-	-/-
221-5-W2-IGT5	North Su	NS2	40.95	-/-	-/-	-/-	-/-	-/-	-/-	-/-	-/-	-/-	-/-	-/-	-/-	-/-	-/-
221-5-W3-M2	North Su	NS2	40.89	-/-	-/-	-/-	-/-	-/-	-/-	-/-	-/-	-/-	-/-	-/-	-/-	-/-	-/-
J2-223-1-W1-IGT8	North Su	NS3	21.22	-/-	-/-	-/-	-/-	1.1	93	21.7	34.6	0.78	251.0	49.3	14.2	112.1	0.52
J2-223-1-W2-IGT7	North Su	NS3	3.42	-/-	-/-	-/-	-/-	0.7	114	7.8	82.9	0.61	222.5	74.8	29.0	119.2	2.39
J2-223-1-W3-M2	North Su	NS3	1.62	-/-	-/-	-/-	-/-	0.2	136	2.7	87.3	0.36	225.9	19.9	13.4	83.0	0.84
J2-223-11-W1-IGT5	North Su	NS4	23.89	-/-	-/-	-/-	-/-	-/-	-/-	-/-	-/-	-/-	-/-	-/-	-/-	-/-	-/-
J2-223-11-W2-IGT6	North Su	NS4	24.63	-/-	-/-	-/-	-/-	-/-	-/-	-/-	-/-	-/-	-/-	-/-	-/-	-/-	-/-
J2-227-10-W1-IGT2	North Su	NS5	7.42	-/-	-/-	-/-	-/-	0.1	64	7.0	31.1	0.60	11.7	28.3	16.1	16.8	0.95
J2-227-10-W2-IGT1	North Su	NS5	7.51	-/-	-/-	-/-	-/-	0.1	673	7.3	397.9	1.22	125.0	56.8	40.9	59.3	0.80
J2-227-10-W3-M2	North Su	NS5	27.43	-/-	-/-	-/-	-/-	0.0	356	5.4	127.3	0.29	115.3	18.2	29.6	89.8	0.68
J2-227-8-W1-IGT4	North Su	NS6	2.03	-/-	-/-	-/-	-/-	0.0	24	5.4	75.5	2.19	8.0	65.8	73.9	244.7	0.87
J2-227-8-W2-IGT3	North Su	NS6	1.57	-/-	-/-	-/-	-/-	0.0	38	6.6	76.3	1.93	7.0	58.2	62.7	92.9	0.64
J2-227-8-W3-M4	North Su	NS6	5.09	-/-	-/-	-/-	-/-	0.0	31	6.3	24.2	0.40	101.9	49.6	29.0	104.1	0.32
J2-223-15-W1-M4	North Su	NS6	3.37	-/-	-/-	-/-	-/-	0.1	15	1.8	12.3	0.16	52.7	8.3	4.6	44.7	0.34
J2-224-6-W1-IGT4	South Su	SS1	5.30	-/-	-/-	-/-	-/-	0.8	46	17.4	247.7	0.40	27.1	127.2	155.3	8697.3	6.95
J2-224-6-W2-IGT3	South Su	SS1	5.52	-/-	-/-	-/-	-/-	0.6	53	18.4	239.0	0.60	21.1	41.5	222.0	8402.7	13.19
J2-224-6-W3-M2	South Su	SS1	37.81	-/-	-/-	-/-	-/-	0.9	252	12.1	520.5	0.41	44.7	27.3	109.0	7872.4	7.65
J2-224-12-W1-IGT1	South Su	SS2	6.77	-/-	-/-	-/-	-/-	0.6	12	8.5	73.5	1.41	24.4	67.7	52.3	168.4	2.74
J2-224-12-W2-IGT2	South Su	SS2	8.43	-/-	-/-	-/-	-/-	0.8	37	14.4	83.1	1.31	33.9	61.9	33.1	209.1	2.20
J2-224-12-W3-M4	South Su	SS2	9.23	-/-	-/-	-/-	-/-	-/-	-/-	-/-	-/-	-/-	-/-	-/-	-/-	-/-	-/-

-/- denotes elements for which no analytical measurement was carried out. BDL denotes elements for which aqueous fluid concentrations were below the analytical detection limit of the method or otherwise not obtainable.

Appendix D1. Measured metal concentrations in "dissolved" fractions of sampled vent fluids from SuSu Knolls

Fluid Sampler ID	Vent Site	Vent Orifice	Mg (mmol/kg)	Li (µmol/kg)	Rb (µmol/kg)	Cs (nmol/kg)	Al (µmol/kg)	Mn (µmol/kg)	Fe (µmol/kg)	Zn (µmol/kg)	Cu (µmol/kg)	Pb (µmol/kg)	Co (nmol/kg)	Cd (nmol/kg)	Ag (nmol/kg)	Sb (nmol/kg)	Au (nmol/kg)
J2-217-2-W1-IGT8	Suzette	SZ1	4.40	642	45.4	1988	< 10	240	656	10.9	24.7	0.72	169.8	48.1	1.2	53.9	0.05
J2-217-2-W2-IGT5	Suzette	SZ1	5.36	683	45.9	1915	< 10	244	657	10.9	11.9	0.28	162.2	17.4	0.6	21.2	0.10
J2-217-2-W3-M2	Suzette	SZ1	5.47	655	47.3	1991	< 10	281	717	23.2	23.2	1.01	205.4	45.9	BDL	72.3	BDL
J2-217-10-W1-IGT1	Suzette	SZ2	8.58	680	40.3	2098	< 10	295	590	4.1	13.0	0.74	32.3	41.2	1.0	41.9	0.38
J2-217-10-W2-IGT2	Suzette	SZ2	8.56	655	41.3	2023	< 10	307	613	6.2	4.8	0.29	39.5	18.7	0.8	12.9	0.17
J2-217-10-W3-M4	Suzette	SZ2	14.69	599	39.4	1814	< 10	311	558	18.4	16.3	1.36	BDL	66.7	24.6	76.9	BDL
J2-219-2-W1-IGT7	Suzette	SZ3	7.16	691	42.7	2144	< 10	283	681	5.5	0.4	0.05	9.6	6.5	BDL	BDL	0.10
J2-219-2-W2-IGT6	Suzette	SZ3	6.13	710	44.5	2200	< 10	291	704	15.7	1.6	0.07	15.3	8.3	0.2	0.8	0.17
J2-219-8-W3-M2	Suzette	SZ3	5.51	757	48.6	2297	< 10	348	802	32.1	29.9	1.90	14.8	99.9	26.8	95.0	0.04
J2-219-10-W1-IGT8	Suzette	SZ4	8.32	643	46.1	2147	< 10	273	365	13.3	0.2	0.08	6.1	6.5	BDL	BDL	BDL
J2-219-10-W1-IGT5	Suzette	SZ4	8.62	672	46.7	2192	< 10	268	291	19.7	0.1	0.05	BDL	12.2	BDL	BDL	0.07
J2-226-2-W1-IGT6	Suzette	SZ5	40.66	178	11.3	512	< 10	61	592	17.6	0.8	1.51	0.4	91.3	BDL	BDL	BDL
J2-226-2-W2-IGT5	Suzette	SZ5	6.31	650	43.7	1877	16.4	239	2527	88.2	1.1	0.06	3.6	17.5	0.7	BDL	0.03
J2-226-2-W3-M2	Suzette	SZ5	20.75	446	33.9	1367	9.9	202	2044	122.1	74.1	2.04	5.9	44.0	38.0	0.2	BDL
J2-226-4-W1-IGT7	Suzette	SZ6	9.08	672	43.1	2167	< 10	315	623	19.3	0.2	0.03	55.9	14.0	BDL	BDL	0.01
J2-226-4-W2-IGT8	Suzette	SZ6	8.02	694	43.3	2192	< 10	324	991	6.6	0.0	0.02	29.3	8.9	BDL	BDL	0.10
J2-226-4-W3-M4	Suzette	SZ6	8.57	709	48.2	2281	< 10	382	704	36.1	1.3	1.77	7.4	102.1	BDL	115.1	BDL

-/- denotes elements for which no analytical measurement was carried out. BDL denotes elements for which aqueous fluid concentrations were below the analytical detection limit of the method or otherwise not obtainable.

Appendix D1. Measured metal concentrations in "bottle-filters" fractions of sampled vent fluids from SuSu Knolls

Fluid Sampler ID	Vent Site	Vent Orifice	Mg (mmol/kg)	Li (µmol/kg)	Rb (µmol/kg)	Cs (nmol/kg)	Al (µmol/kg)	Mn (µmol/kg)	Fe (µmol/kg)	Zn (µmol/kg)	Cu (µmol/kg)	Pb (µmol/kg)	Co (nmol/kg)	Cd (nmol/kg)	Ag (nmol/kg)	Sb (nmol/kg)	Au (nmol/kg)
J2-217-2-W1-IGT8	Suzette	SZ1	4.40	-/-	-/-	-/-	-/-	1.3	3.9	BDL	2.8	0.22	BDL	3.8	10.1	17.9	BDL
J2-217-2-W2-IGT5	Suzette	SZ1	5.36	-/-	-/-	-/-	-/-	1.1	4.4	0.7	5.8	0.37	BDL	9.9	6.2	32.2	BDL
J2-217-2-W3-M2	Suzette	SZ1	5.47	-/-	-/-	-/-	-/-	0.4	23.5	0.1	5.8	0.05	50.2	0.5	5.0	7.8	0.26
J2-217-10-W1-IGT1	Suzette	SZ2	8.58	-/-	-/-	-/-	-/-	1.6	3.8	BDL	3.6	0.67	BDL	22.7	13.9	45.3	BDL
J2-217-10-W2-IGT2	Suzette	SZ2	8.56	-/-	-/-	-/-	-/-	0.8	2.8	0.3	4.3	0.57	BDL	18.5	7.5	37.4	BDL
J2-217-10-W3-M4	Suzette	SZ2	14.69	-/-	-/-	-/-	-/-	0.3	1.4	0.1	0.4	0.05	0.7	BDL	5.4	6.7	0.25
J2-219-2-W1-IGT7	Suzette	SZ3	7.16	-/-	-/-	-/-	-/-	1.1	5.6	0.9	9.5	0.56	BDL	23.1	6.8	31.3	BDL
J2-219-2-W2-IGT6	Suzette	SZ3	6.13	-/-	-/-	-/-	-/-	1.7	5.9	0.6	5.4	0.35	BDL	13.2	4.5	17.1	BDL
J2-219-8-W3-M2	Suzette	SZ3	5.51	-/-	-/-	-/-	-/-	0.6	4.6	0.1	2.2	0.06	2.8	1.6	11.5	5.7	0.37
J2-219-10-W1-IGT8	Suzette	SZ4	8.32	-/-	-/-	-/-	-/-	2.0	113.3	1.4	4.4	1.49	86.0	25.1	14.3	64.0	2.22
J2-219-10-W1-IGT5	Suzette	SZ4	8.62	-/-	-/-	-/-	-/-	0.9	3.3	1.1	0.7	1.36	BDL	39.5	BDL	104.9	BDL
J2-226-2-W1-IGT6	Suzette	SZ5	40.66	-/-	-/-	-/-	-/-	0.7	22.8	8.3	63.8	1.64	BDL	82.8	37.2	34.8	1.08
J2-226-2-W2-IGT5	Suzette	SZ5	6.31	-/-	-/-	-/-	-/-	3.7	50.0	2.4	12.8	1.67	BDL	40.6	28.1	9.9	BDL
J2-226-2-W3-M2	Suzette	SZ5	20.75	-/-	-/-	-/-	-/-	0.5	44.2	0.7	23.1	0.18	0.7	3.3	38.8	29.7	0.47
J2-226-4-W1-IGT7	Suzette	SZ6	9.08	-/-	-/-	-/-	-/-	3.2	7.6	1.2	6.0	1.04	BDL	50.4	12.2	220.5	BDL
J2-226-4-W2-IGT8	Suzette	SZ6	8.02	-/-	-/-	-/-	-/-	2.4	4.9	0.6	0.9	0.83	BDL	41.8	10.6	74.8	BDL
J2-226-4-W3-M4	Suzette	SZ6	8.57	-/-	-/-	-/-	-/-	0.4	1.0	0.1	0.2	0.05	BDL	2.2	8.9	4.3	0.31

-/- denotes elements for which no analytical measurement was carried out. BDL denotes elements for which aqueous fluid concentrations were below the analytical detection limit of the method or otherwise not obtainable.

Appendix D1. Measured metal concentrations in "dregs" fractions of sampled vent fluids from SuSu Knolls

Fluid Sampler ID	Vent Site	Vent Orifice	Mg (mmol/kg)	Li (µmol/kg)	Rb (µmol/kg)	Cs (nmol/kg)	Al (µmol/kg)	Mn (µmol/kg)	Fe (µmol/kg)	Zn (µmol/kg)	Cu (µmol/kg)	Pb (µmol/kg)	Co (nmol/kg)	Cd (nmol/kg)	Ag (nmol/kg)	Sb (nmol/kg)	Au (nmol/kg)
J2-217-2-W1-IGT8	Suzette	SZ1	4.40	-/-	-/-	-/-	-/-	0.7	22	8.5	18.3	0.71	42.4	36.0	20.8	98.5	0.76
J2-217-2-W2-IGT5	Suzette	SZ1	5.36	-/-	-/-	-/-	-/-	0.7	20	8.2	32.7	0.88	40.0	48.5	30.3	186.0	0.04
J2-217-2-W3-M2	Suzette	SZ1	5.47	-/-	-/-	-/-	-/-	1.0	839	6.0	339.7	0.51	BDL	29.3	21.7	92.1	1.41
J2-217-10-W1-IGT1	Suzette	SZ2	8.58	-/-	-/-	-/-	-/-	0.5	6	6.7	7.8	1.63	28.8	16.9	35.4	79.8	0.04
J2-217-10-W2-IGT2	Suzette	SZ2	8.56	-/-	-/-	-/-	-/-	0.9	86	17.0	12.5	1.95	45.2	38.3	25.4	115.6	0.58
J2-217-10-W3-M4	Suzette	SZ2	14.69	-/-	-/-	-/-	-/-	0.2	82	7.6	32.4	0.10	77.4	20.5	16.3	56.7	0.21
J2-219-2-W1-IGT7	Suzette	SZ3	7.16	-/-	-/-	-/-	-/-	1.0	34	15.1	27.9	1.35	36.4	80.6	71.5	134.3	2.55
J2-219-2-W2-IGT6	Suzette	SZ3	6.13	-/-	-/-	-/-	-/-	0.8	73	12.9	30.7	1.15	62.1	81.7	47.9	139.6	1.39
J2-219-8-W3-M2	Suzette	SZ3	5.51	-/-	-/-	-/-	-/-	0.6	126	2.0	59.3	0.25	86.8	11.5	10.0	53.2	0.66
J2-219-10-W1-IGT8	Suzette	SZ4	8.32	-/-	-/-	-/-	-/-	3.5	BDL	26.2	56.1	12.27	1285.1	88.9	216.5	616.5	1.66
J2-219-10-W1-IGT5	Suzette	SZ4	8.62	-/-	-/-	-/-	-/-	0.8	108	5.0	10.4	0.93	104.4	26.9	28.4	118.6	1.67
J2-226-2-W1-IGT6	Suzette	SZ5	40.66	-/-	-/-	-/-	-/-	-/-	-/-	-/-	-/-	-/-	-/-	-/-	-/-	-/-	-/-
J2-226-2-W2-IGT5	Suzette	SZ5	6.31	-/-	-/-	-/-	-/-	0.1	1384	215.4	1016.1	19.29	78.8	1336.0	1387.8	582.1	0.60
J2-226-2-W3-M2	Suzette	SZ5	20.75	-/-	-/-	-/-	-/-	0.2	842	41.1	665.0	7.66	21.9	470.2	584.0	625.8	0.95
J2-226-4-W1-IGT7	Suzette	SZ6	9.08	-/-	-/-	-/-	-/-	0.8	4	3.0	3.9	0.48	32.3	32.6	27.3	85.2	0.34
J2-226-4-W2-IGT8	Suzette	SZ6	8.02	-/-	-/-	-/-	-/-	0.1	152	58.5	561.7	9.16	60.3	419.2	334.4	481.7	0.59
J2-226-4-W3-M4	Suzette	SZ6	8.57	-/-	-/-	-/-	-/-	0.2	7	1.0	4.4	0.10	10.6	6.8	2.4	71.0	0.14

-/- denotes elements for which no analytical measurement was carried out. BDL denotes elements for which aqueous fluid concentrations were below the analytical detection limit of the method or otherwise not obtainable.

Appendix E-1.

List of equilibrium constants (log K) for sulfide and sulfosalt minerals used to construct temperature-activity diagrams for the system Cu-Fe-As-S. Thermodynamic data for sulfides taken from the SUPCRT92 database (Johnson et al., 1992) and for sulfosalts (tennantite) taken from Knight (1977). In the absence of data for the thermodynamic properties of tennantite at elevated pressure, vapor saturation pressures are adopted. Differences in log K values for sulfides at vapor saturation pressure, 170 bar pressure and 250 bar pressure (applicable for depths of hydrothermal systems in the Manus Basin) are the same within error (± 0.5 – 1.0 log units). It can be assumed that the thermodynamic properties of tennantite do not change appreciably over the same range of pressure.

Appendix E1. Thermodynamic equilibrium constants (log K) used to construct phase diagrams

	Log (K) at temperature (°C)									
	0	25	50	75	100	150	200	250	300	350
$HAs(OH)_4 = As(OH)_4^- + H^+$										
log K = 1.570e–02·T – 5.144e–05·T^2 – 9.576	-9.58	-9.21	-8.92	-8.69	-8.52	-8.38	-8.49	-8.87	-9.49	-10.38
$HAs(OH)_5^- = As(OH)_4^- + H_2O$										
log K = 1.252e–03·T – 4.391e–05·T^2 + 3.799e–02	-0.04	-0.03	-0.09	-0.19	-0.35	-0.84	-1.54	-2.47	-3.61	-4.98
$H_2As(OH)_5 = As(OH)_4^- + H^+ + H_2O$										
log K = 1.570e–02·T – 7.829e–05·T^2 – 9.510	-9.51	-9.17	-8.92	-8.77	-8.72	-8.92	-9.50	-10.48	-11.85	-13.61
Pyrite + $H_2O = Fe^{2+} + 2HS^- + 0.5O_2(g)$										
log K = 1.769e–01·T – 2.680e–04·T^2 – 6.275e+01	-62.75	-58.50	-54.58	-50.99	-47.74	-42.25	-38.09	-35.28	-33.80	-33.67
Chalcopyrite + $0.5H_2O + H^+ = Cu^+ + Fe^{2+} + 2HS^- + 0.25O_2(g)$										
log K = 1.468e–01·T – 2.236e–04·T^2 – 5.489e+01	-54.89	-54.66	-54.72	-55.05	-55.66	-57.72	-60.90	-65.20	-70.61	-77.14
Bornite + $0.5H_2O + 3H^+ = 5Cu^+ + Fe^{2+} + 4HS^- + 0.25O_2(g)$										
log K = 3.674e–01·T – 5.326e–04·T^2 – 1.309e+02	-130.90	-130.31	-130.39	-131.14	-132.55	-137.37	-144.86	-155.00	-167.81	-183.28
Tennantite + $17H_2O = 12Cu^+ + 5H^+ + 4As(OH)_4^- + 13HS^- + 0.5O_2(g)$										
log K = 1.129·T – 1.794e–03·T^2 – 4.162e+02	-416.20	-389.10	-364.23	-341.61	-321.23	-287.19	-262.12	-246.01	-238.87	-240.69

Thermodynamic data recalculated for in situ temperature at vapor saturation pressures after Knight (1977) and the modified SUPCRT92 database (Johnson et al., 1992). Data for aqueous species used in calculation of species distributions taken from the modified SUPCRT92 database (Johnson et al., 1992). See text for details.

Appendix E-2.

Complete listing of electron microprobe data for chalcopyrite, bornite, sphalerite, tennantite, pyrite and galena grains in chimney vent deposit samples from the Manus Basin (Vienna Woods, PACMANUS and SuSu Knolls vent fields) during cruise MGLN06MV (Tivey et al., 2007). Data given in wt %.

Appendix E2. Electron Microprobe Analysis of Chalcopyrite in Open Conduit Smokers

	S	Fe	Cu	Zn	Pb	As	Sb	Cd	Ag	Se	Co	Total
					J2_207_1_R1 (*Vienna Woods, fluid pair "VW1"*)							
Spot #1	35.40	30.74	34.61	0.18								100.93
Spot #2	36.24	30.45	34.68	0.77								102.14
Spot #3	35.43	30.95	35.08	0.21	0.17							101.84
Spot #4	35.56	29.96	34.37	0.22								100.11
Spot #5	36.07	30.83	35.15									102.05
Spot #6	35.37	30.25	34.87	0.10	0.18							100.77
Spot #7	35.53	30.43	35.00	0.11								101.07
Spot #8	35.53	30.87	34.08	0.10								100.58
Spot #9	35.91	30.32	34.66	0.33	0.16							101.38
Spot #10	35.37	30.64	34.60	0.16	0.17							100.94
Spot #12	35.36	30.16	35.22	0.24	0.16							101.13
Spot #14	34.84	30.41	34.26	0.63								100.14
Spot #15	35.27	30.40	34.72	0.45								100.84
Spot #16	35.63	30.21	34.90	0.44								101.18
Spot #17	35.96	30.26	34.80	0.52	0.21							101.75
Spot #18	35.80	29.99	33.98	1.14								100.91
Spot #19	35.93	30.59	34.57	0.17								101.26
Spot #20	36.15	30.40	34.28	0.64								101.47
Spot #21	35.13	30.87	34.45	0.16	0.14							100.75
Spot #22	34.73	29.96	33.87	0.12	0.15							98.83
					J2_213_3_R1 (*Roman Ruins, PACMANUS, fluid pair "RMR3"*)							
Spot #1	35.53	30.70	34.75									100.98
Spot #2	35.50	30.42	34.66									100.58
Spot #3	35.12	29.97	34.41	0.12								99.62
Spot #4	35.23	30.82	34.58									100.63
Spot #6	35.16	30.83	35.59	0.12	0.18							101.88
Spot #8	35.12	30.90	34.49		0.22							100.73
Spot #9	35.44	30.80	34.68	0.12	0.18							101.23
Spot #10	35.62	30.47	35.41	0.13	0.19							101.82
Spot #11	35.51	30.06	35.01	0.10	0.20							100.89
Spot #12	35.54	30.76	35.01									101.31
Spot #13	35.23	30.27	34.76	0.09								100.35
Spot #14	35.44	31.19	34.39		0.15							101.17
Spot #15	34.23	30.69	35.07		0.17							100.16
Spot #16	35.09	30.57	34.64		0.22							100.52
Spot #17	35.09	30.75	34.54	0.08	0.14							100.60
Spot #21	35.54	30.22	34.66	0.53								100.95

Values given in wt %. Detection limits are 0.05 for Zn, 0.04 for Co, 0.04 for Cd, 0.04 for Ag, 0.04 for As, 0.03 for Se, 0.09 for Pb, 0.04 for Sb.

Appendix E2. Electron Microprobe Analysis of Chalcopyrite in Open Conduit Smokers

	S	Fe	Cu	Zn	Pb	As	Sb	Cd	Ag	Se	Co	Total
					J2_222_4_R1 (*Roman Ruins, PACMANUS, fluid pair "RMR4"*)							
Spot #1	**35.13**	**30.46**	**34.67**									**100.26**
Spot #2	**35.30**	**30.27**	**34.61**									**100.18**
Spot #3	35.01	30.51	34.66		0.22							100.40
Spot #4	35.22	30.15	34.78									100.15
Spot #5	34.94	30.62	34.74									100.30
Spot #6	35.20	30.54	34.79		0.15							100.68
Spot #7	34.98	30.38	34.77									100.13
Spot #8	34.51	30.38	34.57		0.14							99.60
Spot #9	35.09	30.47	34.56									100.12
Spot #10	35.49	30.64	34.81	0.13	0.22							101.29
Spot #11	34.83	29.95	35.11		0.27							100.16
Spot #12	53.32	45.94	0.59	0.11	0.36							100.32
					J2_213_6_R1 (*Roger's Ruins, PACMANUS, fluid pair "RGR1"*)							
Spot #1	**35.64**	**30.43**	**35.23**		**0.15**							**101.45**
Spot #2	**35.54**	**30.73**	**35.11**									**101.38**
Spot #3	35.67	30.54	35.24		0.23							101.68
Spot #4	35.94	30.70	35.46									102.10
Spot #5	34.84	30.84	35.40									101.08
Spot #6	35.24	30.55	35.63		0.23							101.65
Spot #7	36.12	30.72	35.25									102.09
Spot #10	35.55	30.38	35.72		0.19							101.84
					J2_209_1_R1 (*Satanic Mills, PACMANUS, fluid pair "SM1"*)							
Spot #1	**35.84**	**30.24**	**35.09**	**0.09**								**101.26**
Spot #2	**35.09**	**30.41**	**35.08**									**100.58**
Spot #3	35.65	30.39	34.51									100.55
Spot #4	35.92	30.27	34.80									100.99
Spot #5	35.73	30.15	34.95									100.83
Spot #6	35.60	30.15	34.83									100.58
Spot #7	35.56	30.46	34.82									100.84
Spot #8	35.54	30.07	34.87									100.48
					J2_216_16_R1 (*Fenway, PACMANUS, fluid pair, "F3"*)							
Spot #1	**35.31**	**30.46**	**35.27**							**0.19**		**101.23**
Spot #2	**35.20**	**30.70**	**35.00**							**0.09**		**100.99**
Spot #3	35.23	30.36	35.44							0.13		101.16
Spot #4	35.61	30.50	34.98							0.20		101.29
Spot #5	35.55	30.51	35.13		0.15					0.22		101.56
Spot #6	35.56	29.82	35.83		0.19							101.40
Spot #8	35.20	30.16	35.15		0.18							100.69

Values given in wt %. Detection limits are 0.05 for Zn, 0.04 for Co, 0.04 for Cd, 0.04 for Ag, 0.04 for As, 0.03 for Se, 0.09 for Pb, 0.04 for Sb.

Appendix E2. Electron Microprobe Analysis of Chalcopyrite in Open Conduit Smokers

	S	Fe	Cu	Zn	Pb	As	Sb	Cd	Ag	Se	Co	Total
					J2_217_2_R1 (*Suzette, SuSu Knolls, "SZ1"*)							
Spot #1	34.57	30.10	34.66							0.35		99.68
Spot #2	34.70	30.22	35.16		0.29					0.40		100.77
Spot #3	34.05	29.65	34.92							0.45		99.07
Spot #4	34.46	30.01	34.97							0.27		99.71
Spot #5	34.88	30.41	34.56							0.35		100.19
Spot #6	34.93	30.42	34.67		0.60					0.29		100.91
Spot #7	34.36	29.92	34.61							0.30		99.19
Spot #9	34.83	30.36	34.51							0.25		99.95
Spot #10	35.34	30.27	35.15							0.46		101.22
Spot #11	35.63	30.67	34.88							0.41		101.59
					J2_223_1_R1 (*North Su, SuSu Knolls, "NS3"*)							
Spot #1	34.59	30.35	34.26							0.27		99.47
Spot #2	35.40	30.29	34.69							0.29		100.67
Spot #3	34.88	30.58	34.68							0.36		100.50
Spot #4	35.17	30.46	34.43							0.36		100.42
Spot #19	34.99	30.38	34.63							0.18		100.18
Spot #5	34.76	30.41	34.41							0.40		99.98
Spot #6	35.66	30.31	34.23							0.31		100.51
Spot #7	35.36	29.99	34.71							0.38		100.44
Spot #8	35.22	30.60	34.27							0.33		100.42
Spot #9	35.36	30.21	34.95							0.31		100.83
Spot #10	35.14	30.39	34.43							0.32		100.28
Spot #21	34.62	30.61	34.37		0.14					0.20		99.94
Spot #12	35.32	30.02	34.54							0.31		100.19
Spot #23	35.29	30.43	34.61							0.13		100.46
Spot #13	35.08	30.23	34.60							0.39		100.30
Spot #14	35.10	30.26	34.62							0.19		100.17
Spot #24	34.42	30.06	34.68		0.20					0.30		99.66
Spot #15	35.46	30.50	34.74							0.07		100.77
Spot #16	35.76	30.31	34.78							0.25		101.10
					J2_224_12_R1 (*South Su, SuSu Knolls, fluid pair "SS2"*)							
Spot #1	35.02	30.56	35.44		0.15							101.17
Spot #2	35.16	30.26	34.79		0.15							100.36
Spot #3	34.95	30.32	34.74									100.01
Spot #4	34.48	29.45	35.33		0.18	0.37						99.81
Spot #5	35.41	30.32	35.24		0.16							101.13

Values given in wt %. Detection limits are 0.05 for Zn, 0.04 for Co, 0.04 for Cd, 0.04 for Ag, 0.04 for As, 0.03 for Se, 0.09 for Pb, 0.04 for Sb.

Appendix E2. Electron Microprobe Analysis of Chalcopyrite in Diffuser Smokers

	S	Fe	Cu	Zn	Pb	As	Sb	Cd	Ag	Se	Co	Total
J2_208_2_R3 (*Roman Ruins, PACMANUS, fluid pair "RMR2"*)												
Spot #1	34.71	30.58	34.85	0.11	0.18							100.43
Spot #2	35.95	30.62	35.47	0.19	0.12							102.35
Spot #3	35.73	30.73	35.30		0.18				0.06			102.00
Spot #4	33.71	30.16	35.62	0.08	0.17							99.74
Spot #5	35.64	31.00	35.43		0.20				0.05			102.32
J2_222_1_R1 (*Roger's Ruins, PACMANUS, fluid pair "RGR2"*)												
Spot #1	34.89	29.56	35.69	0.08	0.13				0.19			100.54
Spot #3	34.19	28.36	35.99	0.09	0.28	0.84			0.14			99.89
Spot #7	34.44	28.56	36.02		0.31	0.05			0.20			99.58
J2_209_5_R1 (*Satanic Mills, PACMANUS*)												
Spot #11	34.79	30.20	35.56	0.11	0.12							100.77
Spot #15	34.91	29.53	36.29		0.15				0.05			100.94
Spot #16	34.99	30.13	34.88		0.21							100.21
Spot #21	34.63	29.47	35.37		0.15							99.62
J2_209_6_R1 (*Satanic Mills, PACMANUS, fluid pair "SM2"*)												
Spot #2	35.35	29.19	35.89			0.33						100.76
Spot #5	35.06	29.02	37.16		0.15							101.39
Spot #7	35.33	30.32	35.29									100.94
Spot #8	34.59	28.11	35.96									98.66
Spot #10	35.60	30.81	35.38									101.79
Spot #12	35.25	30.40	35.42									101.07
Spot #13	34.54	28.79	34.34			0.14						97.81
J2_216_2_R1 (*Fenway, PACMANUS, fluid pair "F4"*)												
Spor #1	34.53	30.03	34.65		0.13							99.36
Spor #4	34.74	30.43	34.67		0.13							99.97
Spor #11	34.35	28.86	36.28	0.41	0.19	0.10			0.13			100.32
J2_219_10_R1 (*Suzette, SuSu Knolls, fluid pair "SZ4"*)												
Spor #5	34.53	30.47	35.18		0.16							100.34
Spor #6	34.53	29.83	35.20				0.05					99.61
Spor #7	34.62	30.34	35.32		0.12		0.15					100.55
J2_226_2_R1 (*Suzette, SuSu Knolls, fluid pair "SZ5"*)												
Spot #18	34.97	29.72	35.21	0.12	0.23							100.25
Spot #19	34.89	29.36	35.76	0.16	0.25							100.42
J2_224_6_R1 (*South Su, SuSu Knolls, fluid pair "SS1"*)												
Spot #6	35.68	29.59	35.20						0.12			100.58
Spot #9	35.39	29.92	35.17						0.12			100.60
Spot #13	35.37	29.62	34.67	0.28								99.95

Values given in wt %. Detection limits are 0.07 for Zn, 0.04 for Co, 0.04 for Cd, 0.04 for Ag, 0.04 for As, 0.03 for Se, 0.10 for Pb, 0.04 for Sb.

Appendix E2. Electron Microprobe Analysis of Chalcopyrite in Relict Spires

	S	Fe	Cu	Zn	Pb	As	Sb	Cd	Ag	Se	Co	Total
					J2_210_1_R1 (*Snowcap, PACMANUS*)							
Spot #4	34.26	28.33	36.90		0.25				0.06			99.80
Spot #9	34.52	29.99	35.54	0.15	0.13				0.05			100.37
					J2_210_4_R1 (*Fenway, PACMANUS*)							
Spot #6	34.63	29.32	35.88		0.17							100.00
Spot #8	34.99	30.04	35.37		0.11							100.51
Spot #10	34.79	28.89	35.30	0.11	0.17	0.61			0.05			99.92
Spot #15	26.06	11.38	63.56		0.13							101.13
Spot #16	25.79	11.04	63.61	0.12	0.19							100.75

Values given in wt %. Detection limits are 0.07 for Zn, 0.03 for Co, 0.05 for Cd, 0.04 for Ag, 0.04 for As, 0.04 for Se, 0.10 for Pb, 0.04 for Sb.

Appendix E2. Electron Microprobe Analysis of other Cu-Fe-sulfides in Open Conduit Smokers

	S	Fe	Cu	Zn	Pb	As	Sb	Cd	Ag	Se	Co	Total
					J2_222_4_R1 (*Roman Ruins, PACMANUS, fluid pair "RMR4"*)							
Spot #13	26.30	11.38	64.61	0.09	0.13							102.51
Spot #14	26.49	11.63	63.64		0.17							101.93
Spot #15	26.47	11.40	63.62		0.16							101.65
					J2_213_6_R1 (*Roger's Ruins, PACMANUS, fluid pair "RGR1"*)							
Spot #9	25.83	10.57	65.62									102.02
					J2_216_16_R1 (*Fenway, PACMANUS, fluid pair, "F3"*)							
Spot #7	27.33	11.00	62.60		0.15							101.08
					J2_224_12_R1 (*South Su, SuSu Knolls, fluid pair "SS2"*)							
Spot #6	27.49	5.52	70.12	0.09	0.20							103.42
Spot #7	27.58	12.64	61.27									101.49
Spot #8	27.21	7.86	67.54	0.09	0.14							102.84
Spot #9	27.90	12.15	62.24	0.08								102.37
Spot #10	26.39	3.91	72.57									102.87

Values given in wt %. Detection limits are 0.07 for Zn, 0.03 for Co, 0.05 for Cd, 0.04 for Ag, 0.04 for As, 0.03 for Se, 0.09 for Pb, 0.04 for Sb.

Appendix E2. Electron Microprobe Analysis of other Cu-Fe-sulfides in Diffuser Smokers

	S	Fe	Cu	Zn	Pb	As	Sb	Cd	Ag	Se	Co	Total
J2_222_1_R1 (*Roger's Ruins, PACMANUS, fluid pair "RGR2"*)												
Spot #2	26.25	11.48	62.73	0.09	0.13				1.09			101.77
Spot #4	26.43	11.33	62.78		0.17				0.70			101.42
Spot #8	20.42		79.68	0.08	0.04			0.05	0.46			100.76
Spot #9	20.62		80.91	0.08	0.09				0.47			102.16
Spot #10	20.60		81.23		0.19				0.50			102.52
J2_209_5_R1 (*Satanic Mills, PACMANUS*)												
Spot #9	33.40	2.58	66.03	0.07	0.11				0.11			102.30
Spot #12	33.81	9.96	56.99	0.47	0.28				0.12			101.63
Spot #17	34.32	10.10	56.53	0.11	0.23				0.29			101.58
J2_209_6_R1 (*Satanic Mills, PACMANUS, fluid pair "SM2"*)												
Spot #3	27.20	11.03	62.51		0.14							100.88
Spot #4	27.40	10.20	64.62		0.13							102.35
J2_216_2_R1 (*Fenway, PACMANUS, fluid pair "F4"*)												
Spor #2	26.23	11.36	61.93		0.17				0.11			99.80
Spor #5	28.39	12.60	59.27						0.17			100.43
Spor #10	26.86	11.88	62.96	0.11	0.12				0.35			102.28
J2_224_6_R1 (*South Su, SuSu Knolls, fluid pair "SS1"*)												
Spot #5	25.47	11.09	63.32	0.13					0.59			100.61
Spot #7	25.61	11.15	63.44	0.13					0.57			100.89
Spot #8	25.64	10.92	63.60	0.10					0.46			100.72
Spot #12	27.17	11.83	62.25	0.18					0.25			101.68

Values given in wt %. Detection limits are 0.07 for Zn, 0.03 for Co, 0.05 for Cd, 0.04 for Ag, 0.04 for As, 0.03 for Se, 0.09 for Pb, 0.04 for Sb.

Appendix E2. Electron Microprobe Analysis of other Cu-Fe-sulfides in Relict Spires

	S	Fe	Cu	Zn	Pb	As	Sb	Cd	Ag	Se	Co	Total
					J2_210_1_R1 (*Snowcap, PACMANUS*)							
Spot #2	26.32	11.46	62.89		0.05				0.13			100.85
Spot #3	23.63	2.55	74.78	0.07	0.15				0.19			101.37
Spot #6	26.23	11.38	63.16	0.05					0.14			100.97
Spot #8	26.14	11.45	62.55		0.07				0.12			100.37
Spot #11	27.66	10.81	60.22	0.07	0.12				0.11	0.04		98.99
Spot #13	24.04	1.90	75.05	0.34	0.27				0.08			101.69
Spot #14	22.92	1.17	74.46	0.92	0.19				0.42			100.08
					J2_210_4_R1 (*Fenway, PACMANUS*)							
Spot #5	26.18	11.26	63.89		0.11				0.04			101.48
Spot #11	26.11	11.26	63.60		0.11				0.21			101.29

Values given in wt %. Detection limits are 0.07 for Zn, 0.03 for Co, 0.05 for Cd, 0.04 for Ag, 0.04 for As, 0.03 for Se, 0.10 for Pb, 0.04 for Sb.

Appendix E2. Electron Microprobe Analysis of Wurtzite/Sphalerite in Open Conduit Smokers

	S	Fe	Cu	Zn	Pb	As	Sb	Cd	Ag	Se	Co	Total
				J2_207_1_R1 (*Vienna Woods, fluid pair "VW1"*)								
Spot #26	**33.19**	**4.15**		**60.96**	**0.14**			**0.66**				**99.10**
Spot #27	**32.83**	**3.89**		**63.02**	**0.14**			**0.69**				**100.57**
Spot #28	33.28	3.69		63.44				0.90				101.31
Spot #29	33.31	3.91		63.40	0.12			0.59				101.33
Spot #30	33.23	3.50		62.91	0.17			0.53				100.34
Spot #31	33.48	3.25	0.08	63.13	0.17			0.37				100.47
				J2_213_3_R1 (*Roman Ruins, PACMANUS, fluid pair "RMR3"*)								
Spot #21	33.25	4.99	0.38	61.37	0.15		0.09	1.12				101.36
Spot #22	33.24	2.60	2.35	60.28	0.55	0.33	1.30	0.50	0.13			101.28
Spot #23	34.12	6.63	0.38	62.13	0.22			0.50				104.00

Values given in wt %. Detection limits are 0.03 for Fe, 0.06 for Cu, 0.03 for Co, 0.04 for Cd, 0.04 for Ag, 0.04 for As, 0.03 for Se, 0.10 for Pb, 0.04 for Sb.

Appendix E2. Electron Microprobe Analysis of Wurtzite/Sphalerite in Diffuser Smokers

	S	Fe	Cu	Zn	Pb	As	Sb	Cd	Ag	Se	Co	Total
J2_208_2_R3 (*Roman Ruins, PACMANUS, fluid pair "RMR2"*)												
Spot #9	32.42	0.23	0.53	67.15	0.19		0.40	0.29	0.05			101.26
Spot #10	33.18	0.06		68.61	0.16			0.18				102.19
Spot #12	32.93	0.11		67.90	0.48							101.42
Spot #13	31.08			63.87	3.23							98.18
J2_222_1_R1 (*Roger's Ruins, PACMANUS, fluid pair "RGR2"*)												
Spot #11	31.99	0.49	3.96	62.35	0.49			1.17	0.05			100.51
Spot #12	32.16	0.38	3.05	63.32	0.89	0.25		0.52				100.56
Spot #14	32.05	0.49	2.38	62.27	1.24	0.50		0.72	0.09			99.73
Spot #17	32.57	0.33	1.44	64.66	0.45			0.97	0.06			100.47
Spot #18	32.24	0.22	1.87	64.28	0.42			0.86				99.88
J2_209_5_R1 (*Satanic Mills, PACMANUS*)												
Spot #1	**32.04**		**2.10**	**63.65**	**0.70**			**1.01**				**99.50**
Spot #2	**32.29**	**0.04**	**1.17**	**65.59**	**0.51**			**0.15**				**99.76**
Spot #3	**31.81**		**2.14**	**63.70**	**1.63**			**0.35**				**99.63**
Spot #4	**32.30**		**0.44**	**65.03**	**1.18**			**0.12**				**99.08**
Spot #5	32.28	0.24	3.01	63.50	0.67			0.37				100.06
Spot #6	31.95			64.38	1.65							97.98
Spot #7	32.81	0.06		65.08	0.96							98.91
J2_216_2_R1 (*Fenway, PACMANUS, fluid pair "F4"*)												
Spor #9	31.86	0.12	0.79	63.64	3.30			0.24				99.95
Spor #12	32.81	0.60	0.95	65.11	0.93	0.07		0.21	0.06			100.74
J2_219_10_R1 (*Suzette, SuSu Knolls, fluid pair "SZ4"*)												
Spot #1	31.85	0.19		61.15	4.19	1.34		0.17				98.89
Spot #2	31.41	0.33	0.50	56.08	5.51	1.11	0.58	0.87				96.39
Spot #3	30.66	1.22		56.80	5.69	0.92	0.43	0.27				95.99
J2_226_2_R1 (*Suzette, SuSu Knolls, fluid pair "SZ5"*)												
Spot #3	**32.30**	**0.15**	**0.88**	**65.91**	**1.07**			**0.06**	**0.11**			**100.47**
Spot #5	**33.14**	**0.11**	**0.15**	**67.12**	**0.72**			**0.05**				**101.29**
Spot #6	33.06			65.98	0.73							99.77
Spot #10	32.60			62.55	1.16			1.00				97.31
Spot #12	32.48			65.02	1.51							99.01
Spot #13	31.90			64.67	1.19			0.47				98.24
Spot #14	32.82			65.93	1.02			0.10				99.87
Spot #15	31.99			63.39	0.94			0.86				97.18
J2_224_6_R1 (*South Su, SuSu Knolls, fluid pair "SS1"*)												
Spot #14	31.67			61.81	2.98	0.50		0.07				97.03
Spot #15	32.47			63.65	2.21	0.97		0.42				99.72
Spot #16	32.16			61.89	3.91	1.48		1.11				100.55
Spot #17	32.32	0.12		62.20	3.20	1.17						99.02

Values given in wt %. Detection limits are 0.03 for Fe, 0.07 for Cu, 0.03 for Co, 0.04 for Cd, 0.04 for Ag, 0.04 for As, 0.03 for Se, 0.10 for Pb, 0.04 for Sb

Appendix E2. Electron Microprobe Analysis of Wurtzite/Sphalerite in Relict Spires

	S	Fe	Cu	Zn	Pb	As	Sb	Cd	Ag	Se	Co	Total
					J2_210_4_R1 (*Fenway, PACMANUS*)							
Spot #12	32.51	0.29	0.42	65.36	1.50			0.28				100.36
Spot #13	32.47	0.53	1.88	63.98	1.01			0.61	0.09			100.56
Spot #17	32.14	0.55	2.93	63.17	1.02			0.47	0.05			100.34
					J2_224_5_R1 (*South Su, SuSu Knolls*)							
Spot #8	31.37	0.36	1.51	59.75	4.14	0.86		0.73				98.71
Spot #9	33.15			66.22	1.13	0.27		0.68				101.44
Spot #10	32.60	0.04		62.72	3.62	1.48		0.47				100.92
Spot #13	30.70	0.05	1.34	60.16	6.43	0.66		0.36				99.71
Spot #14	30.78	0.04	2.01	59.16	6.37	0.63		0.51	0.07			99.56

Values given in wt %. Detection limits are 0.03 for Fe, 0.07 for Cu, 0.03 for Co, 0.04 for Cd, 0.04 for Ag, 0.04 for As, 0.03 for Se, 0.10 for Pb, 0.04 for Sb

Appendix E2. Electron Microprobe Analysis of Tennatite in Open Conduit Smokers

	S	Fe	Cu	Zn	Pb	As	Sb	Cd	Ag	Se	Co	Total
						J2_223_13_R1 (*North Su, SuSu Knolls*)						
Spot #1	**32.17**	**1.34**	**50.16**			**16.14**	**1.24**					**101.05**
Spot #2	31.43	0.55	49.88			17.43	0.73					100.03
Spot #3	31.07	0.13	49.78	0.08		17.04	2.02					100.12
Spot #4	31.08	0.08	49.84	0.09		17.73	1.41					100.23
Spot #7	31.62	1.09	49.57			17.77						100.05

Values given in wt %. Detection limits are 0.06 for Zn, 0.03 for Co, 0.04 for Cd, 0.04 for Ag, 0.03 for Se, 0.10 for Pb, 0.04 for Sb

Appendix E2. Electron Microprobe Analysis of Tennatite in Diffuser Smokers

	S	Fe	Cu	Zn	Pb	As	Sb	Cd	Ag	Se	Co	Total
						J2_209_5_R1 (*Satanic Mills, PACMANUS*)						
Spot #10	32.89	1.13	50.37	0.07		17.50						101.96
Spot #13	32.76	2.19	50.77		0.14	16.37	0.18					102.40
Spot #14	32.92	0.23	50.64		0.12	18.25	0.07		0.05			102.29
Spot #20	32.66	5.18	48.33	0.52	0.24	12.68			0.14			99.75
						J2_216_2_R1 (*Fenway, PACMANUS, fluid pair "F4"*)						
Spor #3	28.47	6.63	45.09	0.52	0.12	18.56	2.10		0.13			101.63
Spor #6	27.74	6.19	43.60	0.60	0.12	13.31	8.83					100.40
						J2_226_2_R1 (*Suzette, SuSu Knolls, fluid pair "SZ5"*)						
Spot #1	**32.36**	**0.99**	**51.30**	**0.11**	**0.41**	**12.31**			**1.97**			**99.44**
Spot #2	**32.73**	**2.79**	**51.49**	**0.21**	**0.20**	**12.56**			**1.02**			**100.99**
Spot #8	32.61	2.12	52.88	0.26	0.26	11.72			1.92			101.78
Spot #9	32.35	3.50	50.37	0.25	0.39	12.08			2.46			101.40
Spot #11	32.38	3.54	50.11	1.15	0.42	12.14			2.43			102.17
						J2_224_6_R1 (*South Su, SuSu Knolls, fluid pair "SS1"*)						
Spot #1	**28.89**	**5.16**	**46.55**	**0.44**		**19.01**	**1.54**		**0.08**			**101.68**
Spot #2	**28.78**	**5.06**	**46.43**	**0.47**		**19.97**			**0.09**			**100.80**
Spot #10	28.89	5.16	45.84	1.16		20.07	0.15		0.28			101.55
Spot #11	28.91	4.89	46.16	1.19	0.20	19.86	0.23		0.12			101.56
Spot #14	29.07	5.08	46.29	1.14	0.28	19.89	0.05		0.16			101.96

Values given in wt %. Detection limits are 0.06 for Zn, 0.03 for Co, 0.04 for Cd, 0.04 for Ag, 0.03 for Se, 0.10 for Pb, 0.04 for Sb

Appendix E2. Electron Microprobe Analysis of Tennatite in Relict Spires

	S	Fe	Cu	Zn	Pb	As	Sb	Cd	Ag	Se	Co	Total
						J2_210_1_R1 (*Snowcap, PACMANUS*)						
Spot #5	28.12	5.07	44.76	1.72	0.14	19.81	0.05		0.11			99.79
Spot #7	28.49	5.20	45.03	1.48	0.17	18.83	1.50		0.08			100.78
Spot #10	**28.61**	**5.47**	**45.73**	**1.21**	**0.13**	**19.69**	**0.64**		**0.13**			**101.61**
Spot #12	**28.78**	**5.35**	**45.54**	**1.27**	**0.12**	**19.77**			**0.06**			**100.89**
						J2_210_4_R1 (*Fenway, PACMANUS*)						
Spot #1	**28.69**	**6.27**	**45.12**	**0.71**		**19.70**	**0.64**					**101.13**
Spot #2	**28.56**	**6.25**	**44.61**	**0.57**	**0.13**	**18.78**	**1.77**					**100.67**
Spot #3	**28.53**	**6.19**	**44.94**	**0.69**		**19.03**	**1.55**					**100.92**
Spot #4	**28.41**	**6.13**	**45.83**	**0.63**		**19.55**	**0.96**					**101.50**
Spot #7	28.35	6.16	44.35	0.72	0.12	17.10	4.29					101.08
Spot #9	27.84	6.01	44.32	0.67	0.12	17.14	4.34					100.43
Spot #14	28.68	6.26	45.39	0.67	0.17	19.46	0.75					101.38
						J2_224_5_R1 (*South Su, SuSu Knolls*)						
Spot #1	**28.61**	**1.04**	**45.26**	**7.12**	**0.14**	**19.76**	**0.42**	**0.06**	**0.21**			**102.63**
Spot #4	**28.03**	**0.95**	**44.43**	**7.33**		**19.75**	**0.25**	**0.05**	**0.20**			**101.00**
Spot #6	**28.39**	**0.86**	**44.45**	**6.83**	**0.24**	**19.77**	**0.13**	**0.09**	**0.27**			**101.04**
Spot #11	28.68	0.79	45.10	7.20	0.44	19.92	0.17	0.09	0.21			102.60
Spot #12	28.30	0.68	45.05	7.31	0.56	19.75		0.19	0.20			102.04

Values given in wt %. Detection limits are 0.06 for Zn, 0.03 for Co, 0.04 for Cd, 0.04 for Ag, 0.03 for Se, 0.10 for Pb, 0.04 for Sb

Appendix E2. Electron Microprobe Analysis of Pyrite in Open Conduit Smokers

	S	Fe	Cu	Zn	Pb	As	Sb	Cd	Ag	Se	Co	Total
J2_207_1_R1 (*Vienna Woods, fluid pair "VW1"*)												
Spot #11	55.18	47.56	0.31		0.25							103.30
Spot #13	54.97	47.44			0.22							102.63
Spor #23	**55.12**	**47.47**	**0.05**		**0.22**							**102.86**
Spor #24	**55.05**	**48.40**	**0.22**		**0.18**							**103.85**
Spor #25	54.46	46.64	0.73		0.17							102.00
J2_213_3_R1 (*Roman Ruins, PACMANUS, fluid pair "RMR3"*)												
Spot #18	52.84	45.73		0.78	2.53	1.28						103.16
Spot #20	53.04	45.99		0.79	2.53	0.67						103.02
J2_222_4_R1 (*Roman Ruins, PACMANUS, fluid pair "RMR4"*)												
Spot #16	52.44	45.13	2.12	0.11	0.29							100.09
Spot #17	54.17	47.11	0.47		0.10							101.85
J2_223_1_R1 (*North Su, SuSu Knolls, "NS3"*)												
Spot #17	53.84	45.77	0.23	0.18	0.15	0.56						100.73
Spot #26	53.06	46.24			0.18	0.08						99.55
Spot #27	51.80	44.03	1.31	0.17	0.27	1.00						98.58
J2_223_13_R1 (*North Su, SuSu Knolls*)												
Spot #5	53.11	44.90	0.70									98.70
Spot #9	53.25	46.47	0.37		0.23							100.31
Spot #10	53.79	46.73			0.25							100.77

Values given in wt %. Detection limits are 0.06 for Zn, 0.03 for Co, 0.05 for Cd, 0.04 for Ag, 0.04 for As, 0.03 for Se, 0.09 for Pb, 0.04 for Sb.

Appendix E2. Electron Microprobe Analysis of Pyrite in Diffuser Smokers

	S	Fe	Cu	Zn	Pb	As	Sb	Cd	Ag	Se	Co	Total
					J2_209_6_R1 (*Satanic Mills, PACMANUS, fluid pair "SM2"*)							
Spot #15	54.00	43.78		0.30	3.59	0.12			0.06			101.85
Spot #16	53.00	42.89		0.66	5.39	0.31						102.25
Spot #17	55.33	47.67		0.21	0.44							103.65
					J2_219_10_R1 (*Suzette, SuSu Knolls, fluid pair "SZ4"*)							
Spor #4	50.41	42.92	0.20	0.44	5.16	1.21	0.12					100.45
Spor #8	52.67	44.67	2.06	0.16	1.00	0.70	0.05					101.32
Spor #9	52.74	45.77	1.42		0.56	0.90						101.39
					J2_224_6_R1 (*South Su, SuSu Knolls, fluid pair "SS1"*)							
Spot #18	53.36	44.06		0.36	2.08	0.06						99.92
Spot #19	53.70	45.07		0.22	0.31							99.31
Spot #14	53.72	46.68	0.07	0.10	0.44							101.01
Spot #15	52.99	45.08		0.07	1.06							99.21

Values given in wt %. Detection limits are 0.10 for Zn, 0.03 for Co, 0.05 for Cd, 0.04 for Ag, 0.04 for As, 0.03 for Se, 0.13 for Pb

Appendix E2 Electron Microprobe Analysis of Pyrite in Relict Spires

	S	Fe	Cu	Zn	Pb	As	Sb	Cd	Ag	Se	Co	Total
					J2_224_5_R1 (*South Su, SuSu Knolls*)							
Spot #2	**53.14**	**44.98**	**0.60**	**0.11**	**1.97**				**0.05**			**100.85**
Spot #3	**52.47**	**42.32**	**1.14**	**0.23**	**4.69**							**100.86**
Spot #5	**53.42**	**44.64**	**0.81**	**0.12**	**2.30**							**101.28**
Spot #7	54.27	44.84	0.59	0.93	2.27							102.90

Values given in wt %. Detection limits are 0.07 for Cu, 0.06 for Zn, 0.03 for Co, 0.04 for Cd, 0.04 for Ag, 0.04 for As, 0.03 for Se, 0.10 for Pb, 0.04 for Sb

Appendix E2. Electron Microprobe Analysis of Galena in Diffuser Smokers

	S	Fe	Cu	Zn	Pb	As	Sb	Cd	Ag	Se	Co	Total
					J2_208_2_R3 (*Roman Ruins, PACMANUS, fluid pair "RMR2"*)							
Spot #6	**14.39**				**86.58**			**0.11**	**0.23**			**101.31**
Spot #7	**14.83**		**0.19**		**83.26**				**1.01**			**99.29**
Spot #8	14.13				86.16		0.98	0.07	0.05			101.38
Spot #11	13.64				87.03		0.10	0.11				100.88
					J2_222_1_R1 (*Roger's Ruins, PACMANUS, fluid pair "RGR2"*)							
Spot #15	13.76		0.13	1.43	86.95			0.08				102.35
Spot #16	13.51		0.14	0.72	87.15			0.07				101.59
					J2_209_5_R1 (*Satanic Mills, PACMANUS*)							
Spot #18	13.75			0.72	87.93			0.08				102.48
Spot #19	13.72			0.31	87.80			0.09				101.92
					J2_216_2_R1 (*Fenway, PACMANUS, fluid pair "F4"*)							
Spor #7	13.83			1.51	87.99			0.06				103.39
					J2_226_2_R1 (*Suzette, SuSu Knolls, fluid pair "SZ5"*)							
Spot #4	13.48			0.63	87.82			0.11				102.04
Spot #7	13.80			0.10	87.92			0.05				101.87
Spot #16	13.79				87.85			0.09				101.73
Spot #17	14.12				88.00							102.12

Values given in wt %. Detection limits are 0.03 for Fe, 0.07 for Cu, 0.06 for Zn, 0.03 for Co, 0.04 for Cd, 0.04 for Ag, 0.04 for As, 0.03 for Se, 0.04 for Sb

Appendix E2. Electron Microprobe Analysis of Galena in Relict Spires

	S	Fe	Cu	Zn	Pb	As	Sb	Cd	Ag	Se	Co	Total
					J2_210_1_R1 (*Snowcap, PACMANUS*)							
Spot #1	13.71		0.24	0.63	87.61							102.19

Values given in wt %. Detection limits are 0.03 for Fe, 0.07 for Cu, 0.06 for Zn, 0.03 for Co, 0.04 for Cd, 0.04 for Ag, 0.04 for As, 0.03 for Se, 0.04 for Sb